SERI/TP-212-3675
UC Category: 270
DE91002128

SERI/TP--212-3675

DE91 002128

Annual Report

Solid State Photovoltaic Research Branch

FY 1989

September 1990

Prepared under Task No. PV030101

Solar Energy Research Institute
A Division of Midwest Research Institute

1617 Cole Boulevard
Golden, Colorado 80401-3393

Prepared for the
U.S. Department of Energy
Contract No. DE-AC02-83CH10093

MASTER

NOTICE

This report was prepared as an account of work sponsored by an agency of the United States government. Neither the United States government nor any agency thereof, nor any of their employees, makes any warranty, express or implied, or assumes any legal liability or responsibility for the accuracy, completeness, or usefulness of any information, apparatus, product, or process disclosed, or represents that its use would not infringe privately owned rights. Reference herein to any specific commercial product, process, or service by trade name, trademark, manufacturer, or otherwise does not necessarily constitute or imply its endorsement, recommendation, or favoring by the United States government or any agency thereof. The views and opinions of authors expressed herein do not necessarily state or reflect those of the United States government or any agency thereof.

Printed in the United States of America
Available from:
National Technical Information Service
U.S. Department of Commerce
5285 Port Royal Road
Springfield, VA 22161

Price: Microfiche A01
Printed Copy A13

Codes are used for pricing all publications. The code is determined by the number of pages in the publication. Information pertaining to the pricing codes can be found in the current issue of the following publications which are generally available in most libraries: *Energy Research Abstracts (ERA)*; *Government Reports Announcements* and Index (*GRA* and I); *Scientific and Technical Abstract Reports (STAR)*; and publication NTIS-PR-360 available from NTIS at the above address.

PREFACE

This report summarizes the progress of the Solid State Photovoltaic Research Branch of the Solar Energy Research Institute (SERI) from October 1, 1988, through September 30, 1989. Six technical sections of the report cover these main areas of SERI's in-house research: Semiconductor Crystal Growth, Amorphous Silicon Research, Polycrystalline Thin Films, III-V High-Efficiency Photovoltaic Cells, Solid-State Theory, and Laser Raman and Luminescence Spectroscopy.

Each section of the report was written by the group leader principally in charge of the work. The task in each case was to explain the purpose and major accomplishments of the work in the context of the U.S. Department of Energy's National Photovoltaic Research Program plans.

Approved for

SOLAR ENERGY RESEARCH INSTITUTE

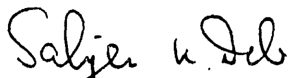

Satyen K. Deb, Manager
Solid State Research Branch

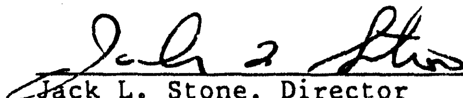

Jack L. Stone, Director
Solar Electric Research Division

TABLE OF CONTENTS

Page

1.0 Introduction 1

1.1 Objective 1
1.2 Organization 1
1.3 Key Accomplishments 1
1.3.1 Semiconductor Crystal Growth 1
1.3.2 Amorphous Silicon 2
1.3.3 Polycrystalline Thin Films 4
1.3.4 III-V High-Efficiency Photovoltaic Cells 6
1.3.5 Solid-State Theory 7
1.3.6 Laser Raman and Luminescence Spectroscopy 8
1.4 Participation in External Cooperative Research 9
1.5 Conclusion 9

2.0 Semiconductor Crystal Growth Research 10

2.1 Introduction 10
2.2 Silicon Crystal Growth 10
2.2.1 Introduction 10
2.2.2 Crystal Growth and Characterization 11
2.2.3 Carbon, Hydrogen, and Oxygen Doping 11
2.2.4 Conclusion 12
2.3 Chalcopyrite Semiconductor Crystal Growth 12
2.3.1 Introduction 12
2.3.2 System Design 13
2.3.3 Summary 14
2.4 Liquid-Phase Preparation of High-Temperature Superconductors 14
2.4.1 Introduction 14
2.4.2 Material Preparation 14
2.4.3 Characterization and Results 15
2.4.4 Summary and Discussion 20
2.5 Summary and Discussion 22
2.6 References 23

3.0 Amorphous Silicon Research 26

3.1 Introduction 26
3.2 Structure and Electronic Properties of Amorphous Silicon 27
3.2.1 Effects on Transport 27
3.2.2 Measurement of Microvoids 27
3.2.3 Attempts to Reduce Microstructure 28
3.3 Metastabilities 28
3.3.1 Modeling the Metastability 29
3.3.2 Experimental Results 30
3.4 a-Si:H Device Modeling 31
3.4.1 Device Modeling 31
3.5 Dangling Bond Defect Transitions 32
3.5.1 Correction for Multiple Reflections in Optical Absorption 32

TABLE OF CONTENTS (Continued)

Page

3.5.2 Limitations of the Integrated Sub-Band-Gap Absorption for Determining the Density of Defects in a-Si:H...... 32
3.5.3 Doping and Hydrogenation by Ion Implantation of a-Si:H.. 33
3.6 Experimental and Theoretical Details........................ 33
3.6.1 Defect Relaxation in a-Si:H Stretched Exponentials, MNR, and Staebler-Wronski Effect.......................... 33
3.6.2 Characterization of Microvoids in Device Quality, Hydrogenated a-Si by Small Angle X-ray Scattering and IR Measurements.................................... 36
3.6.3 Light-Induced Metastable Defects in Rehydrogenated and Post-Hydrogenated a-Si:H.............................. 42
3.6.4 Material Properties of Intrinsic a-Si:H Films Deposited by the Hot Wire Technique............................ 44
3.7 References... 102

4.0 Polycrystalline Thin Films.................................... 112

4.1 Introduction... 112
4.2 Comprehensive Study of the Optical Properties of Thin Film $CuInSe_2$ as a Function of Composition and Substrate Temperature.. 112
4.2.1 Introduction... 112
4.2.2 Experimental Procedures.............................. 113
4.2.3 Results and Discussion............................... 116
4.2.4 Conclusion... 135
4.2.5 Appendix A... 138
4.3 Characterization of Thin Film $CuInSe_2$ and $CuGaSe_2$: The Existence and Identification of Secondary Phases............ 138
4.3.1 Introduction... 138
4.3.2 Results and Discussion............................... 139
4.4 Composition and Substrate Effects on the Structure of Thin Film $CuGaSe_2$.. 145
4.4.1 Introduction... 145
4.4.2 Results and Discussion............................... 145
4.5 Film Microstructure, Morphology, and Electrical Behavior of $CuGaSe_2$.. 148
4.6 X-ray Diffraction Characterization......................... 165
4.7 Characterizations of Electrodeposited $CuInSe_2$ Thin Films: Structure and Deposition Mechanism......................... 181
4.7.1 Introduction... 181
4.7.2 Experimental Conditions.............................. 181
4.7.3 Results and Discussion............................... 183
4.7.4 Conclusion... 197
4.8 Aggregates in Thin Film Polycrystalline $CuInSe_2$.............. 198
4.9 References... 199

TABLE OF CONTENTS (Concluded)

Page

5.0 III-V High-Efficiency Photovoltaic Cells.......... 204

5.1 Introduction.......... 204
5.2 High-Efficiency Solar Cells.......... 204
5.2.1 $Ga_{0.5}In_{0.5}P$/GaAs Tandem Solar Cell.......... 204
5.2.2 GaAs Heteroface Solar Cells.......... 209
5.3 Modeling of Tandem Solar Cells.......... 212
5.4 The Effect of Selenium Doping on the Optical and Structural Properties of $Ga_{0.5}In_{0.5}P$.......... 229
5.5 On-Line Purifiers for CVD.......... 235
5.6 References.......... 237

6.0 Solid-State Theory.......... 240

6.1 Introduction.......... 240
6.2 Stability and Band Offsets of Heterovalent Superlattices Si/GaP, Ge/GaAs, and Si/GaAs.......... 241
6.3 Temperature-Composition Phase Diagrams of Bulk GaInP, AℓGaAs, and GaAsSb.......... 246
6.4 Structures, Thermodynamics, and Optical Properties of Epitaxial Alloys.......... 251
6.5 Stability of Strain Layer Superlattices.......... 255
6.6 Electronic Structure of H_2 in Palladium: Can Solid-State Effects Explain "Cold Fusion"?.......... 257
6.7 Ordering in Semiconductor Alloys.......... 260
6.8 Band Structure of Random Alloys.......... 265
6.9 References.......... 268

7.0 Laser Raman and Luminescence Spectroscopy.......... 269

7.1 Introduction.......... 269
7.1.1 Investigating the Phenomenon of Spontaneous Ordering in $GaInP_2$.......... 269
7.1.2 Raman Scattering Investigations of the Lattice Dynamics of $Cu_xAg_{1-x}InSe_2$ and $CuIn_xGa_{1-x}Se_2$.......... 269
7.2 Polarized Band-Edge Photoluminescence and Ordering in $GaInP_2$.......... 270
7.3 Two-Mode Behavior in Raman Spectrum of $CuIn_xGa_{1-x}Se_2$.......... 277
7.4 References.......... 282

1.0 INTRODUCTION

This report covers the research and development activities of the Solid State Research Branch at the Solar Energy Research Institute (SERI) during the period October 1, 1988, to September 30, 1989.

1.1 Objective

The objectives of the branch are to define and carry out fundamental and applied research on state-of-the-art photovoltaic materials and devices that are consistent with the Department of Energy's (DOE) five-year research plans and to complement subcontract research activities. Additional objectives are to identify research needs and to develop, evaluate, and transfer a coherent base of scientific knowledge and technology to the public and private sectors so that rational decisions can be made on the relevance of different technologies for cost-effective power generation.

1.2 Organization

Consistent with these objectives, research activities within the branch are structured into the following program areas: Semiconductor Crystal Growth, Amorphous Silicon, Polycrystalline Thin Films (involving II-VI compounds and their analogues), III-V High-Efficiency Cells, Solid-State Theory, and Solid-State Spectroscopy. The scope of each of these program areas was chosen carefully so that there would be close integration with research activities conducted outside SERI, including subcontracted research. The bulk of the work discussed here is a continuation of the work discussed in our prior annual reports. In addition to its mainstream activities, the branch also conducts research on high critical temperature (T_c) superconducting thin film and bulk materials. The superconductivity work is funded by DOE's Office of Energy Storage and Distribution. It also conducts solid-state theoretical research supported by the Office of Energy Research (Basic Energy Sciences) in DOE. In FY 1989, the branch had a staff of 31 full-time employees and 15 visiting scientists and students.

1.3 Key Accomplishments

During FY 1989, the members of the Solid State Research Branch made major contributions to advancing the state of the art in most areas of photovoltaic materials and device research. Some of the key accomplishments follow.

1.3.1 Semiconductor Crystal Growth

- No satisfactory procedures were found for controlled doping of carbon and oxygen in high-purity, dislocation-free, float-zoned silicon. Though hydrogen doping could eliminate swirl defects, it introduces additional recombination centers and results in low values of minority charge-carrier lifetime.
- Swirl defects (A- or B-type) and frozen-in defects are found to be carrier recombination centers in dislocation-free, as-grown, float-zoned silicon crystals. The A-type defect has an effective carrier capture range of ~40 μm, as determined by electron beam induced current (EBIC) analysis. The activation energy for formation of the fast cooling, frozen-in defects was

estimated to be about 0.31 eV. Defect formation can be changed by growth conditions, and long minority charge-carrier lifetimes are achieved through moderately high growth speeds and low thermal gradients during crystal growth, by which both swirl-defects and frozen-in defects are avoided. These procedures can attain τ > 20 ms in high-purity, float-zoned silicon.

- We have designed and begun implementation of a precision control system for liquid-encapsulated directional solidification (LEDS) crystal growth of alloys of $CuInSe_2$ with calcium or silver. The goal is to get uniform, crack-free single crystals to be analyzed in house as well as out of house to learn more about the fundamental properties of the material. This information should provide some guidelines to the $CuInSe_2/CuCaSe_2$ polycrystalline thin film researchers so they can improve the performance of photovoltaic solar cells based on these materials.
- We used a liquid-phase process to coat thin rods or wires and flat sheets with the $Bi_2Sr_2CaCu_2O_8$-type, high-temperature superconductor. Reaction temperatures in the range 950°-1150°C form a liquid from mixed oxide starting powders Bi_2O_3, SrO, CaO, and CuO. Substrates passed through the liquid are coated with a multiphase layer that includes a superconducting phase of approximate composition $Bi_2Sr_2Ca_{0.8}Cu_2O_8$.

1.3.2 Amorphous Silicon

- Small angle x-ray scattering (SAXS) has been extensively used to gain insight on the nature of microstructure, such as microvoids, in amorphous silicon (a-Si) thin films. We have made the first SAXS measurements on device quality a-Si:H films deposited by the glow-discharge technique. The best device quality films fabricated by SERI and by subcontractors all show $2\text{-}5 \times 10^{19}/cm^3$ microvoids, each containing about 16-20 missing atoms. By combining these results with infrared (IR) absorption measurements, we deduce that the interior surfaces of these microvoids are unhydrogenated, containing at most 4-9 bonded hydrogen atoms. We have shown that the electronic properties, such as photoconductivity, significantly degrade when the microstructure increases. An inverse correlation between the density of microvoids and the diffusion length of holes and electrons has been established.
- A new hot-wire catalytic deposition technique, which has the potential for fabricating superior material as compared to other conventional methods, is being developed. We have fabricated a large number of intrinsic a-Si:H films at various deposition temperatures to vary the hydrogen content. The transport properties of these films are as good as or better than glow-discharge deposited films. Moreover, we can reduce the hydrogen content to less than 1% and still produce device-quality films that had not been possible using glow-discharge deposition. The process needs to be extended to prepare device quality n- and p-type material and ultimately to the fabrication of a p-i-n device.
- We have devoted considerable effort to trying to understand and control the metastable changes in a-Si induced by light (Staebler-Wronski effect). A popular view of these metastabilities is that they involve hydrogen motion. To further explore the role of hydrogen in these metastabilities, we are developing new models of metastabilities that can be tested by experiment. One model demonstrates that a distribution of defect annealing or production energies is sufficient to explain all the production or annealing data that

the hydrogen diffusion model. In fact, we show that it is the underlying disorder of a-Si, rather than the detailed model, that determines the annealing and production behavior. Another model investigates the role of impurities or dopant atoms in metastable effects in doped films and suggests that bond rearrangement, such as is observed in metastabilities in crystalline silicon, is most important. This model also explores the role of charged dangling bond defects on the metastability.

- We have developed a new theory for the kinetics of annealing and production of metastable defects in a-Si. It is a model of defect controlled relaxation (DCR) in which the defect relaxes without the aid of a diffusing atom. The defect may consist of more than a single atom. The result gives a stretched-exponential-time dependence for defect relaxation and predicts that defect annealing or production obeys a Meyer-Neldel rule. This model is contrasted with the popular hydrogen-diffusion-controlled defect-relaxation (HCR) model. The HCR and DCR models both explain most experimental data. These models give similar results because the defect relaxation kinetics are established by the underlying disorder of the a-Si. Metastable defects arising from microscopic mechanisms such as weak-bond breaking and charge trapping are treated in this model.

- Most of the theoretical work on light-induced effects has concentrated on their role in the transport properties of films. To understand their role in devices, we have made a detailed calculation of the band bending in a p-i-n solar cell resulting from charged defects. Recent experimental work demonstrates that thermodynamic equilibrium statistics are an important factor in determining point-defect concentrations in a-Si:H. It is well known that the concentration of charged defects in a semiconductor depends upon the Fermi energy in equilibrium. The position-dependent Fermi energy in the i-layer of an a-Si:H solar cell therefore results in spatially varying concentrations of dangling bonds. We apply thermodynamic equilibrium statistics to the i-layer of a-Si:H p-i-n solar cells to compare the space charge contributed by the various charged defects, and we calculate the band bending in the i-layer. We find the electric field near the n-i interface is increased considerably by the negative dangling bonds formed because of the high Fermi energy. Point-defect profiles throughout the i-layer are also discussed. Finally, we consider the importance of these results for solar cell characteristics and stability.

- We have developed a new method to analyze long secondary photocurrent transients commonly observed in a-Si. This analysis gave a new powerful spectroscopy technique, permitting one to map the distribution of trapped holes in valence band-tail states. These safe hole traps are located roughly 0.3 to 0.5 eV above the valence band edge. A hole leaves this state by thermal emission to a level about 0.2 eV below the valence band edge. From there it tunnels to a dangling bond where it recombines with an electron. Thus this state above the valence band edge is instrumental in controlling electron-hole recombination and in turn the photoconductivity. During FY 1989, we used this technique to explore light-induced effects. We have been able to show that these safe hole traps convert to midgap recombination centers under light soaking. Thus we conclude that they are the source of the Staebler-Wronski effect.

- As a result of our extensive work with post-deposition hydrogenation on various films, we have been investigating RF hydrogenation during deposition. The original idea was to change the properties of the material after

deposition. However, this was not entirely successful. Nevertheless, a hydrogen-plasma reactive flush between layers has a beneficial effect. We showed this in an investigation of a hydrogen-plasma reactive flush between the p- and i-layer depositions in fabricating solar cells of glass/TCO/p(A-SiC:H)-i(a-Si:H)/metal in a single-chamber, glow-discharge deposition system. Spectral response, photoluminescence, and photovoltaic conversion efficiency measurements show that the hydrogen-plasma reactive flush is effective in reducing the p-i interface recombination of charge carriers and in improving solar cell performance.

- Much of the device modeling is carried out by computer simulation of a device. Although this is capable of high accuracy, the result depends on many parameters that are not well known. Rather than using a mathematically rigorous model, we concentrate on the important physics and develop simple models that give closed form solutions of the transport equations. These then can be used easily by the experimentalist to analyze data. Procedures for analyzing p-i-n solar cells have been obtained that use two closed form expressions, each containing a single unknown i-layer transport parameter. We have shown that this is sufficient to describe the light-intensity and temperature dependence of the current-voltage curve. In addition, the anomolous dependence of photocapacitance on light intensity and voltage has been explained. Excellent agreement between theory and experiment is obtained.

- Charged dangling bonds in high-quality undoped a-Si:H have been detected in two electron spin resonance (ESR) experiments. Shimizu et al., using a combination of constant photocurrent method absorption, CPM, and light-induced ESR (LESR), show that many charged defects are present in undoped a-Si:H. They also find that the density of these charged defects increases with incorporation of carbon, oxygen, and nitrogen alloy constituents. We have reinterpreted LESR data that are the most direct evidence to date that positively charged dangling bond (T3+) and negatively charged dangling bond (T3-) outnumber neutral charged dangling bond (T30) defects in undoped a-Si:H. Therefore, it seems clear that charged dangling bonds are present in all undoped a-Si. Our model is that inhomogeneity, such as that produced by microvoids, can result in charged dangling bonds that far outnumber the more easily observed neutral dangling bonds. This consequence of material inhomogeneity can be modeled with potential fluctuations. The T30 are recombination centers, and the T3+ and T3- defects are electron and hole traps, respectively. Many a-Si:H phenomena are explained and unified by these concepts.

1.3.3 Polycrystalline Thin Films

- A comprehensive study has been made on the optical properties of thin film $CuInSe_2$ as a function of film composition (16 at.% to 26 at.% copper content) and substrate temperature (350° and 450°C) in the near-infrared (NIR) and visible wavelength regions from 500 to 2000 nm. For copper-poor compositions, a decrease in α is observed with increasing copper content in the band-edge region (0.9 to 1.4 ev). For near stoichiometric and copper-rich material, significant sub-band-gap absorption is observed. This absorption is believed to be due to the presence of $Cu_{2-\delta}Se$ secondary phases at grain boundaries and free internal surfaces and for near stoichiometric films increases with increasing substrate temperature. For copper-rich material, the absorption curve exhibits unusually flat behavior at about 1.0 eV. At energies well above the gap (λ <800 nm), all films behave similarly with α

values of (1-2) x 10^5/cm at 500 nm. Measured $\alpha(\lambda)$ curves were substantiated by nearly exact correlation of predicted and observed device quantum efficiency curves using electron probe for microanalysis (EPMA)-deduced values for carrier transport (electron diffusion length, $0.5 < L_d < 1.0$ µm and space charge width, 0.4 < W 0.6 µm). Values for the direct band-to-band transition energy and the magnitude of the valence band splitting due to spin-orbit interaction have also been determined from the optical data.

- The formation, identification, and electrical and optical consequences of copper selenide impurity phase formation in $CuInSe_2$ polycrystalline films have been studied as a function of composition, substrate temperature, and substrate type. It is reasoned that an excess in copper content, above that required for stoichiometry, will be accommodated by the formation of either interstitial defects Cu_i or copper-bearing precipitates. Thermodynamic arguments support the latter for evaporated films in which an overpressure of the selenium species is required for compound formation. Extensive studies on $Cu_{2-\delta}Se$ phases coupled with the compositional and XRD measurements shows $CU_{1.85}Se$ as a likely candidate for coherent (strain-free) nucleation and growth within the host $CuInSe_2$ bulk.

- Based on experimental results, a microstructural model has been formulated. For very copper-poor material (at.% copper < 22) with high bulk ρ, the microstructure is characterized by small single phase grains and with a conduction mechanism exclusively across grain boundaries. For intermediate bulk values of ρ and compositions (22-25 at.% copper), the microstructure appears as predominantly single phase with larger grain sizes, and with an increasing amount of $Cu_{2-\delta}Se$ at grain boundaries. Although the conduction mechanism is still predominantly across $Cu(In,Ga)Se_2$ grain boundaries, percolation effects within the $Cu_{2-\delta}Se$ matrix are possible. For copper-rich compositions, the microstructure takes on a profoundly different nature. The near stoichiometric grains are now "bathed" in a matrix of $Cu_{2-\delta}Se$ sufficient to dominate the conductivity and contribute to significant sub-band absorption. This latter effect is detrimental with regard to device performance in that absorption is free-carrier-like and does not result in electron-hole pair generation.

- Majority ($CuGaSe_2$) and minority ($Cu_{2-\delta}Se$, Ga_2Se_3) phase behavior in $CuGaSe_2$, like $CuInSe_2$, was also shown to be a function of film composition (copper content) and substrate temperature. In addition to this, however, a close relation between substrate type (with regard to differences observed between bare and molybdenum-coated substrates) and selenuim content was also identified as a major factor in understanding the observed film behavior.

- Theoretical x-ray diffractometry (XRD) intensity calculations have been performed for various copper-poor $CuGaSe_2$ and $CuInSe_2$ tetragonal chalcopyrite structures as a function of molecularity (A = [at.%Cu]/[(at.Cu%)+(at.Ga%)]). In this defect adamantine structure, a decrease in copper along the pseudo-binary tie line, Cu_2Se-Ga_2Se_3, results in the generation of copper vacancies, V_{Cu}, and gallium antisites, Ga_{Cu}, in the ratio of 3:1. If the material remains single phase chalcopyrite, a decrease in copper content from stoichiometric $CuGaSe_2$ (25 at.% Cu; A = 0.5) to copper-poor (19 at.% Cu; A = 0.4) results in a significant increase in all Group III superlattice reflections. Support of this structural model was substantial by XRD studies on $CuGaSe_2$ single crystals. In polycrystalline thin films, however, the absence of superlattice peaks and the presence of both cubic and tetragonal

$CuGaSe_2$ in some instances suggests a microstructure consisting of two compositionally distinct phases: a near stoichiometric, chalcopyrite phase and a copper-poor, cubic phase.

- The structure of one-step electrodeposited $CuInSe_2$ films as a function of composition, deposition potential, and annealing conditions was systematically investigated. Films were co-electrodeposited from aqueous ethylenediamine solutions containing Cu(II), In(III), and H_2SeO_3 at a pH of 1.7 onto molybdenum-coated glass substrates. Copper content was varied by variation of the deposition potential between -0.55 and -0.75 volts. Selenium content in as-deposited films was always excessive (>50 at.%) but easily reduced to the desired stoichiometric level (50 at.%) by thermal annealing in argon without any modification of the copper/indium ratio. In addition, thermal annealing had significant effects on film crystallinity. As-deposited films are micro-polycrystalline and exhibit weak and broad diffraction peaks. An increase in annealing temperature from 230° to 450°C increases peak intensity and decreases peak width, indicating larger grain size. A detailed study has been made on the structural and morphological modification of $CuInSe_2$ films of varying composition as a function of annealing conditions.
- The results of chemical treatments utilizing 0.05-0.1 vol.% Br_2 in CH_3OH and 0.1-0.5 M KCN in deionized water on the morphology, composition, and structure of electrodeposited $CuInSe_2$ are reported. The prior solution was observed to function more as a surface leveling (leaching) agent and did not affect composition significantly. The rate of leaching is dependent upon both the Br_2 concentration and solution temperature. The latter solution was found to be more elementally selective with a preference for etching Cu_xSe and selenium in as-deposited material without affecting the $CuInSe_2$ and In_xSe phases and serves to reduce excess selenium in as-deposited material, much like thermal anneals in argon. If unannealed films are treated with KCN, Cu_xSe and selenium impurities are effectively removed leaving only $CuInSe_2$ and In_ySe. Annealing of this material then produces indium-rich (copper-poor) material.

1.3.4 III-V High-Efficiency Photovoltaic Cells

- We have fabricated and characterized a two-terminal $GaInP_2$/GaAs monolithic cascade cell using the atmospheric organometallic chemical vapor deposition (OMCVD) method and achieved 27.3% (one sun, AM1.5) efficiency. The measured cell parameters are J_{sc} = 13.6 mA/cm^2, V_{oc} = 2.29 volts, FF = 0.87, and area = 0.25 cm^2. This is the highest efficiency reported for a two-terminal, tunnel junction-interconnected tandem photovoltaic device (see Section 5.2.1).
- A GaAs n-on-p homojunction with a thin $GaSnP_2$ window layer and a $GaInP_2$/GaAs back surface hetero-interface cell structure was fabricated and achieved a one sun, AM1.5 efficiency of 250%. The V_{oc}, J_{sc}, FF, and total area for this device are 1.05 V, 27.8 mA/cm^2, 85.6%, and 0.249 cm, respectively. The device was grown at 700°C using conventional atmospheric pressure OMCVD (see Section 5.2.2).
- The theoretical efficiencies of series-connected, two-junction solar cells with optimized top-cell thicknesses have been computed. Calculations show that the reduction of the top-cell thickness results in significant increase in the efficiencies for a range of band-gap combinations. For example, in

the case of lattice-matched material systems with band-gap combinations GaAs(1.424 eV)/GaInP(1.90 eV), GaInAs(0.7 eV)/InP(1.35 eV), and Ge(0.8 eV)/GaAs(1.424 eV), thinning the top-cell increases the theoretical efficiencies from 28% to 34%, respectively (see Section 5.3).

- The effect of selenium doping on the optical and structured properties, particularly the ordering phenomena of $GaInP_2$, has been studied under a variety of growth conditions. We have shown that the disordering of $GaInP_2$ films by selenium doping is very similar to that reported previously for zinc and magnesium-doped films. The change from ordered to disordered films takes place as the carrier concentration is increased above $10^{18} cm^{-3}$ for zinc, magnesium, and selenium. The similarity between the effects of all three dopants suggests that the disordering mechanism could be a colligative-type effect (see Section 5.4).

- The effect of using an on-line purifier (ATM Epigrads) during the OMCVD growth of III-V semiconductors on their minority carrier transport properties was evaluated by using a photoelectrochemical spectroscopy technique. The results show that the photocurrent in AℓGaAs is considerably enhanced by the action of the purifier. On the other hand, $GaAsInP_2$ shows a high degree of tolerance to impurities. This observation supports our conclusion that the $GaInP_2$ group of compounds, used in the cascade cell structure, is much less sensitive to impurity problems than is the GaAℓAs group of compounds.

1.3.5 Solid-State Theory

- A "first-principles" approach was carried out for describing the temperature-composition phase diagram of substitutional pseudobinary semiconductor alloys. The calculation includes in a natural way atomic relaxation and self-consistent charge transfer, hence providing a link between the electronic structure and the interaction energies which decide phase stability. A renormalization procedure, whereby distant-neighbor correlations are folded into a compact set of effective near-neighbor correlations, is used and tested against Monte Carlo solutions. This yields the phase diagram and thermodynamic properties. This approach has been applied to five III-V pseudobinary alloys ($Aℓ_{1-x}Ga_x$, As, $GaAs_{1-x}P_x$, $In_{1-x}Ga_x$, As, and $GaSb_{1-x}As_x$) and three II-VI pseudobinary alloys ($Cd_{1-x}Hg$, Te, $Hg_{1-x}Zn_xTe$). We discuss in detail the chemical trends and offer a simple ("ε-G") model which reveals the underlying physical factors controlling such trends.

- First-principles electronic structure calculations for Si_nGe_n superlattices (for n = 4, 6, and 8) grown epitaxially on a (110) silicon substrate reveal a nearly direct band gap (to within ≈0.04 eV for n = 4) despite the pronounced indirectness of its constituents. This is unlike superlattices grown in the [001] direction, which are indirect when grown on silicon and quasi-direct only on substrates with larger lattice constants (e.g., germanium). Transition dipole matrix elements for the lowest energy direct transition vanish for all repeat periods n but are finite for several other new low-energy transitions.

- The excess energy of several III-V and II-VI strained-layer semiconductor superlattices is studied as a function of the repeat period and growth direction. We discover a number of universal features, including the predicted instability for nearly all superlattices with respect to bulk

disproportionation, the identification of chalcopyrite as a metastable ordered structure, and the stability of all thin epitaxial [110] and [201] and most common-anion [001] superlattices relative to coherent phase separation.

- First-principles self-consistent total energy calculations for various configurations of atomic and diatomic hydrogen inside face-centered cubic (fcc) palladium have been carried out to clarify some of the solid-state aspects of the physics of dense hydrogen in metals. We find that the stability of the system is controlled by the relative position of the hydrogen-induced antibonding level with respect to Fermi energy. Diatomic H_2 in crystalline palladium is shown to have but metastable local minima whose internuclear separation are yet larger than that of the isolated H_2 molecule.
- Thermodynamic first-principles theory of stability, including charge-transfer, elastic forces, and atomic relaxations, was developed that reveals the physical origins of stable and metastable ordering in bulk and epitaxial semiconductor alloys.
- Substitutionally random $A_{1-x}B_x$ alloys are usually constructed by randomly occupying each of the N sites of a periodic cell by A or B. We show that it is possible to design special quasirandom structures (SQSs) that mimic for small N (even N = 8) the first few, physically most relevant radial correlation functions of a perfectly random structure far better than the standard technique does. We demonstrate the usefulness of these SQSs by calculating optical and thermodynamic properties of a number of semiconductor alloys.
- First-principles pseudopotential calculations have been carried out for the following column IV/column III-V semiconductor superlattices: $Si_{2n}(GaP)_n$, $Ge_{2n}(GaAs)_n$, and $Si_{2n}(GaAs)_n$. Formation energies with respect to the constituents and valence band offsets have been calculated as a function of repeat period n and growth direction $\vec{G}$ for $n \leq 4$ and $\vec{G}$ = [001], [110], and [111]. The non-lattice-matched Si-GaAs superlattices have been assumed to be grown on silicon substrates. We found that all superlattices were unstable with respect to segregation, and that the [111] direction is the most stable among the superlattices. The unreconstructed polar superlattices [001] and [111] have large internal electric fields, causing the [001] superlattices to reconstruct for $n \geq 2$. Different types of reconstruction give different band offsets. Finally, a simple model for the formation energy based on non-octet bond energies and electrostatic interactions between donor and acceptor bonds is presented.

1.3.6 Laser Raman and Luminescence Spectroscopy

- In an attempt to understand the anamolous band-gap lowering of $GaInP_2$, we have conducted spectroscopic measurements involving polarized photoluminescence. This has resulted in the first experimental evidence for the spontaneous breaking of cubic symmetry in the band structure of OMCVD-grown $GaInP_2$. We show that this effect is related to the spontaneous ordering of the alloy, which leads to the anomalous lowering of the band gap of these films.
- Raman scattering studies of $CuIn_xGa_{1-x}Se_2$ single crystals indicate that the phonons in this alloy show a mixed mode behavior. The phonons below 200/cm exhibit a one-mode behavior, whereas those above 200/cm exhibit a two-mode behavior. The information obtained in this study proved useful in

determining the stoichiometry of this quaternary alloy but also in studying the extent of disorder present in this material.

1.4 Participation in External Cooperative Research

The technical staff of the Solid State Research Branch has continued to work in close collaboration with other research organizations, including several SERI subcontractors. Within the institute, we have maintained close collaborations with the Photovoltaic Measurements and Performance Branch and the Photovoltaics Program Branch. We have also continued to work closely with Boeing Electronics, the Institute of Energy Conversion, International Solar Electric Technologies Corporation, Chronar Corporation, Energy Conversion Devices, Inc., and others. We continued to provide technical support to the Electric Power Research Institute's program on crystalline silicon and a-Si. Members of the branch have actively participated in several workshops, program review meetings, and proposal reviews requested by the Photovoltaics Program Branch. We have benefitted enormously from the participation of many distinguished visitors and postdoctoral scientists from all over the world.

A formal collaborative research program with several laboratories in India under the U.S.-India Science and Technology Initiative (STI) has continued. We are also participating in collaboration with several organizations in Italy and Israel.

1.5 Conclusion

Our research activities in FY 1989 continued to be vigorous with a high degree of productivity. In all research areas, we made original contributions to advancing the state of the art in photovoltaic materials and devices. Progress in all areas has been documented in numerous articles published in scientific and technical journals and in patent disclosures. Several members of the branch have given invited lectures at national and international meetings. SERI's solid-state research has interfaced very effectively with subcontracted research and has made major contributions to the DOE National Photovoltaic Program objectives.

2.0 SEMICONDUCTOR CRYSTAL GROWTH RESEARCH

Investigators

T. F. Ciszek, Principal Scientist and Group Leader
C. R. Schwerdtfeger, Associate Scientist (from March, 1989)
C. Evans, Master Technician (through January, 1989)
T. Schuyler, Master Technician
C. Sarris, Part-Time Student Employee

2.1 Introduction

Crystal growth research activities were conducted in three primary areas or material systems: silicon, chalcopyrites, and high-T_c superconductors. In silicon, we concluded our study of growth parameter effects on minority charge-carrier lifetime. We also investigated methods for deliberate oxygen and carbon doping of high-purity silicon, and grew dislocation-free crystals in a partial hydrogen ambient to study the effect on lifetime.

The effort in chalcopyrite crystals focused on fabrication and installation of a bank of three small, high-pressure growth furnaces for liquid-encapsulated directional solidification (LEDS) of $CuInSe_2$ and chalcopyrite alloys. The furnaces are based on a prototype design we reported last year with the addition of computer control for long-duration growth runs that we feel are required to attain high-quality material for fundamental property and characterization studies in support of the thin film effort.

Our activities in high-T_c superconductor materials included attainment of characterization capability for low-field alternating current (ac) susceptometry and resistivity between 5 K and 300 K, as well as critical current density. We employed these techniques to characterize the superconductor materials fabricated by our superconductor filament and sheet coating process, and we also performed low-field susceptometry measurements on individual mm-size $YBa_2Cu_3O_{7-\delta}$, $ErBa_2Cu_3O_{7-\delta}$, and $Bi_2Sr_2Ca_{0.8}Cu_2O_x$ single crystals. We continued development of our superconductor filament and sheet coating process on a small scale. High-T_c superconductors have potential application in photovoltaic-generated energy transmission and storage.

2.2 Silicon Crystal Growth

2.2.1 Introduction

The newer high-efficiency silicon photovoltaic cell designs require long minority charge-carrier lifetime silicon materials [1], since lifetime is one of the most important parameters concerning cell efficiency [2]. At dopant concentrations lower than $10^{17}/cm^3$, bulk lifetime is mainly determined by Shockley-Read-Hall recombination rather than band-band Auger recombination and band-gap narrowing. Grain boundaries, dislocations, and other large lattice defects, as well as deep level impurities, are known to lower lifetime very substantially.

Even when silicon crystals are single and dislocation-free, types of micro-defects like swirls (A, B-type) and D-type defects may exist [4,5]. These defects are all visible by x-ray topography or chemical etching after copper

decoration. In addition, fast cooling of crystals can produce frozen-in defects [6]. To date, a few reports [6-8] dealing with defect effects on carrier recombination were done either with low-purity, crucible-grown silicon crystals or by post-growth heat treatments. In a previous publication [9], we reported lifetimes of float-zoned silicon containing different defects.

The lifetimes observed in high-purity, dislocation-free, float-zoned silicon are usually about an order of magnitude higher than those seen in dislocation-free, Czochralski-grown crystals. Oxygen contamination from the quartz crucible and carbon contamination from the graphite resistance heaters used in Czochralski growth are frequently blamed for the lifetime reduction, but a quantitative analysis of carbon and oxygen effects on the lifetime of otherwise high-purity, dislocation-free, single silicon crystals is needed. Conversely, hydrogen doping is thought to benefit silicon material properties when the silicon is amorphous or multicrystalline, but again the effects on lifetime of dislocation-free single crystals is not characterized. In our silicon activities during the past year, we investigated some carbon, oxygen, and hydrogen doping methods for otherwise high-purity, dislocation-free, float-zoned silicon. The study of microdefect effects on minority charge carrier lifetime τ has been concluded.

2.2.2 Crystal Growth and Characterization

The silicon crystals were grown by single-turn (RF) coil float-zoning, with three pass purifications under a high vacuum of $\sim 1 \times 10^{-6}$ torr prior to final dislocation-free crystallization in an argon atmosphere. Crystal diameters ranged 10-34 mm. The growth rates were in the range of 2-7 mm/min, depending on specific experiments. Crystal rotation was 7 rpm in most cases.

Minority carrier lifetime was measured by photoconductive decay with a digital oscilloscope-computer system [10]. A single bar method [11] was used to obtain lifetime profiles. For this, a sample was opaquely masked on the two ends and most of the total surface, only allowing a certain portion of the sample length to be exposed to incident pulsed light. The macroscopic lifetime distribution was obtained by changing the position of the exposed area along the sample length. The pulsed light sources used here were either a xenon strobe with a 0.5-mm-thick silicon filter or a 930-nm GaAs:Si diode array; the latter has less power output but sharper cutoff.

2.2.3 Carbon, Hydrogen, and Oxygen Doping

Since the segregation coefficient of carbon in silicon is much less than 1, we used a "pill-doping" method in which all the dopant is placed at the starting end of the silicon feed rod. This results in a nearly uniform distribution of dopant along the rod after the float-zone crystal growth pass is completed. We tried slurries of finely ground, high-purity graphite mixed in acetone, but these typically would not adhere to the silicon rod. A commercial material, Aqua-Dag, was also tried and demonstrated better adherence. Carbon levels up to about 5×10^{16} were achieved, as measured by infrared (IR) spectroscopy. However, numerous control and comparison experiments indicated that the carbon effects on lifetime were not consistent, and it is likely that other contaminants were entering the silicon along with the carbon.

The segregation coefficient of oxygen in silicon is near 1, and oxygen must be continuously supplied during the crystal growth pass for uniform doping. We tried several doping methods: insertion of a small-diameter, high-purity quartz rod in the molten zone during crystal growth; pre-oxidation of the high-purity feed rod surface by heating it in a diffusion-furnace tube under a partial oxygen ambient before crystal growth; and the use of a partial oxygen ambient during crystal growth. None of these approaches were satisfactory. Too little oxygen could be incorporated by the first approach. The second approach tended to form a silicon-oxide skin that flaked away during the crystal growth pass and disrupted growth. The third approach either did not introduce enough oxygen (if the concentration in the ambient was low) or else formed a thin oxide skin with problems similar to the second approach when the amount of oxygen in the ambient was increased. As in the case of carbon doping, no useful data were obtained with oxygen doping.

Hydrogen doping has been previously reported for float-zoned silicon and was used to eliminate swirl defects in early studies [12]. But later on it was found to cause other defects that make crystals more brittle. We grew some crystals in a 10% hydrogen/90% argon atmosphere. We confirmed that swirl defects were nearly eliminated by growth in the partial hydrogen ambient. However, a few large, hydrogen-caused defects were seen by x-ray topography in these dislocation-free, hydrogen-doped crystals. A crystal grown under similar conditions but in pure argon has intensely striated swirl defects. We know from earlier work that the presence of swirl defects degrades τ. Despite the low swirl defect density in the hydrogen-doped crystals, an extremely low lifetime was measured for this material relative to that measured for the crystals grown in pure argon (~100 ms versus ~2,000 ms). Since the large defects caused by hydrogen are sparse in the x-ray topographs, this low-lifetime value is unlikely to be attributed to them and may be due to some much smaller, hydrogen-caused haze defects that appear to be gettered near the larger defects. In any case, hydrogen doping appears to be detrimental rather than beneficial in high-purity, dislocation-free single crystals.

2.2.4 Conclusion

No satisfactory procedures were found for controlled doping of carbon and oxygen in high-purity, dislocation-free, float-zoned silicon. Though hydrogen doping could eliminate swirl defects, it introduces additional recombination centers and results in low values of minority charge carrier lifetime.

A low thermal gradient (i.e., large crystal diameter) near the growth interface is preferred for avoiding both swirl defects and fast cooling defects. At a given thermal gradient, a growth speed just high enough to avoid swirl defects should be adopted to avoid excessive cooling effects. These procedures can attain $t > 20$ ms in high-purity, float-zoned silicon.

2.3 Chalcopyrite Semiconductor Crystal Growth

2.3.1 Introduction

With new advances and interest in $CuInSe_2$ thin films, we must better understand some of the fundamental material properties. We hope to grow the best available single crystals of $CuInSe_2$ alloyed with gallium or silver in the form $Cu_xAg_{1-x}In_yGa_{1-y}Se_2$ with either x or y = 1, but not both. These alloys

may then be used for fundamental characterization. By precision motion and temperature control, we should be able to produce uniform, crack-free crystals using an LEDS method [13]. In this section, we will describe the project development to date.

Previously, we built a prototype high-pressure furnace with manual controls which was used to make large-grained, polycrystalline $CuInSe_2$, $Cu_xIn_{1-x}Se_2$, and InP by LEDS [14]. The preliminary results indicated the need for longer growth runs in a steeper temperature gradient to eliminate stress fractures and constitutional supercooling effects. To achieve the stability and control required for 1- to 2-month growth runs, we have designed a computer-controlled system with precision stepper motor drives to use with the three high-pressure furnace chambers we built last year.

The primary goal of this effort was to design a pulling mechanism that would move an ampule through a temperature gradient at a minimum speed less than 0.004 mm/min (less than 0.6 cm/day). In addition, the computer should have the capability of controlling the temperature through a proportional-integral-differential (PID) loop on each furnace simultaneously with run-time adjustment.

Constitutional supercooling, which causes solid-liquid interface instability (eventually leading to propogation and composition inhomogeneity), can be overcome by using a steep temperature gradient in which to freeze the melt. An appropriate furnace core must be designed and profiled.

2.3.2 System Design

The chamber is designed to handle up to 80 atmospheres of pressure. As in our previous work, we will use argon to overpressure an open quartz ampule which contains elemental copper, indium, selenium, and a liquid encapsulant B_2O_3. The combination of a liquid encapsulant and the high pressure will keep the selenium vapors from escaping the melt. In fact, we should be able to put an excess of selenium in the melt to ensure a p-type crystal.

The 20-mm-i.d. ampule will hang from a 3/16-in. pull rod. The rod will go through a teflon compression feedthrough and connect to a coupler at the top. The coupler is in turn connected to a 40 revolution/inch lead screw and stepper motor. The stepper motor has a 100:1 gear reduction box which allows the 12,800 steps per revolution to reduce to 1.28 million steps for each revolution of the lead screw. Forty lead screw revolutions per inch translates to just over 5 Angstroms per step. The stepper motors for each furnace will be controlled by an indexer capable of receiving commands from the computer. The indexers are able to control the stepper motors as slowly as 0.001 revolution/s. This translates to an ampule speed less than 0.5 μm/min. At this rate, it would take 260 days to travel 15 cm. Fortunately, once the crystal has solidified, we can increase the speed such that it sees an effective cooling rate less than 1°C/h. The cooling rate is determined by the temperature gradient and travel speed. For instance, if the furnace has a temperature gradient of 70°C/cm, the travel speed would need to be about 0.00175 mm/min to achieve 1°C/h.

The temperature control in the furnace is critical with such slow growth speeds. Type K thermocouples will be used to detect the furnace temperature.

Th computer will compare that temperature to a predefined setpoint and adjust the power to the furnace accordingly. The setpoint can be constant valued, linearly ramped up or down, or adjusted to any set of values the user inputs in a file. With a constant setpoint, it may be changed at any time during the run.

All of these operations are performed by a commercial software package called LabTech Control. During the run, several CRT screens can be viewed, many graphs can be monitored, and variables such as temperature setpoint or PID loop parameters can be adjusted.

2.3.3 Summary

We have designed and begun implementation of a precision control system for LEDS crystal growth of $CuInSe_2$ alloys with gallium or silver. The goal is to get uniform, crack-free single crystals to be analyzed in house as well as out of house to learn more about the fundamental properties of the material. This information should provide some guidelines to the $CuInSe_2/CuGaSe_2$ polycrystalline thin film researchers so that they can improve the performance of photovoltaic solar cells based on these materials.

2.4 Liquid-Phase Preparation of High-Temperature Superconductors

2.4.1 Introduction

Superconductivity in the Bi-Sr-Cu-O system was first reported by Michel et al. [15] at a transition temperature T_c of 7 to 22 K. The dramatic increase of T_c obtained by Maeda, Tanaka, Fukutomi, and Asano [16] via addition of calcium to the system led to considerable scientific and technological interest. Many research investigations have focused on understanding the superconducting characteristics [17-22] and structure [21-26] of this material system. That work was done primarily on sintered oxide pellets processed at temperatures in the 800°-900°C range. Several crystal growth results have also been reported [27-31]. More recently, superconducting Bi-Sr-Ca-Cu-O fibers [32], wires [33-35], and strips [35] have been made by several investigators. High critical current (J_c) values ($>10^4$ A/cm^2) in high magnetic fields B (>25 T) have been seen with some of the wire materials [34]. Here, we will report on the composition and superconducting properties of mixed-phase superconducting coatings formed on thin, long substrates by a liquid-phase process [35].

2.4.2 Material Preparation

Schematic drawings of the processes we used for coating substrates are shown in Figure 2-1. Powders of the four oxides Bi_2O_3, SrO, CaO, and CuO with ACS-grade or higher purity levels were mixed, ground, and tamped into 99.8% alumina crucibles. When heated to temperatures in the range 950°-1150°C, the powders became liquid. Rod, wire, or sheet substrates were inserted into the oxide melt and withdrawn at a controlled rate in the dip-coating method. A continuous version of the coating process was carried out by moving a long substrate upward at a controlled rate through a hole in the bottom of the crucible. Here, a relationship of the form $h = A/\phi - B$ governs stable containment of the melt, where ϕ is the diameter of the hole in the crucible bottom, h is the maximum stable melt height in the crucible, and A and B are constants [36]. We typically used melt heights on the order of 3-5 mm with a

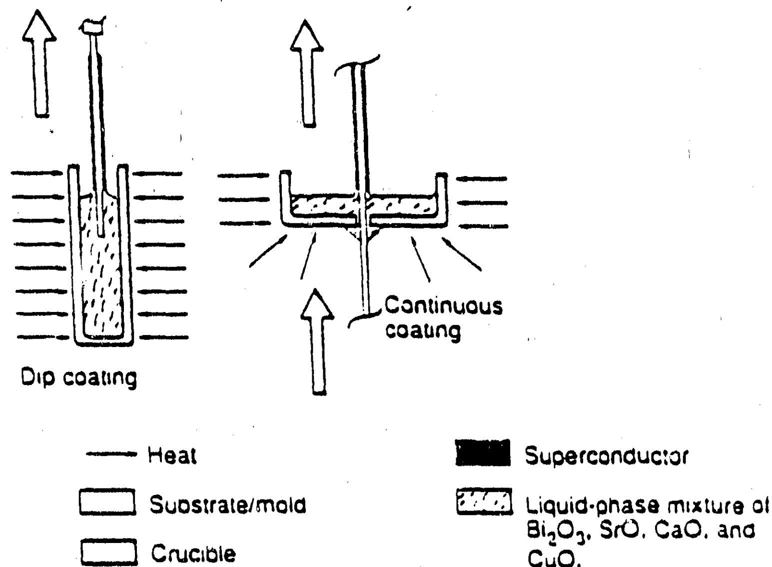

Figure 2-1. Schematic drawings of a dip-coating process (left) and continuous-coating process (right) for liquid-phase deposition of superconductor layers on substrates

hole diameter of 1 mm. Figure 2-2 is a photograph of the continuous coating process in operation. Continuous lengths of up to 170 mm (limited by the pulling mechanism) were coated.

Pulling speeds between 2 and 1800 mm/min were used to move the substrates through the liquid oxides. Resistance heating was used for the dip-coating method, and RF heating at 28 MHz frequency was used for continuous coating. The atmosphere was air, oxygen, or nitrogen. Al_2O_3 substrates were used for growth of most of the coatings that will be discussed; however, platinum and other metals have also been successfully used. The substrate diameters or thicknesses ranged from 25 μm to 3 mm.

Numerous atomic-ratio starting compositions produced superconducting material. The specific ones we will discuss in this paper include Bi:Sr:Ca:Cu = 2:2:1:2 (or molar ratio Bi_2O_3:SrO:CaO:CuO = 1:2:1:2), 2:2:2:1, 1:1:1:1, and 0.875:2:10:5. In all cases, post-growth annealing was required to make the coatings superconductive. This process typically consisted of heating the coated substrates to 860°-875°C for 2 h or less in air, oxygen, or nitrogen.

2.4.3 Characterization and Results

2.4.3.1 Composition and Morphology

Figure 2-3 shows typical coated wire, rod, and sheet substrates after growth. The coatings are black and possess a texture attributable to the presence of mixed phases with differing individual morphologies. Coating thicknesses in the range of 5 μm to several hundred micrometers were obtained. Thickness varied with substrate temperature, melt temperature, residence time of the substrate in the liquid, and pulling speed.

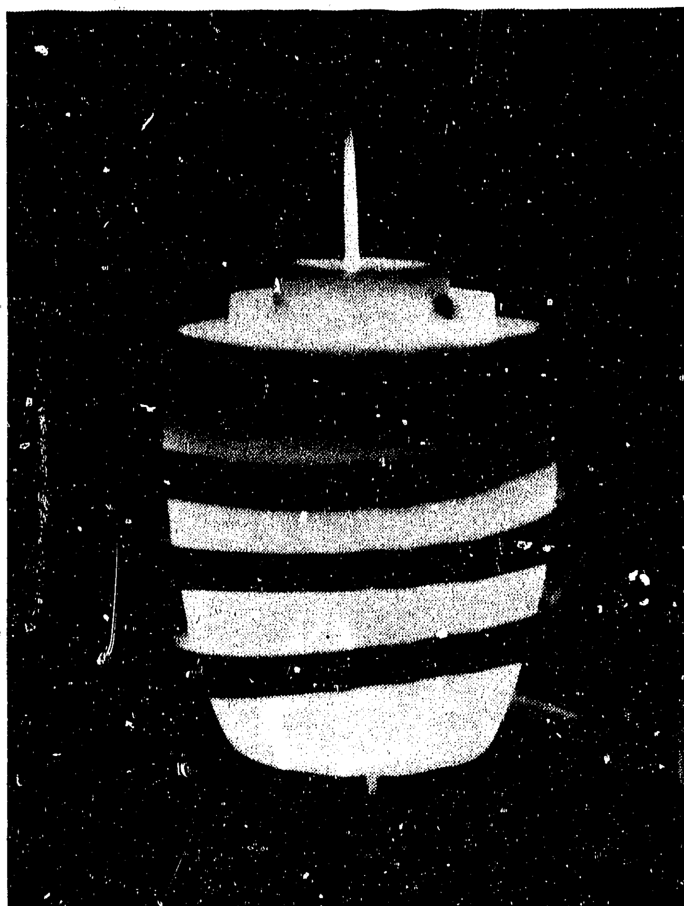

Figure 2-2. Continuous coating of a 0.7-mm-diameter filament

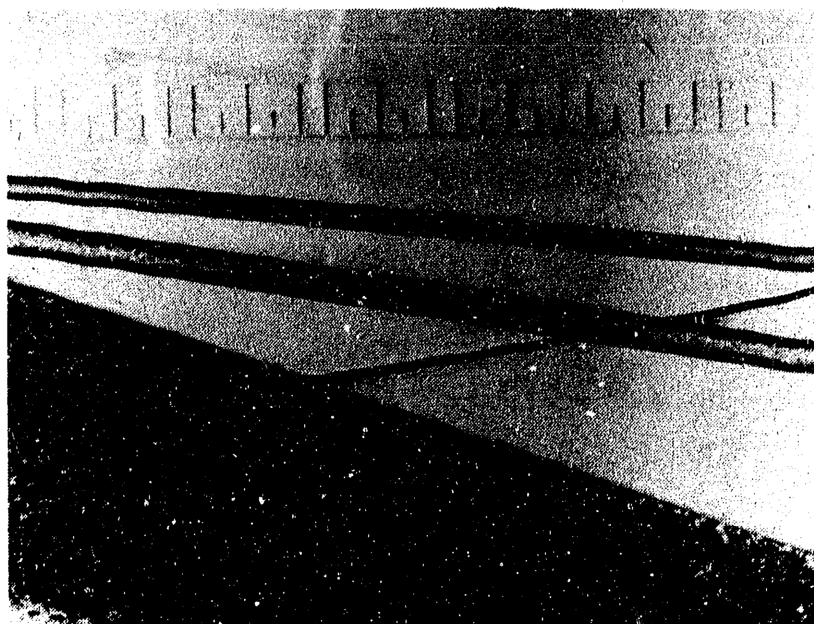

Figure 2-3. Typical wire, rod, and sheet geometries coated with the Bi-Sr-Ca-Cu-O superconductor

Energy dispersive spectroscopy (EDS) was used to determine filament and sheet coating compositions. An ISI-50A scanning electron microscope and a Tracor Northern EDS system were used for standardless quantitative analysis. A single-crystal 2212 superconductor was analyzed as a calibration check, and the analysis of its composition via EDS agreed within 2 at. % with that obtained by the more accurate electron probe microanalysis (EPMA) performed on the same crystal sample. However, both EDS and EPMA indicated low calcium content compared to the ideal stoichiometric atomic percentages 14:14:7:14.

In this discussion, we will present detailed EDS results for coatings obtained from the 2:2:1:2 starting powder composition. The composition/morphology relationships seen in coatings made from the other mixtures are analogous. As shown in Figure 2-4(a), the general morphology consists of a relatively smooth, plate-like, primary phase with darker, elongated needles dispersed within it. The needles lie within the surface plane of the coating and tend to be longer and wider for thicker coatings. Figure 2-4(b) shows the less uniform morphology of a sheet coating near an edge, with a greater variety of needle sizes and shapes. This typical morphology was similar for coatings made from each starting mixture, differing only by the number of needles present in a given area. The 0.875:2:10:5 mixture had a substantially higher concentration of needles than did the 2:2:1:2 or 2:2:2:1 mixtures. The plate-like, light-colored background material is the superconducting phase and is consistently slightly bismuth-rich, strontium-poor, and calcium-poor compared to the ideal 2:2:1:2 stoichiometry for both sheet coatings and filament coatings (Figure 2-5). Similar deviations from ideal stoichiometry have been reported by other investigators [37].

Most of the long, narrow needles on each sample exhibit a bismuth-poor composition near 0:1:1:4 (Figure 2-6), like that previously reported by Dou et al. [38]. We also see a variation from this composition in some shorter, wider needles, which typically contain more calcium and less copper (also shown in Figure 2-6) than that in the 0:1:1:4 needles. On some samples, we see a third dominant composition near 0:1:4:3, and the morphology is similar to that of the 0:1:1:4 needles. A 0:0:2:1 Ca-Cu-O phase has been reported [39] for a sintered pellet material; we did not observe it in our samples. Slight morphological differences appear to exist between the three observed needle-like phases, but further investigation is required to confirm these trends.

All three needle types are seen on both as-grown and annealed sheet and filament coatings. Typical annealing conditions consisted of 0.2-2 h at 860°-875°C in flowing oxygen, followed by slow cooling to room temperature. Apparently, annealing near 860°C does not alter the needle compositions.

In addition to these needles, several impurities were present. Small cubic and tetragonal growths on the surface of the coatings were caused mainly by aluminum contamination from the crucibles and included oxides of Sr-Ca-Al, Sr-Al, and Sr-Ca. Small "popcorn like" surface features usually consisted of calcium oxides.

2.4.3.2 Superconducting Properties

The superconductivity of the coatings was observed for a large range of starting oxide powder compositions. Before measuring the electrical resistance and magnetic susceptibility of the coatings, post-growth annealing was carried out

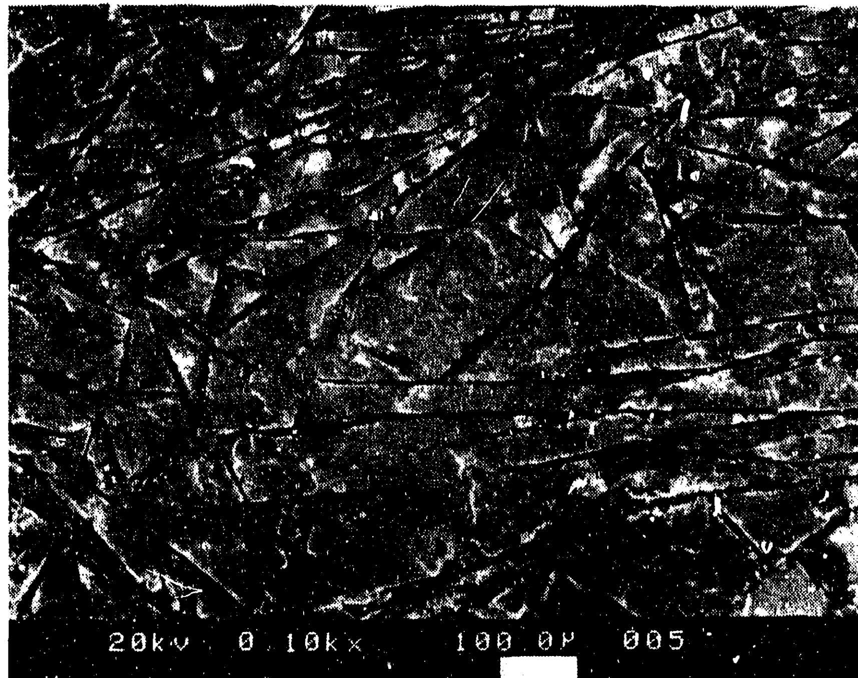

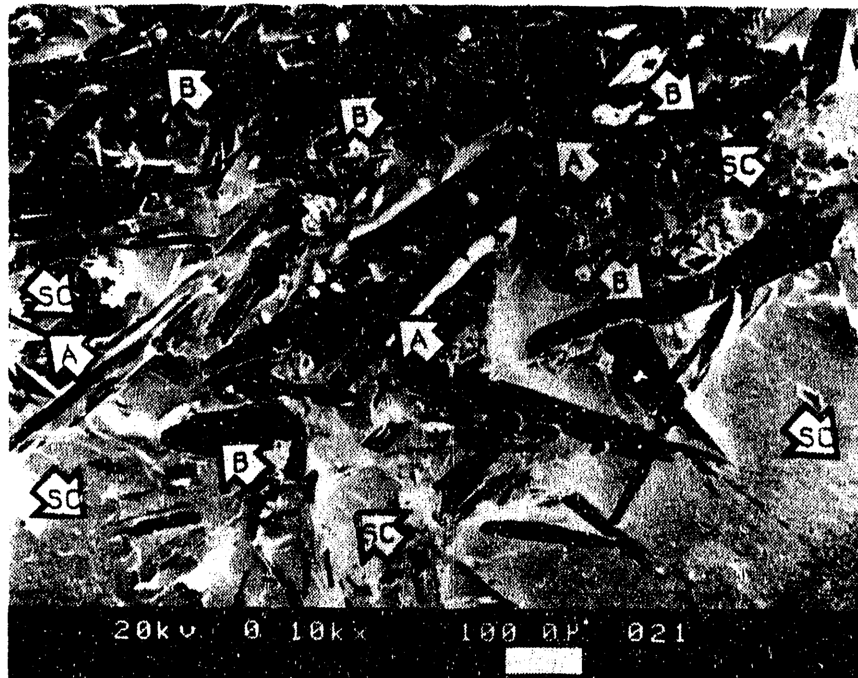

Figure 2-4. **SEM micrographs of the morphologies of 2:2:1:2 mixtures coated on an alumina sheet: (a) typical coating morphology with predominantly 0:1:1:4 needles, (b) less typical morphology with various needle compositions.** The lighter, smooth-flowing areas labeled 'SC' are superconducting regions (see Fig. 2-5); the dark needles labeled 'A' and 'B' are Bi-poor regions (see Fig. 2-6).

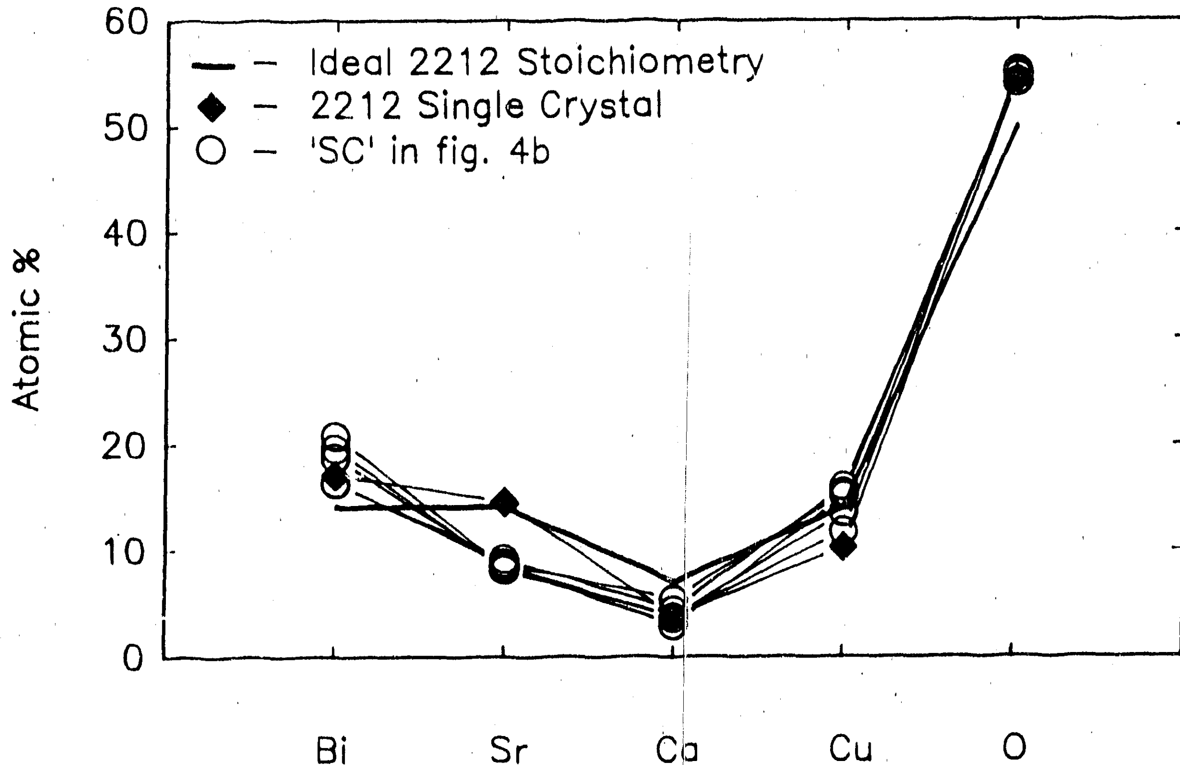

Figure 2-5. Elemental composition measured by EDS for a reference "2:2:1:2" single crystal and several typical superconducting regions on a coated sheet substrate (labeled 'SC' in Fig. 2-4(b)). The composition for ideal 2:2:1:2 stoichiometry is also shown as a heavy line.

as described in the previous section. The shorter annealing times and lower temperatures were used for thinner samples. Both low-field ac magnetic susceptibility and direct current (dc) resistance were measured as a function of temperature with a Lakeshore Cryotronics Inc. model 7000 ac susceptometer fitted with an accessory resistance probe. Annealed evaporated-silver contact pads were applied to the samples for the resistance measurements. The sample volume for the contactless susceptibility measurements was typically 2 to 4 × 10^{-9} m^3.

Figure 2-7 shows the resistivity versus temperature curves for coatings grown from three different oxide-starting powder compositions with element ratios Bi:Sr:Ca:Cu = 2:2:1:2, 2:2:2:1, and 0.875:2:10:5. Superconducting transition onset temperatures were between 80 K and 90 K for all three. The 2:2:1:2 and 0.875:2:10:5 batches yielded coatings that showed a small component of the higher ≈110 K transition onset. The highest zero-resistance temperature, 76 K, was achieved with the 2:2:2:1 starting composition.

Low-field ac susceptibility χ was measured on coatings that were removed from the substrates after annealing. Variation of the real χ' and imaginary χ'' components with temperature are shown in Figure 2-8 for two different sets of

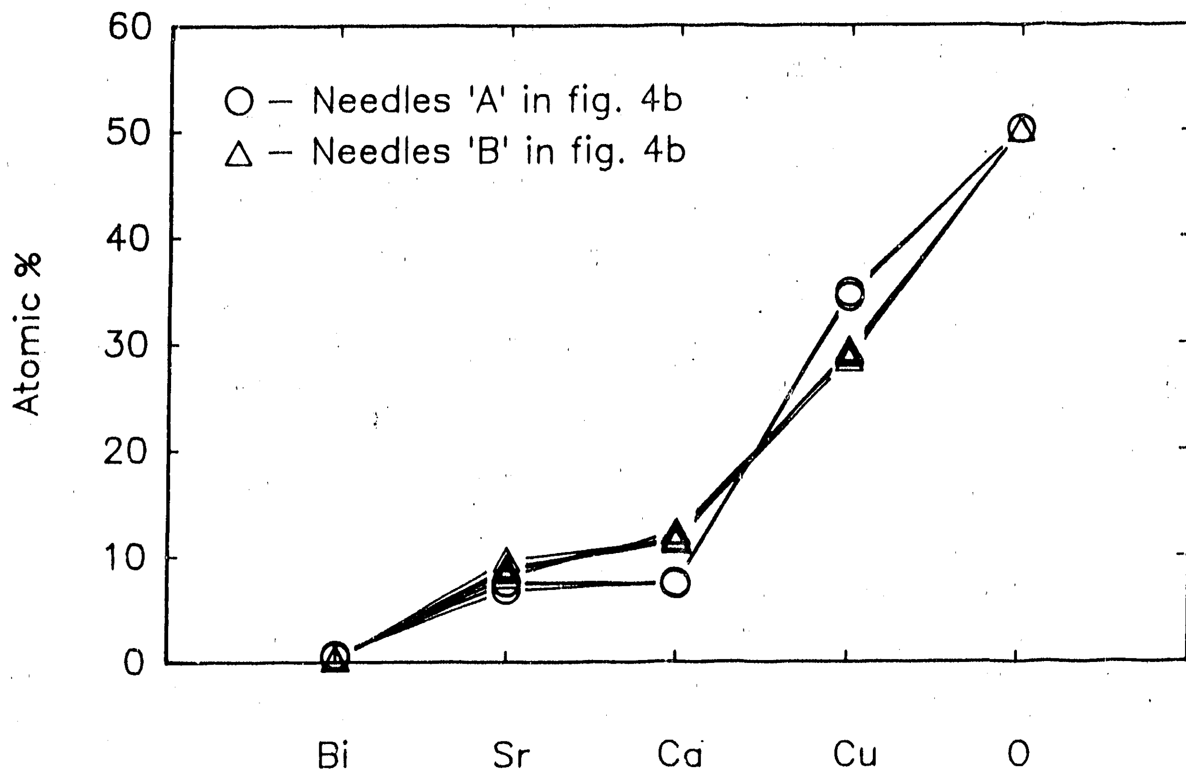

Figure 2-6. Elemental compositions of two types of needles coated on a sheet substrate: (-O-) Bi-poor composition near 0:1:1:4 of needles labeled 'A' in Fig. 2-4(b); (-Δ-) Ca-rich, Cu-poor composition (relative to 0:1:1:4) of needles labeled 'B' in Fig. 2-4(b)

element ratios in the starting oxide powder mixture. The two samples were examined under similar measurement conditions. For Bi:Sr:Ca:Cu = 1:1:1:1, the ac field was 1 Oe, the dc field was 0 Oe, the frequency was 100 Hz, and the demagnetization correction factor was 0.087; for Bi:Sr:Ca:Cu = 2:2:1:2, the ac field was 1.5 Oe, the dc field was 0 Oe, the frequency was 125 Hz, and the demagnetization correction was 0.079. The samples were oriented with their flat surface and longest dimension parallel to the magnetic field. The sample dimensions were on the order of 10 mm long by 2 mm wide by 0.2 mm thick. The specimen grown from the excess calcium mix exhibited a higher transition onset temperature, sharper transition, and lower intergranular coupling losses (as evidenced by the smaller χ'' peak) than did the one grown from the stoichiometric mix, but it had a smaller volume fraction of superconducting material (approximately 60% versus 80%).

2.4.4 Summary and Discussion

We have described a simple liquid-phase process for applying Bi-Sr-Ca-Cu-O coatings to wire or ribbon substrates in both a batch (or dipping) mode and a continuous coating mode. With appropriate post-growth annealing, these coatings become superconductors. Currently, their transition onset temperatures

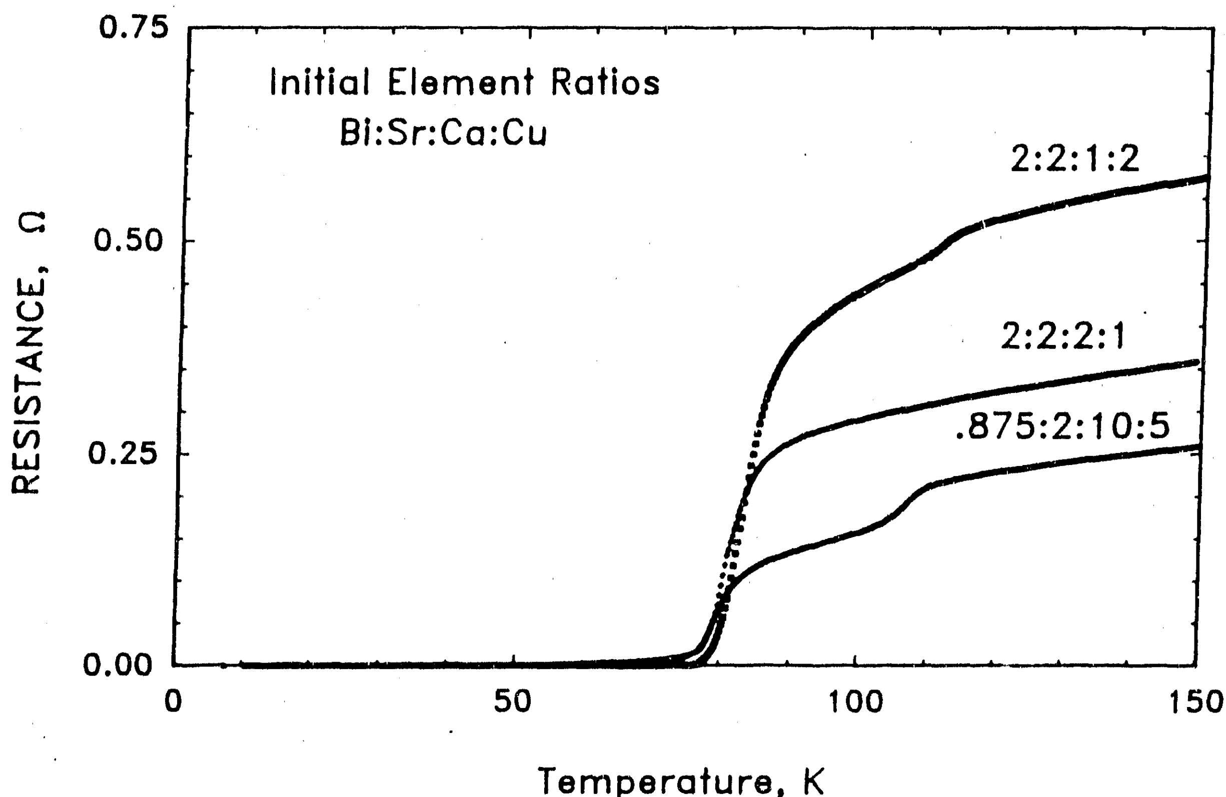

Figure 2-7. Resistance vs. temperature for superconductor coatings grown from the liquid phase using three different element ratios in the starting oxide powder mixture

are in the range of 80-90 K, and zero-resistance temperatures as high as 76 K have been achieved. The wire and ribbon coatings contain several phases. The typical morphology consists of a dominant superconducting phase near 2:2:1:2 composition in which several bismuth-deficient, needle-like phases are interspersed. The most prevalent of these has a composition 0:1:1:4. But variations with higher calcium and lower copper contents are sometimes present. A 0:1:4:3 needle phase with morphology nearly identical to that of 0:1:1:4 occasionally appears. Further study is required to determine the detailed morphological differences between these three varieties of needles in melt-grown Bi-Sr-Ca-Cu-O superconductors.

The superconducting phase is composed of interconnected plate-like crystals lying in the plane of the coating. As in the case of single crystals grown from the liquid [30], the calcium content of the coatings is lower than expected for 2:2:1:2 stoichiometry. In addition, the strontium content is somewhat low and the Bi and Cu contents are slightly high. This tendency appears to hold for a wide range of starting powder compositions. However, susceptibility measurements indicate that excess calcium addition to the starting melt may raise the Meissner onset temperature and improve the intergranular coupling.

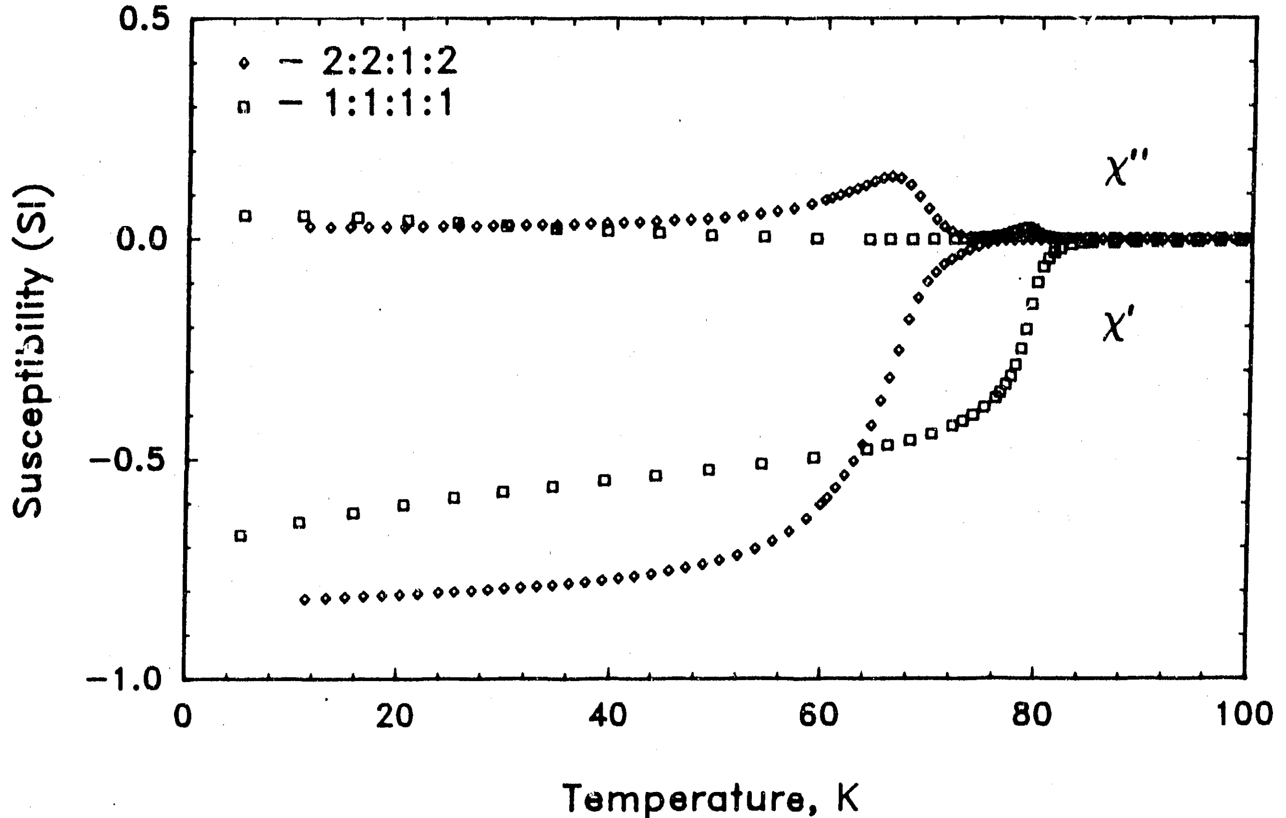

Figure 2-8. Low-field ac magnetic susceptibility (both real or cM and imaginary or cN components) for two different element ratios in the starting oxide powder mixture N

2.5 Summary and Discussion

No satisfactory procedures were found for controlled doping of carbon and oxygen in high-purity, dislocation-free, float-zoned silicon. Though hydrogen doping could eliminate swirl defects, it introduces additional recombination centers and results in low values of minority charge-carrier lifetime.

Swirl defects (A- or B-type) and frozen-in defects are found to be carrier recombination centers in dislocation-free, as-grown, float-zoned silicon crystals. The A-type defect has an effective carrier capture range of ~40 μm, as determined by electron beam induced current (EBIC) analysis. The activation energy for formation of the fast-cooling, frozen-in defects was estimated to be about 0.31 eV. Defect formation can be changed by growth conditions, and long minority charge-carrier lifetimes are achieved through moderately high growth speeds and low thermal gradients during crystal growth, by which both swirl defects and frozen-in defects are avoided. These procedures can attain τ > 20 ms in high-purity, float-zoned silicon.

We have designed and begun implementation of a precision control system for LEDS crystal growth of alloys of $CuInSe_2$ with gallium or silver. Our goal is

to obtain uniform, crack-free single crystals to be analyzed in house as well as out of house to learn more about the fundamental properties of the material. This information should provide some guidelines to the $CuInSe_2/CuGaSe_2$ polycrystalline thin film researchers so that they can improve the performance of photovoltaic solar cells based on these materials.

We used a liquid-phase process to coat thin rods or wires and flat sheets with the $Bi_2Sr_2CaCu_2O_8$-type, high-temperature superconductor. Reaction temperatures in the range 950°-1150°C form a liquid from mixed oxide starting powders Bi_2O_3, SrO, CaO, and CuO. Substrates passed through the liquid are coated with a multiphase layer that includes a superconducting phase of approximate composition $Bi_2Sr_2Ca_{0.8}Cu_2O_8$. Connectivity between grains of the superconducting phase is sufficient to achieve superconductivity of the coating as a whole (after suitable post-growth annealing) for a surprisingly large range of starting oxide powder compositions. Analytical results for the composition of some of the observed phases were obtained through EDS and EPMA. The superconducting properties were determined by low-field ac magnetic susceptometry and four-contact resistivity measurements for temperatures between 5 K and 100 K. Superconducting transition onsets above liquid nitrogen temperatures were observed for several starting compositions. Continuous coating has been demonstrated for thin rods and wires in lengths up to 170 mm.

2.6 References

1. R.M. Swanson, 18th IEEE Photovoltaic Specialists Conference Record, Las Vegas, 1985, p.604.

2. A.R. Mokahshi, T. Daud and A.H. Kachare, 18th IEEE Photovoltaic Specialists Conference Record, Las Vegas, 1985, p.573.

3. T.F. Ciszek, Solar Cells, 21 (1987) p.81.

4. A.J.R. De Kock, Appl. Phys. Lett. 16 (1970) p.100.

5. J. Chikawa, T. Abe, and H. Harada, in H.R. Huff, T. Abe and B. Kolbesen (eds.), Semiconductor Silicon, 1986, Electrochem. Soc., Pennington, NJ), 1986, p.61.

6. J. Knobloch, B. Voss, and K. Leo, 18th IEEE photovoltaic Specialist Conference Record, Las Vegas, 1985, p. 445.

7. K. Graff and H. Pieper, J. Electronic Materials 4 (1975) p.281.

8. D.C. Wong and G.F. Wakefied, Lifetime Factors in Silicon, American Society for Testing and Materials, Philadelphia, PA, 1980, p.87.

9. T.H. Wang, T.F. Ciszek, and T. Schuyler, Solar Cells, will be published in June or July, 1988.

10. T.F. Ciszek, T.H. Wang, T. Schuyler, and A. Rohatgi, accepted for publication in J. Electrochem. Soc.

11. F.G. Vieweg-Gutberlet, P.E. Siegesleitner, and M. Stallhofer, Lifetime Factors in Silicon, American Society for Testing and Materials, Philadelphia, PA, 1980, p.183.

12 T.F. Ciszek, in H.R. Huff, R.R. Bugess (eds.), Semiconductor Silicon 1973, 1973, p.150.

13. T.F. Ciszek, "Melt Growth and Some Properties of $Cu_xAg_{(1-x)}InSe_2$ and $CuIn_yGa_{(1-y)}Se_2$ Chalcopyrite Alloy Crystals," J. Crystal Growth 79 (1986) p.689.

14. T. F. Ciszek and C. D. Evans, "A Simple High-Pressure Furnace for Liquid-Encapsulated Bridgman/Stockbarger Crystal Growth," J. Crystal Growth 91 (1988) p.533.

15. C. Michel, M. Hervieu, M.M. Borel, A. Grandin, F. Deslandes, J. Provost, and B. Raveau, Z. Phys. B68 (1987) p.421.

16. H. Maeda, Y. Tanaka, M. Fukutomi, and T. Asano, Japan. J. Appl. Phys. Letters 27 (1988) L209.

17. M. Uehara, Y. Asada, H. Maeda, and K. Ogawa, Japan. J. Appl. Phys. Letters 27 (1988) L665.

18. K. Togano, H. Kumakura, H. Maeda, K. Takahashi, and M. Nakao, Japan. J. Appl. Phys. Letters 27 (1988) L323.

19. H. Katayama-Yoshida, Y. Yonezawa, H. Hirooka, Y. Okabe, T. Takahashi, T. T. Sasaki, M. Hongoh, K. Yamada, T. Suzuki, S. Hosoya, M. Sato, T. Ciszek, and S.K. Deb, Physica C153 (1988) p.425.

20. C. Politis, Appl. Phys. A45 (1988) p.261.

21. R.M. Hazen, C.T. Prewitt, R.J. Angel, N.L. Roy, L.W. Finger, C.G. Hadidiacos, D.R. Veblem, P.J. Heaney, P.H. Hor, R.L. Meng, Y.Y. Sun, Y.Q. Quang, Y.Y. Xue, Z.J. Huang, L. Gao, J. Bechtold, and C.W. Chu, Phys. Rev. Letters 60 (1988) p.1174.

22. M.A. Subramanian, C.C. Torardi, J.C. Calabrese, J. Gopalakrishnan, K.J. Morrisey, T.R. Askew, R.B. Flippen, U. Chowdhry, and A.W. Sleight, Science 239 (1988) p.1015.

23. T.M. Shaw, S.A. Shivashankar, S.J. La Placa, J.J. Cuomo, T.R. McGuire, R.A. Roy, K.H. Kelleher, and D.S. Yee, Phys. Rev. B37 (1988) p.9856.

24. J.M. Tarascon, Y. Le Page, P. Barboux, B.G. Bagley, L.H. Greene, W.R. McKinnon, G.W. Hull, M. Giroud, and D.M. Hwang, Phys. Rev. B37 (1988) p.9382.

25. T. Kijima, J. Tanaka, Y. Bando, M. Onoda, and F. Izumi, Japan. J. Appl. Phys. Letters 27 (1988) L369.

26. Y. Matsui, H. Maeda, Y. Tanaka, and S. Horiuchi, Japan. J. Appl. Phys. Letters 27 (1988) L361.

27. J.Z. Liu, G.W. Crabtree, L.E. Rehn, Urs Geiser, W.K. Kwok, P.M. Baldo, Jack M. Williams, and D.J. Lam, Phys. Lett. A 127 (1988) p.444.

28. High-Tc Update 2 No. 5, (1988) p.2.

29. L.F. Schneemeyer, R.B. van Dover, S.H. Glarum, S.A. Sunshine, R.M. Flemming, B. Batlogg, T. Siegrist, J.H. Marshall, J.V. Waszczak, and L.W. Rupp, Nature 332 (1988) p.422.

30. T. F. Ciszek, J. P. Goral, C. D. Evans, and H. Katayama-Yoshida, J. Crystal Growth 91 (1988) p.312.

31. T. F. Ciszek and C. D. Evans, in: Proceedings of Industry-University Advanced Materials Conference II, Ed. F.W. Smith (Advanced Materials Institute, Golden, CO, USA, ISBN 0-9624027-0-2, 1989) p. 512.

32. R.S. Feigelson, D. Gazit, D.K. Fork, T.H. Geballe, Science 240 (1988) p.1642.

33. M. Minura, H. Kumakura, K. Togano, and H. Maeda, Appl. Phys. Letters 54 (1989) p.1582.

34. K. Heine, J. Tenbrink, and M. Thoner, submitted to Appl. Phys. Letters.

35. T.F. Ciszek and C. D. Evans, in: Science and Technology of Thin-Film Superconductors, Eds. R.D. McConnell and S.A. Wolf (Plenum Publishing Corp., New York, 1989) p. 301.

36. J.L. Hurd and T.F. Ciszek, J. Crystal Growth 59 (1982) p.499.

37. J. van den Berg, C.J. van der Beek, P.H. Kest, J.A. Mydosh, M.J.V. Menken, and A.A. Menovsky, Superconductor Science and Technology 1 (1989) p.249.

38. S.X. Dou, H.K. Liu, A.J. Bourdillon, N.X. Tan, and C.C. Sorrell, Physica C 158 (1989) p.93.

39. H. Jaeger, M. Aslan, K. Schulze, and G. Petzow, Submitted to J. Crystal Growth, February 7, 1989.

3.0 AMORPHOUS SILICON RESEARCH

Investigators

R. Crandall, Principal Investigator and Group Leader
H. Branz, Staff Scientist
J. Carapella, Research Technician
A. Langford, Staff Scientist
H. Mahan, Senior Scientist
T. McMahon, Senior Scientist
B. Nelson, Associate Scientist
K. Sadlon, Staff Scientist
S. Tsuo, Senior Scientist
D. Baker, Visiting Scientist
S. Salamon, Visiting Scientist
M. Fleet, Visiting Scientist
X. Deng, Visiting Professional
R. Galliano, Visiting Scientist
Y. Xu, Research Technician
D. Williamson, Visiting Scientist

3.1 Introduction

During FY 1989, a number of our ideas on metastable defects in hydrogenated amorphous silicon (a-Si:H) were confirmed. Both the modeling effort and the experimental effort support each other. The experimental effort has been strengthened by two new and powerful characterization techniques that have improved our understanding of microstructure and metastability.

The extensive work on microstructure carried out at SERI in the past was based on inferences of microstructure from infrared absorption and band tail broadening. This year, we were successful in making small angle x-ray scattering (SAXS) measurements on a-Si:H that were two or three orders of magnitude more sensitive than any previous measurements, permitting the first determination of the microstructure in device quality a-Si:H.

A new trap spectroscopy technique was developed that allows us to determine the distribution of trapped holes in valence band tail states. These states are particularly important because they are instrumental in determining photoconductivity. Further, we have been able to show that they are the precursors to light-induced dangling bond formation.

The effort on devices produced a new processing step using a hydrogen plasma to improve photovoltaic efficiency, and we are now making tandem cells from a-Si:H in preparation for fabricating a-Si:H amorphous germanium tandem cells.

A significant portion of our effort is devoted to the light-induced metastabilities or Staebler-Wronski effect. We have gained considerable understanding of this effect and have developed new models that are in much better agreement with experiment than are existing ones.

During the year, we continued collaborations with the National Institute of Standards and Technology, Jet Propulsion Laboratories, University of Colorado, Colorado School of Mines, University of Illinois, Harvard, Chronar, Energy Conversion Devices, and Solarex. Visiting scientists from The Indian Association for the Cultivation of Science and LAMEL-CRN in Italy interacted strongly with the group during the year. Students from Colorado School of Mines and Colorado University also worked with members of our group.

A brief account of some of the achievements of the Amorphous Silicon Research Group follows.

3.2 Structure and Electronic Properties of Amorphous Silicon

The effect of microstructure on the electronic properties of a-Si:H still comprises a sizeable fraction of our effort. The introduction of SAXS has dramatically increased our knowledge of the microstructure of a-Si:H. This year we showed that even the best device quality a-Si:H contains a significant number of microvoids. This type of structure is apart from the effects of impurities, which can act as isolated entities such as traps, scattering centers, or recombination centers. Impurities, however, can also generate microvoids. An example of this is carbon, which usually bonds to three hydrogen atoms in a methyl group with the remaining bond being to a silicon. Fluorine is another impurity that forms voids by terminating silicon bonds.

3.2.1 Effects on Transport

We have known for some time that the electronic properties, such as photoconductivity, significantly degrade when the microstructure increases. However, the exact cause of this degradation is still unknown. Last year we showed, contrary to previous conjectures, that the increase in the number of dangling bond defects is not the major cause of the degradation of the transport properties. This year, we found that structure also affects the ambipolar diffusion length. An inverse correlation exists between the number of microvoids and the diffusion length.

One way in which structural modifications can have deleterious effects on transport is through potential fluctuations due either to charged defects or dielectric constant variations. These potential fluctuations can affect the transport through electron and hole scattering or give rise to modifications of the band tails. Another effect is that they will promote the formation of large densities of charged defects. To describe this condition, we have considered the thermodynamics of the dangling bond defect in a-Si:H assuming there are medium-range electrostatic potential fluctuations whose peak-to-peak magnitude is greater than the (positive) effective correlation energy. Results showed that significant concentrations of charged dangling bonds will result--negative defects with transition energies below the Fermi energy (E_F) in regions of high potential and positive defects with transitions above E_F in regions of low potential. We discuss some consequences of these charged dangling bonds for transport and photostability in a-Si:H in Section 3.6.4.1.

3.2.2 Measurement of Microvoids

Because microvoids in a-Si:H are such an important quantity, we need easy-to-use, quantitative techniques to measure them. A decrease in density is, of course, a good indication of void formation. However, density measurements are tedious and not amenable to routine evaluation of films. Thus we have made correlations of density changes and the absorption bands due to the Si-H vibrations and the width of the Urbach edge to the optical absorption. We have found linear changes in these with density and now use their change as a routine measure of the amount of microstructure. The best measure of microstructure is SAXS. However, since these measurements require large amounts of material with special preparation conditions, they are not routine. Nevertheless, we have been able to make quantitative measurements of the size and number of microvoids and compare these with the Urbach edge and IR absorption to give a quantitative relationship among the various measurement techniques.

We have made the first SAXS measurements on device quality a-Si:H deposited by glow discharge. The best films produced at SERI and by subcontractors all show 2-5 x 10^{+19} microvoids containing 16-20 missing atoms. By combining these results with IR absorption measurements, we deduce that the interior surfaces of these voids are largely unhydrogenated, containing at most 4-9 bonded hydrogen atoms. Details of this work are in Section 3.6.2.

3.2.3 Attempts to Reduce Microstructure

Because the microstructure has such serious effects on transport, we have tried various methods to reduce it. One method, Kaufmann ion beam rehydrogenation, has improved the transport properties of non-device-quality films. However, this method does not improve device quality material. Many reports have shown that rehydrogenation or posthydrogenation of a-Si:H reduced the Staebler-Wronski effect in a-Si:H. To verify this finding, we made a systematic investigation of the photostability properties of a variety of rehydrogenated and posthydrogenated a-Si:H films. We find that their light-induced degradation properties follow the same dependence on the initial photoconductivity values regardless of the deposition or processing method. We have also found, indirectly through photoconductivity, that the absolute and relative degradation in photoconductivity values seems to decrease with increasing initial defect-state densities. We believe many of the reported observations of reductions of the Staebler-Wronski effect are actually due to poor material qualities. Details of this work are in Section 3.6.3.

3.2.3.1 Hot Wire Deposition

A new deposition technique that may have some potential for fabricating superior material is the hot-wire catalytic decomposition technique. In this deposition process, silane gas is thermally decomposed on a high-temperature filament, which is followed by subsequent evaporation of atomic silicon and hydrogen, enabling a-Si:H film growth on a heated substrate. We are currently exploring this technique for two reasons. First, previous results suggest that growth rates higher than those obtained using the glow-discharge technique can be obtained, without a significant reduction in film properties. We would like to quantify and extend those results. Secondly, we believe that this technique may have particular advantages in the production of a-Si:H based alloys. Excellent film properties have already been reported for a-SiGe:H, and we plan to make a similar study for the a-SiC:H alloy system. We have fabricated a large number of a-Si:H films at various deposition temperatures to vary the hydrogen content. The transport properties of these films are as good or better than those for glow-discharge-deposited films. In addition, we can reduce the hydrogen content to below 1 at. % and still produce device quality material. This has not been possible using glow-discharge deposition. We have reason to believe that these low hydrogen content films may be more stable against light-induced degradation. However, we are just beginning to investigate this phenomenon. Details of this work are in Section 3.6.4.

3.3 Metastabilities

Since the metastable changes induced by light (Staebler-Wronski effect) are such an important problem in a-Si:H (they degrade solar cell efficiency), we have devoted considerable effort to trying to understand these changes and

control them. A popular view of these metastabilities is that they involve hydrogen motion. If this were the case, then they could be minimized by reducing the amount of hydrogen in the film. However, this is not possible using glow discharge deposition without severely degrading the transport properties. Nevertheless, there is a current effort in the community to reduce the hydrogen content of the films. If hydrogen is not involved in the Staebler-Wronski effect, this could be a wasted effort. Another idea is that microstructure causes the Staebler-Wronski effect. Since it is so important to decide among these models, we are carrying out detailed experiments designed to test the validity of these ideas.

3.3.1 Modeling the Metastability

To further explore the role of hydrogen in these metastabilities, we are developing new models of metastabilities that can be tested by experiment. One model demonstrates that a distribution of energies for defect annealing or defect production is sufficient to explain all the defect production or annealing data that exist in the literature. The results of this model are the same as those of the hydrogen diffusion model. In fact, we show that it is the underlying disorder of the a-Si:H that determines the defect annealing and production behavior. Another model investigates the role of impurities or dopant atoms in metastable effects in doped films and suggests that bond rearrangement such as is observed in metastabilities in crystalline silicon is most important. This model also explores the role of charged dangling bond defects on the metastability.

3.3.1.1 Meyer-Neldel Rule

We have developed a new theory for the kinetics of annealing and production of metastable defects in a-Si:H. It is a model of defect-controlled relaxation (DCR) in which the defect relaxes without the aid of a diffusing atom. The defect may consist of more than a single atom. The result gives a stretched-exponential time dependence for defect relaxation and predicts that defect annealing or production obey a Meyer-Neldel rule (MNR). This model is contrasted with the popular hydrogen-diffusion-controlled, defect-relaxation (HCR) model. The HCR and DCR models both explain most experimental data. These models give similar results because the defect-relaxation kinetics are established by the underlying disorder of the a-Si:H. Metastable defects arising from microscopic mechanisms (such as weak bond-breaking and charge trapping) are treated in this model. Details of this work are in Section 3.6.1.

3.3.1.2 Charged Dangling Bonds in Undoped a-Si:H

Charged dangling bonds in high-quality, undoped a-Si:H have been detected in two electron spin resonance (ESR) experiments. Shimizu et al., using a combination of constant photocurrent method absorption, constant photocurrent method (CPM), and light-induced ESR (LESR), showed that many charged defects are present in undoped a-Si:H. They also found that the density of these charged defects increases with incorporation of carbon, oxygen, and nitrogen alloy constituents. We have reinterpreted LESR data of Ristein et al., to show it is the most direct evidence to date that positively charged dangling bonds (T_3^+) and negatively charged dangling bonds (T_3^-) outnumber neutral charged dangling bonds (T_3^0) in undoped a-Si:H. Therefore it seems clear that

charged dangling bonds are present in all undoped a-Si:H. Our model is that inhomogeneity, such as that produced by microvoids, can result in charged dangling bonds that outnumber the more easily observed neutral dangling bonds despite a positive, effective correlation energy. We have modeled this material inhomogeneity with potential fluctuations. The T_3^o are recombination centers and the T_3^+ and T_3^- defects are electron and hole traps, respectively. Many a-Si:H phenomena are explained and unified by these concepts. Details of this work are in Section 3.6.4.1.

3.3.1.3 Effect of Charged Dangling Bonds on Solar Cells

Most of the theoretical work on light-induced effects has concentrated on their role in the transport properties of films. To understand their role in devices, we have made a detailed calculation of the band bending in a p-i-n solar cell resulting from charged defects. Recent experimental work demonstrates that thermodynamic equilibrium statistics are an important factor in determining point-defect concentrations a-Si:H. It is well known that the concentration of charged defects in a semiconductor depends upon the E_F in equilibrium. The position-dependent E_F in the i-layer of an a-Si:H solar cell therefore results in spatially varying concentrations of dangling bonds. We apply thermodynamic equilibrium statistics to the i-layer of a-Si:H p-i-n solar cells to compare the space charge contributed by the various charged defects and to calculate the band-bending in the i-layer. We find the electric field near the n-i interface is increased considerably by the negative dangling bonds formed because of the high E_F. Point-defect profiles throughout the i-layer are discussed. Finally, we consider the importance of these results for solar cell characteristics and stability. Details of this work are in Section 3.6.4.2.

3.3.1.4 Entropy in Metastable-Charged Defect Transitions

Since there is such a close connection between metastable effects in a-Si:H and those in crystalline solids, we have been following the crystalline literature in detail. We have found many parallels between the defects in the two systems. One particular example is found in a recent experiment on crystalline silicon, in which a deep level transient spectroscopy (DLTS) signal suddenly disappears during cooling. To explain this puzzling result, we propose a new theory of entropy-driven, charge-state-controlled metastability in semiconductors. The entropy change due to metastable-defect ionization near 300 K reduces the Gibbs free energy by up to 0.1 eV. This affects equilibrium populations of the various defect charge states and configurations. Details of this work are in Section 3.6.4.3.

3.3.2 Experimental Results

During FY 1988 we developed a new method to analyze secondary photocurrent transients commonly observed in a-Si:H. This analysis gave a new powerful spectroscopy technique, permitting one to map the distribution of trapped holes in valence band tail trapped states. These safe hole traps are located roughly 0.3 to 0.5 eV above the valence band edge. A hole leaves this state by thermal emission to a level about 0.2 eV above the valence band edge. From there it tunnels to a dangling bond, where it recombines with an electron. Thus this state above the valence band edge is instrumental in controlling electron-hole recombination and in turn the photoconductivity. During

FY 1989, we used this technique to explore light-induced effects. We have been able to show that these safe hole traps convert to midgap recombination centers under light soaking. Thus we conclude that they are the source of the Staebler-Wronski effect. In addition, we have attempted to determine which of the microscopic defect models are consistent with these changes in the safe-hole-trap distributions by studying their changes during light soaking and annealing cycles. During annealing experiments above room temperature, recovery of safe hole traps converted below room temperature is much faster than the recovery of safe hole traps converted at room temperature. We conclude that the exact configuration for lattice-relaxed metastable defects originating from safe hole traps depends on the temperature at which they are formed, and we discuss how each of the three most specifically stated models can explain such results. Details of this work are in Section 3.6.4.5.

3.4 a-Si:H Device Modeling

As a result of our extensive work with post-deposition hydrogenation on various films, we have been investigating RF hydrogenation during deposition. The original idea was to change the properties of the material after deposition. However, this was not entirely successful. Nevertheless, a hydrogen-plasma reactive flush (H-plasma flush) between layers has a beneficial effect. We showed this in an investigation of a H-plasma flush between the p- and i-layer depositions in fabricating solar cells of glass/TCO/p(a-SiC:H)-i(a-Si:H)-n(a-Si:H)/metal in a single-chamber, glow-discharge deposition system. Spectral response, photoluminescence, and photovoltaic conversion efficiency measurements show that the H-plasma flush is effective in reducing the p-i interface recombination of charge carriers and in improving solar cell performance. Details of this work are in Section 3.6.4.6.

3.4.1 Device Modeling

Much of the device modeling is carried out by computer simulation of a device. Although this method is capable of high precision, the result depends on many parameters that are not well known. Rather than using a mathematically rigorous model, we concentrated on the important physics and developed simple models that give closed form solutions of the transport equations. These then can be used easily by the experimentalist to analyze his data. Procedures for analyzing p-i-n solar cells are obtained that use two closed form expressions, each containing a single, unknown i-layer transport parameter. We show that this is sufficient to describe the light intensity and temperature dependence of the current-voltage curve. In addition, the anomalous dependence of photocapacitance on light intensity and voltage is explained.

One of the predictions of this modeling is that the carrier with the larger mobility-lifetime ($\mu\tau$) product determines the photovoltaic behavior. We were able to verify this on a device by making direct measurements of the electron and hole $\mu\tau$ products on a 10-μm-thick a-Si:H p-i-n solar cell. The $\mu\tau$ products, determined from charge collection using strongly absorbed light, are $\mu\tau_h = 2.2 \times 10^{-8} cm^2/V$ and $\mu\tau_e = 3.0 \times 10^{-7} cm^2/V$, for holes and electrons, respectively. Measurements of the drift length, $l_d = \xi\tau_e + \xi\tau_h$, using uniformly absorbed light and analyzed using the uniform field model, give $l_d = 2.9 \times 10^{-7} cm^2/V/s$. These results are the first experimental evidence that the carrier with the larger $\mu\tau$ product determines the photovoltaic behavior. Details of this work are in Section 3.6.4.6.

3.5 Dangling Bond Defect Transitions

We have resolved the longstanding controversy over the anomalously large subgap optical absorption energies in n-type (1.1 eV) and p-type (1.3 eV) hydrogenated a-Si:H. Adler suggested that these large values are incompatible with a positive effective correlation energy of the dangling bond defect and a 1.7-eV band gap. Kocka proposed that dopant-defect pairing deepens each dangling bond transition energy by about 0.5 eV in doped a-Si:H. We assume no deepening due to pairing, a positive correlation energy of 0.2 eV consistent with the observation of dark ESR in undoped a-Si:H, and dangling-bond relaxation energies of 0.2 to 0.3 eV, which are indicated by previous theoretical and experimental work. The postulate of vertical optical transitions then reduces the anomaly from about 0.9 to 0.4 eV. This residual anomaly may be explained by electronic-level deepening in doped a-Si:H caused by disorder-induced potential fluctuations of 0.2 eV half-width. Details of this work are in Section 3.6.4.7.

3.5.1 Correction for Multiple Reflections in Optical Absorption

The IR absorption of a-Si:H is used routinely to yield quantitative compositional information such as the hydrogen content and film quality. However, to calculate the integrated absorbances of features in the spectra, multiple internal reflections in the film must be accounted for. In practice, this has been done either by mathematically estimating the degree of multiple reflections or by using substrates designed to eliminate the reflections, typically wedged or roughened crystalline silicon (c-Si). To determine the best method, we compare these techniques on the basis of accuracy and ease of substrate preparation.

Device quality a-Si:H was glow-discharge deposited simultaneously on a variety of c-Si substrates: double-polished, single-polished (rough side), single-polished (polished side), roughened, and wedged. Correction for multiple reflections in the spectrum of a-Si:H on a double-polished substrate gives the same absorbance as that on a wedged substrate. This confirms the accuracy of the correction for multiple reflections and shows it is unnecessary to prepare wedged substrates. The transmission spectra of the Si-H peak at 630 cm^{-1} are identical for all non-wedged substrates regardless of surface roughness. Thus, there is no advantage to deliberately roughened substrates and no need for double-polished substrates. Details of this work are in Section 3.6.4.8.

3.5.2 Limitations of the Integrated Sub-Band-Gap Absorption for Determining the Density of Defects in a-Si:H

Photothermal deflection spectroscopy (PDS) and CPM are routine, easy-to-use techniques for measurement of small optical absorption coefficients in thin films. They are used to determine the Urbach absorption edge and the density of midgap states. An investigation of the commonly used procedure for calculating the density of states in the gap from optical absorption data shows that it is used improperly. We find that, in general, the proportionality coefficient between the density of states and the integrated sub-band-gap absorption is not unique. The sum rule has been misused since integration of the excess subgap absorption is terminated either at a fixed energy or at an energy which does not include all optical transitions to the conduction band.

We estimate the errors arising from this procedure can be as large as a factor of 10. Details of this work are in Section 3.6.4.9.

3.5.3 Doping and Hydrogenation by Ion Implantation of a-Si:H

The feasibility of using ion implantation for doping a-Si:H films has been demonstrated. However, further improvements of the properties of ion-implantation-doped a-Si:H and a better understanding of the doping process are needed. To discriminate between the effects of doping and the effects of bombardment damage introduced by the implantation process, we have compared the properties of our boron-doped samples with silicon-implanted samples. It is known that samples doped by ion implantation at concentrations less than 1020 at./cm^3 exhibit doping efficiencies lower than those of samples doped in the gas phase during film growth. We show experimental results that indicate two possible mechanisms that could lead to poor electrical activity: the implantation-induced disorder may introduce compensating centers for the p-type dopants or a high electrically inactive fraction of the dopants due to either interstitial positioning or three-fold coordination. Details of this work are in Section 3.6.4.10.

3.6 Experimental and Theoretical Details

3.6.1 Defect Relaxation in a-Si:H Stretched Exponentials, MNR, and Staebler-Wronski Effect

Annealing of metastable defects (MSD) usually follows a stretched exponential time dependence and obeys an MNR relating the annealing activation energy E_a to the attempt frequency ν. These relations hold for the Staebler-Wronski effect, quenched-in, bias-stress induced, and defects in solar cells. Such behavior is a good test of the validity of models of MSDs. Jackson [1], assuming a hydrogen-diffusion-controlled defect relaxation (HCR), derived expressions for production and annealing kinetics. He obtained both stretched exponential relaxation and the MNR, explaining a large number of experiments. He argued that this proved that hydrogen was involved in MSDs. In addition, he showed the connection between the MNR and multiple-trapping transport. Using a model of DCR [2], we derived similar annealing kinetics without the assumption that hydrogen diffusion was involved in the defect reactions. The weak-bond breaking [3] without hydrogen involvement and the charged dangling bond [4] models are microscopic mechanisms that fit the formalism. Since both HCR and DCR models explain the central features of annealing, they are not unique and can be distinguished.

Figure 3-1 [2] shows E_a as a function of the logarithm of ν for annealing of most of the metastable effects that have been observed. The data are determined from the annealing time constant $\tau_a = \nu^{-1} \exp(E_a/k_BT)$. It is remarkable that all the experimental annealing energies (0.3 eV-1.8 eV), from a wide variety of measurements on doped and undoped a-Si:H, scatter about a straight line. This type of plot shows that the data obey the MNR, implying a common feature to all the data.

Since both the HCR and DCR models explain the data in Figure 3-1, one needs further experimental tests to distinguish between the models. A central feature in both models is the exponential distribution of activation barriers encountered during defect production or annealing. It is these exponential distributions that produce the stretched exponential annealing and the MNR. However, the form of the distributions are different. The defect distribution in the HCR model is $N_d = N_1 \exp[-E/E_c]$, and in the DCR model it is $N_d = N_2 \exp[+E/E_c]$. In both cases, disorder produces the exponential distribution of activation barriers.

These different distributions have important consequences. In the HCR model, the many low barriers, with faster transition rate, anneal first. Because of their larger numbers they dominate the observed decay. The few high barriers, with the slower transition rate, anneal later and are difficult to observe. In the DCR model, the few low barriers anneal first. The many high barriers, with the slower transition rate, anneal later. Because of their larger numbers, they dominate the observed decay.

Both models produce a stretched exponential for the number N(t) of relaxing defects. It is $N(t) = N(0) \exp(-[t/\tau_a]^{\alpha})$, where $\alpha = k_BT/E_c$ and E_c is a characteristic energy determined from the slope of the line in Figure 3-1. The different barrier height distributions produce slightly different annealing E_a expressions. In the DCR model [2], it is

$$E_a = E_c \ln(\nu) + E_max + E_c \ln([1-\alpha]/\omega), \qquad (3\text{-}1)$$

where ω is a lattice vibration frequency and E_max is maximum barrier height surmounted for a degradation time t_d. A crude estimate is $E_max = k_BT \ln(\nu t_d)$. Thus, E_a will increase with t_d. The corresponding MNR for the HCR model is [1]

$$E_a = E_c \ln(\nu) + E_c \ln(\alpha/AD_o o), \qquad (3\text{-}2)$$

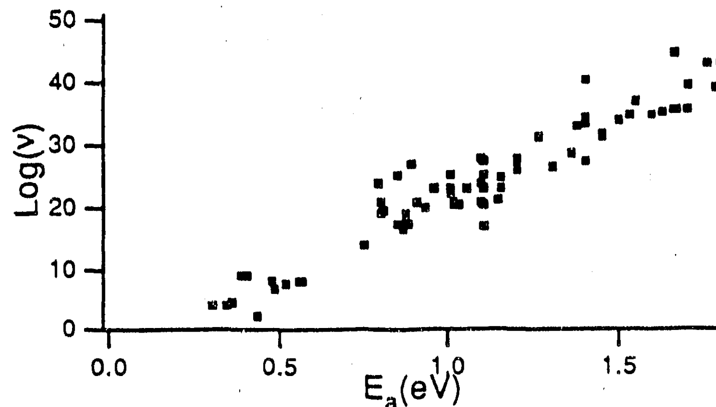

Figure 3-1. MNR behavior for a-Si:H

where A is a constant and D_{oo} is a microscopic hydrogen diffusion coefficient. This expression is of the same form as Eq. 3-1 and will equally well explain the data in Figure 3-1. However, it does not contain a term equivalent to $E_{m}ax$ so that E_a does not depend on degradation time. Equations 3-1 and 3-2 are both expressions of the MNR relating E_a to ν.

These two models can be distinguished experimentally by varying the amount of degradation to change the relative populations of the low and high barriers. The most direct way to view this is to form the function $S(t) = t\delta N(t)/\delta t$, which is the distribution of annealing defects with a maximum at $t = \tau_a$. The plot of S(t) in Figure 3-2 shows that the DCR distribution moves to longer time and hence higher energy [5] for longer t_d. The HCR distribution only increases in size because its τ_a does not change with t_d.

The experimental situation favors the DCR model. Guha et al. [6] show that degradation at higher temperature produces harder-to-anneal defects. This implies that degradation is thermally activated. Since then, various workers have shown that longer degradation times at a fixed temperature produce recombination center [7], spin [8], solar cell [9], and conductivity [10] changes that are harder to anneal. The data of Deng and Fritzsche [10] for the change in the dark conductivity after light soaking in Figure 3-3 show that the annealing time increase with longer degradation time. The number of defects also increases as shown by the larger conductivity changes. The distribution of annealing times for conductivity relaxation can be found from S(t), shown in Figure 3-4.

Figure 3-4 shows that increasing degradation time changes S(t) at longer rather than shorter annealing times. If we assume that S(t) is proportional to the energy distribution of annealing defects, then these data show that the number of defects with higher energy increases with longer degradation time, but the number of low-energy defects is saturated at short degradation time. Examples of this behavior can be found in Ref. 9, where the actual number of defects was determined from transient capacitance.

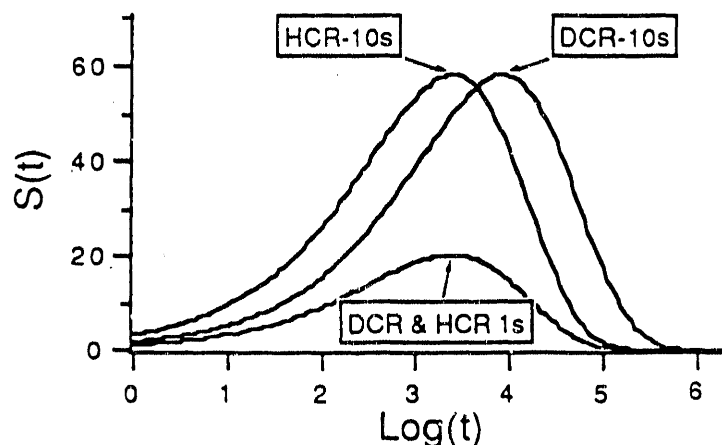

Figure 3-2. Comparisons of the distribution of annealing times for the HCR and DCR models for t_d=1 s and 100 s. The N(0) was calculated using the stretched exponential form for degradation.

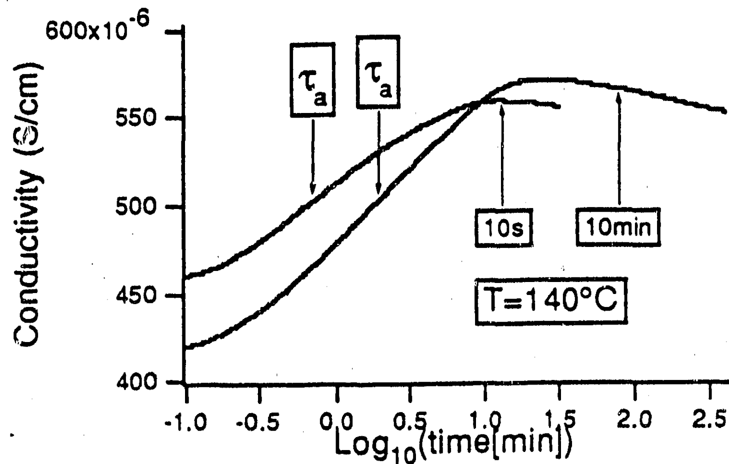

Figure 3-3. Data for a lightly phosphorous-doped sample following 10 s and 10 min degradations. Data from Fig. 3-5, Ref. 10. The τ_a are determined from the maximum of the plots in Fig. 3-4.

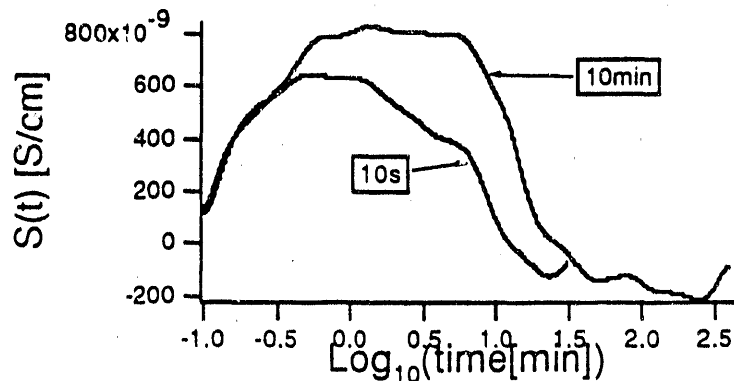

Figure 3-4. Data in Fig. 3-3 processed to form $S(t) = t\delta\,(\text{conductivity})/\delta t$

Two different models to explain the annealing kinetics of MSDs were shown to give substantially the same results. The reason they give the same form of annealing is that both distributions arise from the fundamental disorder of a-Si:H. The models can be distinguished by varying the degradation time.

3.6.2. Characterization of Microvoids in Device Quality, Hydrogenated a-Si by Small Angle X-ray Scattering and IR Measurements

The size, shape, and number density of microvoids in device quality glow-discharge-deposited hydrogenated a-Si has been obtained by SAXS. By combining the SAXS results with IR measurements, we deduce that the interior surfaces of these microvoids are largely unhydrogenated, containing at most 4-9 bonded hydrogen atoms. We suggest that these hydrogen atoms are the clustered hydrogen atoms previously detected by multiple-quantum nuclear magnetic resonance (NMR).

Microstructure in hydrogenated a-Si:H has been extensively studied in the past few years. Probes of microstructure include multiple-quantum NMR [11], calorimetry experiments involving H_2 [12], IR spectroscopy [13-15], positron annihilation spectroscopy [16], hydrogen evolution experiments [17], scanning electron microscopy (SEM) [18], and small angle scattering [19-21]. All of these techniques suggest or demonstrate the existence of microvoids in non-device-quality a-Si:H. However, it is unclear whether device quality a-Si:H has microvoids or can be considered a homogeneous material. Evidence to date on device quality material is at best indirect and conflicting. Calorimetry experiments indirectly suggest 10- to 40-Å-diameter microvoids, SEM suggests columnar microstructure, and multiple-quantum NMR indicates clustered hydrogen. Nevertheless, device quality a-Si:H shows no low-temperature hydrogen evolution peak indicative of a heterogeneous microstructure [17], and previous SAXS measurements [20-21] showed no detectable scattering, suggesting a homogeneous medium. Earlier, we used SAXS [22-23] to measure microvoids in a-SiC:H and in a-Si:H.

In the present study, we extended and quantified preliminary results reported earlier [22-23] on device quality, glow discharge a-Si:H. We find a small but distinct SAXS signal indicative of microvoids in every device quality, glow discharge sample. We analyzed these data to obtain the microvoid size, shape, and number density. By combining the SAXS results with IR measurements, we deduced that the interior surfaces of the microvoids are largely unhydrogenated, containing at most 4 to 9 bonded hydrogen atoms. We suggest that these hydrogen atoms are one source of clustered hydrogen atoms previously detected by multiple-quantum NMR. Finally, a comparison of microvoid number densities with gap state densities indicated that the unhydrogenated bonds must reconstruct to reduce the number of dangling bonds to the levels observed in device quality a-Si:H.

The SERI a-Si:H samples used in this study were deposited on the anode of an RF (13.56-MHz) glow discharge reactor using device quality conditions [24] (i.e., substrate temperature of 250°C, flow rate of 70 cm^3/min at standard temperature and pressure (SCCM) SiH_4, chamber pressure of 700 mT, and RF power 30 mW/cm^2) in a cross-flow geometry. For each sample, two sequential depositions were made. The first was made onto 10-μm-thick, iron-free aluminum foil and a single-polished c-Si substrate. After deposition, the foil was cut into eight strips and stacked for the SAXS measurements. No attempt was made to account for the shape of the radial distribution function in this scattering regime, since its shape for a material without microvoids is unknown. IR measurements on the sample deposited on c-Si determined both the total bonded-hydrogen content from the Si-H bending mode (H_630) and the integrated intensities of the Si-H stretch modes centered at 2070 cm^{-1} [I(2070)] and 2000 cm^{-1} [I(2000)]. I(2070) has been linked to microvoids [13,15,22,23, 25,26,27,28]. The second deposition on 7059 glass was used for PDS measurements of the midgap state density [29]. Film thicknesses were typically 2-4 μm. We also obtained a device quality a-Si:H sample from Dr. S. Guha of Energy Conversion Devices, Inc. (ECD) for SAXS analysis. To demonstrate the quality of the a-Si:H material used in this study, the efficiencies of single-junction solar cells, fabricated using identically prepared material as the intrinsic layer, are greater than 10% for both the SERI [24] and ECD [30] samples under AM 1 illumination.

In Figure 3-5, we show Guinier plots [31] for three SERI samples and the ECD sample, where I(h) is the SAXS signal from the a-Si:H film, $h \equiv (2\pi/2)(2\theta)$ is

the scattering parameter, λ = 1.54 Å, and 2θ is the scattering angle. (The data reduction procedure used to obtain I(h) is discussed elsewhere [23].) Since in a Guinier approximation $I(h) = I_o \exp(-R_g^2 h^2/3)$, the slope of a linear fit in such a plot yields the radius of gyration R_g, which characterizes the size of the electron density fluctuations. Previous SAXS publications [32-33] have argued that the observed signals were due to microvoids and not low-density, hydrogen-rich tissue-like material; we agree with this interpretation and have also addressed this issue in a SAXS study of a-SiC:H [22,23]. To explore the shape of the microvoids, SAXS scans were made on two of the samples tilted at an angle of 45° with respect to the beam axis and compared to the non-tilted data. The SAXS curves were identical, suggesting that the microvoids are either spherical or randomly oriented [31]. If a spherical shape is assumed, the microvoid radii are $(5/3)^{1/2} R_g$ ~4.4 Å for the SERI samples and ~5.0 Å for the ECD sample. For a randomly oriented ellipsoid, with the ratio of major to minor axes equal to 2, values of a (6.2 Å, 5.1 Å) and b (3.1 Å, 2.6 Å) are obtained for "cigar-like" and "pancake-like" microvoids, respectively, with R_g = 3.4 Å [34].

To obtain the microvoid number density, we used the formula $\int hI(h)dh = K(\Delta p)^2, \nu_f(1-\nu_f)$ [23], where the left-hand side is the integrated SAXS signal appropriate for a line source, Δp is the difference in electron densities for our two phase material, and ν_f is the microvoid volume fraction. To obtain the constant K, we determined the density deficiency of a sample deposited at 125°C (ν_f = 0.06) by the flotation method [35] and equated this density deficiency to the integrated SAXS intensity of that sample [23,36]. Thus, the ν_f values of the present samples can be determined [37]. In addition, using these values of ν_f, we calculated the total number of missing atoms per microvoid and the resultant microvoid number densities [23]. These results are presented in Table 3-1, where both spherical and ellipsoidal (a = 2b, numbers in parentheses) microvoid shapes are assumed [38]. The microvoid densities lie in the low to mid $10^{19}/cm^3$ range.

It is not clear why SAXS signals were not obtained previously [20-21] from device quality a-Si:H. We suggest that the small scattering signal from the iron-free aluminum foil, the low background counting rate (0.19-0.20 ct/s), the high efficiency of the x-ray detector in the 8 keV (copper anode) region, and the use of long counting times (~8 h/scan) enable the present small SAXS signals to be detected.

Several comments can be made from correlations between the SAXS and IR results. First, we have calculated the total hydrogen contents of the SERI films from IR spectroscopy to be 8-9 at.%, or 4.0-4.5 x 10^{21} H/cm^3. The data analysis followed that of Brodsky et al. [39], with the proportionality constant [40] of the Si-H 630/cm bending mode, $A_W = 1.6 \times 10^{-19}/cm^2$. Previous measurements of I(2070) indicated microvoids [13,15,22,25,26,27,28], but did not quantify how much hydrogen was bonded in this stretch mode. We now quantify the number of hydrogen atoms bonded in the Si-H 2070/cm (H_{2070}) shifted stretch mode, and assume that they are bonded on the surfaces of the presently discussed microvoids because of the linear relationship between H_{2070} and ν_f presented elsewhere [23, 41]. Figure 3-6 shows a deconvolution which is typical of all our samples, where the complete Si-H stretch mode is deconvoluted into two Gaussians of variable peak position and intensity but of equal full width at half maximum (FWHM); the best fit (χ^2 indicator) was obtained with

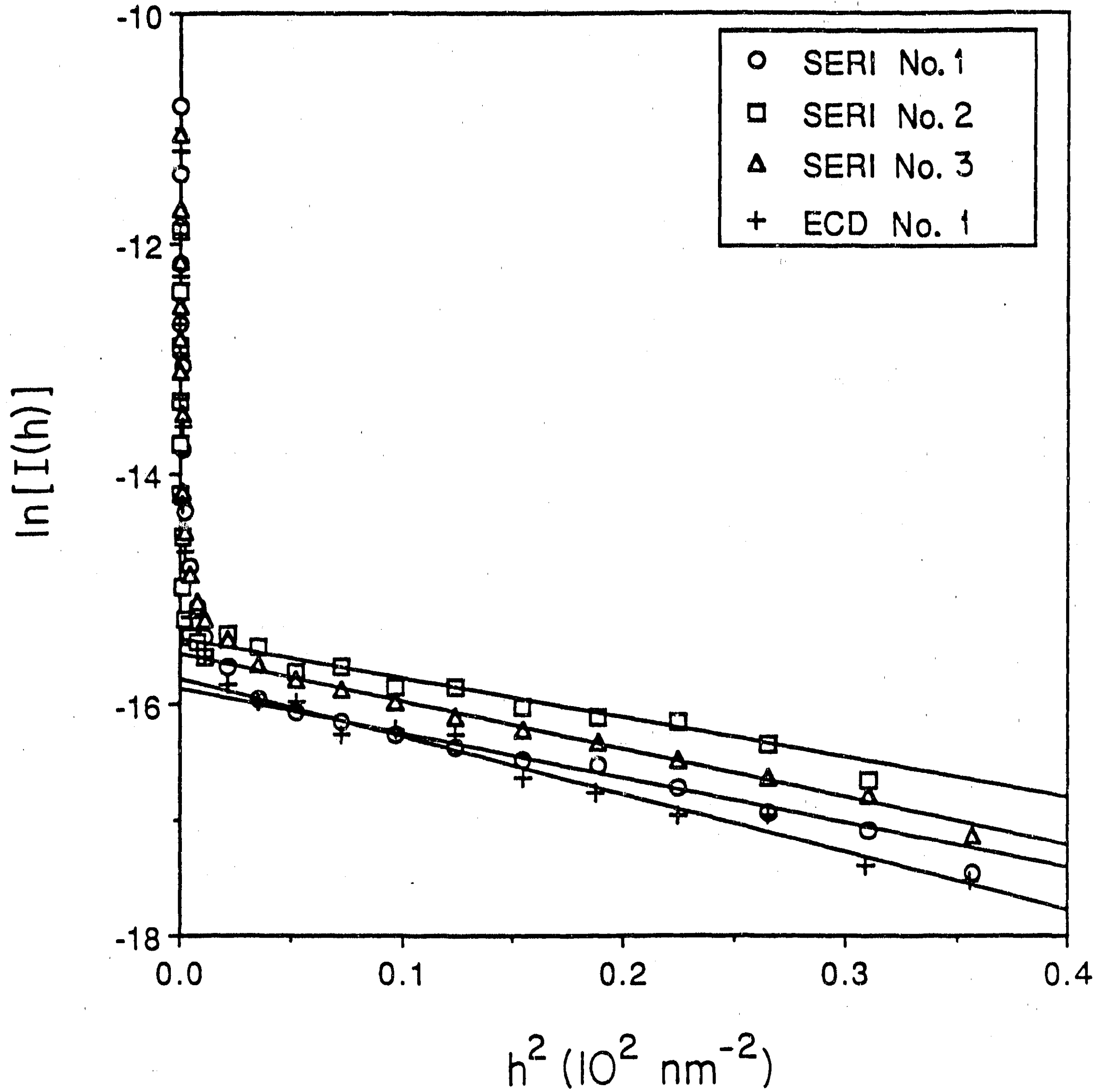

Figure 3-5. Guinier plots for the device quality a-Si:H films. The open symbols (□,Δ,o) represent SAXS results for the three SERI samples, while the symbol (+) represents SAXS data for the ECD sample.

Table 3-1. SAXS Results

Film	R_g	ν_f	Total Number Missing Atoms/cm^3	Number Missing Atoms/Void	Microvoid Number Density (/cm^3)
SERI #1	3.30	0.015	7.3×10^{20}	16 (12)	4.5×10^{19} (6.1×10^{19})
SERI #2	3.41	0.012	6.0×10^{20}	18 (14)	3.3×10^{19} (4.3×10^{19})
SERI #3	3.53	0.014	7.0×10^{20}	20 (16)	3.5×10^{19} (4.4×10^{19})
ECD #1	3.89	0.010	5.0×10^{20}	26 (20)	1.9×10^{19} (2.5×10^{19})

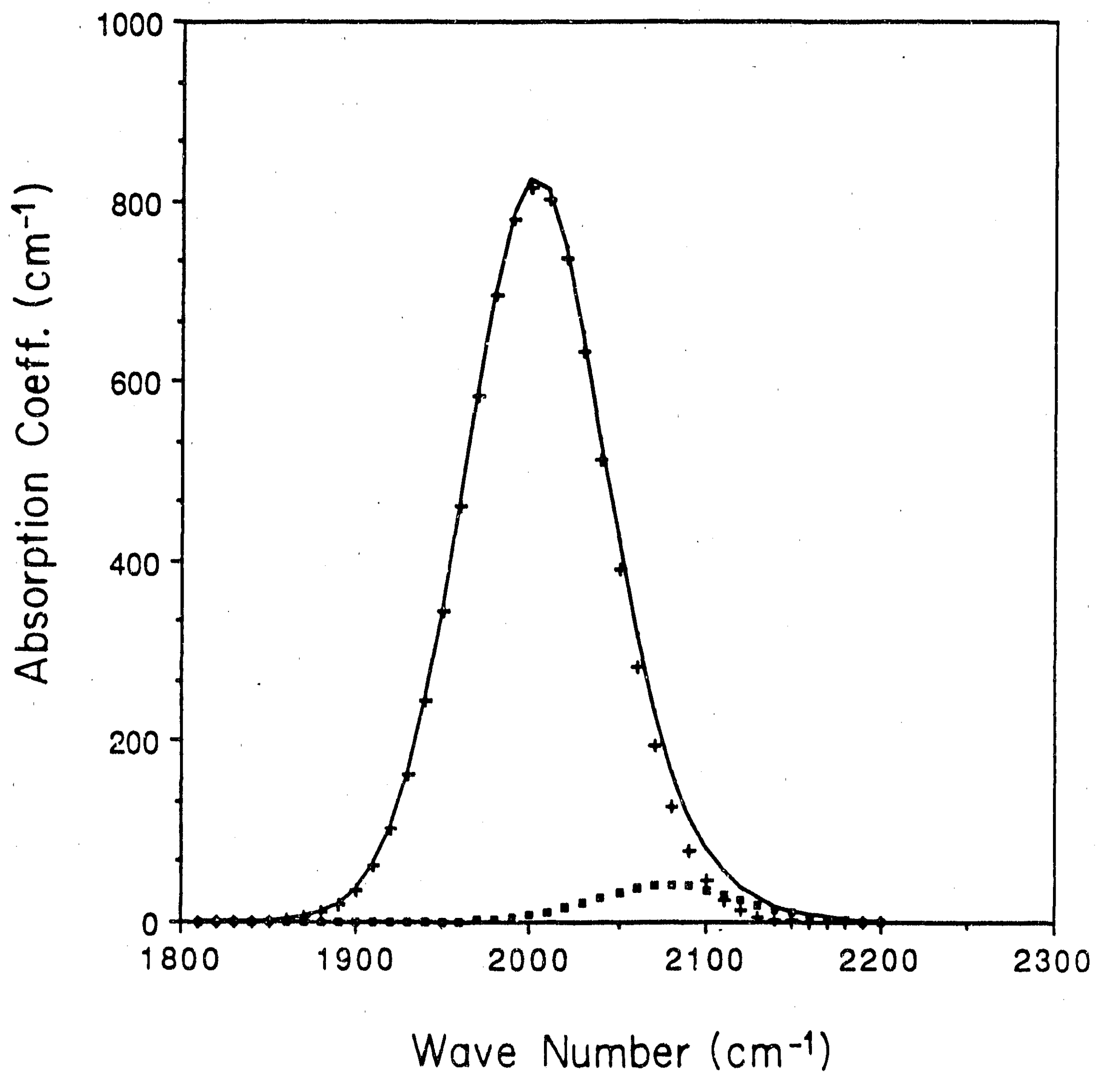

Figure 3-6. Typical IR deconvolution of the Si-H stretch mode (solid line) into components centered at 2000/cm (+) and ~2070/cm (□) wave numbers, respectively. Equal FWHMs were assumed for the two peaks.

the frequency of the small peak at ~2070-2080/cm. This peak position is consistent with the fact that the complete IR scans of these samples showed a very small absorption peak in the 845-890/cm range, suggesting that I(2070) may be due at least in part to the SiH_2 [or $(SiH_2)_n$] bonding configuration [42]. Since neither the FWHM nor the proportionality constant A_s for I(2070) has been firmly established [40,43], assumptions are made to obtain H_{2070}. We estimate H_{2070} by three methods. In the first, we assume equal FWHMs and identical proportionality constants A_s for the two peaks shown in Figure 3-6. For this method, $H_{2070} = (I(2070)/[I(2070) + I(2000)I]H_{630}$. The second method is identical to the first, except that we allow the FWHM of the 2070/cm mode to be narrowed from ~85/cm to ~70/cm, consistent with the narrowing of this mode observed [44] in lower substrate temperature deposited a-Si:H. Finally, for the third method we calculate $H_{2070} = I(2070)A_s$, where $A_s = 1.4 \times 10^{20}/cm^2$ is the average proportionality constant for the Si-H 2070/cm mode [40,43,45]. We thus obtain H_{2070} in the range 1.5-3.5 x $10^{20}/cm^3$ for the three SERI samples, or < 0.7 at.% H. When we now divide these numbers by the respective microvoid number densities for each film, and average the results of the three methods, the number of bonded hydrogen atoms per microvoid becomes 5 to 9 if spherical microvoids are assumed and 4 to 7 if (unoriented) ellipsoidal (a = 2b) microvoids are assumed. These numbers are in excellent agreement with the number of clustered hydrogen atoms found using the multiple quantum NMR technique [11], and they support the correlation found [14] between clustered hydrogen and I(2070). Therefore, we suggest that one source of 5-8 clustered hydrogen atoms detected by multiple-quantum NMR is found on those bonded on the surfaces of microvoids of R_g~3.4 Å, as detected here by SAXS.

Secondly, we constructed a ball-and-stick model of a microvoid of ~20 missing atoms and estimated that the number of surface atoms having bonds which protrude into the microvoid is ~1.25 times the number of atoms missing in a microvoid. Therefore, within the framework of this model, the number of surface sites on a microvoid available for hydrogen bonding (15-25) in a-Si:H is significantly larger than the number of bonded hydrogen atoms estimated to sit on a typical microvoid surface (5-9). This shows that these microvoid surfaces are not heavily hydrogenated. Note that since at least some of H_{2070} is due to dihydride bonding, the fraction of the surface bonds that are hydrogenated is even smaller than would be indicated by a simple ratio of the above numbers.

Third, PDS measurements of the number of midgap states in these samples gave <5 x $10^{15}/cm^3$ midgap states. Based on published correlations between PDS and ESR data, we deduced that our samples contain ~10^{-4} dangling bonds per microvoid. It was thus unclear whether the dangling bonds observed in device quality a-Si:H were even associated with these microvoids. In any case, these results clearly showed that bonds on the microvoid surfaces that were unhydrogenated must reconstruct to reduce the number of dangling bonds to the levels observed here. Dangling bonds have been postulated to reconstruct during H_2 evolution experiments [26].

Finally, we found that the hydrogen bonded in the 2000/cm mode cannot all be bonded on the microvoid surfaces. From the previous discussion, $H_{2000} = H_{630} - H_{2070}$ ~3.8 x $10^{21}cm^{-3}$. This means that, on the average, 60-100 of these hydrogen atoms must be bonded on each microvoid surface. This is unreasonable not only because of the lack of surface sites needed to accommodate these hydrogen atoms, but also because the multiple-quantum NMR technique

observed clusters of at most 5-8 hydrogen atoms in device quality a-Si:H. In addition, calculations [46] predict that these microvoids are too large to produce enough screening to shift the Si-H frequency from ~2080/cm, observed for both SiH and SiH_2 bonds on crystalline silicon surfaces [13], down to 2000/cm observed in device quality a-Si:H. On the other hand, part of H_{2000} may contribute to the proton NMR clustered phase (5-8 atoms) [47] but be bonded in microvoids smaller than the ones reported here. Such small microvoids (i.e., multivacancies) would be small enough such that the electrostatic screening would be effective and at the same time, from scattering-angle limitations of the SAXS apparatus, produce a negligibly small SAXS signal. We estimate that the integrated SAXS signal due to multivacancies would be at most 10% of the total SAXS signals we observed.

3.6.3 Light-Induced Metastable Defects in Rehydrogenated and Post-Hydrogenated a-Si:H

Hydrogenated a-Si:H exhibits an increase in defects after prolonged illumination and a reduction of these defects after thermal annealing. This metastable, light-induced effect was first discovered by Staebler and Wronski [48], who observed that the photo- and dark conductivities of an undoped a-Si:H film both decreased after optical exposure. The detailed mechanism of the effect is not completely understood at present. It is generally believed that this effect can be observed in all a-Si:H films regardless of the deposition method. However, recently there have been many reports that showed that rehydrogenation or post-hydrogenation of a-Si:H using an atomic hydrogen source reduced the Staebler-Wronski effect in a-Si:H [49-53]. The objective of this study was a systematic investigation of the photostability properties of a variety of rehydrogenated and post-hydrogenated a-Si:H films.

All films used were undoped, a-Si:H, or a-Si:H:F films, less than 800 nm thick, deposited on Corning 7059 glass substrates. All the depositions were done in a load-locked, single-chamber, RF glow discharge deposition system with a base vacuum level of less than 1×10^{-8} torr and a leak rate of 2×10^{-5} SCCM. The impurity levels in these samples were much lower than those that might influence the photostability behavior of a-Si:H [54]. State-of-the-art a-Si:H films and photovoltaic solar cells, with efficiencies around 10%, have been deposited in this system. Rehydrogenated a-Si:H films were obtained by first reducing the hydrogen content of glow-discharge-deposited a-Si:H by heating them to above 540°C and then rehydrogenating them with a Kaufman ion-beam source [49,55]. (Typical ion-beam-hydrogenation conditions are described in Ref. 55.) An important advantage of using rehydrogenated a-Si:H is that the effects of ion-beam hydrogenation can be studied without the complications of high-impurity levels and poor microstructures typically associated with physical-vapor-deposited (PVD) or high-temperature chemical-vapor-deposited (CVD) a-Si:H.

In addition to ion-beam hydrogenation, we have also studied RF hydrogenation of a-Si:H films by using a pure-hydrogen-gas glow discharge in the RF glow discharge deposition system. We found that the RF hydrogenation has a much higher etch rate, up to 5 nm/min, and a slower hydrogenation rate than the Kaufman ion-beam hydrogenation method. We were unable to RF-hydrogenate a fully dehydrogenated a-Si film to an a-Si:H film with more than 5 at.% hydrogen. The RF-hydrogenated films used in this study were obtained by post-hydrogenating as-deposited a-Si:H (about 9 at.% hydrogen and an optical band

gap of 1.75 eV) to about 10 at.% hydrogen and an optical band gap of 1.80 eV. To get more uniformly distributed post-hydrogenated hydrogen content, we deposited a-Si:H films using a periodic-etching-deposition (PED)-CVD method [56]. The RF-generated hydrogen plasma both etches and hydrogenates the deposited a-Si:H. In this method, the RF glow discharge deposition of the a-Si:H film is interrupted about every 30 nm for RF hydrogenation. The resulting films have about the same hydrogen content, optical band gap, and dark- and photoconductivities as films obtained by continuous deposition. Since there have been reports of improved photostability due to fluorine incorporation in a-Si:H [57-58], we have also studied the photostability properties of the a-Si:H:F films deposited by this PED-CVD method using a XeF_2 etch gas as described in Ref. 56. Both a-Si:H:F films deposited by the PED-CVD method of cycling the SiH_4 flow and by the constant deposition method of having a constant SiH_4 and XeF_2 flows were used in our photostability study. All samples used in our photostability study were either as-deposited or thermally annealed for at least one hour at 150°C. Rehydrogenated or post-hydrogenated films were also thermally annealed after RF or ion-beam hydrogenation.

To study the illumination-induced degradations in photoconductivities, we first measured the AM1 photo- and dark conductivities of the samples in the as-deposited or annealed state. The samples were then illuminated under AM1 light for about 20 hours. The absolute changes in photoconductivity plotted against the initial photoconductivity values for the samples we studied are shown in Figure 3-7. All samples degraded after illumination; the amount of degradation depended on the initial photoconductivity value. The relative changes in photoconductivity plotted against the initial photoconductivity values are shown in Figure 3-8. It is obvious that the relative degradation in photoconductivity decreases rapidly once the initial photoconductivity value is below about 3×10^{-5} s/cm, regardless of the sample preparation method. It is also interesting to note that, if the initial photoconductivity is below 1×10^{-5} s/cm, the relative degradation in photoconductivity is so small that it gives the impression that the sample has little or no Staebler-Wronski effect. Since the samples we studied all had similar impurity levels and similar optical band gaps (between 1.70 and 1.85 eV), the differences in photoconductivity values before degradation were mainly due to the differences in the defect densities in the as-deposited or annealed materials. Materials with higher initial defect densities have less absolute and relative degradation in the photoconductivity values after illumination. This decrease in the relative degradation of the photoconductivity is obviously not a reduction of the Staebler-Wronski effect, nor is it due to any improvements of the intrinsic properties of the material. Actually, it is an indication of poor material quality. To prove this point more conclusively, we must measure more directly the defect-state densities of the materials and compare them with the relative degradations. We have measured the defect-state densities of some of our samples using a sub-band-gap absorption measurement technique called PDS [59]. However, the PDS measurements are surface sensitive, and the surface properties of the samples used in this study varied greatly due to the different preparation methods. We were unable to get meaningful results out of the PDS measurements. Another sub-band-gap absorption measurement method CPM [60] can measure defect-state densities with less sensitivity to the surface than that of PDS. We have started these measurements recently.

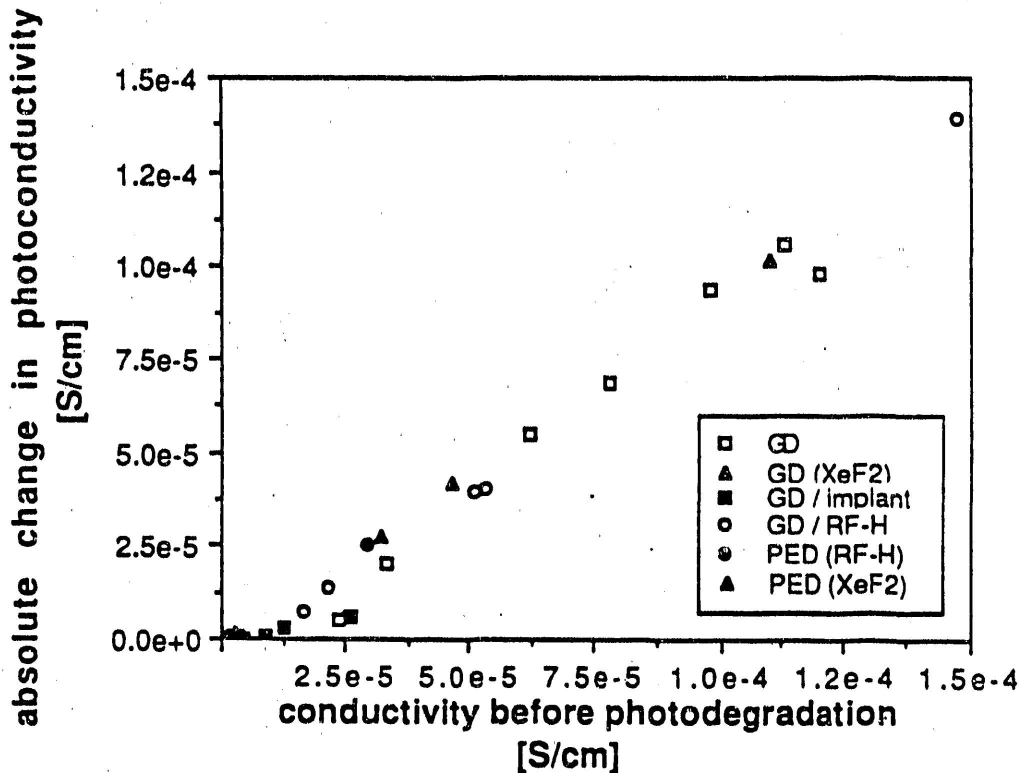

Figure 3-7. The absolute changes in photoconductivity after light-induced degradation plotted against the initial photo-conductivity values. Samples studied include glow-discharge-deposited a-Si:H (GD), glow-discharge-deposited a-Si:H:F (GD(XeF_2)) using a constant flow of a SiH_4 and XeF_2 gas mixture, ion-beam-dehydrogenated a-Si:H (GD/implant), RF-hydrogen-plasma-posthydrogenated a-Si:H (GD/RF-H), PED-CVD-deposited a-Si:H (PED(RF-H)) using RF hydrogen plasma for the etching cycles, and PED-CVD-deposited a-Si:H:F (PED(XeF_2)) using XeF_2 gas for the etching cycles.

We have studied the light-induced degradation of photoconductivity in a variety of undoped a-Si:H and a-Si:H:F samples depcsited in the same chamber. We have found that their light-induced degradation properties follow the same dependence on the initial photoconductivity values regardless of the deposition method. We have also found, indirectly through photoconductivity, that the absolute and relative degradations in photoconductivity values seem to decrease with increasing initial defect-state densities. We believe many of the reported observations of reductions of the Staebler-Wronski effect are actually due to poor material qualities.

3.6.4 Material Properties of Intrinsic a-Si:H Films Deposited by the Hot Wire Technique

In this section, we will present preliminary results on the properties of hydrogenated a-Si:H films deposited by the hot wire technique. In this deposition process, silane gas is thermally decomposed on a high-temperature

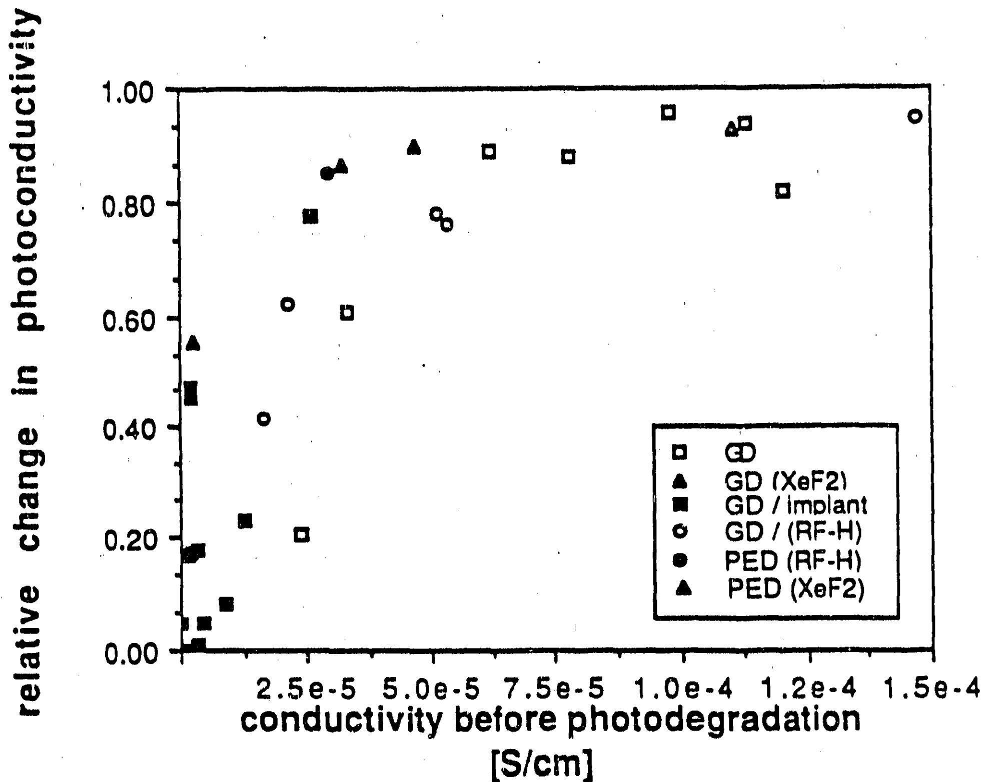

Figure 3-8. The relative changes in photoconductivity after degradation plotted against the initial photoconductivity values for the same samples shown in Fig. 3-7.

filament, which is followed by subsequent evaporation of atomic silicon and hydrogen, enabling a-Si:H film growth on a heated substrate. This technique was first reported by Matsumura et al. [61-66], and was subsequently studied extensively by Doyle et al. [67]. We are currently exploring this technique for two reasons. First, previous results suggest that growth rates higher than those obtained using the glow discharge technique can be obtained without a significant reduction in film properties. We would like to quantify and extend those results. Secondly, we believe that this technique may have particular advantages in the production of a-Si:H-based alloys. Excellent film properties have already been reported for a-SiGe:H [64], and we plan to make a similar study for the a-SiC:H alloy system.

The hot wire source consists of a single .020-inch-diameter tungsten wire attached to a high-current, high-vacuum feedthrough. This is mounted on an ultra-high vacuum, stainless-steel conflat deposition system that is pumped by a Balzers Turbo pump and has a base pressure of ~5 x 10^{-8} torr. The substrate is externally heated by a disc-type resistance heater. To provide the a-Si:H deposition conditions, we combined certain aspects of the work of Matsumura et al. [61-66] and of Doyle et al. [67] (i.e., T_s = 100°-500°C, filament current ~ 12 amps, SiH_4 flow rate of 20 SCCM, and a chamber pressure (7 mT) low enough to minimize gas collisions before the particles reached the substrate). In this preliminary study, we fixed the filament current, SiH_4 flow rate, and chamber pressure, and examined the a-Si:H film quality as a function of substrate temperature. The deposition procedure consisted of heating the filament to its desired temperature in vacuum, introducing the SiH_4 to make the

film, turning off the SiH_4, and finally letting the filament cool down, again in vacuum. SIMS measurements of the tungsten content on selected samples has indicated the need of a shutter. To date, approximately 20 a-Si:H films have been deposited and analyzed.

Figure 3-9 shows the amount of hydrogen in our films plotted versus the substrate temperature. The hydrogen content was obtained from the integrated intensity of the SiH 630/cm IR mode, using the analysis of Brodsky et al. [68], with $A_w=1.6 \times 10^{19} cm^{2}$. To date, we have succeeded in varying the hydrogen content from ~15 at.% to < 1 at.%. Data for glow discharge a-Si:H films made at SERI using substrate temperatures 40°C $<T_s<$250°C are shown for comparison. The substrate temperatures quoted in the figure are the values measured by an external thermocouple; we estimate that the filament may heat the substrate by as much as 50°C.

In Figures 3-10 and 3-11, we present an analysis of the hydrogen bonding in our films as a function of the total hydrogen content as determined previously. In particular, the SiH stretch mode has been deconvoluted into two Gaussian modes located at ~2000/cm and 2070/cm, respectively, assuming that the two peaks have identical half-widths. Also shown are the data for the previously mentioned series of glow discharge a-Si:H films. As can be seen, the bonding in our hot wire films is similar to that in the glow discharge samples, with the possible exception that the higher hydrogen content hot wire samples may contain more 2000/cm bonded hydrogen. More hot wire samples deposited at lower substrate temperatures are needed to confirm this trend.

In Figures 3-12 and 3-13, we present photo-(σ_L) and dark (σ_D) conductivity data on our samples, again as a function of the total hydrogen content. In Figure 3-12 we present the actual data, and in Figure 3-13 we show the σ_L/σ_D ratio. Several comments can be made concerning the data. First, the hot wire films have better electronic properties than do the glow discharge films at higher hydrogen contents (i.e., the values of σ_L remain high as the hydrogen content is increased, while the σ_L values for glow discharge films containing similar amounts of hydrogen are significantly reduced). Secondly, the values of σ_L and σ_D for the hot wire films may be significantly influenced by tungsten contamination. In particular, selected films with $\sigma_D \sigma 10^{-9}$ exhibit varying degrees of tungsten contamination, while two films with $\sigma_D \sim 10^{-11}$ do not show this contamination. Excluding the problem of tungsten contamination, a comparison of film properties of device quality glow discharge a-Si:H films with hot wire a-Si:H films of similar hydrogen content suggests that the two types of films may be similar. In addition to the IR and conductivity behavior, measurements of the optical band gap (~1.72 eV), Urbach edge (50 mV), midgap state density (2-4 x $10^{15} cm^{-3}$) by photo-thermal deflection spectroscopy, and the full width at half maximum of the Raman Si-Si transverse optical mode (62/cm) on hot wire films containing 7-9 at.% hydrogen all suggest high-quality material.

We conclude this study with some random comments. First, for the conditions used in this study, one filament lasted 5-6 depositions and needed to be changed only because the filament became brittle upon heating and broke when we tried to clean excess a-Si:H off the support rod. In addition, we find that the first film made with a new filament shows more tungsten contamination than the subsequent films, which is reflected in higher values for σ_D and sometimes σ_L. Secondly, our deposition rates ranged from 1.9 to 6.7 Å/s, and

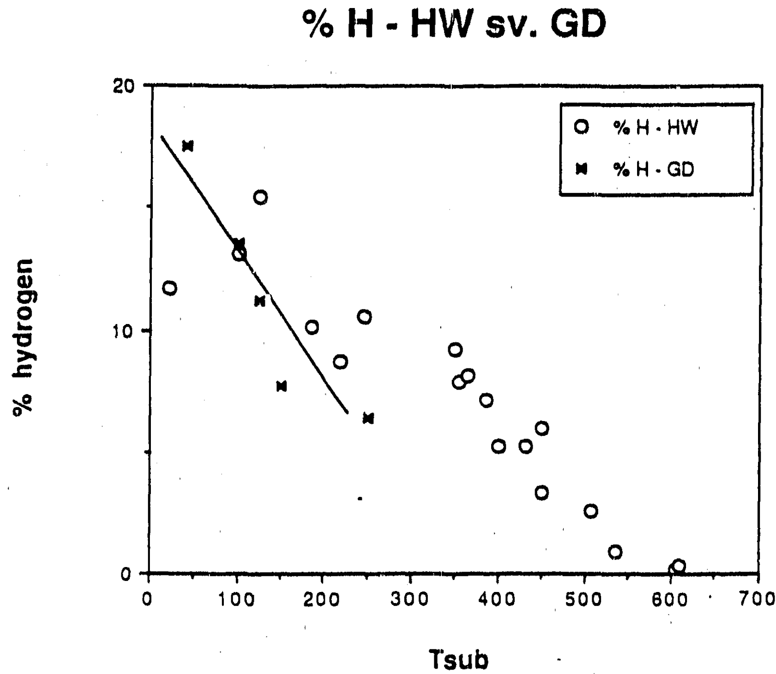

Figure 3-9. Hydrogen content (at.%), as determined from the absorption strength of the 630/cm SiH wagging mode, vs. substrate tem perature (°C) for hot wire (o) and glow discharge (x) a-Si:H samples

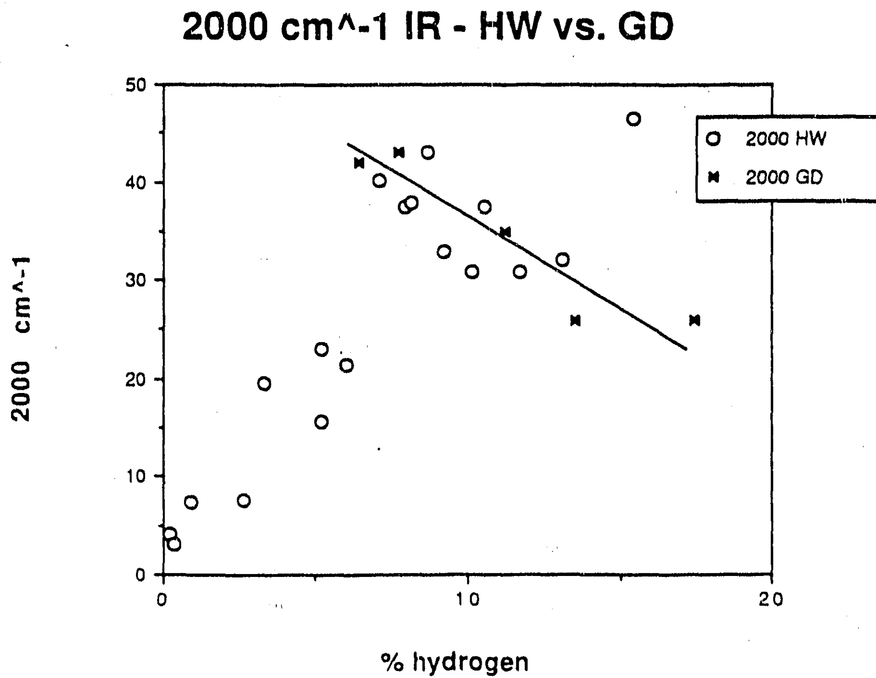

Figure 3-10. Absorption strength of the SiH 2000/cm stretch mode vs. hydrogen content (at.%) for hot wire (o) and glow discharge (x) a-Si:H

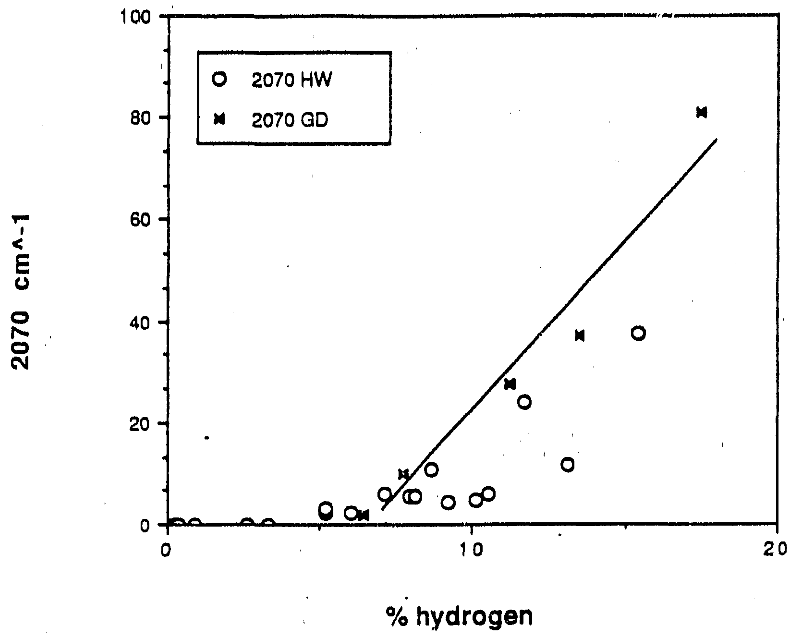

Figure 3-11. Absorption strength of the SiH 2070/cm stretch mode vs. hydrogen content (at.%) for hot wire (o) and glow discharge (x) a-Si:H

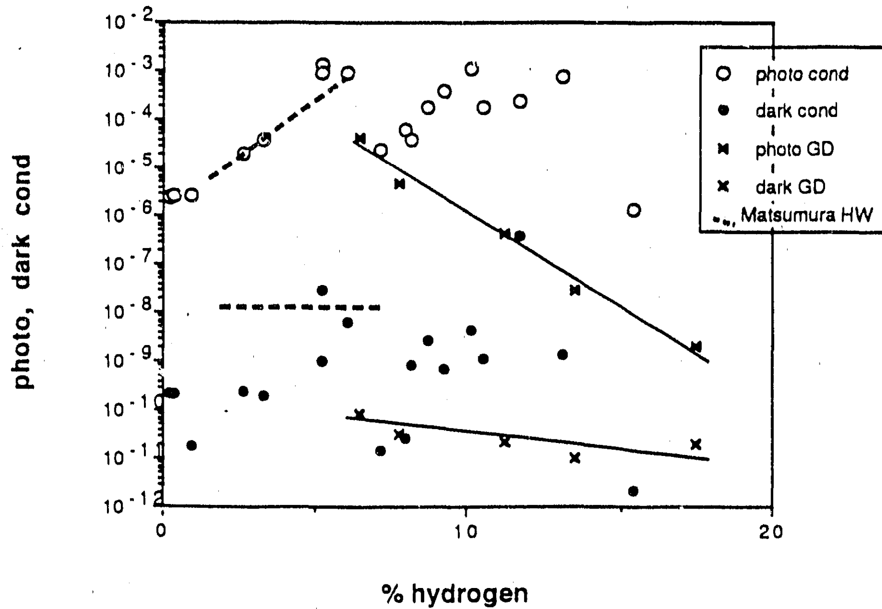

Figure 3-12. σ_L and σ_D for hot wire and glow discharge a-Si:H films vs. hydrogen content (at.%). The dashed line (---) indicates the results of Matsumura [66].

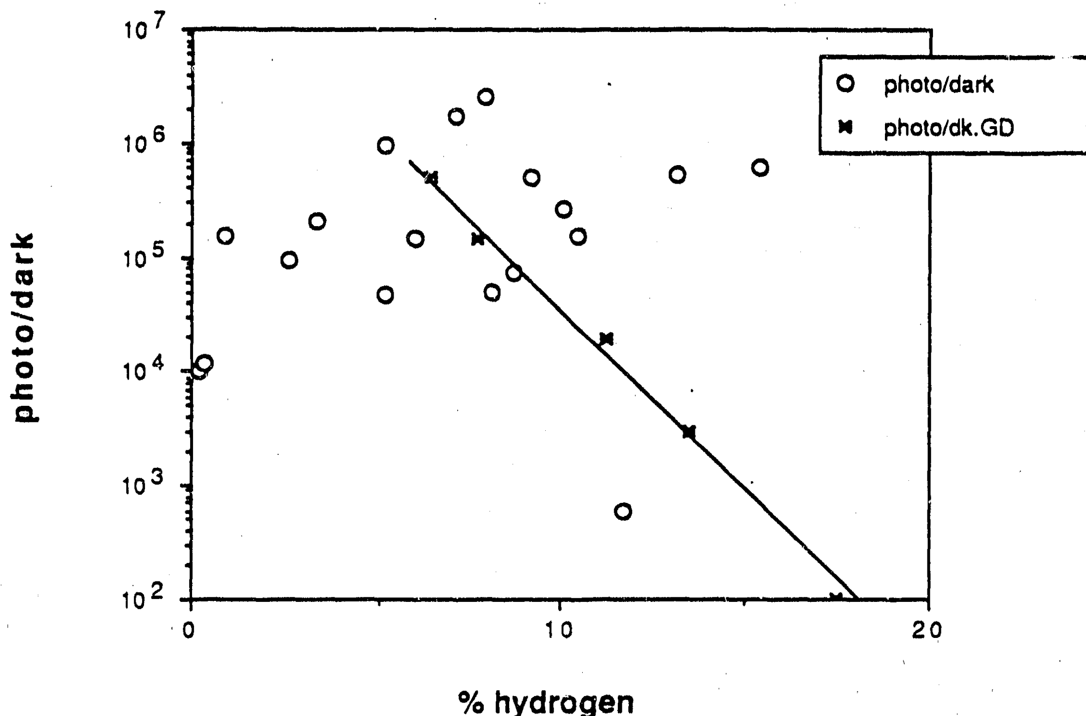

Figure 3-13. σ_L/σ_D vs. hydrogen content (at.%) for hot wire (o) and glow discharge (x) a-Si:H films

we saw no correlation between deposition rate and film properties over this range. Finally, we suggest that this technique may be ideally suited for alloy depositions. In particular, a previously reported correlation [69-70] between IR and SAXS data for glow-discharge-deposited a-SiC:H suggests that the incorporation of methyl (CH_3) groups into the growing film may influence microvoid formation. Such methyl groups may be caused by the incomplete dissociation of methane in the plasma as compared to the more complete dissociation of silane. If the hot wire technique can equally dissociate both the carbon and silicon source gases, then an improvement in a-SiC:H material quality may be possible.

3.6.4.1 Charged Dangling Bonds: Key to Electronic Transport, Recombination, and Metastability in Hydrogenated a-Si:H

The g = 2.0055 ESR signal in undoped a-Si:H is usually attributed to neutral threefold-coordinated silicon dangling bond (T_3^0) defects. In a homogenous film, the presence of T_3^0 defects would imply that the T_3 effective correlation energy (U_{eff}) is positive and that there can be no charged dangling bonds (T_3^+ or T_3^-) present. However, recent measurements [71-72] clearly demonstrate that device quality, as well as poorer quality a-Si:H, is inhomogeneous. Consequently, there is not necessarily a contradiction between a positive U_{eff} and the presence of T_3^+ and T_3^- in undoped a-Si:H. In this

section, we will review some recent evidence for charged dangling bonds, describe theory which predicts them, and explain their electronic properties.

The IR-LESR experiment [73] has been analyzed [74] to determine that T_3^+ and T_3^- are more prevalent than T_3^0 defects in undoped a-Si:H. Excitation with visible light results in electron-hole pair creation. The large LESR signals of these charges after they thermalize to the band-tail states normally prevents observation of the smaller LESR signal due to defect absorption. In contrast, sub-band-gap IR illumination permits observation of the LESR that results from defect absorptions.

Ristein et al. [73] performed IR-LESR on several a-Si:H samples. All their data are examined in a separate publication [74]. We discuss here a single, 8-μm-thick undoped glow discharge a-Si:H sample because this thick sample is likely dominated by its bulk.

Dark ESR measurement showed there are $1.5 \times 10^{16}/cm^2$ T_3^0 defects in the film. These are characterized by a narrow (g~2.0055, half-width ≈ Δ~5G) line. Equal narrow and broad components are easily distinguished in the LESR seen during illumination with 1.96-eV red light because carriers excited into the bands quickly thermalize into the bandtails from which they recombine in pairs. Electrons trapped in states isoenergetic with the conduction band tail produce the narrow line (g~2.0048, Δ~4G). Holes in states isoenergetic with the valence band tail produce the broad line (g~2.011, Δ~18G). In contrast, the LESR signal for 1.17-eV IR illumination has a 3:1 ratio of narrow to broad spins. The narrow line is an unresolvable combination of g = 2.0048 and g = 2.0055 lines [73]. There are $6 \times 10^{16}/cm^3$ spins in the broad line.

The density of states in a-Si:H is as sketched in Figure 3-14. Figure 3-14(a) (adapted from Ref. 73) shows only positively correlated T_3^0 defects. Figure 1b shows the charged dangling bonds formed in regions of large potential magnitude [see Sec. 3-14(3)]. The T_3^- defects have (-/0) transition levels below E_F, while the T_3^+ defects have (0/+) transition levels above E_F. One-step bulk transition processes are marked by solid arrows in Figure 3-14. Possible second steps that can occur before de-excitation are marked by dashed arrows. The inset indicates the number of narrow (n) and broad (b) spins that result from each transition. As pointed out in Ref. 73, processes indicated in Figure 3-14(a) cannot account for a larger narrow line than the broad line. To model LESR spectra having $n_n > n_b$ with bulk processes, Figure 3-14, schematic diagrams of the density of electronic transition levels in a-Si:H for (a) T_3^0 defects and (b) T_3^+ and T_3^- defects in regions of large negative and positive V, respectively, T_3^+ and T_3^- must be included.

Figure 3-14(b) shows process 5, in which an electron is excited out of a T_3^- defect. This produces two narrow spins (2n). Process 6 is an excitation of a hole out of a T_3^+ defect (b+n). Charge neutrality suggests that the density of T_3^+ and T_3^- are equal. Equal de-excitation rates for processes 5 and 6 will result in production of 3 narrow spins for each broad spin in agreement with the IR-LESR result [73]. From the size of the broad line, we conclude that there are at least $6 \times 10^{16}/cm^3$ of both T_3^+ and T_3^- in this undoped a-Si:H sample, compared to only 1.5×10^{16} T_3^0 defects.

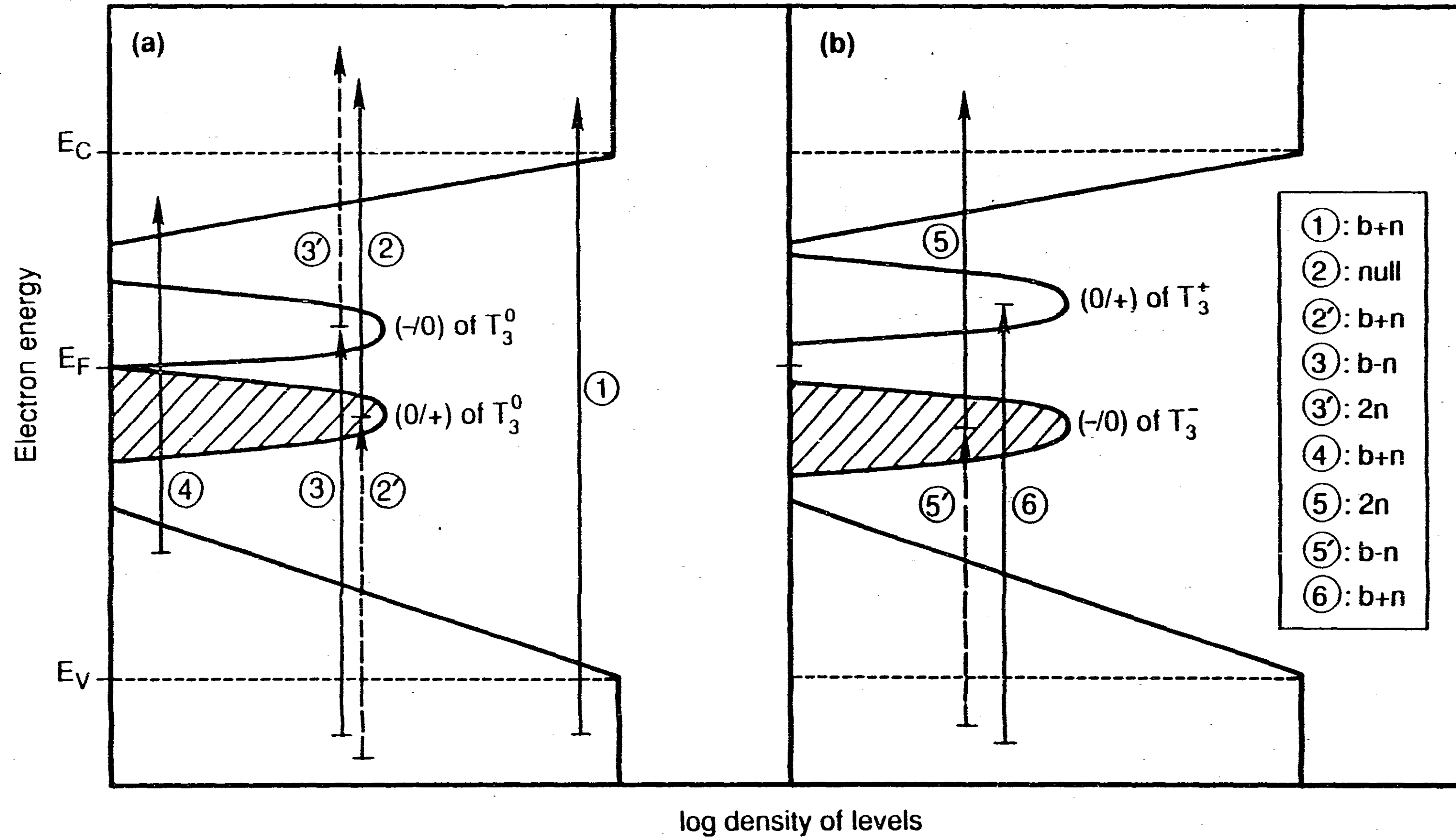

Figure 3-14. Schematic diagrams of the density of electronic transition levels in a-Si:H for (a) T_3^0 defects and (b) T_3^+ and T_3^- defects in regions of large negative and positive V, respectively. T_3^+ and T_3^- must be included.

Recent SAXS measurements [71] of device quality a-Si:H show density fluctuations attributed to 3 to 5 x $10^{19}/cm^3$ of 7-Å-diameter microvoids. Baum et al. [72] found by multiple-quantum NMR that there are about $10^{20}/cm^3$ of four- to seven-hydrogen clusters. These measurements suggest inhomogeneity of the a-Si:H on a length scale of 20 to 30 Å.

In a recent publication [75], we modeled the disorder as potential fluctuations with magnitude greater than an invariant and positive value of U_{eff}, and found T_3^+ and T_3^- would likely outnumber the T_3^0 defects. These potential fluctuations may be due to disorder-induced dipoles, charges on microstructural surfaces, or strain fluctuations. In short, a positive (negative) potential results in a reduced formation energy for T_3^- (T_3^+) defects locally. The thermodynamic equilibrium density of the charged defects increases exponentially with the magnitude of this potential, but the density of T_3^0 defects is unaffected. From our analysis of various experiments [75], we think that 10^{17} to 10^{18} cm^{-3} of charged defects are formed, about one per 100 fluctuations.

Although $U_{eff} > 0$, the position of the electronic transition levels of the T_3^+ and T_3^- defects (in different regions of the film) are as shown in Figure 3-14(b). Quantum confinement effects in a 50-Å superlattice [76] suggest that the inelastic scattering length of a carrier is greater than 50 Å. Consequently, an extended state carrier does not scatter into the 20-30 Å potential valleys, and the mobility edges are not position dependent. The defect states, however, are localized and therefore feel the effect of the local potential. It requires additional energy to ionize a T_3^- (T_3^+) defect formed in a region of high (low) potential to an extended state. The transition level of a charged defect at position x is deepened by eV(x) [compare Figures 3-14(a) and 3-14(b)]. The level deepening observed [77] for charged T_3 in doped a-Si:H is due, in part, to this effect [78].

Many phenomena, including IR and thermal quenching of photoconductivity, safe hole trapping, double-injection mobility enhancement, and light-induced metastability can be explained by the presence of T_3^+ and T_3^- defects in a-Si:H. Their interpretation in the context of our model is described elsewhere [75]. Here, we explain why T_3^+ and T_3^- act as carrier traps but T_3^0 defects are effective recombination centers.

The T_3 is a trivalent defect. Consequently, recombination can follow either of two pathways. Through the (-/0) transition, T_3^0 traps an electron to become T_3^- and this traps a hole to become T_3^0 and complete a recombination. Using the (0/+) transition pathway, the defect alternates between T_3^+ and T_3^0. Trapping and emission of holes can also use either transition (-/0) or (0/+). In hole trapping through (-/0), for example, the T_3^0 emits a hole to become T_3^- and captures a hole to become T_3^0. Trapping and emission of electrons can also proceed through either (0/+) or (-/0).

In general, transitions near midgap function as recombination centers; those near the conduction band edge are electron traps and those near the valence band edge are hole traps. The exact energies that divide trap levels from recombination levels are the trap quasi-Fermi levels [79]. These depend on illumination intensity, temperature, and the ratio of electron-to-hole-capture rate constants for the defect species and transition involved. For a given transition (q/q+1), b_n is the rate constant for capture of an electron to

T_3^{q+1} and b_p is the rate constant for capture of a hole to T_3^q. Because $b_n/b_p<<1$ for a (-/0) transition, a (-/0) anywhere in the lower half of the gap is likely to act as a hole trap. Near and above midgap, a (-/0) transition functions as a recombination center. For a small range of energy near the conduction band edge, (-/0) is an electron trap. Conversely, $b_n/b_p>>1$ for the (0/+) transition, and those in the upper half of the gap will usually function as electron traps while transitions near and below midgap are recombination centers.

Consider the transitions illustrated in Figure 3-14. The transitions of T_3^0 will be recombination centers under most conditions due to their positions in the gap. Those of T_3^+ and T_3^- will more often function as carrier traps. These differences between the charged and neutral T_3 defects' transition positions are even greater when equilibrium hybridization is considered [78].

Recent IR-LESR data [73] are the most direct evidence to date that T_3^+ and T_3^- outnumber T_3^0 defects in undoped a-Si:H. This consequence of material inhomogeneity can be modeled with potential fluctuations. The T_3^0 are recombination centers, and the T_3^+ and T_3^- defects are electron and hole traps, respectively. Many a-Si:H phenomena are explained and unified by these concepts.

3.6.4.2 Defect Equilibrium Thermodynamics in Hydrogenated a-Si:H: Consequences for Solar Cells

Recent experimental work [80] demonstrates that thermodynamic equilibrium statistics are an important factor in determining point-defect concentrations in hydrogenated a-Si:H. It is well known that the concentration of charged defects in a semiconductor depends upon the E_F in equilibrium [81]. As pointed out by Smith [82], the position-dependent E_F in the i-layer of an a-Si:H solar cell therefore results in spatially varying concentrations of dangling bonds. In this section, we will discuss the application of thermodynamic equilibrium statistics to the i-layer of a-Si:H p-i-n solar cells to compare the space charge contributed by the various charged defects and to calculate the band-bending in the i-layer. We found the electric field near the n-i interface increased considerably by the negative dangling bonds formed because of the high E_F. Point-defect profiles throughout the i-layer are discussed. Finally, we consider the importance of these results for solar cell characteristics and stability.

In a p-i-n solar cell, E_F relative to E_c and E_v depends upon position x. Usually, a model of the undoped a-Si:H density of states is assumed and the i-layer space change is calculated from E_F. In calculating the band-bending from the density of states and Poisson's equation, only the band tails are usually considered [85] because of the low density of neutral dangling bonds, T_3° (< 10^{16} cm-3), found in device quality a-Si:H. In a defect-thermodynamic model, space charge in the form of charged dangling bonds cannot be neglected. E_F positions far from midgap can induce formation of large numbers of charged dangling bonds. For example, n-type a-Si:H is known to contain up to about $10^{18}/cm^3$ of equilibrium T_3 defects. Similar densities can be expected to form in the i-layer near the n-i interface, where the position of E_F is comparable to that in the n-layer. In addition to the occupied band-tail levels, space charge in thermodynamically created T_3^+ and T_3^- defects must be considered when solving Poisson's equation for the form of the band bending.

Near the n-i interface, E_F lies in the conduction band tail and high densities of these states are occupied to form T_4^-. From transport results [84], we take a conduction-band-tail density of the form

$$N_c(E) = N_o \exp[(E-E_c)/kT_c], \tag{3-3}$$

from E_c - 0.13 eV to midgap, with N_o = 2 x $10^{22}/cm^3$ eV and kT_c = 27 eV. Integrating from midgap to E_F yields the total density of T_4^-, as a function of E_F:

$$N(T_4^-) = 5 \times 10^{20}/cm^3 \exp[(E_F-E_c)/27 \text{ meV}]. \tag{3-4}$$

These data are plotted as a solid line in Figure 3-15.

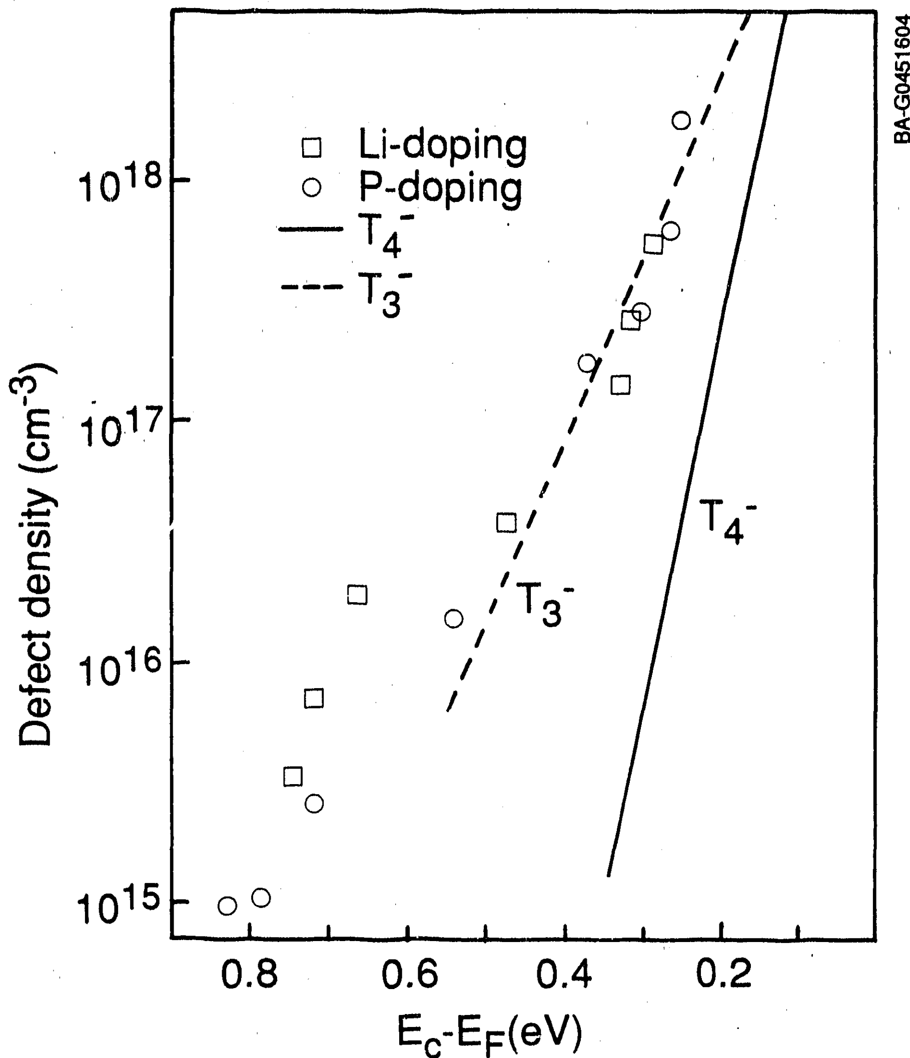

Figure 3-15. **Defect densities in a-Si:H as functions of E_cE_F.** Data points are from Ref. 6. The dashed line approximates the T_3^- density from 0.6 to 0.2 eV below E_c; this approximation is used in the text to find the band bending near the n-i interface. The solid line is the T_4^- density computed from the results of Ref. 5.

In this figure, we also plotted the defect densities obtained by Pierz et al. [85] for lithium- and phosphorus-doped a-Si:H films. The defect density was extracted from constant-photocurrent optical-absorption measurements and the value of $E_c - E_F$ was found from the T-dependence of dark conductivity [85]. These T_3^- defect densities approximate the exponential behavior for E_F between 0.2 and 0.5 eV below E_c that is predicted by thermodynamic theory. The density of T_3^- was larger than that of T_4^- in the region of interest between 0.2 and 0.6 eV below E_c. We concluded that most of the negative space charge near the n-i interface is in dangling bonds, not band tails. We approximated the data of Ref. 85 for the density of T_3^- defects by:

$$N(T_3^-) = 10^{20}/cm^3 \exp[(E_F - E_c)/57 \text{ meV}]. \quad (3\text{-}5)$$

This corresponds to the dashed line in Figure 3-16 and fits the data well from 0.2 to 0.6 eV below E_c.

We were unaware of comparable data relating T_3^+ density to E_F in p-type a-Si:H. So, instead we correlated separate reports of the defect-density and E_F dependences on dopant gas concentrations. This uncertain procedure suggested roughly $3 \times 10^{17}/cm^3$ of T_3^+ defects at $E_F = E_v + 0.4$ eV and an order of magnitude fewer at $E_v + 0.6$ eV. Such values are roughly comparable to T_4^+ densities. It was therefore difficult to determine the dominant species contributing to the space charge near the p-i interface. It was clear, however, that elevated densities of T_3^+ are found there.

To compute the band bending due to the i-layer space charge, we solved Poisson's equation together with the expression of Eq. (3-4) or of Eq. (3-5) for the charged defect density. Closed-form solutions to this problem for equal exponential conduction and valence band tails has been obtained [4], and we adapted the solution to the thermodynamic description of charged-defect density.

Figure 3-16(a) illustrates the calculated band bending near the n-i interface of a 5000-Å-thick solar cell. The dashed line is the usual $E_c(x)$ profile for T_4^- conduction band tail space charge [from Eq. (3-4)], and the solid line is the band bending for the actual T_3^- space-charge [from Eq. (3-5)]. In both cases, $E_F^n = E_c - 0.2$ eV. For T_3^- space charge, a density of $2 \times 10^{18}/cm^3$ T_3^- defects at the interface falls to about $2 \times 10^{16}/cm^3$ within the first 200 Å.

The electric fields are shown in Figure 3-16(b). The surface field is nearly an order of magnitude larger for T_3^- than for T_4^- space charge. For T_3^- space charge, the electric field falls within 500 Å from the surface value of 5×10^5 V-cm^{-1} to roughly twice its uniform value at the cell center. In the case of T_4^- space charge, the electric field attains its uniform value within 300 Å of the interface. The uniform fields are about 2.1×10^4 V-cm^{-1} for the T_4^- space charge and 1.4×10^4 V-cm^{-1} for the T_3^- space charge. The electric field in the uniform region of the i-layer is about 50% higher in the case of T_4^- space charge due to the smaller potential drop across the n-i interface layer.

We compute the band bending near the p-i interface using the a-Si:H valence band tail. As discussed above, it is unclear from the literature whether T_4^+ or T_3^+ dominates the space charge. In either case, with $E_F^p = E_v + 0.4$ eV the interface field of about 5×10^4 V-cm^{-1} falls nearly to its uniform value

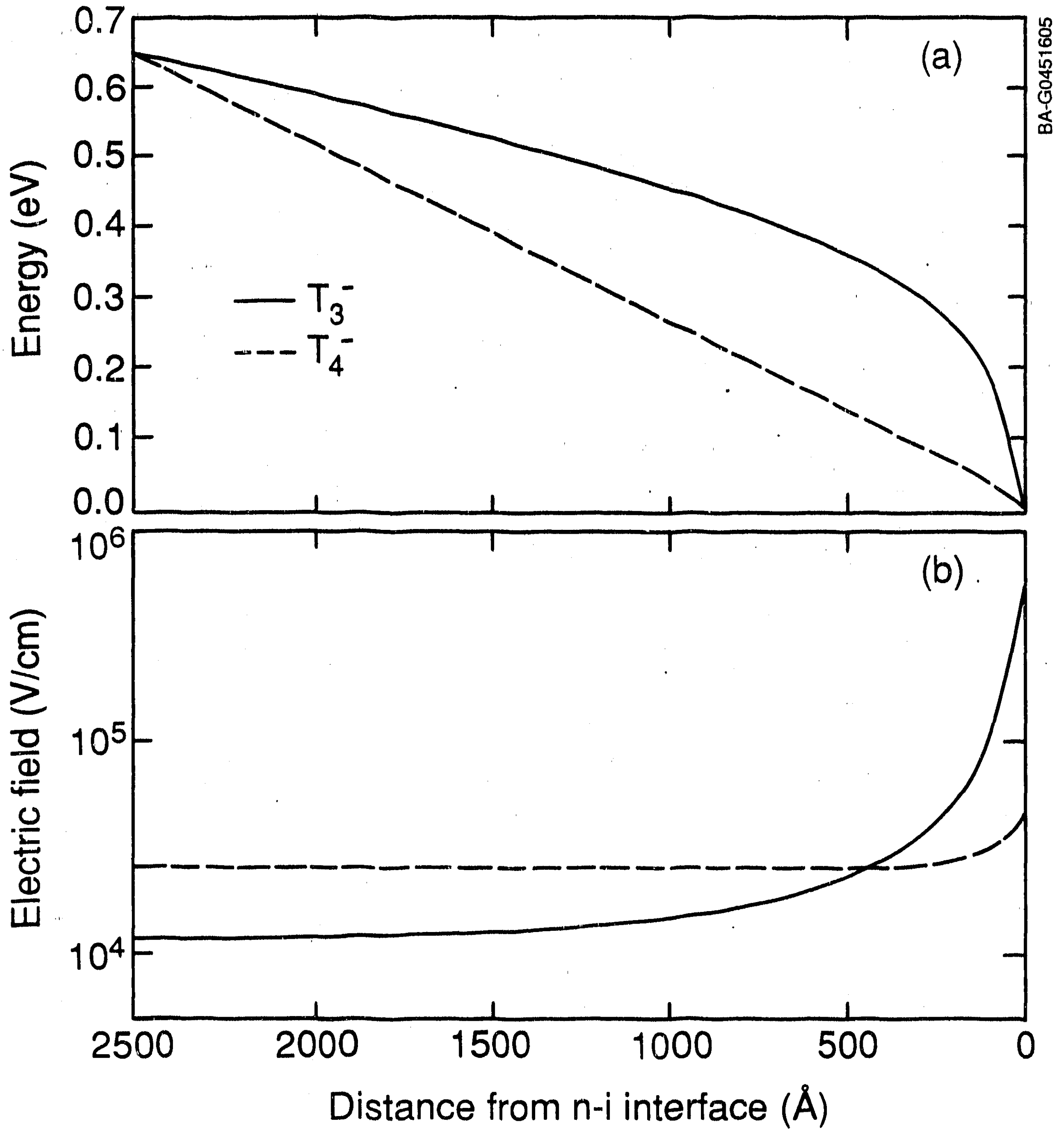

Figure 3-16. (a) E_c and (b) electric field near the n-i interface of a 5000-Å-thick p-i-n cell. Dashed curves are calculated for the equilibrium T_3^- space-charge density of Eq. 3. Solid curves are for T_4^- space charge only.

within about 400 Å of the interface. The T_3^+ density drops from above $10^{17}/cm^3$ at the interface to roughly $10^{16}/cm^3$ in this distance.

These calculations have a number of important consequences for solar cells. Large space-charge densities due to charged dangling bonds increase the electric field near the interface. Large interface fields prevent back diffusion of photogenerated electrons into the p-layer and of photogenerated holes into the n layer [86]. Once the potential changes by about 0.4 eV from its n-i interface value, the electric field is roughly constant through most of the i-layer thickness in the dark.

While there are large densities of T_3^+ or T_3^- defects near each interface, these high densities are confined to thin layers with high electric fields. Because of the high field, the defects' effect on recombination may not be great. However, Adler [88] proposed that the Staebler-Wronski effect [89] is caused by capture and stabilization of electrons on T_3^+ defects and of holes on T_3^- defects. Such a neutralization of space charge will cause a reduction of the near-interface field and a concomitant increase in back diffusion. Because T_3^- densities are greater than T_4^- densities, the effect of light soaking will be much more pronounced at the n-i interface than at the p-i interface, where the T_3^+ and T_4^+ densities are comparable. If all T_3^- defects near the interface converted to metastable T_3^0 defects, the interface field would collapse from the T_3^- to the T_4^- curve of Figure 3-16(b).

Experimental data are consistent with these predictions. Light soaking of n-i-p and p-i-n solar cells suggests the main effect is a decrease in electric field near the n-i interface [11]. Blue-light soaking through the n-layer harms cell performance much more than comparable soaking through the p-layer [90,91]. For all light-soaking wavelengths and directions, the greatest Staebler-Wronski decrease in current collection (30%-40%) is observed when measurement is made with blue light illumination through the n-layer [91]. For n-side illumination, the dramatic drop in blue response is accompanied by a small increase in red response [91], which can be attributed to the enhancement of electric field in the uniform region.

We applied recent advances in the thermodynamics of point defects in a-Si:H and computed the band bending, electric-field profile, and defect densities in the solar cell i-layer. Future work will focus on more detailed calculation of the effects on solar cell performance of charged dangling-bond defects and experimental tests of the theory.

3.6.4.3 Ionization Entropy and Charge-State-Controlled Metastable Defects in Semiconductors

Charge-state-controlled (CSC) metastable defects are observed in doped crystalline semiconductors, including silicon [92], InP [93], CdTe [94] and $Ga_{1-x}Al_xAs$ [95]. Metastable defect configurations can be obtained by cooling devices under conditions of non-equilibrium carrier density or by rapid cooling without applied bias. CSC metastable defects may also be important in doped [96] and undoped [97] hydrogenated a-Si:H.

The stable configuration of a defect at temperature T corresponds to the minimum of its Gibbs free energy of formation G, given by G = H - TS. Here, hydrogen is the formation enthalpy and S is the formation entropy. Recently,

Hamilton et al. [98] proposed that entropy differences between configurations of metastable defects can cause spontaneous configuration changes at a critical temperature. These are driven by inversion of the ordering of the Gibbs free energies of the different configurations. The authors reported observation of unusual phenomena in DLTS experiments on n-type silicon (e.g., sudden disappearance of a signal during cooling) which they attribute to such an entropy-driven transition. They did not, however, identify the metastability they observed as a consequence of a CSC defect.

In this work, we extended the theory of Ref. 98 to the entropy differences among charge states of CSC metastable defects. Typically, there are entropy differences at 300 K of up to about 5 k_B (0.4 meV-K^{-1}) per defect between states differing by one electron charge. At room temperature, the entropy differences in G can be 0.1 eV, comparable to or larger than the enthalpy differences between defect configurations. Therefore, the ionization entropy must be included in the analysis of experiments on CSC metastable defects. We also proposed that the entropy-driven metastable defect observed by Hamilton et al. [98] is an example of this phenomenon---a CSC defect for which the dominant entropy term is the ionization entropy.

Figure 3-17 shows schematic configuration-coordinate diagrams for a CSC defect which could be found in an n-type semiconductor. The solid curves are the enthalpy (i.e., G at T = 0). Stable and metastable states (local minima in G) are found at the atomic configurations Q_1 and Q_2. D is the un-ionized defect containing the maximum number of majority carriers it can stabilize. D^+ is the singly ionized state formed by releasing an electron into the semiconductor conduction band. In Figure 3-17, the stable equilibrium configurations at T = 0 depend on charge state. The ground state of the unionized defect is $D(Q_1)$, and the ground state of the ionized defect is $D^+(Q_2)$. $D(Q_2)$ and $D^+(Q_1)$ are metastable states. For large enough entropy differences among the configurations and/or charge states of the defect, finite temperature alters the shapes and/or relative positions of these curves.

We proposed that the largest entropy difference is between the ionized and unionized states. This reduces G for D^+ at finite temperature, as shown by the dashed curve in the schematic Figure 3-17. We consider the consequences after describing the ionization entropy term. The ionization entropy is a convenient way to represent the T-dependence of the electronic ionization energy which results from the electron-phonon interaction [99]. From the work of several groups [99-104], we estimated the entropy increase upon ionization of a defect ΔS_I to be 2.5 k_B to 4 k_B (0.22 to 0.35 meV-K^{-1}) in silicon at about 250 K. This range reflects experimental uncertainty.

From DLTS data, Lang et al. [100] computed that the electron ionization entropy at 250 K of the gold-acceptor defect in Si is 3.00 k_B and 3.87 k_B in two different samples. For hole ionization from the gold-acceptor, Lang et al. [100] find ΔS_I = 1.74 k_B, and their analysis of the data of Engstrom and Grimmeiss [101] yielded ΔWS_I = 2.9 k_B.

Van Vechten and Thurmond [102] argued that the entropy change upon ionization of a tightly bound (deep) carrier from a defect approximately equals the entropy of electron-hole-pair creation ΔS_{CV}. The ionization results in one free carrier and a charge on the defect whose entropy is equivalent to that of the second free carrier created during electron-hole-pair excitation. They

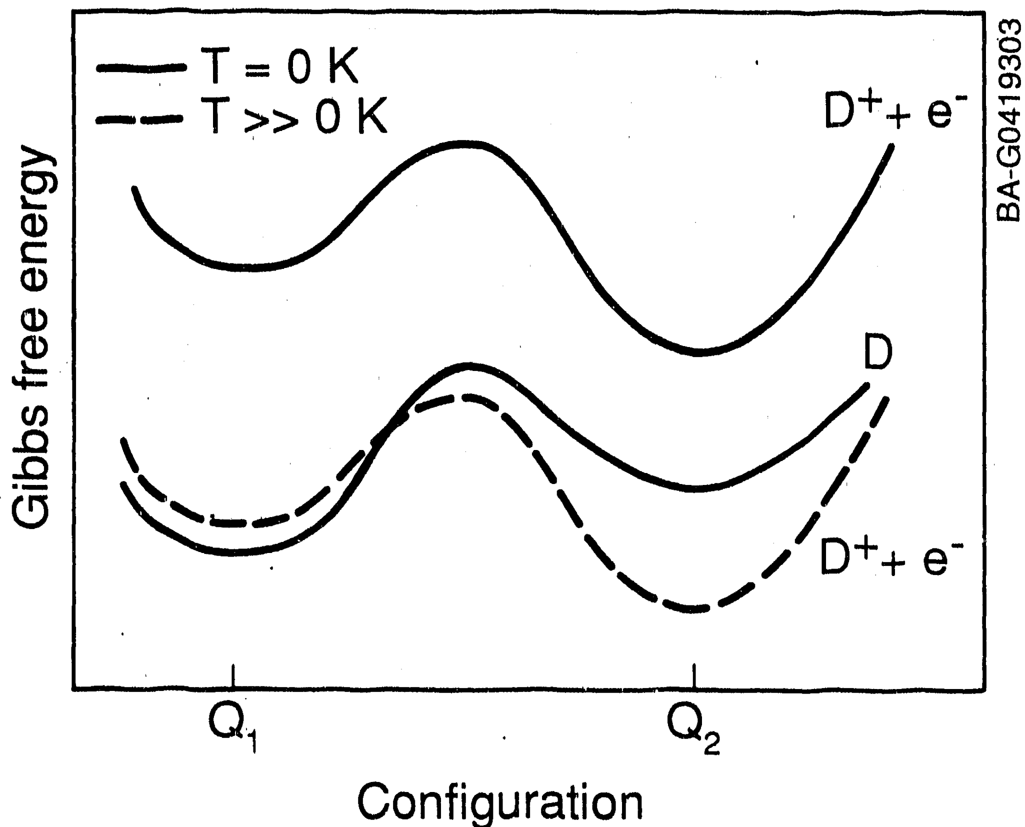

Figure 3-17. Schematic configuration-coordinate diagrams at absolute zero (solid curves) and at finite temperature (dashed curve) for a CSC metastable defect. D is the un-ionized defect, and $D^+ + e^-$ is the singly ionized state with its free conduction electron.

supported this assumption by analysis of a variety of experiments on defect formation and ionization in silicon and germanium [102].

Thurmond [103] showed from band-gap measurements that ΔS_{CV} was about 2.7 k_B in silicon at 250 K. These measurements also showed that ΔS_{CV} increase rapidly with T from 0 to about 500 K, and more slowly at higher temperatures [65]. Heine and Van Vechten [99] calculated both the magnitude and T-dependence of ΔS_CV from the lattice-mode softening caused by the electron-hole pair and obtain approximate agreement with experiment results. More recently, Jellison and Modine [104] found ΔS_{CV} was about 4 k_B at 250°C by polarization modulation ellipsometry of the silicon direct gap.

Table 3-2 exhibits $\Delta S_{CV}(T)$ (adapted from Ref. 103) and the Gibbs free energy difference of a singly ionized defect state, $G(0\ K) - G(T) = T\Delta S_I$, between 0 and 350 K in silicon. We assume that $\Delta S_I = \Delta S_{CV}$. Note that G changes by 28 meV between 150 and 250 K. This can significantly alter equilibrium occupation statistics during DLTS for the various charge states of metastable CSC defects.

Table 3-2. **Ionization Entropy and the Resulting Change in Gibbs Free Energy of Ionized Defects in Si ($T\Delta S_I$) (assuming $\Delta S_I = \Delta S_{CV}$)**

T (K)	0	100	150	200	250	300	350
$\Delta S_I(k_B)$*	0	1.3	1.9	2.3	2.7	3.0	3.2
$T\Delta S_I$(meV)	0	11	25	40	58	78	97

*Reference 103.

In this research, we focused on defects in silicon but note that ΔS_I is thought to be larger in other semiconductors. In GaAs, Ge, and GaP, ΔS_{CV} at 250 K are 5.25 k_B, 4.47 k_B, and 4.65 k_B, respectively [102,103]. From DLTS of the EL2 center in GaAs, Pons [105] estimated an electron ionization entropy of 2.9 k_B and a hole ionization entropy of 6.0 k_B at 300-400 K.

Studies of CSC metastable defects at finite T must include the entropy term in G. The most dramatic effects will be observed at a critical temperature T_c, at which the energy ordering of the local minima in G is changed [98]. In the hypothetical schematic of Figure 3-17, the dashed curve represents a temperature sufficient to drive the ionized ground state below that of the un-ionized state. On heating, $D(Q_1)$ reconfigures spontaneously to $D^+(Q_2)$ above T_c.

Let's examine a specific CSC metastable defect model that explains in detail the unusual DLTS data of Ref. 98 for a metastable defect in electron-irradiated, n-type silicon. Figure 3-18 is a schematic of our proposed configuration-coordinate diagrams at three different temperatures. Inaccessibly high energy states of the defect are not shown. We choose energies and temperatures to obtain approximate quantitative agreement with the data of Ref. 98. The ionization entropies and resulting changes in G with temperature are taken from Table 3-2. We recognize that our model is not necessarily unique in explaining the data of Ref. 98, but it exemplifies the principles of ionization-entropy-driven transitions and suggests further experiments.

Figure 3-18(a) shows G curves at T = 0, with $D(Q_1)$ as the defect's ground-state. At $T = T_c \sim 150$ K, the curve G of D^+ is reduced by 25 meV relative to $D(Q_1)$ and G of D^{++} (the doubly ionized defect) is reduced by 50 meV. Consequently, at $T = T_c$, $D^+(Q_2)$ and $D(Q_1)$ are isoenergetic [Figure 3-18)]. At T~250 K (above T_c), $T\Delta S_I$ is 58 meV for D^+ and 116 meV for D^{++}. $D^+(Q_2)$ now lies below $D(Q_1)$ and is therefore the system ground state (Figure 3-18(c). The enthalpy differences (ΔH) that will be measured by DLTS at any temperature [106] for the defect in configurations Q_1 and Q_2 are shown by dashed arrows in Figure 3-18(a). Activation enthalpies $\Delta H(Q_1)$ and $\Delta H(Q_2)$ correspond to the low-temperature and high-temperature peaks, respectively, reported in Ref. 98 (each about 0.2 eV).

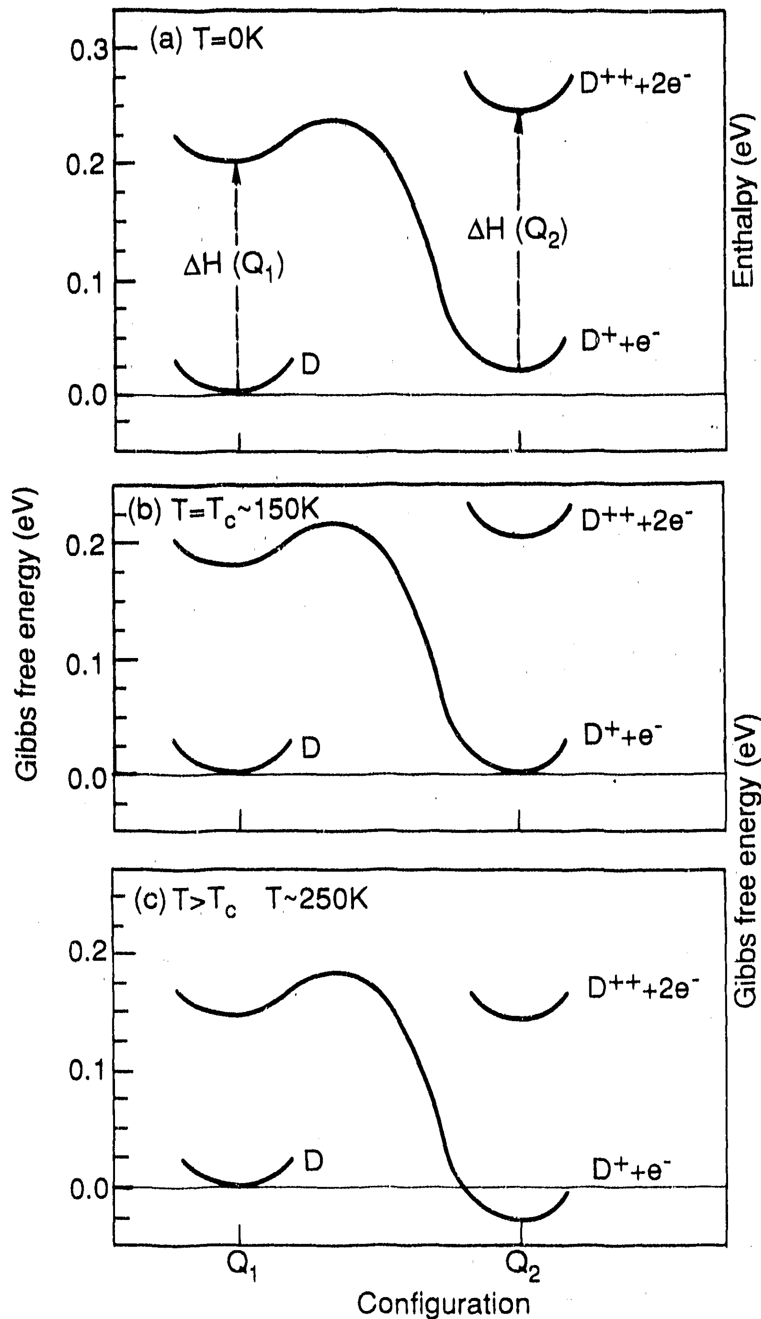

Figure 3-18. **Schematic configuration-coordinate diagrams of the model CSC defect at three different temperatures.** The T=0 diagram (a) represents both enthalpy and Gibbs free energy; the other diagrams (b,c) represent G. Energies are measured relative to the energy of $D(Q_1)$. This model accounts for the unusual DLTS data of Ref. 7.

The following predictions of our model and thermodynamics are evident from Figure 3-18 and correspond to the observations in Ref. 98:

- After annealing at $T > T_c$, defects are in the ground state $D^+(Q_2) + e^-$. Above T_c, DLTS during cool-down measures $\Delta H(Q_2)$ associated with the transition $D^+(Q_2) \rightarrow D^{++}(Q_2) + e^-$.
- The DLTS signal associated with $\Delta H(Q_2)$ vanishes abruptly during cooling through T_c. For $T < T_c$, $D(Q_1)$ becomes the ground state and the defects $D^+(Q_2)$ convert spontaneously to $D(Q_1)$. Below T_c, only $\Delta H(Q_1)$ associated with the transition $D(Q_1) \rightarrow D^+(Q_1) + e^-$ is observed.
- For experimental conditions in which the DLTS transition $\Delta H(Q_2)$ is observed while cooling through T_c, each filling pulse enables conversions from $D^+(Q_2)$ to $D(Q_1)$ and a concommitant loss of the DLTS signal associated with $\Delta H(Q_2)$. This decreasing $\Delta H(Q_2)$ signal competes with the increasing $\Delta H(Q_1)$ signal to create a noisy DLTS spectrum. The signal associated with $\Delta H(Q_1)$ rises with decreasing T for two reasons: an increasing number of defects convert to Q_1, and the peak of the DLTS signal is approached.
- This CSC defect exhibits identical DLTS spectra after cooling with and without applied reverse bias because $D(Q_1)$ is the low-temperature ground state. After reverse-bias cooling, DLTS filling pulses at $T < T_c$ convert the defect to $D(Q_1)$ and the transition $\Delta H(Q_1)$ is observed in a DLTS spectrum taken during heating.

While the thermodynamics of this defect system are evident from Figure 3-18, reconfiguration kinetics depend upon barrier heights and carrier concentrations. We continue with a discussion of the causes of history-dependent kinetics. We focus in particular upon the observation [98] of a kinetic barrier to the $Q_1 \rightarrow Q_2$ reconfiguration during heating above T_c, which contrasts sharply with the apparently barrierless $Q_2 \rightarrow Q_1$ reconfiguration observed during cooling.

In both cases, the DLTS measurement procedure alternated filling and depletion pulses which determine at any moment those pathways for reconfiguration available to the defect. On cooling from the high-T ground state $D^+(Q_2)$, the reconfiguration to the low-T ground state $D(Q_1)$ occurred during the filling pulse. The excess electrons drove the transition from $D^+(Q_2)$ to $D(Q_1)$. During the depletion pulse, the defect did not capture an electron and convert to Q_1.

On heating from the low-T ground state $D(Q_1)$, the defect was unlikely to ionize and convert to Q_2 during the filling pulse. Instead, we expected the transition to occur during the depletion pulse. However, the ionization and reconfiguration reaction, $D^+(Q_1) \rightarrow D^{++}(Q_2) + e^-$, was evidently inhibited by a kinetic barrier. Without a microscopic model of the defect, we were unable to describe this barrier. We noted only that the barrierless $Q_2 \rightarrow Q_1$ cooling transition and the kinetically inhibited $Q_1 \rightarrow Q_2$ heating transition occurred through different ionization states of the defect. This feature of our model can explain the observation of history-dependent defect configurations.

To construct accurate T-dependent configuration-coordinate diagrams for this defect, we suggest further experiments. Slow heating and cooling rates and

carefully controlled filling and depletion pulse lengths permit determination of defect reconfiguration rates [107]. Isothermal capacitance transients near T_c after a step change in temperature or illumination should be useful. Electron spin resonance above and below T_c may determine whether the ground states have different charges, thereby distinguishing between the present model and that of Ref. 98.

In summary, we have extended the concept of entropy-driven metastability [98] to CSC metastable defects. The entropy term in G, TS, increased by nearly 0.1 eV upon ionization of these defects at typical experimental temperatures. The relative value of G for the ionized and un-ionized states is therefore T-dependent. At a critical temperature, entropy can alter the ordering of the Gibbs free energies of local minima in G, and spontaneous charge-state and configuration changes may result. We have proposed a specific CSC metastable defect model that includes entropy-driven transitions to explain all the major features of the unusual DLTS data of Ref. 98. The DLTS data of Londos [108], which show features that appear at a temperature independent of the rate window, also suggested these entropy-driven transitions of CSC defects. Even when such spontaneous transitions are not observed, the ionization entropy term must be included in the correct analysis of CSC metastable defect systems.

3.6.4.4 Safe Hole Trap Conversion Properties and Microscopic Models

Previously, we concluded that safe hole traps (i.e., states located 0.4 to 0.5 eV above the valence band edge with long occupancy times for trapped holes) are the source of metastable dangling bonds induced by light-soaking. During annealing experiments, the recovery of safe hole traps converted at 163 K was much faster than the recovery of safe hole traps converted at room temperature. We conclude that the exact configuration for lattice-relaxed metastable defects originating from safe hole traps depends on the temperature at which they were formed. In this section, we will discuss how each of the three most specifically stated models can explain such results.

Until recently, light-induced degradation in hydrogenated a-Si:H was measured only in terms of defects produced--usually the three-fold coordinated dangling bond (DB). Many microscopic models use as the source of their metastable DBs states located in the valence band tail. These models include the weak bond breaking model with lattice relaxation [109,110], the weak bond breaking/hydrogen insertion [111-114], and the T_3^-/T_3^0 conversion model [115,116].

We have developed and applied a new technique to determine safe hole trap distributions from secondary photocurrent transients that is especially sensitive to hole traps with long trapping times [117]. We concluded that hole traps 0.4 to 0.5 eV above the valence band with long occupancy times converted with light soaking to metastable DBs, and we were able to measure their restoration with annealing [118].

Safe hole traps have two important properties: they are spatially isolated from other valence band-tail states and DBs so that tunneling enhanced recombination of trapped holes is unlikely, and the capture-rate constant of electrons to trapped holes in these states is orders of magnitude smaller than the capture rate constant of electrons to DBs. Safe hole traps manifest themselves in the following way [118]:

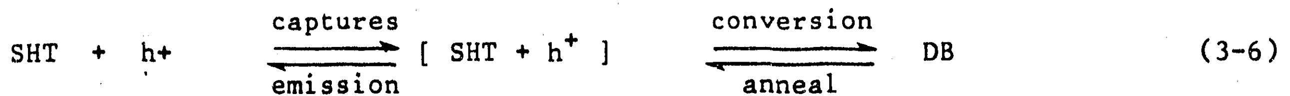

$$\text{SHT} + h+ \underset{\text{emission}}{\overset{\text{captures}}{\rightleftharpoons}} [\text{ SHT} + h^{+}] \underset{\text{anneal}}{\overset{\text{conversion}}{\rightleftharpoons}} \text{DB} \qquad (3\text{-}6)$$

where

SHT = safe hole traps
h^+ = holes.

During exposure to light, safe hole traps capture h^+, forming the SHT+h^+ complex. From there the trapped hole is usually emitted to shallower, more delocalized states, through which it tunnels to a doubly occupied DB completing the normal recombination process. On rare occasions, however, the safe hole trap remains occupied long enough so that the reaction in Eq. 3-6 proceeds further to the right, permitting conversion to a metastable DB. The safe hole traps with the longest occupancy times convert first. The spectrum of safe hole traps converted by 20 min of light-soaking at 630 nm with a flux of 7.5 x 10^{15} photons/cm^2 s at 309 K (shown in Figure 3-19) and at 163 K (shown in Figure 3-20) is a solid curve.

The difference between B and B* is striking: Four times as many safe hole traps convert as a result of the 163 K light-soaking, and they anneal much faster at lower temperature. We must conclude that defects are stabilized differently for states B and B^*. The two-level system with a distribution of activation energies E_a used by Jackson and Stutzmann [119] to explain the effect of temperatures above 25°C on the light-soaking and annealing behavior of the excess spin density is unable to account for our results below 25°C. Jackson and Stutzmaan [119] concluded, after annealing studies of samples light-soaked at temperatures of 25° to 125°C, that the same generation kinetics are present independent of temperature. But due to back annealing during soaking at higher temperatures, spins with the smaller values of E_a are absent. We, on the other hand, find that a 163 K soaking forms few if any defects with the longer annealing times found for the 309 K soaking.

We define the set of position coordinates $\{Q_i\}^j$ for the ith atom in a group of about one hundred atoms for a localized volume of the disordered lattice in the state j = A, B, or B*. In a-Si, many sets $\{Q_i\}^j$ will have nearly the same total, ground-state energy $E(\{Q_i\}^j)$. Figure 3-21 also shows $\{Q_i\}^j$ for each of these states after hole capture as the excited states A', B', or B*'.

During light-soaking at 163 K, smaller potential barriers with heights designated by E* in Figure 3-21 may be passed over as the lattice proceeds to configurations such as B*; configurations such as B', and therefore B, will not be created because of the larger potential barrier height E separating it from A'; we inferred that configurations such as B are virtually non-existent because of their strikingly different anneal kinetics. State B* is frozen in as long as the defect is held at 163 K in the dark. Upon heating to 303 K for only 3 min, 75% of the defects in configuration B* converted back to state A as shown in Figure 3-20. Perhaps only one small barrier had to be surmounted to return to A. A mild anneal eliminates the remaining defects.

On the other hand, upon light-soaking at 309 K, configurations such as B that are isolated by higher potential barriers such as E were now thermally accessible. To arrive at configuration B, the lattice may or may not have to pass

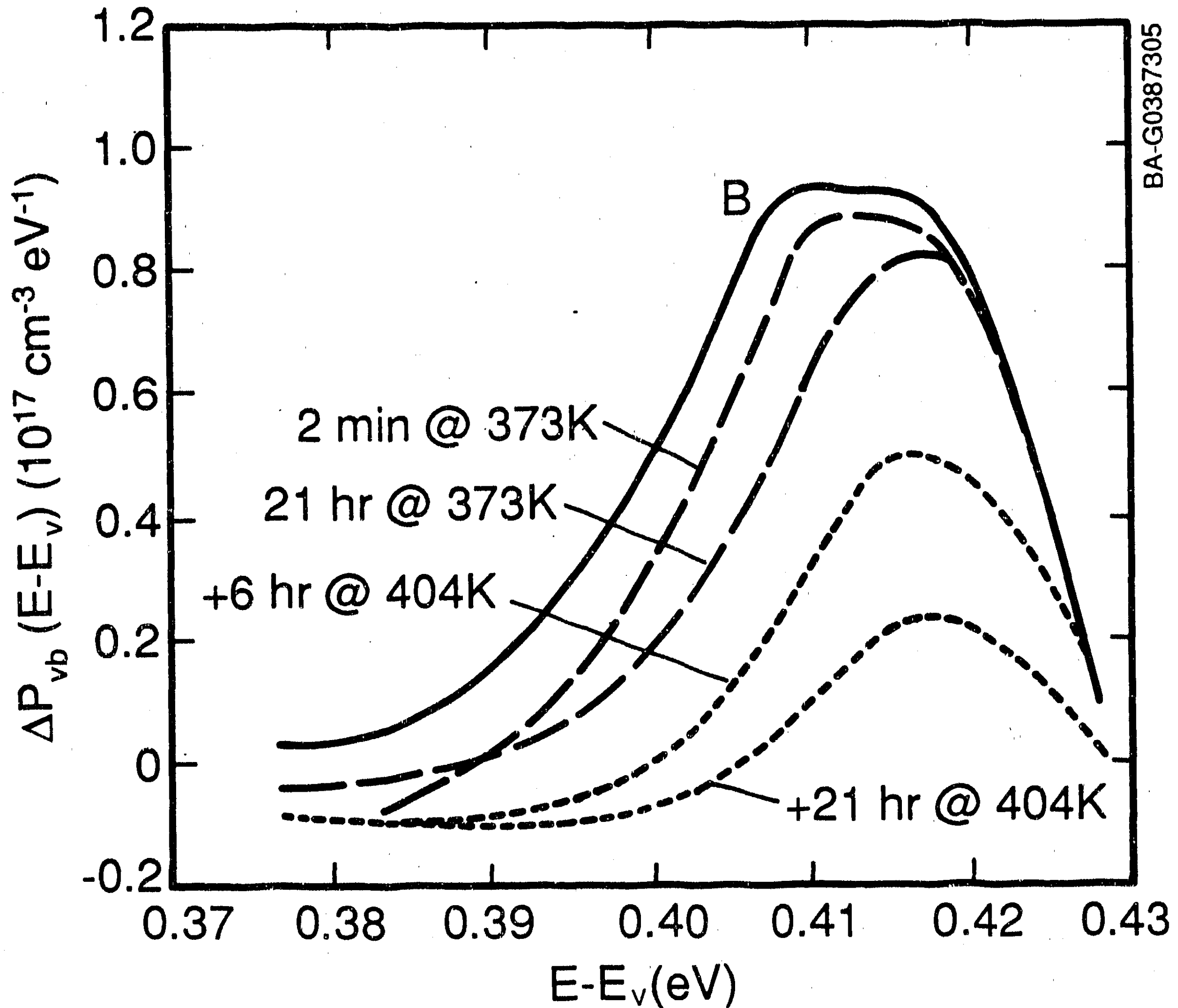

Figure 3-19. Converted safe hole traps versus E − E_v after light-soaking at 309 K (———) and with partial recovery after annealing at 373 K (— — —) and 404 K (------). (From Ref. 10.)

through intermediate configurations such as B*. Many B*s would be passed over to produce Bs. After light-soaking, many B*s would quickly anneal back to A; by the time the sample was cooled for the safe hole trap measurment, few defects would be left in configurations such as B*. More and higher potential barriers isolating state B from state A resulted in defects that are more difficult to anneal (see Figure 3-21). In other words, the final stabilized defect configuration depended upon the temperature during soaking.

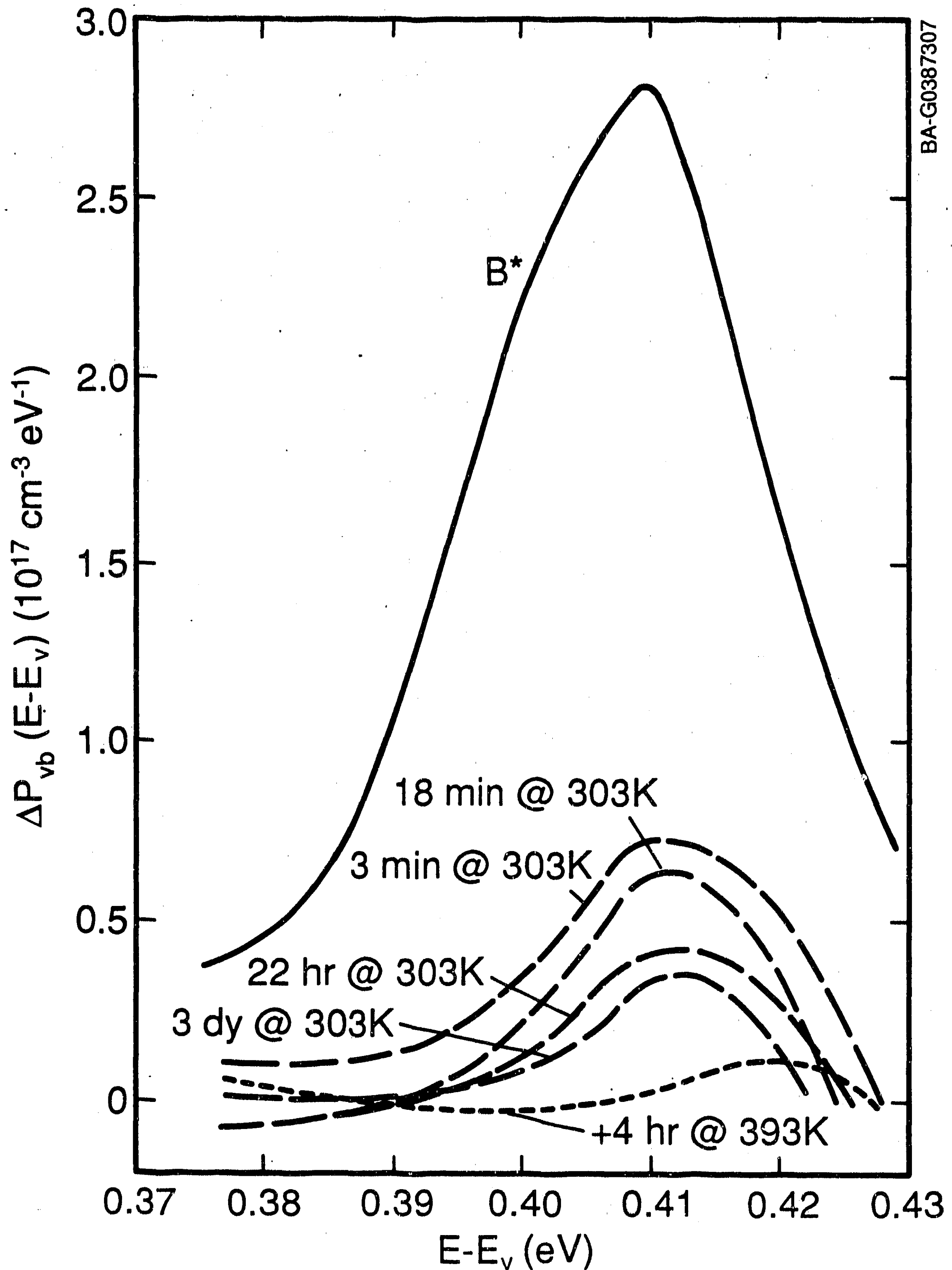

Figure 3-20. Converted safe hole traps versus E - E_v after light-soaking at 163 K (———) and with partial recovery after annealing at 303 K (— — —) and 393 K (------). (From Ref. 10.)

In this model, highly strained Si-Si bonds located deep in the valence tail were the source of the metastable DB. If they were isolated spatially from existing DBs, long hole occupancy times resulted and were the safe hole traps. We suggested that for a safe hole trap with a trapped hole to convert to a defect configuration with a relaxed lattice surrounding two DBs (i.e., for Eq. 3-6 to proceed all the way to the right) one or more reconfigurations of the local lattice in the excited state must occur. Stutzmann et al. [112] argued that when a weak bond traps a hole, the back bonds distort, stabilizing the hole. We proposed that rehybridization of the back bonds of second and third nearest neighbors was involved, thus explaining all the intermediate potential minima in Figure 3-21. The net result was a relaxation leading to an increase in the interatomic distance or a distortion of the σ-symmetry [110]. The deeper states converted first because these bonds were weaker and because thermal emission times were longer.

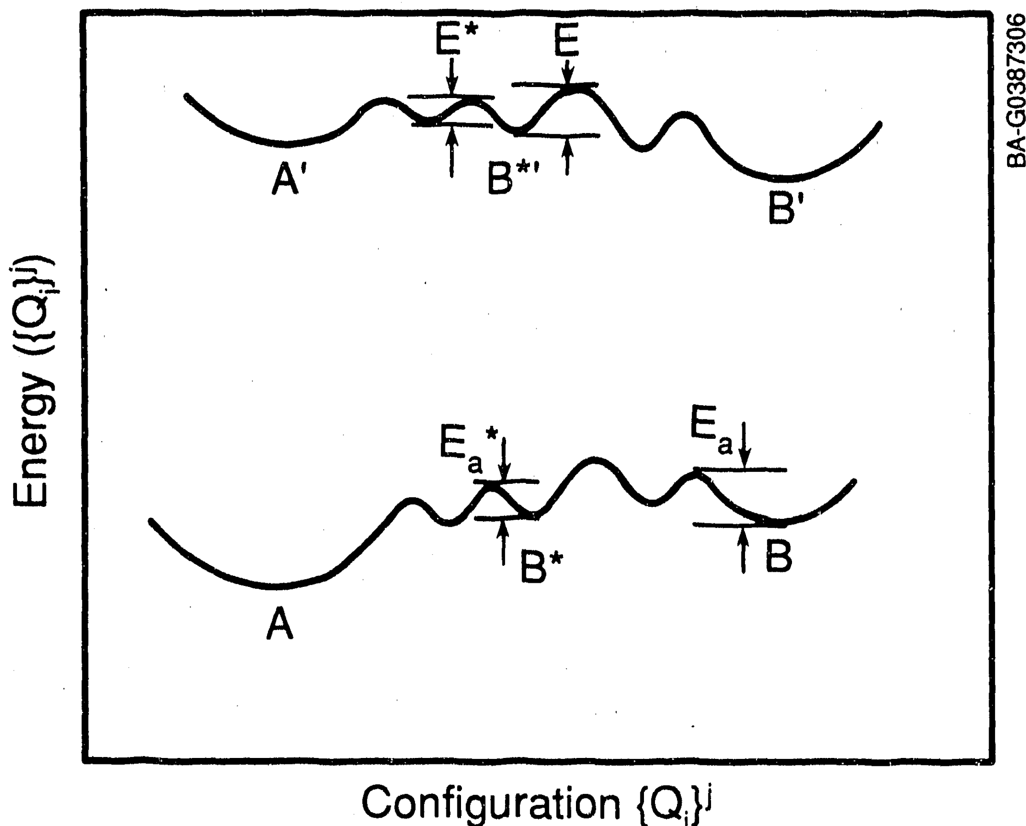

Figure 3-21. Total configurational energy versus configurational coordinates for the atomic site locations $\{Q_i\}$ for state j. See the text for a description of amorphous states.

Proponents argued that a weak Si-Si bond is broken with one of the sites becoming metastabily occupied by a hydrogen atom that is temporarily liberated from a Si-H bond [111-114]. In the mobile-hydrogen model prosposed by Street and Winer [114], hydrogen is freed from a Si-H bonding site and diffuses thermally through the matrix inserting into weak Si-Si bonds with strengths varying exponentially. Hydrogen inserted into a weak Si-Si bond can be detrapped thermally to interstitial sites, where it is mobile until it finds either another weak bond or an isolated DB. Such a model agrees well with our observations, since at 163 K most hydrogen atoms will move only one step to occupy neighboring sites. These are probably shallower, relatively stronger Si-Si bonds since there are more of them. Such converted safe hole traps will anneal back quickly.

At room temperature, hydrogen will be freer to move through the shallower Si-Si bonds until only the weakest and deeper, perhaps more distant but fewer in number, Si-Si bonds are found. Hydrogen inserted in these deeper, more remote Si-Si sites will have much longer annealing times [120]. Figure 3-21 applies if we imagine the potential minima as being the configurational energy of hydrogen inserted into neighboring weak bond sites.

Branz and Silver [116] have argued that T_3^- centers (i.e., s^2p^3-hybridized DBs lying below E_F), stabilized as a result of potential fluctuations, may be the source of safe hole traps. The T_3^- is a good trap and a poor recombination center because of its negative charge. Not many details are known about this conversion model; if the potential barrier argument were imposed for the rehybridization/stabilization process of a T_3^-, then we could equally well explain our results if the safe hole traps were due to T_3^- states. The deeper T_3^- states will convert first since hole emission times are longer.

Each of the three microscopic models could explain the fact that defects induced at lower temperature anneal more easily. In each, the shorter anneal times found for lower temperature light-soakings are due to fewer steps and lower formation barriers between states A and B^*.

3.6.4.5 Hydrogen-Plasma Reactive Flushing for a-Si:H p-i-n Solar Cell Fabrication

Hydrogenated amorphous silicon p-i-n solar cells deposited in a single-chamber, glow discharge deposition system often have the problem of residual boron doping at and near the p- and i-layer interface (p/i interface). This problem increases carrier recombination and reduces the cell's blue-light response and overall conversion efficiency [121]. High-vacuum pumping, silane or argon gas flush, or combinations of the three are normally used after the p-layer deposition to reduce the residual diborane gas concentration in the reactor. However, these methods are not very effective in removing the diborane molecules and adsorbed boron atoms adhering to the electrodes and walls of the reactor. These diborane molecules and boron atoms are released (gettered) at the beginning of the i-layer deposition by the SiH_4 plasma, which results in an undesirably high level of boron in the i-layer near the p/i interface. Recently, Collins [122] suggested that a layer of high-boron-content, CVD a-Si:H:B film resulting from thermal decomposition of B_2H_6:SiH_4 gas may deposit atop the p-layer and on electrodes and chamber walls immediately after the p-layer deposition. Such a layer cannot be removed by vacuum pumping or gas flushing and may degrade the properties of the p/i interface. Multiple-chamber deposition systems [121,123] have been used to reduce the

boron cross-contamination problem. However, because of their mechanical simplicity and low cost, single-chamber deposition systems are still being widely used. Catalano and Wood [124] reported that a reactive NF_3 gas flush can be used to scavenge diborane after the p-layer deposition and can improve the short-wavelength response in the solar cells.

In this section, we describe a simpler, 30-second or shorter, H-plasma flush that has similar effects. Improvements in the properties of a-Si:H p-i-n solar cells, both with and without an undoped, graded-band-gap buffer layer between the p- and i-layers [125], are observed when the H-plasma flush is used in the deposition process instead of the conventional silane gas flush and high-vacuum pumping.

All cells were fabricated in an RF glow discharge deposition system with a single-chamber deposition reactor and a load-lock vacuum chamber for introducing and removing substrates into and out of the system. The reactor walls and RF electrodes were made of stainless steel. A base vacuum of less than 1×10^{-8} torr in the reactor was achieved by cryogenic pumping before deposition. The reactor leak rate is less than 3×10^{-7} torr·liter/s. The transparent conducting oxide (TCO)-coated glass substrates, supplied by Asahi Glass Co., Ltd., have a fluorine-doped tin oxide layer with a sheet resistivity of 10 ohms/square, a 10% haze, and a maximum optical transmission of about 85%.

Our baseline p-i-n cell structure was TCO/a-$Si_{1-x}C_x$:H(p)/a-Si:H(i)/a-Si:H(n)/Ag. The 15-nm-thick p-layer was deposited at 180°C for 50 seconds using a gas mixture of 0.15% B_2H_6, 27% SiH_4, and 73% CH_4; a total gas flow rate of 80 sccm; and a reactor pressure of 0.7 torr. After the p-layer deposition, the RF power was turned off and the reactor was flushed by leaving a 10-sccm SiH_4 flow on for about 5 min. Then the reactor chamber was pumped down to 10^{-8} torr vacuum for an hour or more. The 540-nm i-layer and the 30-nm n-layer were deposited at 250°C at a deposition rate of 0.18 nm/s. A SiH_4 flow rate of 70 sccm and a pressure of 0.7 torr were used for i- and n-layer depositions. The PH_3-to-SiH_4 gas ratio was 1% for the n-layer deposition. A typical i-layer deposited in our system had an optical band gap E_o of 1.76 eV, a dark-conductivity activation energy E_a of 0.76 eV, an AM1 photoconductivity value of 1×10^{-4} S/cm, and a photo-to-dark conductivity ratio of 3×10^6. The p-layer had an E_o of 2.02 eV, an E_a of 0.32 eV, and a conductivity of 9×10^{-6} S/cm. The n-layer had an E_o of 1.72 eV, an E_a of 0.24 eV, and a conductivity of 6×10^{-2} S/cm.

A 6-nm-thick, undoped, graded-band-gap a-$Si_{1-x}C_x$:H buffer layer (b-layer) [125] between the p- and i-layers was sometimes added to our baseline p-i-n cell structure (denoted p-b-i-n). This layer was deposited in 30 seconds by linearly decreasing the CH_4 flow rate from 45 sccm to zero while keeping the SiH_4 flow (11 sccm) and the chamber pressure (0.7 torr) constant. The deposition was interrupted again after the b-layer deposition and the reactor chamber pumped down to high vacuum before reintroducing SiH_4 for i-layer deposition. The addition of the b-layer improved the open-circuit voltage V_{oc} but not the fill factor (FF) of our p-i-n cells. In this study, we investigated the effects of using a short, RF H-plasma flushing step after the p-layer deposition instead of the standard chamber-cleaning procedure of SiH_4 gas flush and high vacuum pumping. This H-plasma flushing step was used for both the p-i-n structure (denoted p_f-i-n) and the p-b-i-n structure (denoted p_f-b-i-n). The plasma for the reactive flush was maintained with a hydrogen

flow rate of 30 sccm, a reactor chamber hydrogen pressure of 4 torr, and an RF power density of 0.07 W/cm^2. The original objective of this RF H-plasma study was to investigate the possibility of increasing the optical band gap and conductivity of the p-layer, similar to what has been observed in studies of ion-beam hydrogenation of a-Si [126,127]. However, we found that the RF hydrogen plasma was ineffective in these aspects, even though cell properties were improved by the H-plasma flush. Although the hydrogen plasma etches undoped a-Si:H at the rate of 1.8 nm/min, no detectable etching was found for p-type a-Si:H after up to one hour of H-plasma etching. There were also no significant changes in optical band gap and conductivity of the p-layer after RF hydrogenation.

Solar cells fabricated in this study were tested as deposited, with no post-deposition treatments such as reverse-bias annealing, which sometimes improves device performance. The TCO-coated glass substrate, the vacuum-evaporated Ag back contact, and the baseline p-i-n structure used were similar for all cells, so that the effects of the buffer layer and hydrogen plasma could be studied. Cell efficiency measurements were performed under AM1.5, global illumination conditions. Cell parameters reported in this paper were averaged values of at least six identically but separately prepared cells to reduce effects due to slight process variations in the cell fabrications. The photoluminescence (PL) measurements were performed at a sample temperature of 78 K using an argon-ion laser at 488-nm wavelength for excitation. A PbS photoconductive detector cooled to dry-ice temperature was used for photon detection.

The RF H-plasma reactive flush between the p- and i-layer depositions improved V_{oc} and the short-circuit current density J_{sc} in the p-i-n and p-b-i-n cells (as shown in Table 3-3). The area of each cell was about 0.050 cm^2. Eleven p-i-n cells, eleven p_f-i-n cells, six p-b-i-n cells, and seven p_f-b-i-n cells were used for averaging cell parameters in Table 3-3. In addition, many cells were fabricated using various methods of high-vacuum pumping or combinations of SiH_4, H_2, CH_4, and Ar gas flushes, or both, between the p- and i-layer depositions. No significant improvements over our baseline cells were observed after these nonreactive methods were used. Sputter-cleaning the electrodes with an argon plasma between the p- and i-layer depositions also did not result in any significant improvements in device properties. Using a XeF_2 vapor, which spontaneously etches Si and a-Si:H without plasma assistance [128], to etch a-Si off the reactor walls and electrodes after p-layer deposition did improve the V_{oc}, but it reduced the FF of the p-i-n device.

The beneficial effect of the H-plasma flush on the V_{oc} can be seen for as short a flush time as 13 seconds. We have not observed any of the cell improvements to depend on the duration of the H-plasma flush. We typically used a 30-second flush. Interestingly, similar degrees of improvement in V_{oc} and J_{sc} were observed, regardless of whether the deposited p-layer came in contact with the hydrogen plasma during the H-plasma flush. In many cases, we deliberately isolated the p-layer in the load-lock vacuum chamber away from the hydrogen gas and plasma during the H-plasma flush and observed the same device performance improvements as those that resulted from our usual H-plasma flush with the sample left in the reactor. This indicated that the effect was mainly due to reactive flushing by the hydrogen plasma (i.e., the ions and radicals of the hydrogen plasma removing diborane molecules and boron atoms adsorbed to the reactor chamber walls and electrodes). The possibilities that the RF plasma was hydrogenating the p-layer and that dangling bonds were

passivated at the p/i interface by the hydrogen plasma were obviously not important factors in the device improvements caused by the H-plasma flush. The beneficial effects of the H-plasma flush were also not due to the hydrogen plasma etch removal of the CVD a-Si:H:B films discussed by Collins [122], for three reasons: the device improvements resulting from the H-plasma flush were observed even when the p-layer had no contact with the hydrogen plasma; our p-layers were deposited at a relatively low substrate temperature, 180°C, which should reduce the CVD of a-Si:H:B in the reactor; and it is difficult for a hydrogen plasma to etch a-Si:H:B, as we mentioned earlier. Since we also interrupted the silane plasma after b-layer deposition, we tried adding a H-plasma flush between the b- and i-layer depositions in p-b-i-n cells. We observed no improvements in device performance with this addition.

Table 3-3 shows that the most obvious improvement in the p-i-n device parameters resulting from the H-plasma flush occurred in the V_{oc}. The average improvement in V_{oc} from the p-i-n cells to the p_f-i-n cells was 0.039 V, and the average improvement in V_{oc} from the p-b-i-n cells to the p_f-b-i-n cells was 0.013 volts. This improvement was probably due to the decrease in the effective recombination velocity of carriers at the p/i interface [129]. The reduced p/i interface carrier recombination by the H-plasma flush was most likely due to reduced boron contamination at the p/i interface region. Short-circuit currents (I_{sc}), taken at 400-nm and 600-nm wavelengths, showed that the shorter wavelength I_{sc} improved more than the longer wavelength I_{sc} (Table 3-3) with the application of the H-plasma flush step for both p-i-n and p-b-i-n cells. The relative I_{sc} values in Table 3-3 were obtained by dividing the average I_{sc} values of each type of cell obtained at a 400-nm or 600-nm wavelength by the average I_{sc} values of the p-i-n cells at the same wavelength. The significantly higher improvements in I_{sc} at the shorter wavelengths indicated again that the cell improvement occurred near the p/i interface.

Table 3-3. Average Cell Parameters for Four Cell Structures
The structures, p_f-i-n and p_f-b-i-n, represent cells with an H-plasma flush after the p-layer deposition in the conventional p-i-n and p-b-i-n structures, respectively.

Cell Structure	V_{oc} (V)	J_{sc} (mA/cm^2)	FF (%)	Efficiency (%)	I_{sc},400 nm (relative)	I_{sc},600 nm (relative)
p-i-n	0.769	15.2	66	7.8	1	1
p_f-i-n	0.808	16.2	67	8.6	1.59	1.19
p-b-i-n	0.849	15.6	66	8.7	1.59	1.22
p_f-b-i-n	0.862	17.7	63	9.6	1.82	1.24

We also studied the light-biased, spectral response curves of a p_f-i-n cell with and without a one-volt reverse bias and found that the two curves were almost identical. This result is similar to the spectral response properties of cells treated with NF_3 reactive flushing observed by Catalano and Wood

[124] and indicates a reduced recombination loss at the p/i interface. It is interesting to note that the average p_f-i-n cell efficiency we obtained was similar to the average efficiency of our conventional p-b-i-n cells. The H-plasma flush process is, however, much simpler to implement in a single-chamber, glow-discharge deposition system than the deposition of a graded-band-gap buffer layer.

We studied the photoluminescence spectra of the p/i interface region by using samples with a 12-nm-thick p-layer followed by a 50-nm-thick i-layer deposited on Corning 7059 glass substrates. The samples were prepared with and without the H-plasma flush between the p- and i-layers. The excitation laser beam illuminated the samples through the i-layer. We found that the PL signal strength from the 1.2-eV main band of the samples with the H-plasma flush was about 50% larger than those of the samples without the flush. Since this luminescence peak was identified as resulting from a radiative tunneling transition between band tail states [130], the stronger PL signals observed in the H-plasma-flushed samples indicated, once more, that the densities of p/i interface states and/or defect states in the i-layer near the p/i interface were reduced by the H-plasma flush. The PL signals detected from the 0.60-eV defect band were about 200 times smaller than that of the 1.2-eV main band. We did not see any significant difference between the two types of samples in the defect band PL signal. The main PL band signals from a p-i sample with no H-plasma flush (p-i) and a p-i sample with the H-plasma flush (p_f-i) are shown in Figure 3-22. Also shown is the PL main band signals from a 50-nm-thick i-layer. This represents the PL signal strength of our i-layer material without its having been reduced by p/i interface and residual boron contaminations. PL measurements also detected no difference between p_f-i samples that were left in the reactor in contact with the H-plasma during the reactive flush and a sample that was moved to the load-lock chamber not in contact with the hydrogen plasma during the reactive flush. Secondary ion mass spectroscopy (SIMS) depth-profiling measurements using an oxygen beam for sputtering to optimize the boron sensitivity were made on p-i samples with and without the H-plasma flush. Similar to the report by Catalano and Wood [124], we did not find any significant differences between the two boron depth profiles. This indicates that the excessive residual boron contamination, removed by the H-plasma flush, was probably localized at the metallurgical p/i interface and was hard to identify by the depth-resolution of SIMS.

We demonstrated that the application of a simple, 30-second or shorter, H-plasma flush after the deposition of the p-layer of an a-Si:H p-i-n solar cell was effective in scavenging residual diborane molecules and adsorbed boron atoms in a single-chamber, glow discharge deposition reactor and can significantly improve the efficiency of the solar cell. Spectral response, PL and V_{oc} measurements showed that the cell efficiency improvement was due to a reduction in the recombination of charge carriers at the p/i interface.

3.6.4.6 Direct Measurement of the Mobility-Lifetime Product of Holes and Electrons in a p-i-n Solar Cell

Considerable effort has been devoted to measuring transport properties of electrons and holes using time of flight techniques [131]. This method measures electron and hole drift mobilities and drift lengths [132] on a time scale of 10^{-6} s or less. We have explored a simpler method to determine these parameters from quasi-direct-current (dc) measurements on p-i-n solar cells.

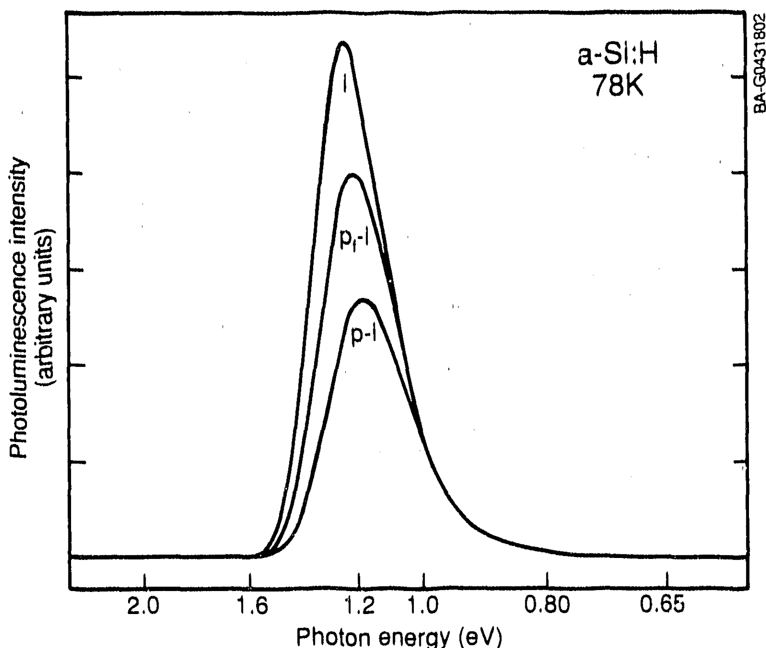

Figure 3-22. Photoluminescence spectra of a sample (i) with a 50-nm-thick, intrinsic a-Si:H layer deposited on glass, a sample (p-i) with a 12-nm-thick p-layer followed by a 50-nm-thick i-layer deposited on glass, and a sample (p_f-i) with a hydrogen-plasma reactive flush applied between p- and i-layer depositions. An Ar-ion laser at 488-nm wavelength was used for the excitation.

There have been many attempts to model the current-voltage curve of an a-Si:H p-i-n solar cell. Computer simulations offer the advantage of accurate calculations without approximations. Unfortunately, the final result is only as good as the input parameters, which are many and not accurately known. Simple expressions, based on approximate solutions of the transport equations, are much easier to use and have few unknown parameters. However, the approximations are not always justified. One of the earliest approximations was a modification of the Hecht expression,

$$J_t = J_o \, (l_d/L) \, [1-e(-L/l_d)] \; , \tag{3-7}$$

where J_o is the saturated current when all the carriers are transported across the i-layer, L is the sample thickness, and l_d is the drift length. This expression is only valid for single carrier transport when the electric field is uniform. The drift length is

$$l_d = \mu \; \tau \; E \; , \tag{3-8}$$

where μ is the photocarrier mobility, τ is its trapping time, and E the electric field. At low fields, the current is linear with field. At high fields, it saturates at the value J_o.

However, Eq. 3-7 is not valid for two carrier currents because it violates current continuity [133]. Nevertheless, this expression is still used to analyze two carrier photocurrents with the further assumption that μ and τ are for the hole. The justification is that because the hole has the smaller $\xi\tau$ product it will limit the current. This is an intuitive argument that is not always true. In fact, if space charge due to the photogenerated carriers can be neglected, then the hole will not limit the current because electrons and holes each make equal contributions to the current [135]. A carrier's contribution is, at low fields, equal to l_d/L because the carrier drifts a distance equal to its drift length before being trapped. During this transit, it induces a charge e l_d/L in the external circuit. Now both electrons and holes do this so that the total induced charge is proportional to the sum of the drift lengths of electrons and holes. From this argument, we clearly see that the carrier with the larger mobility-lifetime product will induce the most charge and thus carry the bulk of the current. In fact, a closed form solution to the two carrier transport equations can be obtained when the field is assumed to be uniform [133]. In this so-called uniform field approximation, the current is given by an expression identical to Eq. 3-7, with the drift length written as $l_d = (\mu\tau|_h + \mu\tau|_e)E$.

This simple physical picture breaks down when space charge distorts the electric field [134]. The carrier with the shorter drift length contributes most to the space charge because a larger number of these carriers is required to carry the current when it is the majority carrier. Near the p-i interface, the electron is the minority carrier so that the bulk of the current is carried by the holes. The opposite situation prevails at the n-i interface. The relative space charge contribution is given by the inverse of the ratio of the drift lengths. Experimentally, it does not appear that photogenerated space charge can produce significant field distortion in the usual a-Si:H p-i-n cell at room temperature [135]. However, at low temperature or for thick cells, a photogenerated space charge will distort the electric field and the simple uniform field model cannot be used.

In this section, we have described methods for measuring current-voltage on thick p-i-n solar cells that can be illuminated with strongly absorbed light through either side. In this case, there is only a single type of carrier in the bulk of the i-layer, where there is little light absorption. Therefore, recombination cannot take place. A carrier is either transported across the i-layer or trapped in a deep trap. It is a good approximation to view the region of light absorption as a contact that supplies just enough charge that can be transported by the bulk. The general description of bulk transport is quite complex and cannot be described by elementary expressions. Fortunately, there are two limiting regimes describable in elementary terms: (1) At lower light intensity or high voltage, insufficient space charge is produced in the i-layer to distort the electric field. Therefore, the current is given by Equation 3-7. (2) For large light intensity or low voltage, space charge distorts the field and the current is a pure single carrier space charge limited current, given by [136]

$$J_{sc} = \varepsilon\mu_d V^2 L^{-3}, \tag{3-9}$$

where ε is the static dielectric constant, μ_d is the drift mobility and V is the voltage across the i-layer.

The current is carried by the smaller of J_{sc} or J_t. At sufficiently low voltage or high light intensity, the current is always given by Eq. 3-9 and at high enough voltage by Eq. 3-7. The transition region cannot be described adequately by these approximations. What is observed in an actual cell depends on experimental conditions; for example, we take $\mu_d = 1.0 cm^2/Vs$, $L = 0.5 \times 10^{-4} cm$, and $V = 1$ V. Then $J_{sc} \sim 10\ A/cm^2$. Typical $J_o < 10^{-3} A/cm^2$ so that space charge effects could only be observed at voltages below about 0.01 V. However, for these low voltages, diffusion must be included [133] and the approximations made are not valid. However, for larger L or lower μ_d, space charge transport can be observed as we will demonstrate in the next section.

The solar cell is a standard p-i-n device with a 10-μm i-layer and a semitransparent titanium metal contact to the n-layer. We measured ac photocurrents at room temperature using a chopping frequency of 23 Hz and light of either 400-nm or 750-nm wavelength. The strongly absorbed, 400-nm light supplied electrons or holes to the i-layer when illumination was through the p- or n-layers, respectively. The 750-nm light is nearly uniformly absorbed, producing both electrons and holes.

Figure 3-23 shows photocurrent data. One curve represents illumination through the p-layer, one through the n layer using 400-nm wavelength light, and one using 750-nm light. The data clearly show a large difference for the two illumination directions using strongly absorbed light. Analysis of the data using Equation 3-7 gives:

$$\mu\tau|_h = 2.2 \times 10^{-8} cm^2/V \text{ and } \mu\tau|_e = 3.0 \times 10^{-7} cm^2/V .$$

Thus, the hole drift length is about one-tenth that of the electron. These values agree well with those determined by time of flight [131]. However, the current-voltage curve under uniformly absorbed light is nearly that for electron transport alone. This result clearly demonstrates that the carrier with the shorter drift length does not determine the current-voltage curve. As predicted by the two-carrier uniform-field model [131], the carrier with longer drift length determines the photovoltaic behavior.

For low voltage, the curve for hole transport Δ in Figure 3-23 does not show the linear dependence on voltage predicted by Eq. 3-7 because the current in this regime is carried by a space charge limited current flow, Eq. 3-9. At higher voltage, there is no space charge limitation and the current is trap-limited, obeying Eq. 3-7. The data were analyzed for the collection length in this high-voltage region. The slope of the linear portion of the current-voltage curve between 25 and 50 volts was used to find l_d. If there were no space charge effects, then the curve would be displaced to lower voltage and the linear region would extrapolate to the origin. Low light intensities were used to avoid more dramatic space charge effects. At the highest light intensity, space-charge-limited current flow is observed to nearly 90 volts. In this case, the current obeys Eq. 3-9, with $\mu_d = 2.9 \times 10^{-6} cm^2/V/s$. This value is much less than that determined from time of flight measurements [131]. However, on the time scale of these measurements, the demarcation level has moved toward the center of the gap so that the drift mobility should decrease accordingly.

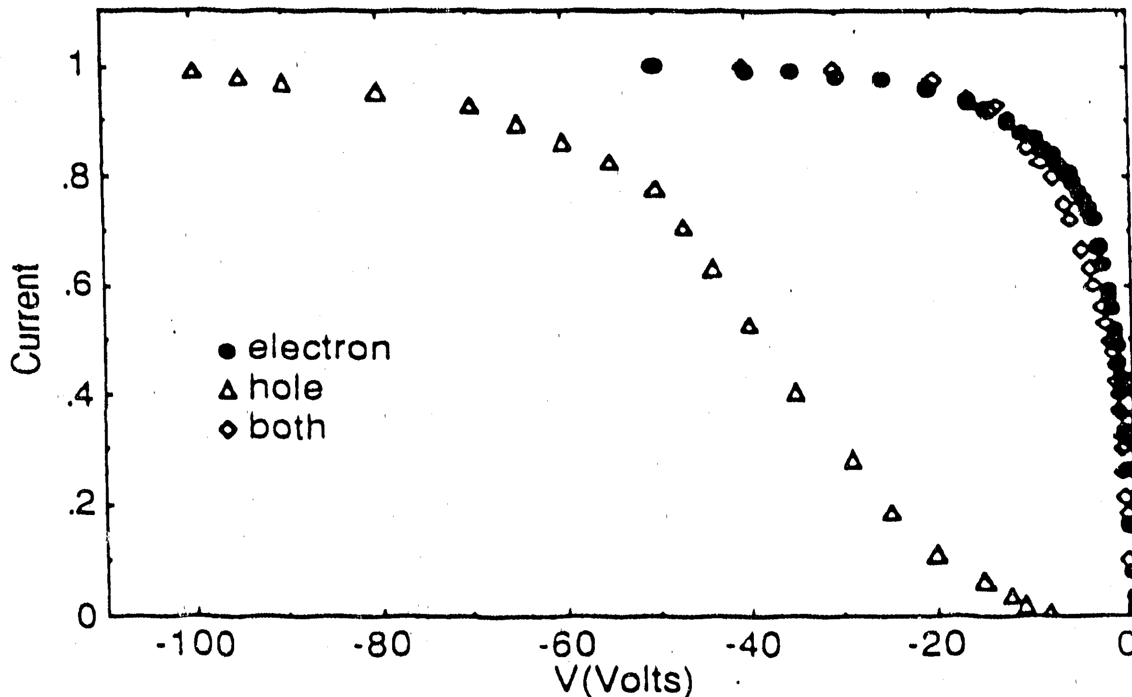

Figure 3-23. Current-voltage curves. (o) 400-nm light through the p-layer, J_o = 8.3nA/cm; (Δ) 400-nm light through the n layer, J_o = 8nA/cm; (◇) 750-nm light through the p-layer, J_o = 10nA/cm.

For electron transport, we observed no clear space-charge limited-current flow region. This is expected because of the much higher electron drift mobility. If the i-layer were only 0.5 μm thick, as in a typical solar cell device, it would be virtually impossible to observe space-charge-limited transport. Similarly, if the i-layer were thicker than 10 μm, space-charge transport for electrons could be observed. Experimental data show that for two-carrier transport in a-Si:H, the carrier with the longer drift length determines the photocurrent. This confirms the result of the uniform field approximation.

3.6.4.7 Explanation of the Anomalously Large Defect-Optical-Absorption Energies in Doped a-Si:H

In this work, we propose a two-part solution to the long-standing controversy [137,138] over defect-optical-absorption energies in doped hydrogenated a-Si:H: recognition that optical transitions are vertical and potential fluctuations. Subgap optical absorption energies of about 1.1 and 1.3 eV have been observed in n-type and p-type a-Si:H, respectively [139]. These are widely thought to correspond to $T_3^- \rightarrow T_3^0 + e^-$ and $T_3^0 \rightarrow T_3^+ + h^+$ transitions of the threefold-coordinated silicon dangling bond, T_3. With an a-Si:H optical band gap of E_g~1.7 eV, this result seems to imply that the $T_3^- \rightarrow T_3^0$

transition lies well below the $T_3^o \rightarrow T_3^+$ transition, meaning the effective correlation energy (U_eff) of the dangling bond is negative by more than 0.5 eV [137]. However, most workers [140] favor a positive U_eff for the dangling bond, primarily because an equilibrium ESR signal attributed to the neutral dangling bond is observed for a range of E_F positions near midgap.

There is significant electron-phonon coupling affecting the measured dangling-bond energy levels. As suggested by Balagurov et al. [141], the controversy over the optical absorption experiments is largely resolved by recognizing that optical transitions are vertical (i.e., no atomic relaxation occurs during the absorption). The observed absorption energies in n-type and p-type a-Si:H are then consistent with the band gap, without the need to assume either large negative correlation energy [137] or large electronic-level deepening by dopant-defect pairing [138]. However, the analysis indicates a smaller, disorder-induced, electronic-level deepening of about 0.2 eV, which may be understood in an electrostatic potential fluctuation model.

There is no unique position of a-Si:H electronic transition levels that can be applied to the analysis of all experiments. The large electron-phonon coupling at the defect precludes this. Large lattice relaxations mean that a theory of electronic-transition levels must distinguish among the various non-equilibrium and the thermodynamic equilibrium experiments. In this section, we will examine how much optical transition energies can be expected to differ from equilibrium transition energies.

The effective correlation energy of the T_3 defect is estimated by probing with ESR the dependence of thermodynamic equilibrium T_3^o densities upon Fermi energy position [142]. U_eff is positive and approximately 0.2 eV. This indicates that the electronic level associated with the transition from a relaxed T_3^o to a relaxed T_3^- is at a higher electron energy level than the transition from a relaxed T_3^+ to a relaxed T_3^o. If the optical transitions corresponded to these thermodynamic transitions, we would expect

$$E^n + E^p = E_g - U_eff. \tag{3-10}$$

Here, E^n (see Figure 3-24) and the analogous E^p are the transition energies for charged dangling-bond ionization (between fully relaxed defects) in n-type and p-type materials, respectively. However, there is no relaxation of a defect's final state in an optical absorption experiment [143]. To describe why the experimentally determined sum of optical transitions is about 2.4 eV, much larger than the 1.5 eV predicted by for fully relaxed transitions, we must first consider the nature of relaxed and unrelaxed dangling bonds in a-Si:H.

Let Q^q represent the fully relaxed configuration of T_3^q. In this notation, the fully relaxed defects are denoted by T_3^+ (Q^+3), T_3So(Q^o). As suggested by Adler [144], T_3^+, T_3^o, and T_3^- are isoelectronic with column III, IV, and V atoms, respectively. When relaxed, each adopts the hybridization that its isoelectronic analog has in threefold-coordinated gas molecules. To a good approximation, Q^o is an arrangement of the three neighboring atoms at the corners of a tetrahedron. This configuration arises from the sp^3 hybridization of electronic states that minimizes the total energy of T_3^o. Q^+ is an approximately planar, sp^2-hybridized, configuration with 120° bond angles that

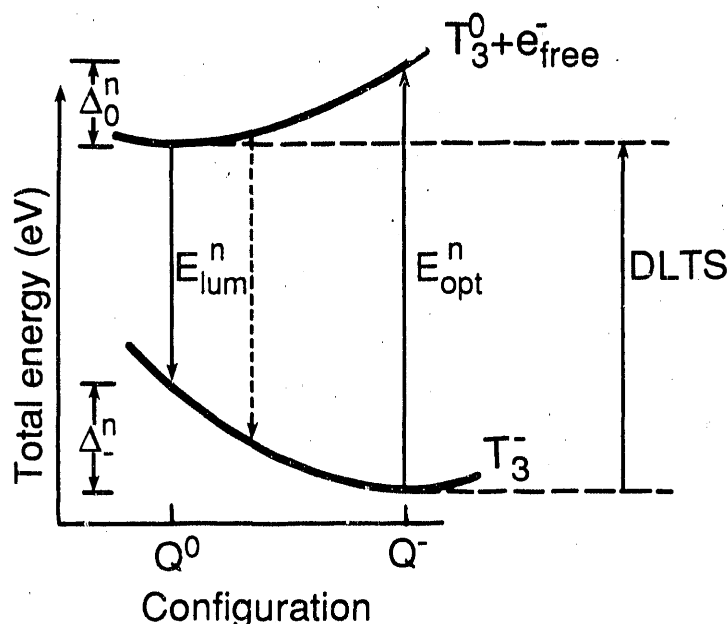

Figure 3-24. Defect formation energy of the T_3^- and T_3^o defects in n-type a-Si:H. Relaxation energies are from Ref. 145. Transition energies are indicated by arrows.

minimizes the energy of T_3^+. In Q^-, the bond angles are about 90°, reflecting the s^2p^3 unhybridized bonding. Total energy calculations [145] confirm that distinct energy-minimizing configurations Q^+, Q^o, and Q^- do form in the solid but suggest that the hybridization is not quite as complete as in the idealized configurations described earlier.

In general, T_3^+ (Q^s) denotes a dangling bond of charge r, in the configuration appropriate to the T_3^s relaxed state. A T_3^- defect which loses an electron without relaxing is denoted by T_3^o (Q^-). Several first-principles calculations of the relaxation energies of charged and neutral dangling bonds in a-Si:H have been undertaken [145,146]. These calculations show that misconfiguration raises the defect formation energy between 0.2 and 0.3 eV. Relaxation energies from Ref. 145 were used to draw each curve of Figure 3-24.

Optical absorption in n-type material by excitation of an electron out of a relaxed T_3^- by a photon of energy hν is represented by hν + T_3^- (Q^-) -> T_3^o (Q^-) + e_{free}. If the T_3^o then relaxes to Q^o, the photoluminescence upon reabsorption of the electron is represented by e_{free} + T_3^o (Q^o) -> T_3^- (Q^o) + hν - E^n_{FC}), where E^n_{FC} is the Franck-Condon shift energy in n-type a-Si:H and n is the same energy in each equation. Figure 3-24 is a schematic of the vertical optical and luminescence transitions in n-type a-Si:H, assuming relaxation energies taken from Ref. 145 and complete relaxation of all initial states. Typical values of experimentally observed energies in both n-type and

p-type a-Si:H follow. Experimentally, a 0.3 eV Franck-Condon shift between the n-type optical and luminescence energies is seen, indicating

Experiment	$E^n{}_{opt}$	$E^n{}_{lum}$	$E^n{}_{FC}$	$E^p{}_{opt}$	$E^p{}_{lum}$	$E^p{}_{FC}$
Energy (eV)	1.1	0.8	0.3	1.3	0.9	0.4

strong electron-phonon coupling at the dangling-bond defect. Tajima et al. [147] showed directly that $E^n{}_FC > 0.2$ eV by observing the excitation-energy dependence of the defect photoluminescence band. Theory [145] would predict a slightly larger Franck-Condon shift of about 0.45 eV, indicating that complete relaxation of the luminescence initial state is not obtained. This does not affect predictions of optical absorption energies because the process begins with an equilibrium state.

The absorption energy that would be observed for complete relaxation of both initial and final states E^n is indicated in Figure 3-24. This corresponds to the transition between thermodynamic equilibrium defect states. As described earlier, it is measurement of these thermodynamic transition positions that yields the positive value of U_eff. From Figure 3-24, the vertical optical transition in n-type material is larger:

$$E^n{}_opt = E^n + 0.2 \text{ eV}.$$

From similar arguments, the optical transition in p-type material is

$$E^p{}_opt = E^p + 0.3 \text{ eV},$$

where 0.3 eV is the relaxation energy from Q^+ to Q^o of the $T_3{}^o$ final state [145]. Substituting these two expressions in Equation 3-10 yields

$$E^n{}_opt + E^{po}pt = E_g - U_eff + 0.5 \text{ eV}. \tag{3-11}$$

A sum of optical transition energies $E^n{}_opt + E^n{}_opt$ greater than E_g is, therefore, expected because the incident photon must supply sufficient energy to leave the defect in an unrelaxed final state. The remaining 0.4-eV discrepancy between Equation 3-11 and the experimental results is explained in Section 3.6.4.8.

Disorder in a-Si:H has often been modelled by electrostatic potential fluctuations. Some of the applications of this model are listed in Ref. 148. Figure 3-25 includes a schematic of these fluctuations and of the resulting electronic transition energies in n-type a-Si:H. The conduction- and valence-band mobility edges E_c and E_v, like E_F, do not depend on the electrostatic potential V(x) at the position x. The mobility edges are not position dependent in the potential fluctuations [149]; they separate electronic states extended through the entire solid from localized states [150]. However, the energy required to ionize a defect to the band edge does depend on V(x) because the carrier is localized in the initial state but not in the final state. Due to the electrostatic attraction of the electron to the region, more energy is needed to ionize a T_3^- to T_3^o in regions of positive V(x) than in regions of negative or zero V(x). This results in the transition energy positions sketched in Figure 3-25(a). However, as we shall see, the regions of highest absorption energy actually dominate the observed absorption

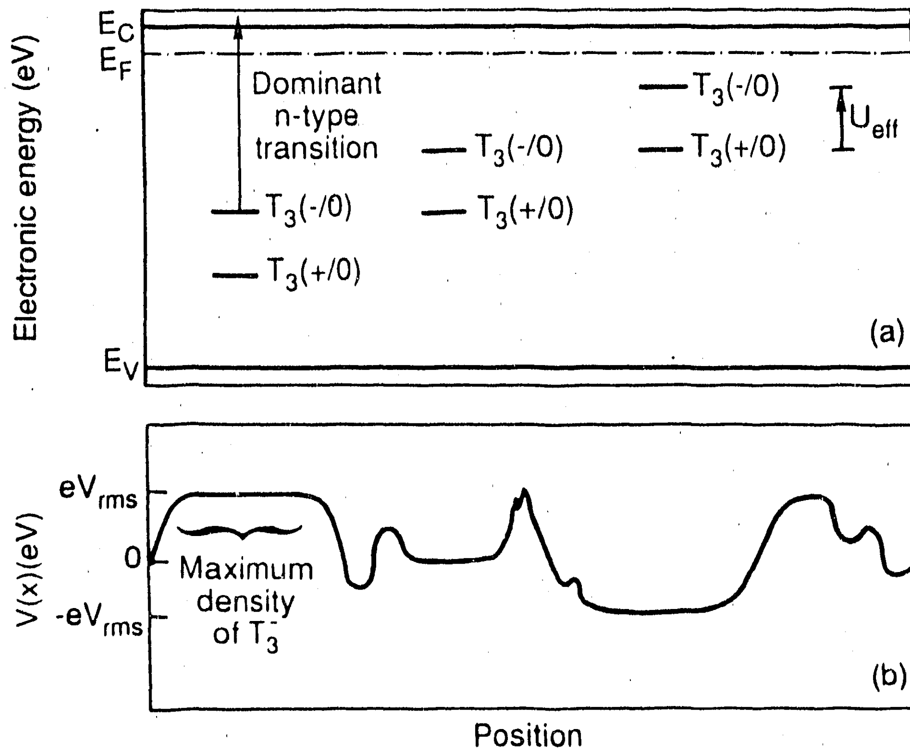

Figure 3-25. Schematics of electrostatic potential fluctuations. (a) Dependence of electronic transition levels of the T_3 defect in a-Si:H on potential fluctuations. The dominant observed transition $T_3^- \rightarrow T_3^o$ is indicated. (b) The position-dependent potential, eV(x), with the region of maximum defect density indicated.

energies due to spatially nonuniform defect concentrations. This gives rise to the observed electronic transition-level deepening. It should also be noted that U_{eff} is independent of V(x), and the $T_3^o + h^+$ transition energy is greatest in regions of low electrostatic potential.

Recent work [151] shows that dangling bond densities in device quality a-Si:H are largely determined by thermodynamic equilibrium statistics [152]. The concentration of the dangling bond is determined by a structural freeze-in temperature T^* and is given by

$$n(T_3^q) = n_s i \exp(-F[T_3^8]/kT^*) \ , \qquad (3\text{-}12)$$

where $F[T_3^q]$ is the formation energy of the dangling bond species, T_3^q, which is consistent with the position of E_F.

The formation energies of charged defects depend upon V(x), but those of neutral defects do not. Thus, $F[T_3^o]$ is independent of V(x) and the formation energies of the charged dangling bonds are

$$F[T_3^+, \nu(x)] = F_o[T_3^+] + eV(x) \quad (3-13)$$

and

$$F[T_3^-, \nu(x)] = F_o[T_3^-] - eV(x) ,$$

where e is the electronic charge and F_o is the formation energy of a defect at V = 0, the mean value of V(x).

When thermodynamic equilibrium is established in a doped film, the charged defects will form preferentially in certain regions according to Eqs. 3-12 and 3-13. In n-type material, the T_3^+ defects are found in exponentially greater numbers in regions of greatest positive V(x). As described above, these defects have the largest ionization energy. Due to their great numbers, they will dominate the observed experimental energies and this effect will deepen the observed electronic-transition levels, $T_3^- \rightarrow T_3^o$, in n-type a-Si:H. Similarly, T_3^+ defects formed in regions of negative V(x) will dominate the experimental observations and have transition levels further from E_v than the minority of T_3^+ defects formed in other regions. Since $E^n{}_opt$ and $E^p{}_opt$ are each increased by roughly the root-mean-square potential fluctuation half-width eV_rms, Eq. 3-11 becomes

$$E^n{}_opt + E^n{}_opt = E_g - U_eff + 0.5\ eV + 2\ eV\ _rms.$$

Thus, the experimental data suggest that eV_rms ~ 0.2 eV. It should be noted that the thermodynamic equilibrium theory of defect densities suggests that when eV_{rms} exceeds $U_{eff}/2$, copious charged dangling bonds form [148] in undoped a-Si:H.

The long-standing controversy over an anomaly of about 0.9 eV in the sum of optical absorption energies in doped a-Si:H is largely resolved by recognizing that optical transitions are to unrelaxed final states of the defect. This resolution uses a positive value of U_eff and significant (0.2 to 0.3 eV) relaxation energies of dangling bond defects. The anomaly of about 0.4 eV that remains can be explained by electronic-level deepening due to potential fluctuations of 0.2 eV half-width. A more complete treatment in the thermodynamic-equilibrium-model framework of this anomaly and other experimental results in doped a-Si:H are given in Ref. 139.

3.6.4.8 Correction for Multiple Reflections in Infrared Spectra of Amorphous Silicon

In IR spectroscopy of a-Si:H, multiple internal reflections of the IR beam give an apparent absorbance which is greater than the actual absorbance. In the seminal paper by Brodsky, Cardona, and Cuomo [153], the interference-free transmittance is approximated by

$$T_{film} = (1-R)^2 e^{-8},1d\ /\ (1-R^2 \alpha d) , \quad (3-14)$$

where R is an empirically determined interface multiple reflection loss, α is the absorption coefficient, and d is the film thickness. This expression is for a freely supported film but, except for substrate absorptions, it is the same for a film on a substrate since in either case there are two air interfaces. In terms of the absorption-free transmission of the substrate T_o, this becomes

$$T_{film} = \frac{4T_o^2 e^{-\alpha d}}{(1+T_o)^2 - (1-T_o)^2 e^{-\alpha d}} . \qquad (3\text{-}15)$$

This expression accounts for reflections at the film-air and substrate-air interfaces. Based on R = 30% for the c-Si refractive index of 3.42, approximately 8% of the transmitted beam undergoes two internal reflections before joining the primary transmitted beam, and 1% undergoes four internal reflections. Most researchers either cite this work or choose techniques that eliminate interference fringes from the spectrum. This can be done through substrate choice, wedged or roughened c-Si, or measurement conditions such as using a resolution lower than the fringe period.

To confirm the accuracy of the technique used in our laboratory, we deposited device quality, glow discharge a-Si:H simultaneously on double-polished, single-polished (rough side), single-polished (polished side), roughened, and wedged c-Si substrates and compared the IR spectra. In an unexpected result, the spectrum of the Si-H wag at 630/cm did not change with surface roughness, except for the noise level. We present here an assessment of substrate choice and analysis method for quantitative analysis of IR spectra.

Films were deposited in a standard RF glow discharge deposition system under conditions that produce device quality films: 500 mtorr SiH_4, 250°C substrate temperature, and 1.4 Å/min deposition rate. The plasma diameter was 13 cm, and a uniform film could be deposited on up to six substrates. The uniformity was confirmed by placing matched, double-polished substrates in different deposition positions. For the IR comparison, the following c-Si substrates were used: double-polished (Monsanto, p-type), single-polished (Monsanto, n-type and Siltec, p-type), roughened, and wedged. To prepare the roughened samples, the polished side of Siltec c-Si was lapped with size 600 abrasive grit. To make the 2° wedged samples, Siltec c-Si was attached to a wedged holder and the unpolished side was ground with 5 μm Al_2O_3 and polished with 1 μm Al_2O_3. The thickness was measured on Corning 7059 glass substrates using an Alpha-Step profiler. IR transmission spectra were measured with either a Nicolet 7199 FTIR at 2/cm resolution or a Perkin-Elmer 580B at either 1.4/cm or 6.8/cm resolution. The total reflectance and the diffuse reflectance were measured in the near IR using an ACTA reflectance sphere on a Beckman UV-5240 spectrometer.

Before proceeding further, we must address a practical difficulty in integrating the 630/cm peak which arises from the substrate c-Si phonon mode at 615/cm. Unless the substrate and reference c-Si are perfectly matched, this peak will interfere with the a-Si:H peak. This is demonstrated in Figure 3-26. Spectrum (a) is the single-polished c-Si substrate showing the peak at 615/cm. Spectrum (c) is 9700 Å of a-Si:H deposited on this substrate and measured versus a matched reference c-Si piece. In spectrum (b), the reference c-Si is thicker than the substrate, so there is an indentation in the 630/cm peak due to the 615/cm peak; in spectrum (d), the reference is thinner and the substrate absorption forms a clear shoulder. We have found that a single 10-cm-diameter c-Si wafer has enough thickness variation from the center to the edges to produce this degree of reference mismatch. Often the shoulder is not as pronounced and may not be recognized as a contribution from the substrate

absorption. The slope and offset from 100% of the baselines are due to differences in the relative scattering of the substrate and reference c-Si.

Because of the interference of the c-Si absorption at 615/cm, we find more reliable integrations of the 630/cm peak from integrating just the high-frequency side of the peak from 640/cm to 740/cm and multiplying by a scaling factor of 1.91 ± 0.05. This factor is the ratio of the integrated absorbance of the entire peak to that of the high-frequency side measured for samples with well-matched references. An additional source of uncertainty in the integration comes in drawing the baseline. Because of the curvature in the spectra, a linear baseline is inappropriate and, with a poorly matched reference, the appearance of c-Si peaks compounds the difficulty in establishing the baseline. As shown in Figure 3-26, this gives a 10% uncertainty in the integration for well-matched substrates and a greater uncertainty for poorly matched substrates.

To confirm that Eq. 3-15 succeeded in extracting the actual absorbance from a spectrum with multiple reflections, we simultaneously deposited 6700 Å of a-Si:H on wedged and double-polished substrates. Spectra of the substrates [Figure 3-27(a) and (b)] taken at a nominal 1.4/cm resolution demonstrated that the interference fringes evident in the double-polished c-Si are eliminated by the 2° wedge. The fringe period was ~2.8/cm at 1000/cm, corresponding to the substrate thickness of 0.05 cm. The variations in the amplitude of the fringes were due to changes in instrument resolution with wavelength. The abrupt change in fringe amplitude, for example at 2000/cm, occurred at filter changes with corresponding changes in slit width. The substrates have major peaks at 615/cm and 1110/cm, with smaller peaks in between.

Spectra of a-Si:H on these substrates are shown in Figure 3-27(c) and (d). For clarity, the resolution was reduced to 6.8 cm^{-1} so that the fringes were not visible. We have verified that the spectrum at low resolution is simply the average of the fringes seen at higher resolution. We have also compared the spectra from the Perkin-Elmer 580B to the Nicolet 7199 FTIR and found that they are the same. In the case of the FTIR, the spectra were measured at 2/cm resolution but the interference fringes could be eliminated by removing the second burst in the interferogram before transforming. The spectra have the characteristic Si-H stretch at 2000/cm and the wag at 630/cm. As is typical for high-quality films, the SiH_2 peaks at 2100/cm, 840/cm, and 890/cm were not apparent. As expected, the size of the peaks was greater on the double-polished substrate than on the wedged substrate because of the approximately 10% of the beam, which has 3 or 5 passes through the film.

To quantitatively compare these spectra, the absorbances of the 630/cm and 2000/cm peaks were integrated using Brodsky's technique. The measured transmission T_m was read from the spectrum at 10/cm intervals and normalized to an absorption-free background by dividing by the baseline transmission. For a spectrum referenced to c-Si, $T_m = T_{film}/T_o$. Eq. 3-15 could then be solved for α,

$$e^{-\alpha d} = \frac{-2T_o + [4T_o^2 - T_m^2(1-T_o)^2(1+T_o)^2]^{1/2}}{T_m\ (1-T^o)^2}, \qquad (3\text{-}16)$$

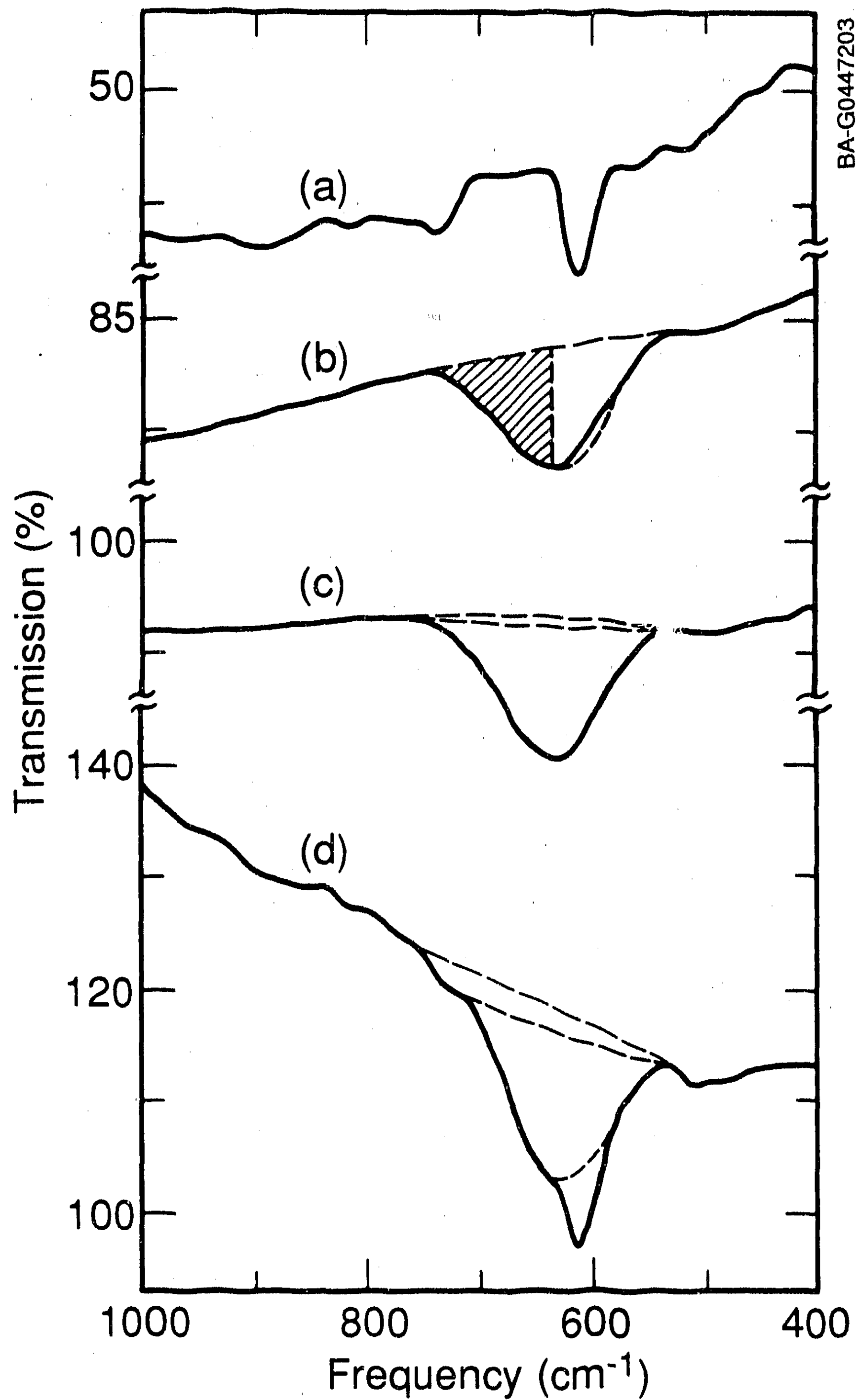

Figure 3-26. **Spectra of a c-Si substrate referenced to air (a), and of 9700 Å of a-Si:H on this substrate referenced to c-Si of different thicknesses.** The reference is thicker than the substrate in (b), well matched in (c), and thinner in (d). In spectrum (b), we show the region which we integrate, and spectra (c) and (d) illustrate the baseline uncertainty.

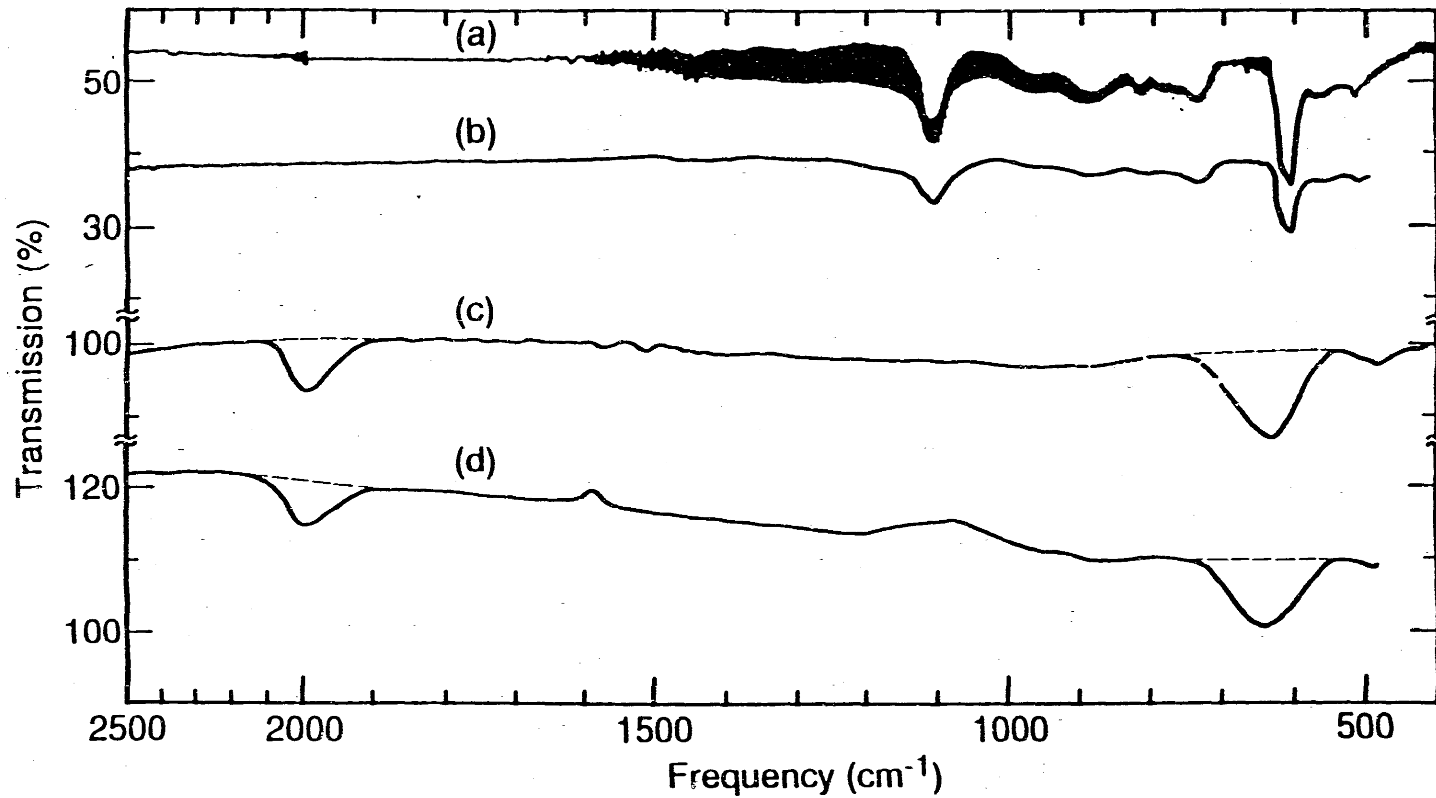

Figure 3-27. Spectra of (a) a double-polished c-Si substrate and (b) a wedged substrate measured with 1.4/cm resolution. The same substrates after deposition of 6700 Å of a-Si:H, where (c) is double-polished and (d) is wedged shown at a resolution of 6.8/cm.

from which the integrated absorption is obtained:

$$I = \int \alpha(\omega)/\omega \; d\omega \; . \tag{3-17}$$

Table 3-4 illustrates the integration procedure using the spectrum in Figure 3-26(b). Table 3-5 shows the integrated absorbances calculated using Eq. 3-16, with $T_o = 0.54$ compared to the absorbances calculated without internal reflections via

$$e^{-\alpha d} = T_m \; . \tag{3-18}$$

The integrated absorbance of films on double-polished substrates calculated using Eq. 3-16 equal those on wedged substrates calculated using Eq. 3-18. In other words, this confirms that the method used by Brodsky accurately accounts for the effect of multiple internal reflections of the IR transmission spectrum of a-Si:H. This method represents approximately a 20% correction to the integrated absorbance. A refinement on this technique would include reflections at the film-substrate interface [154]. Because the index of refraction of a-Si:H is similar to that of c-Si, this represents less than a 1% change in the integrated absorbance. When measuring spectra of alloys such as a-SiGe:H or a-SiC:H, reflections at this interface become more noticeable.

Brodsky applied the expression for multiple reflections, Eq. 3-15, to films on double-polished c-Si for which $T_o = 0.54$ both theoretically and experimentally. Commonly, single-polished substrates are used, which scatter light and reduce the measured transmission. The scattering increases with frequency, and, thus, T_o decreases with frequency. By measuring the transmission and the diffuse and specular reflectance of different substrates at 2500/cm, we confirmed that the decrease in transmission corresponds to an increase in diffuse scattering and a decrease in specular scattering (Figure 3-28). We thus anticipated that the measured specular reflectance should be used in Eq. 3-14, and that it would depend on substrate roughness and frequency. With the decrease in specular reflectance, the number of multiple passes through the sample was expected to decrease, producing a decrease in the amplitude of the measured IR peaks (as for the wedged substrate in Figure 3-27.

To investigate this possibility, substrates with varying degrees of specular reflectance were prepared. Figure 3-29 shows spectra of the c-Si substrates referenced to air. The double-polished substrate has approximately 54% transmission throughout this region. The single-polished and roughened substrates have lower transmission, which decreases with increasing frequency. For each substrate, a matched reference piece was chosen such that a double-beam spectrum of the substrate before deposition versus the reference is flat and featureless with 100% transmission.

a-Si:H was deposited on these substrates simultaneously. IR spectra were measured versus the matched references. The striking result in Figure 3-30 is the similarity of all the spectra. The 630/cm peak magnitude is unchanged with substrate, and the 2000/cm peak is different only on the roughened substrate, where is it slightly larger. This is in contrast with the prediction that the peak size would decrease with increasingly scattering substrates.

Table 3-4. Calculation of Integrated Absorbance[a] of Si-H Wag in Fig. 3-26(b) Spectrum using Brodsky's Correction with T_0 = 0.54

$\omega(cm^{-1})$	$T_m(\%)^b$	$\alpha(cm^{-1})$
740	99.5	45
730	99.0	90
720	98.0	177
710	96.9	275
700	95.3	417
690	93.8	562
680	92.2	709
670	90.1	912
660	88.6	1058
650	87.6	1163
640	87.0	1226

[a] $I = \int_{540}^{740} \alpha(\omega)/\omega \, d\omega = 1.9 \int_{640}^{740} \alpha(\omega)/\omega \, d\omega = 1.9$

$$\sum_{640}^{740} \alpha(\omega)/\omega \, \Delta\omega = 189 \text{ cm}^{-1}.$$

[b] Normalized by dividing by the baseline.

Table 3-5. Integrated Absorbances (in cm^{-1}) of Si-H Peaks at 2000 and 630 cm^{-1} Calculated from Spectra in Fig. 3-26 with and without Brodsky's Correction for Multiple Internal Reflections

Substrate	Brodsky Correction (T_0 = 0.54)		No Multiple Internal Reflections	
	I(2000)	I(630)	I(2000)	I(630)
Double-polished 1	37[a]	212[a]	45	250
Double-polished 2	39[a]	216[a]	46	354
Wedged	33	178	39[a]	211[a]

[a] Numerals identify the analysis method which is expected to be correct for each substrate type.

We analyzed these spectra using Brodsky's method. The question in applying Eq. 3-16 to a sample which is not deposited on double-polished c-Si is what value to use for T_0. Instead of using the double-polished value of 54%, one might measure the substrate transmission directly from Figure 3-29. Alternatively, recognizing that T_0 is introduced in Eq. 3-15 to describe R, one can measure the specular scattering directly (Figure 3-28) and return to Eq. 3-14 to get α. Since the same film was deposited on all the substrates in Figure 3-30, the correct analysis is that which gives the same integrated absorption for all the samples.

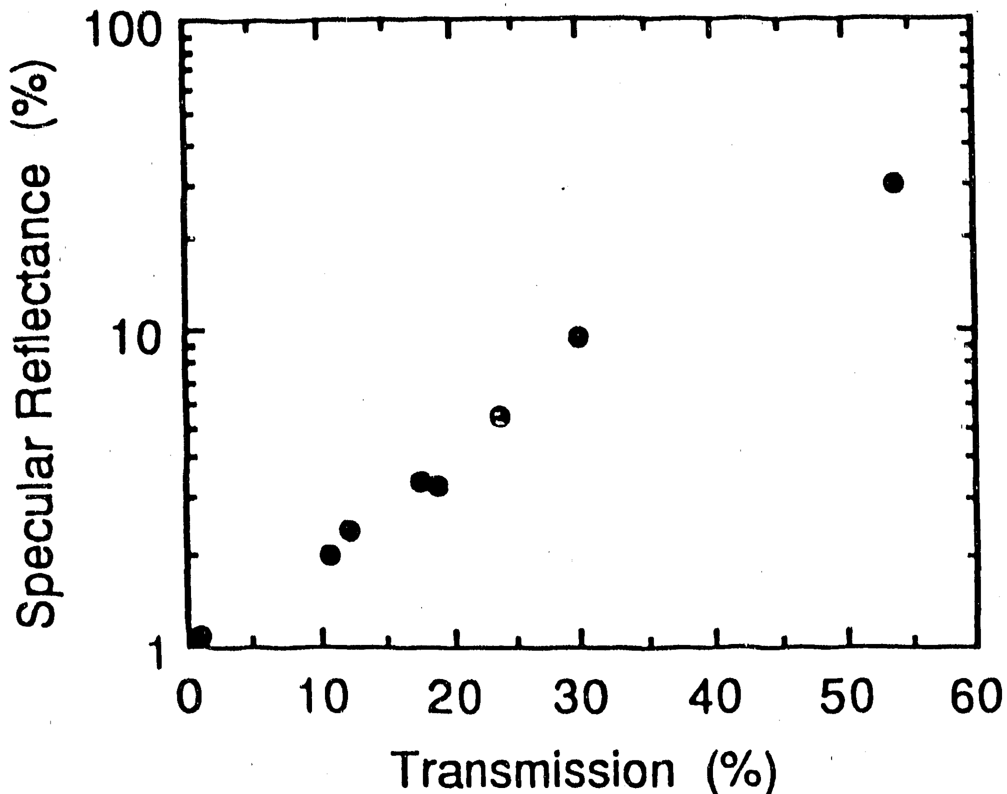

Fig. 3-28. The decrease in specular reflectance with a decrease in transmission for c-Si substrates with varying degrees of surface roughness

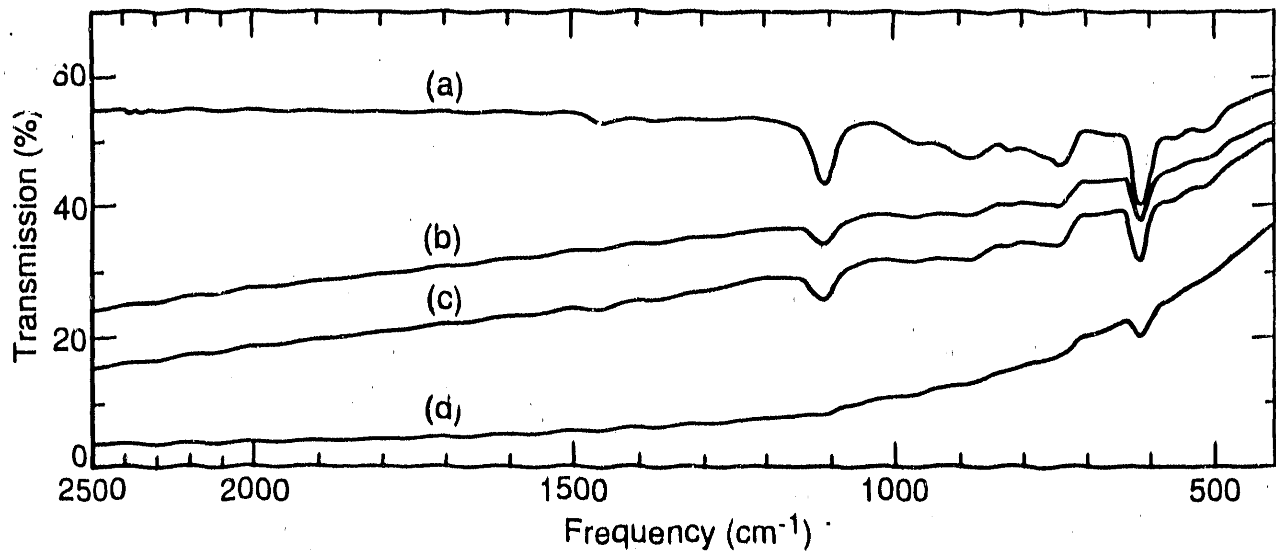

Figure 3-29. c-Si substrates referenced to air: (a) double-polished, (b) Siltec single-polished, (c) Monsanto single-polished, (d) roughened

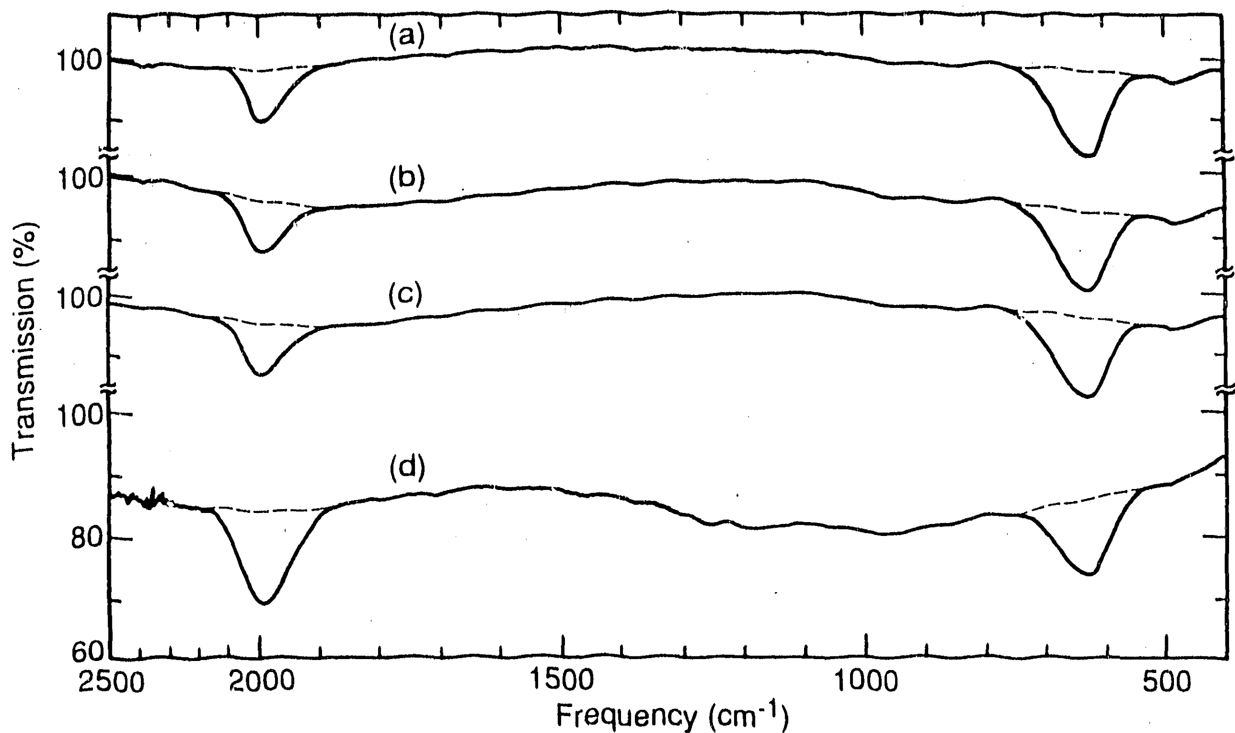

Figure 3-30. 9700 Å of a-Si:H deposited simultaneously onto the substrates in Fig. 3-29. The peak heights are unchanged for all substrates except for the increase in the 2000 cm^{-1} peak on the roughened substrate.

In Table 3-6, the various treatments of the multiple reflections are compared. The primary result is that for the 630/cm peak, in spite of the varying degrees of substrate roughness, a consistent integrated absorbance is obtained when all the samples are treated like the double-polished sample with $T_o = 0.54$. When multiple reflections are not considered, the apparent integrated absorbances are 20% too large. If the measured transmission of the substrate is used for T_o, the calculated absorbances can be grossly incorrect. A scattering substrate has a low transmission which, in Eq. 3-15, implies a high reflectance, therefore, Brodsky's correction gives a large reduction to the measured absorbance. In the case of the roughened substrate, the calculated absorbance at 2000/cm is reduced by an order of magnitude. If the specular reflectance is measured directly and used in the correction, then for the double-polished substrates it is equivalent to using $T_o = 0.54$ and in the limit of very scattering substrates it is equivalent to omitting the correction for multiple reflections. At 630/cm, the most consistent results are obtained by using $T_o = 0.54$ for all non-wedged substrates.

The fact that roughened substrates have the same contribution from multiple internal reflections as polished substrates may be coincidental. For a roughened substrate, the IR beam is not normal to the substrate surface and therefore refraction results in an angular distribution in the primary transmitted beam. The angular distribution after internal reflections is greater, which would suggest that a smaller percentage of the light reaching the detector has undergone multiple internal reflections than for a polished surface. However, the efficiency of internal reflection increases as the angle of incidence decreases, which would tend to increase the contribution from multiple reflected light for rough substrates. Apparently, these two effects cancel out for the 630/cm mode. At 2000/cm, where the decrease in substrate transmission is evidence of greater scattering, the effect of increased reflectance due to oblique incidence dominates, and the size of the peak actually increases on the roughened substrate. Since in the region of the 630/cm peak the single-polished substrates do not scatter significantly, these competing effects are not of concern in the calculation of hydrogen content from the IR spectra.

Because of the effect of a roughened surface on the absorption at 2000/cm, we looked for differences in spectra of films deposited on the polished versus the rough side of Siltec single-polished c-Si and of substrates that were further roughened with size 600 grit. This comparison is particularly important as films are often deposited on the unpolished side of single-polished substrates to improve the adhesion. For the single-polished substrate, the spectrum was unchanged for deposition on either surface and was identical to that on a double-polished substrate. For the roughened substrate, the 630/cm peak was the same as on the double-polished substrate for deposition on either surface. The 2000/cm peak was 40% larger for the film deposited on the polished side and 80% larger for the film deposited on the rough side.

For these films, accounting for multiple internal reflections in the IR spectra of a-Si:H constitutes a 20% correction to the integrated absorbance. This correction is greater for thinner films or films with a lower hydrogen content. With the use of a wedged substrate, which removes the reflected beams from the primary beam, we have confirmed that the technique of Brodsky, Cardona, and Cuomo [153] accurately accounts for the multiple reflections. Since it is much simpler to apply their correction than to fabricate wedged substrates, we recommend this approach.

Table 3-6. Integrated Absorbances (in cm^{-1}) of Si-H Peaks at 2000 and 630 cm^{-1} with Various Corrections for Multiple Internal Reflections

Substrate	Brodsky Correction (T_0 = 0.54)		No Multiple Internal Reflection		Brodsky Correction T_0 = Measured Substrate Transmission		Brodsky Correction Measured Substrate Specular Reflectance	
	I(2000)	I(630)	I(2000)	I(630)	I(2000)	I(630)	I(2000)	I(630)
Double-polished 3	43	203	52	239	44	203	43	206
Double-polished 4	37	187	44	220	37	180	37	189
Single-polished 1[a]	35	204	41	239	22	181	40	216
Single-polished 2[b]	41	197	48	232	18	150	47	218
Roughened	95	182	112	216	10	96	110	208

[a]Supplied by Siltec.
[b]Supplied by Monsanto.

There are a number of ways to remove the interference fringes from the IR spectrum. Typical approaches are to roughen the substrates or to reduce the resolution of the spectrometer. With FTIR, removing the second burst from the interferogram eliminates the fringes. We have found that whether the substrate is double-polished, single-polished, or deliberately roughened, for the 630/cm mode Brodsky's correction should be applied using the same reflectance as in the double-polished case. In other words, removing the interference fringes from the IR spectrum does not eliminate multiple internal reflections in the sample. These results indicate that it is unnecessary to buy the more expensive double-polished substrates and counterproductive to roughen substrates since this increases the noise in the spectrum without eliminating the multiple reflections.

For substrates that were roughened with size 600 grit, the mode at 2000/cm is actually increased compared to that on a double-polished substrate. This is attributed to the increase in the diffuse scattering, even though from the decrease in the specular reflectance the multiple passes through the film might have been expected to decrease. This is a further caveat against the use of roughened substrates. On the other hand, we find for single-polished substrates that the spectrum is unchanged with deposition on the rough or polished side so the rough side may be used to increase adhesion.

3.6.4.9 Limitations of the Integrated Sub-Band-Gap Absorption for Determining the Density of Defects in a-Si:H

A commonly used method for determining the density of defects (N_d) in a-Si:H is to integrate the excess sub-band-gap absorption (ISA) in the region of energies lower than about 1.5 eV. The relation is

$$N_d = 7.9 \times 10^{15} \times \int \Delta\alpha(h\nu)d(h\nu) \quad , \tag{3-19}$$

where the value of the prefactor is determined by comparing values of N_d with the electron spin densities and is also compared with theory [155]. The excess optical absorption coefficient $\Delta\alpha(h\nu)$ is the difference between the experimentally measured value and $\alpha_0 \exp(h\nu/E_0)$; α_0 and E_0 are the fitting parameters of the exponential band-tail absorption.

Equation (3-19) is a modification of a more general sum rule procedure, in which the density of defects in a material is equated, through various constants (index of refraction, etc.), to the integral of the absorption coefficient versus the energy, extended over the entire defect absorption band [156]. For the case of a-Si:H, the integral should be extended to all the energies related to electron transitions from the defect states (in the gap) to all the conduction-band final states. As a practical matter, however, this cannot be done for the a-Si:H excess absorption spectra because of the exponentially increasing number of transitions between occupied valence band-tail states and empty conduction band states at energies higher than 1.5 eV, which overwhelm the contribution to the absorption from midgap defects.

We will proceed by calculating the absorption coefficient as a function of photon energy [$\alpha(h\nu)$] for well-defined densities of states that will include specialized midgap distributions, $N_d(E)$, and then compare the integrated value of $N_d(E)$ with the result obtained from Eq. 3-19. By definition, $\alpha(h\nu)$ is the integral of the product of the density of occupied initial states N(E) and

the unoccupied final states G(E') of every electron transition characterized by an energy difference of hν:

$$\alpha(h\nu)= [const/h\nu) \times \int N(E)\ G(E')\ \delta(E-E'-h\nu)\ dE\ dE'] \ . \qquad (3\text{-}20)$$

The σ function ensures that the final state energy E' is hν higher than the initial state energy E. The matrix elements for transitions between extended states and from localized to extended states are assumed constant with energy, an assumption introduced by Davis and Mott [157]. However, the basic conclusion of this work would be unaffected if we were to introduce a functional dependence for the matrix elements. Integration of Eq. 3-20 with respect to E' yields

$$\alpha(h\nu) = (const/h\nu) \times \int N(E)\ G(E+h\nu)\ dE \ . \qquad (3\text{-}21)$$

The constant was found to be 4.34×10^{-38} eV^2cm^5 by Vanecek [158] by comparing the measured value of α(2.5 eV) to the value calculated using Eq. 3-21 with only the extended states included in the integral. Figure 3-31 shows the density of states assumed in our study. The conduction band density is taken to be the free electron distribution, $6.7 \times 10^{21}(E-E_c)^{1/2}$ [159]. The zero energy is set at the conduction band mobility edge E_c, with decreasing energies toward the valence band mobility edge E_v. A similar dependence is assumed for the valence band.

In our first example to test the ISA method of determining subgap defect densities, we added delta function distribution for $N_d(E)$ at each of three energies, E_i = -0.9, -1.1, and -1.3 eV, in addition to the usual exponentially varying conduction and valence band tails, assumed to have characteristic energies of 30 and 50 meV, respectively. The total density of states is fixed at a value $2 \times 10^{16}/cm$ and is defined by the following distribution:

$$N_d{}^i(E) = 2 \times 10^{16}\delta(E-E_i)/cmeV \ . \qquad (3\text{-}22)$$

Equation 3-21 is now used to calculate the absorption coefficient as a function of the energy for each $N_d{}^i(E)$, the results of which are plotted in Figure 3-32.

As expected, the absorption coefficient goes to zero for photon energies less than E_i-E_c, while following a $(E-E_i)^{1/2}$ energy dependence at higher energies. We can see from Figure 3-32 that the ISA density of defects calculated from Eq. 3-19 over the range of energy between 0 and 1.5 eV (i.e., to where the exponential contribution becomes dominant) varies by almost an order of magnitude.

In the absence of the exponential tail state absorption, we would have been able to see more of the contribution to the ISA from Δα(hν) at higher energies. Had the total number of transitions to the conduction band been considered from each $N_d{}^i(E)$, the ISA for the three curves of Δα(hν) would have given the same result. This clearly demonstrates the flaw in the ISA method.

Practically speaking, subgap defects in a-Si:H are not expected to take on this σ-function form. In Figure 3-33, we show four Gaussian energy dependencies for $N_d{}^i(E)$, with full-widths-at-half-maximum (FWHM) from 0 (delta-function case) up to 0.32 eV. In each case, the total density of states is

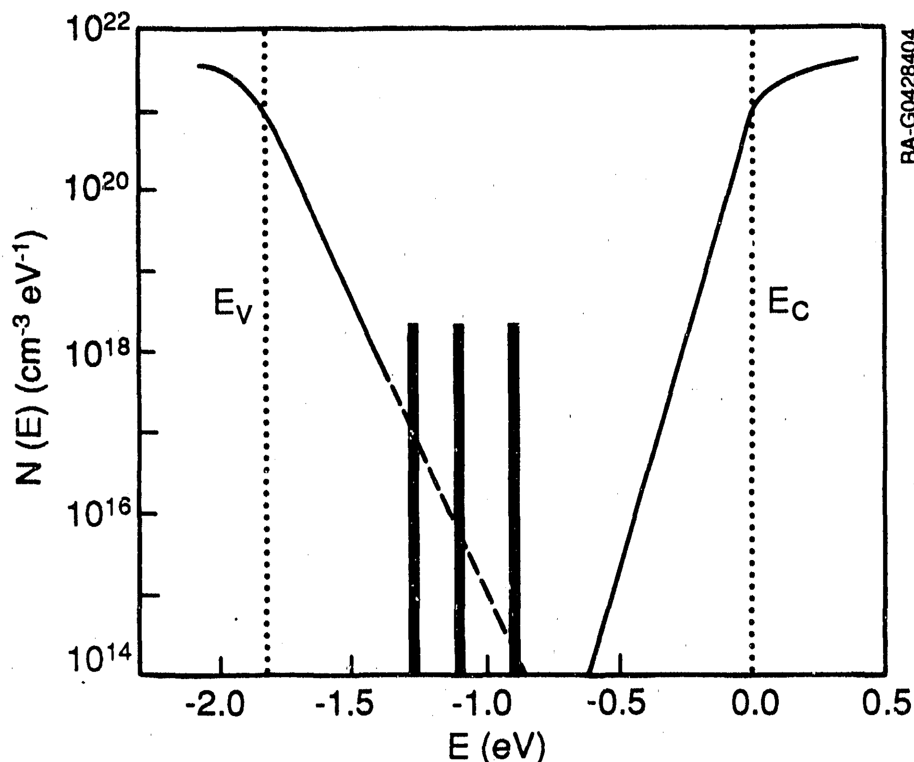

Figure 3-31. Assumed density of states for each of three σ-function distributions peaked at three positions. The total number of states is fixed at E_i = -0.9, -1.1, and -1.3 eV for each case. The valence and conduction exponential band tails have characteristic energies of 30 and 50 meV, respectively. A square root density of states for the valence and conduction bands is assumed.

kept constant at 2 x 10^{16} states/cm^3, with the peak fixed at 1.0 eV below the conduction band. Figure 3-34 shows the excess subgap absorption calculated using Eq. 3-21 for each of the four distributions, along with the ISA densities. These values of ISA density vary less dramatically with increasing FWHM than for the previous case, where the position of the density of subgap states is altered.

Moreover, if neither the width nor the position of the subgap defect is altered, a 1:1 correlation will exist between ISA values and real defect density, and a constant of proportionality may be determined experimentally. However, the equality between the measured spin density and the ISA density should not be expected as implied in Ref. 155 for a couple of reasons: as explained above, all of the initial-state subgap defect transitions are not included for hν < 1.5 eV; as the position of the defect density approaches the valence band tail, it contributes less and less to the ISA defect density; finally, the ISA method should be used with caution when applied to all types of a-Si:H films since all subgap defects may not have spin. Using the same prefactor in Equation 3-19 for films with spinless defects (e.g., charged defects), is presumptuous unless transition matrix elements for each type of defect are the same.

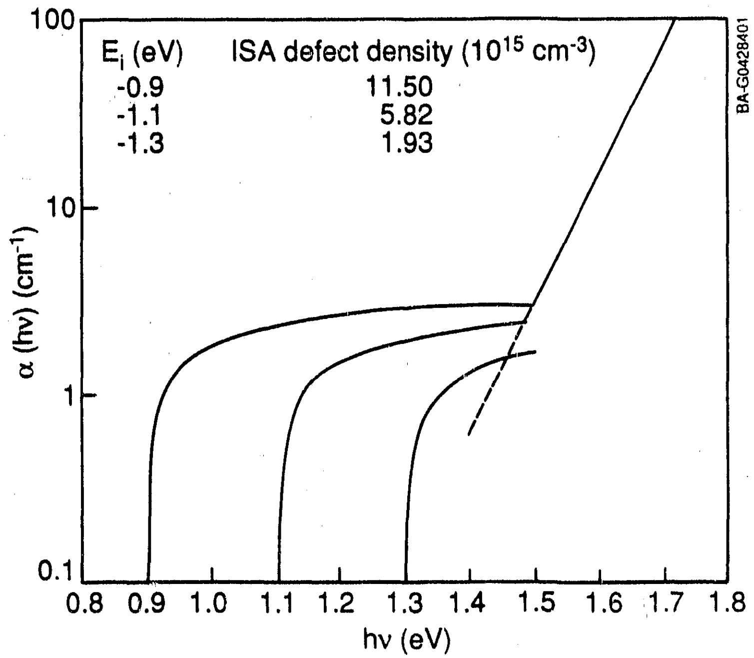

Figure 3-32. Calculated values of the excess absorption corresponding to the three distributions in Fig. 3-31 as a function of the photon energy. Also shown is a typical exponential absorption edge characterized by a characteristic energy E_0 = 50 meV. The corresponding ISA densities from Eq. 3-19 are listed in t.

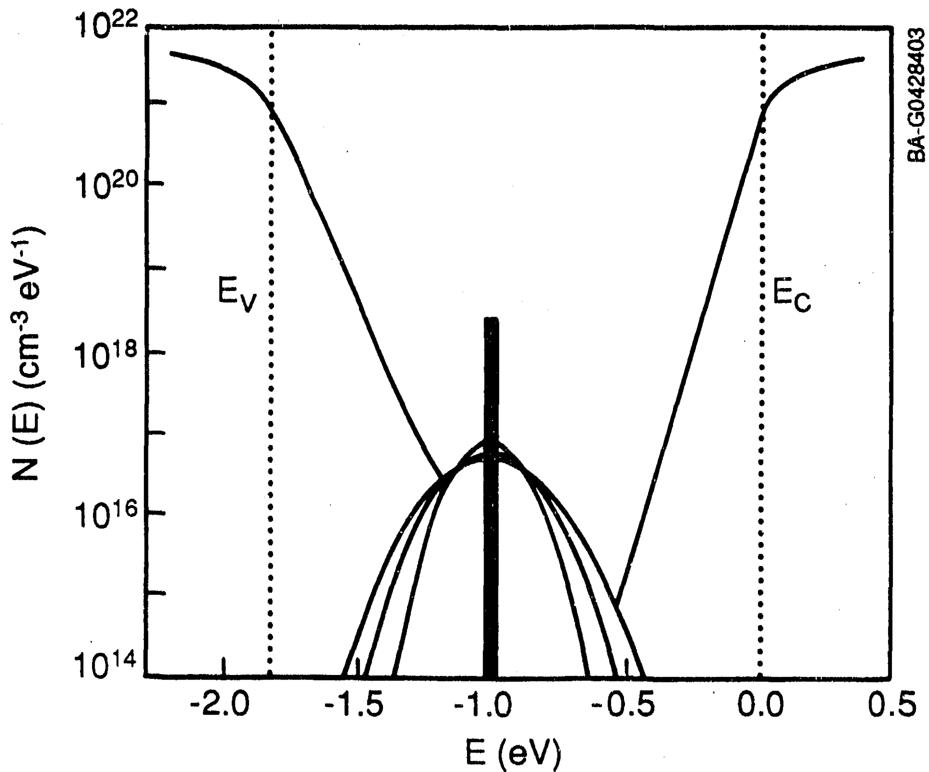

Figure 3-33. Assumed density of four Gaussian densities of states in the gap peaked at the same position, each having a different FWHM ranging from 0 (σ-function case) to 0.32 eV.

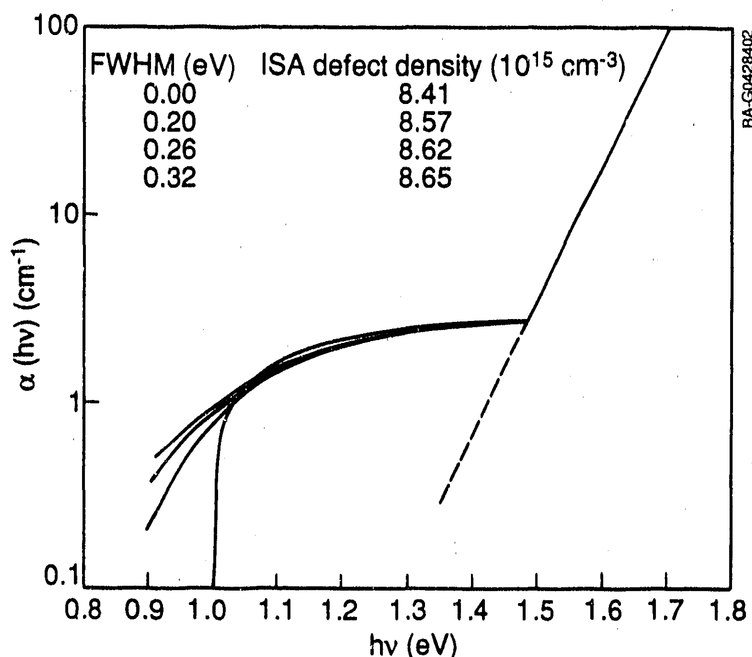

Figure 3-34. Calculated values of the excess absorption corresponding to the distributions in Figure 3-33 as a function of the photon energy. Also shown is a typical exponential absorption edge characterized by a characteristic energy E_0 = 50 meV. The corresponding ISA densities from the equation are listed in the figure.

We have clearly shown the limitations of applying the ISA method to the excess subgap absorption in a-Si:H. Depending on the position of the density of states in the gap, a factor of 10 error may result from using the ISA method. The error in the evaluation is intrinsic to the technique and cannot be avoided due to the exponential tail state absorption. Finally, only if the defect to be studied is restricted in some sense to one type (e.g., neutral dangling bonds in undoped films) can a single constant of proportionality be expected to equate the subgap defect density to the ISA.

3.6.4.10 Doping and Hydrogenation by Ion Implantation of a-Si:H

The feasibility of using ion implantation for doping a:Si films has been demonstrated [160-163]. However, further improvements of the properties of ion-implantation-doped a-Si:H and a better understanding of the doping process are needed. In this section, we discuss our analysis of boron doping of a-Si:H using ion implantation. To discriminate between the effects of doping and the effects of bombardment damage introduced by the implantation process, we have compared the properties of our boron-doped samples with silicon-implanted samples. It is known that samples doped by ion implantation at concentrations less than 10^{20} at./cm^3 exhibit doping efficiencies lower than those of samples doped in the gas phase during film growth. We will show experimental results that indicate two possible mechanisms that could lead to poor electrical activity; that is, the implantation-induced disorder may

introduce compensating centers for the p-type dopants or a high electrically inactive fraction of the dopants due to either interstitial positioning or threefold coordination.

The experiments were performed by using high-quality, intrinsic a-Si:H films deposited by RF glow discharge of SiH_4 in a load-locked, single-chamber system. Corning 7059 glass and single-crystal silicon were used as substrates to allow electrical, optical, and IR characterizations of the films. The films were ion-implanted at room temperature, with boron and silicon ions at concentrations between 10^{18} and 10^{21} at./cm^3. Homogeneous implantation profiles throughout the 0.3-μm film thickness were obtained by varying the energy of the implanted ions. The optimum implantation conditions and the concentration profiles were calculated using a computer code that makes use of the Ziegler-Biersack-Littmark (ZBL) theory [164]. Special care was taken during ^{28}Si implantation to avoid the simultaneous implantation of N_2 contaminants.

After ion implantation, the samples were annealed in a furnace, under vacuum (~10-2 torr) at 260°C for 1 hour. This temperature is about the same as the film deposition temperature, and it was reported [161,165] to provide the best annealing conditions. The samples were further implanted with H^+ ions for either 40 minutes or 80 minutes at 640 eV ion-beam energy and 0.5 mA/cm^2 ion-beam current density using a Kaufmann type ion source [166]. During hydrogen implantation, the samples were kept at a temperature of 200°C on a rotating stage for better implantation homogeneity. The samples containing 4 x 10^{19} B^+/cm^3 and 8 x 10^{19} Si^+/cm^3 were exposed to the hydrogen beam for 3 hours. Longer exposures, up to 6 hours, did not produce further significant changes in the room temperature dark conductivities ($\sigma_R T$). At 640 eV, hydrogen ions only penetrate about 10 nm into the film. After implantation, the hydrogen atoms diffuse through the remainder of the film [166]. An estimate of the diffusion coefficient D observed in our samples at 200°C gives a value of D = 10^{-14}(cm^2/s), which is four orders of magnitude higher than previously reported [167]. A more detailed study of these results is in progress.

Conductivity measurements on the intrinsic films used in this study were carried out using a planar silver contact geometry. The $\sigma_R T$ values were in the range of 1 - 3 x 10^{-11} S/cm, and photoconductivity values (σ_L) under global AM1.5 illumination were between 10^{-5} and 10^{-4} S/cm. The dark conductivity activation energies E_o were measured between 17° and 200°C and were found to be between 0.75 and 0.85 eV. The optical band gaps E_g evaluated by the Tauc method [168] were between 1.75 and 1.80 eV. Hydrogen contents, determined by IR spectroscopy, were about 9%-10%.

Electrical characteristics of post-annealed and post-hydrogenated a-Si:H samples implanted with boron, phosphorus, or silicon at a dose of 10^{20} at./cm^3 are reported in Ref. 163. The present study extends our analysis to different atomic concentrations of boron and silicon. Figure 3-35 shows $\sigma_R T$ vs. dopant concentration of our boron-doped samples compared with results published by Kalbitzer et al. [160]. The dash-dotted curve, also from Ref. 160, describes samples doped by gas phase during film deposition. Our boron-doped samples have $\sigma_R T$ values two to three orders of magnitude higher than those obtained by Kalbitzer et al. [160] using implantation, except for the higher doses where all three curves converge. Our samples are about 0.3 μm thick, whereas the samples of Ref. 1 are only about 0.1 μm thick. The thickness dependence of

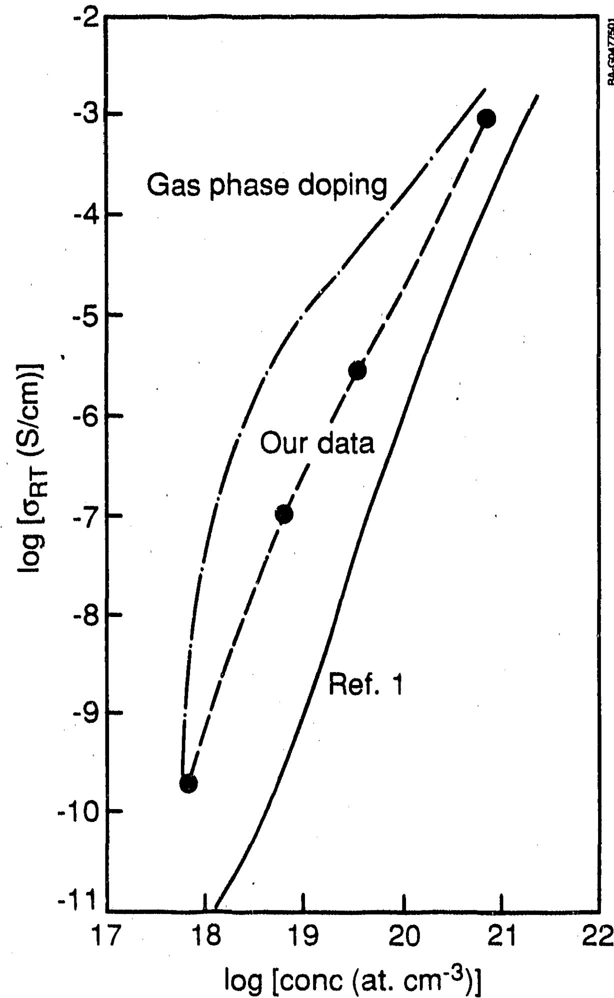

Figure 3-35. Room temperature dark conductivity $\sigma_R T$ vs. implanted boron concentration, compared with previously published data

conductivity [169] can account for one order of magnitude increase in conductivity. Although we implanted the samples at room temperature and annealed afterward, and Kalbitzer et al. [160] implanted on heated samples, we do not believe this contributed to the conductivity differences. Therefore, the larger conductivities measured in our samples may have to be explained by other factors to be discussed later. Figure 3-36 shows $\sigma_R T$ values of boron- and silicon-implanted samples, after annealing for 1 hour at 260°C (dashed curves) and after hydrogenation (dash-dotted curves). The $\sigma_R T$ values of boron-implanted samples after hydrogenation are considerably lower than those

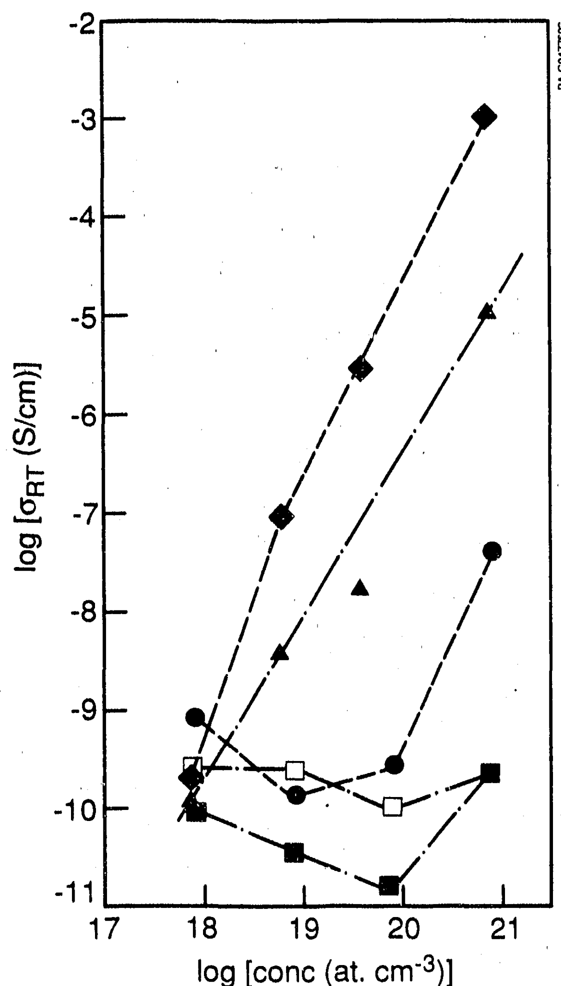

Figure 3-36. Experimental values of $\sigma_R T$ vs. implanted concentration: ▶ boron annealed; ◆ boron annealed and hydrogenated; ● silicon annealed; ■, □ silicon annealed and hydrogenated for 40 and 80 minutes, respectively

implantations and annealings, and they reach values comparable to those reported in Ref. 160. In the case of silicon implantation, a better passivation (lower dark conductivity) seems to be obtained after 40 minutes of hydrogen irradiation. We believe this might be due to the already observed effects of hydrogen-related introduction of acceptor-like defect centers [170]. Figure 3-37 shows the E_a values versus the implanted concentrations. The boron-doped samples have steadily decreasing E_a values down to 0.27 eV before hydrogenation and considerably higher values, at higher boron concentrations, after hydrogenation. In the case of silicon-implanted samples, before hydrogenation, the activation energy is constant at about 0.75 eV and

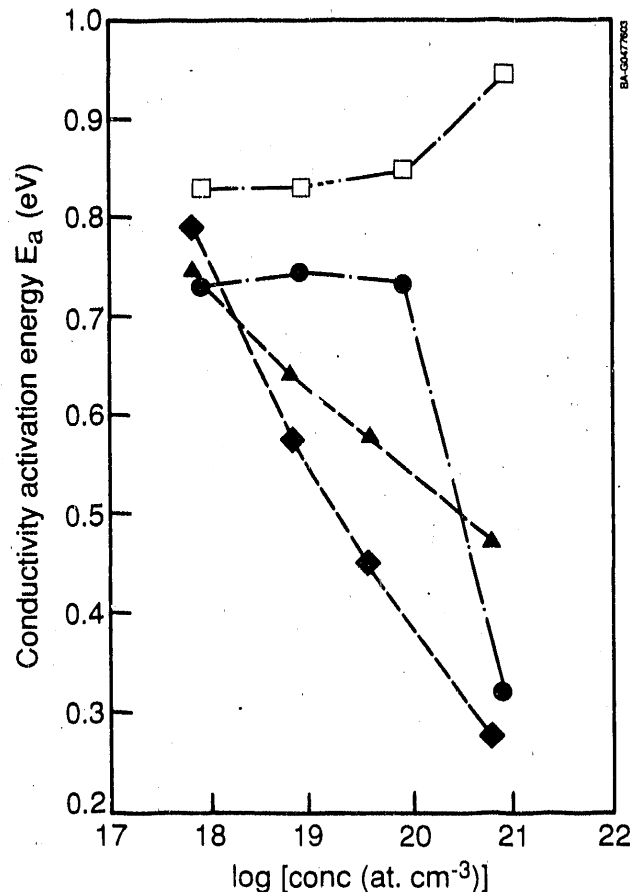

Figure 3-37. Dark conductivity activation Energy E_a vs. implanted concentration: ▶ boron annealed; ◆ boron annealed and hydrogenated; ● silicon annealed; □ silicon annealed and hydrogenated for 80 minutes

then abruptly decreases to about 0.3 eV for the highest implanted concentration (10^{21} at./cm^3). After hydrogenation, E_a becomes constant (0.80-0.85 eV) for the lower doses and increases to 0.94 eV for the higher doses. The band gap E_g is constant at 1.83 eV. Figure 3-38 shows the dark conductivity pre-exponential factor σ_o versus implanted concentration. Whereas in the case of boron-implanted samples there is only a moderate decrease in σ_o with increasing dose, silicon-implanted samples show a large decrease, at the highest concentration of 10^{21} at./cm^2. The values of 10^{-2}-10^{-3} S/cm are typical of conduction in the variable range hopping regime [165]. A plot of ln σ vs. σ $T^{-1/4}$ between 200° and -150°C shows a well-defined straight line. Dark conductivities of boron-doped samples between 200°C and room temperature

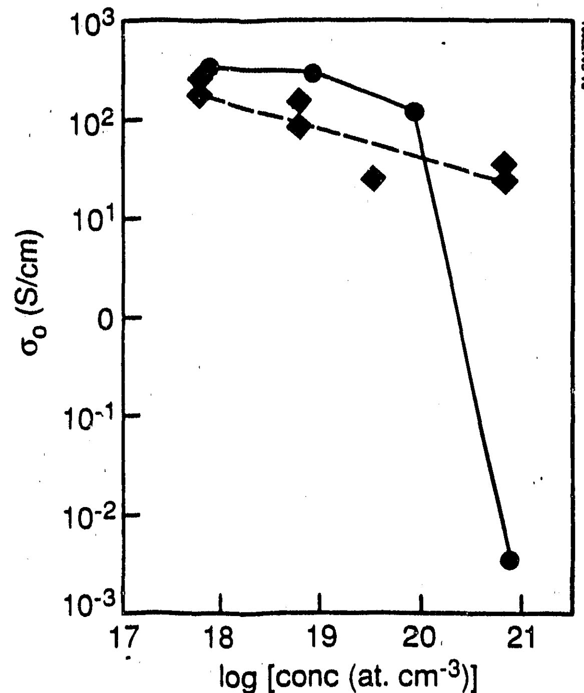

Figure 3-38. Dark conductivity preexponential factor σ_o vs. implanted concentration: ◆ boron annealed and hydrogenated; ● silicon annealed

show instead the T^{-1} dependence characteristic of the extended state conduction. For better understanding of the role of hydrogen on the electrical characteristics, the sample doped with boron at 4×10^{19} cm^{-3}, which was post-hydrogenated to a high hydrogen concentration of ~16% (only Si-H bonds detectable by IR absorption), was then annealed at increasing temperatures between 150° and 350°C and the $\sigma_R T$ was measured. It was observed that $\sigma_R T$ increased with temperature up to 350°C and then started decreasing again. We think that this behavior qualitatively supports Pankove's model [171] of boron de-activation by hydrogen. The model, in fact, hypothesizes a transition from four- to threefold coordination with the formation of a weaker Si-H bond due to the perturbation introduced by the presence of the nearby boron. Subsequent annealing should, as in fact it does, release the hydrogen and restore the Si-B four fold coordination. We believe that the lower electrical activity measured by Kalbitzer et al. [160] might be due to a similar effect of dopant de-activation by hydrogen. This may explain why their samples have lower conductivities than ours, as we mentioned earlier. From these reported experimental results, we can draw the following conclusions:

- The damage introduced by the implantation of silicon atoms can be removed almost completely by low-temperature annealing (260°C) for implanted doses up to 10^{20} at./cm^{-3}. For the highest doses, however, at which some irreversible structural change seems to take place, good electrical and optical characteristics can be restored by post-hydrogenation.

- Boron implantation at room temperatures, followed by annealing at 260°C, gives good electrical activity and the implantation damage is annealed out, even at the highest doses. At this regard, however, we should remember that the damage introduced by the implantation of boron atoms in silicon is very limited because the mass of boron is small compared to the mass of the silicon target atoms.

- Post-hydrogenation of boron-implanted films gives rise to de-activation of the dopant. Electrical activity can, however, be restored by hydrogen evolution; qualitatively, the data seem to confirm the validity of Pankove's model [171].

- Low-energy hydrogen implantation seems to generate the conditions for highly enhanced hydrogen diffusion (diffusion coefficient at 200°C ~10^{-14}. A more detailed study of this effect is under way.

3.7 References

1. W. B. Jackson, Phys. Rev. B38 (1988) p. 3595.

2. R. S. Crandall, Mat. Res. Soc. Symp. Proc. 149 (1989) in press.

3. S. R. Eliot, Philos. Mag. B39 (1979) p. 349 ; D. L. Staebler and C. R. Wronski, J. Appl. Phys. 51 (1980) p. 3262; J. Pankove and J. E. Berkeyheiser, Appl. Phys. Lett. 38 (1980) p. 456.

4. D. Adler, Solar Cells. 9 (1983) p. 133.

5. The energy scale is related to the time scale in the usual way by $E = kBT\ln(\nu t)$.

6. S. Guha, C.-Y. Huang, and S. J. Hudgens, Appl. Phys. Lett. 45 (1984) p. 50.

7. T. J. McMahon and R. Tsu, Appl. Phys. Lett. 51 (1987) p. 412.

8. M. Kumeda, H. Yokomichi, A. Morimoto, and T. Shimizu; Jpn. J. Appl. Phys. 25 (1986) L654.

9. R. S. Crandall, Phys. Rev. B36 (1987) p. 2645.

10. X.-M. Deng and H. Fritzsche, Phys. Rev. B36 (1987) p. 9378.

11. J. Baum, K. K. Gleason, A. Pines, A. N. Garroway and J. A. Reimer, Phys. Rev. Lett. 56 (1986) p. 1377.

12. Y. J. Chabal and C. K. N. Patel, Reviews Mod. Phys. 59 (1987) p. 835.

13. H. Wagner and W. Beyer, Solid State Commun. 48 (1983) p. 585.

14. K. K. Gleason, M. A. Petrich, and J. A. Reimer, Phys. Rev. B36 (1987) p. 3259.

15. A. H. Mahan, P. Raboisson, and R. Tsu, Appl. Phys. Lett. 50 (1987) p. 335; A. H. Mahan, P. Menna, and R. Tsu, Appl. Phys. Lett. 51 (1987) p. 1167.

16. V. G Bhide, R. O. Dusane, S. V. Rajarshi, A. D. Shaligram and S. K. David, J. Appl. Phys. 62 (1987) p. 108.

17. W. Beyer, H. Wagner, and H. Mell, MRS Symp. 49 (1985) p. 189.

18. R. C. Ross, A. G. Johncock, and A. R. Chan, J. Non-Cryst. Solids 66 (1984) p. 81.

19. N. J. Shevchik and W. Paul, J. Non-Cryst. Solids 16 (1974) p. 55.

20. A. J. Leadbetter, A. A. M. Rashid, R. M. Richardson, A. F. Wright, and J. C. Knights, Solid State Commun. 33 (1980) p. 973.

21. P. D'Antonio and J. H. Konnert, Phys. Rev. Lett. 43 (1979) p. 1161.

22. A. H. Mahan, B. P. Nelson, R. S. Crandall, and D. L. Williamson, 2nd Int. Conf. on Amorphous and Crystal SiC and Related Materials (IEEE, New York, 1989), in press.

23. D. L. Williamson, A. H. Mahan, B. P. Nelson, and R. S. Crandall, Appl. Phys. Lett. (Aug. 1989), in press.

24. Y. S. Tsuo, Y. Xu, R. S. Crandall, H. Ullal, and K. Emery, MRS Spring 1989 Meeting, in press. Typical material parameters of the intrinsic layer are also given.

25. W. Beyer, H. Wagner, and H. Mell, MRS Symp. 95 (1987) p. 317.

26. W. Beyer, <u>Tetrahedrally Bonded Amorphous Semiconductors</u> (Plenum, New York, 1985) p. 129.

27. A. H. Mahan, P. Raboisson, D. L. Williamson, and R. Tsu, Solar Cells 21, (1987) p. 117.

28. A. H. Mahan, P. Raboisson, P. Menna, and R. Tsu, MRS Symp. 95 (1987) p. 361; A. H. Mahan, A. Mascarenhas, D. L. Williamson, and R. S. Crandall, MRS Symp. 118 (1988) p. 641.

29. W. B. Jackson and N. M. Amer, Phys. Rev. B25 (1982) p. 5559.

30. S. Guha, J. Yang, P. Nath, and M. Hack, Appl. Phys. Lett. 49 (1986) p. 218.

31. A. Guinier and G. Fournet, <u>Small Angle Scattering of X-Rays</u> (John Wiley, New York, 1955), p. 30.

32. A. J. Leadbetter, A. A. M. Rashid, N. Colenutt, A. F. Wright, and J. C. Knights, Solid State Commun. 38 (1980) p. 957.

33. R. J. Temkin, W. Paul, and G. A. N. Connell, Adv. in Phys. 22 (1973) p. 581.

34. The ellipsoid eccentricity can only be increased to the point where the minor axis diameter becomes approximately that of a Si-Si bond length (2.35Å), which happens for a/b = 4 for a cigar-like microvoid, and 3 for a pancake-like microvoid. Since we have no reason to presuppose a large eccentricity for our samples, we have chosen an intermediate case (a/b = 2).

35. P. Menna, A. H. Mahan, and R. Tsu, 19th IEEE PV Spec. Conf. (IEEE, New York, 1987), p. 832.

36. Because of uncertainties in geometrical factors which are involved in a theoretical calculation of the constant K, we have chosen to determine this quantity experimentally. Nevertheless, the theoretical and experimental values of K agree to within a factor of 2.

37. We could equally well have chosen for normalization purposes the a-$Si_{0.7}C_{0.3}$:H sample used for normalization in the a-SiC:H study of Refs. 12 and 13; were we to do this, there would be minimal change (±.001 in ν_f) in the present results.

38. For this choice of axes, the number of missing atoms and the microvoid number densities are virtually identical for the cigar-like and pancake-like microvoids.

39. M. H. Brodsky, M. Cardona, and J. J. Cuomo, Phys. Rev. B16 (1977) p. 3556.

40. H. Shanks, C. J. Fang, L. Ley, M. Cardona, F. J. Demond, and S. Kalbitzer, Phys. Stat. Sol. B 100 (1980) p. 43.

41. A. H. Mahan, D. L. Williamson, B. P. Nelson, and R. S. Crandall, Proceedings, MRS Symposium E (San Diego, April 1989), in press.

42. The picture of dihydride configurations residing on internal (microvoid) surfaces has been proposed elsewhere. See, e.g., M. L. Albers, J. Shinar and H. R. Shanks, J. Appl. Phys. 64 (1988) p. 1859 and references therein.

43. M. Cardona, Phys. Stat. Sol. B 118 (1983) p. 463.

44. D. E. Soule, G. T. Reedy, E. M. Peterson and J. A. McMillan, A.I.P. Conf. Proc. 73 (1981) p. 89.

45. This value was obtained using sputtered a-Si:H that had hydrogen predominantly in the H_{2070} mode. See Ref. 30.

46. W.-J. Sah, H.-K. Tsai, and S. C. Lee, Abstracts of the 20th Intl. Conf. on Solid State Devices and Materials (Tokyo, Aug. 1988), p. 243.

47. W. E. Carlos and P. C. Taylor, Phys. Rev. B26 (1982) p. 3605.

48. D. L. Staebler and C. R. Wronski, "Reversible Conductivity Changes in Discharge-Produced Amorphous Si," Appl. Phys. Lett. 31 (1977) pp. 292-294.

49. Y. S. Tsuo, E. B. Smith, and S. K. Deb, "Ion Beam Hydrogenation of Amorphous Silicon," Appl. Phys. Lett. 51 (1987) pp. 1436-1438.

50. Y-F. Chen, "Elimination of Light-Induced Effect in Hydrogenated Amorphous Silicon," Appl. Phys. Lett. 53 (1988) pp. 1277-1278.

51. T. Ishimura, Y. Okayasu, H. Yamamoto, and K. Fukui, "A Study on the Surface Reaction in the Growth of Amorphous Silicon by Intermittent Deposition Method," Proceedings of the 20th IEEE Photovoltaic Specialists Conf., (IEEE, New York), Sept. 1988.

52. H. Ohagi, M. Yamazaki, J. Nakata, J. Shirafuji, K. Fujibayashi, and Y. Inuishi, "Optical Degradation of a-Si:H Films with Different Morphology and Preparation of Degradation-Resistive Films," Tech. Digest of the International Photovoltaic Science and Engineering - 3, Tokyo, Japan, 1987, pp. 671-674.

53. P. A. Thomas and J. C. Flachet, "Effect of Hydrogenation on the Conductivity of UHV-deposited Amorphous Silicon," Philos. Mag. B 51 (1985) pp. 55-66.

54. C. C. Tsai, M. Stutzmann, and W. B. Jackson, "The Staebler-Wronski Effect in Undoped a-Si:H: Its Intrinsic Nature and the Influence of Impurities," AIP Conference Proceedings No. 120, Optical Effects in Amorphous Semiconductors, 1984, pp. 242-249.

55. Y. S. Tsuo, X. J. Deng, E. B. Smith, Y. Xu, and S. K. Deb, "Ion Beam Rehydrogenation and Posthydrogenation of a-Si:H," J. Appl. Phys. 64 (1988) pp. 1604-1607.

56. Y. S. Tsuo, R. Weil, S. Asher, A. Nelson, Y. Xu, and R. Tsu, "Deposition and Etching of a-Si:H:F Using Silane and Xenon Difluoride," Proceedings of the 19th IEEE Photovoltaic Specialists Conf., (IEEE, New York) 1987, pp. 705-708.

57. M. Janai, M. Stutzmann, and R. Weil, "The Absence of the Staebler-Wronski Effect in Fluorinated Amorphous Silicon," Solar Cells 14 (1985) pp. 191-192.

58. R. Weil and B. Pratt, "Reduced Staebler-Wronski Effect in Hydrogenated Amorphous Silicon Containing Fluorine," private communication.

59. W. B. Jackson, N. M. Amer, A. C. Boccara, and D. Fournier, "Photothermal Deflection Spectroscopy and Detection," Appl. Optics 20 (1981) pp. 1333-1334.

60. M. Vanecek, A. Abraham, O. Stika, J. Stuchlik, and J. Kocka, "Gap States Density in a-Si:H Deduced from Subgap Optical Absorption Measurement on Schottky Solar Cells," Phys. Stat. Sol. (a) 83 (1984) pp. 617-623.

61. H. Matsumura and H. Tachibana, Appl. Phys. Lett. 47 (1985) p. 833.

62. H. Matsumura, H. Ihara, and H. Tachibana, Proceedings of the 18th IEEE Photovoltaic Specialists Conf., (IEEE, New York) 1985, p. 1277.

63. H. Matsumura, Japan. J. Appl. Phys. 25 (1986) L949.

64. H. Matsumura, Appl. Phys. Lett. 51 (1987) p. 804.

65. H. Matsumura, Mat. Res. Symp. 95 (1987) p. 261.

66. H. Matsumura, Mat. Res. Symp. 118 (1988) p. 43.

67. J. Doyle, R. Robertson, G. H. Lin, M. Z. He, and A. Gallagher, J. Appl. Phys. 64 (1988) p. 3215.

68. M. H. Brodsky, M. Cardona, and J. J. Cuomo, Phys. Rev. B16 (1977) p. 3556.

69. D. L. Williamson, A. H. Mahan, B. P. Nelson, and R. S. Crandall, submitted to Applied Physics Letters.

70. A. H. Mahan, B. P. Nelson, R. S. Crandall, and D. L. Williamson, Int'l Conf. on Hydrogenated Amorphous Silicon Devices and Technology, IBM, Yorktown Heights, November 1988, (IEEE, New York), in press.

71. D. L. Williamson, A. H. Mahan, B. P. Nelson, and R. S. Crandall, Appl. Phys. Lett., in press.

72. J. Baum, K. K. Gleason, A. Pines, A. N. Garroway, and J. A. Reimer, Phys. Rev. Lett. 56 (1986) p. 1377.

73. J. Ristein, J. Hautala, and P. C. Taylor, Phys. Rev. B40 (1989) p. 88.

74. H. M. Branz, Phys. Rev. B41 (1990) p. 7887.

75. H. M. Branz and M. Silver, unpublished; H. M. Branz and M. Silver, in Amorphous Silicon Technology-1990, eds. A. Madan et al., (MRS, Pittsburgh), in press.

76. K. Hattori, T. Mori, H. Okamoto, and Y. Hamakawa, Phys. Rev. Lett. 60 (1988) p. 825.

77. J. Kocka, J. Non-Cryst. Solids 90 (1987) p. 91.

78. H. M. Branz, Phys. Rev. B39 (1989) p. 5107.

79. J. G. Simmons and G. W. Taylor, Phys. Rev. B4 (1971) p. 502.

80. For example, Z E. Smith and S. Wagner, Phys. Rev. B32 (1985) p. 5510; R. A. Street, J. Kakalios, and T. M. Hayes, Phys. Rev. B34 (1986) p. 3030.

81. W. Shockley and J. Moll, Phys. Rev. 119 (1960) p. 1480; Y. Bar-Yam, D. Adler, and J. D. Joannopoulos, Phys. Rev. Lett. 57 (1986) p. 467; H. M. Branz, Phys. Rev. B39 (1989) p. 5107.

82. Z E. Smith, in Advances in Amorphous Semiconductors, ed. by H. Fritzsche (World Scientific, Singapore, 1988) p. 409.

83. R. S. Crandall, in Disordered Semiconductors, ed. by M. A. Kastner, G. A. Thomas, and S. R. Ovshinsky (Plenum, New York) 1987, p. 603.

84. W. E. Spear, J. Non-Cryst. Solids 59&60 (1983) p. 1.

85. K. Pierz, W. Fuhs, and H. Mell, Proceedings of the 19th Intl. Conf. on the Physics of Semiconductors, Warsaw, Poland, Aug. 1988.

86. D. Gutkowicz-Krusin, C. R. Wronski, and T. Tiedje, Appl. Phys. Lett. 38 (1981) p. 87.

87. R. S. Crandall in Amorphous Silicon Technology, ed. by A. Madan, M. J. Thompson, P. C. Taylor, P. G. LeComber, and Y. Hamakawa (MRS, Pittsburgh) 1988, p. 593.

88. D. Adler, Solar Cells 9 (1983) p. 133.

89. D. L. Staebler and C. R. Wronski, Appl. Phys. Lett. 31 (1977) p. 292.

90. Y. Uchida, M. Kamiyama, Y. Ichikawa, T. Hama, and H. Sakai, Technical Digest of the International PVSEC-1 (Kobe, Japan), 1984, p. 217.

91. J. P. Xi, Y. S. Tsuo, J. U. Trefny, and T. J. McMahon, Proceedings of the 18th IEEE Photovoltaic Specialists Conference, (IEEE, New York) 1985, p. 519.

92. A. Chantre and D. Bois, Phys. Rev. B31 (1985) p. 7979; A. Chantre, Phys. Rev. B32 (1985) p. 3687; L. W. Song, X. D. Zhan, B. W. Benson, and G. D. Watkins, Phys. Rev. Lett. 60 (1988) p. 460.

93. M. Stavola, M. Levinson, J. L. Benton, and L. C. Kimerling, Phys. Rev. B30 (1984) p. 832; M. Levinson, M. Stavola, P. Besomi, and W. A. Bonner, Phys. Rev. B30 (1984) p. 5817.

94. G. Zoth and W. Schroter, Phil. Mag B58 (1988) p. 623.

95. D. V. Lang, in Deep Centers in Semiconductors, edited by S. T. Pantelides (Gordon and Breach, New York), 1986, p. 489.

96. H. M. Branz, Phys. Rev. B38 (1988) p. 7474.

97. D. Adler, Solar Cells 9 (1983) p. 133; R. S. Crandall, Phys. Rev. B36 (1987) p. 2645.

98. B. Hamilton, A. R. Peaker, and S. T. Pantelides, Phys. Rev. Lett. 61 (1988) p. 1627.

99. V. Heine and J. A. Van Vechten, Phys. Rev. B13 (1976) p. 1622.

100. D. V. Lang, H. G. Grimmeiss, E. Meijer, and M. Jaros, Phys. Rev. B22 (1980) p. 3917.

101. O. Engstrom and H. G. Grimmeiss, J. Appl. Phys. 46 (1975) p. 831, as cited in Ref. 9.

102. J. A. Van Vechten and C. D. Thurmond, Phys. Rev. B14 (1976) p. 3539; and B22 (1976) p. 3551.

103. C. D. Thurmond, J. Electrochem. Soc. 122 (1975) p. 1133

104. G. E. Jellison, Jr., and F. A. Modine, Phys. Rev. B27 (1983) p. 7466.

105. D. Pons, Appl. Phys. Lett. 37 (1980) p. 413.

106. The slope of the DLTS emission rate on an Arrhenius plot is ΔH (see, e.g., Ref. 9).

107. M. Levinson, J. Appl. Phys. 58 (1985) p. 2628.

108. C. A. Londos, Solid State Commun. 62 (1987) p. 719.

109. J. I. Pankove, Appl. Phys. Lett. 37 (1980) p. 705.

110. M. Stutzmann, Phil. Mag. B56 (1987) p. 63.

111. H. Dersch, J. Stuke, and J. Beichler, Appl. Phys. Lett. 38 (1981) p. 456.

112. M. Stutzmann, W. B. Jackson, and C. C. Tsai, Phys. Rev. B32 (1985) p. 23.

113. G. Muller, Proc of the MRS 118 (1988) p. 285.

114. R. A. Street and K. Winer, Phys. Rev. B40 (1989).

115. D. Adler, J. Phys. Paris 42 (1981) pp. c4-3.

116. H. M. Branz and M. Silver, unpublished; H. M. Brand and M. Silver, in Amorphous Silicon Technology-1990, eds. A. Madan et al., (MRS, Pittsburgh) 1990, in press.

117. T. J. McMahon and R. S. Crandall, Phys. Rev. B39 (1989) p. 1766.

118. T. J. McMahon and R. S. Crandall, P. Mag. 61 (1990) p. 425.

119. W. B. Jackson and M. Stutzmann, Appl. Phys. Lett. 49 (1986) p. 957.

120. M. S. Bennett, J. L. Newton, K. Rajan, and A. Rowthwarf, J. Appl. Phys. 62 (1987) p. 3968.

121. G. Rajeswaran, P. E. Vanier, R. R. Corderman, and F. J. Kampas in Proceedings of the 18th IEEE Photovoltaics Specialists Conference (IEEE, New York), 1985, pp. 1271-1276.

122. R. W. Collins, Appl. Phys. Lett. 53 (1988) p. 1086.

123. Y. Kuwano and M. Ohnishi, J. Phys. (Paris) Colloq. 42 (1981) pp. C4-1155.

124. A. Catalano and G. Wood, Amorphous Silicon Technology, edited by A. Madan, M. J. Thompson, P. C. Taylor, P. G. LeComber, and Y. Hamakawa (MRS, Pittsburgh), 1988, pp. 581-586.

125. R. R. Arya, A. Catalano, and R. S. Oswald, Appl. Phys. Lett. 49 (1986) p. 1089.

126. Y. S. Tsuo, X. J. Deng, E. B. Smith, Y. Xu, and S. K. Deb, J. Appl. Phys. 64 (1988) p. 1604.

127. X. J. Deng, Y. S. Tsuo, and J. U. Trefny in Proceedings of the Industrial-University Advanced Materials Conference, March 6-9, 1989, Denver, Colorado, to be published.

128. Y. S. Tsuo, R. Weil, S. Asher, A. Nelson, Y. Xu, and R. Tsu in Proceedings of the 19th IEEE Photovoltaics Specialists Conference (IEEE, New York), 1987, pp. 705-708.

129. I. Sakata and Y. Hayashi, Appl. Phys. A39 (1986) p. 277.

130. R. A. Street in Semiconductors and Semimetals, 21B, ed. by J. I. Pankove (Academic Press, Inc.), 1984, pp. 197-244.

131. J. M. Marshall, R. A. Street, and M. J. Thompson, J. Non. Cryst. Sol. 66 (1984) p. 175.

132. The the drift length is the mean distance a charge moves in the direction of the electric field before trapping.

133. S. Crandall, J. Appl. Phys. 54 (1983) p. 7176.

134. R. S. Crandall, J. Appl. Phys. 55 (1984) p. 4418.

135. R. S. Crandall, J. Kalina, and A. E. Delahoy, Mat. Res. Soc. Symp. Proc. 118 (1980) p. 593.

136. M. A. Lampert and R. B. Schilling in Semiconductors and Semimetals, edited by A. Beer, 6, (Academic, New York), 1970, pp. 1-95.

137. D. Adler in Optical Effects in Amorphous Semiconductors, ed. by P. C. Taylor and S. G. Bishop (AIP, New York), 1984, p. 70.

138. J. Kocka, J. Non-Cryst. Solids 90 (1987) p. 91.

139. The experimental literature is reviewed in H. M. Branz, Phys. Rev. B39 (1989) p. 5107. A rigorous treatment of transition-level positions is also given.

140. For example, R. A. Street, J. Non-Cryst. Solids 77 & 78 (1985) p. 1 and other references in these volumes.

141. L. A. Balagurov, E. M. Omel'yanovskii, A. G. Petukhov, N. M. Starikov, and M. G. Foigel', Sov. Phys. Semicond. 21 (1987) p. 987.

142. M. Stutzmann and W. B. Jackson, Solid State Commun. 62 (1987) p. 153.

143. J. M. Ziman, Principles of the Theory of Solids, (Cambridge Univ. Press, Cambridge), 1964, p. 275.

144. D. Adler in Semiconductors and Semimetals, 21B, ed. by J. I. Pankove (Academic Press, New York), 1984, p. 10.

145. Y. Bar-Yam and J. D. Joannopoulos, Phys. Rev. Lett. 56 (1986) p. 2203.

146. A. Redondo, W. A. Goddard III, T. C. McGill, and G. T. Surrat, Solid State Commun. 20 (1976) p. 733, as cited by D. C. Allan and J. D. Joannopoulos, in The Physics of Hydrogenated Amorphous Silicon II, ed. by J. D. Joannopoulos and G. Lucovsky (Spring-Verlag, Berlin), 1984, p. 5.

147. M. Tajima, H. Okushi, S. Yamasaki, and K. Tanaka, Phys. Rev. B33 (1986) p. 8522.

148. H. M. Branz and M. Silver, unpublished; H. M. Branz and M. Silver in Amorphous Silicon Technology, eds. A. Maden et al., (MRS, Pittsburgh), 1990, in press.

149. H. Fritzsche, J. Non-Cryst. Solids 6 (1971) p. 49. (MRS, Pittsburgh), 1990, in press.

150. Fluctuations of order 20 / are envisioned. The observation of quantum confinement effects in a 50 / superlattice means that 50 / is a lower limit to the coherence length of electrons in extended states [K. Hattori, T. Mori, H. Okamoto, and Y. Hamakawa, Phys. Rev. Lett. 60 (1988) p. 825]. Consequently, the total energy of an extended state is not affected by the potential fluctuations.

151. For example, Z E. Smith, and S. Wagner, Phys. Rev. B32 (1985) p. 5510; R. A. Street, J. Kakalios, and T. M. Hayes, Phys. Rev. B34 (1986) p. 3030; T. J. McMahon and R. Tsu, Appl. Phys. Lett. 51 (1987) p. 412.

152. Y. Bar-Yam, D. Adler, and J. D. Joannopoulos, Phys. Rev. Lett. 57 (1986) p. 467.

153. M. H. Brodsky, M. Cardona, and J. J. Cuomo, Phys. Rev. B16 (1977) p. 3556.

154. E. C. Freeman and W. Paul, Phys. Rev. B16 (1978) p. 4288.

155. W. B. Jackson and N. M. Amer, Phys. Rev. B25 (1982) p. 5559.

156. D. L. Dexter, Phys. Rev. 101 (1956) p. 48.

157. E. A. Davis and N. F. Mott, Phil. Mag. 22 (1970), p. 903.

158. M. Vanecek, J. Kocka, J. Stuchlik, Z. Kozisek, O. Stika, and A. Triska, Solar Energy Mat. 3 (1983) p. 411.

159. G. A. N. Connell, Topics in Applied Physics 36, Amorphous Semiconductors, ed. M.H. Brodsky (Springer-Verlag, Berlin), 1979, p. 98.

160. S. Kalbitzer, G. Muller, P. G. LeComber, and W. E. Spear, Phil. Mag. B41 (1980) p. 439.

161. S. Vavilov, I. P. Akimchenko, and V. V. Krasnopevtsev, Phys. Stat. Sol. A94 (1986) p. 343.

162. A. V. Dvurechenskii, V. A. Dravin, I. A. Ryazantsev, A. K. Antonenko, and I. G. Landochkin, Phys. Stat. Sol. A95 (1986) p. 635.

163. R. Galloni, Y. S. Tsuo, and F. Zignani, Nucl. Inst. and Meth. in Phys. Res. B39 (1989) p. 386.

164. J. F. Ziegler, J. P. Biersack, and U. Littmark, in The Stopping and Range of Ions in Solids, 1 (Pergamon Press, New York), 1985.

165. G. Muller and P. G. LeComber, Phil. Mag. B43 (1981) p. 419.

166. Y. S. Tsuo, X. J. Deng, Y. Xu, A. K. Barua, S. Asher, and S. K. Deb, Mat. Res. Soc. Symp. Proc. 118 (1988) p. 153.

167. R. A. Street, C. C. Tsai, J. Kakalios, and W. B. Jackson, Phil. Mag. B56 (1987) p. 305.

168. J. Tauc, Optical Properties of Solids, (North-Holland, Amsterdam), 1972.

169. D. G. Ast and M. H. Brodsky, Phil. Mag. B41 (1980) p. 273.

170. N. M. Johnson, F. A. Ponce, R. A. Street, and R. J. Nemanich, Phys. Rev. B35 (1987) p. 4166.

171. J. I. Pankove, Cryst. Lett. Def. and Amorph. Mat. 11 (1985) p. 203.

4.0 POLYCRYSTALLINE THIN FILMS

Investigators

R. Noufi, Senior Scientist and Task Leader
D. Albin, Staff Scientist
F. J. Pern, Staff Scientist
J. Tuttle, Staff Scientist
J. Dolan, Master Technician
J. Carapella, Master Technician (as of September, 1989)

4.1 Introduction

The task objectives are to fabricate and investigate promising thin film solar cell material and devices to contribute to the goals of achieving 15% efficiency. The primary goals are (1) to increase the understanding of materials processes, (2) to increase the understanding of materials and their properties that are critical to device performance; (3) to investigate a low-cost, large-area fabrication process, such as electrodeposition; and (4) to help to solve fundamental problems that will help the $CuInSe_2$ technology become viable.

The task entails the fabrication and characterization of thin films and photovoltaic devices of ternary and quaternary semiconductor materials. The approach is to study the fundamental properties of the material and relate these properties to photovoltaic applications. The material of emphasis is $CuInSe_2$ polycrystalline thin films. Other materials such as $CuGaSe_2$ are studied for use in conjunction with $CuInSe_2$. We identify and study those fundamental material properties crucial to the performance of the device, such as stoichiometry and defect chemistry of the films; effect of composition and annealing treatment on the fundamental properties; modification of the physical and chemical properties of the films to achieve better device performance parameters, especially open circuit voltage (V_{oc}); feasibility to bring the electrodeposition of $CuInSe_2$ as a low-cost, large-area process to state of the art.

The expected results are a comprehensive data base and a better understanding of the properties of $CuInSe_2$ and $CuGaSe_2$ polycrystalline thin films that are critical to the device performance; the use of the above studies to effect improved device parameters, especially V_{oc} (0.5-0.6 V); the demonstration of $CuInSe_2$ electrodeposition as a low-cost, large-area process to produce state-of-the-art $CdS/CuInSe_2$ devices; and the demonstration that the program total results have contributed to the advancement of the $CuInSe_2$ technology.

4.2 Comprehensive Study of the Optical Properties of Thin Film $CuInSe_2$ as a Function of Composition and Substrate Temperature

4.2.1 Introduction

$CuInSe_2$ polycrystalline materials belong to a larger family of I-III-VI_2 ternary semiconductor compounds, many of which have been studied extensively because of their potential electro-optical applications [1,2]. Specifically, $CuInSe_2$ is of interest to the photovoltaics technology because of its

desirable band gap ($E_g \approx 1.0$ eV) and relatively high absorption coefficient ($\alpha = 10^4$-10^5/cm). Photovoltaic devices consisting of a polycrystalline $CuInSe_2$-based absorber are quickly proving to be the most economically viable, high-efficiency thin film solar cell technology, with efficiencies approaching 14% [3].

The electro-optical, structural, and morphological properties of $CuInSe_2$, and the corresponding device performance, are highly dependent on film composition, defect chemistry, and growth parameters such as substrate temperature. For example, the bulk resistivity increases from 10^{-1}-10^6 ohm-cm with a change in copper content from 26-21 at. % [4]. Additionally, the cubic/tetragonal phase stability in a related ternary compound, $CuGaSe_2$, has been shown by both x-ray diffraction [5] and optical techniques [6] to be dependent on composition. To date, other investigators have reported on the compositional dependence of various electro-optical properties of thin film $CuInSe_2$ [7], such as photoconductivity [8], charge transport [9], thermally stimulated current [10], and electrical conductivity [11].

In this report, the index of refraction n and the absorption coefficient α are presented, with significant emphasis on the latter. The absorption data are presented for a wide range of compositions and are related to deposition parameters and post-deposition treatments. The absorption coefficient and band gap are of special interest in modeling the observed quantum efficiency of $CdS/CuInSe_2$ devices. Spectral response data indicate poor current generation in the near-infrared (NIR) region, while electron beam induced current (EBIC) measurements [12] suggest response deep into the bulk of the $CuInSe_2$. This behavior, however, is inconsistent with a sharp heterojunction model and the high absorption coefficients previously reported [13,14]. A junction model that is consistent with the absorption data reported here and spectral response simulations that agree with actual device measurements will be presented.

Values for the direct valence to conduction band transition energies, and corresponding values for the spin-orbit interaction energy, are extracted from the absorption data and are related to compositional variations. The existence of secondary impurity phases in near stoichiometric and copper-rich material (at. % Cu > 24) is presented and related to observed band-gap narrowings. As measurement and calculation errors have a profound effect upon calculations of optical constants, a general error analysis, including the effects of scattered transmittance, diffuse reflectance, and data analysis techniques, is discussed in detail.

4.2.2 Experimental Procedures

4.2.2.1 Film Preparation

$CuInSe_2$ thin films were prepared by vacuum thermal evaporation of the constituent elements [15] onto heated 1 in. × 2 in. substrates of polycrystalline Al_2O_3 and 7059 glass. Actual substrate surface temperatures (T_s) of 350° and 450°C were verified by calibration. Two film thicknesses of the same composition were obtained from a single run by shielding one-half of the substrate assembly during a portion of the deposition. Copper arrival rates were varied, while indium and selenium arrival rates were held approximately constant in order to obtain compositions ranging from 16 to 26 at. % Cu. This

composition range roughly represents the at. % Cu below and above that of isolated layers in a multilayer $CuInSe_2$ photovoltaic device [15]. Our results will, therefore, allow us to characterize any homogenous or discrete mixture of the initial layer stoichiometries.

Our sample preparation technique [7] effectively produced four compositionally equivalent samples per run, allowing for multiple analytical techniques. The quality of films deposited on glass was quite good, with specular appearance and good thickness uniformity (±5.0%) as measured by a Tencor profilometer. Thickness determination was also made optically by an iterative technique (see Section 4.2.2.2). Compositional determination was accomplished by a Cameca MBX Electron Probe for Micro-Analysis (EPMA) on film portions of thickness $t > 1.0$ µm to within ±0.5 at. %. To assure a good compositional correlation between films of different thicknesses, several very thin films ($t = 150$-300 nm) were analyzed by quantitative Rutherford backscattering (RBS) to within ±0.2 at. %.

Hereafter, the notation Cu/In/Se utilized in the text and the figures will represent the composition of the film in atomic percent of the constituent elements. In cases where appropriate, the composition will be followed by the thickness of the film in Angstroms (Å) and the substrate temperature during deposition in degrees centigrade (°C).

4.2.2.2 Optical Analysis

Optical measurements were performed with a 5240 Beckman spectrophotometer in the NIR and visible (VIS) wavelength (λ) range, 500-2000 nm, with an integrating sphere to measure diffuse and total reflectance (R_{diff} and R_{tot}, respectively) and scattered and total transmission (T_{scatt} and T_{tot}, respectively). The lower-wavelength/high-energy limit is significant in that it represents the cutoff of photon penetration to the $CuInSe_2$ absorber in a $CdS/CuInSe_2$ device structure. Data were acquired and stored at intervals of 1 nm in the VIS up to 800 nm, and 4 nm in the NIR above 800 nm. Reflectance measurements were normalized to the absolute reflectance of a $BaSO_4$ plate used in the reference beam. To obtain measurable transmittance data well above the band edge, film thicknesses in the range of 150-400 nm were utilized for analysis. For better accuracy below the band edge, where $T_{tot} + R_{tot} \approx 100\%$ for very thin films, several films of thickness $t > 1.5$ µm were analyzed down to 800 nm.

To calculate the optical constants from the acquired data requires formulas that relate measured values of R_{tot}, T_{tot}, and t to the real and imaginary components of the index of refraction ($\tilde{n} = n - ik$) for an absorbing film on a transparent substrate. The extinction coefficient k is related to α by the expression $\alpha = 4\pi k/\lambda$. We will primarily speak in terms of the latter when presenting data. Several authors have discussed methods for the determination of optical constants and thicknesses of thin films in this manner [16-18]. The common approach is to consider the reflection and transmission of light at the three interfaces of the air/film/substrate/air multilayer system and express the results in terms of Fresnel coefficients. For transmission at normal incidence and reflection at near-normal incidence, the multiply reflected amplitudes can be summed to infinity without significant error. (The equations, expressed in the form $f_1(n,k)=(1+R)/T$ and $f_2(n,k)=(1-R)/T$, are given in Section 4.2.5 for reference.)

An unfortunate complication associated with these relations is the existence of multiple solutions for singular values of R_{tot}, T_{tot}, and t. We may readily solve $F_2(n,k) = f_2(n,k) - (1-R)/T = 0$, finding singular values of k for a fixed value of n. However, the functional nature of $F_1(n,k) = f_1(n,k) - (1+R)/T$, with k fixed, is oscillatory about $F_1 = 0$. The result is multiple solutions for n with a given k. In rare instances, we can extract from the results a continuous dispersion curve, n vs. λ. In most cases, however, we must delve deeper into the problem. For example, a measurement error in thickness of as little as 1% can produce a bifurcation of the dispersion curve in the neighborhood of the band edge. Denton et al. [17] described a method to eliminate discontinuities of this origin by varying the value of t about the measured value until an acceptable dispersion curve results. The resultant value of t therefore corresponds to the exact thickness of the film.

This technique was utilized with some success for $CuInSe_2$ thin films in this study that were predominantly single phase, and the results for one such film will be presented. The situation, however, is further complicated if the sample contains a significant amount of a secondary phase or exhibits excessive sub-bandgap absorption or both. In the discussion, we will show that near-stoichiometric and copper-rich films appear to contain a $Cu_{2-\delta}Se$ secondary phase. By a significant amount, we mean material sufficient to dominate the bulk conductivity. In such a case, the iterative technique described here fails as well.

To maintain continuity among results in our study, we will not utilize the iterative technique beyond the cursory examination that will be presented. Instead, the issue will be addressed in a separate publication. We feel confident in doing so because comparative calculations indicate there is little error incurred in determining k with a fixed value of n over the wavelength region of interest. The values for the absorption coefficient presented here will therefore be singular solutions to the relation $F_2(n,k) = 0$ with $n = 2.9$. This value of n represents, approximately, the median of index values presented in the literature [19,20].

There has been some discussion in the literature concerning the applicability of Denton's formulas to "non-ideal" thin films (i.e., films with non-zero surface roughness) [18,21-23]. The formulas are based upon coherent radiation normally incident on a perfectly smooth surface and account for multiple interface Fresnel reflections. The general argument is that artificial enhancement of the extinction coefficient can occur due to destructive interference between the specular and coherent non-specular components of reflection. There are modifications to these formulas which account for these phenomena, but they are limited by their neglect of non-normal components of scattered radiation and the condition that the root-mean-square surface roughness divided by the wavelength σ/λ is << 1. The latter condition is not satisfied for moderately rough films in the visible range. These shortcomings are addressed in this study by the measurement of diffuse and scattered components of reflected and transmitted radiation. Data will be presented characterizing the significance of T_{scatt} and R_{diff} for different compositions, as well as an analysis of the potential errors incurred by ignoring these components. (For a more comprehensive discussion of scattering phenomena, the reader is referred to Haas and Thun [24].)

4.2.3 Results and Discussion

4.2.3.1 Total Transmittance and Reflectance

$T_{tot}(\lambda)$ and $R_{tot}(\lambda)$ spectra for two compositions of thin film $CuInSe_2$ are shown in Figure 4-1. The data presented here have been normalized according to the procedures described earlier. Included in the figure is the scattered (diffuse) component of transmission (reflection) for the copper-rich film. The behavior of this data is representative of the two regimes of composition that will be discussed throughout the paper.

Two observations can be made about their relative differences. First, near stoichiometric/copper-rich films exhibit an onset of absorption at higher photon wavelengths than do copper-poor films, which manifests as a lower "effective" band gap. Second, diffuse reflectivity and scattered transmittance are observed in the measurements, the most significant of which occurs for copper-rich film compositions. This is easily understood if we inspect the film surface morphology by scanning electron microscopy (SEM) of samples from each regime (Figure 4-2). The copper-poor film is smooth and specular in nature, while the copper-rich film is rough and appears dull to the naked eye. According to Bennett and Porteus [25], the scattering amplitude will increase with σ according to the relation $1 - e^{-(4\pi\sigma/\lambda)^2}$.

A simple means of quantifying the scattering phenomena is to plot the ratio of scattered to total transmittance above, at, and below the band edge (Figure 4-3). For wavelengths greater than 1300 nm, a baseline scatter level of 2%-5% is observed for all compositions. At 800 nm, the trend is significantly different, with copper-rich films exhibiting up to 17% scatter. The ultimate effect of the scattering is to increase the effective radiation pathlength in the material and thus alter the film thickness appropriate for the calculations. This will not, however, produce significant error in our calculated absorption coefficients.

Of special interest to photovoltaic device performance is the scatter observed in a $CdS/CuInSe_2$ multilayer system. Data for such a system, consisting of a 3.0-μm window layer of CdS deposited on a very thin film of $CuInSe_2$, are included in Figure 4-3. Throughout the transparent region of CdS, the scattered component of transmission for the multilayer system is significantly greater than that of an isolated $CuInSe_2$ thin film, ranging from 8% at 1800 nm to 28% at 800 nm. If this phenomenon carries over into actual $CdS/CuInSe_2$ devices, the impact is to effectively decrease the depth of photon penetration and subsequent carrier generation. At present, this effect is not quantifiable since we do not know the angular dependence of the scattering.

4.2.3.2 Index of Refraction $\hat{n} = n - ik$

Calculated values of the absorption coefficient α for a range of film compositions deposited at T_s = 350°C are plotted in Figure 4-4. Although measurements were made down to 500 nm on most samples, little variation among different compositions is observed below 800 nm. We, therefore, will concentrate our analysis in the NIR (800-2000 nm). Near the band edge (0.9-1.4 eV), for the data gathered in this study, there is a decrease in α with copper concentration for copper-poor compositions. For near stoichiometric and copper-rich material which exhibit degenerate, free-carrier-like electrical properties,

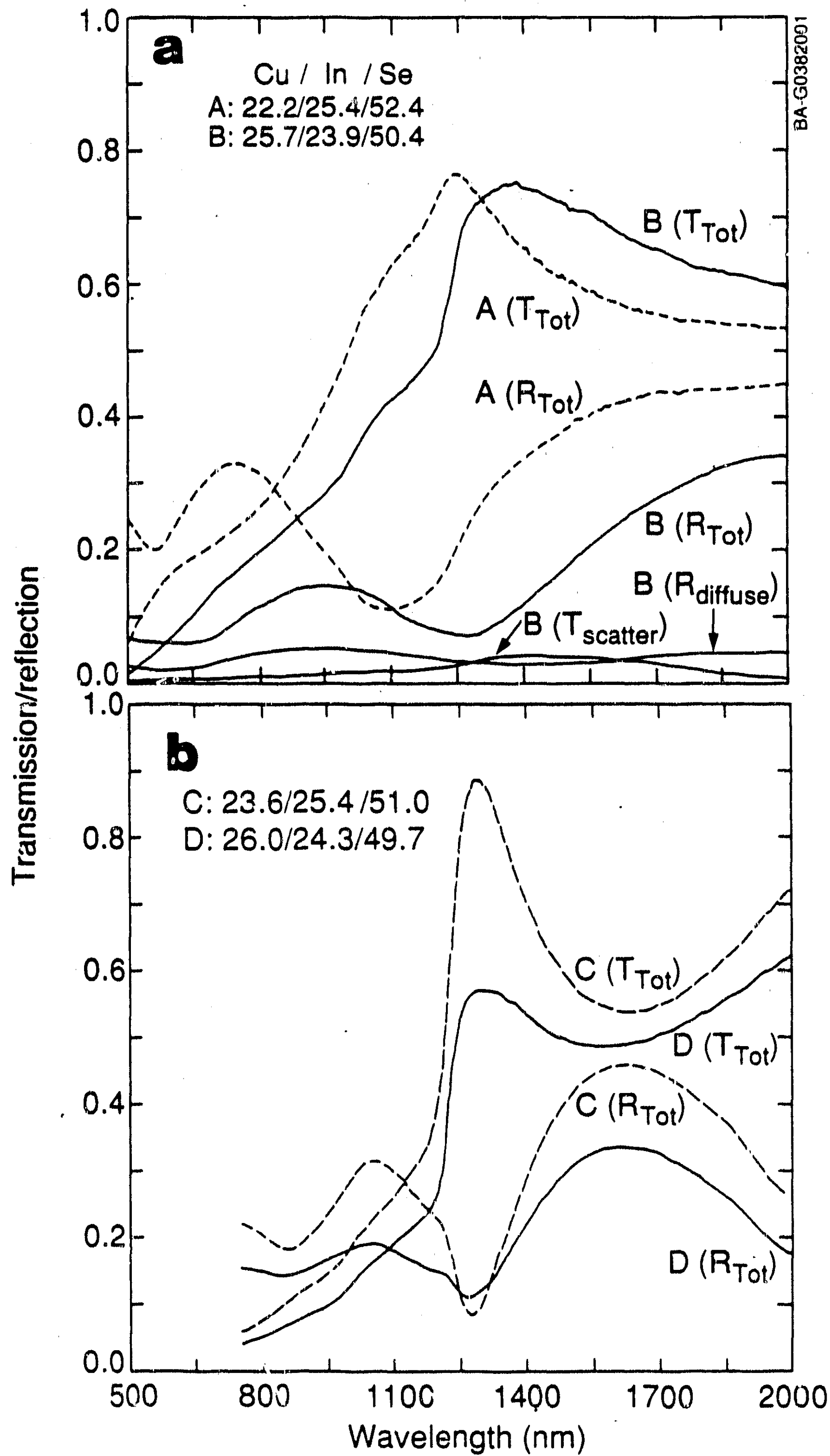

Figure 4-1. Transmission/reflection spectra for two compositions of thin film $CuInSe_2$ (at. % Cu/In/Se, thickness, T_s). (a) 22.2/25.4/52.4, 1780 Å, 450°C; (b) 25.7/23.9/50.4, 3550 Å, 350°C.

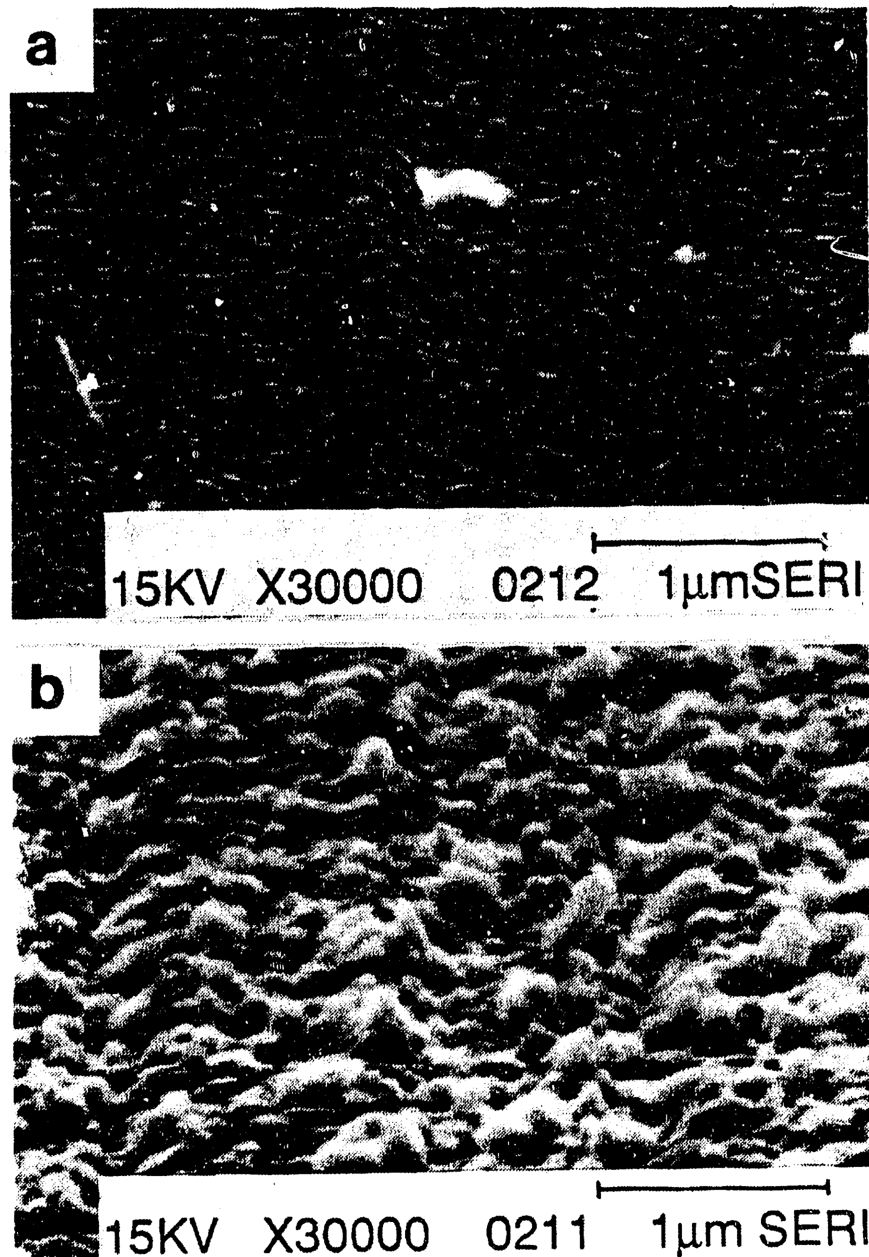

Figure 4-2. SEM micrographs of copper-poor and copper-rich thin film $CuInSe_2$ on 7059 glass substrates. (a) 22.2/25.4/52.4, 1780 Å, 450°C; (b) 26.0/24.0/50.0, 2960 Å, 350°C.

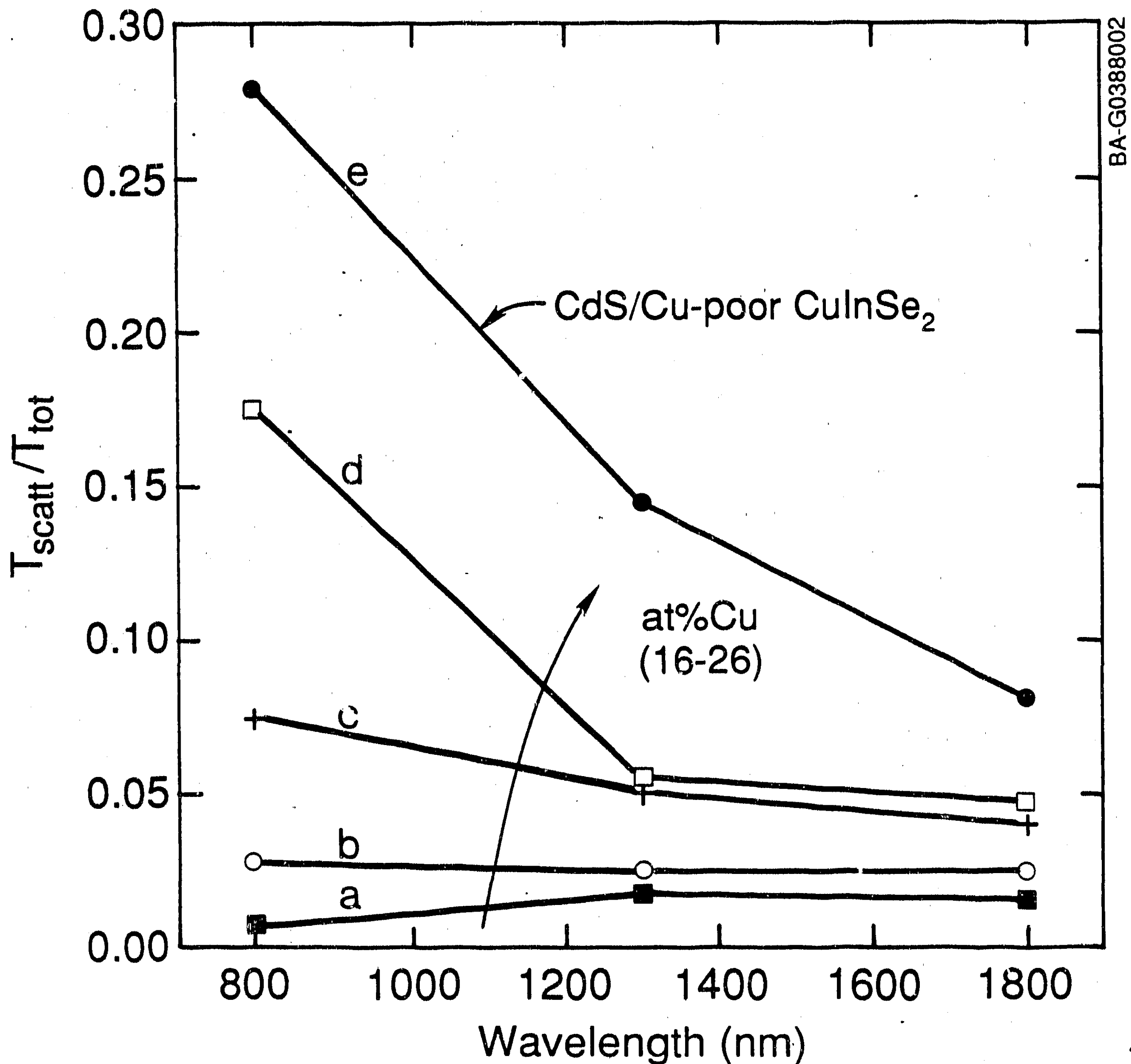

Figure 4-3. Ratio of $T_{scatter}/T_{tot}$ vs. wavelength for four compositions of thin film $CuInSe_2$ and a $CdS/CuInSe_2$ multi-layer structure. (a) 22.2/25.4/52.4, 1780 Å, 450°C; (b) 24.2/25.0/50.8, 1850 Å, 350°C; (c) 25.7/23.9/50.4, 3550 Å, 350°C; (d) 25.0/24.6/50.4, 3560 Å, 350°C; (e) 21.9/26.5/51.7, 1700 Å, with 3.0 μm CdS.

significant sub-band-gap absorption is observed. For copper-rich material only, the absorption curve exhibits unusually flat behavior at about 1.0 eV, or slightly above the "effective" band gap of the material.

At a substrate temperature of 450°C, a similar trend in α with composition is observed. However, a narrow region of composition appears to exhibit a marked difference. For material with 24 < at. % copper < 25, films grown at 350°C exhibit significant sub-band-gap absorption whereas films deposited at 450°C

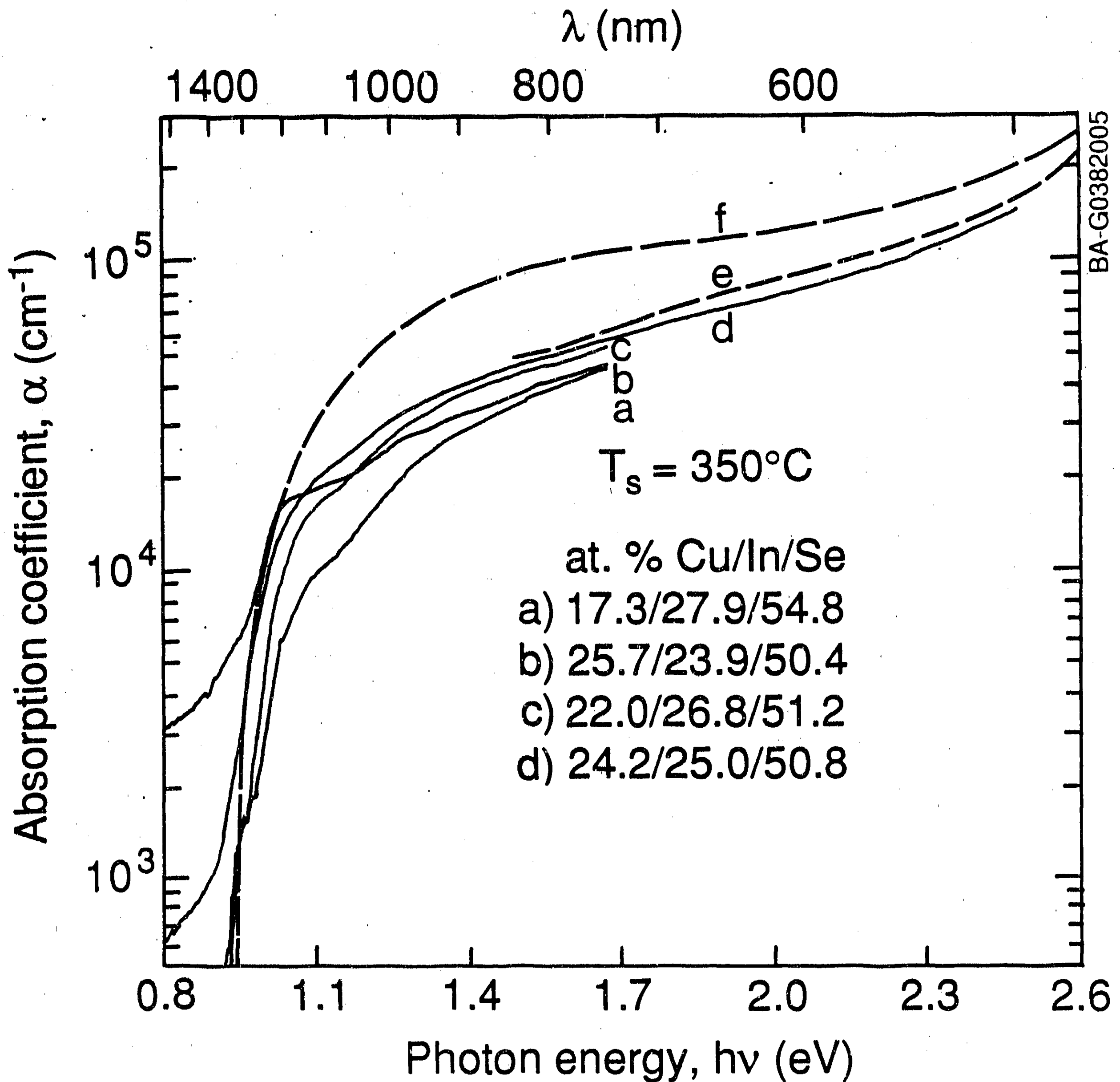

Figure 4-4. Absorption coefficient α vs. incident photon energy for four compositions of thin film $CuInSe_2$ deposited at 350°C

do not (Figure 4-5). The phenomenon of sub-band-gap absorption in thin film $CuInSe_2$ is believed to be related to the presence of the secondary phase, $Cu_{2-\delta}Se$, at grain boundaries and free surfaces. The variation seen among different substrate temperatures suggests a detailed balance between incident copper fluxes, T_s, and the consequent formation of this secondary phase. These effects will be discussed again later.

The decrease in α with copper concentration observed in the moderately absorbing region just above the band edge is not completely understood at this time. A variation in n sufficient to produce these differences is unlikely, though

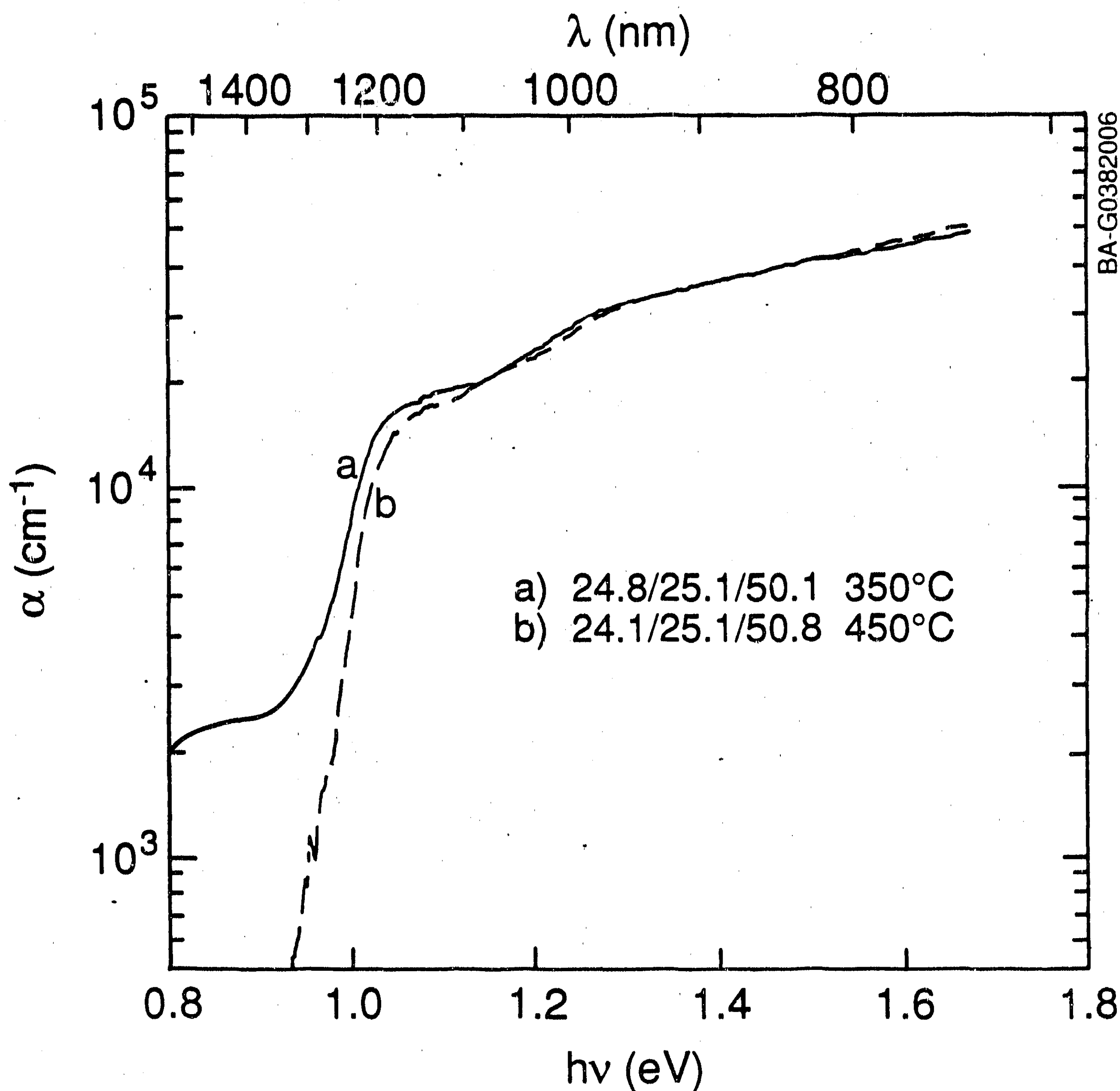

Figure 4-5. Absorption coefficient of similar compositions of thin film $CuInSe_2$ deposited at different substrate temperatures. (a) 24.8/25.1/50.1, 350°C; (b) 24.1/25.1/50.8, 450°C.

it has not been ruled out. In Figure 4-4, the absorption data for all compositions converge at the energy extrema, implying similar band gaps and densities of states away from the gamma (Γ) point. A more likely candidate, therefore, is a perturbation of the band structure near the Γ-point. This perturbation is related to the quantity and nature of the defects, which include vacancies (V_{Cu}) and anti-sites (In_{Cu}) [26] in heavily compensated copper-poor material. A structural versus composition study under way is expected to lend additional insight into the dependence.

For comparison purposes, absorption data from two additional sources are shown in Figure 4-4. The data by Meakin [13] are compiled from various sources on both single-crystal and polycrystalline thin film material. The most significant differences observed from the data reported here are near the band edge. This will have a dramatic effect on spectral response simulations, as will be discussed in detail below. The second data set originates from scanning ellipsometry measurements made at AT&T Laboratories [20] on single-crystal material fabricated elsewhere. In this case, there is good agreement with the absorption data presented here for thin film material.

An alternative means of corroborating the absorption data reported here was to investigate the effect of thickness on the optical properties of polycrystalline $CuInSe_2$. As we described earlier, the film preparation technique used produced compositionally equivalent films of different thicknesses (e.g., 0.20 µm and 1.20 µm). Two such films were measured, and a comparison of the resultant absorption spectra indicated no differences.

For selected films, the real and imaginary parts of the index of refraction can be determined simultaneously. There exist multiple branches to the solution curves for n, as previously discussed. The branches converge, producing a nearly continuous n versus λ dispersion curve, when an appropriate value for the film thickness is utilized in the calculations. This convergence phenomenon is exhibited in Figure 4-6, where data are presented for a copper-poor film deposited at 450°C. One branch, shown as the broken line, represents a disallowed solution and is discarded. The allowed solution for n shows only mild fluctuations in this wavelength range. This would suggest that the decision to fix n at 2.90 for the calculations was quite reasonable. Included in the figure are single-crystal data as determined by ellipsometry [20].

4.2.3.3 Transition Energies

Values for the direct valence to conduction band transition energies, and the corresponding valence band splitting due to the spin-orbit interaction, can be extracted from the optical data. The fundamental transition E_g is derived by extrapolating $(\alpha h\nu)^2$ versus $h\nu$ to the photon energy axis intercept. This is illustrated in Figure 4-7, with obvious differences noted between copper-rich and copper-poor samples. The range of calculated direct-band-gap values is 0.95 eV to 1.01 eV (Figure 4-8). With only a few exceptions, all samples fabricated at 350°C have transition energies less than 0.99 eV, while films fabricated at 450°C exhibit transition energies above 0.99 eV. The exceptions are for copper-rich material ($x > 0.5$) fabricated at 450°C (E_g = 0.96 eV) and for very copper-poor material ($x < 0.45$) fabricated at 350°C ($E_g \sim 1.0$ eV).

The lower values of the fundamental transition energies and the unusual flattening of the $(\alpha h\nu)^2$ versus $h\nu$ curve above and below the primary transition appear only in the analysis of near stoichiometric and copper-rich material. The origin of these features is suspected to be the $Cu_{2-\delta}Se$ secondary phase, though the exact causal relationship has not been determined. It is known that sufficient amounts of $Cu_{2-\delta}Se$ will dominate the conductivity of polycrystalline $CuInSe_2$ since the phase is degenerate p-type. The consequence is tailing in the valence band, band gap narrowing, and possibly free-carrier-like absorption.

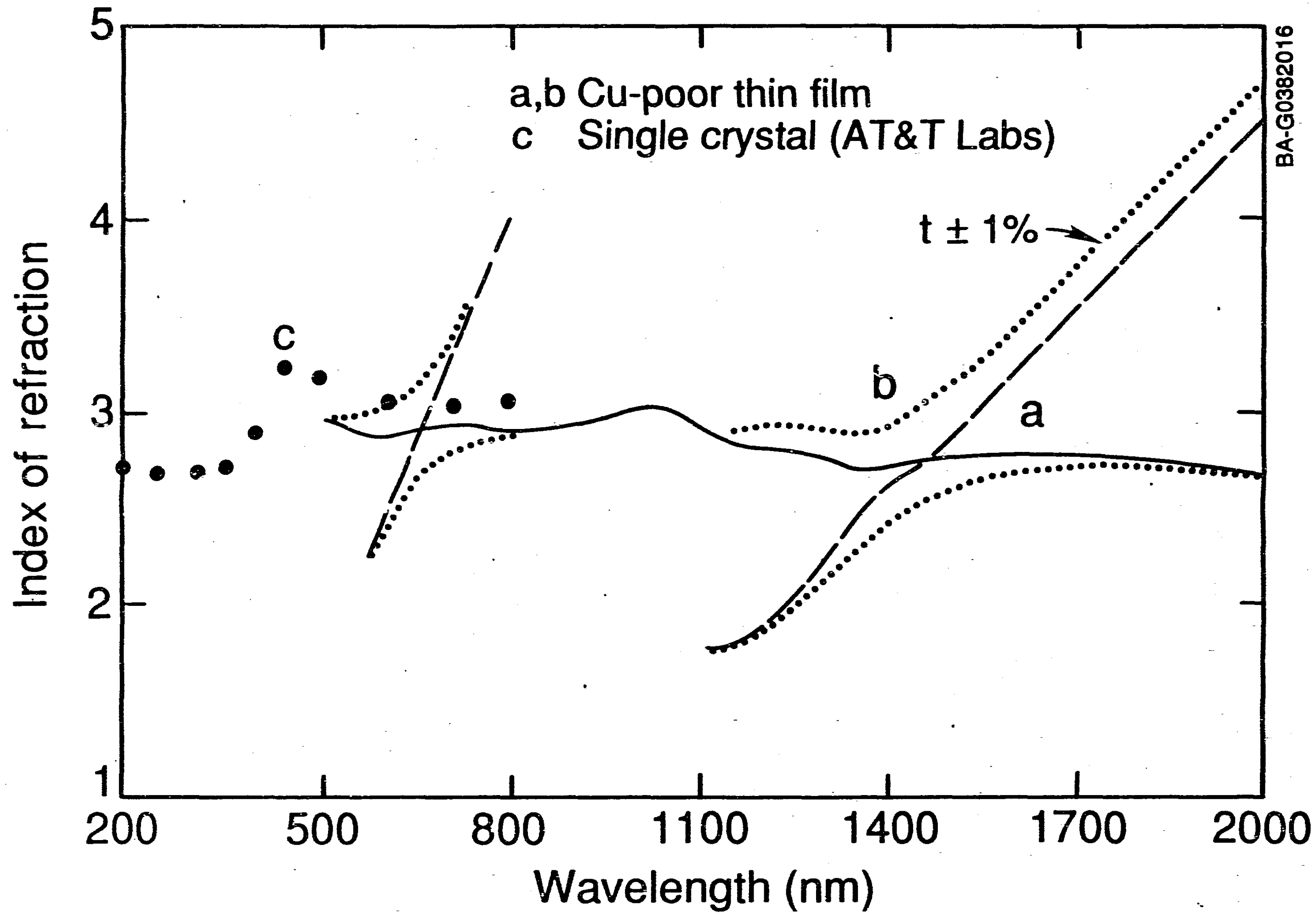

Figure 4-6. **The real component of the index of refraction n plotted vs. λ for a copper-poor film deposited at 450°C.** (a) allowed (solid line) and disallowed (broken line) solutions for correct film thickness, (b) non-convergent solution (dotted line) for incorrect film thickness, (c) data from Ref. 20.

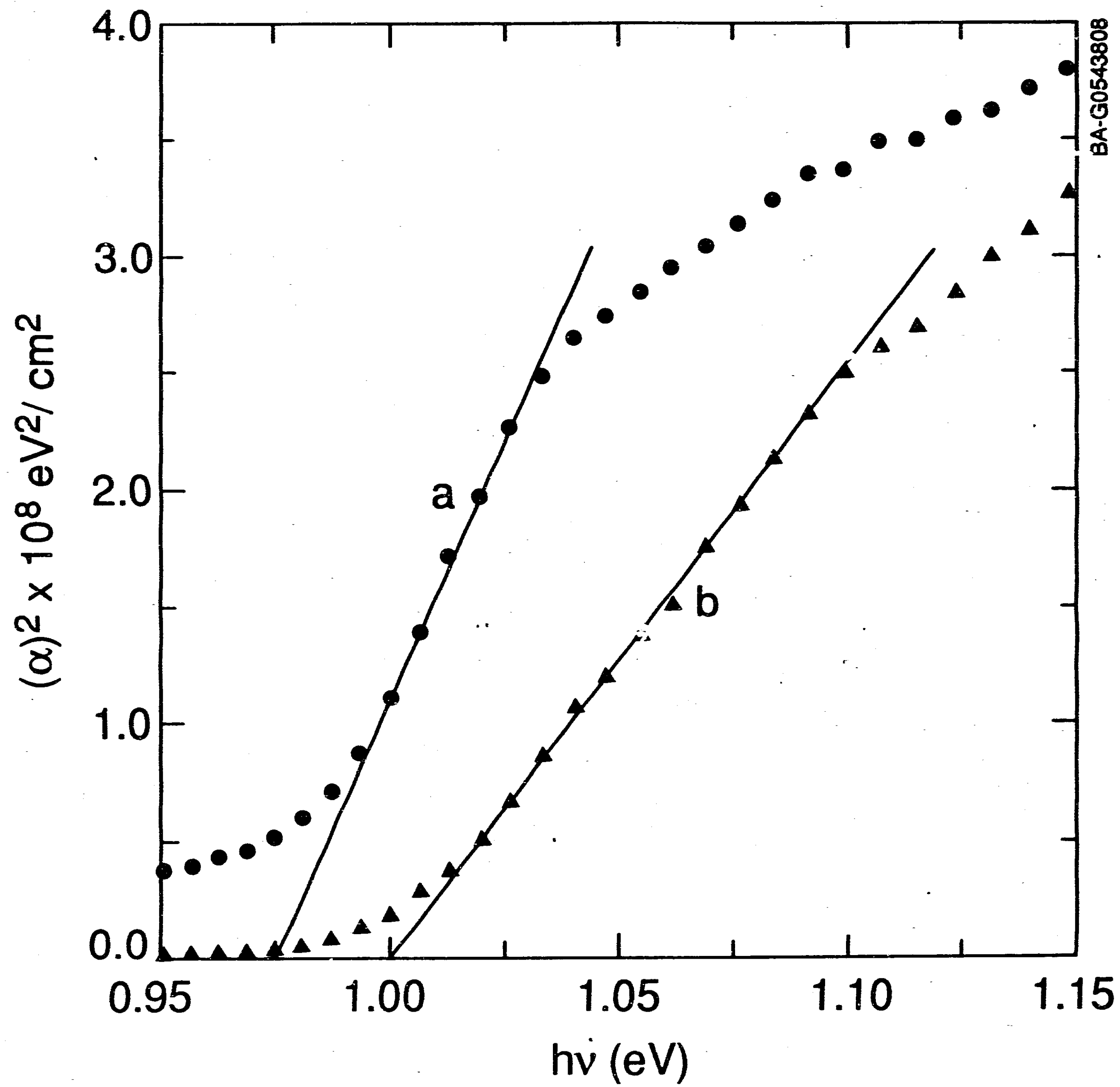

Figure 4-7. Dependence of the parameter $(\alpha h\nu)^2$ on photon energy for two thin films deposited at 350°C. (a) 25.7/23.9/50.4, (b) 22.0/26.8/51.2.

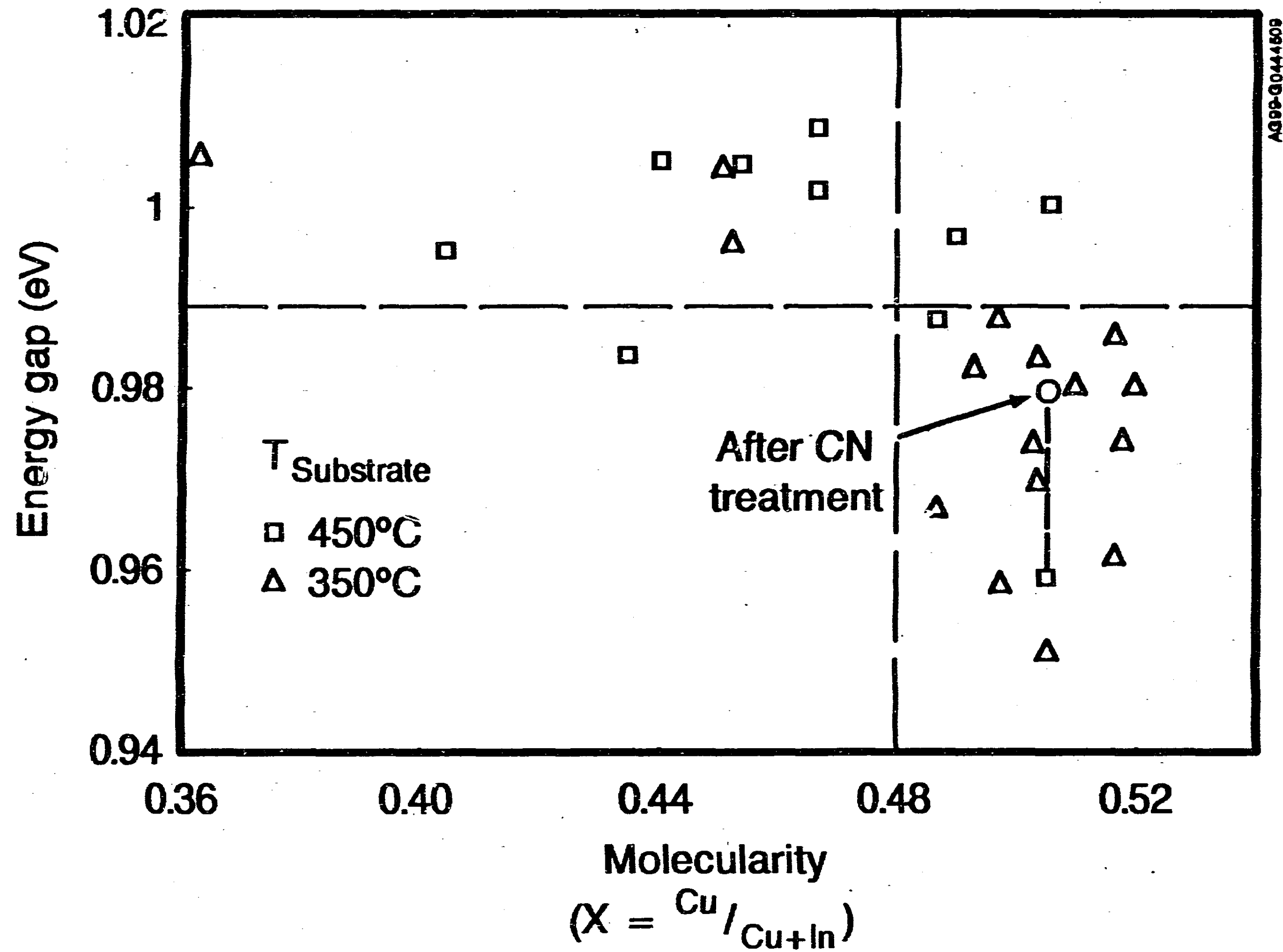

Figure 4-8. Dependence of energy gap on molecularity, x = Cu/(Cu + In), and substrate temperature. (□) T_s = 450°C, (△) T_s = 350°C, (○) sample remeasured after 30 seconds chemical treatment.

The presence/absence of $Cu_{2-\delta}Se$ in our films can be rationalized as follows: At a T_s of 450°C, the formation of $Cu_{2-\delta}Se$ is not favorable until there is an excess of the copper species at the substrate surface, above that which is necessary to create stoichiometric material; at a T_s of 350°C, the formation of $Cu_{2-\delta}Se$ is more favorable and proceeds until the local surface concentration of copper is severely depleted. The demarcation line for this phenomenon is at at. % copper ≈ 23 ($0.45 < x < 0.48$). We have confirmed the presence of this phase by applying selective chemical treatments, such as cyanide, to remove it and subsequently observing a drop in sub-band-gap absorption and an increase in extrapolated transition energy values (Figure 4-9). The increase seen for this copper-rich sample is 0.02 eV.

For copper-rich material, the data above and below the primary transition in Figures 4-7 and 4-9 are characterized by variable regions of constant slope in the $(\alpha h\nu)^2$ versus $h\nu$ curve. In some cases, the intermediate linear region is characteristic of a direct allowed transition of 0.88 eV, but we are unable to identify its source. Cu_2Se, the logical secondary phase, has a band gap greater than 1.0 eV. When this transition is extrapolated above 1.0 eV, the fundamental edge of the $CuInSe_2$ shifts, in this case, from 0.97 to 0.99 eV. In other films, however, the absorption data in this region cannot be fit to any transition model. It is reasoned, therefore, that these regions actually represent a single band-band transition where the parabolic model is only valid at the onset of absorption and deviates in k-space away from the zone center.

By assuming an additive absorption model and through extrapolation of the primary transitio· in copper-poor material to higher energies, a second transition is obser·ed in the range 1.17-1.22 eV, indicating a spin-orbit valence band splitting (Δ_{so}) of 0.21-0.24 eV [Figure 4-10(a)]. In Figures 4-10(a) and 4-10(b), α' represents the difference between the calculated values of the absorption coefficient α_{calc} and the extrapolated value from the primary transition, α_{extrap}. In the other compositional regime, it is the intermediate rather than the primary transition that is extrapolated in order to calculate α' [Figure 4-10(b)]. For these films, the linear behavior of the $(\alpha' h\nu)^2$ and the accurate values for Δ_{so} extracted support the conjecture made earlier concerning the nature of the intermediate transition.

The values for the spin-orbit splitting calculated here are in good agreement with single-crystal values reported elsewhere [1]. There is only a mild dependence of the splitting on stoichiometry, the higher values representing near stoichiometric and copper-rich material. Since the built-in compressive/dilative distortion of this compound along the c-axis is negligible, crystal field splitting is not observed.

4.2.3.4 Device Modeling

In order to substantiate the optical absorption data presented here, we need to explore its ramifications on the performance of an actual $CuInSe_2$-based solar cell. In the context of this report, it is not appropriate to approach the modeling of this device in great detail. The reader is referred to works by Böer [27] and Rothwarf [28] for in-depth analyses of $CdS/CuInSe_2$ heterojunction devices. Instead, we will present a simple heterojunction model that will predict the internal quantum efficiency of this device and compare the resulting spectra with actual data obtained by spectral response measurements.

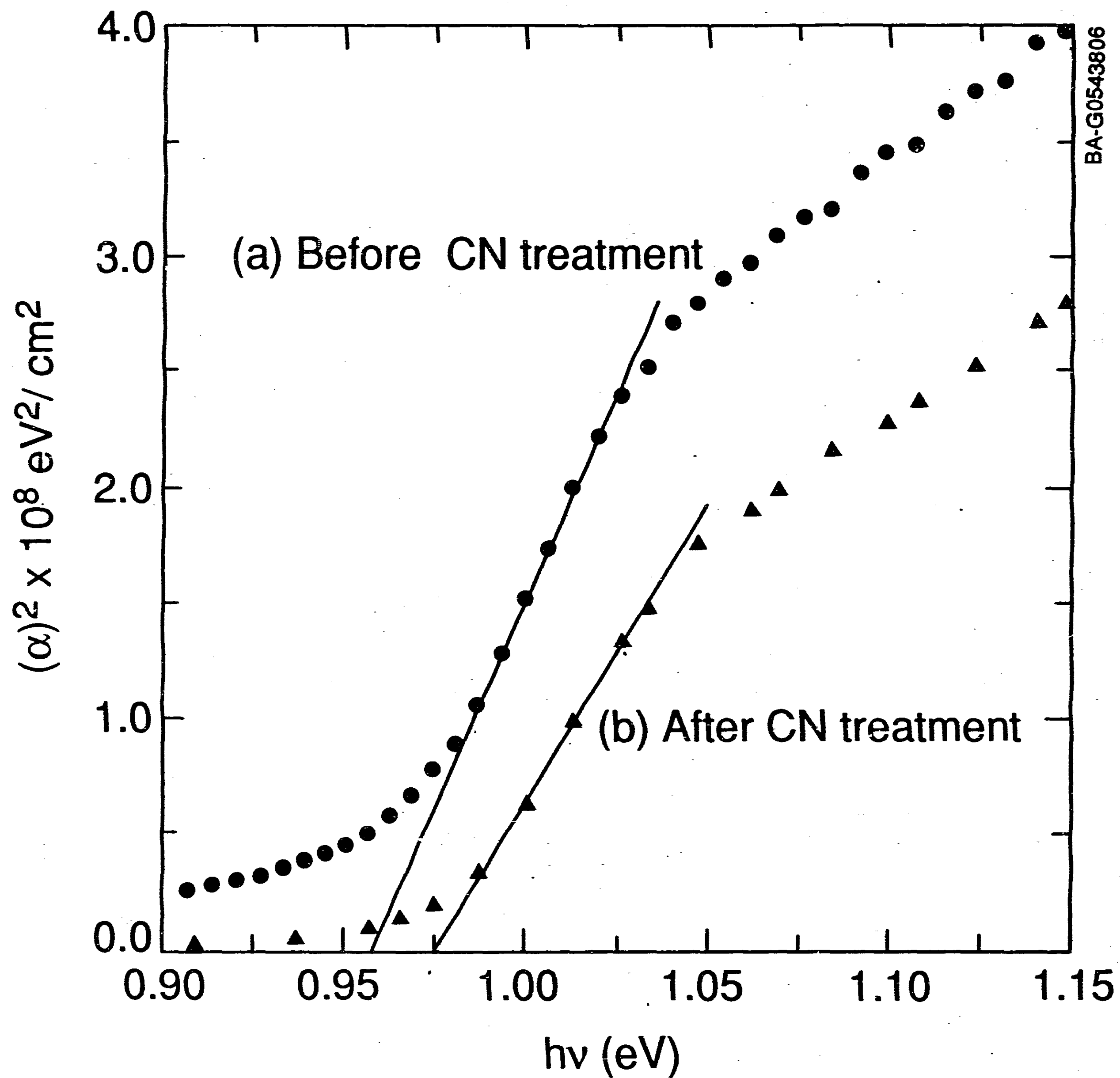

Figure 4-9. **Shift of fundamental transition to higher energy following chemical treatment aimed at removing $Cu_{2-\delta}Se$.** (a) before, (b) after treatment.

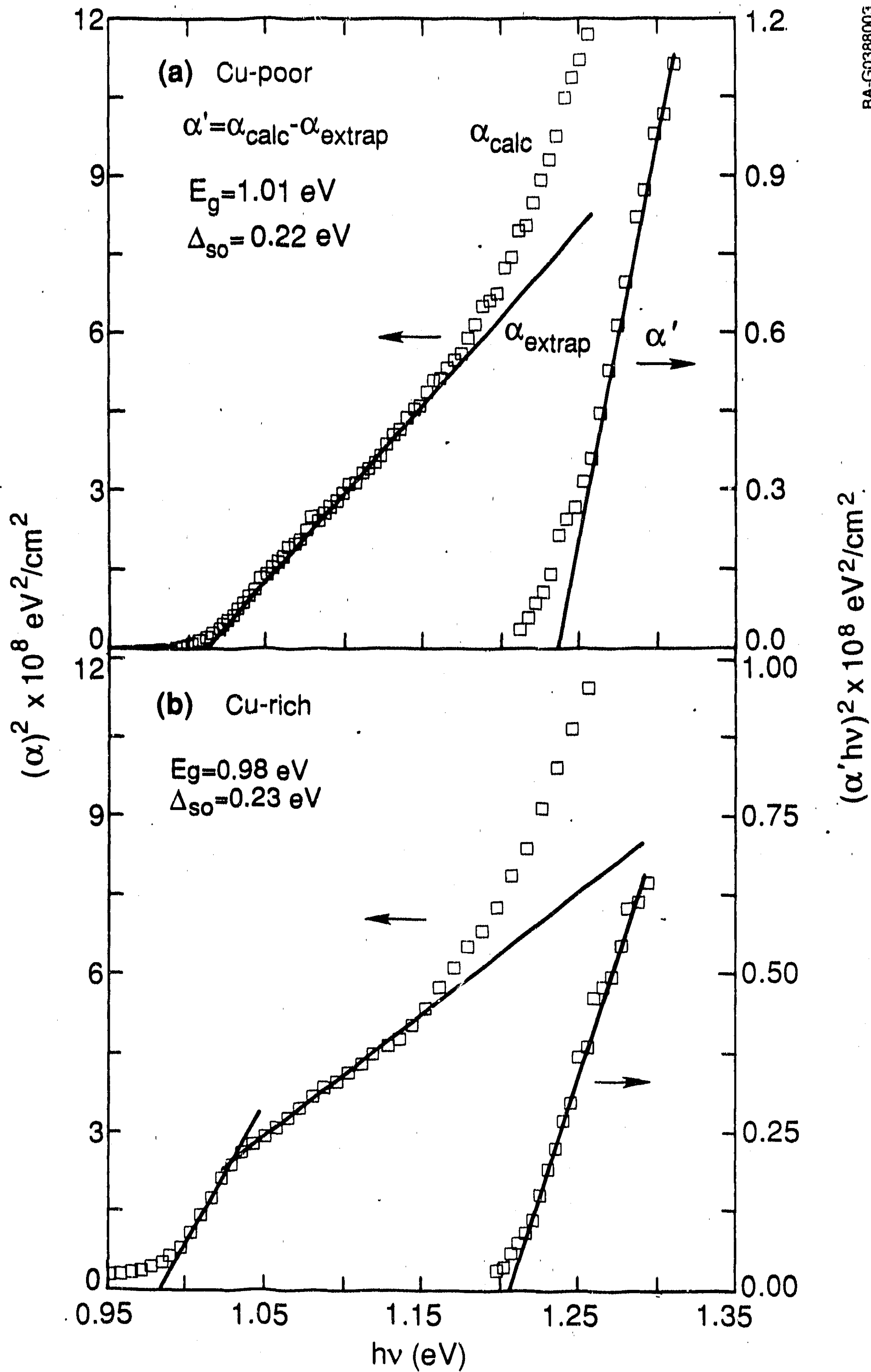

Figure 4-10. **Extrapolation of (a) primary transition for a copper-poor film and (b) intermediate transition for a copper-rich film to determine higher-order direct transition**

In order for this discussion to be complete, some details of the device fabrication procedure will be presented. For a complete discussion of the procedures, the reader is referred to Mickelson and Chen [29]. The most common $CdS/CuInSe_2$ thin film device structure is shown in Figure 4-11 in the form of a cross-sectional SEM micrograph. The $CuInSe_2$ absorber layer is fabricated in a "bi-layer" structure. The first layer of $CuInSe_2$ (2.5 μm) is evaporated at T_s = 350°C and is copper-rich, typically 25.4/24.9/49.7, in order to establish good electrical contact to the molybdenum back electrode. The second layer (0.8 μm) is evaporated at T_s = 450°C and is copper-poor, typically 19.5/28.5/52.0. The copper-poor layer is very resistive (≈ 10^5 Ω-cm) and is necessary to establish a good interface with the CdS window layer. The resultant composite structure has a composition of 23.5/26.0/50.5 and can be considered quasi-homogenous throughout the bulk, with a graded copper-poor layer at the interface. The variation in composition that is seen in the bi-layer structure is the primary driving force for determining the electro-optical properties of $CuInSe_2$ as a function of stoichiometry.

Superimposed on the micrograph is a junction electron-beam-induced current (JEBIC) linescan representing the charge collection efficiency profile of the heterostructure. (The JEBIC measurement technique is described in detail elsewhere [12,30].) The peak in the charge collection efficiency is considered the device junction and, in this case, resides in the $CuInSe_2$ absorber. It is generally accepted that the device is a one-sided heterojunction, with one edge of the space charge region (SCR) coincident with the heteroface. There is some disagreement, however, as to the spatial extent of the SCR, W, and the value of the diffusion coefficient of minority carriers L_d in the $CuInSe_2$. From the JEBIC linescan presented here for a typical $CdS/CuInSe_2$ device, one can extract a W value of 0.4-0.6 μm and a L_d of 0.5-1.0 μm [31]. As we will show, the resultant spectral response simulations will depend upon the values of W and L_d chosen together rather than separately.

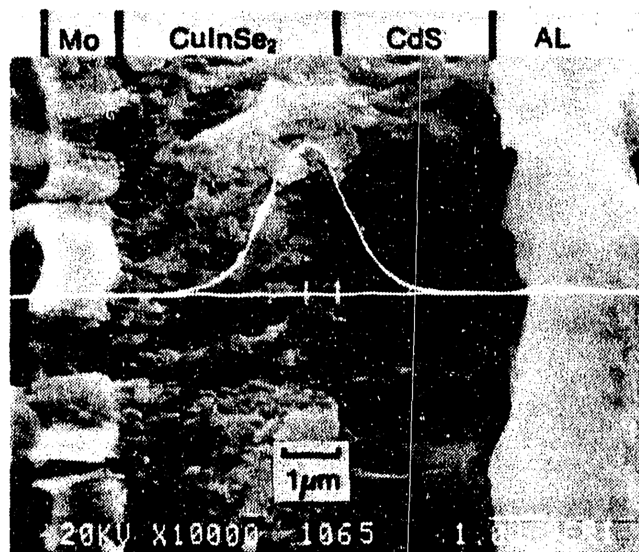

Figure 4-11. Cross sectional SEM micrograph of $CdS/CuInSe_2$ device. Superimposed is a JEBIC linescan of the device.

A few additional assumptions are made concerning the charge collection efficiency of the device structure. Within the SCR, the collection efficiency is considered to be unity and recombination within the SCR is neglected. Outside the SCR, the collection efficiency drops off with x (the point of e-h pair generation) as $e^{-(x-x_i)/L_d}$, where x_i is the location of the edges of the SCR within the $CuInSe_2$. In this model, $x_1 = 0$ and $x_2 = W$. A charge collection profile with $L_d = 1.0$ µm is presented in Figure 4-12 as the dashed line. Given the junction profile and the absorption spectra $\alpha(\lambda)$, we can calculate the spectral response by convoluting the normalized EBIC signal $J(x)/J_0$ with the optical generation function $G(x) = \alpha(\lambda)e^{-(\alpha x)}$. A plot of $G(x)/\alpha$ for different values of α is shown in Figure 4-12. The resulting equation for the spectral response $QE(\lambda)$ for light entering through the CdS, to an absorber of thickness d, for a one-sided heterojunction, is given by

$$QE(\lambda) = \int_0^d \frac{J(x)}{J_o} \alpha(\lambda) e^{-\alpha(\lambda)x} dx$$

$$= \alpha(\lambda) \left[\int_0^W e^{-\alpha(\lambda)x} dx + \int_W^d e^{-\alpha(\lambda)x} e^{-(x-W)/L_d} dx \right]$$

$$= 1 - \frac{1}{\alpha(\lambda)L_d + 1} \left[e^{\alpha(\lambda)W} + \alpha(\lambda)L_d e^{(W/L_d - \alpha(\lambda)d - d/L_d)} \right]$$

With this relationship, and the $\alpha(\lambda)$ data files at 4-nm intervals, we can generate $QE(\lambda)$ spectra for different values of L_d and W. In the calculations that follow, the value of absorber thickness d utilized is 3.5 µm and the $\alpha(\lambda)$ spectra is from a sample of composition 23.7/25.2/51.0. In Figure 4-13, a $QE(\lambda)$ simulation is performed, with $L_d = 0.7$ µm and $W = 0.5$ µm, exhibiting good agreement with a $CdS/CuInSe_2$ device fabricated at Boeing. Similar agreement is achieved for a continuum of L_d and W values, as exhibited in Curve A of Figure 4-14. The substantial data base of devices measured by EBIC suggests a narrow region of allowable values, indicated by the shaded region.

If we consider L_d and W values within the shaded region and utilize $\alpha(\lambda)$ spectra presented by Meakin (Figure 4-4), the resultant $QE(\lambda)$ spectra is 900-1300 nm, a response that is far too high in the NIR (Figure 4-13). By performing a similar series of $QE(\lambda)$ calculations with this $\alpha(\lambda)$ data as described before, one obtains a second continuum of L_d and W values (Curve B, Figure 4-14) that produce consistent $QE(\lambda)$ spectra. There does not appear to be, however, any combination of L_d and W that is observed in the device analyses.

The absorption data presented here are consistent with the charge collection configuration and the measured spectral response observed in actual high efficiency $CdS/CuInSe_2$ devices. Although the heterojunction model utilized in this analysis neglects some observed device phenomena, such as SCR recombination, we are confident that the consistency of the calculated $QE(\lambda)$ and the measured internal $QE(\lambda)$ is justifiable proof of the argument presented.

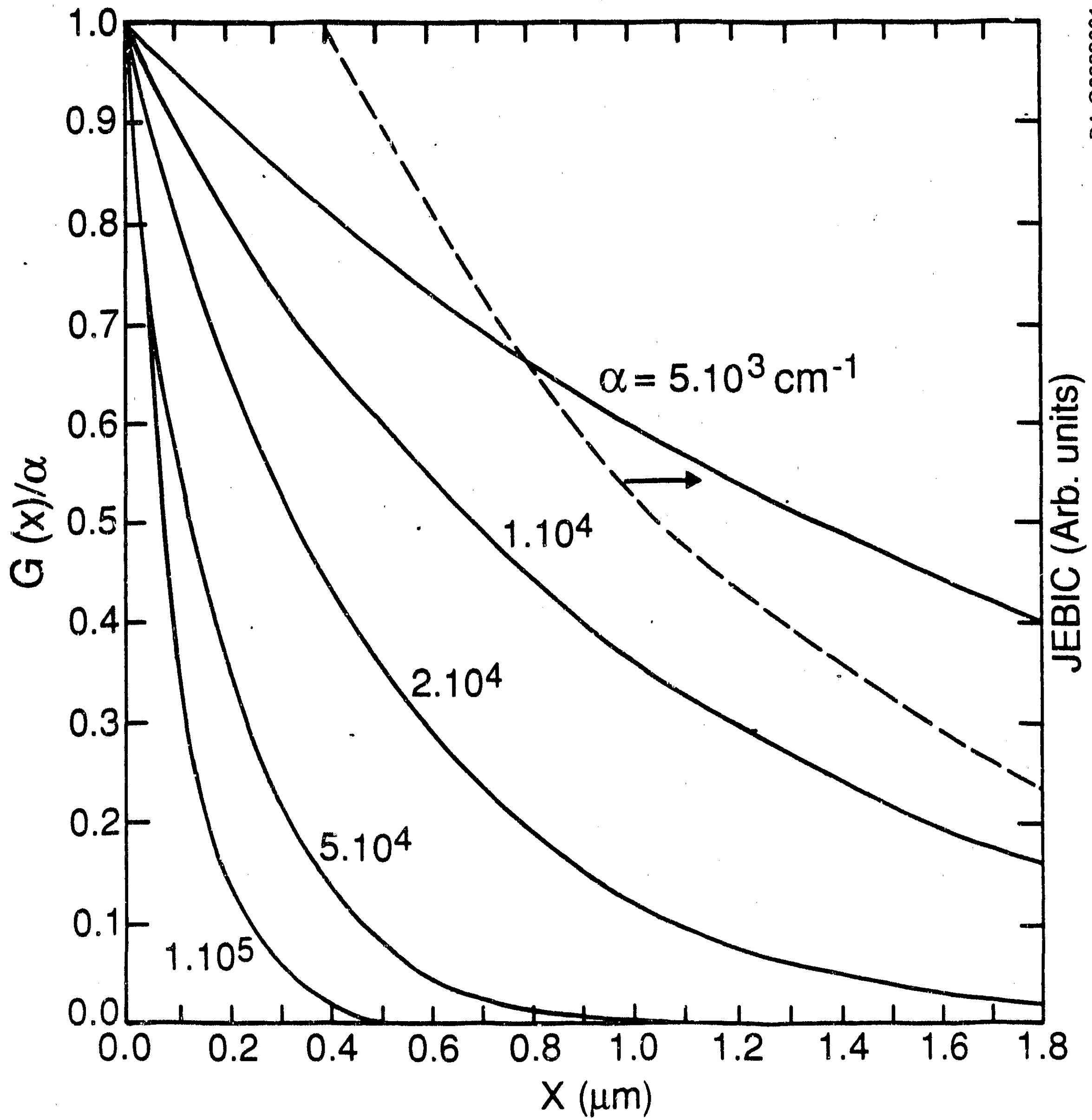

Figure 4-12. Plot of the normalized optical generation function (solid line) and EBIC junction profile vs. distance from heteroface (dashed line) in a $CdS/CuInSe_2$ device structure

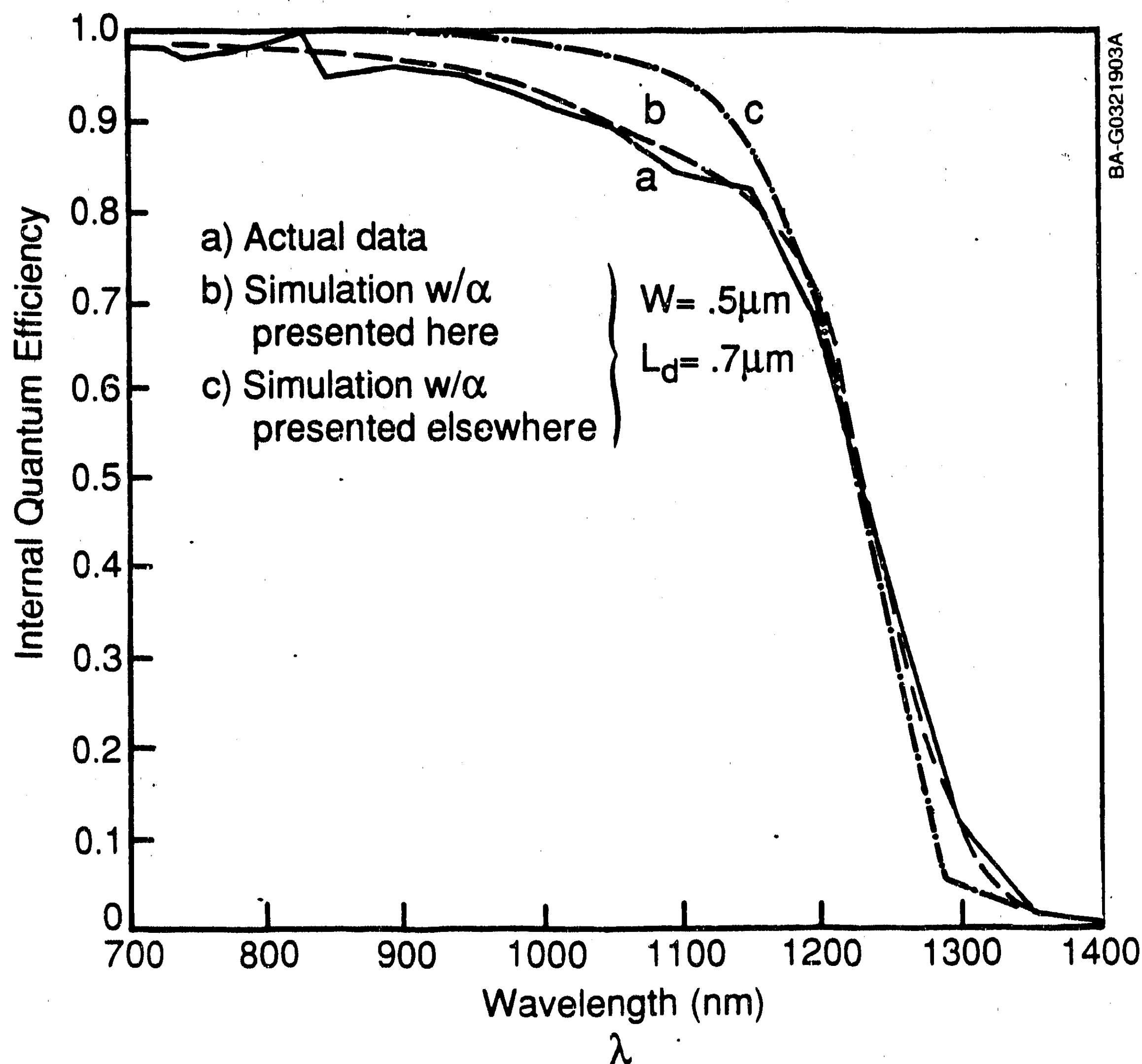

Figure 4-13. Internal quantum efficiency of a $CdS/CuInSe_2$ device (a); comparative simulations, QE(λ), utilizing absorption data presented here (b) and from Ref. 13 (c).

4.2.3.5 Error Analysis

Absorption coefficients for thin film $CuInSe_2$ presented here are significantly lower than previously published data. It would seem appropriate, therefore, to examine potential sources of error in our experimental procedures. The three obvious choices are errors in measurement, errors in calculation, and errors in interpretation. As we have attempted to be objective in our presentation of the data, so the latter choice will be left up to the reader. As for the former two, they are in many ways intimately related. We will separate them in the context of measured and non-measured quantities.

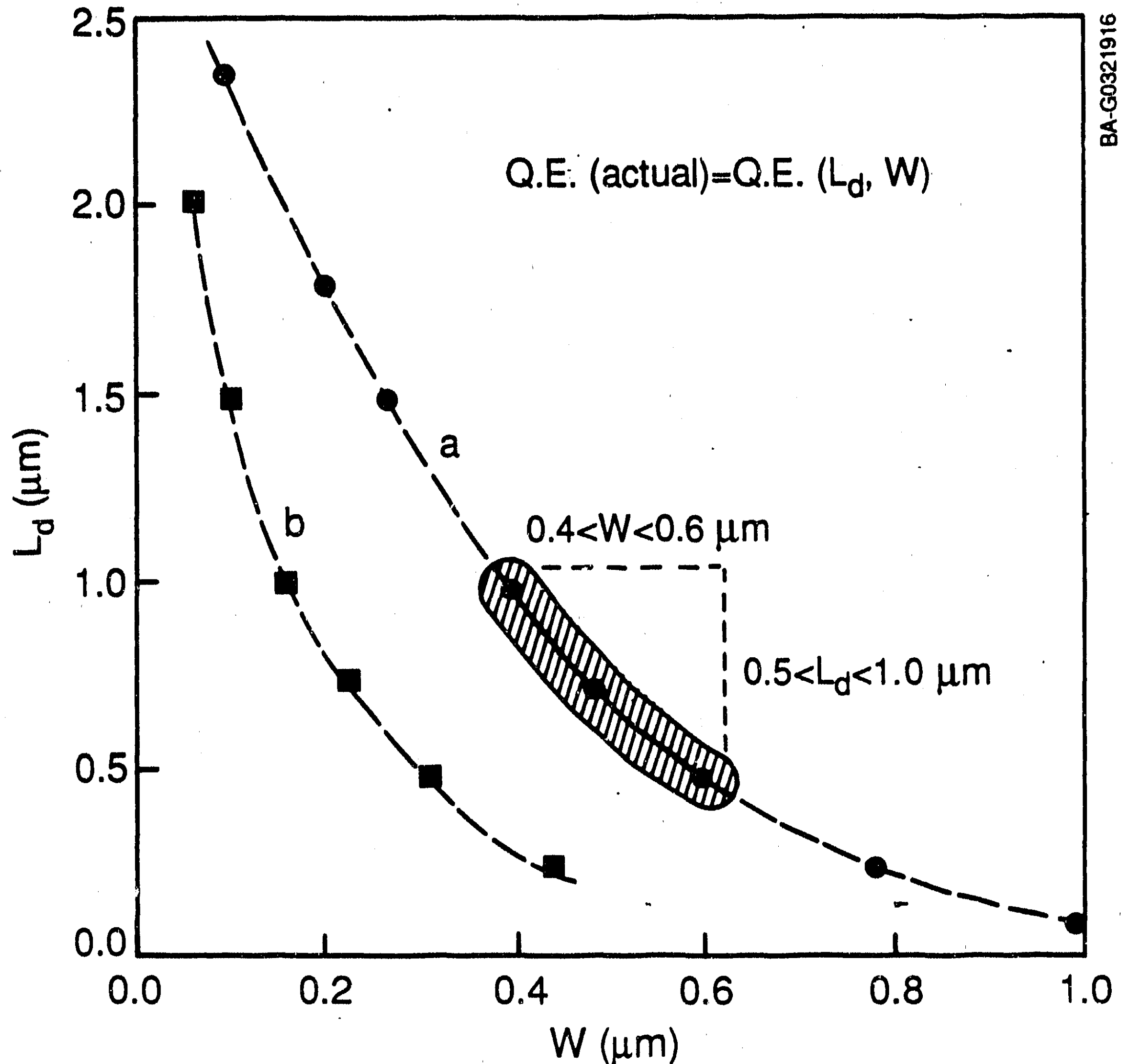

Figure 4-14. Cross-sectional SEM micrograph of a $CdS/CuInSe_2$ device. Superimposed is a JEBIC linescan of the device.

Measurement error has several origins. There is systematic and random measurement error which can be introduced by either the instrumentation or the operator. Probable sources of systematic error in our system include 0% and 100% baseline, reference beam reflectance, and losses associated with non-absorbed light. We will briefly consider the first and second sources and follow with an analysis of the third. Other sources of systematic and random error include non-linearity of the detector, random noise, and the process of signal conversion/transfer. In this analysis, the magnitudes of these sources can be considered negligible.

As part of the experimental procedure, we correct the first and second possible sources prior to data analysis so they can safely be disregarded. This correction is accomplished by normalization to a measured 0% and 100% T_{tot} reference line and a National Bureau of Standards $BaSO_4$ reflectance standard, respectively. Consequently, only losses associated with non-absorbed light need be considered as a source of systematic error in our measurements. The minimization of losses related to non-absorbed radiation involved the positioning of the sample relative to the beam such that the reflected and transmitted intensities were a maximum. In this analysis, we have considered losses that account for up to 5% of the measured R_{tot} and T_{tot} spectra. An example of such a loss would be uncollected scattered transmittance and diffuse reflectance.

Figure 4-15 illustrates the effect on the calculated values of α of several measurement error types for representative copper-rich and copper-poor films. Included in the figure is the result of a ±10% error in the measurement of thickness. This calculation is based upon a fixed value of n and does not address the n versus λ dispersion issue discussed earlier. $\Delta\alpha(\lambda)$ is simply calculated as the difference $\|\alpha(\lambda) - \alpha'(\lambda)\|$, where $\alpha'(\lambda)$ is calculated with modified values of the dependent variables. One can conclude that the dominant source of error is uncollected transmittance, such as scatter, that occurs at energies at or below the fundamental edge. In this region, however, α is small so the absolute error is also small. For copper-poor films, failure to measure scattered transmittance manifests itself in artificially high absorption below the band edge (Figure 4-16). For copper-rich films, measurement of scattered and diffuse radiation components reduces, but does not remove, the subgap absorption artifacts that are observed. For all compositions, the effect of errors for photon energies above the band edge becomes negligible.

Calculation error has several origins in this study. The effects of scatter on the calculations were discussed earlier. The primary source is the index of refraction value that is fixed at 2.9 in these calculations. Near the band edge and in the ultraviolet (UV), we can expect the index of refraction to deviate from its value in the transparent region. This was observed in Figure 4-6 for a copper-poor film that is predominantly single phase. Preliminary calculations for near stoichiometric and copper-rich material suggest a slightly larger deviation within the absorbing region. For the purpose of discussion, a deviation in n of ± 1.0 is investigated in Figure 4-17, with some variation in α observed. The upper and lower curves in the figure, representing solutions to $F_2(n,k) = 0$ with n = 1.9 and 3.9, can be considered an envelope within which α must lie. A variation in *n*, therefore, can be considered a probable cause for the unidentified kinks observed in the α versus $h\nu$ curves for copper-rich material. The effect, however, is difficult to verify due to the discontinuous nature of the n versus λ dispersion curve for multiphase material.

When considering the error mechanisms discussed and the magnitudes of α in the different wavelength regions used for analysis, gross errors probably do not exist. We can therefore conclude that the experimental and data analysis techniques utilized in this study to calculate the absorption coefficient of thin film $CuInSe_2$ are quite acceptable.

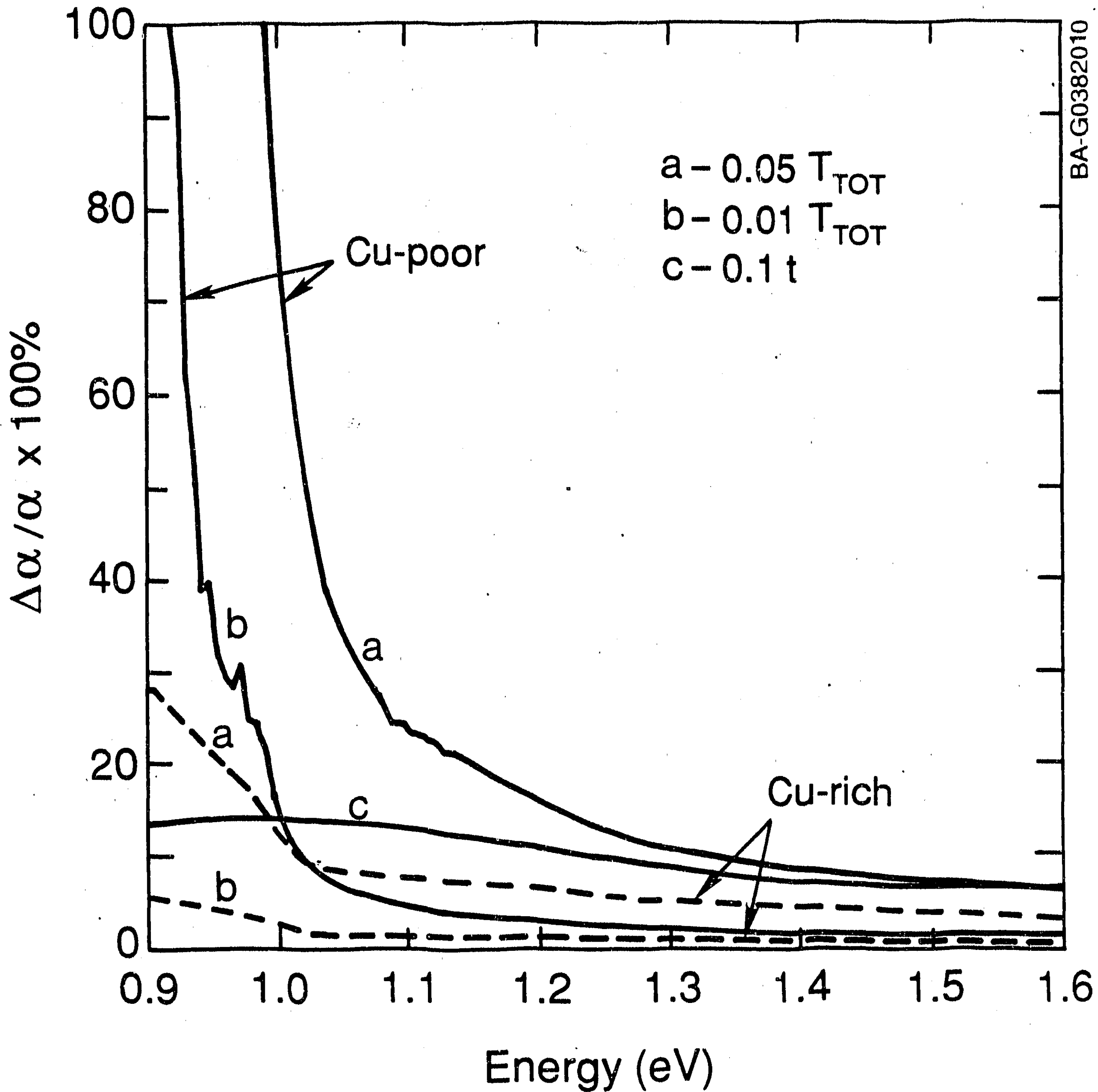

Figure 4-15. Relative error in calculated α induced by measurement error for a copper-rich (dashed line) and a copper-poor (solid line) film. (a) 1% and (b) 5% error in T_{tot}, (c) 10% error in thickness.

4.2.4 Conclusion

The values for α presented here represent upper limits on the absorption coefficient for thin film $CuInSe_2$. Although minor variations are observed among different compositions and growth parameters, the optical properties of the material are dominated by the degree and manner of polycrystallinity, such as rough surfaces and secondary phases at grain boundaries. The values for the band gap and spin-orbit interaction energies can be accurately extracted from

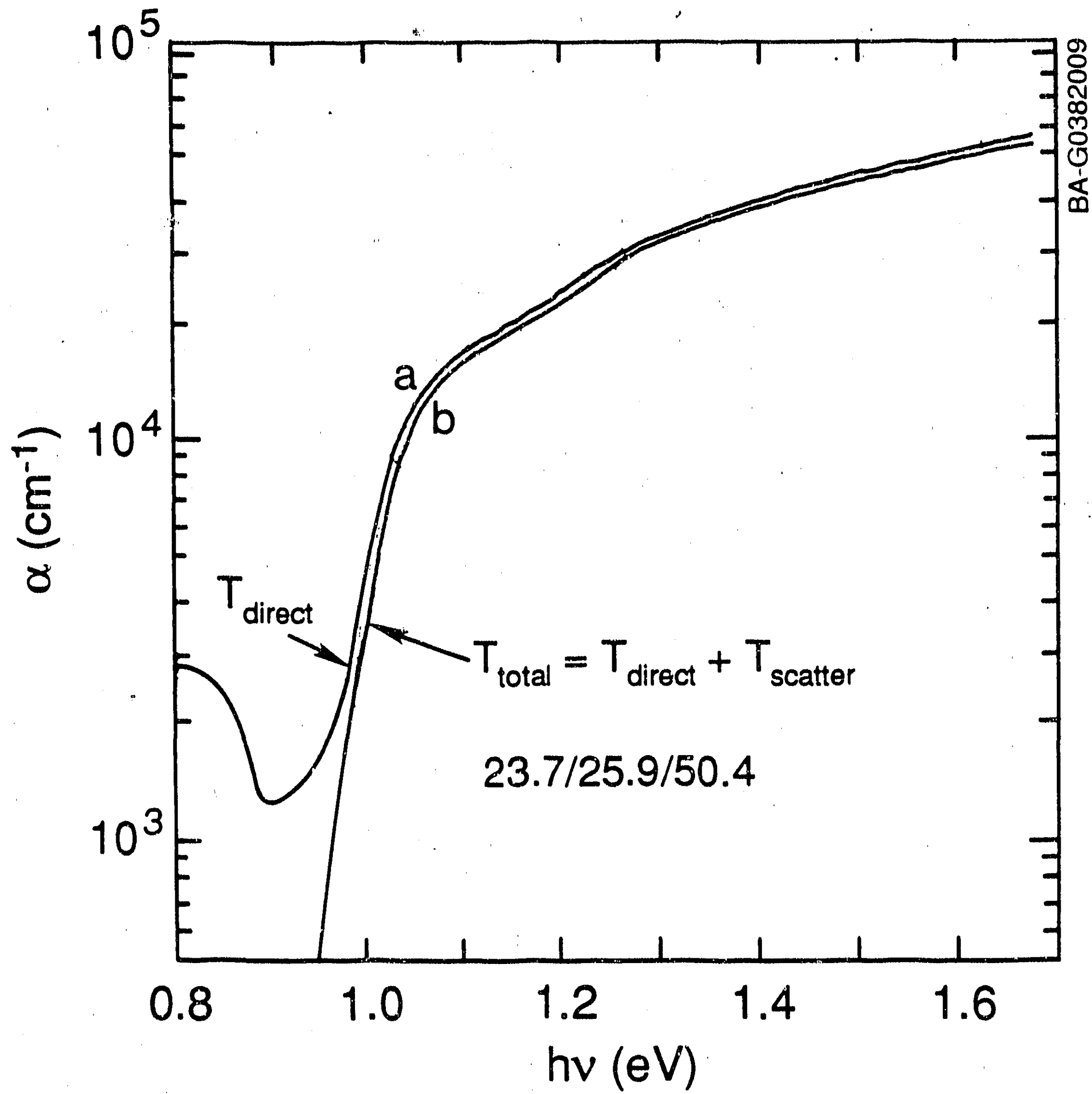

Figure 4-16. Difference in calculated α if $T_{scatter}$ is not collected. (a) T_{direct}, (b) $T_{tot} = T_{direct} + T_{scatter}$.

the optical data. The determination of optical constants of thin films from transmission and reflection measurements without significant error requires attention to diffuse and scattered components.

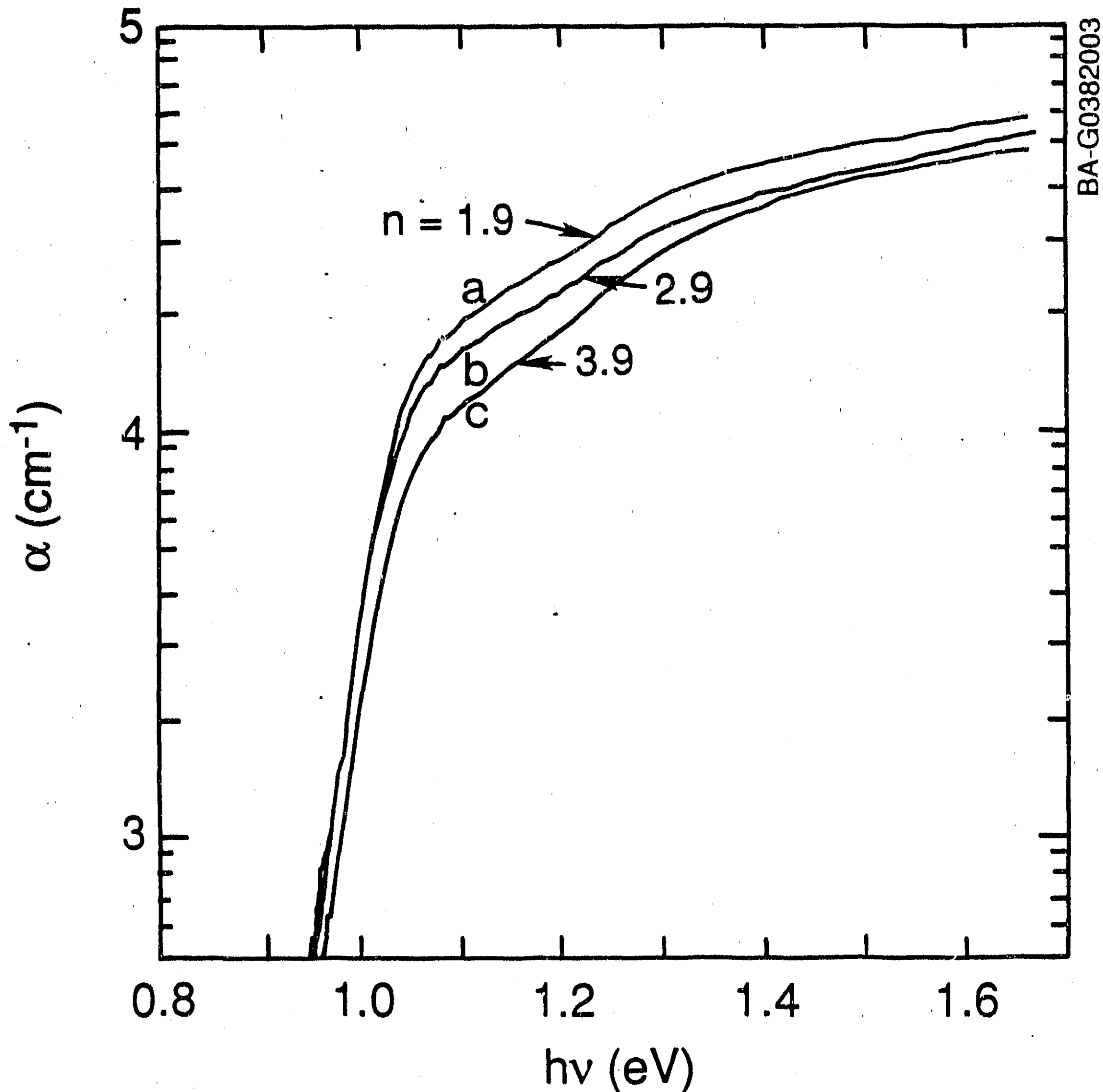

Figure 4-17. Variations in calculated α for different values of the index of refraction N. (a) 1.9, (b) 2.9, (c) 3.9.

When correlated with observed junction profiles, the optical data agree well with measured $CdS/CuInSe_2$ device spectral response. The data also provide useful insight into the effects on device performance of a multicompositional profile within the absorber layer and of photon scattering within polycrystalline materials.

4.2.5 Appendix A

For a single absorbing film on a transparent substrate, the formulas relating the measured values (at normal incidence) of R_{tot}, T_{tot}, and film thickness t_1 to the real and imaginary components of the index of refraction for the absorbing film are given by:

$f_1(n_1,k_1) =$

$$\frac{1+R}{T} = \frac{1}{4n_0n_2(n_1^2+k_1^2)} [(n_0^2+n_1^2+k_1^2)\{(n_1^2+n_2^2+k_1^2)\cosh 2\alpha_1 + 2(n_1n_2)\sinh 2\alpha_1\}$$

$$+ (n_0^2-n_1^2-k_1^2)\{(n_1^2-n_2^2+k_1^2)\cos 2\gamma_1 - 2n_2k_1\sin 2\gamma_1\}]$$

$f_2(n_1,k_1) =$

$$\frac{1-R}{T} = \frac{1}{2n_2(n_1^2+k_1^2)} [n_1\{(n_1^2+n_2^2+k_1^2)\sinh 2\alpha_1 + 2n_1n_2\cosh 2\alpha_1\}$$

$$+ k_1\{(n_1^2-n_2^2+k_1^2)\sin 2\gamma_1 + 2n_2k_1\cos 2\gamma_1\}]$$

where $\gamma_1 = (2\pi\nu_1\tau_1Å\lambda)$, $\alpha_1 = 2\pi\kappa_1\tau_1Å\lambda$ with the absorption coefficient $\alpha = \alpha_1/t_1$, $n_1 - ik_1$ is the complex refractive index of the film being measured, λ is the wavelength at which R and T are measured, $n_2 - ik_2$ is the complex refractive index of the substrate ($k_2 = 0$), and n_0 is the refractive index of air (i.e., $n_0 = 1$).

4.3 Characterization of Thin Film $CuInSe_2$ and $CuGaSe_2$: The Existence and Identification of Secondary Phases

4.3.1 Introduction

Photovoltaic devices consisting of a polycrystalline $CuIn_xGa_{1-x}Se_2$-based absorber are quickly proving to be the most economically viable, high-efficiency, thin film solar cell technology. $ZnO/CdS/CuInSe_2$ solar cell devices presently exhibit efficiencies exceeding 14% [32]. The electro-optical, structural, and morphological properties of $CuInSe_2$ and $CuGaSe_2$, and the corresponding device performance, are highly dependent on film composition, defect chemistry, and growth parameters (such as substrate temperature) and are dominated by the degree and manner of polycrystallinity (such as rough surfaces and secondary phases at free surfaces and grain boundaries). The absorption coefficient α and band gap E_g are of special interest in modeling the observed quantum efficiency of $CdS/CuInSe_2$ devices. (A complete treatise on this subject is presented elsewhere [33-35], including details on material fabrication, data acquisition and analysis, and device modeling.) In this report, the relationship between observed sub-band-gap absorption in copper-rich $CuInSe_2$ and $CuGaSe_2$ films, hereafter referred to as $Cu(In,Ga)Se_2$, and the presence of a $Cu_{2-\delta}Se$ secondary phase are discussed. By analyzing isolated $Cu_{2-\delta}Se$ thin films, it is possible to speculate on the concurrent growth mechanism of the two materials and estimate the volume percent constituency of the secondary phase.

The presence of $Cu_{2-\delta}Se$ is not, however, limited to copper-rich compositions of $Cu(In,Ga)Se_2$. Its presence is observed optically and by chemical treatments in copper-poor material, though there appears to be a substrate temperature dependence [34]. This would suggest a detailed balance between incident copper and selenium fluxes, substrate temperature, and the subsequent formation of the secondary phase, either intragranular or at grain boundaries and free surfaces. The general argument concerning the formation of the phase is based on valence stoichiometry and the formation of anti-site defects, in this case Cu_{In} [36]. When there is a concentration of copper in the solid solution above that which is required to form stoichiometric $Cu(In,Ga)Se_2$, the excess can be accommodated either by copper interstitials (Cu_i), secondary phase precipitates, or Cu_{In} anti-site defects. The latter condition is not allowed, as it would force the average number of electrons per atomic site to be different than four, a condition that cannot be balanced by cation vacancies (V_{In}) as is observed in the corollary situation with an excess of In. Although the thermodynamics of the gas and solid phase reactions is beyond the scope of this report, it is reasonable to conclude that the reaction will favor the formation of a $Cu_{2-\delta}Se$ precipitate over Cu_i due to the abundance of the selenium species in the local environment. A full investigation of this issue, as well as that of phase identification and characterization, will be the subject of a future publication. In this communication, the problem will be addressed first by examining evidence for the presence of $Cu_{2-\delta}Se$, followed by a brief structural and optical characterization of a mixed phase $Cu_{2-\delta}Se$ thin film and a discussion of chemical treatments targeting its removal, and then finally by proposing a basic microstructural model that may aid in explaining the observed optical phenomena.

4.3.2 Results and Discussion

In Figure 4-18, the absorption coefficients for thin films of $CuInSe_2$ and $CuGaSe_2$ of various compositions and $Cu_{2-\delta}Se$($\delta \approx 0.15$), deposited on transparent substrates at temperatures ranging from 350° to 500°C, are presented. Significant sub-band-gap absorption is evident in near stoichiometric and copper-rich films, indicative of valence band tailing, the presence of a secondary phase, or both conditions. Very copper-poor films, on the other hand, exhibit sharp optical transitions indicative of nearly single-phase material.

To understand the optical and phase behavior of thin film $Cu_{2-\delta}Se$, the material ($\approx$ 1.0 μm) was deposited in vacuum by coevaporation of the constituent elements onto heated (400°C) 7059 glass and Mo/Al_2O_3 substrates. The resultant films were analyzed by EPMA and were found to have a $\delta = 0.15$. The films appeared silver-blue and exhibited bulk resistivity (ρ) on the order of 10^{-3} Ω-cm. The films were subsequently characterized by spectrophotometry in the NIR and by powder x-ray diffractometry (XRD) from 2θ = 10-110. The optical results in the form of absorption coefficients are presented in Figure 4-18 and suggest semimetallic behavior.

The results of the XRD measurements are given in Figure 4-19 for a portion of the diffraction spectrum. The films deposited on glass exhibited preferred orientation, while the films simultaneously deposited on Mo/Al_2O_3 substrates appeared to be of a mixed amorphous/microcrystalline nature. Three distinct families of phases have been identified (in order of maximum peak intensities): cubic $Cu_{2-\delta}Se$, orthorhombic Cu_2Se, and cubic $CuSe_2$. Within the cubic $Cu_{2-\delta}Se$ family, three compounds are reported by the Joint Council on Powder

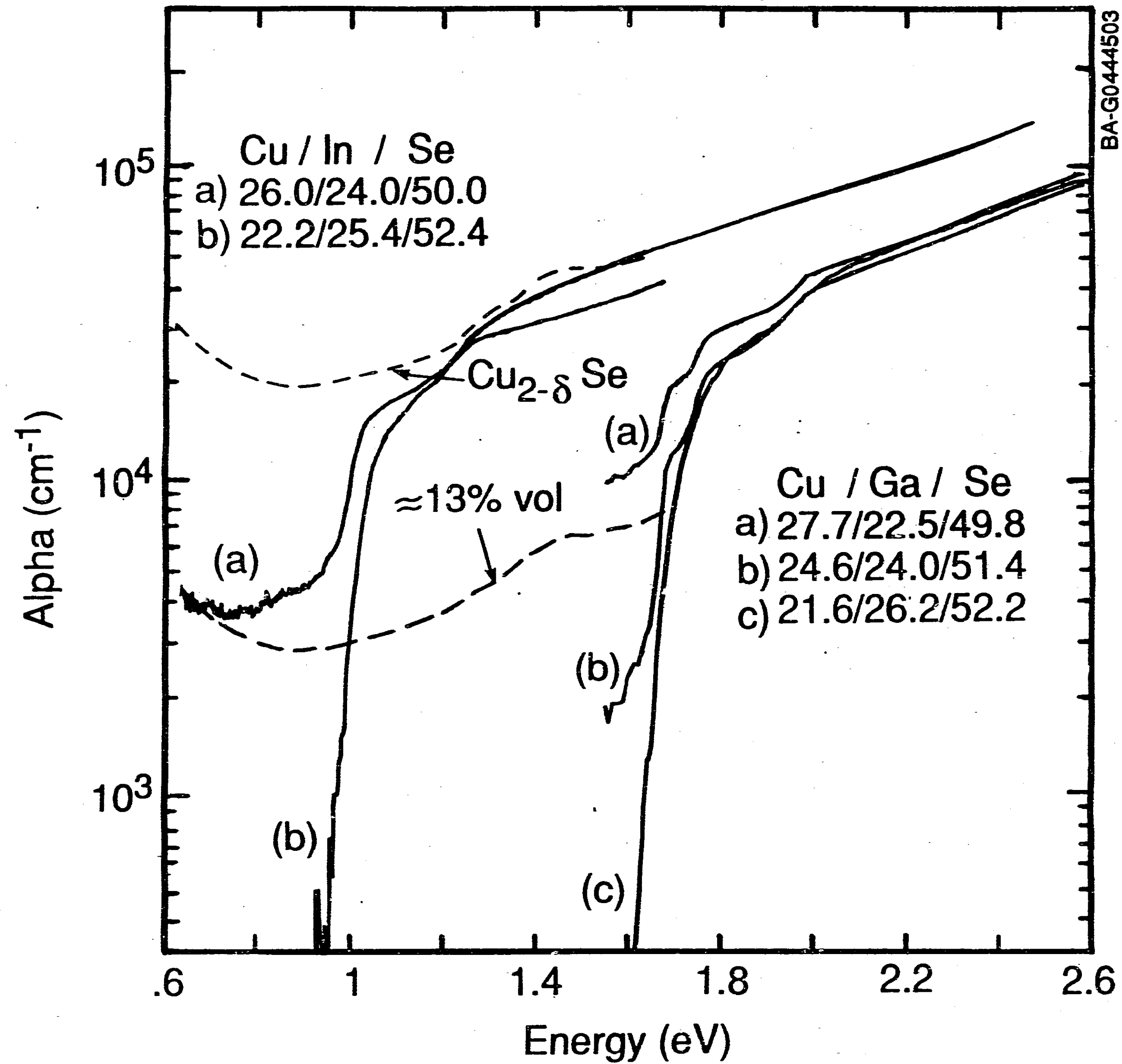

Figure 4-18. Absorption coefficient α vs. incident photon energy for thin films of $CuInSe_2$, $CuGaSe_2$, and $Cu_{2-\delta}Se$ ($\delta = 0.15$)

Diffraction Studies (JCPDS): δ = 0.0, 0.15, and 0.25, the latter being reported as Cu_7Se_4 with lattice parameters approximately twice that of the others. An exact identification of the phases present has not been achieved and may prove to be very difficult due to scarcity of comprehensive data. With the similarity of lattice parameters, a_0 = 5.782 Å and 5.739 Å for $CuInSe_2$ and $Cu_{1.85}Se$, respectively, it seems logical to conclude that the cubic phases of $Cu_{2-\delta}Se$ are the most likely candidates for nucleation and growth on the grain boundaries of $Cu(In,Ga)Se_2$. The very nearly identical values of a_0 in $Cu_{2-\delta}Se$ and $CuInSe_2$, however, make XRD detection in thin films of the mixture very difficult due to the overlap of diffraction peaks. In very copper-rich material, though, a peak is observed at $2\theta \approx 30.93$, which corresponds to either the (002) line for $Cu_{2-\delta}Se$, or the (200):(004) doublet in $CuInSe_2$. The peak does not appear in material with at. % Cu < 27, suggesting the secondary phase as the likely origin.

In the $CuGaSe_2$:$Cu_{2-\delta}Se$ system, the situation is a bit more promising. The lattice parameter for $CuGaSe_2$ (a_0 = 5.612 Å) is sufficiently different to allow for resolution of related tetragonal and cubic peaks. A recent publication [37] on the composition/structure relationship in thin film $CuGaSe_2$ has identified two peaks associated with the Cu_7Se_4 phase mentioned above.

To verify the presence of a $Cu_{2-\delta}Se$ phase, NaCN-based chemical treatments selective to its removal have been applied to copper-rich material and the resulting film characterized for electrical, optical, and compositional changes [34]. The results are presented in Figure 4-20 and indicate, for treated material, a substantial drop in sub-band-gap absorption with a corresponding rise in the extrapolated band gap [34], a 10-1000 times increase in bulk resistivity, and a change in composition of copper and selenium in the ratio of about 2:1, suggesting a loss of $Cu_{2-\delta}Se$. Similar effects are observed in $CuGaSe_2$ films as well [35,37].

With this analysis in mind, we formulated a microstructural model on the growth and coexistence of a $Cu_{2-\delta}Se$ secondary phase in thin film $Cu(In,Ga)Se_2$ as a function of measured copper content (Figure 4-21). However, for near stoichiometric and copper-rich films, this value is not representative of the copper stoichiometry of the $CuInSe_2$ phase. For very copper-poor material (at. % Cu < 22) with high bulk ρ, the microstructure is characterized by small single-phase grains and with a conduction mechanism exclusively across grain boundaries. For intermediate bulk values of ρ and compositions 22 < at. % Cu < 25, the microstructure appears as predominantly single phase with larger grain sizes and with an increasing amount of $Cu_{2-\delta}Se$ at grain boundaries. The relative amounts of each phase will be a strong function of both the elemental fluxes and the substrate temperature during film growth. The conduction mechanism is still predominant across $Cu(In,Ga)Se_2$ grain boundaries, although for near stoichiometric compositions percolation within the $Cu_{2-\delta}Se$ matrix is possible. The $Cu_{2-\delta}Se$ may or may not contribute to the absorption of light.

For copper-rich compositions, the microstructure may take on a profoundly different character. The near stoichiometric grains are now bathed in a matrix of $Cu_{2-\delta}Se$ sufficient to dominate the conductivity. This becomes clear in material with at. % Cu > 27 following NaCN treatments in that the films appear to disintegrate, leaving undissolved $CuInSe_2$ particles in solution. Significant photon absorption by the $Cu_{2-\delta}Se$ is now expected and is observed for

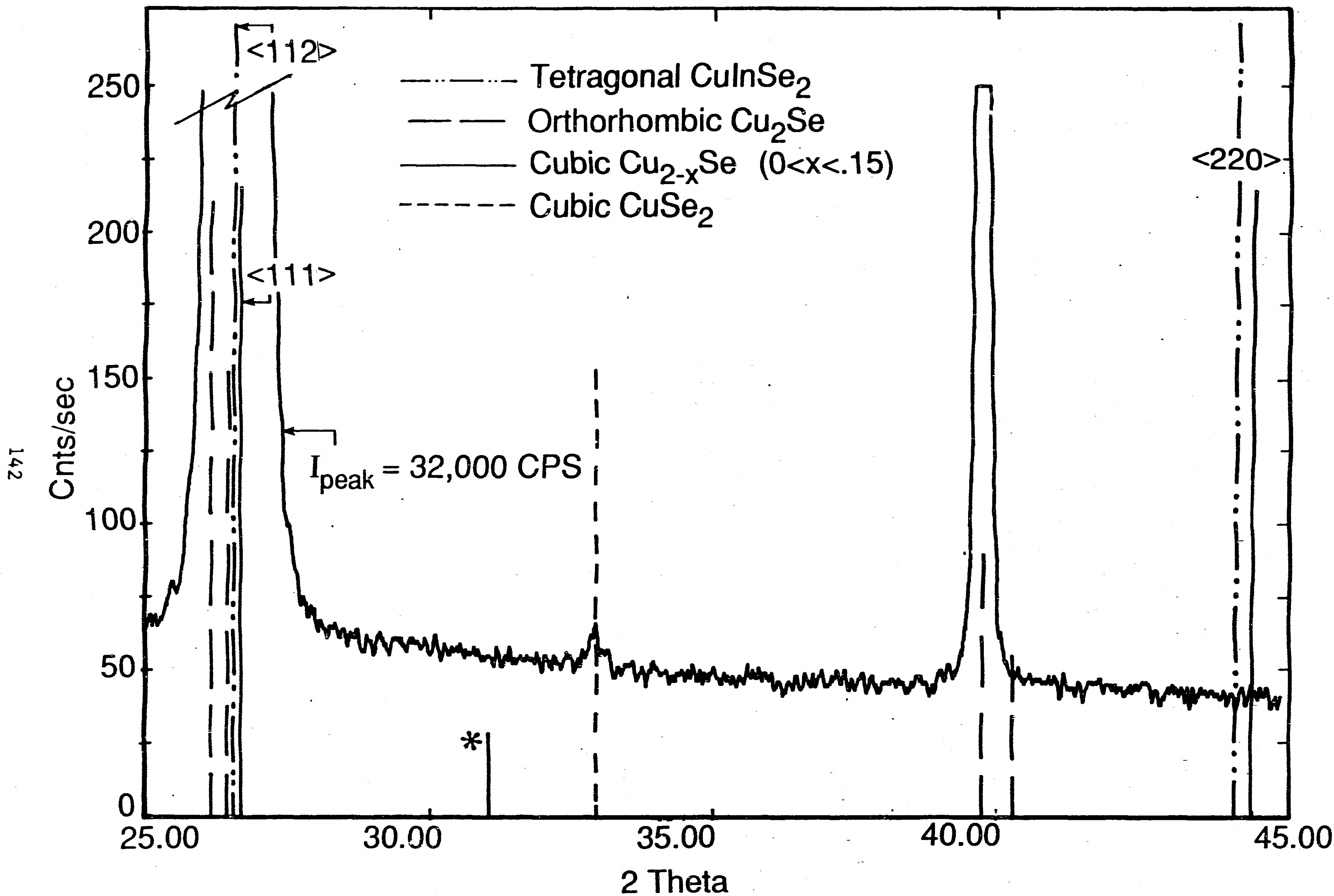

Figure 4-19. XRD spectra for thin film $Cu_{2-\delta}Se$ (δ = 0.15), deposited on a glass substrate, indicating peak positions for phases suspected to be present

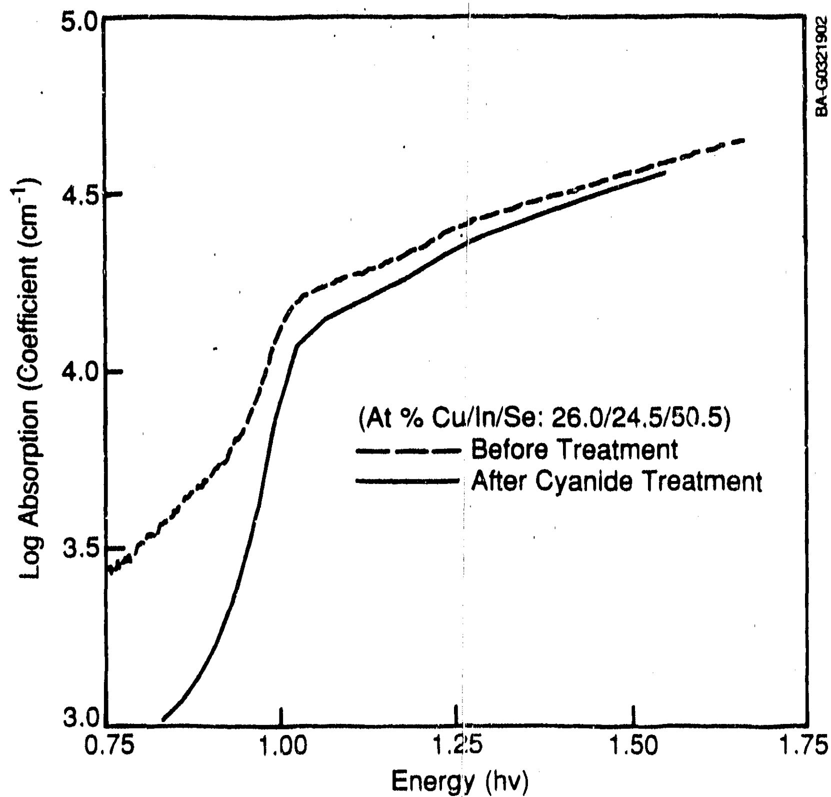

Figure 4-20. $CuInSe_2$ thin film sample characterized for electrical, optical, and compositional changes following NaCN chemical treatments

copper-rich compositions in Figure 4-18. When we consider the material in a device configuration, it is important to note that the absorption is of a free carrier nature in the semimetallic $Cu_{2-\delta}Se$ and therefore will not produce photogenerated carriers.

To quantify the $Cu_{2-\delta}Se$ content of the films, we refer back to the optical measurements presented in Figure 4-18. The analysis would suggest a means by which the sub-band-gap absorption could be fit to a volume percent of $Cu_{2-\delta}Se$,

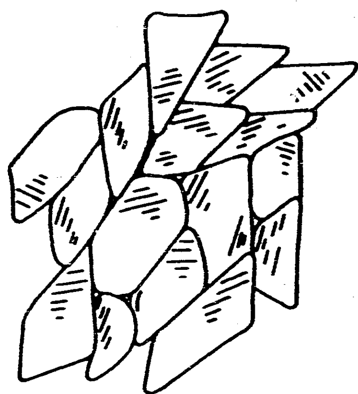

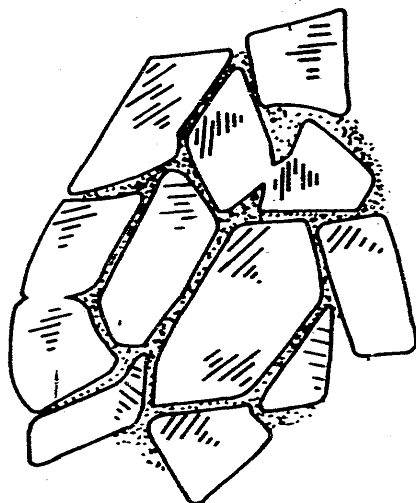

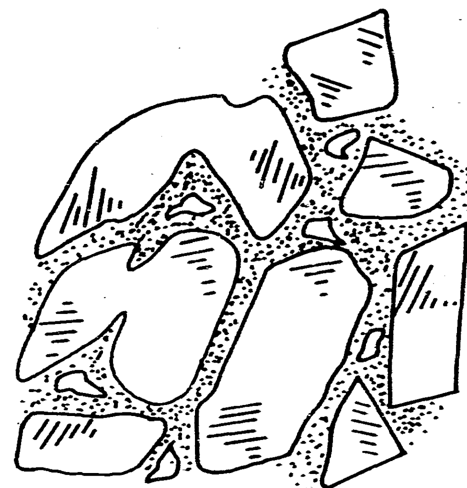

at% Cu<22
$10^5\ \Omega$-cm

22<at%Cu <25
10^1-$10^5\ \Omega$-cm

at% Cu >25
10^{-2}-$10^1\ \Omega$-cm

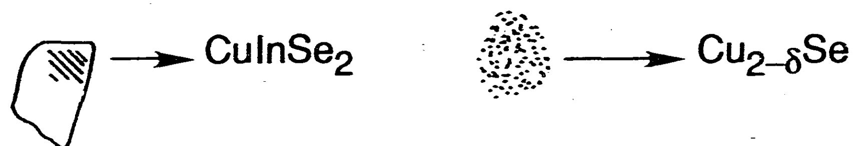

Figure 4-21. Microstructural model of polycrystalline thin film $CuInSe_2$ as a function of composition

as the phase will be the only contributing factor to absorption below the band edge. By adjusting the film thickness value used in the calculation of α of the secondary phase, the resulting absorption spectra can be fit with that measured in the mixture. For the near stoichiometric and copper-rich films of Figure 4-18, the volume percent can be estimated to be in the 5%-15% range.

Although these preliminary experiments are not comprehensive in nature, they do present a picture suggesting that $Cu_{2-\delta}Se$ plays an important role in the electro-optical and structural behavior of thin film $CuInSe_2$ and $CuGaSe_2$ deposited by vacuum evaporation.

4.4 Composition and Substrate Effects on the Structure of Thin Film $CuGaSe_2$

4.4.1 Introduction

Ternary semiconducting compounds of composition $A^{I}B^{III}C_2^{VI}$ and of chalcopyrite structure have received a great deal of interest because of their potential electro-optical applications. Thin film solar cells based on polycrystalline $CuInSe_2$ ($E_g \approx 1.0$ eV) have demonstrated efficiencies exceeding 14% [38]. However, $CuGaSe_2$ with a band gap of 1.67 eV has shown less promise in stand-alone devices. A tandem arrangement of both ternary compounds could increase efficiencies considerably, with theoretical calculations, at AM 1.5 and global reference spectrum (ASTM E 892) at 1000 W/m^2, yielding efficiencies above 33% [39].

Studies on the opto-electronic properties of $CuGaSe_2$ thin films of various compositions have been published [40-42]. Albin et al. [43] have studied the XRD pattern of $CuGaSe_2$ thin films evaporated onto Al_2O_3 and Corning 7059 glass. They note in their study that the (112) peak undergoes an increase in the 2θ position with increasing molecularity X defined as

$$X = \frac{\text{Cu (at. \%)}}{\text{Cu (at. \%)} + \text{Ga (at. \%)}} .$$

4.4.2 Results and Discussion

In this paper, we show that this structural trend, as a function of composition for $CuGaSe_2$ thin films, is not consistent for all types of substrates (e.g., Al_2O_3, 7059 glass, Mo/Al_2O_3, and Mo/7059 glass). Also, we show how the presence/absence of impurity phases modifies the molecularity of the $CuGaSe_2$ and how such modification influences the variation in the (112) 2θ peak position.

$CuGaSe_2$ polycrystalline thin films were deposited by three-source evaporation from the elements in vacuum (2×10^{-6} torr). Deposition rate control for the copper and gallium sources was obtained using an electron impact emission spectroscopy monitor (EIES). A 5-MHz quartz crystal oscillator was used to monitor the selenium rate. Elemental rates for the copper, gallium, and selenium fluxes ranged between 0.5-1.5 Å/s, 2.8-6.0 Å/s, and 10-14 Å/s, respectively. The resulting film growth rates varied from 4.5 to 15 Å/s. The film thicknesses were 1.0-2.0 μm. Compositional control was obtained by varying the Cu/Ga ratio delivered to the substrate.

Four different types of substrates were used: polycrystalline alumina (Al_2O_3), polycrystalline alumina with a magnetron-sputtered molybdenum layer (Mo/Al_2O_3), Corning 7059 glass, and 7059 glass with a magnetron sputtered molybdenum layer (Mo/glass). The thicknesses of the molybdenum layers varied between 1.0 and 2.7 μm. The substrate temperature during deposition of 450°C was obtained by using a graphite cloth heater. Film compositions were measured by wavelength dispersive x-ray fluorescence spectroscopy (WDS) with ±0.5 at. % accuracy.

XRD measurements were made using a Rigaku Dmax vertical goniometer and controller system with a rotating copper anode x-ray generator. A graphite monochromator ($2\alpha = 26.57°$) was used in the diffracted beam to remove CuK_β as well as fluorescent and incoherent radiation. Operating conditions of 40 kV and 60 mA were typical. Scanning step widths of 0.01° and counting times of one second per step were used throughout the measurements. A beam divergence slit of 1/2°, combined with sample dimensions not less than 2x1 cm^2, eliminated angular intensity variations due to irradiated area size.

As the penetration depth of the x-ray beam is greater than twice the thicknesses of the $CuGaSe_2$ films, Mo and Al_2O_3 characteristic diffraction lines were observed in the diffraction pattern. These patterns were used as internal standards to eliminate sample plane displacement errors. This error represents the major source of diffractometer-measured error [44]. The thicknesses of the $CuGaSe_2$ and Mo films, which were measured using a Tencor profilometer to within an accuracy of ± 2%, were incorporated in this correction.

The XRD pattern for the $CuGaSe_2$ samples that was evaporated onto Mo/Al_2O_3 and Mo/glass agrees well with published work on single crystals [45,46] with regard to the tetragonal-type structure of the compound and its peak positions; however, the sample compositions were not reported in those works. In this study, XRD patterns exhibited preferred orientation in the close-packed (112) plane, thus enhancing the intensity of the (112) peak at the expense of the rest of the pattern. In copper-poor samples evaporated on Al_2O_3 and glass, the (111) becomes the dominant peak due to the formation of a cubic phase, tentatively identified as sphalerite.

Figure 4-22 shows (112) peak positions as a function of molecularity for $CuGaSe_2$ samples evaporated at 450°C onto different substrates. The observed (112) peak positions indicate a variation in the unit cell structure. The 2θ variation on Al_2O_3 and glass substrates is attributed to the cubic-to-tetragonal phase change (i.e., the change from the copper-poor to the copper-rich phase). The change in the 2θ value was calculated using the Bragg formula and the equilibrium interplanar spacings as 0.167°. The corresponding 2θ values for the (111) cubic and (112) tetragonal indices using lattice parameter values from Jaffe and Zunger [47] are 27.519° and 27.686°, respectively. Figure 4-23 demonstrates such a shift between the tetragonal and cubic phases. Patterns with a diffraction peak lying somewhere between the ideal (112) tetragonal and the (111) cubic peak positions are broader and are composed of two convoluted peaks, indicating possible phase mixing. However, for the molybdenum-coated substrates of Al_2O_3 and glass, an opposite effect is observed. 2θ increases with decreasing film molecularity from the near-stoichiometric/copper-rich region into the copper-poor region. This signifies a decrease in d-spacing resulting from strain induced by increasing vacancy

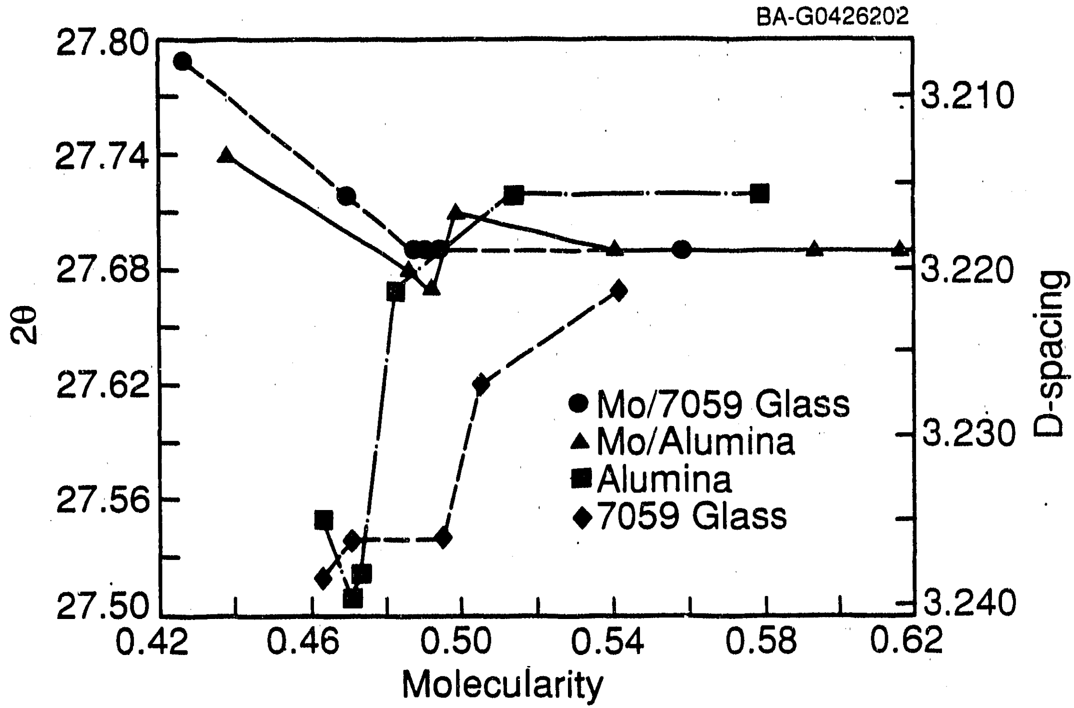

Figure 4-22. 2-θ variation of the (112) peak with molecularity for $CuGaSe_2$ films deposited on different substrate surfaces

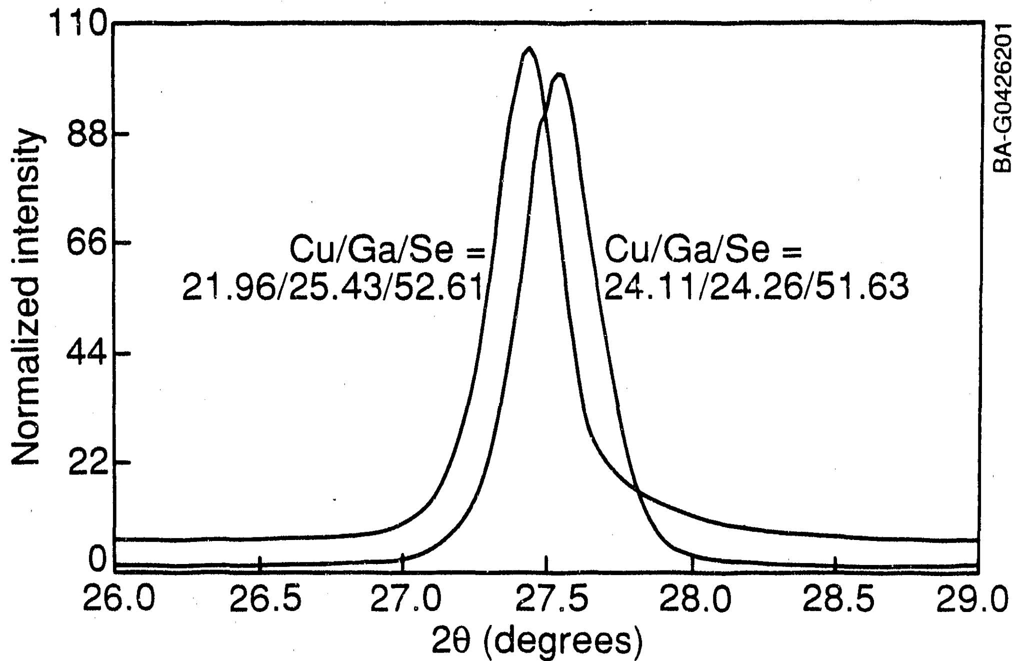

Figure 4-23. (112) peak position shift due to phase change from a tetragonal to a cubic structure

concentration. The leveling off in the 2θ position in the copper-rich region implies secondary phase formation rather than the formation of copper-rich $CuGaSe_2$.

The molecularity X determined from the film composition could not, hence, be considered to represent the "actual" composition of $CuGaSe_2$, but rather of $CuGaSe_2$ plus any impurity phases present. To eliminate such impurity phases, a chemical treatment was used in which the film was dipped for 5 minutes in a 1-M solution of NaCN. NaCN readily dissolves copper, selenium, and $Cu_{2-x}Se$ complexes while being inert to the ternary $CuGaSe_2$.

The WDS results for the NaCN-treated samples showed considerable drops in film molecularity. For the copper-rich samples, this drop was attributed to the removed impurity phases. Figure 4-24(a) shows a typical XRD pattern for such samples. The two strong peaks [(222) and (440)] for Cu_7Se_4 are clearly visible, indicating the presence of this impurity phase. After the same sample has been treated with NaCN, the $CuGaSe_2$ peaks do not shift or hardly vary in intensity [Figure 4-24(b)], but the Cu_7Se_4 peaks completely disappear. WDS data for composition changes due to chemical treatment corroborate this observation. The molecularity of the treated films, regardless of how copper-rich was the original sample, never exceeded 0.5. Such results are in agreement with published work [11,12] on the Cu-Ga-Se phase diagram, limiting the chalcopyrite $CuGaSe_2$ phase to $0.4 \le X \le 0.5$. Figure 4-25 shows the variation of the (112) peak position with molecularity for $CuGaSe_2$ evaporated onto a Mo/Al_2O_3 substrate before and after the NaCN treatment. The molecularity of untreated films shifts to lower X values after treatment (primed numbers).

We conclude that the d-spacing (2θ) variation with the molecularity of $CuGaSe_2$ polycrystalline thin films is dependent on the nature of the substrate. Therefore, it is important to specify the substrate and the molecularity in structural studies. In addition, one has to be careful to specify the "actual" molecularities after correcting for the composition of other phases.

4.5 Film Microstructure, Morphology, and Electrical Behavior of $CuGaSe_2$

The nucleation and growth of thin films is a complex process involving three separate steps: the mechanism of adsorption (including both the mass transfer of reactant species and chemical kinetics of presubstrate reactions); the mechanism of surface reaction (including surface diffusion and chemical kinetics of surface reactions); and desorption (including mass transfer and readsorption mechanisms). In the most general sense, the resultant combination of these factors for a compound film is reflected in how the composition of the film differs from the incident flux composition. If we assume that all incident atoms directed from the three separate sources stick (i.e., unity sticking coefficient), the required elemental fluxes R for the growth of stoichiometric $CuGaSe_2$ at a film growth rate of 1 Å/s is given by:

$$\underset{(\text{Å/s})}{R} = \frac{(N)10^{24}}{a^2c} \; \frac{1}{A} \; \frac{MW}{\rho} ,$$

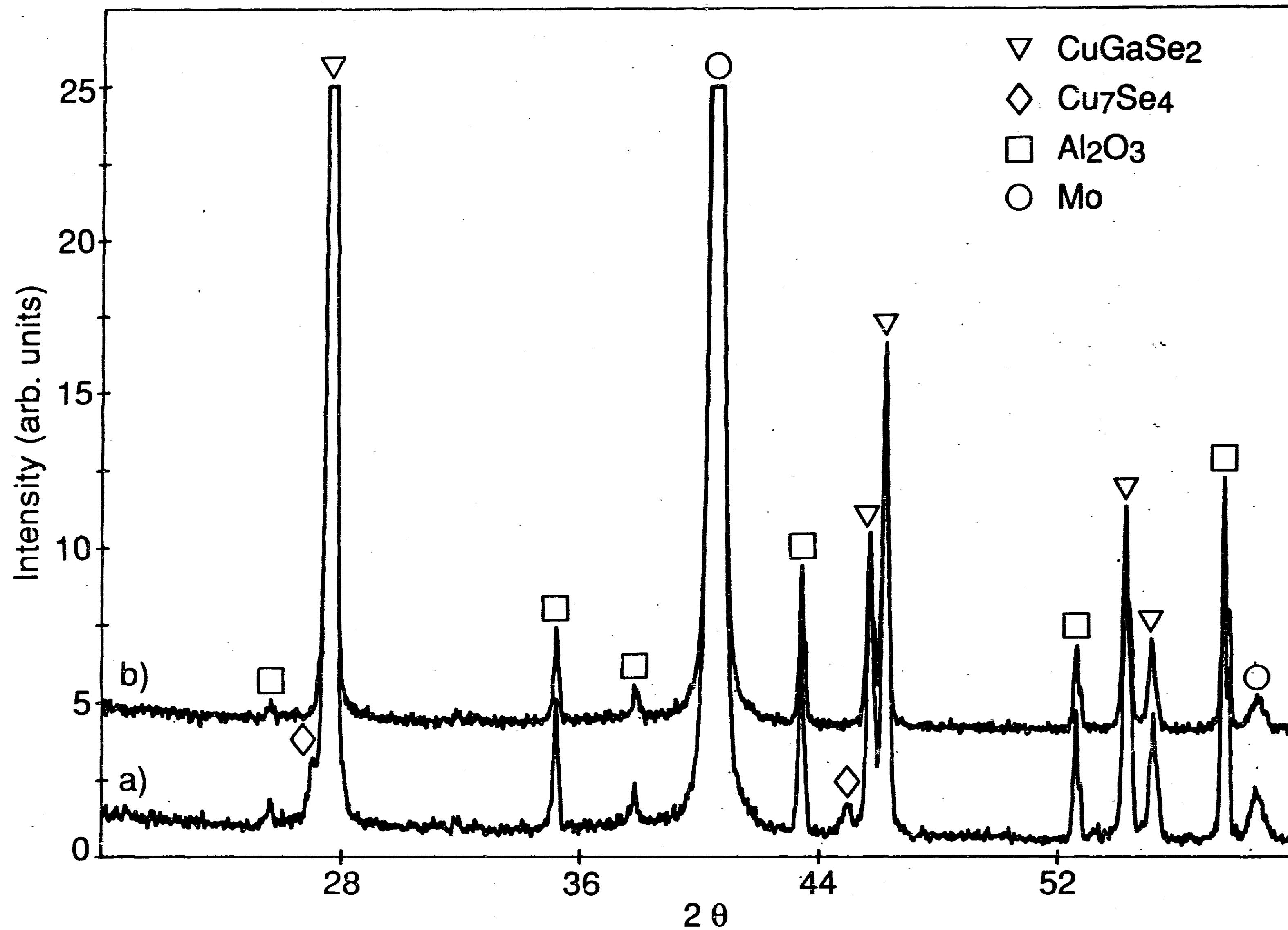

Figure 4-24. XRD patterns for copper-rich $CuGaSe_2$. (a) as-deposited showing the (222) and (440) peaks of the impurity phase Cu_7Se_4, (b) after treatment with NaCN, showing the absence of Cu_7Se_4.

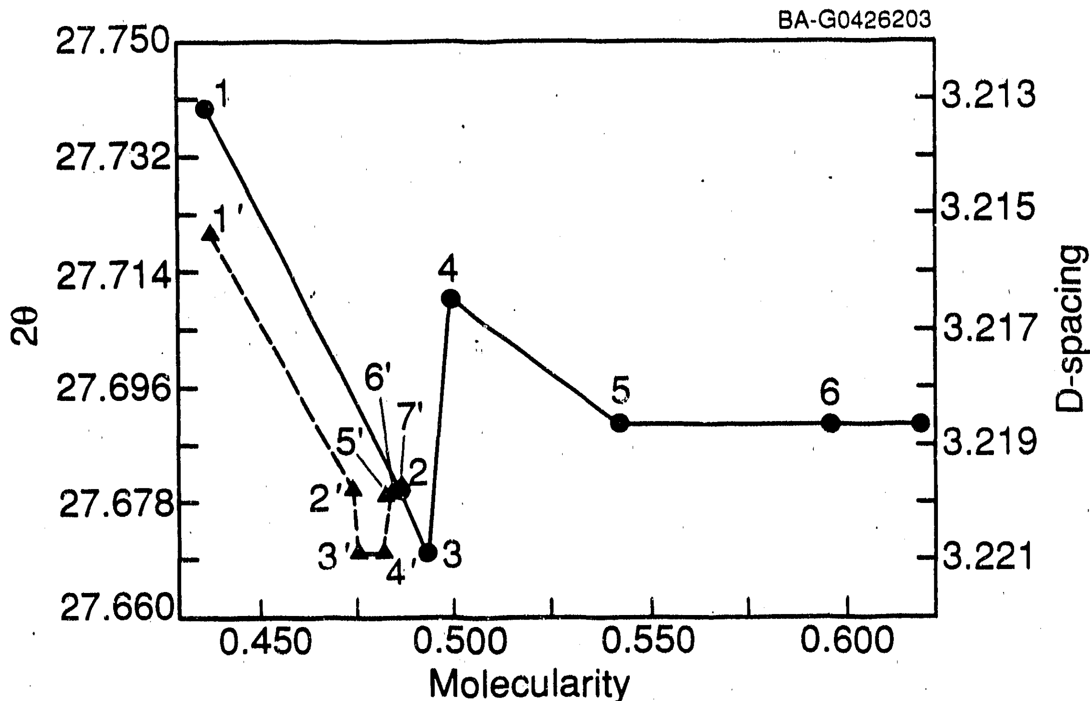

Figure 4-25. Effect of NaCN treatment on 2-θ variation with molecularity. Solid lines indicate as-deposited films; dashed lines are NaCN treated. The substrate is Mo/Al_2O_3.

where N is equal to 4 for both copper and gallium, and equal to 8 for selenium; MW is the elemental molecular weight; ρ is the elemental density; A is Avogadro's number; and a and c are the unit cell parameters. For 1 Å/s film growth, the corresponding copper, gallium, and selenium rates required are 0.135, 0.225, and 0.628 Å/s, respectively, in the ideal ratios of 1:1.7:4.7. This relationship is shown in Figure 4-26 by the solid lines. However, due to the mechanisms discussed previously, the actual required rates for stoichiometric growth deviate from these lines shown by a representative group of elemental fluxes necessary for a measured film growth rate of about 8 Å/s.

We can define a sticking or elemental incorporation coefficient S for each element, where

$$S = \frac{\text{actual rate}}{\text{rate for } S=1} ,$$

which can be taken directly from Figure 4-26. For the case shown, the corresponding incorporation coefficients for copper, gallium, and selenium are 0.95, 0.37, and 0.45, respectively, and indicate the general characteristic of Cu-ternary growth (that is, the overall film growth rate) is almost entirely dependent upon the copper flux. Comparison of a series of stoichiometric films grown at different temperatures and rates shows the same approximate behavior, and overpressures of copper, gallium, and selenium were on average 1.09, 2.5, and 3.3, respectively, times what was to be expected assuming unity sticking. With this understanding, the necessary elemental fluxes required for a pre-determined film growth rate of stoichiometric material could be calculated. For instance, a film growth rate of 3 Å/s would require elemental fluxes of

$$(3)(0.135)(1.09) = 0.442 \text{ Å/s Cu}$$
$$(3)(0.225)(2.50) = 1.69 \text{ Å/s Ga}$$
$$(3)(0.628)(3.30) = 6.22 \text{ Å/s Se} .$$

In actuality, although the copper and gallium fluxes can be approximately determined a priori by this technique, the selenium rate appears to be relatively independent of the elemental rate and for film growth rates < 10 Å/s can be fixed constant at about 11-12 Å/s. Rates lower than this result in impurity phase formation and poor $CuGaSe_2$ formation.

A detailed analysis of these general characteristics could not be attempted due to problems with drifting rate calibrations attributed to the window coating by selenium. This is unfortunate since comparison of rates with film composition and phase behavior outside the process window of good $CuGaSe_2$ formation can lead to better insight regarding the growth mechanism. A comparison of film compositions as related to substrate was possible, however, and is shown in Figure 4-27 for the glass and molybdenum/alumina examples.

All these compositions were generated solely by variation of the copper rate while maintaining gallium and selenium nearly constant. This variation allowed

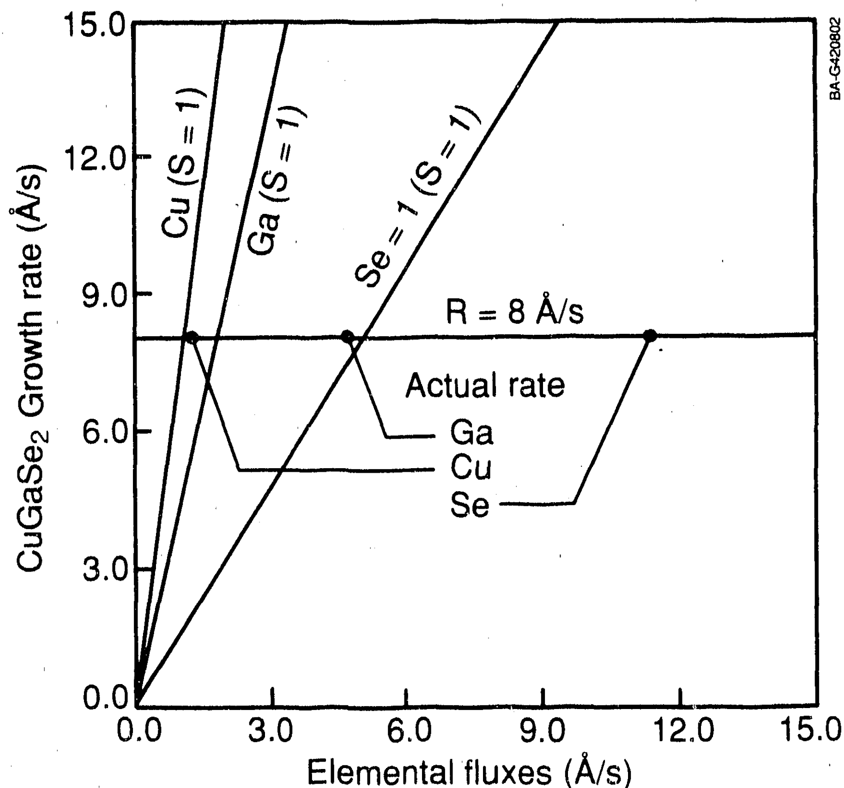

Figure 4-26. CuGaSe^2 growth rate diagram

the film composition, for a given substrate and T_s, to adjust in a direction parallel to the Cu_2Se-Ga_2Se_3 tie line. Variation of gallium or selenium alone, while maintaining the other two constant, was impractical since neither of these species appear to affect film composition as much and will generally result in impurity phase formation. By adjustment of copper, however, we follow the pseudobinary path, which according to the phase diagram of $CuGaSe_2$ should allow us to lie close to the single-phase field of $CuGaSe_2$. Another observation from Figure 4-27 is that films deposited on glass substrates are higher in selenium than are films deposited on molybdenum/alumina, while films deposited on alumina (not shown in Figure 4-27 for clarity) exhibit compositions between the two. In fact, it was impossible to obtain compositions with $\Delta Z < 0$. Only on molybdenum/alumina were films with $\Delta Z < 0$ possible, largely in the case that films were also copper-rich (i.e., $\Delta X > 0$). This fact greatly hindered any defect chemistry studies on these films since compensation effects due to a transition from $\Delta Z > 0$ to $\Delta Z < 0$ were not possible for films grown on insulating glass and alumina, while films grown on molybdenum/alumina could not be analyzed by conventional 4-point and Hall techniques due to the conducting molybdenum layer.

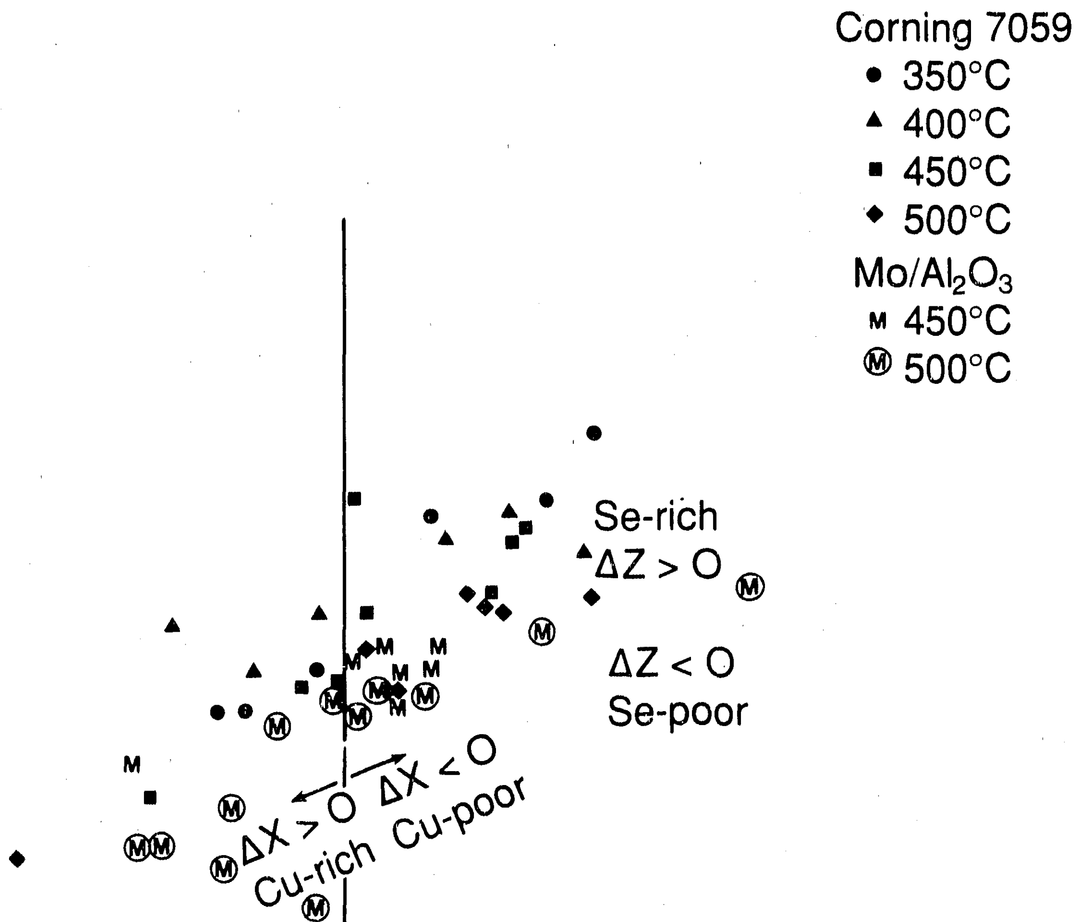

Figure 4-27. $CuGaSe_2$ film composition vs. substrate and T_s

To explain why films deposited on molybdenum-coated surfaces exhibit lower selenium content, a quick thermodynamic treatment of the problem is helpful. Surfaces characterized by metallic-conducting behavior can undergo bond relaxation and reconstruction at the surface better than more rigid, covalently bonded materials (like ceramic glass and alumina). Consequently, this relaxation reduces the surface energy of molybdenum more than the latter case such that the surface-vapor energy term γ_{sv} is smaller. The heterogeneous nucleation of a condensate phase c onto a substrate phase s in a vapor phase v is dependent upon the wetting characteristics of the system, where, from Young's equation,

$$\gamma_{sv} - \gamma_{sc} = \gamma_{vc} \cos\theta ,$$

where γ_{sv}, γ_{sc}, and γ_{vc} are the interfacial surface energies between the substrate-vapor, substrate-condensate, and vapor-condensate, respectively, and θ is the contact angle through the condensate. As θ decreases, wetting increases and the nucleation rate will increase [50]. If we consider our two cases, that of a high γ_{sv} for the glass substrate and a lower γ_{sv} for the molybdenum/alumina, it is probable that the system described by the nucleation of phase c (selenium) on the glass substrate exhibits better wetting due to elimination of the high-energy glass surface. Consequently, from this simple argument it becomes clear why films deposited on both alumina and glass should be higher in selenium. (Note: Coating by selenium is favored over gallium due to the much higher surface tension of the latter; i.e., at 240°C, the surface tensions of gallium and selenium are 697 and 88, respectively [51,52].)

The effect of substrate temperature T_s was also noticeable. In general, an increase in T_s causes a general shift of film composition toward the binary line regardless of substrate type. This may be related to the constituent vapor pressure of selenium and not necessarily some equilibrium condition governed by the pseudobinary as compositions on molybdenum/alumina substrates actually become selenium-deficient with increasing T_s. Unfortunately, this effect could not be used to create selenium-deficient films on glass or alumina due to a deleterious surface reaction for these films at increasingly high temperatures, as will be shown later.

Detailed analysis of the impurity phase content of films deposited on both glass and molybdenum/alumina substrates at $T_s \approx 400°$, 450°, and 500°C showed that a variety of phases could possibly exist in conjunction with the majority $CuGaSe_2$ phase. The detection of these phases required extremely careful XRD work due to low impurity content (I/I_0 typically < 1.0). Identification of these phases was restricted to certain ranges in d-spacing, which may be indicative of some mechanism by which the phase grows simultaneously with $CuGaSe_2$. Figures 4-28, 4-29, and 4-30 illustrate representative ranges in 2θ where these impurities were found. These impurities are referred to as the (112) hump, 50° hump, and 79° hump, respectively. The designation of the (112) hump lies in its proximity to the (112) $CuGaSe_2$ reflection and covers a range in d-spacing from 3.32 to 3.40 Å from film to film. Similarly, the 50° and 79° humps correspond to reflections from impurity d = 1.824 and 1.212 Å, respectively.

In order to assign probable impurity phases to these reflections (which are not related to possible $CuGaSe_2$ preferably oriented peaks), the initial necessary condition was that the phase have at least one (hkl) spacing given

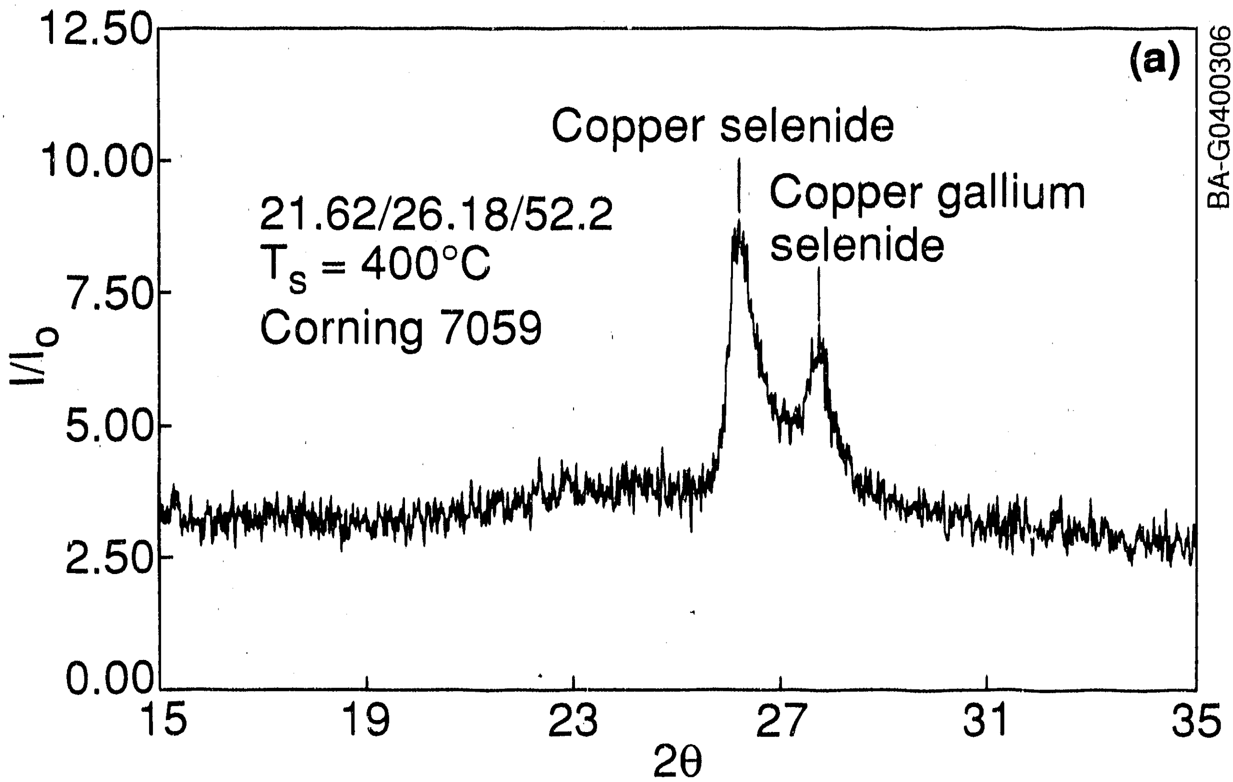

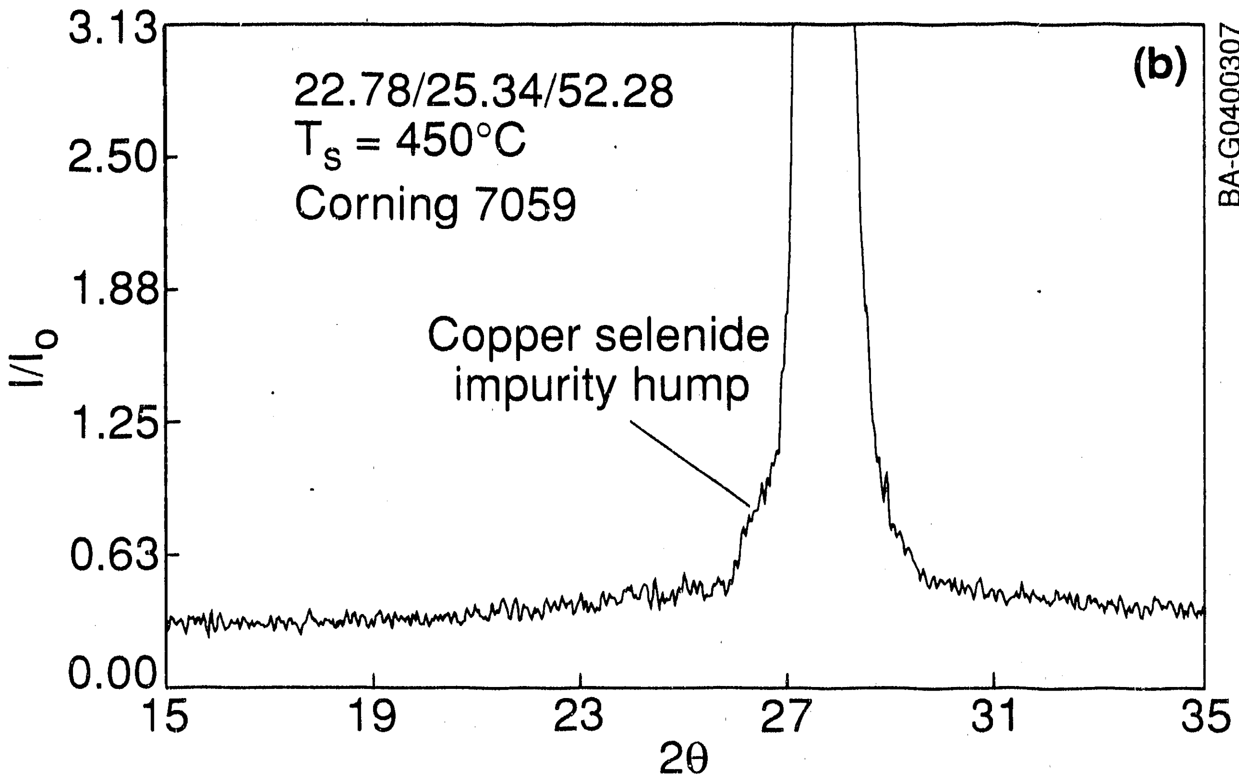

Figure 4-28. (112) hump impurity phases

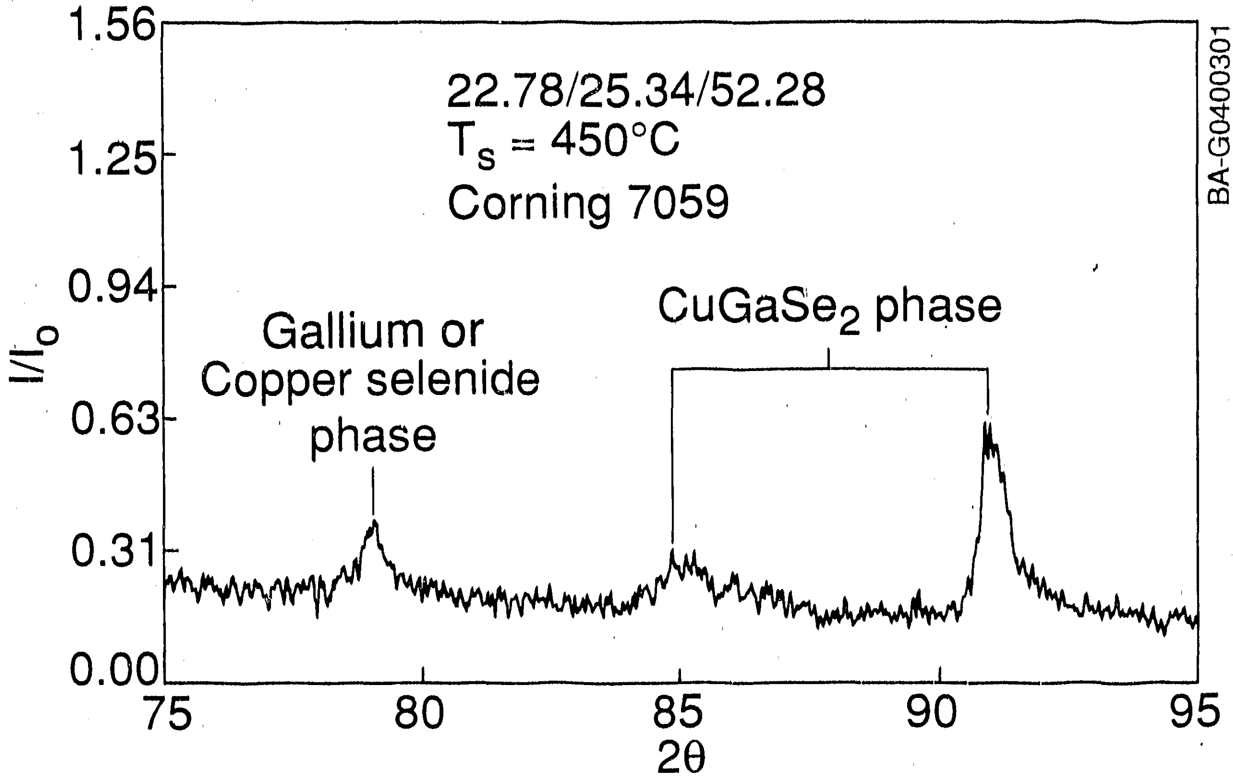

Figure 4-29. 79° hump impurity phase

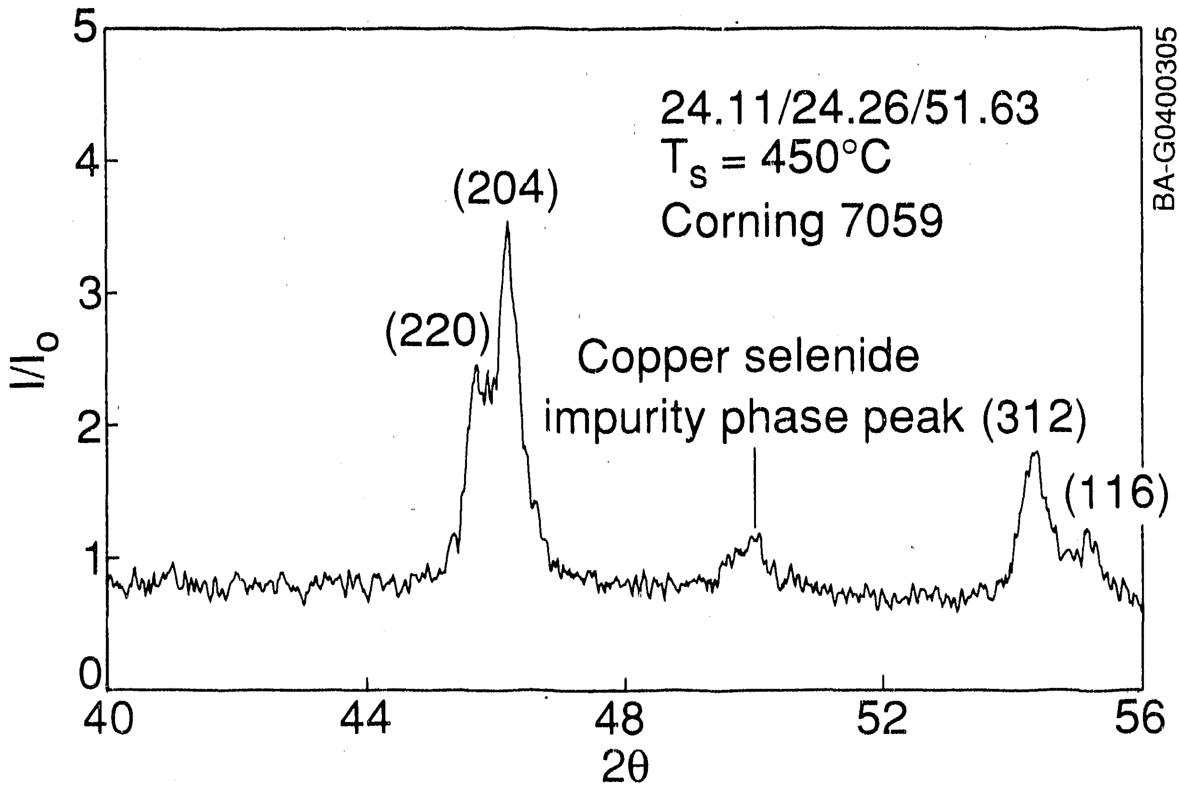

Figure 4-30. 50° hump impurity phase

by the above designations. With this minimal requirement, a variety of possible phases attributable to these peaks were grouped as presented in Table 4-1. Included in this table are the JCPDS card number, as well as d-spacing of the nearest match and the relative random orientation I/I_0. Due to preferred orientation effects, the values of I/I_0 only serve as a qualitative means for identification. Careful analysis of each grouping, including reported acquisition accuracy as well as composition, lead to the assignments that the (112) and 50° humps were likely due to copper selenide while the 79° hump was probably Ga_2Se_3 and possibly copper selenide. Oxide modifications were not thought probable for several reasons. First, all processing is done at high vacuum using ultra-pure elements. Second, those phases which typically contained some indication of an oxide phase were typically copper-poor, while EPMA results showed the small possibility of oxygen incorporation (typically < 1.0 at. %) only in copper-rich films. Last, oxygen plasma treatments did not appear to affect these phases. The selenium phase shown in the 50° hump group was reported as a high-pressure form and was also eliminated. By systematically relating the presence or absence of these three impurity groupings (to a series of 31 variable composition films deposited on glass and molybdenum/alumina substrates), process phase diagrams were constructed in the vicinity of stoichiometric $CuGaSe_2$ at three temperatures (as shown in Figures 4-31, 4-32, and 4-33). Identification of chalcopyrite (CH) or sphalerite (ZB) $CuGaSe_2$ in these figures was accomplished by techniques described later. From these diagrams, it is generally observed that film compositions closer to the pseudobinary contain less impurity phases. For films deposited on glass, an increase in temperature appears to promote the formation of these phases, while the opposite trend is observed for copper-poor films deposited on molybdenum/alumina.

The occurrence of $CuSe_2$ in copper-rich compositions on glass and alumina is believed to be the major factor for explaining the observed electrical behavior of copper-ternary films as a function of copper content [53,54]. If we plot the film bulk resistivity, as determined by 4-point probe, as a function of ΔX for these films, we see a strong trend between composition and resistivity (as shown in Figure 4-34).

Copper-poor compositions are characterized by highly resistive material ($\rho \sim 10^5$ Ω-cm), while copper-rich compositions show almost degenerate behavior ($\rho < 1.0$ Ω-cm). Initially, this effect has been attributed to the degenerate, p-like behavior of $CuSe_2$; however, from our detailed phase analysis, copper-poor compositions also contain $CuSe_2$. One possible explanation for the high-resistive nature of this $CuSe_2$-containing material may be related to the film morphology.

Besides the disjunct behavior in electrical resistivity shown in Figure 4-34, there is a similar demarcation in the film morphology at $\Delta X \simeq 0$. Representative examples of this behavior are shown in Figures 4-35 through 4-44 on the following pages for various compositions deposited on glass, alumina, and molybdenum/alumina at temperatures of 400°, 450°, and 500°C. Films deposited on insulating substrates required a 200-Å gold layer deposited by evaporation for good imaging. Films on molybdenum/alumina required no additional processing.

Table 4-1. $CuGaSe_2$ Impurity Phases

Copper Selenide: d = 3.32 - 3.4 Å (112 Hump)

Impurity Phase	I/I_o	d (Å)	JCPDS
$\delta CuSe$	100	3.206	27-186
αCu_2Se	80	3.38	4-0839
$\beta CuSe$	65	3.369	27-183
CuSe	80	3.37	26-556
CuSe	60	3.35	6-0427
Cu_2Se	60	3.36	19-401
CuSe	40	3.35	20-1020
Cu(1.85)Se	90	3.33	6-0680
αCu_2Se	50	3.365	27-1130
Se_2O_5	100	3.37	20-1047
SeO_3	100	3.33	20-1046
SeO_3	100	3.30	15-640
Cu_7Se_4	100	3.29	26-557

Copper Selenide: d = 1.824 Å (50° Hump)

Impurity Phase	I/I_o	d (Å)	JCPDS
$\beta CuSe$	40	1.823	27-184
$\delta CuSe$	20	1.831	27-185
$CuSe_2$	25	1.834	18-453
CuSe	60	1.819	6-0427
Cu_3Se_2	80	1.831	19-402
CuSe	70	1.820	20-1020
Cu_5Se_4	30	1.817	21-1016
$CuSe_2$	60	1.827	25-309
Se	30	1.187	27-601
SeO_2	14	1.829	22-1314
Ga_2O_3	35	1.814	6-0503

Table 4-1. $CuGaSe_2$ Impurity Phases (Concluded)

Gallium Selenide and Copper Selenide:
d = 1.212 Å (79° Hump)

Impurity Phase	I/I_o	d(Å)	JCPDS
$CuSe_2$	4	1.212	19-400
Cu_5Se_4	20	1.205	21-1016
βGa_2O_3	20	1.210	11-370
αGa_2O_3	4	1.209	6-0503
SeO_2	6	1.2105	22-1314
Ga_2Se_3	10	1.211	5-0724

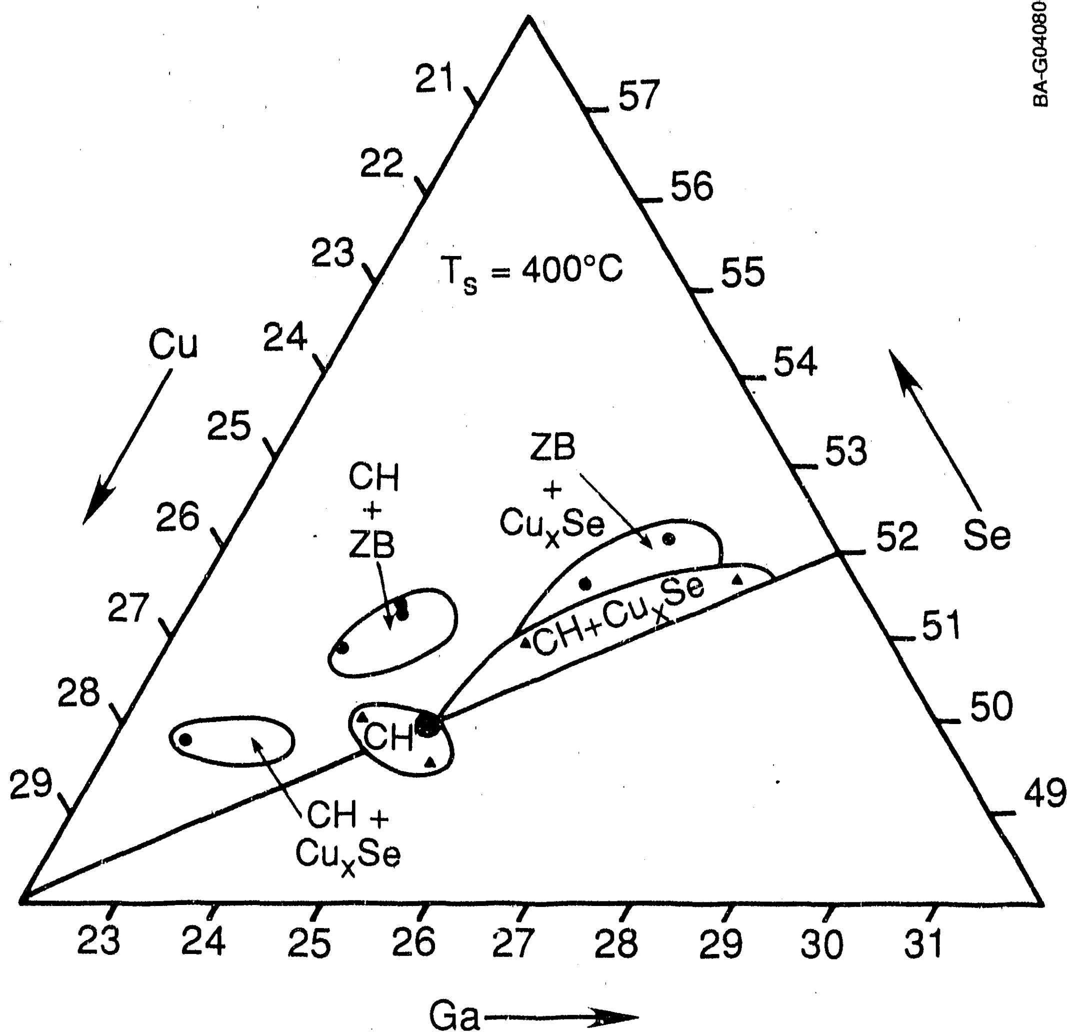

Figure 4-31. $CuGaSe_2$ process phase diagram (T_s = 400°C)

Figure 4-32. $CuGaSe_2$ process phase diagram (T_2 = 450°C)

The most noticeable feature of the film morphology is the formation of larger grained $CuGaSe_2$ as copper content is increased. This behavior is clearly visible on glass while less evident on alumina and molybdenum/alumina substrates due to the increased roughness of these substrates. This behavior has recently been proposed by Dimmler et al. as a consequence of the anisotropy of the close-packed selenium and cation planes in chalcopyrite [55]. For copper-rich films, isometric crystals of tetragonal bipyramid structure are favored while decreasing copper causes the (112) planes of selenium to grow, preferably resulting in a tetrahedral bisphenoid hemihedron as shown in Figure 4-45.

This growth behavior appears to indicate that the large-grained crystals existing in conjunction with the finer-grained structures near the structural transition point (Cu/Ga ≈ 1.0) may be copper-rich compared to the matrix. A

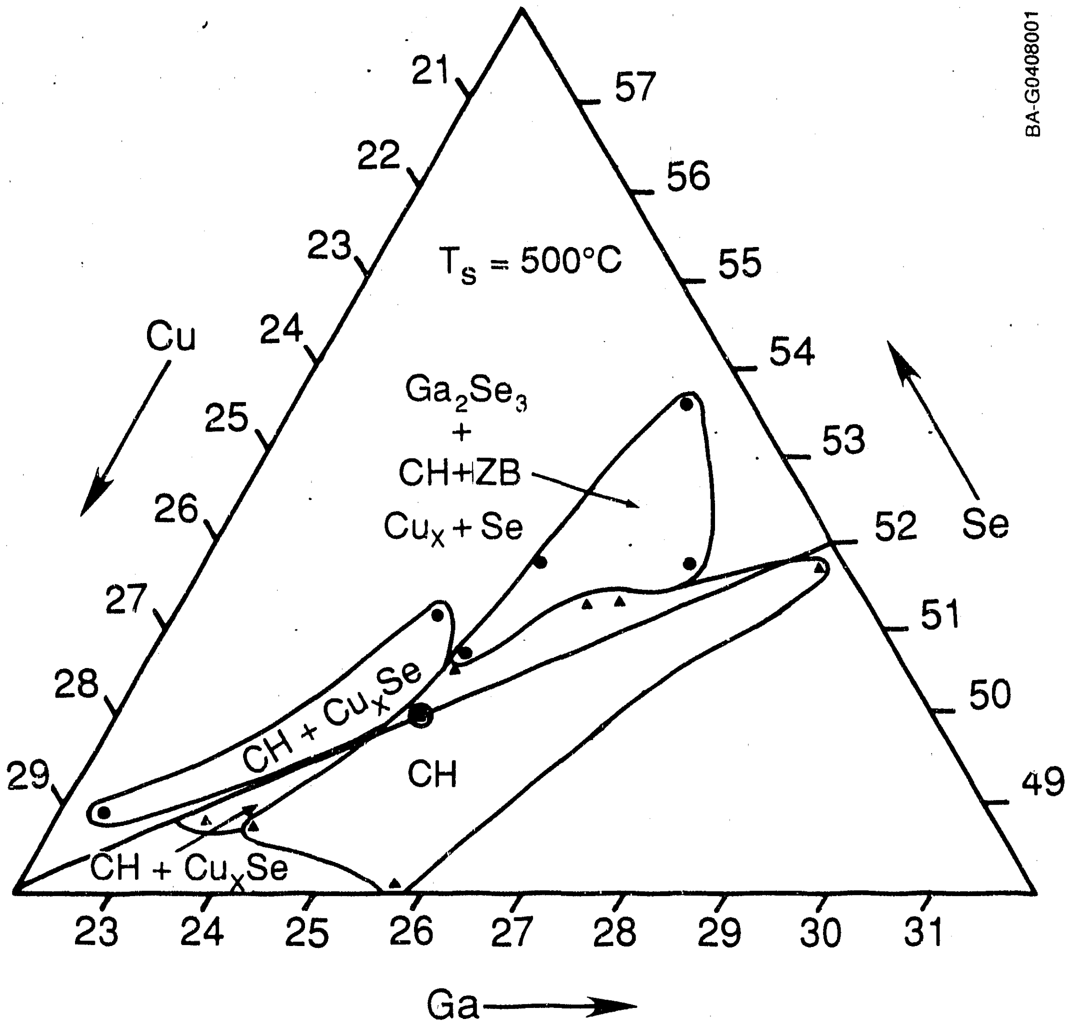

Figure 4-33. $CuGaSe_2$ process phase diagram [T_s = 500°C (- glass; - molybdenum/alumina)]

qualitative analysis of this possibility (using a spot scan EDXA on a JEOL 35C electron microscope) appears to substantiate this possibility. A quantitative compositional measurement was not possible due to lack of processing software on this instrument (the JEOL was mainly used for imaging purposes); however, normalized integrated intensities indicated that the large-grained structures contain slightly more copper and gallium (metal/Se ratio = 0.667 versus 0.663) in support of Dimmler's theory.

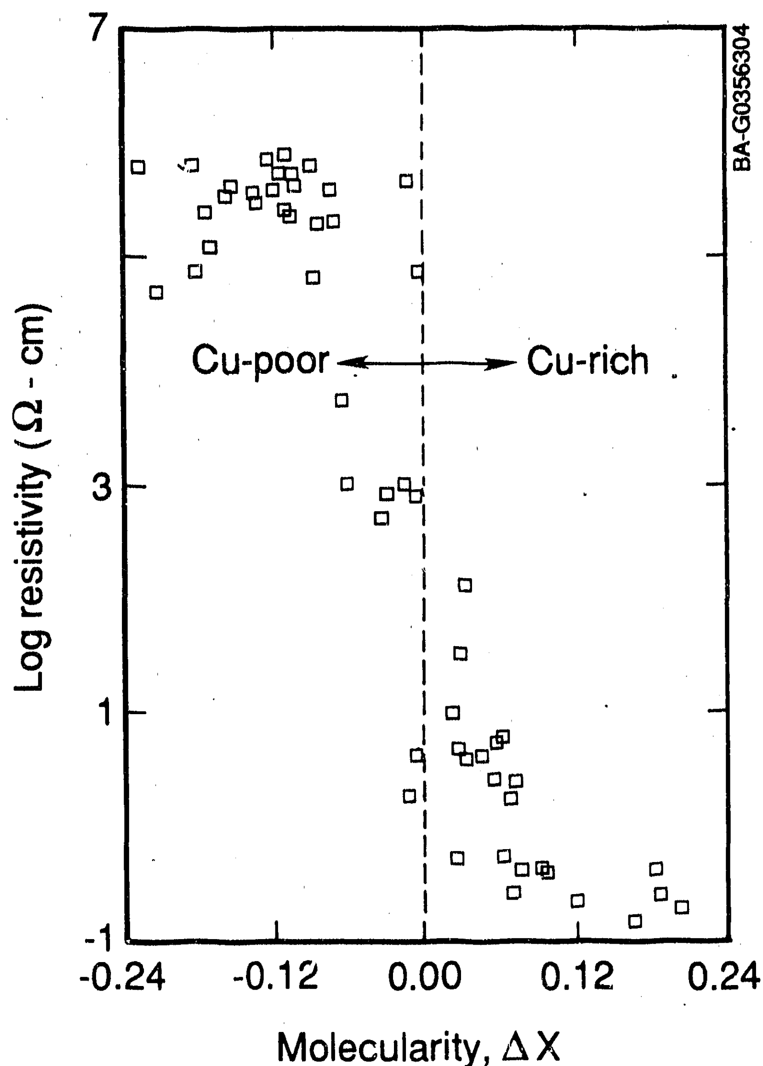

Figure 4-34. $CuGaSe_2$ bulk film resistivity vs. composition (7059-Al_2O_3 substrates)

Another more consequential observation related to device fabrication is seen in the behavior of copper-poor films deposited on glass as temperature increases. Copper-poor compositions at 400° and 450°C appear to be fine grained and well defined with no unusual characteristics. However, at T_s = 450° and 500°C, the surface is drastically altered with the appearance of surface pits and mottling. This behavior is also visible to a lesser degree on a 22.14/25.68/52.18 at. % composition deposited on alumina at T_s = 450°C. This behavior is extremely important since high-efficiency $CuInSe_2$ devices usually

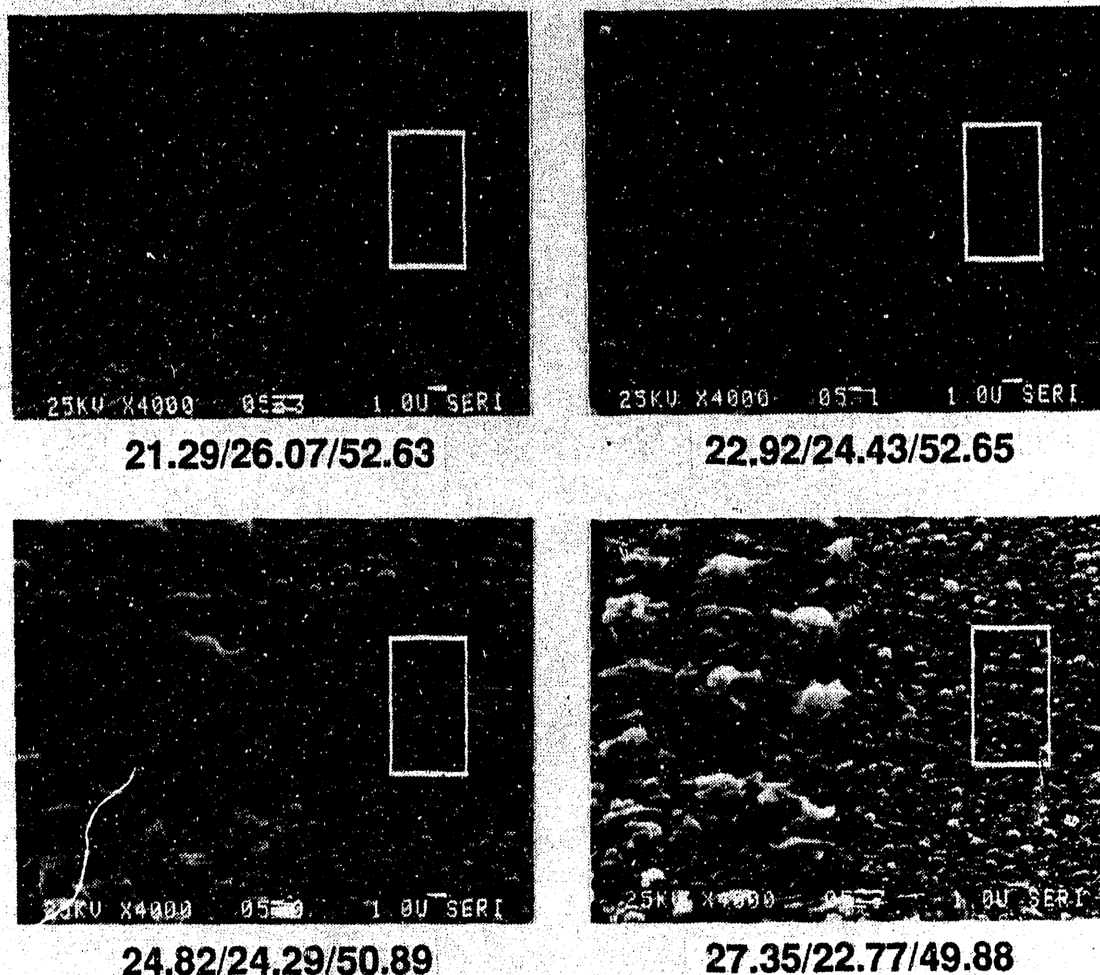

Figure 4-35. SEM morphology (Corning 7059 substrate, T_s = 350°C, t = 1-2 μm)

require a bilayer structure where, near the end of the run, the substrate temperature is increased from 350° to 450°C while simultaneously reducing the copper flux [56]. If the same two-step process is applied in the case of $CuGaSe_2$ bilayer devices, the observed mottling behavior could be present directly at the interface of a heterojunction device. To date, the efficiency of $CdS/CuGaSe_2$ devices has exhibited reasonably good V_{oc} behavior but appears to suffer in short circuit current (I_{sc}) output. Interface recombination, perhaps introduced by a damaged surface like those shown for this case, might lead to such a decrease in I_{sc}. The behavior does not seem to be visible for

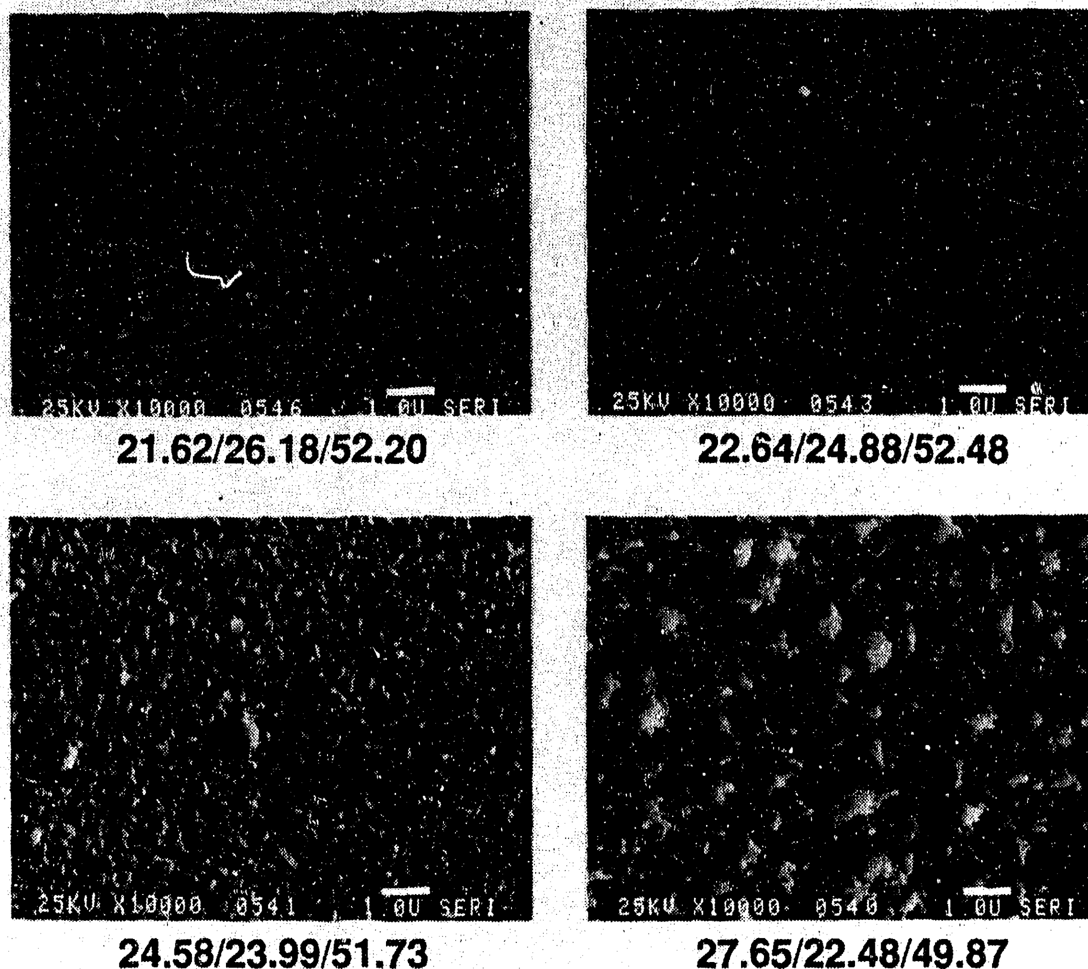

Figure 4-36. SEM morphology (Corning 7059 substrate, T_s = 400°C, t = 1-2 μm)

films deposited on molybdenum/alumina, although the increased roughness of this substrate/coating system might hinder such identification. Interestingly, ohmic contact problems to GaAs have been attributed to phase separation of gallium and arsenic on the surface due to the high surface energy of gallium [57,58]. The same behavior may be occuring in cooper-poor $CuGaSe_2$.

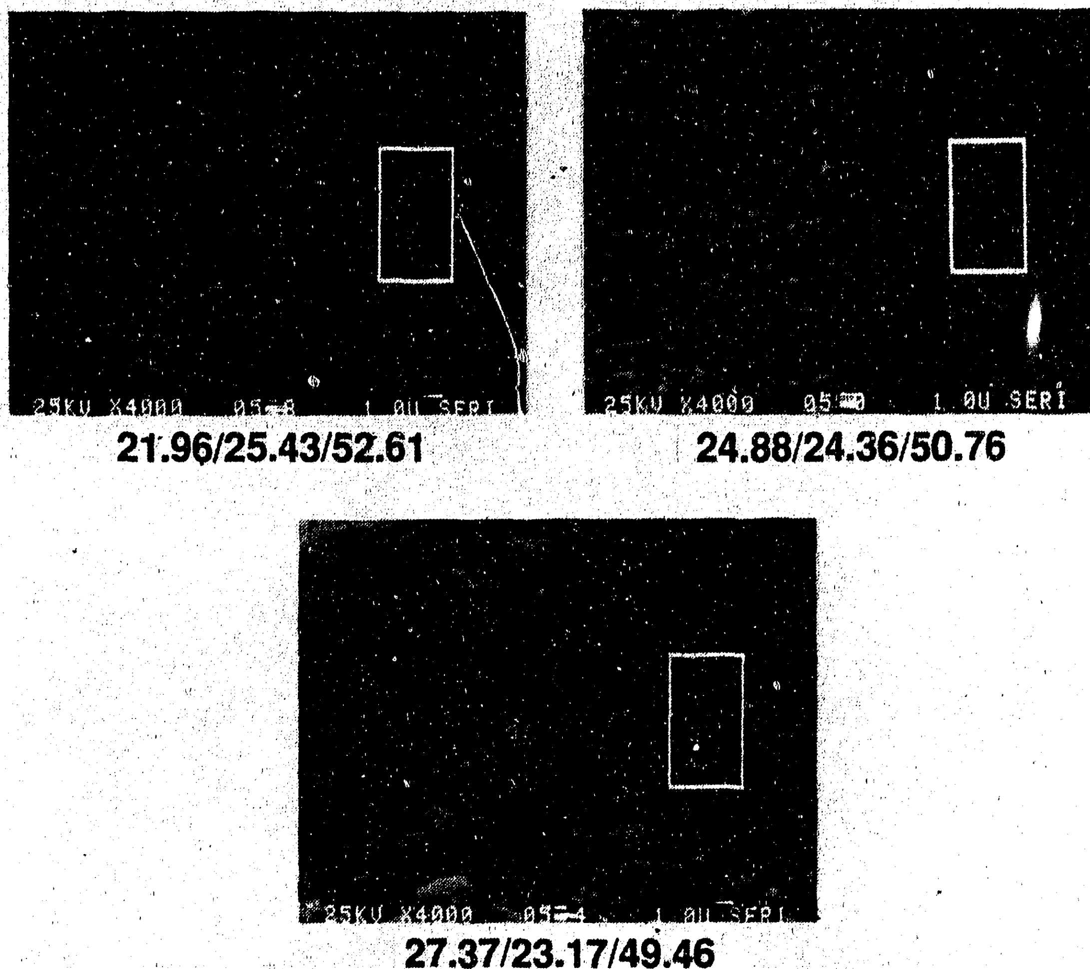

Figure 4-37. SEM morphology (Corning 7059 substrate, T_s = 450°C, t = 1-2 μm)

Due to the limited spatial extent of the pits (2-3 μm wide, 200-300 Å deep), spot scan EDXA was unable to detect any phase separation; however, high-resolution Auger probe analysis (shown in Figure 4-46) appears to indicate some compositional differences between the pits and film surface. The particular scan shown was obtained after a 5-second sputtering. The oxygen and carbon decrease with sputtering at 20 seconds.

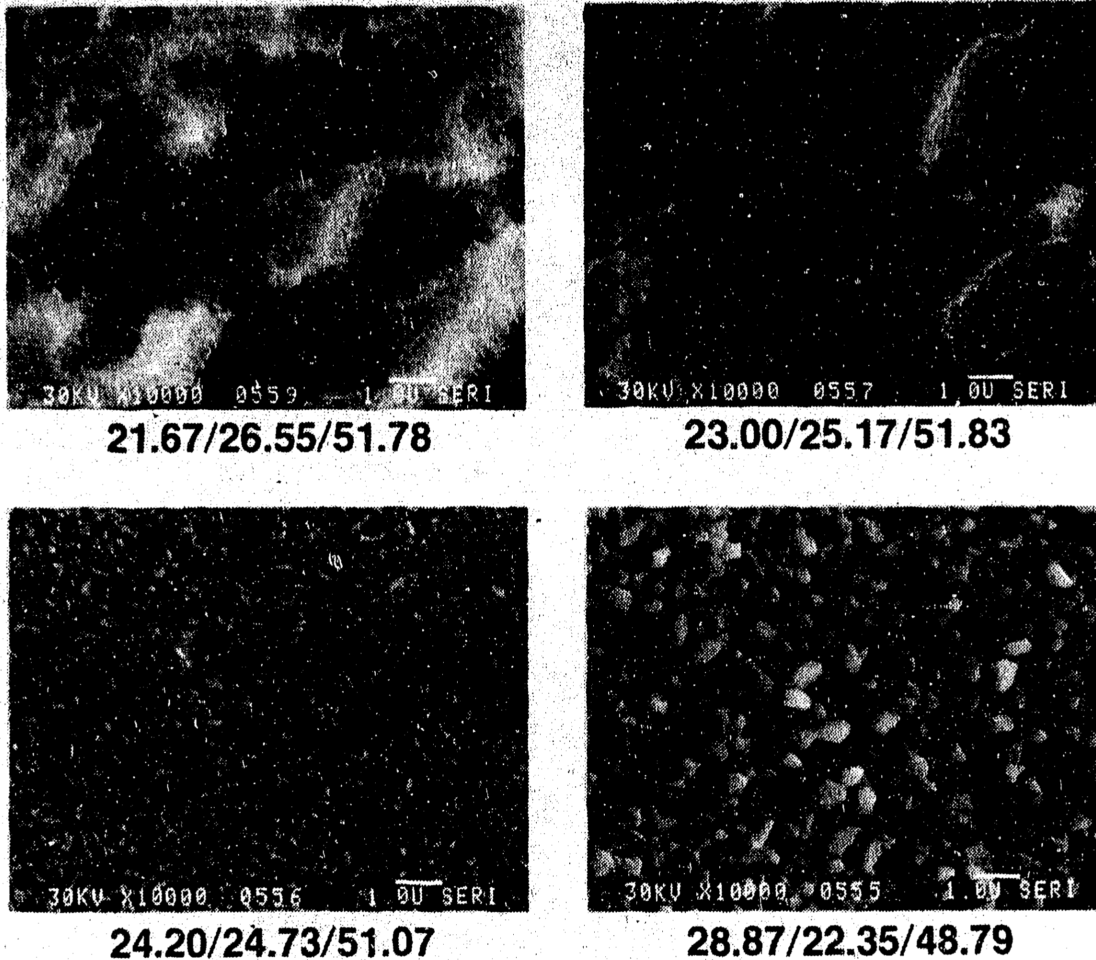

Figure 4-38. SEM morphology (Corning 7059 substrate, T_s = 350°C, t = 1-2 μm)

4.6 X-ray Diffraction Characterization

Preferred orientational growth of $CuGaSe_2$ on glass substrates was studied as a function of composition and substrate temperature to determine if film anisotropy might affect subsequent optical measurements. Orientation studies were not performed on alumina and molybdenum/alumina substrates due to interference effects by substrate peaks, although in general all films studied exhibited high (112) orientation. This condition also occurred with films deposited on glass, with the exception of films grown at $T_s \leq 400°C$, in which

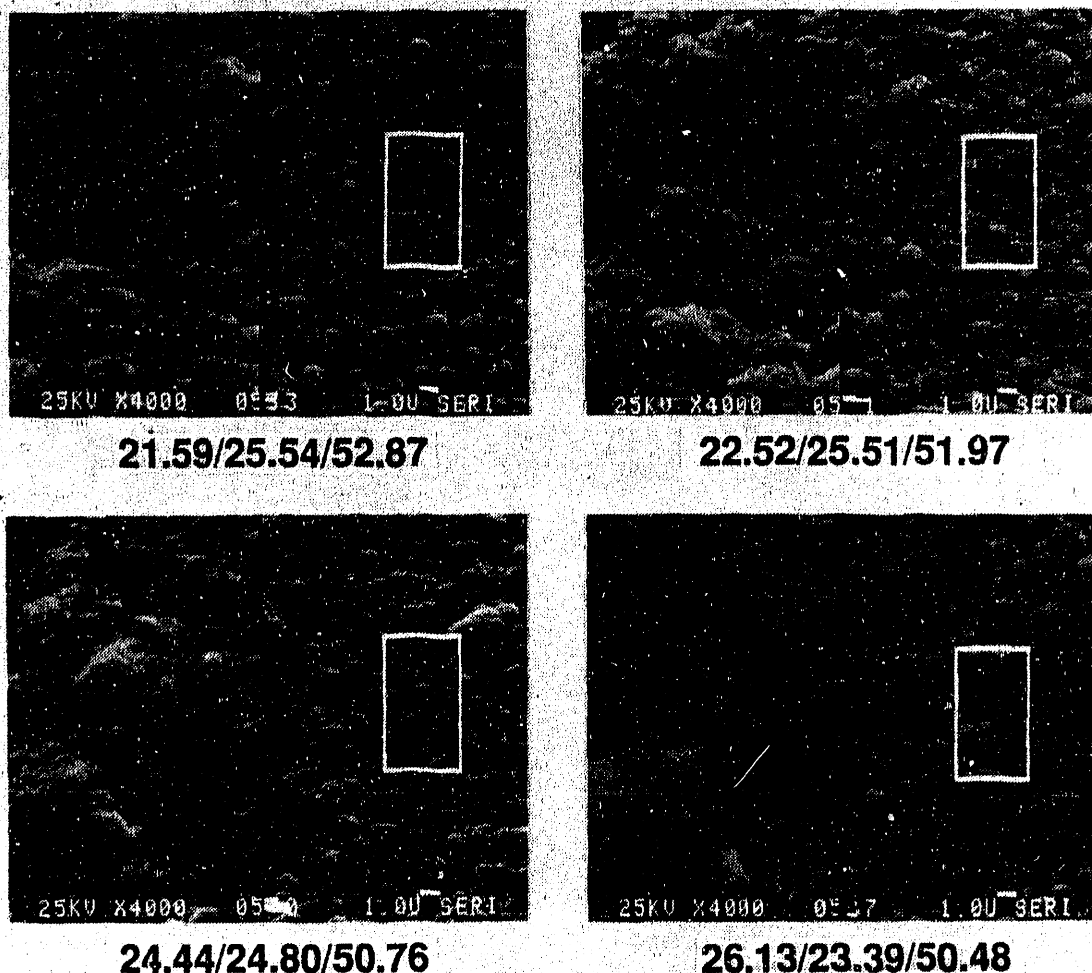

Figure 4-39. SEM morphology (bare alumina Substrate, T_s = 350°C, t = 1-2 μm)

a strong (220) orientation occurs. A Lotgering plot of orientation was prepared using net intensities normalized to a random pattern (shown in Figure 4-47). As shown, a strong difference in orientation exists for copper-poor films deposited at temperatures above and below approximately 425°C. Actual x-ray spectra for films as a function of composition at a substrate temperature of 400°C are shown in Figure 4-46, where the behavior is clearly shown. Also evident in this figure is the enhanced splitting or doublet formation characteristic of the tetragonal chalcopyrite phase for stoichiometric and copper-rich films. This is a clear indication of order-disorder effects as a function of composition, which will be described in later detail.

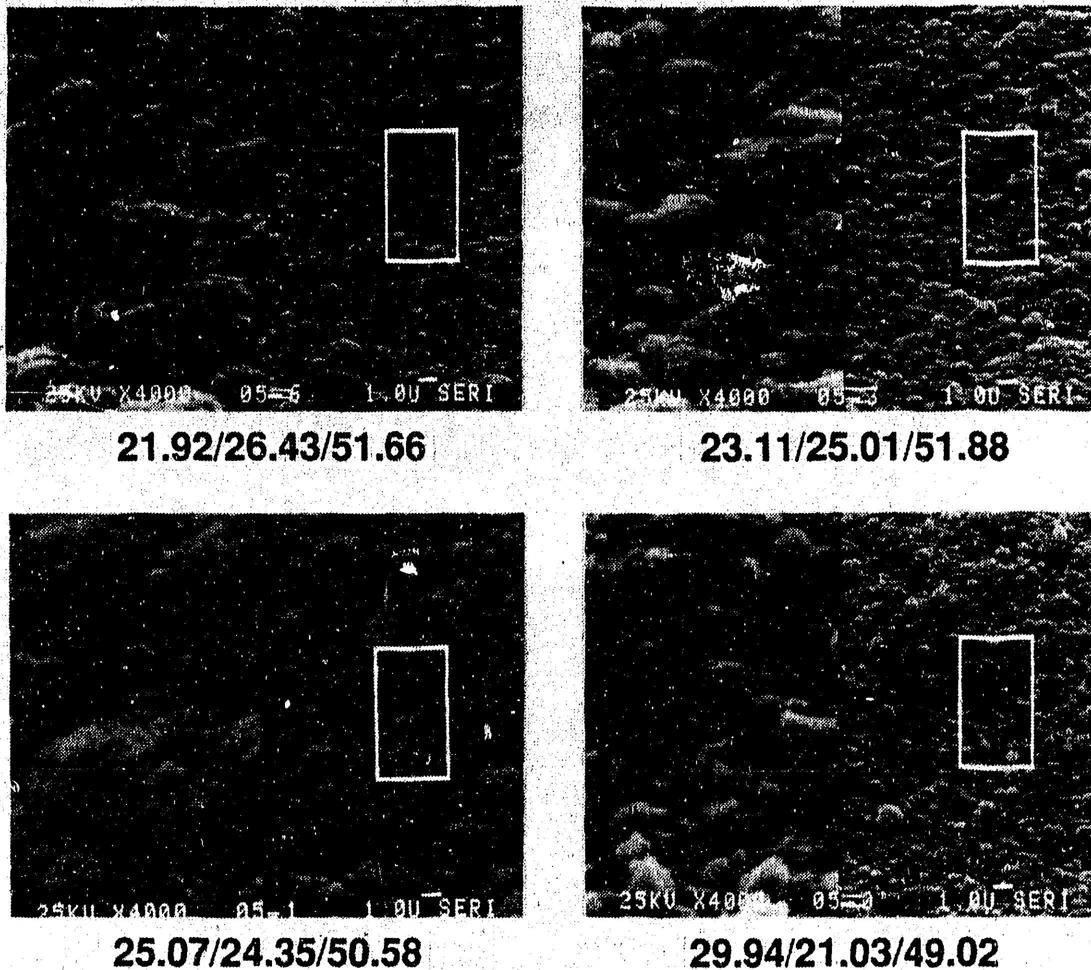

Figure 4-40. SEM morphology (bare alumina substrate, T_s = 400°C, t = 1-2 μm)

Theoretical structure factors $|F_{hkl}|$ required for subsequent XRD-integrated intensity calculations can be represented in trigonometric form as:

$$|F_{hkl}| = \left[\left(\sum_{i=1}^{N} f_i \cos 2\pi(hu_i + kv_i + lw_i)\right)^2 + \left(\sum_{i=1}^{N} F_i \sin 2\pi(hu_i + kv_i + lw_i)\right)^2\right]^{1/2} ,$$

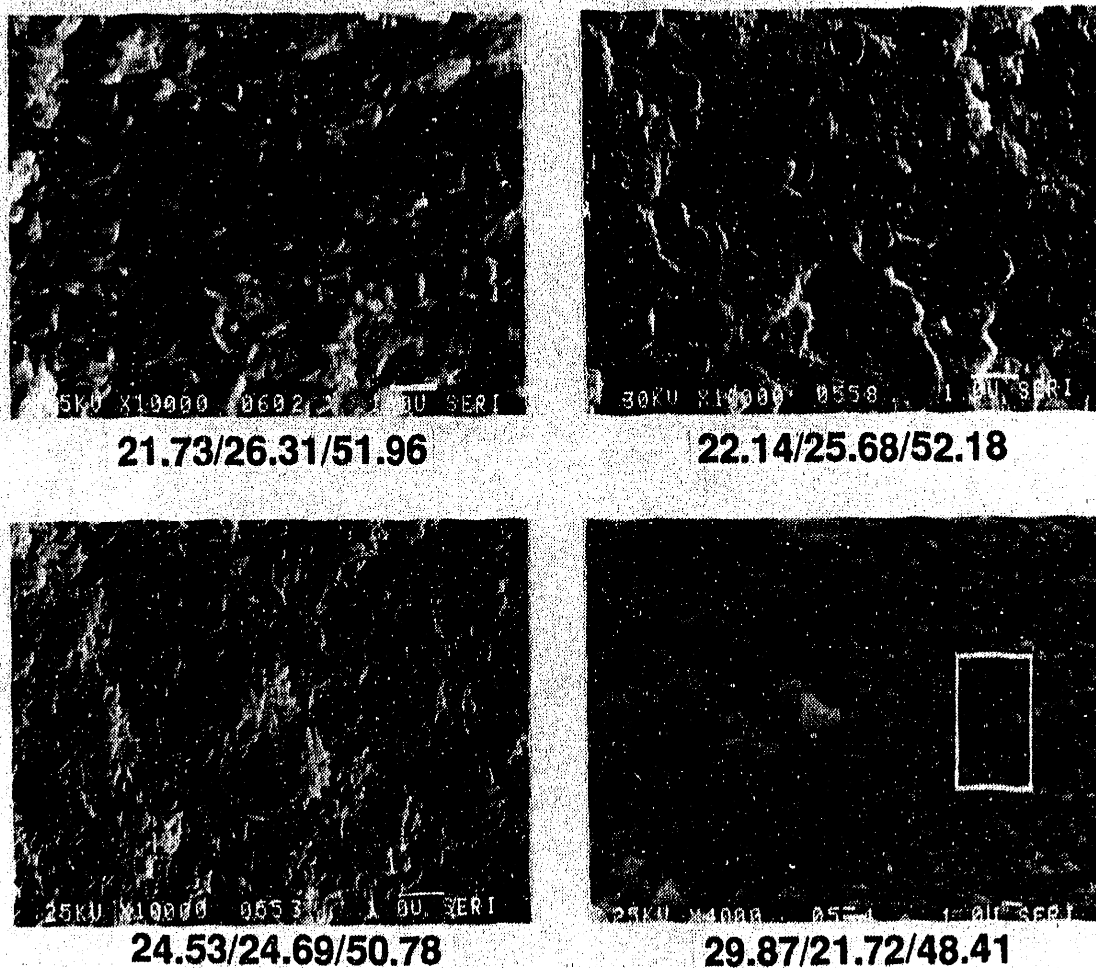

Figure 4-41. SEM morphology (bare alumina substrate, T_s = 450°C, t = 1-2 μm)

where f_i are the appropriate atomic scattering factors located at u_i, v_i, and w_i, and N is summed over all atoms of the unit cell. This calculation, however, assumes a perfectly ordered lattice and does not consider the possibility of randomized defect concentrations (i.e., vacancies, antisites, interstitials) believed to be prevalent in chalcopyrite materials. Phase diagram studies validate a large defect solubility by reporting relatively wide single-phase chalcopyrite fields, sometimes extending beyond 10 mol %. Although vacancy ordering at very high concentrations (50% copper sites

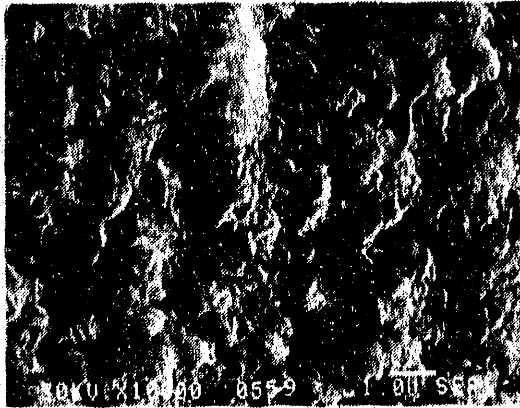

22.25/26.42/51.33

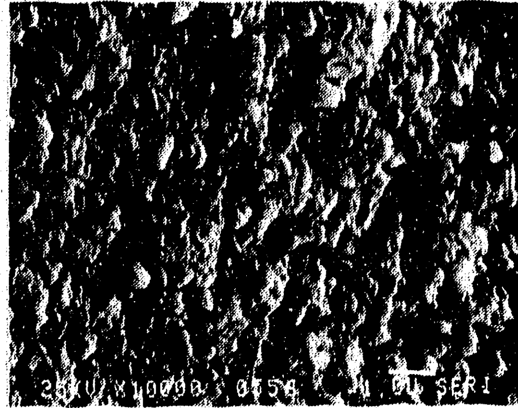

25.10/24.74/50.17

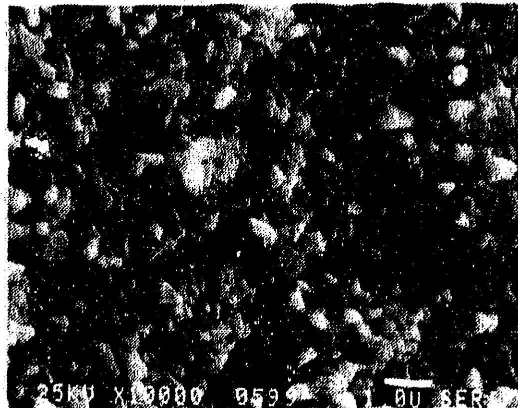

26.45/23.77/49.78

Figure 4-42. SEM morphology (bare alumina substrate, T_s = 500°C, t = 1-2 μm)

vacant) may result in a structural change from chalcopyrite to thiogallite, the work of Mikkelsen would seem to indicate the lack of such vacancy ordering. Mikkelsen does indicate, however, that such a possibility might exist and would require highly detailed peak intensity analysis. The various attitudes regarding defect ordering, defect complex formation, and extended defects are discussed in a recent summary text by Mrowec [59]. According to Anderson's view [60], statistically distributed point defects should only occur at at. % concentrations $<$ 0.10%; however, as pointed out by Mrowec, some discrepancies exist.

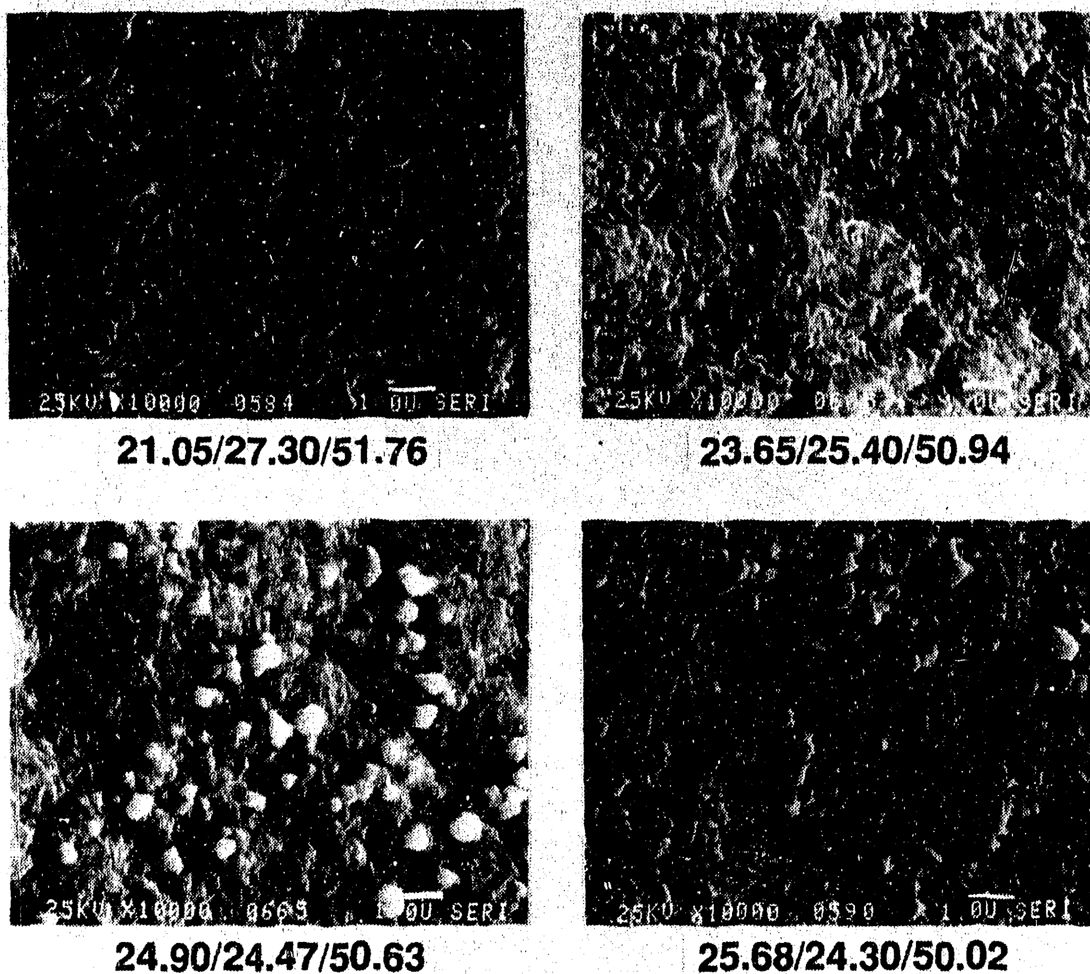

Figure 4-43. SEM morphology (bare alumina substrate, T_s = 400°C, t = 1-2 μm)

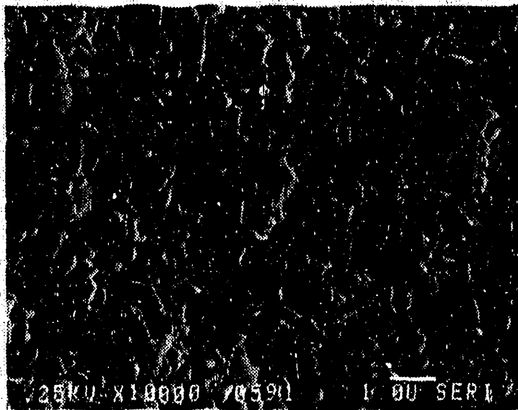

20.92/27.57/51.51

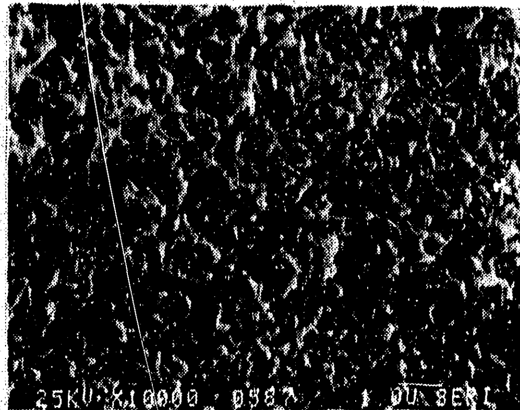

23.44/25.52/51.04

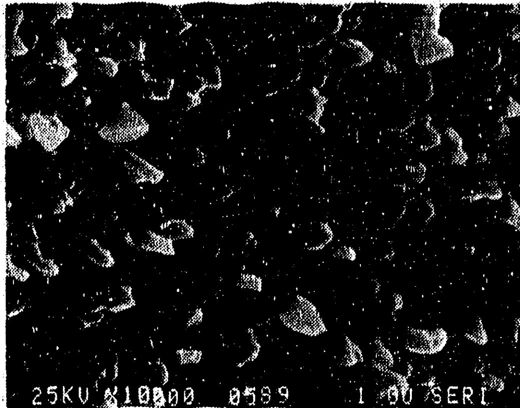

25.90/25.26/48.84

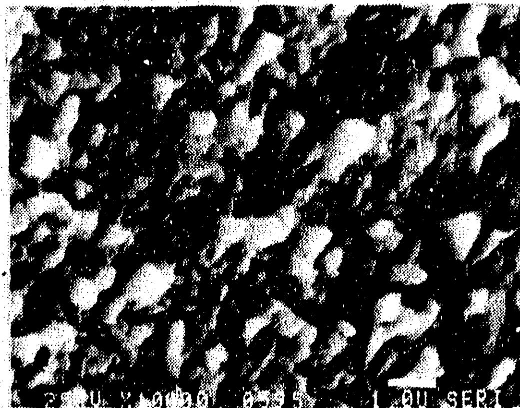

27.23/23.97/48.80

Figure 4-44. SEM morphology (bare alumina substrate, T_2 = 500°C, t = 1-2 μm)

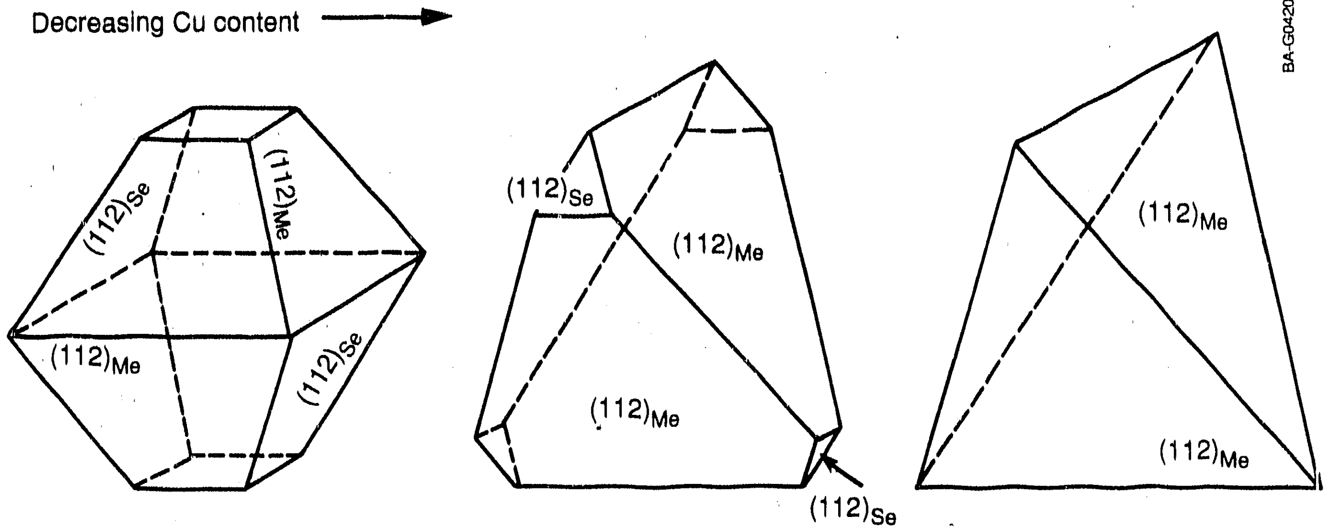

Figure 4-45. Grain morphology change predicted for compositional change (note the disappearance of [112] Se, Ref. 41)

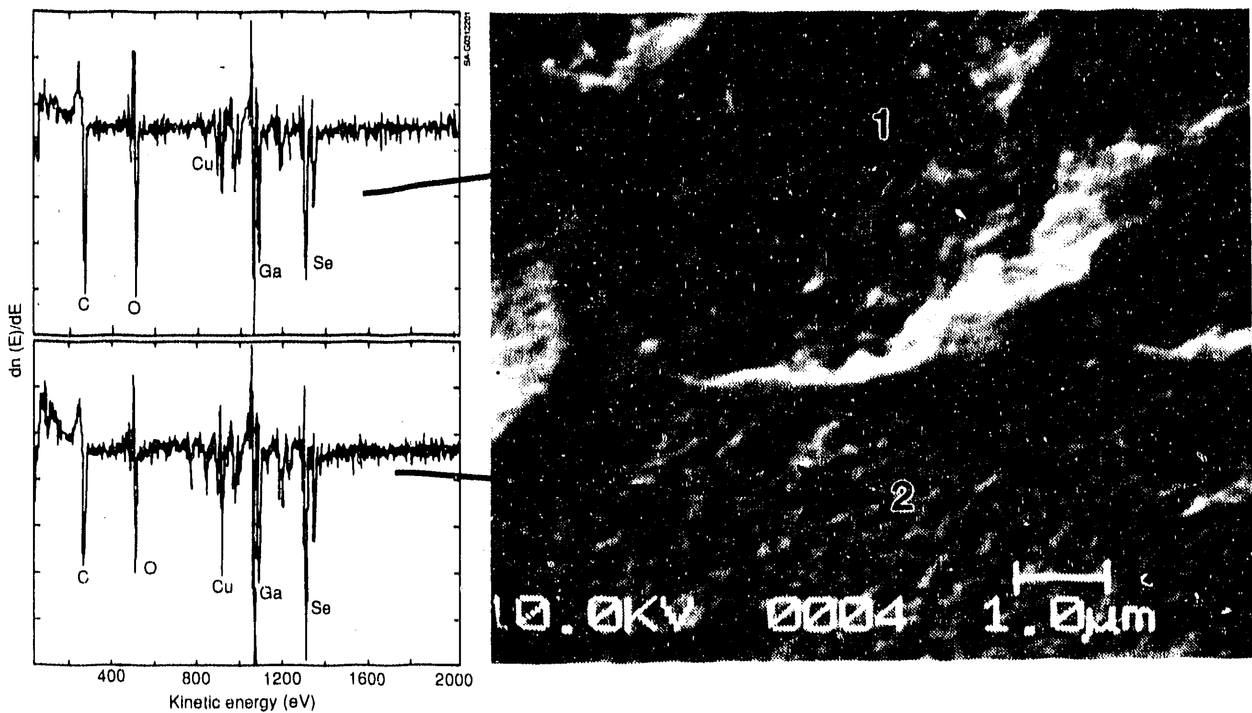

Figure 4-46. Auger scan of surface pit phenomena

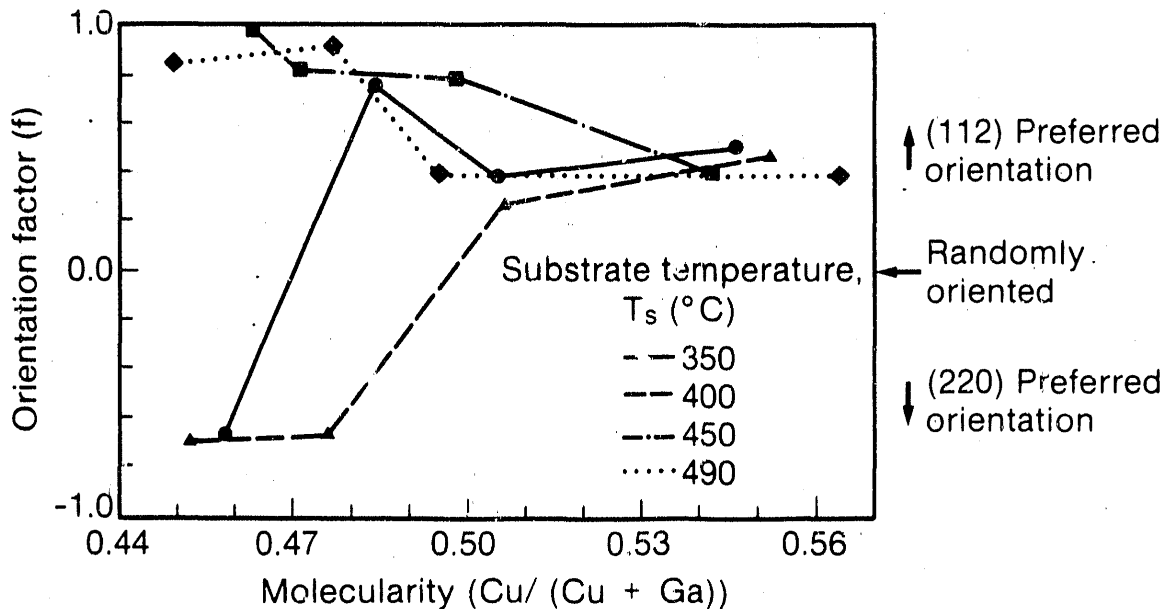

Figure 4-47. Lotgering plot of (112) orientation vs. film composition

For example, in $Fe_{1-y}O$, cation vacancies of up to 12 at. % exist in a non-interacting fashion as determined by defect chemistry results. In any case, the question as to whether films grown at high temperature and quickly cooled to room temperature represent equilibrium remains to be answered. Oxides in which defect ordering did occur when vacancy concentrations exceeded Anderson's value underwent disordering at elevated temperatures.

At this point, we decided to investigate whether the large existence field of chalcopyrite $CuGaSe_2$ could be better quantified by constructing a structural model, consistent with observed electrical (p-type) behavior, for copper-poor compositions. Calculations involving the effect of randomly distributed point defects require modification of the atomic scattering factor f_i. The effective scattering term is an at. % average of the constituent atoms occupying that site:

$$f_{eff} = \sum (at.\ \%i) f_i / 100,$$

where a vacancy is represented by setting $f_i = 0$. In this fashion, vacancies and antisites are easily incorporated within theoretical estimates of intensity. A short program was written in BASIC to handle intensity calculations including structure, temperature, and anomalous dispersion effects. Atomic scattering factors were based upon the Thomas Fermi-Dirac statistical model results for neutral atoms with data fitted to an 8th-degree polynomial with anomalous dispersion terms $\Delta f_i'$ and $i\Delta f_i''$ for CuK_α radiation taken from Cromer's compilation. Debye-Waller temperature factors were obtained from the single-crystal refinement of Abrahams and Bernstein [61], in which the isotropic terms were used. All calculations were for $CuK_{\alpha1\alpha2}$ radiation.

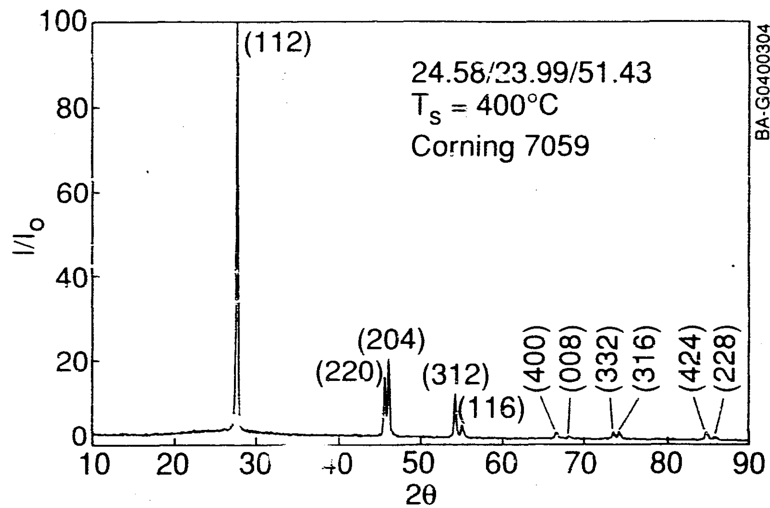

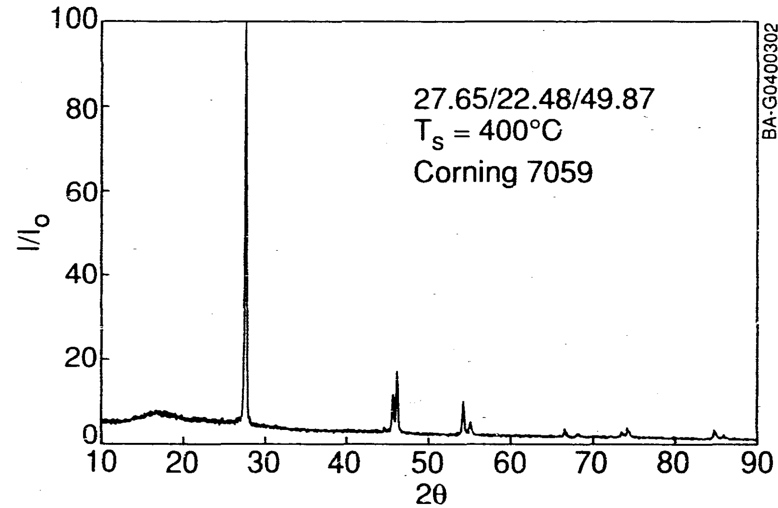

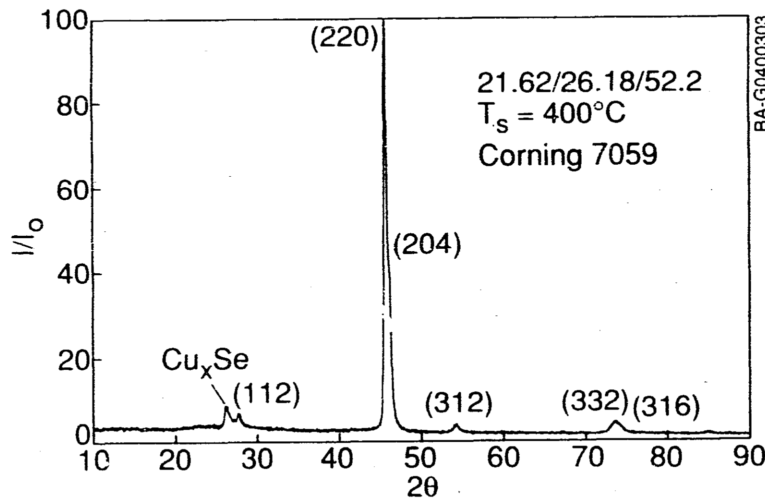

Figure 4-48. Preferred orientation shift for films with $T_s \leq 400°C$

XRD structure factors are based upon the atomic positions, where u, the group VI atom displacement parameter, was set to 0.25. Allowed reciprocal lattice vectors fall into one of three categories [62]. Group (i) vectors correspond to sphalerite vectors and have tetragonal Miller indices given by (h,k,l/2) unmixed. Group (ii) vectors are dependent only upon the anion scattering factor and have indices given by (h,k) even (l/2) odd, or vice versa. Group (iii) vectors involve both an anion term (which vanishes for u = 0.25) as well as a cation ionicity term based upon the difference in cation scattering factors and are often referred to as superlattice peaks. The indices of this grouping are given by (h) even (k,l) odd, or (k) even (h,l) odd. From these relationships, various requirements were established for checking computer calculations involving I-III-VI_2 structures: (1) if u = 0.25 and $f_I = f_{III}$, then only group (i) reflections exist (i.e., the material is zincblende); (2) if $f_I = f_{III}$, then F_{hkl} is symmetrical around u = 0.25; (3) if u = 0.25, then group (ii) reflections become extinct; and (4) group (ii) reflections are independent of changes in f_I, f_{III} scattering.

According to the model of Groenink and Janse, the defect chemistry of the chalcopyrites can be described by stoichiometric deviations in molecularity and valency. To provide a systematic approach to our calculations of defect-dependent structure factors, we therefore consider first the case of copper-poor ΔX variations at ΔZ = 0, in which compositions are generated along the binary tie line $(Cu_2Se)_A$ - $(Ga_2Se_3)_{1-A}$ with the molecularity, A=[Cu]/([Cu]+[Ga]). With a further restriction that the anions form a perfect lattice (i.e., no vacancy/interstitial combinations), we can normalize the atomic fractions to that of a defect adamantine structure. In this case, we have chosen the more energetically favorable gallium antisite model rather than the interstitial model. Calculations for the latter have not been made as yet. XRD intensities are now calculated by modification of the atomic scattering terms:

$$f_{Cu} = 2A\left(\frac{2}{3 - 2A}\right) f_{Cu} + \left[2(1 - A)\left(\frac{2}{3 - 2A}\right) - 1\right] f_{Ga},$$

where

$$f_{Cu} = f_{Cu} + \Delta f'_{Cu} + i\Delta f''_{Cu} \text{ , and}$$

$$f_{Ga} = f_{Ga} + \Delta f'_{Ga} + i\Delta f''_{Ga} \text{ .}$$

The variation in $|F_{hkl}|$ (electrons/unit cell), including temperature and anomalous dispersion effects for various group (iii) reflections as a function of composition, are shown in Figure 4-49. Although variations in F_{hkl} for any (hkl) can be observed, the magnitude change is small, generally less than 10-20 electrons/unit cell for the compositional range studied, and appears to be independent of theta. Consequently, the effect should be more dramatic in the lower-intensity group (iii) reflections.

Since XRD intensities predicted in this fashion are relative, it is necessary to establish a baseline intensity profile before investigating composition-XRD intensity relationships. This profile provides a reference from which changes in peak intensity can be correlated with composition in support of a given structural model such as the one previously presented. To demonstrate the merit of this approach, we used the (101) peak as a reference for setting empirical detection limits for other low-intensity peaks. This choice was not altogether arbitrary in that the (101) reflection is reportedly the lowest

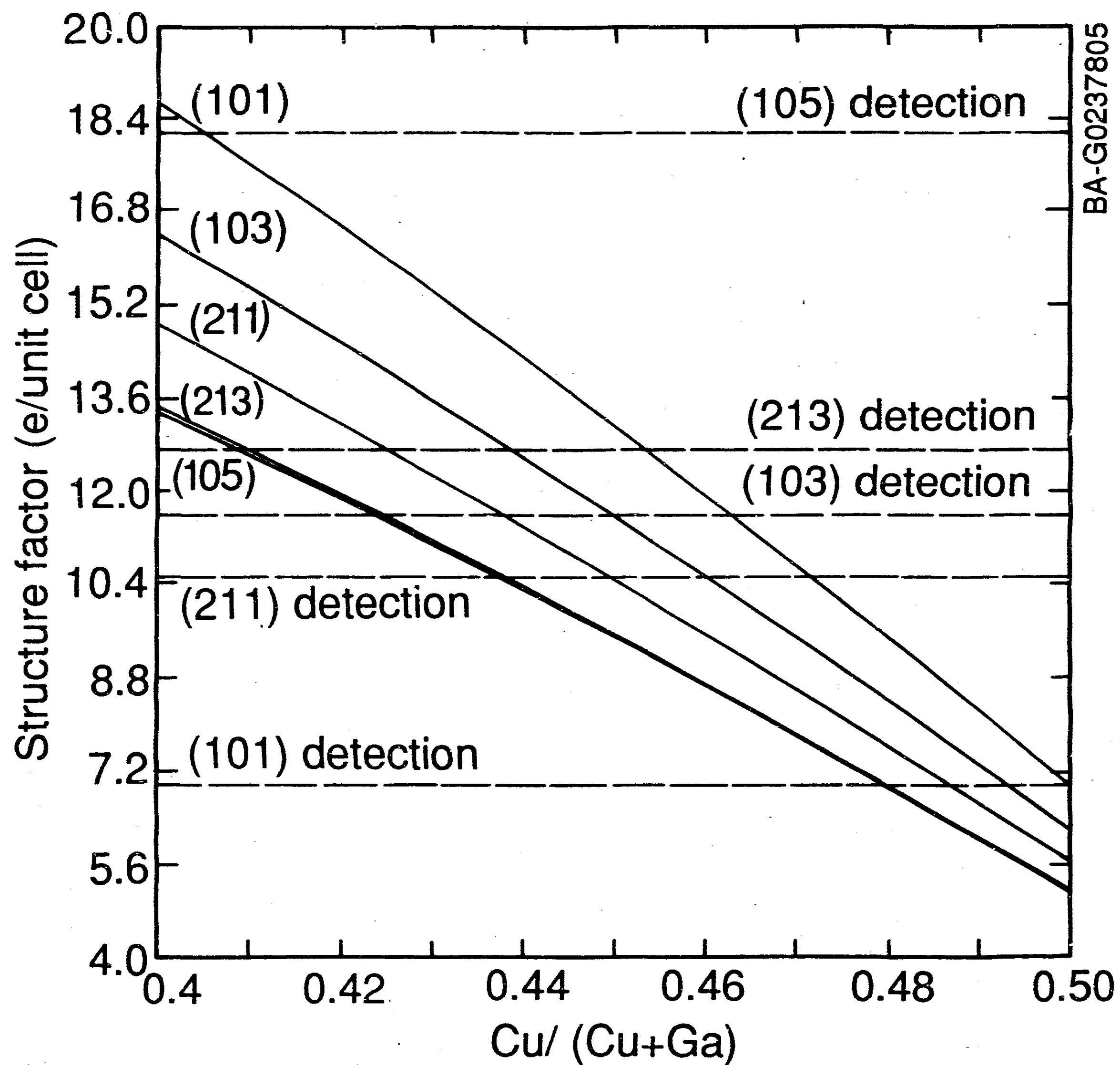

Figure 4-49. Variation in group (iii) reflections vs. molecularity based on a defect adamantine model. Curves A, B, C, D, and E correspond to the (101), (103), (211), (213), and (105) reflections, respectively.

intensity [63] and one of the lowest intensity [64] peaks observed in powder diffraction of $CuGaSe_2$ crystals grown from stoichiometric and copper-rich melts. If we assume these crystals themselves to be stoichiometric (final compositions were not reported), we can reference the (101) detection limit at A = 0.5 as shown in Figure 4-49. By normalization of both theta-dependent Lorentz-polarization and planar-multiplicity factors, detection limits for remaining peaks can be determined. As shown in Figure 4-49, the only group (iii) peak observed at perfect stoichiometry was assigned to the (101) peak. With decreasing molecularity (increasing V_{Cu} and Ga_{Cu} defects), structure factors for the remaining peaks all increase such that at a composition of A ~ 0.45, both the (211) and (103) peaks should become visible. The (213) peak becomes visible at a composition of A ~ 0.412, with the (105) reflection remaining hidden for $0.4 \leq A \leq 0.5$.

To test the validity of Figure 4-49, we obtained and analyzed a sample of copper-poor single crystal with an EPMA-determined composition of 22.1 at. % copper, 27.75 at. % gallium, and 50.05 at. % sellenium (crystal courtesy of T. Cizek) [65]. The appropriate location on the molecularity tie line is shown in Figure 4-49. As shown in Figure 4-50, the (102) and (211) peaks were indeed present while the (105) and (213) reflections were absent, as predicted by the results given in Figure 4-49. (The peak at 43.75° 2θ was identified as probably Cu_2Se - JCPDS #27-1131 or #4-839 and not as the (213) peak. Peak locations were calculated using a,c parameters obtained from the (200), (004) reflections of the same crystal.) Finally, it is worth mentioning that the (103) reflection has not been previously reported, either in powder [63,64] or single-crystal work [61].

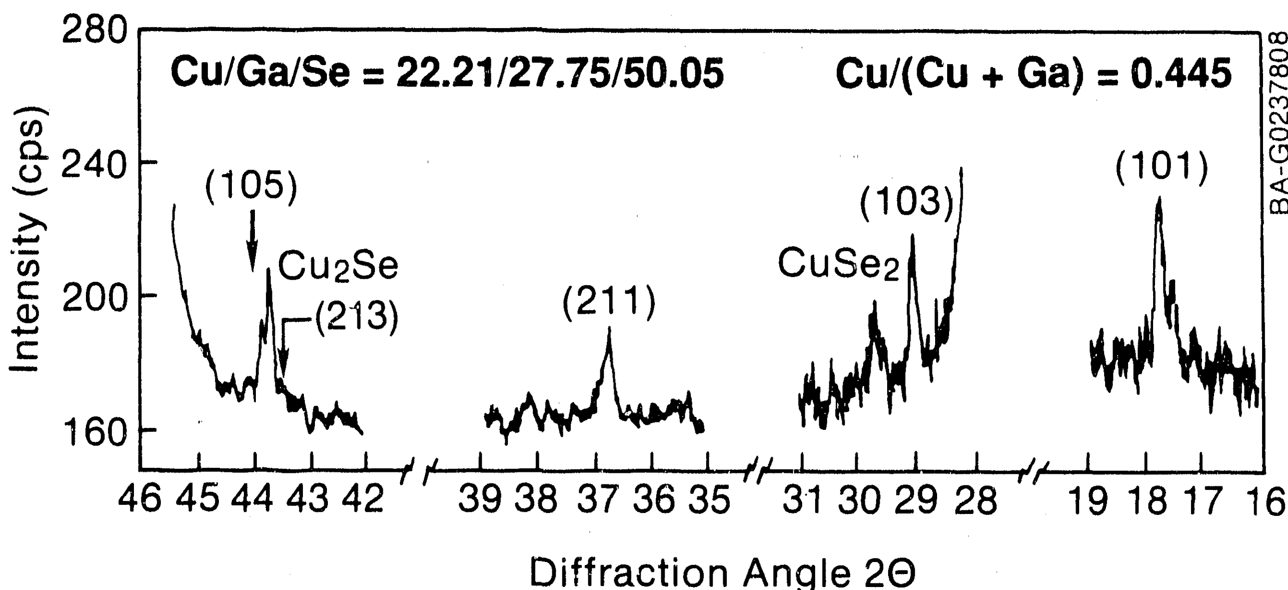

Figure 4-50. Single-crystal verification of a defect adamantine model

Diffraction patterns of evaporated copper-poor $CuGaSe_2$ thin films do not, however, exhibit these group (iii) reflections. If orientation effects are momentarily ignored, we are faced with two subtle possibilities: we have oversimplified the defect structure, or copper-poor $CuGaSe_2$ thin films are no longer chalcopyrite [i.e., all group (iii) reflections are extinct]. In consideration of the first of these, it is highly probable that additional defects other than the V_{Cu} - Ga_{Cu} pair exist in copper-poor material. Formation energy calculations of intrinsic defects in $CuInSe_2$ indicate the probabilistic nature of the anion vacancy. However, due to the inability of $CuGaSe_2$ to type convert and therefore always exhibit p-type behavior, the formation of V_{Se} (donor) must involve a subsequent compensation mechanism, in this case the Se_i (acceptor) or a reduction in Ga_{Cu} antisites (donor). The large formation energy of the anion interstitial warrants the latter mechanism. The effect of this donor-balancing mechanism involving V_{Se} and Ga_{Cu} defects on the (103) reflections is shown in Figure 4-51.

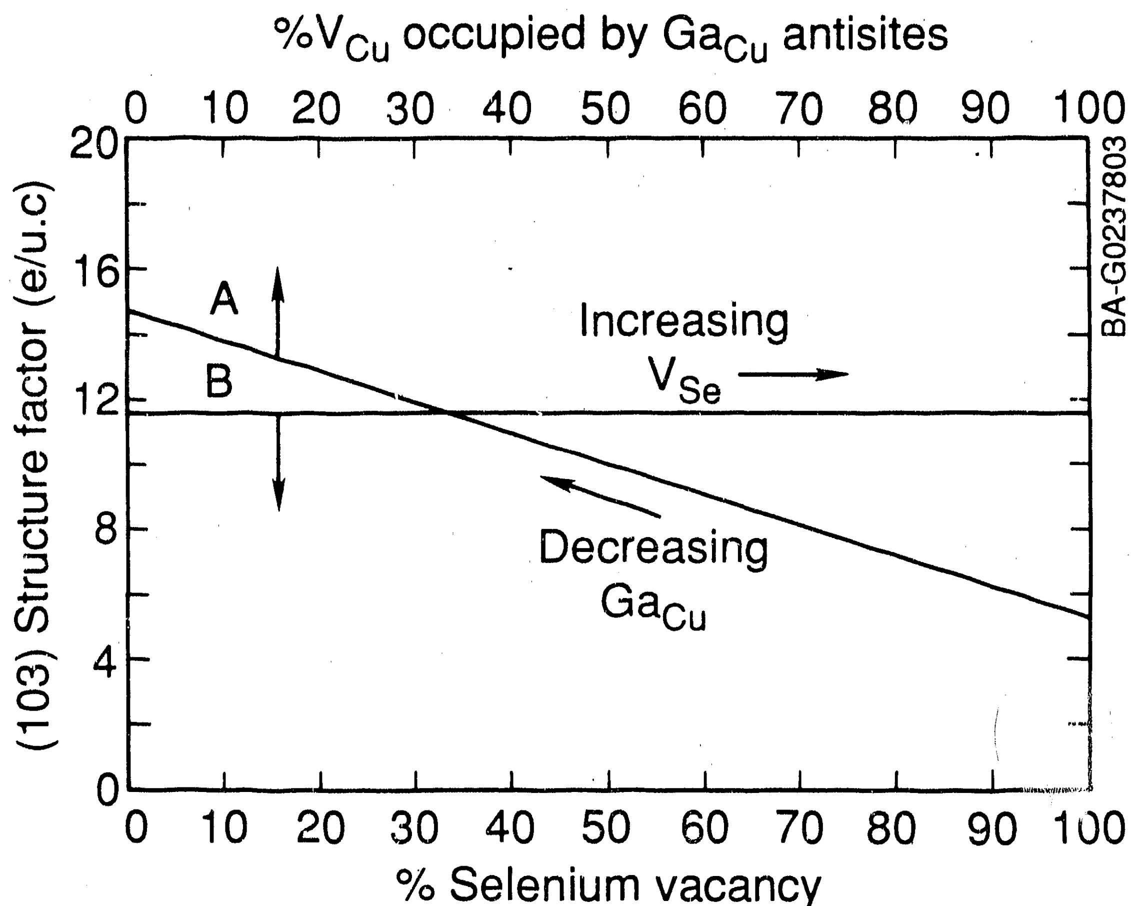

Figure 4-51. Effect of the V_{Se} - Ga_{Cu} balancing mechanism on (103) superlattice reflection

In this figure, the top abscissa represents the occupation of Ga_{Cu} antisites as a percentage of the total V_{Cu} concentration for A = 0.45 and a nominal 5% V_{Se} concentration. The bottom abscissa shows the effect of selenium vacancies as a percentage of total anion sites at the same composition and one-third of the V_{Cu} occupied by Ga_{Cu}. Since copper and gallium scatter with nearly the same efficiency, it was expected that an increase in Ga_{Cu} defects would reduce the increase in $|F_{103}|$ caused by increased copper vacancies. This was indeed the case as shown in Figure 4-51. The presence of V_{Se}, meanwhile, has no effect on $|F_{103}|$ since u = 0.25 for $CuGaSe_2$ and anion contributions to group (iii) reflections are absent. Consequently, if V_{Se} defects are compensated by a reduction in Ga_{Cu} defects, from electrical and energy considerations, the structure factor $|F_{103}|$ would actually increase in copper-poor tetragonal material. The second possibility, that copper-poor $CuGaSe_2$ films are not chalcopyrite, therefore seems to be a more plausible explanation for the absence of the (103) and (211) peaks in lieu of any preferred orientation effects. However, a tetragonal phase is indeed present in copper-poor films, which generates the idea of phase and compositional separation.

The convolution of group (i) cubic and tetragonal phase peaks usually requires an analysis of group (ii) and (iii) peaks for structure determination. The large difference in cation scattering of tetragonal $CuInSe_2$, for instance, generates readily visible group (iii) peaks. For $CuGaSe_2$, however, the similarity of cation scattering reduces the intensity of all group (iii) reflections such that only the (101) peak can typically be found. A nearly ideal selenium lattice also eliminates the presence of any group (ii) reflections. Fortunately, a large tetragonal distortion (c/a = 1.96) provides easy resolution of various group (i) hkl doublets, including the (220)/(204), (312)/(116), (008)/(400), and (332)/(316) pairs [66,67]. The presence of these doublets in $CuGaSe_2$ films as a function of composition and substrate temperature are shown in Figure 4-52. Clearly, as the films become increasingly copper poor, the doublets become less resolved, qualitatively indicating a transition from chalcopyrite to sphalerite.

Although the absence of doublets, as well as superlattice peaks, is indicative of disorder, it is not definitive proof because of the tendency of oriented growth for evaporated films. Definite proof of the tetragonal to cubic effect was, however, obtained by analysis of the (112) peak shift with film composition. Order-to-disorder transitions result in loss of the tetragonal distortion associated with the tetragonal phase. If we assume this distortion is due to either tension (c/a >2.0) or compression (c/a <2.0) along the [001] direction, we should observe a shift $\Delta 2\theta$ as the (112) tetragonal plane reverts to the (111) cubic plane. This effect, greatest for large distortions, is given by

$$\Delta 2\theta = 2(\sin^{-1}\{(\lambda^2/4a^2)[h^2 + k^2 + (1/\delta)^2]\}^{1/2}$$

$$-\sin^{-1}\{(\lambda^2/4a^2)[h^2 + k^2 + (1/2)^2]\}^{1/2}) ,$$

where h,k,l and δ=c/a are referred to as the tetragonal parameters.

Table 4-2 is a comparison of the integrated intensities, d(hkl), 2θ, structure factor, and normalized intensities for both tetragonal and cubic sphalerite, the latter based on the previous c-axis distortion. The intensity-independent

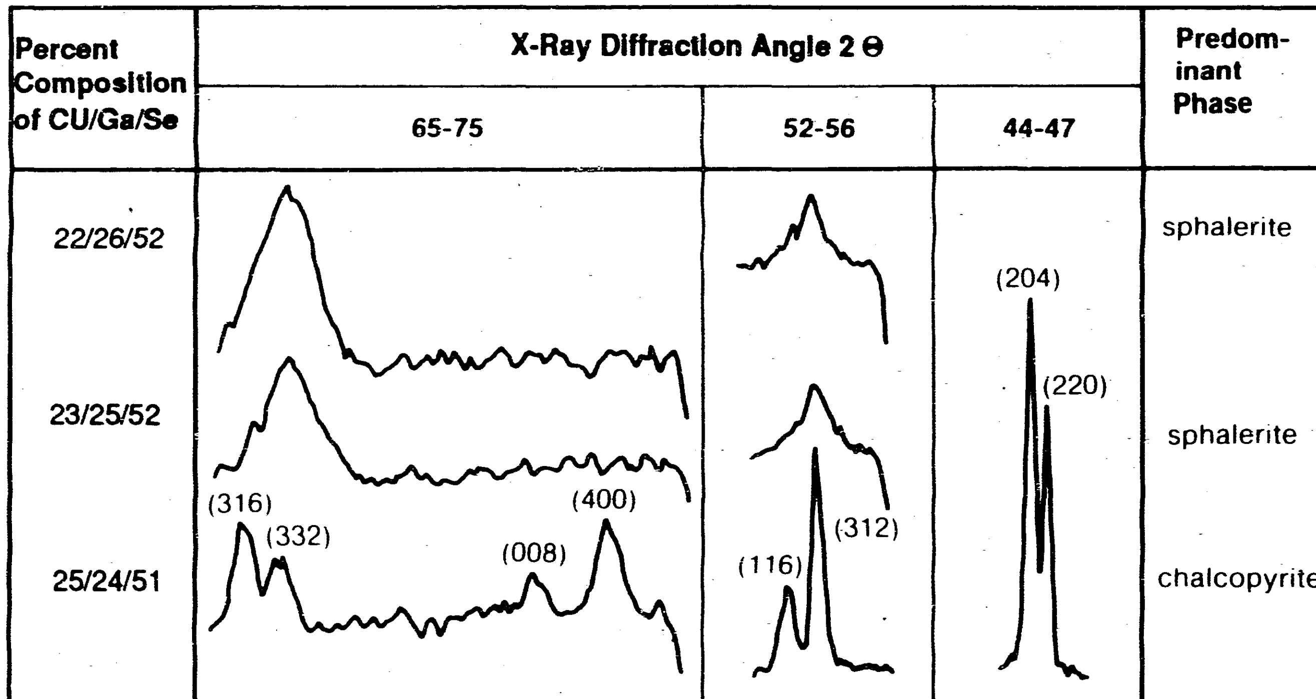

Figure 4-52. Peak splitting behavior vs. composition and substrate temperature for $CuGaSe_2$ deposited on glass substrates

differences of theta shifts offer a significant advantage for studying the structural disorder. For instance, the shift in 2θ when order-disorder occurs for the (112) and (008) reflections are 0.17° and 1.34°, respectively, which is easily resolved in practice.

4.7 Characterizations of Electrodeposited $CuInSe_2$ Thin Films: Structure and Deposition Mechanism

4.7.1 Introduction

Polycrystalline thin films of $CuInSe_2$ prepared by vacuum evaporation processes have been shown to be stable semiconductor materials for photovoltaic application, with an efficiency of 14.1% recently reported for devices that featured a configuration of $CuInSe_2$/(Cd,Zn)S/ZnO [68-70]. The structural properties of the sputtered and vacuum-evaporated $CuInSe_2$ thin films fabricated by single-source, two-source, and three-source methods have been characterized by several groups [71-73]. However, differences exist in whether the $CuInSe_2$ thin films of In-rich composition (Cu/In < 1) are chalcopyrite or sphalerite.

In addition to preparing the $CuInSe_2$ thin films using the several deposition processes in vacuum systems, co-electrodeposition from a single solution has been shown capable of producing device quality materials [74-79]. Investigations of the structure of the co-electrodeposited $CuInSe_2$ thin films also produced varying results. For example, Qiu and Shih [75] reported a chalcopyrite structure for both copper-rich and indium-rich thin films with preferred orientation in (112) plane, while Pottier and Maurin [80] reported a preferred orientation in (220,204) plane for the $CuInSe_2$ thin films on Ti or nickel made from acidic citrate solutions. Ueno et al. [81] reported chalcopyrite structures for slightly selenium-poor, indium-rich $CuInSe_2$ thin films electrodeposited from a pH = 1 sulfate bath after annealing at 600°C.

To better understand the structural characteristics of the $CuInSe_2$ thin films prepared in our work [77-79], we systematically investigated the structural effects of film composition as a function of deposition potentials, annealing conditions, oxidation by air, and chemical treatments. Elucidation of the deposition/formation mechanism of the $CuInSe_2$ thin films was based on the results of compositional and corresponding structural change upon chemical treatments. Our findings from this work are given in the following subsections.

4.7.2 Experimental Conditions

Single-layer $CuInSe_2$ thin films (2-2.5 μm) were co-electrodeposited from aqueous ethylenediamine solutions containing Cu(II), In(III), and H_2SeO_3 at pH = 1.70. The instrumentation, deposition method, and annealing setup are the same as described in Ref. 77. Thin film molybdenum (Mo)-coated glass substrates were used to minimize background interference in the XRD measurements. The molybdenum thin films (2-3 μm) were prepared by plasma sputtering.

XRD measurements were performed on a Rigaku "Rotaflex" spectrometer using copper Kα lines. Identical operation conditions were employed for all measurements in order to minimize the variations of measured spectra in band width and peak intensity. A wafer of single-crystal silicon (111) was used to

Table 4-2. Theoretical XRD Intensities for Tetragonal and Cubic Phases of $CuGaSe_2$

Tetragonal Chalcopyrite					Cubic Sphalerite				
(hkl)	d(hkl)	2θ	$\|F\|_e^{2-2m}$	I/I_o	(hkl)	d(hkl)	2θ	$\|F\|_e^{2-2m}$	I/I_o
101	5.002	17.73	45.75	.147					
112	3.222	27.69	77956	100	111	3.241	27.52	28274	100
103	3.076	29.03	36.3	.04					
200	2.807	31.88	1278	.61	200	2.807	31.88	1276	.897
004	2.758	32.46	1273	.29	002	2.807	31.88		
211	2.448	36.71	29.9	.04					
213	2.074	43.65	24.7	.02					
105	2.010	45.10	24.4	.12					
220	1.985	45.71	[illegible]9392	21.8	220	1.985	45.71	99421	64.3
204	1.967	46.14	98304	42.2	202	1.985	45.71		
301	1.845	49.39	20.8	.007					
312	1.690	54.28	41123	24.8	311	1.693	54.19	41235	36.8
116	1.668	55.04	40360	11.8	113	1.693	54.19		
224	1.611	57.18	1078	.29	222	1.621	56.81	1077	.289
323	1.434	65.05	12.7	.005					
305	1.427	65.39	12.5	.002					
400	1.403	66.64	59207	5.8	400	1.403	66.64	59242	8.55
008	1.379	67.98	57356	2.7	004	1.403	66.64		
332	1.287	73.62	25247	4.1	331	1.288	73.53	25307	12.13
316	1.277	74.26	24881	7.9	313	1.288	73.53		
420	1.255	75.78	951	.14	420	1.255	75.77	946	.86
404	1.251	76.10	949	.14	402	1.255	75.77		
208	1.238	77.05	943	.14	204	1.255	75.77		
424	1.143	84.87	39185	10.3	422	1.146	84.56	39484	15.35
228	1.133	85.80	38408	5.0	224	1.146	84.56		

a_o = 5.614 B_{Cu} = 1.356 Å^2 Perfect stiochiometry assumed

c_o = 11.032 B_{Ga} = 1.607 Å^2

B_{Se} = 1.023 Å^2

λ = 1.541838 Å

determine the intrinsic instrumental line broadening, which in turn was used for correction in grain-size calculation as described in the text. The peak positions reported here are in the values of 2θ degrees.

The composition of the $CuInSe_2$ thin films before and after annealing was analyzed by a Cameca MBX EPMA equipped with three WDS spectrometers and a Tracor Northern TN-2000 automation system. Thin films of thermal-evaporated $CuInSe_2$ of known composition were used as reference. Auger depth profiling was conducted on an Auger spectrometer.

4.7.3 Results and Discussion

4.7.3.1 Annealing Effects

On $CuInSe_2$ thin film composition, the single-layer $CuInSe_2$ thin films made by a single potential from the current solution formulation at pH = 1.7 were normally excessive in selenium (Se > 50 at. %), while the indium/copper ratio increased as the deposition potential became more negative. These results are shown in Figure 4-53 as the curves in the solid line for a series of $CuInSe_2$ deposited between -0.55 and -0.75 V (versus a SSCE reference electrode). This observation indicates *in situ* potential-dependent deposition rates of the copper, selenium, and indium. The increase of indium concentration in the films at more negative potentials in fact provides the basis for making $CuInSe_2$ of bilayer configuration as desired in this work [77,78].

Heat treatment of the as-deposited films is needed to remove the excess selenium. The effect of annealing on film composition is illustrated as the dashed curves in Figure 4-53 for the three elements. In the figure, the atomic % of the selenium decreased to near 50 at. % (as desired) while the copper/indium ratio remained basically unchanged after annealing at 400°C for 30 minutes in flowing argon. Similar conservations of copper/indium ratios were also observed by Qiu and Shih [75] on their electrodeposited thin films annealed in vacuum-sealed quartz tubes.

In addition to removing the excess selenium, the crystallinity of the annealed $CuInSe_2$ thin films was found to increase substantially. The effect of annealing temperature on the thin films was examined by XRD for a series of copper-rich $CuInSe_2$ films deposited identically. The results (Figure 4-54) produced three main diffraction peaks: (112), (204,220), and (312,116). The as-deposited film [Figure 4-54(a)] has micropolycrystallines that gave weak and broad diffraction peaks. Upon heating at 230°C for 25 minutes (a pre-annealing step to remove excess selenium), the film crystallinity was improved as indicated by the increased peak intensity and narrower peak width [Figure 4-54(b)]. Further annealing at higher temperatures (from 300° to 450°C) resulted in systematically increased peak intensity and decreased peak width [Figures 4-54(c)-4-54(f)], reflecting enlarged grain size. In addition, two small peaks at 17.2° and 35.7° appeared on the films annealed at ≥350°C. These are (101) and (211) peaks, characteristic of chalcopyrite structure. On the other hand, a shoulder peak at 25.4° next to the main (112) peak gradually decreased and finally disappeared upon annealing at 300°C. The component responsible for the shoulder peak was assigned to be an impurity phase of In_xSe, which was also observed on indium-rich films; but its exact composition could not be positively identified even after a thorough examination through the JCPDS data cards.

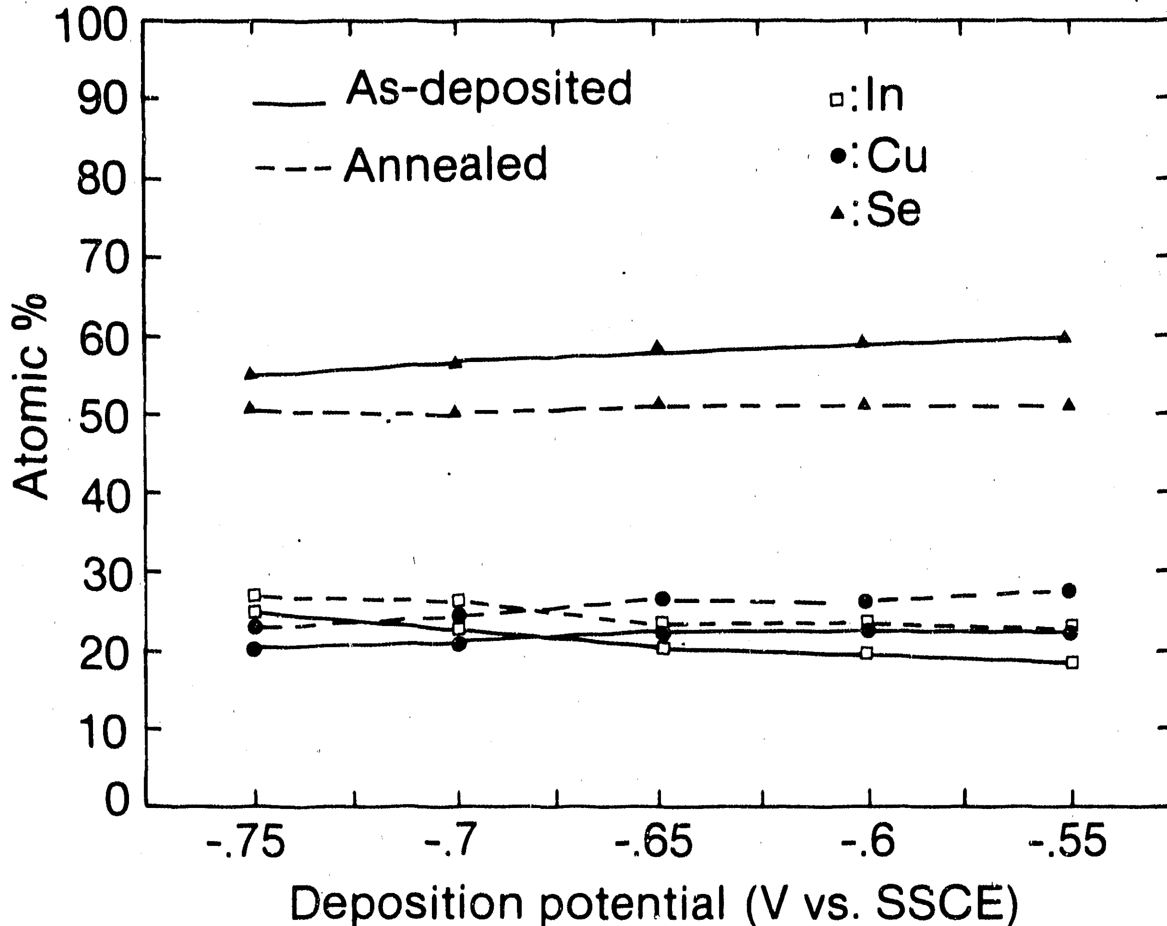

Figure 4-53. Thin film compositions for samples deposted between -0.55 and -0.75 V before (solid lines) and after (dashed lines) annealing at 400°C for 25 min

The annealed thin films displayed different growth rates in peak intensity as the annealing temperature increased (as seen in Figure 4-54). The intensities of the three main peaks are analyzed and are plotted in Figure 4-55(a). The (112) peak increased significantly faster than the two doublets, (204,220) and (116,312), indicating a preferred structural orientation in the (112) plane. The preferred orientation factor of (112) plane, **f(112)**, for the annealed $CuInSe_2$ thin films as a function of annealing temperature was analyzed by calculating the fraction of (112) peak intensity over the sum of intensity of all peaks within a given measuring 2θ range [82-83]. The range for this study is between 15° and 85° (2θ degree). The results are shown in Figure 4-55(b). Meanwhile, the grain size was calculated by using the following equation [84]:

$$(W_{observed})^2 = (W_{real})^2 + (W_{line\ broadening})^2$$

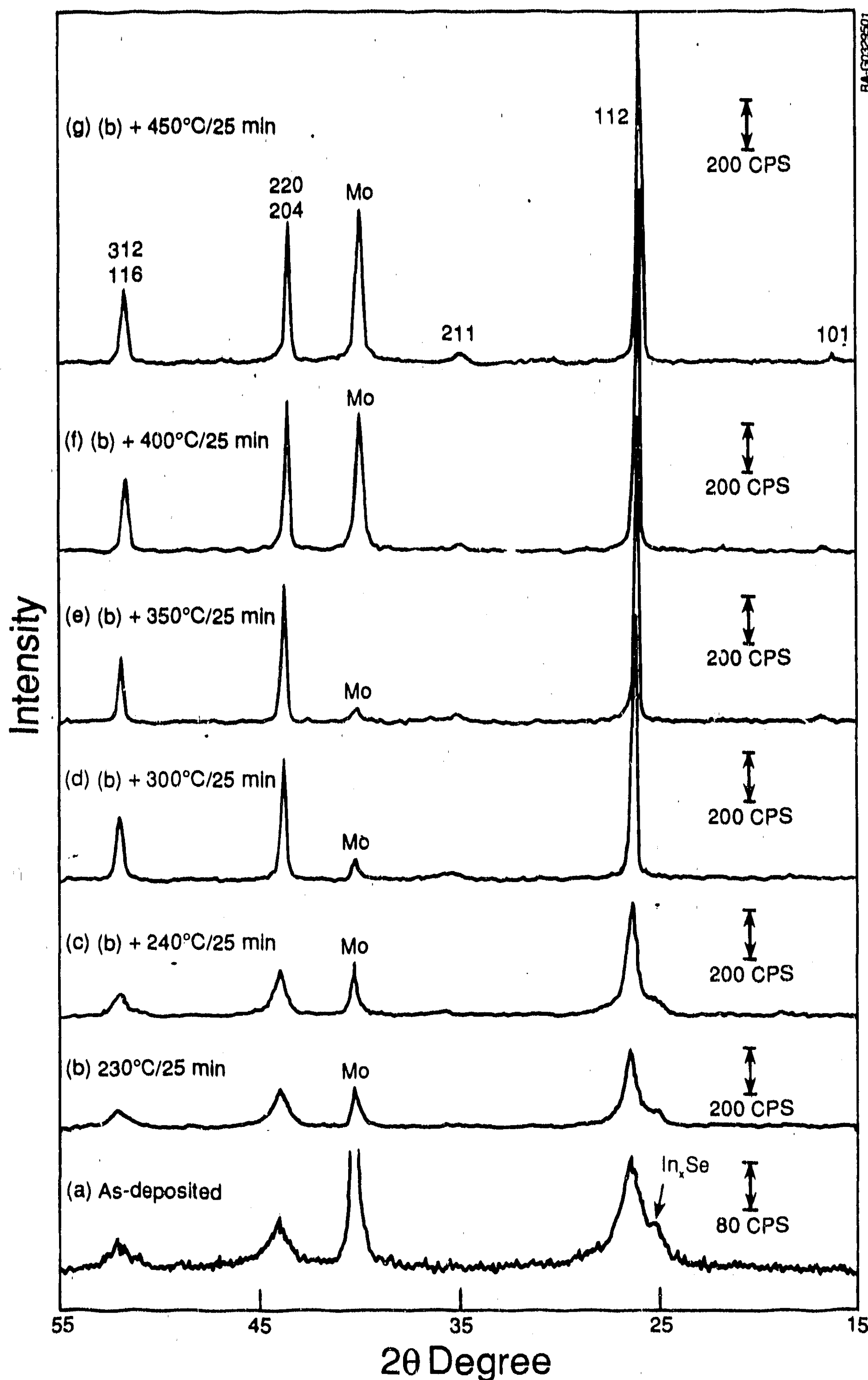

Figure 4-54. XRD spectra for electrodeposited copper-rich thin films. The films were heated at 230°C for 25 min to remove excess selenium, followed by higher annealing temperatures for 25 min in flowing argon. (a) As-deposited film, (b) heated at 230°C, (c) annealed at 240°C, (d) annealed at 300°C, (e) annealed at 350°C, (f) annealed at 400°C, and (g) annealed at 450°C.

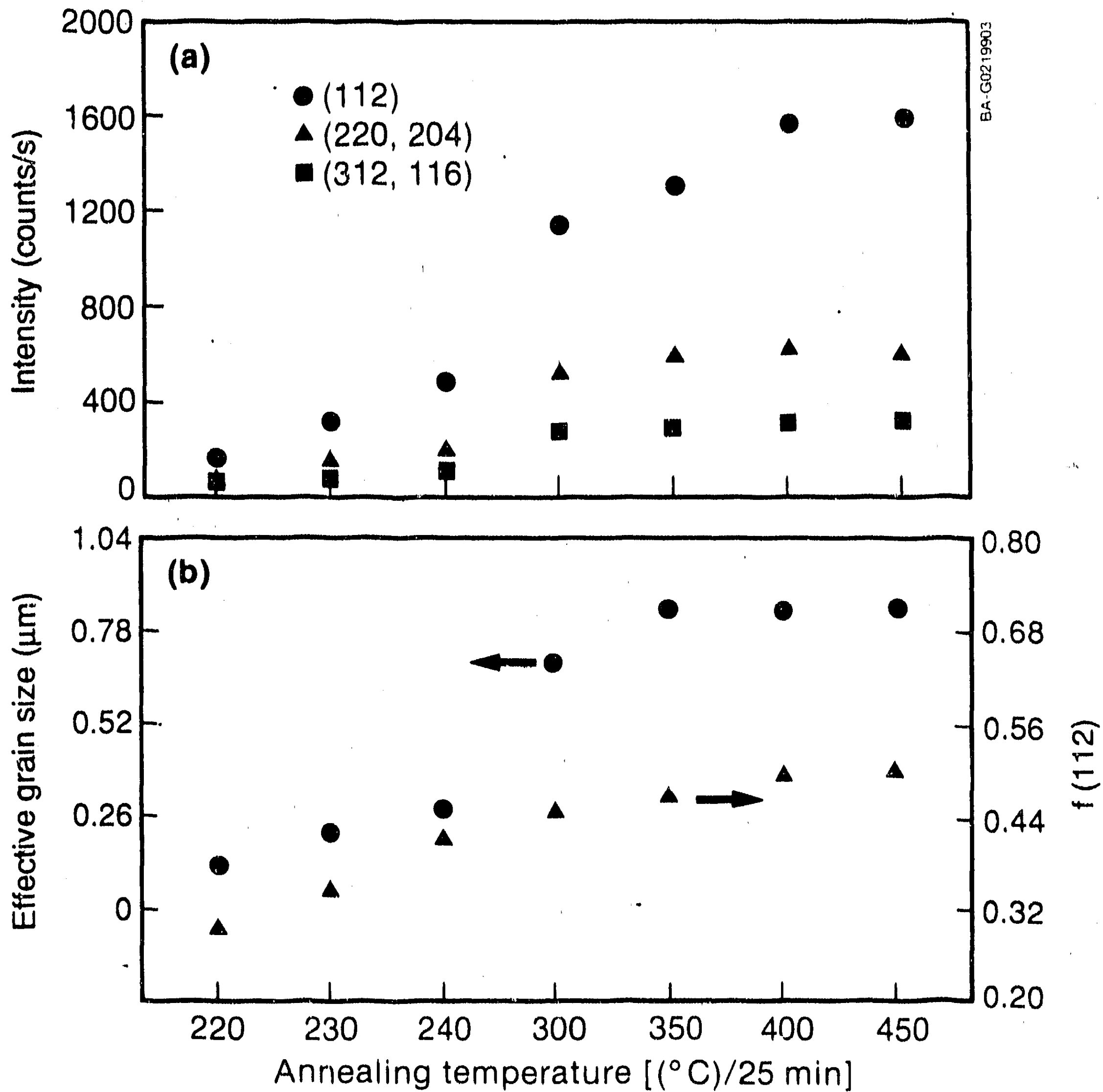

Figure 4-55. (a) Analysis of XRD intensity for three main diffraction peaks, (112), (220,204) and (312,116), as a function of annealing temperature shown in Fig. 4-54. (b) Grain size and preferred (112) orientation factor, f(112), analyzed for the same samples.

where W is the full width at half peak height. The last term is for the intrinsic line broadening on the peak width due to instrument factor [84], which was assessed by using a single-crystal silicon (111) wafer. The corrected values of grain sizes (W_{real}) thus derived are shown in Figure 4-55(b), together with the f(112) factors. An f(112) factor up to 0.71 and a grain size up to 0.1 µm are obtained for the annealed copper-rich films. For comparison, a number of vacuum-evaporated, single-layer $CuInSe_2$ thin films of copper-rich and indium-rich compositions were also examined in the same manner. The results indicate that the vacuum-evaporated films could have a f(112) factor as high as 0.85 and a corrected grain size about 20% larger than

that of the electrodeposited thin films. The observed plateaus in Figure 4-55(b) on peak intensity and grain size for films annealed at temperatures ≥400°C suggest an annealing temperature of 400°C for 25 minutes would be appropriate for the $CuInSe_2$ thin films.

The effects of annealing time at a higher temperature of 440°C were also investigated, with the results shown in Figure 4-56. The sample set was first annealed at 440°C for 20 minutes and measured with XRD, followed by additional annealing for 15 minutes and second XRD measurements. A longer annealing time (35 minutes) significantly increased the grain size of copper-rich films but did little on indium-rich films [as seen in Figure 4-56(a)]. The f(112) factor, however, was not correspondingly improved for copper-rich films after a longer annealing time [Figure 4-56(b)]. The f(112) factor for indium-rich films, on the contrary, suffered a considerable decrease. The results shown in Figure 4-56(b) indicate that a long annealing time at a high temperature such as 440°C probably is not desirable for the indium-rich films, since a large loss of preferred orientation may occur, apparently a consequence of an increased degree of randomization of indium atoms in the unit cells [84].

The preferred orientation, structure, and grain size were strongly affected by the thin film composition. Figure 4-57 compares the XRD spectrum of (a) a detailed analysis of an annealed copper-rich film to that of (b) an indium-rich film. In the former, all characteristic superlattice peaks of chalcopyrite structure [such as (101), (103), (211), (301), and so on] are clearly obtained for the copper-rich film. A similar XRD pattern was obtained for the vacuum-evaporated, copper-rich film. The similarity indicates the copper-rich films made by the two methods are identical as having chalcopyrite structure. In contrast, the indium-rich film is clearly absent of any of the superlattice peaks of chalcopyrite [Figure 4-57(b)]. In addition to the structural difference, the indium-rich films are very resistive after annealing as compared to the very conductive copper-rich films.

More detailed XRD analysis revealed a totally different structure for the indium-rich films, which was identified as a disordered version of chalcopyrite (i.e., a cubic sphalerite). This conclusion was reached because the characteristic peaks of that chalcopyrite were absent. This finding is in full accord with the difference calculated for the theoretical XRD peaks that may be present in a tetragonal chalcopyrite as compared to those found in a cubic sphalerite structure [84]. It should be pointed out that the peak shift due to the very small difference in c-axis was too small to be observable in XRD spectra. For example, the tetragonal chalcopyrite has an axis ratio of $c/a = 11.621/5.782 = 2.01$, and the cubic sphalerite has a ratio of $c/a = 2.00$; the displacement of the (112) peak will be a mere 0.045° (2θ). A larger peak shift of 0.23° is calculated for the (116) peak, but it could not be resolved in the doublet (312,116) in the measurement. These results indicate that a structural transition exists for the electrodeposited $CuInSe_2$ from a tetragonal to a cubic as the film composition varies from copper-rich to indium-rich. An unambiguous result is the monitored decrease and eventual disappearance of the (211) peak at 35.7°, characteristic of chalcopyrite, as a result of an increased indium/copper ratio (from <1 to >1) in the film composition (as illustrated in Figure 4-58). Figure 4-59 shows a plot of the (211) peak intensities obtained for the sample sets of Figure 4-58 and another. A nearly linear relationship is observed in Figure 4-59 for the two sample sets that

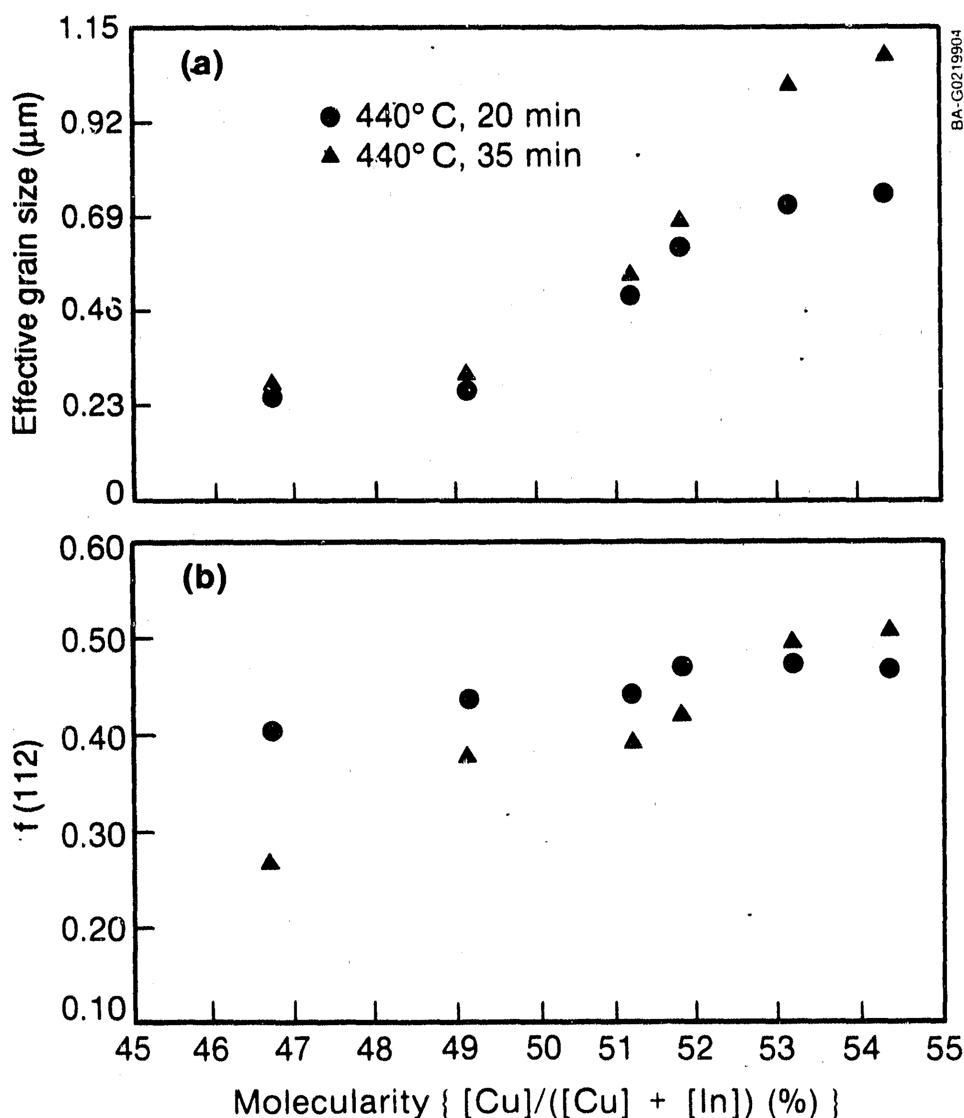

Figure 4-56. Grain size (a) and f(112) factor (b) as a function of molecularity for thin films annealed at 440°C for 20 min and 35 min

were prepared separately, indicating that the decline of the (211) peak is a consequence of an intrinsic physical property of the film composition. The gradual change from a tetragonal (ordered) to a cubic (disordered) structure apparently arose from the increased randomization of indium atoms in the unit cell of indium-rich $CuInSe_2$ thin films. The Cu_2Se-In_2Se_3 pseudobinary phase diagrams for the $CuInSe_2$ system, given by Palatnik and Rogacheva [85] and Fearheiley [86], indicate that a homogeneous solid solution of γ phase can exist for indium-rich $CuInSe_2$, while a copper-rich $CuInSe_2$ solid solution will precipitate into two phases as $CuInSe_2$ and Cu_2Se.

In comparison, Qiu and Shih [75] reported a chalcopyrite structure for both annealed copper-rich and indium-rich thin films made in their electrodeposition work. A number of vacuum-evaporated $CuInSe_2$ thin films of copper-rich

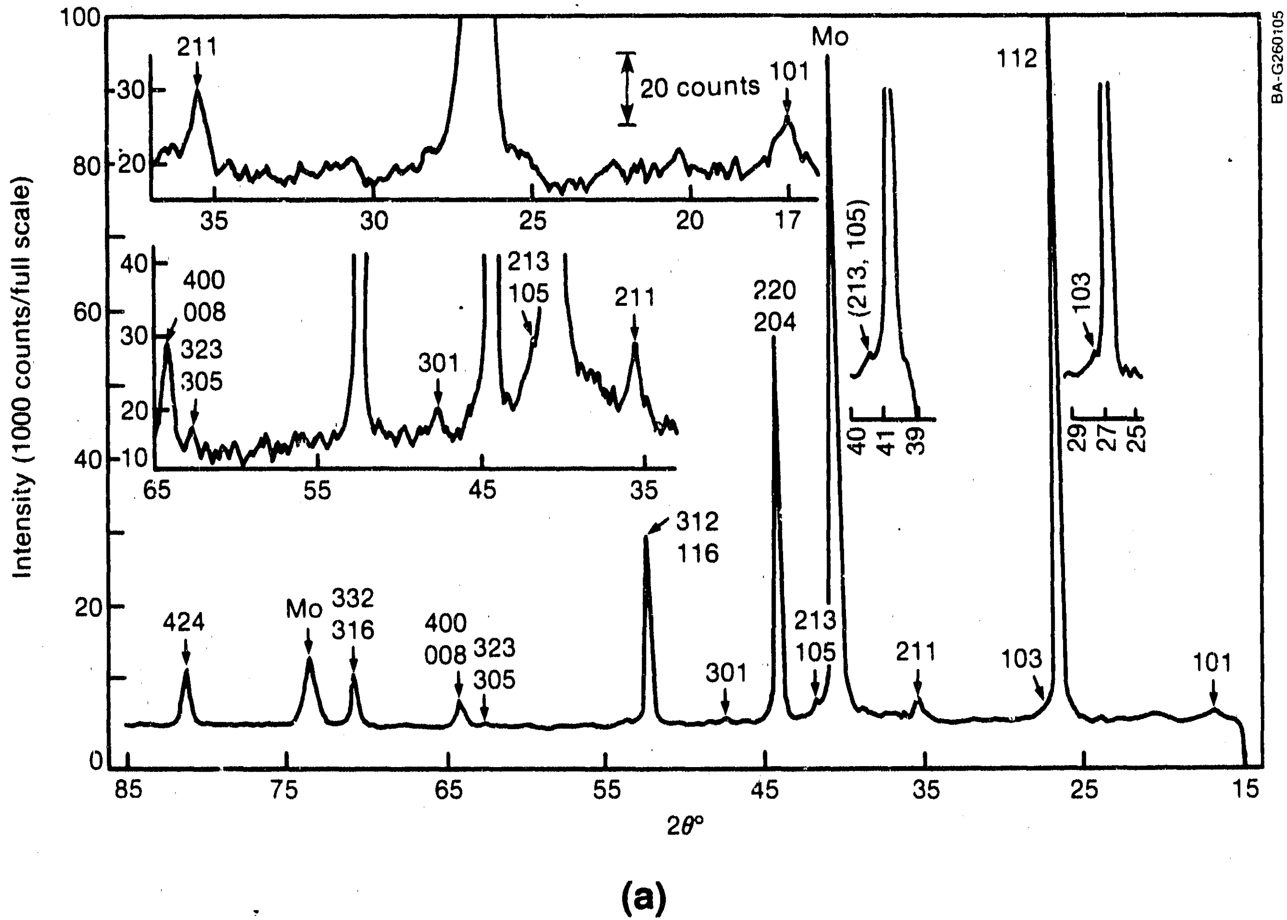

Figure 4-57. XRD spectra for annealed copper-rich (a) and indium rich (b) $CuInSe_2$ thin films

and indium-rich compositions in single-layer and bilayer configurations were also examined. For single-layer copper-rich films, the XRD analysis showed the structure to be chalcopyrite. For single-layer indium-rich films, the XRD spectra still showed characteristic peaks of chalcopyrite structure. Similar XRD results were also obtained for the bilayer films. Apparently, some inherent differences in structure existed between the electrodeposited and vacuum-evaporated indium-rich films. Dhere et al. [81], however, reported a chalcopyrite structure for Cu-rich films and a sphalerite structure for indium-rich films prepared by a three-source vacuum evaporation method. For comparison, metal site disorder resulting in structural change from chalcopyrite to sphalerite was reported for $ZnSnP_2$ by Ryan et al. [87].

In summary, the physical differences between the copper-rich and indium-rich $CuInSe_2$ thin films are given in Table 4-3. and the electrodeposited indium-rich films are compared to the vacuum-evaporated films in Table 4-4.

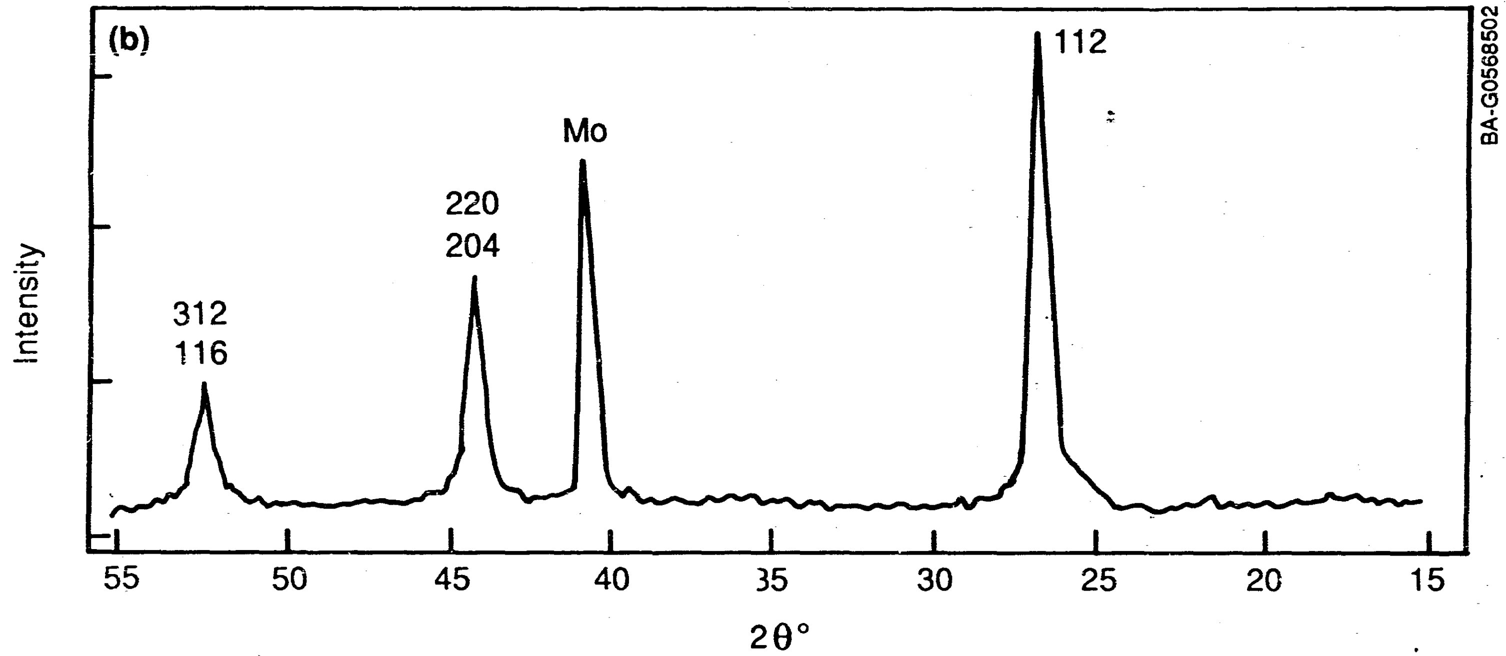

Figure 4-57. XRD spectra for annealed copper-rich (a) and indium-rich (b) $CuInSe_2$ thin films (concluded)

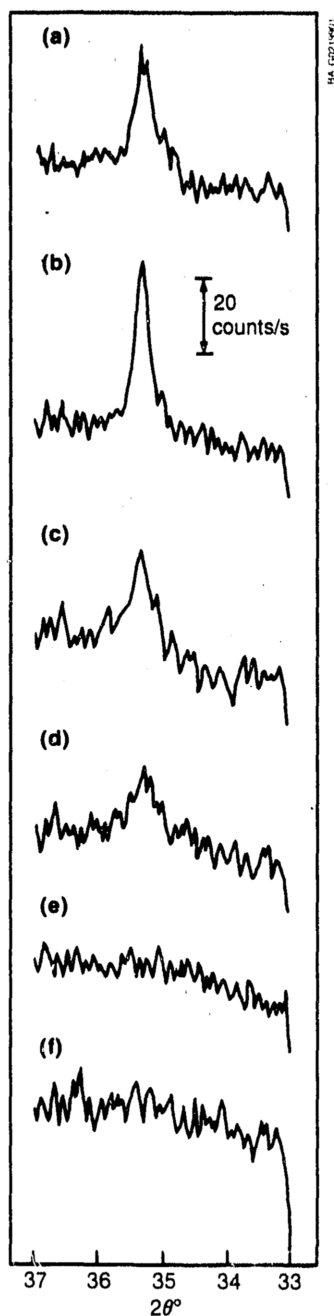

Figure 4-58. Monitored decrease and eventual disappearance of (211) peak for a series of annealed $CuInSe_2$ thin films electrodeposited at (1) -0.55 V, (b) -0.60 V, (c) -0.65 V, (d) -0.70 V, (e) -0.75 V, and (f) -0.80 V. The film composition varied from copper-rich (a-d) to indium-rich (e,f).

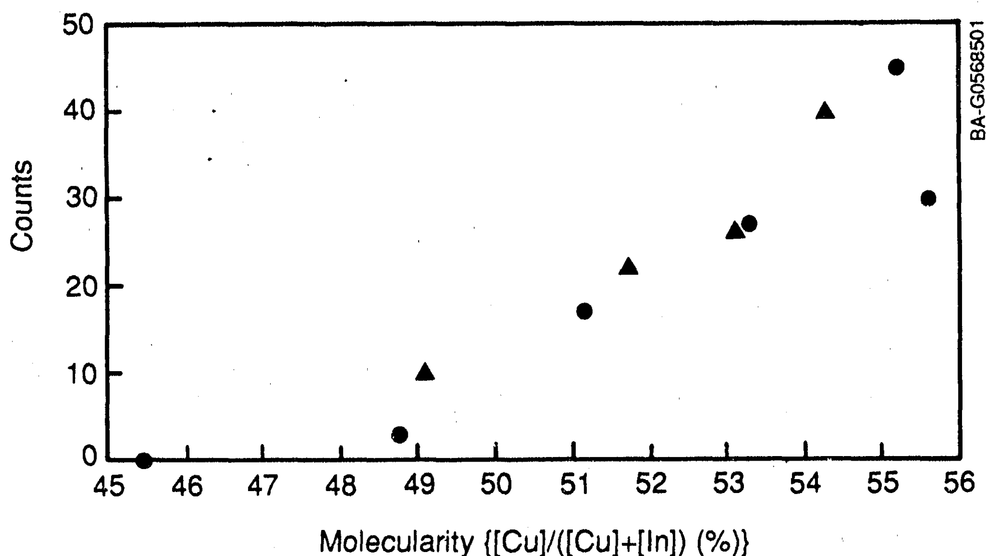

Figure 4-59. A plot of (211) peak intensity for the sample sets of Fig. 4-58 (o) and another (Δ)

4.7.3.2 Effect of Oxygen (Air) Presence in Annealing

The annealing of the electrodeposited $CuInSe_2$ thin films normally was conducted in flowing argon gas. By introducing air during annealing, the film composition and structure were adversely affected. The resulting films are very conductive regardless of whether they were originally copper-rich or indium-rich. Composition analysis by EPMA showed that a large fraction of selenium was replaced by oxygen. The oxygen content in the films increased as the annealing temperature was increasingly higher than 300°C. The oxidized films were examined by XRD, and the results are given in Figure 4-60. The oxidized films showed several foreign peaks, the strongest at 30.5°, which are identified to originate from In_2O_3. The intensity of these foreign peaks increased as the annealing temperature increased, which is in accord with the results of EPMA composition analysis showing that the percentage of selenium underwent a large decrease (to 20 atm. % - 30 atm. %) while the percentage of oxygen increased. Results of Auger depth profiling analysis revealed the bulk of the films was oxidized since the depth profile curve of oxygen is parallel to that of the indium profile. Accordingly, the presence of air or oxygen during annealing would result in the displacement of selenium and hence the formation of In_2O_3 in the films that renders them highly conductive.

Table 4-3. Thin Film Composition Characteristics

Cu-Rich Films	In-Rich Films
Chalcopyrite	Sphalerite
Large grain	Small grain
Low resistance	High resistance

Table 4-4. Structural Differences in In-Rich Thin Films

Sample	Composition Cu%/In%/Se%	Superlattice Peaks
Vacuum evaporated	20.01/28.68/49.31	present
Electrodeposited	21.77/26.87/51.36	absent
	20.53/28.56/50.92	absent

4.7.3.3 Effect of Chemical Treatments on Thin Film Composition

Chemical treatments were conducted for two purposes: to reduce surface roughness and reduce impurity phases, and to elucidate the thin film deposition and formation mechanisms.

Two etchants were used: one was 0.05%-0.1% (v/v) Br_2 in CH_3OH, and the other was 0.1-0.5 M KCN in deionized water. The Br_2/CH_3OH solution acted to remove the $CuInSe_2$ thin film as a surface leveling (leaching) agent more than to change the film composition. Its surface-leveling power depends on the concentration of Br_2 and the temperature of the solution. The micrographs in Figure 4-61 illustrate the surface-leveling effect of a 0.1% Br_2/CH_3OH solution. The as-deposited film, which was purposely used in this study, showed large, rough black pittings around the defective spots of molybdenum. After a 30-second treatment at room temperature, the rough pittings were effectively removed and a smoother film surface was produced. On the other hand, the compositional change of a vacuum-evaporated, copper-rich thin film after a 30-second treatment at 35°C in a 0.1% Br_2/CH_3OH solution was relatively small. The film composition of copper/indium/selenium (atm. %) changed from 25.58/24.22/50.20 to 24.92/24.88/50.20.

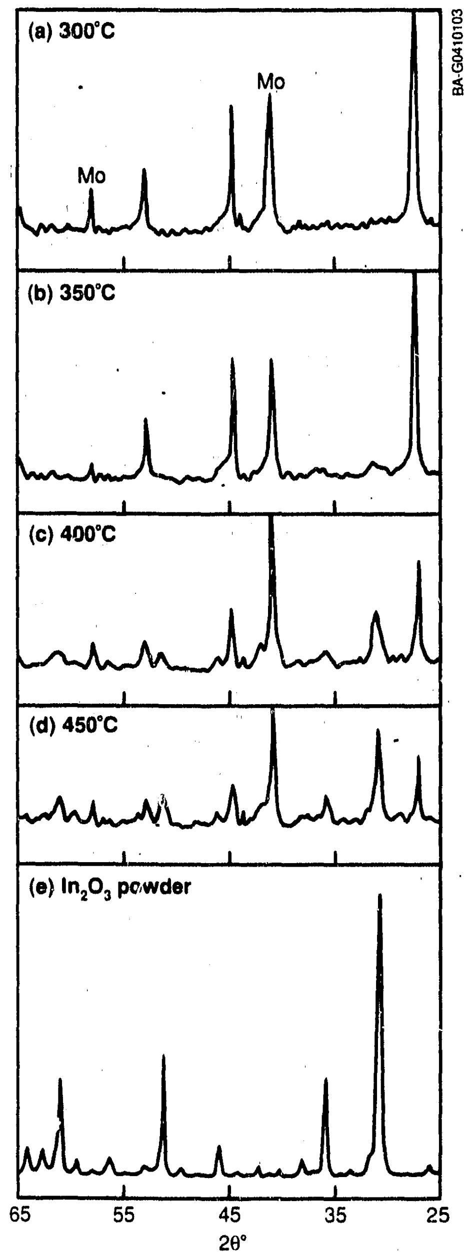

Figure 4-60. XRD spectra showing the oxidation of elecrodeposited $CuInSe_2$ thin films due to the presence of air during annealing. The films were heated at 200°C for 20 min before annealing at (a) 300°C, (b) 350°C, (c) 400°C, and (d) 450°C. The XRD spectra (a-d) are compared to (e) for pure In_2O_3 powder. The foreign peaks due to In_2O_3 origin are marked with * (b-d).

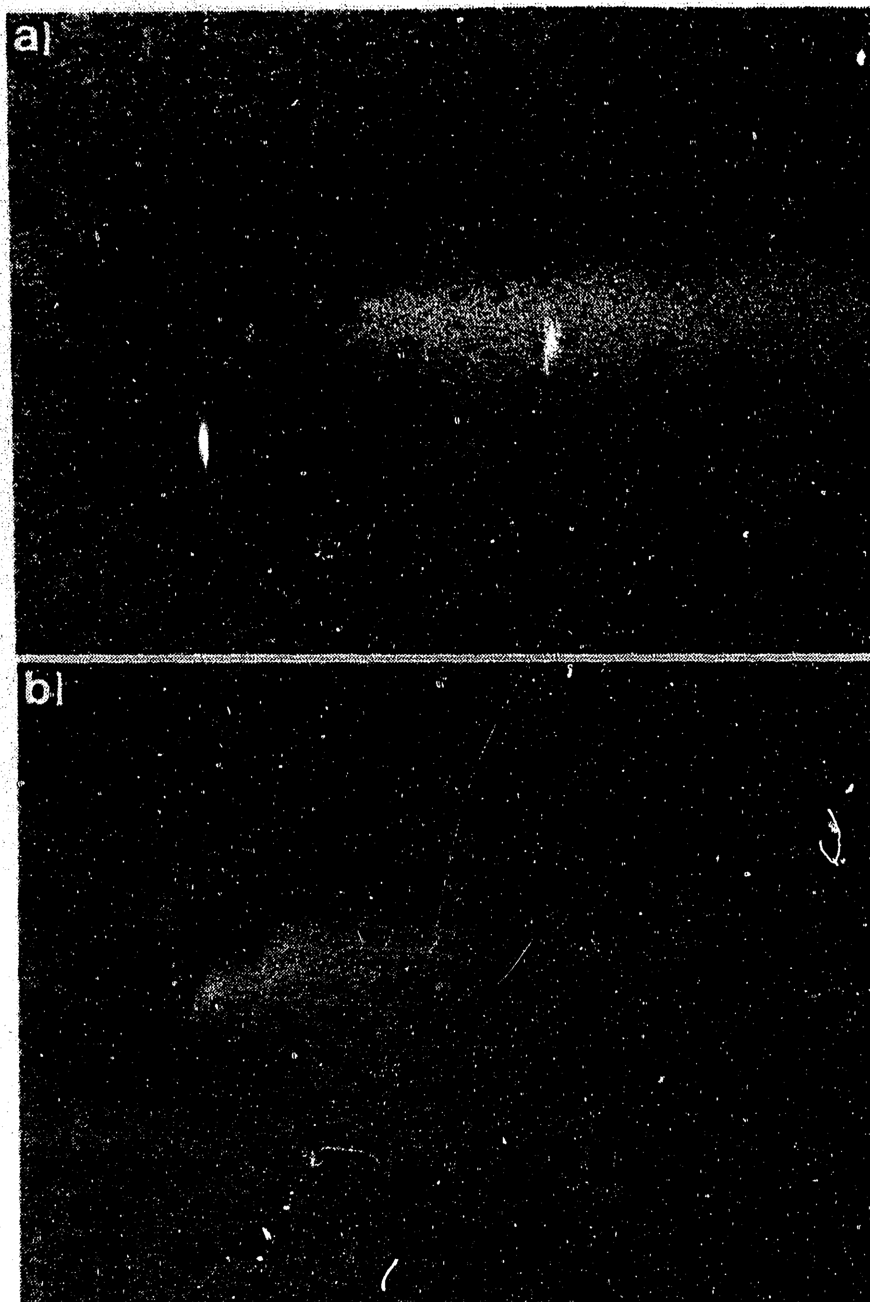

Figure 4-61. Optical micrographs illustrating the leveling effect of chemical treatment with 0.1% Br_2/MeOH for the rough and uneven surface morpology around a defect spot on a $CuInSe_2$ thin film (a) before and (b) after treatment at 30°C for 30 seconds

The etching power of aqueous KCN solution was found to be more selective than the Br_2/CH_3OH solution. In a solubility test of inorganic compounds, powders of CuSe, Cu_2S, CdS, sulfur, selenium, and electrodeposited Cu_xSe thin films dissolved rapidly in KCN solutions at room temperature. In contrast, single-crystal $CuInSe_2$, In_2Se_3 powder, and electrodeposited In_xSe thin films showed either no effect or very slow dissolution. The observations indicate that the KCN solution is capable of effectively removing excess selenium in the electrodeposited $CuInSe_2$ thin films and selectively etching away the Cu_xSe impurity phases, but leaving pure $CuInSe_2$ and indium selenides intact. The KCN etching mechanisms for selenium and Cu_2Se seem to involve the ring opening of Se_8 by CN^- followed by sequential breaking of selenium as $SeCN^-$ and the complexation of Cu^+ with CN^- ions into $[Cu(CN)_4]^{3-}$, respectively [88,89]. Table 4-5 shows the composition changes due to treatment in 0.50-M KCN for the electrodeposited $CuInSe_2$ before and after annealing and for the vacuum-evaporated copper-rich and indium-rich $CuInSe_2$ thin films. For the as-electrodeposited copper-rich films, KCN etching resulted in indium-rich films with a reduced percentage of selenium. Post-treatment annealing at 400°C for 1 hour showed little composition change. If the electrodeposited films were annealed prior to KCN treatment, the etching removed relatively small amounts of Cu_xSe and resulted in near stoichiometric or slightly indium-rich film composition. Similar results are obtained for vacuum-evaporated copper-rich film. In contrast, the indium-rich films showed nearly no composition change after KCN etching. If the as-electrodeposited copper-rich films were heated at 250°C for 20 minutes to remove excess selenium, the film compositions reached a constant value after 4 minutes of a 0.50-M KCN treatment. The final films are nearly stoichiometric.

XRD analysis was employed to examine the structural effects for the films that are KCN treated followed by annealing. For the as-electrodeposited copper-rich films, annealing at 400°C as usual would result in a chalcopyrite structure as discussed earlier. No change was observed after the films were subjected to KCN treatment. If the films were KCN-treated prior to annealing, their compositions became indium-rich (see Table 4-5). Follow-up annealing would result in a sphalerite structure since no characteristic peaks of chalcopyrite were observed in XRD spectra. The films were very resistive, just as the annealed films that were initially indium-rich as electrodeposited. The latter films would be even more indium-rich if KCN treatment was administered prior to annealing.

Chemical treatments were then used to further understand the thin film deposition and formation mechanisms. The thin film deposition/formation mechanism is derived from the results described in previous sections. First, we know that the as-deposited $CuInSe_2$ thin films possess excess selenium, which can be removed by heating at 250°C for 20 minutes. Second, earlier work demonstrated that the indium concentration in the film is closely related to the concentration of H_2SeO_3 in the solution (i.e., as the selenium deposition rate increased, the indium content in the film increased, indicating the deposition of indium required sufficient reaction sites provided by the selenium). Third, KCN treatment of the unannealed copper-rich and indium-rich films would decrease the Cu_xSe and selenium in the films and result in indium-rich films, but the same treatment on the annealed films showed a negligible effect, indicating that the as-deposited films are made of four components: $CuInSe_2$, Cu_xSe, In_xSe, and selenium. The relative amount of Cu_xSe and In_xSe determines

Table 4-5. Chemical Etching Effect on Film Composition

0.50-M KCN Etching Time (min/°C)	Film Composition (at. %) Before Cu/In/Se	After Cu/In/Se
2.5/40°C	21.70/18.48/59.41	21.83/25.46/52.72
1.0/40°C	22.23/21.62/56.16	20.87/26.32/52.81
(60/400°C)		21.59/26.69/51.72
(60/400°C)	25.08/24.50/50.42	
2.0/45°C		25.02/25.25/49.73
(350°C/evp)	26.77/23.94/49.30	
2.0/22°C		24.21/25.10/50.69
(450°C/evp)	23.76/25.74/50.50	
1.5/22°C		23.68/25.65/50.67

the overall film composition (whether KCN-treated or not) and the final structural characteristics after the films are annealed. Accordingly, the overall deposition reaction and thin film formation can be described qualitatively by the following equation:

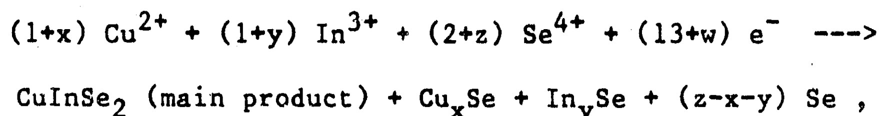

$$(1+x)\ Cu^{2+} + (1+y)\ In^{3+} + (2+z)\ Se^{4+} + (13+w)\ e^- \ \text{--->}$$

$$CuInSe_2\ \text{(main product)} + Cu_xSe + In_ySe + (z-x-y)\ Se\ ,$$

where $x,y,z < 1$ and represent the uncertainty of the exact values, and w is the number of excess electrons needed to meet the sum of x, y, and z.

Upon heating at 250°C, excess selenium is vaporized and the impurity phases of Cu_xSe and In_ySe partially combine into $CuInSe_2$. The combination increases as the annealing temperature and time are increased (see Figure 4-54). After annealing, only the remaining Cu_xSe will be etched off by KCN. If the unannealed films are treated with KCN, the net components will be only $CuInSe_2$ and In_ySe, which produce indium-rich films upon annealing.

4.7.4 Conclusion

The structural characteristics of electrodeposited $CuInSe_2$ thin films are investigated. Effects of annealing temperature and time on preferred orientation and grain size, film composition on chalcopyrite (ordering) - sphalerite (disordering) transition, presence of air during annealing, and chemical treatment on film composition and structure are systematically studied. The thin film deposition/formation mechanisms are accordingly derived.

4.8 Aggregates in Thin Film Polycrystalline $CuInSe_2$

Corroborating the Weizmann Institute of Science (WIS) results, "aggregate structures" in thin film $CuInSe_2$ on molybdenum on 7059 glass were observed using EBIC. The planar EBIC micrograph (Figure 4-62) illustrates the current loss (dark) at the aggregate boundaries. Quantitative EBIC line scans show the current loss at the boundaries (at 20 kV beam voltage) to range from ~20% to 50%. This behavior has only been observed where the molybdenum back contact has been deposited on 7059 glass, as compared to the more common soda lime glass, due to the difference in thermal expansion coefficients between the 7059 glass and the molybdenum back contact in conjunction with the heating during evaporation. The relevance for the technology, of course, is the current loss.

Ongoing collaborations with International Solar Electric Technology (ISET) revealed that no JEBIC shifts occurred in the material, in contrast to the deposited and sputtered $CuInSe_2$ cases. This effect indicated that there is either little or no oxygen in the material to be desorbed by the electron beam, or that whatever oxygen is in the material is stable with respect to the electron beam. SERI SIMS ion depth profiles, however, revealed that (the unsuspected) oxygen was present at a concentration approximately five times that of the evaporated films ($\sim 5 \times 10^{19}$ cm^{-3}). Follow-up experiments with hydrazine treatments (an oxygen scavenger) of the ISET devices exhibited considerably diminished performance -- as has been the case in the evaporated films that clearly depend on oxygen for optimal performance. Having noted a high concentration of oxygen in ISET's material and its electronic role, the question becomes what role the oxygen is playing, if different from what is suspected in the evaporated film case (passivation of donor defects on the grain surfaces).

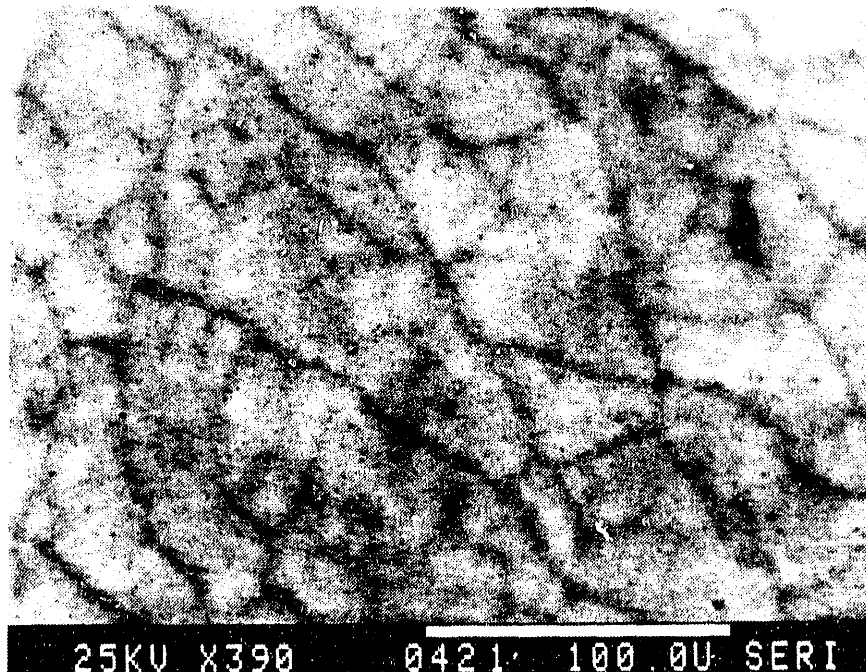

Figure 4-62. Planar EBIC micrograph for a $CuInSe_2$ film on Mo/7059 glass

4.9 References

1. J.L. Shay and J.H. Wernick, Ternary Chalcopyrite Semiconductors: Growth, Electronic Properties, and Applications (Fermagon Press, Oxford), 1975.

2. J.C.W. Folmer, J.A. Turner, R. Noufi, and D. Cahen, J. Electrochem. Soc. 132 (1985) p. 1319.

3. K. Mitchell, C. Eberspacher, J. Ermer, and D. Pier, in Proceedings of the 20th IEEE PV Specialists Conference, Las Vegas, NV (IEEE, New York), 1989, p. 1384.

4. R. Noufi, R. Axton, C. Herrington, and S.K. Deb, Appl. Phys. Lett. 45 (1984) p. 668.

5. D.S. Albin, R. Noufi, and J. Tuttle, J. Appl. Phys. 64 (1988) p. 4903.

6. D.S. Albin, J.R. Tuttle, J. Goral, A. Mason, R. Noufi, and S.H. Risbud, in Proceedings of the 20th IEEE PV Specialists Conference, Las Vegas, NV (IEEE, New York), 1989, p. 1495.

7. J.R. Tuttle, D. Albin, J. Goral, C. Kennedy, and R. Noufi, Solar Cells 24 (1988) p. 67.

8. V. Ramanathan, T. Datta, and R. Noufi, Appl. Phys. Lett. 51 (1987) p. 746.

9. R. Vaidhyanathan, R. Noufi, T. Datta, R.C. Powell, and S.K. Deb, in Proceedings of the 15th IEEE PV Specialists Conference, Orlando, FL (IEEE, New York), 1981, p. 1054.

10. T. Datta, R. Noufi, and S.K. Deb, J. Appl. Phys. 59 (1986) p. 1548.

11. T. Datta, R. Noufi, and S.K. Deb, Appl. Phys. Lett. 47 (1985) p. 1102.

12. R.J. Matson, R. Noufi, D. Ahrenkiel, R.C. Powell, and D. Cahen, Solar Cells 16 (1986) p. 495.

13. J.D. Meakin, SPIE J. 543 (1985) p. 108.

14. T.J. Coutts and C.R. Osterwald, Solar Cells 22 (1987) p. 201.

15. R. Noufi and J. Dick, J. Appl. Phys. 58 (1985) p. 3884.

16. O.S. Heavens, Optical Properties of Thin Solid Films, (Butterworth, London), 1955.

17. R.E. Denton, R.D. Campbell, and S.G. Tomlin, J. Phys. D: Appl. Phys. 5 (1972) p. 852.

18. C.L. Nagendra and G.K.M. Thutupalli, Applied Optics 20 (1981) p. 2747.

19. W. Hôrig, H. Neumann, V. Savalev, and J. Lagzdonis, Phys. Lett. 78A (1980) p. 189.

20. D.E. Aspnes, AT&T Laboratories, private communication.

21. I. Filinski, Phys. Stat. Sol. (b) 49 (1972) p. 577.

22. J. Szczyrbowski and A. Czapla, Thin Solid Films 46 (1977) p. 127.

23. R. Swanepoel, J. Phys. E: Sci. Instrum. 17 (1984) p. 896.

24. G. Haas and R.E. Thun, Physics of Thin Films (Academic Press, New York), 1967.

25. H.E. Bennett and J.O. Porteus, J. Opt. Soc of Amer. 51 (1961) p. 123.

26. L.S. Palatnik and E.I. Rogacheva, Sov. Phys. Doklady 12 (1967) p. 503.

27. K.W. Böer, Solar Cells 16 (1986) p. 591.

28. A. Rothwarf, Solar Cells 16 (1986) p. 567.

29. R.A. Mickelson and W.S. Chen, in Proceedings of the 16th IEEE Photovoltaic Specialists Conference, San Diego, CA (IEEE, New York), 1982, p. 784.

30. H.J. Leamy, J. Appl. Phys. 53 (1982) p. R51.

31. A. Rothwarf, in Proceedings of the 18th IEEE Photovoltaic Specialists Conference, Las Vegas, NV (IEEE, New York), 1985, p. 1424.

32. K. Mitchell, C. Eberspacher, J. Ermer, and D. Pier, in Proceedings of the 20th IEEE Photovoltaic Specialists Conference, Las Vegas, NV (IEEE, New York), 1989, p. 1384.

33. J.R. Tuttle, D. Albin, J. Goral, C. Kennedy, and R. Noufi, Solar Cells 24 (1988) p. 67.

34. J.R. Tuttle, D.S. Albin, R.J. Matson, and R. Noufi, J. Appl. Phys, in press.

35. D.S. Albin, J.R. Tuttle, J. Goral, A. Mason, R. Noufi, and S.H. Risbud, Proceedings of the 20th IEEE Photovoltaic Specialists Conference Las Vegas, NV (IEEE, New York), 1989, p. 1495.

36. L.S. Palatnik and E.I. Rogacheva, Sov. Phys. Doklady 12 (1967) p. 503.

37. H. Hallak, D.S. Albin, and R. Noufi, Appl. Phys. Lett., in press.

38. K. Mitchell, C. Eberspacher, J. Ermer, and D. Pier, in Proceedings of the 20th IEEE Photovoltaic Specialists Conference Las Vegas, NV (IEEE, New York), 1989, pp. 1384-1389.

39. W. H. Bloss, J. Kunmerle, F. Pfisterer, and H. W. Schock, in Proceedings of the 17th IEEE Photovoltaic Specialists Conference Kissimmee, FL (IEEE, New York), 1984, pp. 715-720.

40. R. Noufi, R. Powell, C. Herrington, and T. Coutts, Solar Cells 17 (1986) p. 303.

41. B. Dimmler, H. Dittrich, R. Menner, and H. W. Schock, in Proceedings of the 19th IEEE Photovoltaic Specialists Conference, New Orleans, LA (IEEE, New York), 1987, pp. 1454-1460.

42. J. Tuttle, D. Albin, J. Goral, C. Kennedy, and R. Noufi, Solar Cells 24 (1988) p. 67.

43. D. Albin, R. Noufi, J. Tuttle, and J. Goral, J. Appl. Phys. 64:10 (1988) p. 4903.

44. B. D. Cullity, Elements of X-ray Diffraction (Addison-Wesley Publishing Co., Inc., New York), 1978, p. 359.

45. L. Mandel, R. D. Tomlinson, and M. J. Hampshire, J. Appl. Cryst. 10 (1977) p. 130.

46. B. Grzeta-Pleukovic, S. Popovic, B. Celustka, and B. Sautec, J. Appl. Cryst. 13 (1980) p. 311.

47. J. E. Jaffe and A. Zunger, Phys. Rev. B28 (1983) p. 5822.

48. L. S. Palatnik and E. K. Belova, Izv. Akad. Nauk SSSR, Neorgan. Mater. 3 (1967) p. 967.

49. J. C. Mikkelsen, J. Electron. Mater. 10:3 (1981) p. 541.

50. W. D. Kingery, H. K. Bowen, and D. R. Uhlmann, Introduction to Ceramics, (John Wiley and Sons), 1976.

51. Karasaev, Sadumkin, and Kukhno, Zh. Fiz. Khim. 41 (1967) p. 654.

52. Korolkov and Igumnova, Izv. A. N., OTN 6 (1961) p. 95.

53. W. Arndt, B. Dimmler, H. Dittrich, J. Kimmerle, R. Menner, F. Pfisterer, and H. W. Schock, in Proceedings of the 20th IEEE Photovoltaic Specialists Conference, Las Vegas, NV (IEEE, New York), 1988.

54. J. Tuttle, D. Albin, J. Goral, C. Kennedy, and R. Noufi, Solar Cells 24 (1988) p. 67.

55. B. Dimmler, H. Dittrich, R. Menner, and H. W. Schock, in Proceedings of the 19th IEEE Photovoltaic Specialists Conference, New Orleans, LA (IEEE, New York), 1987, pp. 1454-1460.

56. R. Noufi and J. Dick, J. Appl. Phys. 58:10 (1985) p. 3884.

57. J. L. Freeouf and J. M. Woodall, Appl. Phys. Lett. 39 (1981) p. 727.

58. S. D. Offsey, J. M. Woodall, A. C. Warren, P. D. Kirchner, T. I. Chappel, and G. D. Pettit, Appl. Phys. Lett. 48 (1986) p. 475.

59. S. Mrowec, Defects and Diffusion in Solids - An Introduction (Elsevier Scientific Publishing, Materials Science Monographs, 5), 1980.

60. J. S. Anderson, Defects in Oxides, National Bureau of Standards, Special Publication No. 364, 1972.

61. S. C. Abrahams and J. L. Bernstein, J. Chem. Phys. 61 (1974) p. 1140.

62. J. E. Jaffe and A. Zunger, Phys. Rev. B28:10 (1983) p. 5822.

63. B. Grzeta-Plenkovic, S. Popovic, B. Celustka, and B. Santic., J. Appl. Cryst. 13 (1980) p. 311.

64. L. Mandel, R. D. Tomlinson, and M. J. Hampshire, J. Appl. Cryst. 10 (1980) p. 130.

65. T. F. Ciszek, C. D. Evans, and S. K. Deb, "Ternary and Multinary Compounds," in Proceedings of the 7th International Conference, S. K. Deb and A. Zunger, eds., (Materials Research Society), 1987, p. 195.

66. D. Albin, R. Noufi, J. Tuttle, and S. H. Risbud, to be published in Conference Proceedings of the "Advanced Characterization Techniques for Ceramics" Symposium, 41st Meeting of the American Ceramic Society; West Coast Regional.

67. D. Albin, R. Noufi, J. Tuttle, J. Goral, and S. H. Risbud, J. Appl. Phys. 64:10 (1988) p. 4903.

68. R.A. Mickelson and W.S. Chen, in Proceedings of the 16th IEEE Photovoltaic Specialists Conference, San Diego, CA, Sept. 27-30, 1982 (IEEE, New York), 1982, pp. 781-785.

69. R.A. Mickelson and W.S. Chen, in Proceedings of the 7th International Conference on Ternary and Multinary Compounds, Snowmass, CO, Sept. 10-12, 1986 (MRS, Pittsburgh), 1986, pp. 39-47.

70. K. W. Mitchell, C. E. Eberspacher, J. Ermer, K. Pauls, and D. Pier, in Proceedings of the Polycrystalline Thin Film Program Meeting, SERI/CP-211-3550, Lakewood, CO, August 16-17, 1989, (SERI, Golden, CO), 1989, pp. 199-205.

71. N.G. Dhere, M.C. Lourenco, R.G. Dhere, and L. L. Kazmerski, Solar Cells 16 (1986) pp. 369-380.

72. E. R. Don, R. Hill, and G. J. Russell, Solar Cells 16 (1986) pp. 131-142.

73. S. Isomura, A. Nagamatsu, K. Shinohara, and T. Aono, Solar Cells 16 (1986) pp. 143-153.

74. I. Shih and C.X. Qiu, in Proceedings of the 19th IEEE Photovoltaic Specialists Conference, New Orleans, LA, May 4-8, 1987 (IEEE, New York), 1987, pp. 1291-1294.

75. C.X. Qiu and I. Shih, Solar Energy Materials 15 (1987) pp. 219-223.

76. C.X. Qiu and I. Shih, Can. J. Phys. 65 (1987) pp. 1011-1014.

77. F.J. Pern, R. Noufi, A. Mason, and A. Swartzlander, in Proceedings of the 19th IEEE Photovoltaic Specialists Conference, New Orleans, LA, May 4-8, 1987 (IEEE, New York), 1987, pp. 1295-1298.

78. F.J. Pern, J. Goral, R.J. Matson, T.A. Gessert, and R. Noufi, Solar Cells 24 (1988) pp. 81-90.

79. F.J. Pern, A. Mason, and R. Noufi, Presented in the 174th J. Electrochem. Soc. Meeting in Chicago, IL, Oct. 9-14, 1988.

80. D. Pottier and G. Maurin, J. Appl. Electrochem. 19 (1989) pp. 361-367.

81. Y. Ueno, H. Kawai, T. Sugiura, and H. Minoura, Thin Solid Films 157 (1988) pp. 159-168.

82. F.K. Lotgering, J. Inorg. Nucl. Chem. 9 (1959) p. 113.

83. J.U. Knickerbocker and D.A. Payne, Ferroelectrics 37 (1981) pp. 733-736.

84. H. Lipson and H. Steeple, Interpretation of X-Ray Powder Diffraction Patterns (Macmillan, London), 1970.

85. L.S. Palatnik and E.I. Rogachev, Dokl. 12 (1967) p. 503.

86. M.L. Fearheiley, Solar Cells 16 (1986) pp. 91-100, and references cited therein.

87. M.A. Ryan, M. W. Peterson, D.L. Williamson, J.S. Frey, G.E. Maciel, and B.A. Parkinson, J. Mater. Res. 2 (1987) pp. 528-537.

88. F.A. Cotton and G. Wilkinson, Advanced Inorganic Chemistry, 3rd ed., Chapters 15, 22, and 25 (Wiley, New York), 1977.

89. Stability Constants of Metal-Ion Complexes, Section I: "Inorganic Ligands," compiled by Lars Gunnar Sillen, The Chemical Society (Burlington House, London), 1964, p. 110.

5.0 III-V HIGH-EFFICIENCY PHOTOVOLTAIC CELLS

Investigators

J. M. Olson, Senior Scientist and Group Leader
E. E. Beck, Technician
A. E. Blakeslee, Senior Scientist
A. E. Kibbler, Staff Scientist
S. R. Kurtz, Staff Scientist
P. J. M. Faine, Visiting Professional

5.1 Introduction

The objective of this work is to develop an understanding of, and solutions to, the problems inherent in the fabrication of high-efficiency, multijunction cascade solar cells using such III-V semiconductor materials as GaAs, GaP, InP, GaInP, and AlGaAs. The major areas of research include metal-organic chemical vapor deposition (MOCVD), material analysis, and device fabrication and characterization.

Most of the past year's work has been directed toward the development of the lattice- and current-matched $Ga_{0.5}In_{0.5}P$/GaAs cascade solar cell. This cell has a one-sun, air-mass (AM) 1.5 theoretical efficiency of 34%, but exhibits few of the problems typical of lattice-mismatched heterostructures. Progress and highlights in this area are presented and discussed.

5.2 High-Efficiency Solar Cells

5.2.1 $Ga_{0.5}In_{0.5}P$/GaAs Tandem Solar Cell

Multijunction photovoltaic cells have the potential for achieving solar energy conversion efficiencies in excess of 30% [1]. The simplest multijunction device is a monolithic, two-terminal, two-junction structure. The two junctions are stacked vertically. The top junction is designed to absorb and to convert the blue portion of the solar spectrum. The bottom junction absorbs and converts the red portion of the spectrum that is not absorbed by the top junction. To achieve maximum energy conversion efficiency, the junctions must be fabricated from materials that are of high electronic quality. They must also be current matched, i.e., they must generate equal currents when exposed in the tandem configuration to the solar spectrum. The current matching is determined by the relative band-gap energies of the two materials.

For a monolithic, two-junction tandem device epitaxially deposited on a substrate that also serves as the bottom cell, the quality of the top cell generally will be adversely affected by any lattice mismatch between the bottom and top cell materials. Heretofore, current-matched semiconductors with band-gap energies of 1.1 eV and 1.7 eV have received the most attention. This combination of band gaps yields the maximum AM1.5 conversion efficiency of 36% [1]. However, there does not exist within the III-V alloy system a material that is both current- and lattice-matched to an inexpensive, commercially available bottom-cell substrate material with a band gap of

1.1 eV (such as silicon). For the band-gap combination of 1.4 eV and 1.9 eV, the maximum theoretical AM1.5 efficiency is 34% [1]. GaAs has a band gap of 1.42 eV, and at least two III-V alloys exist with band gaps of 1.9 eV that are also lattice-matched to GaAs, namely $Al_{0.4}Ga_{0.6}As$ and $Ga_{0.5}In_{0.5}P$ (hereafter, $GaInP_2$). The $Al_{0.4}Ga_{0.6}As$/GaAs system has been studied in the past [2] but with mixed results, presumably because of problems with the growth of high-quality, oxygen-free AlGaAs and the fabrication of a high-conductance cell interconnect. The tandem combination of GaAs and $GaInP_2$ has received relatively little attention despite the fact that it exhibits few of the problems commonly encountered with AlGaAs.

In this discussion, we report the details of the fabrication and characterization of a two-terminal $GaInP_2$/GaAs tandem device with an efficiency of 27.3% (one-sun, AM1.5). Advantages and problems unique to $GaInP_2$ will also be discussed. We will show, for example, that the electronic quality of $GaInP_2$ is relatively insensitive to wide variations in the growth conditions, and that the design of the device structure must account for the well-known band gap anomaly in $GaInP_2$.

A schematic of the $GaInP_2$/GaAs monolithic cascade cell is shown in Figure 5-1. The structure was grown in a vertical, air-cooled reactor at one atmosphere using MOCVD, the detailed aspects of which are described elsewhere [3,4]. The group III source gases were trimethylindium, trimethylgallium, and trimethylaluminum; the group V source gases were arsine and phosphine. The dopant sources were diethylzinc and hydrogen selenide. The arsine and phosphine were purified on-line by passing them over a gettering compound supplied by Advanced Technology Materials, Inc. (ATM) (see Section 5.5). The optoelectronic properties [5] and photovoltaic quality [4] of the materials listed above are complex and coupled functions of the growth temperature, T_g, the V/III ratio, composition, dopant type and concentration, and substrate quality. The effects of some of these factors are presented below. Generally, however, the cascade device is grown at T_g = 700°C. The phosphides are grown with V/III = 30 and a growth rate of 80-100 nm/min; the arsenides are grown with V/III = 35 and a growth rate of 120-150 nm/min, with the exception of the GaAs tunnel diode, which is grown at a rate of 40 nm/min.

The absorbers of both subcells are doped with zinc to a level of $1\text{-}4 \times 10^{17}/cm^3$. The emitters and window layers are doped with selenium at about $10^{18}/cm^3$. Both layers of the GaAs tunnel diode are heavily doped at concentrations approaching $10^{19}/cm^3$. Tunnel diodes grown under conditions simulating the fabrication of a full cascade device have a series resistance of $10^{-3}\text{-}10^{-2}$ ohm cm^2, and exhibit other characteristics that are similar to those reported by Saletes et al. [6]. For example, they are relatively stable at 700°C for at least 30-40 min.

The front and back contacts to all the devices reported in this section were of electroplated gold. Because of the high dopant concentration in both the GaAs substrate and the top GaAs contacting layer (not shown in Figure 5-1), no thermal annealing of either contact is required. The front contact is defined by photolithography and obscures approximately 5% of the total cell area. The cell perimeter is also defined by photolithography and a mesa etch that uses a sequential combination of concentrated hydrochloric acid and an ammonia:peroxide:water solution. The ammonia/peroxide solution is also used to remove the GaAs contacting layer between the gold grid fingers. The

antireflection coating (ARC) is a double layer of evaporated ZnS and MgF_2, with thicknesses of 60 and 120 nm, respectively.

The cell efficiency was measured using the multisource simulator method of Glatfelter and Burdick [7]. The simulated solar spectrum was adjusted using two reference cells. One reference cell was a $GaInP_2$ top cell and the second was a GaAs cell coated with the GaAs tunnel junction and a layer of $GaInP_2$ to simulate the optical transmission to the GaAs bottom cell in the actual tandem device. The spectrum of the simulator was adjusted with filters until both reference cells produced the correct ASTM E892-87 global, short-circuit current at 1000 W/cm^2. Using this spectrum, the current of the cascade cell was then measured.

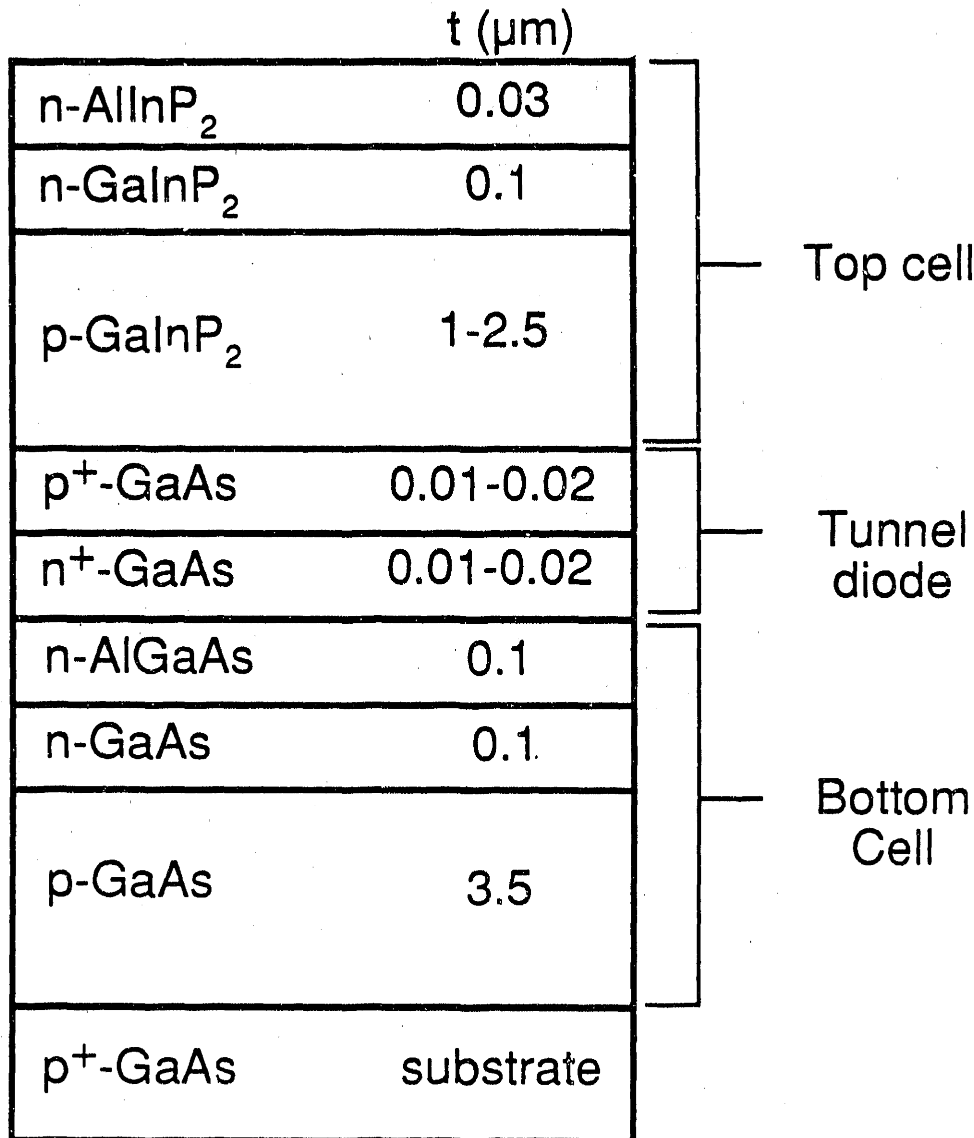

Figure 5-1. Schematic cross section of the $GaInP_2$/GaAs tandem structure. An electroplated gold grid on a heavily doped n-type GaAs contacting layer is not shown.

The best efficiency measured to date for this device is 27.3% (one sun, AM1.5). The short-circuit current density (J_{sc}), open circuit voltage (V_{oc}), and fill factor (FF), were 13.6 mA/cm^2, 2.29 V, and 0.87, respectively. The area of this device was 0.25 cm^2 and the band gap of the top cell was 1.85 eV. This is the highest efficiency reported for a two-terminal, tunnel-junction-interconnected tandem photovoltaic device and represents a significant improvement with respect to our previously reported work [4]. Recently, Chung et al. [8] have reported a 27.6%-efficient monolithic AlGaAs/GaAs solar cell. This device has a metal, as opposed to a tunnel-junction, interconnect and includes a prismatic cover slip to eliminate the photocurrent loss associated with grid shadowing. In our case, the use of the prismatic cover slip would boost the efficiency from 27.3% to 28.7%.

Numerous factors affect the efficiency of multijunction solar cells. They include the electronic quality of the top and bottom cell materials, the band gap and thickness of the top cell, the design of the ARC, and the thickness and passivating properties of the window layers. Some of these factors are discussed in the following paragraphs. The bulk electronic quality of $GaInP_2$ as a function of growth parameters is illustrated in Figures 5-2(a) and 5-2(b). Plotted is the relative white-light photocurrent generated at an electrolyte/$GaInP_2$ junction as a function of the $GaInP_2$ growth temperature, the V/III ratio and lattice mismatch between the GaInP and the GaAs. This photocurrent is a function mainly of the minority carrier diffusion length in the $GaInP_2$ and, therefore, is a suitable quantity to use as a measure of quality [9]. The highest relative currents shown in Figure 5-2(a) for $GaInP_2$ are indicative of a minority carrier diffusion length in the range of 3-6 μm and a peak internal quantum efficiency of about 90%. The evidence in Figure 5-2(a) indicates that the quality of $GaInP_2$ is relatively insensitive to T_g and V/III. This finding is contrary to previous reports where the photoluminescence intensity of $GaInP_2$ grown by MOCVD was found to increase by a factor of 10^3 when the growth temperature [10] decreased from 675° to 650°C or the V/III ratio [11] increased from 100 to 200.

The effect of lattice mismatch is shown in Figure 5-2(b). The lattice mismatch (proportional to $\Delta\theta$, the Bragg peak separation) is measured using the rocking mode x-ray diffraction technique. As expected, the photocurrent decreases rapidly for tensional strains greater than some critical mismatch strain. For material grown in compression, the photocurrent increases with increasing mismatch. This increase is due to a concomitant decrease in the band gap of the $Ga_xIn_{1-x}P$. This result is contrary to a previous report [12] that suggested that precise control of the composition of $GaInP_2$ was required to achieve device-quality material.

A model that couples the optical properties of the double layer ARC with those of the underlying junction's materials was developed for this study. The reflection coefficient (R) of an $AlInP_2$-coated $GaInP_2$ epilayer is about 30% for wavelengths between 450 and 900 nm. A ZnS and MgF_2 ARC with thicknesses of 60 and 120 nm, respectively, reduces R to less than 2% over the same range of wavelengths. While these thicknesses are close to those calculated from simple quarter wavelength considerations, the detailed effects of these antireflection layers is considerably more complicated. For example, the optical modeling studies show that the current matching between the top and bottom cells is a strong function of the ZnS and MgF_2 thicknesses. Further details will be discussed in a future paper.

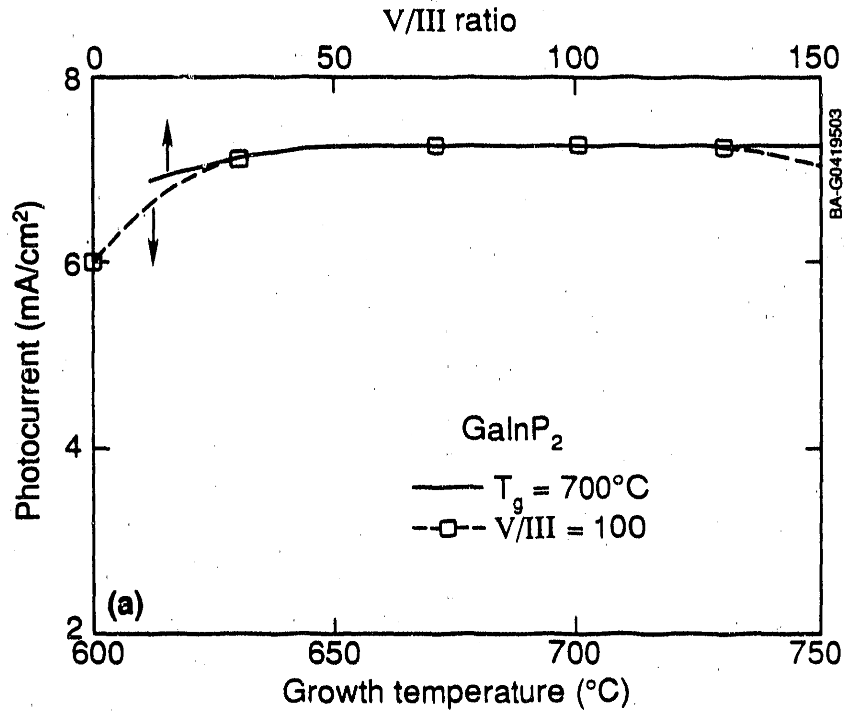

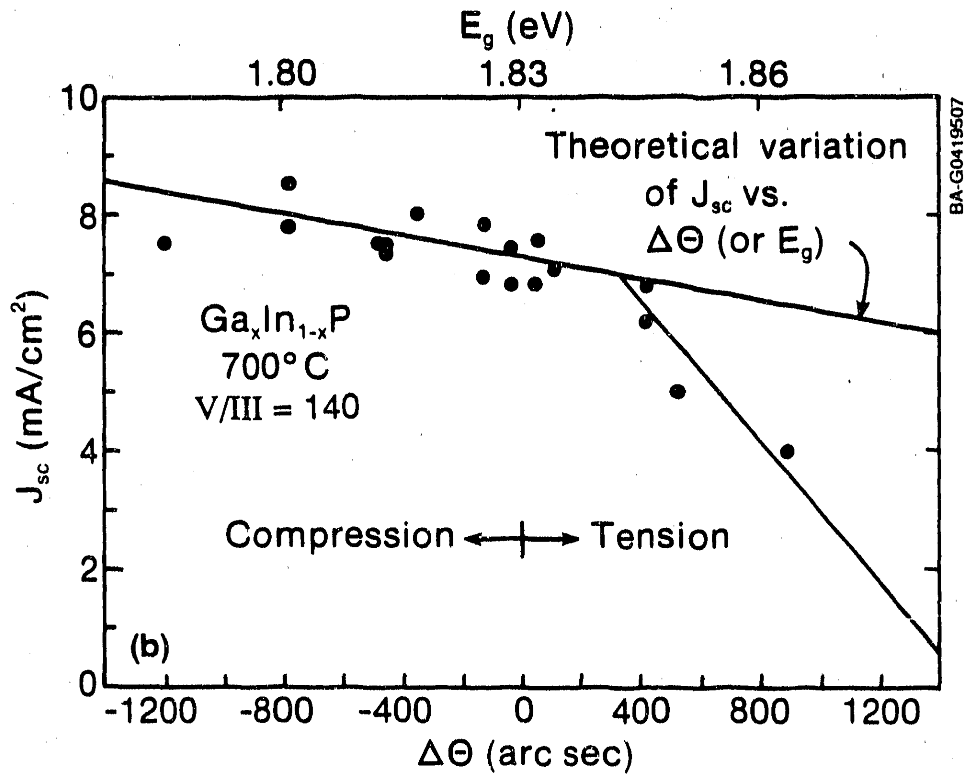

Figure 5-2. **Photocurrent versus (a) T_g and V/III for $GaInP_2$, and (b) band gap or lattice mismatch as measured by x-ray diffraction.** A $\Delta\Theta$ of 100 arc-s corresponds to a lattice mismatch of about 3.5×10^{-4}.

Using a similar optical model, we have calculated that a 30-nm layer of AlInP and 30-nm-thick GaAs tunnel junction each absorb approximately 3% of the light destined for the respective underlying subcell. It is reasonable to assume that most of this light is not converted into external current, and the tandem cell current therefore suffers a net loss of 3%.

It has been shown that AlInP passivates the surface of GaAs [13], reducing the surface recombination velocity (S) to less than 1000 cm/s. For the $AlInP_2$/$GaInP_2$ interface, S has not been measured. However, controlled experiments have shown that the blue response and total short-circuit current density of $GaInP_2$ solar cells are enhanced by the use of an AlInP window layer.

For the $GaInP_2$/GaAs tandem cell, a significant potential loss mechanism is associated with current matching between the top and bottom cells. As stated in the introduction, the top cell and bottom cell currents (J_T and J_B, respectively) are determined primarily by the band gaps of the top and bottom cell materials. It was assumed in previous treatments of this problem that the subcells were infinitely thick and that quantum efficiencies were equal to 100%. With these assumptions, for a bottom cell band gap of 1.42 eV, the optimum top cell band gap for an AM1.5 solar spectrum is 1.93 eV. Since the nominal or classical band gap of $GaInP_2$ is 1.9 eV, we expect that for a thick, high-quality $GaInP_2$ top cell on a GaAs bottom cell, $J_T/J_B > 1$. To make matters worse, the band gap of OMCVD-grown $GaInP_2$ can be as low as 1.82 eV. The solution to this problem is to reduce the thickness of the $GaInP_2$ top cell. A calculation of the expected effect is shown graphically in Figure 5-3. These calculations suggest that top cell thicknesses in the range of 500-1000 nm, depending on the top cell band gap and quantum efficiency, should yield a current-matched tandem structure at a current level that changes only slightly with top cell band gap. The device in Figure 5-1 has a top cell band gap of 1.85 eV and a top cell thickness of 0.8 μm. This thickness is slightly larger than the optimum value, so that this device may not be current matched. Efforts to reduce the thickness of the $GaInP_2$ top cell and achieve higher conversion efficiencies are currently under way.

5.2.2 GaAs Heteroface Solar Cells

A GaAs n-on-p homojunction with a thin $GaInP_2$ window layer and a $GaInP_2$/GaAs back surface heterointerface was fabricated with a one-sun, AM1.5 efficiency of 25%. The V_{oc}, J_{sc}, and FF for this device are 1.05 V, 27.8 mA/cm^2, and 85.6%, respectively. The cell's I-V plot is shown in Figure 5-4. A schematic of the device structure is shown in Figure 5-5. The cell has a total area of 0.249 cm^2 with a grid coverage of about 5%. It is similar in design to a conventional AlGaAs/GaAs heteroface cell except that the AlGaAs window layer and back surface heterobarrier are replaced with $GaInP_2$. The $GaInP_2$ is lattice-matched to GaAs and has a band gap of about 1.85 eV in this case. The $GaInP_2$/GaAs interface has been shown previously [13] to exhibit ultralow interface recombination velocities.

The device was grown at 700°C using conventional, atmospheric pressure MOCVD as described in Section 5.2.1. The ratio of V/III = 30. The photovoltaic quality of both $GaInP_2$ and GaAs is relatively insensitive to growth conditions and to trace levels of oxygen and water. Consequently, no extraordinary treatments of the source gases were required for the growth of this device and

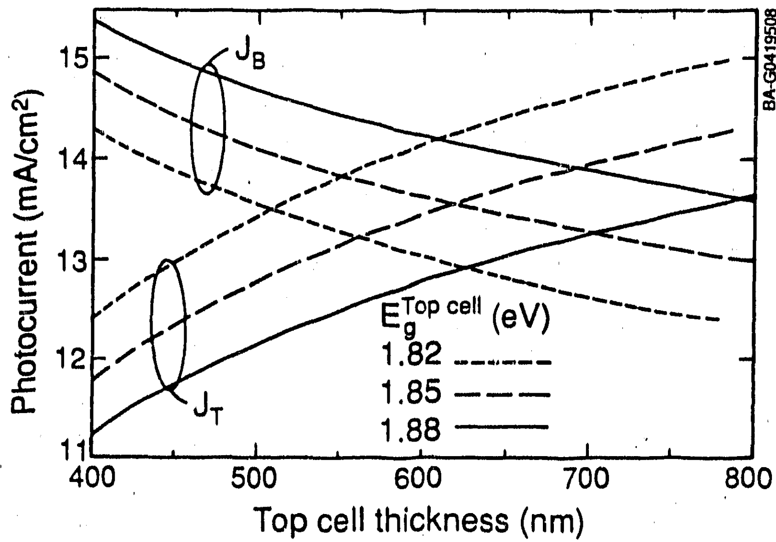

Figure 5-3. Calculated top and bottom cell current densities (J_T and J_B, respectively) as a function of $GaInP_2$ top cell thickness for three different $GaInP_2$ band gaps. In a series-connected tandem cell, the cell current is limited by the smaller subcell current. Maximum efficiency for a given band gap occurs when $J_T = J_B$.

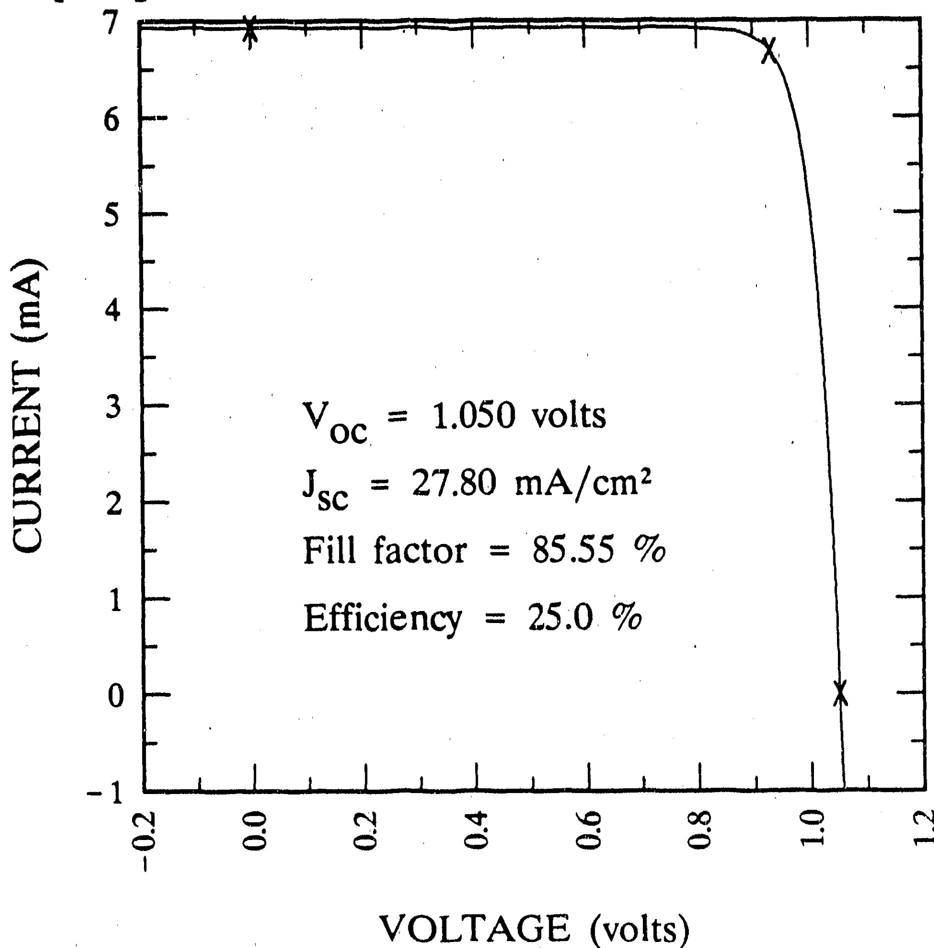

Figure 5-4. The current versus voltage plot for the device in Fig. 5-5 under one-sun illumination

Layer	t (micron)	
MgF_2	0.12	COATING
ZnS	0.065	
n - $GaInP_2$	0.03	CELL
n+ - GaAs	0.1	
p - GaAs	3.5	
p - $GaInP_2$	0.1	
p+ - GaAs	substrate	

Figure 5-5. Schematic cross section of the GaAs heteroface solar cell. The contacting and metalization layers are not shown.

we expect that the efficiency of this device will not change significantly for growth temperatures in the range of 600°-750°C.

As with the tandem device described in Section 5.2.1, the absorber is doped to a level of 1-4 $\times$ $10^{17}/cm^3$, while the emitter is doped to about $10^{18}/cm^3$. Both front and back contacts were also essentially the same as described in Section 5.2.1. A double ARC of evaporated ZnS and MgF_2 was applied to the finished device.

Compared to previous work, this record high efficiency and high V_{oc} are attributed to the low interface recombination velocity ($S < 2$ cm/s) of the $GaInP_2$/GaAs heterointerface [13]. This low S reduces the dark current in the device, yielding a higher V_{oc}.

Other than the insensitivity of $GaInP_2$ to oxygen and water, its use as a window layer would appear to be inferior to that of AlGaAs. The band gap is relatively low and according to Olsen et al. [12], the composition must be precisely controlled to maintain a lattice-matched and, therefore, low S interface with GaAs. However, preliminary experiments indicate that for thin (<30 nm) $GaInP_2$ window layers, neither of these poses serious problems. Figure 5-6 shows the external quantum efficiency of a comparable GaAs cell with a thin $GaInP_2$ window layer. There is no dramatic drop in the quantum efficiency for wavelengths shorter than 670 nm. This finding could imply that there is significant collection of the minority carriers generated within the $GaInP_2$ window layer. Other experiments have shown that the composition of the $GaInP_2$ can be adjusted by 10% with no measureable change in the efficiency of these devices.

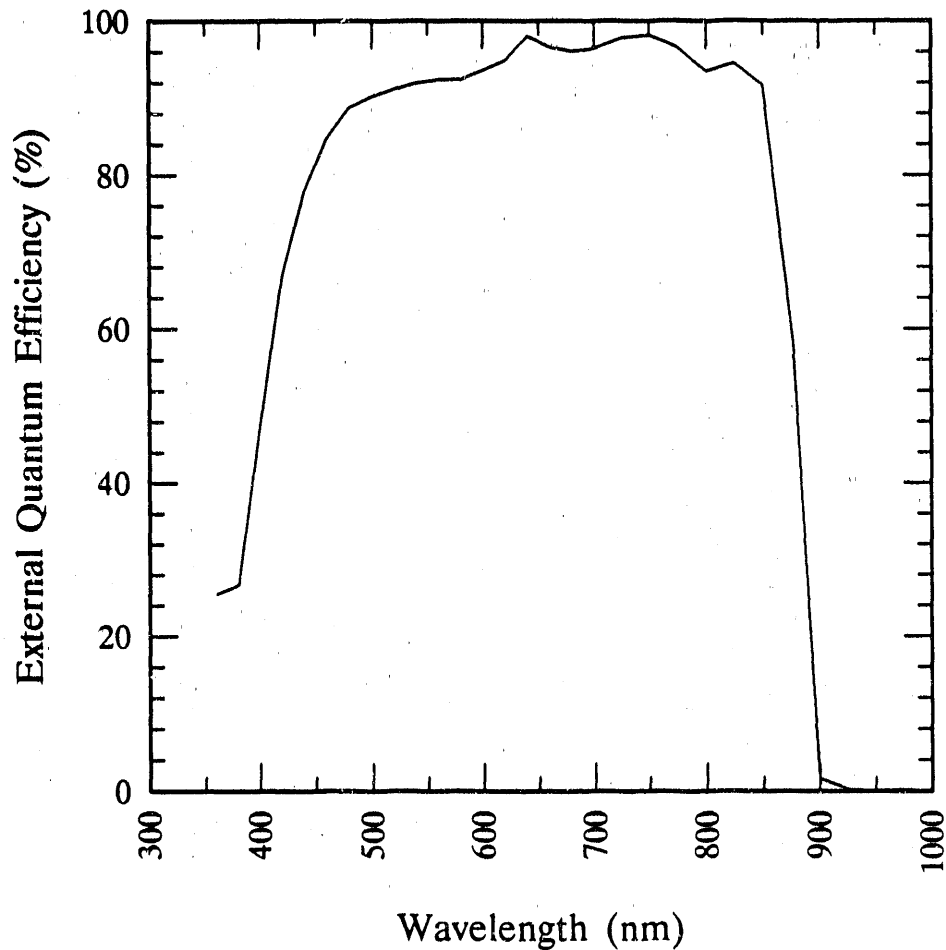

Figure 5-6. External quantum efficiency versus wavelength for the device in Fig. 5-4

5.3 Modeling of Tandem Solar Cells

The theoretical efficiency of a single-junction solar cell depends on the band gap [14]. If a high band gap is chosen to obtain a high-voltage cell, the current is low because most of the solar spectrum is sub-band-gap light and, therefore, is not absorbed. If the band gap is decreased so that most of the spectrum is absorbed, then the voltage of the cell is decreased. By using a multijunction cell, it is possible to obtain a high-voltage cell while still effectively collecting the low-energy photons. Despite the large potential gain in efficiency, it is only recently that two-junction tandem solar cells have surpassed the highest efficiencies reported for single-junction cells [15,8].

The theoretical efficiencies of two-junction tandem solar cells have been reported [1,16,17] to be strong functions of the band-gap choices for the top and bottom cells unless four-terminal devices are used. In practice, four-terminal cells tend to be impractical since the cost of the cells is usually doubled and the problems of heat-sink design are significantly greater. The series-connected, two-junction configuration has always been considered the most practical but has been discouraged since the theoretical models have shown only a narrow range of band-gap combinations to yield potentially high efficiencies [1,16,17]. From this small range, only a handful of material combinations exists.

Here we report the theoretical efficiencies of series-connected, two-junction solar cells with optimized top cell thicknesses. Reduction of the top cell thickness results in significant increases in the efficiencies for a range of band-gap combinations. The primary increase in efficiency results from an increase in current as the top cell thickness is optimized. For ideal cells (i.e., cells with low surface-recombination velocities), the thinner top cells also lead to increased values of V_{oc}, resulting in even greater improvements in the efficiencies. In practice, the top cell thickness is a parameter that can be controlled easily and accurately. Thus, a number of new material combinations can be considered as candidates for high-efficiency, two-junction solar cells.

The theoretical solar cell efficiencies were calculated for AM1.5 global, AM1.5 direct normal, and, in some cases, AM0 spectra, using the irradiance standards published by Hulstrom et al. [18] and trapezoidal integration. The total power densities are 964 W/m^2 and 768 W/m^2, for the global and direct normal spectrums, respectively.

In contrast to previous publications, which assumed that each cell was infinitely thick [1,16,17] (i.e., absorbed all of the light with energy greater than the material's band gap), we calculated [19] the short-circuit currents as a function of the top cell thickness:

$$J_T = \sum_{\lambda} e\, I_o(\lambda)\, \Delta\lambda\, (1 - \exp[-\alpha(\lambda)t]) \tag{5-1}$$

and

$$J_B = \sum_{\lambda} e\, I_o(\lambda)\, \Delta\lambda\, \exp\left[-\alpha(\lambda)t\right] ,$$

where J_T and J_B are the photocurrents of the top and bottom cells, respectively; e is the electronic charge; $I_o(\lambda)$ is the incident intensity as a function of wavelength (taken from the spectral tables of Hulstrom et al. [18]); $\alpha(\lambda)$ is the absorption coefficient of the top cell material; and t is the thickness of the top cell. The integration step width ($\Delta\lambda$) was 1/30 of the wavelength step shown in the tables [18].

The J_{sc} values of the cell were then taken as the lesser of J_T and J_B. The thickness of the top cell was adjusted to obtain $J_T = J_B$ whenever possible (i.e., whenever $J_T > J_B$ for the infinite-thickness cells), ± 1 $\mu A/cm^2$. This arbitrary limit gave an accuracy of about 0.1% for the thickness and 0.01% for J_{sc} in most cases.

The reverse saturation current density (J_o) was calculated for each cell as the sum of the currents for the n- and p-type layers using the cell design in Figure 5-6:

$$J_o = e\left(\frac{D_e}{\tau_e}\right)^{1/2} \frac{n_i^2}{N_A} \left[\frac{S_e\left(\frac{\tau_e}{D_e}\right)^{1/2} \cosh\left(\frac{x_p}{D_e \tau_e}\right) + \sinh\left(\frac{x_p}{D_e \tau_e}\right)}{S_e\left(\frac{\tau_e}{D_e}\right)^{1/2} \sinh\left(\frac{x_p}{D_e \tau_e}\right) + \cosh\left(\frac{x_p}{D_e \tau_e}\right)} \right] +$$

$$e\left(\frac{D_h}{\tau_h}\right)^{1/2} \frac{n_i^2}{N_D} \left[\frac{S_h\left(\frac{\tau_h}{D_h}\right)^{1/2} \cosh\left(\frac{x_n}{D_h \tau_h}\right) + \sinh\left(\frac{x_n}{D_h \tau_h}\right)}{S_h\left(\frac{\tau_h}{D_h}\right)^{1/2} \sinh\left(\frac{x_n}{D_h \tau_h}\right) + \cosh\left(\frac{x_n}{D_h \tau_h}\right)} \right], \qquad (5\text{-}2)$$

where N_A and N_D are the acceptor and donor concentrations taken from Figure 5-7; S_h and S_e are the surface-recombination velocities in the n- and p-type materials; and x_p and x_n are the thicknesses of the p- and n-type layers, respectively. D_e and D_h are the diffusion constants for electrons and holes, respectively, calculated from the Einstein relationship:

$$D_e = \frac{kT\mu_e}{e}$$

and

$$D_h = \frac{kT\mu_h}{e} \qquad (5\text{-}3)$$

where k is Boltzmann's constant; T is the temperature in Kelvin; and μ_e and μ_h are the mobilities of electrons and holes, respectively. The intrinsic carrier concentration (n_i) was calculated from

$$n_i^2 = N_c N_v \exp\left(\frac{-E_g}{kT}\right)$$

$$= 4M_c M_v \left(\frac{2\pi kT}{h^2}\right)^3 \left(m_e^* m_h^*\right)^{3/2} \exp\left(\frac{-E_g}{kT}\right) , \qquad (5\text{-}4)$$

where N_c and N_v are the densities of state in the conduction and valence bands, respectively; M_c and M_v are the number of equivalent minima in the conduction and valence bands, respectively; h is Planck's constant; m_e^* and m_h^* are the effective masses of the electrons and the holes, respectively, and E_g is the band gap. The minority carrier lifetimes, τ_e and τ_h, were calculated from

$$\frac{1}{\tau_e} = \frac{1}{\tau_{SRH}} + BN_A$$

and

$$\frac{1}{\tau_h} = \frac{1}{\tau_{SRH}} + BN_D , \qquad (5\text{-}5)$$

where τ_{SRH} is the Shockley-Read-Hall lifetime and B is the direct band-to-band recombination coefficient. Equation 5-2 is often written as a function of the minority carrier diffusion lengths

$$L_e = \sqrt{\tau_e D_e} \text{ and } L_n = \sqrt{\tau_h D_h} .$$

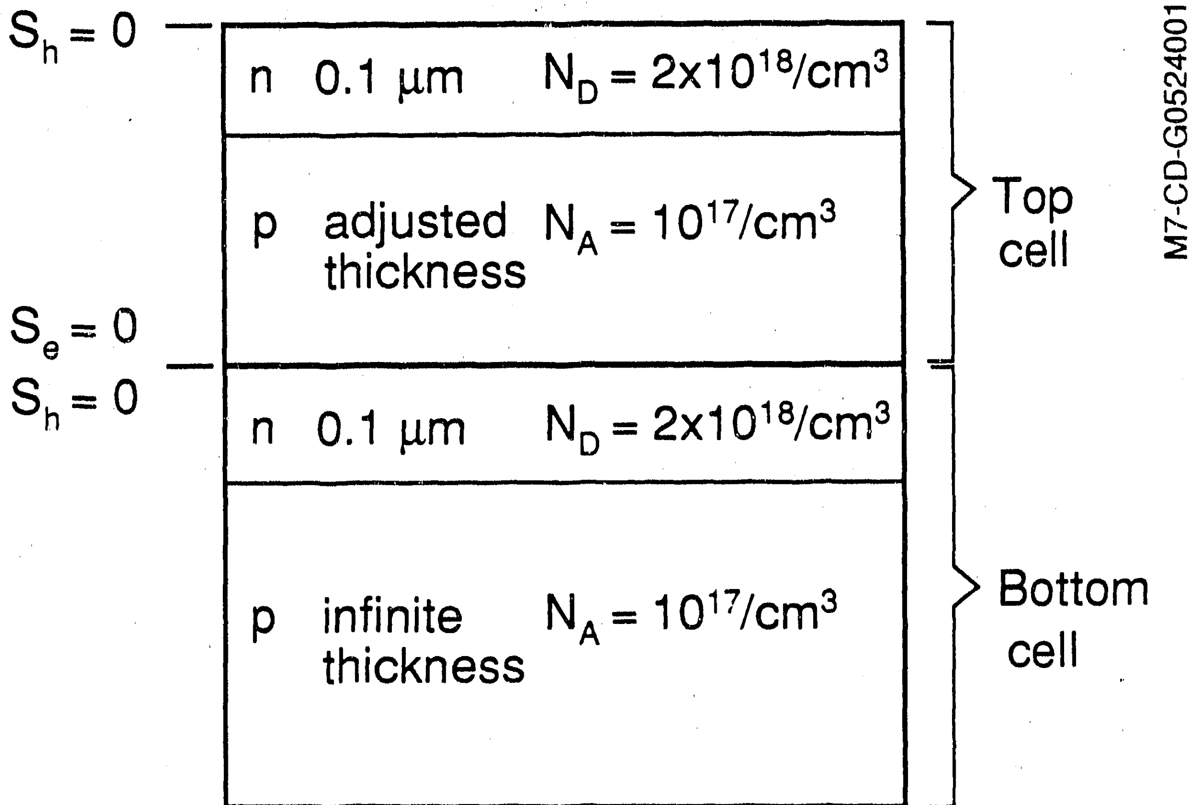

Figure 5-7. Schematic of the tandem solar cell used in the model

Ideally, the reverse saturation currents would be calculated in each case using the parameters for a known material of that band gap. However, this is not practical, and parameters for the two material models presented in Table 5-1 were used. These parameters approximate the properties of $GaInP_2$ (model A) and GaAs (model B). These were chosen as the top cell (model A) and bottom cell (model B) for the most detailed studies because the tandem cell using GaAs and $GaInP_2$ is likely to achieve a high efficiency [15]. Although its theoretical efficiency (34%) is not as high as some other combinations, this tandem cell has the advantages of being a lattice-matched system and also containing no aluminum. These greatly simplify the design and growth of the cell and may lead to higher experimental efficiencies despite the slightly lower theoretical efficiency. In addition to the set of calculations using model A for the top cell and model B for the bottom cell, we calculated efficiencies using model B for both cells. The results from this latter set of calculations should be of more general interest since GaAs is the best-known direct-gap material.

Table 5-1. Material parameters for models A and B. The values have been chosen to simulate $Ga_{0.5}In_{0.5}P$ and GaAs, respectively.

Parameter	Model A	Model B
M_c	1	1
M_v	3	1
μ_e (cm^2/Vs)	4000	8500
μ_h (cm^2/Vs)	200	400
m_e^*/m_e	0.155	0.067
m_h^*/m_e	0.460	0.473
τ_{SRH}(s)	10^{-5}	10^{-5}
B (s/cm^3)	7.5×10^{-10}	7.5×10^{-10}
α (μm^{-1})	$4.55(E-E_g)^{1/2} + 2.05(E-Eg-0.1)^{1/2}$	$3.3(E-Eg)^{1/2}$

V_{oc} was calculated [19] from:

$$V_{oc} = \frac{kT}{e} \ln\left(\frac{J_{sc}}{J_o} + 1\right) . \quad (5\text{-}6)$$

The power from the cell is given by the product of the cell voltage (V) and cell current (J), and was maximized by satisfying the condition

$$\frac{d(JV)}{dJ} = 0 , \quad (5\text{-}7)$$

where the cell voltage was calculated from the combined current-voltage curves:

$$V = \frac{kT}{e} \left[\ln\left(\frac{J + J_T}{J_{oT}} + 1\right) + \ln\left(\frac{J + J_B}{J_{oB}} + 1\right) \right] . \quad (5\text{-}8)$$

J_{oT} and J_{oB} are the reverse saturation currents for the top and the bottom cells, respectively. This represents an improvement over the previously used method [1,16,17] of calculating the maximum power points of the two separate cells.

The isoefficiency contour plot is shown for the AM1.5 global spectrum in Figure 5-8(a), using model B to calculate both J_o values and α. For comparison, the corresponding plot assuming an infinite thickness for the top cell is shown in Figure 5-8(b). Figures 5-9(a) and 5-9(c) show isoefficiency contour plots similar to those shown in Figure 5-8, except that model A was

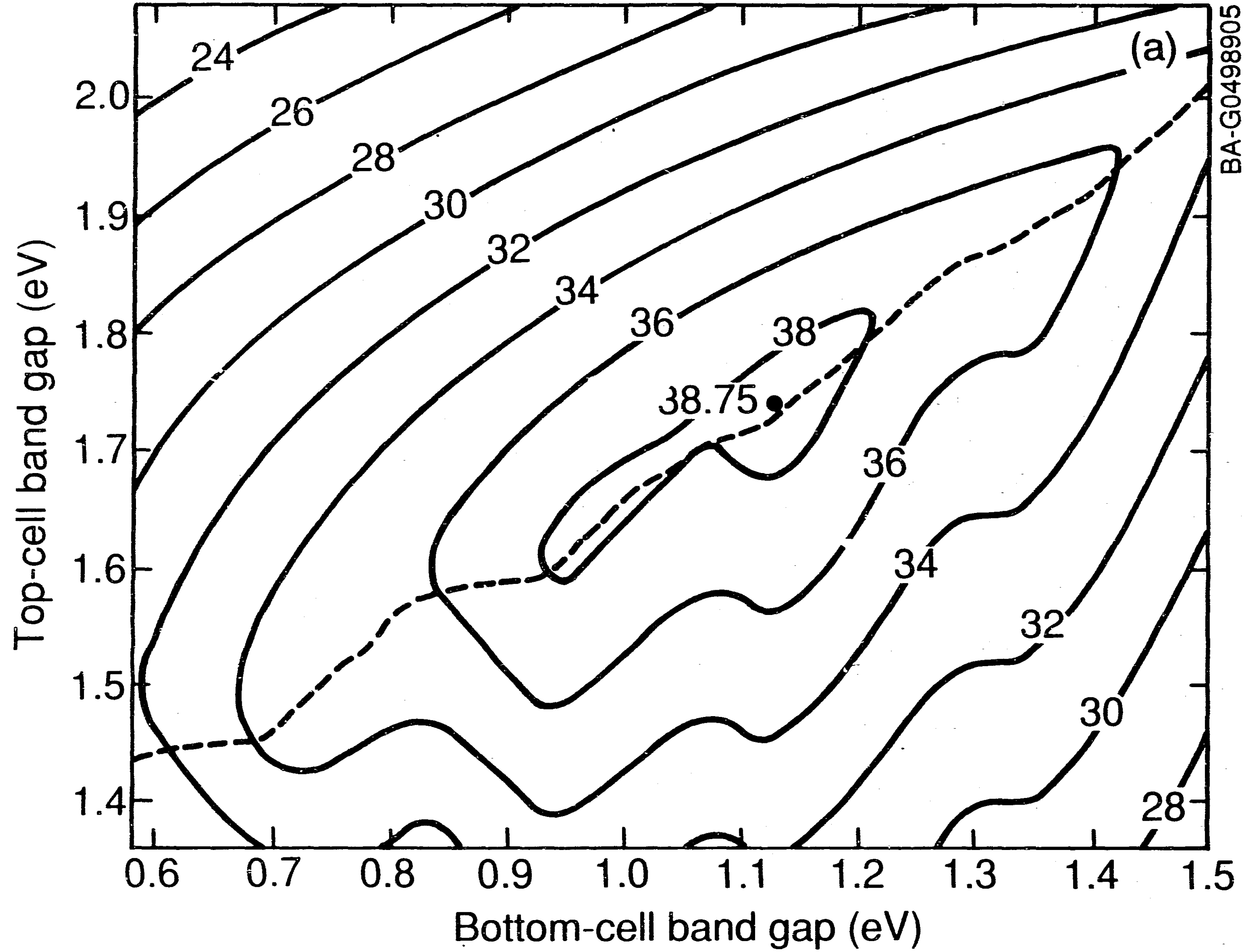

Figure 5-8(a). Isoefficiency contour plot for the AM1.5 global spectrum

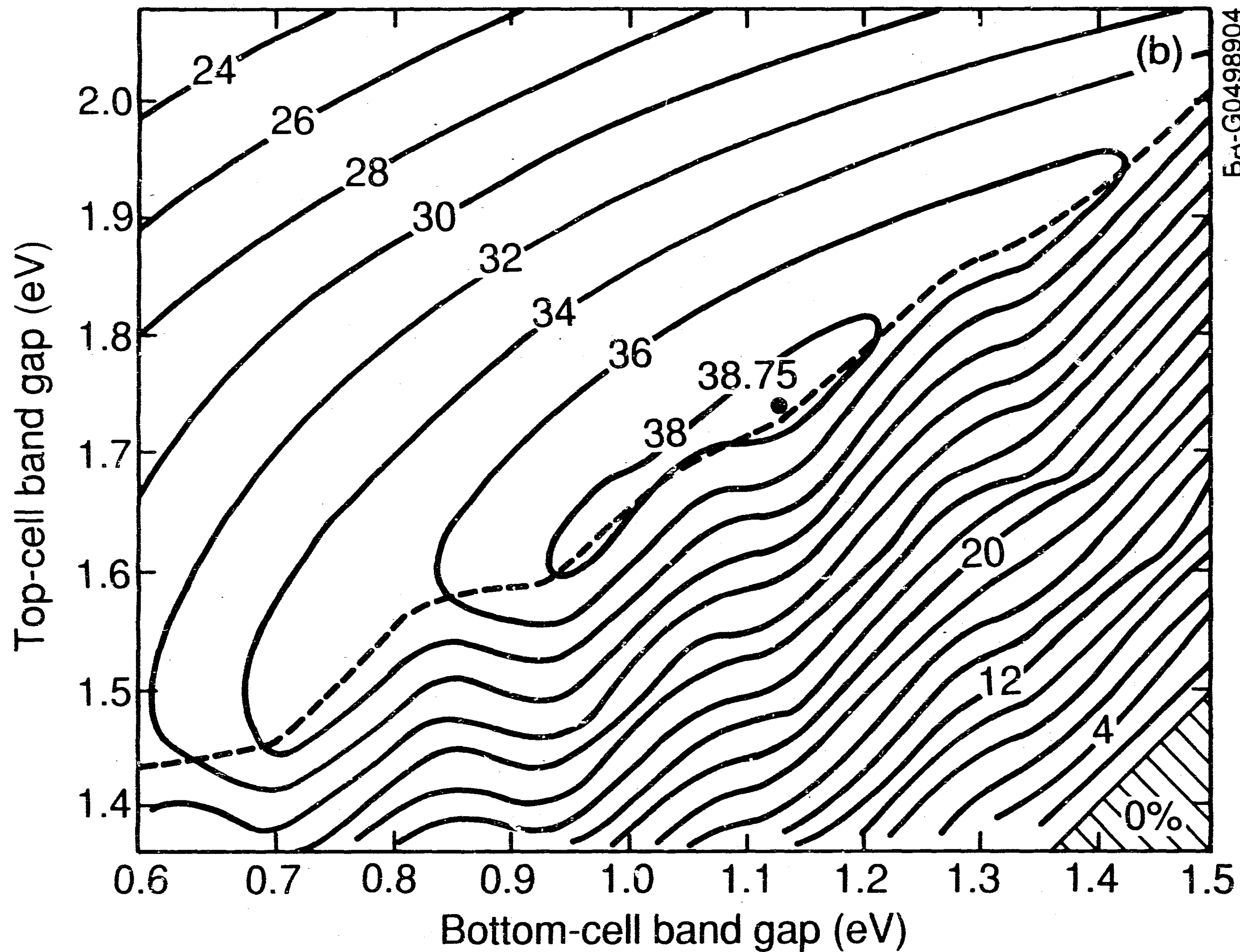

Figure 5-8(b). Isoefficiency contour plot assuming an infinite thickness for the top cell

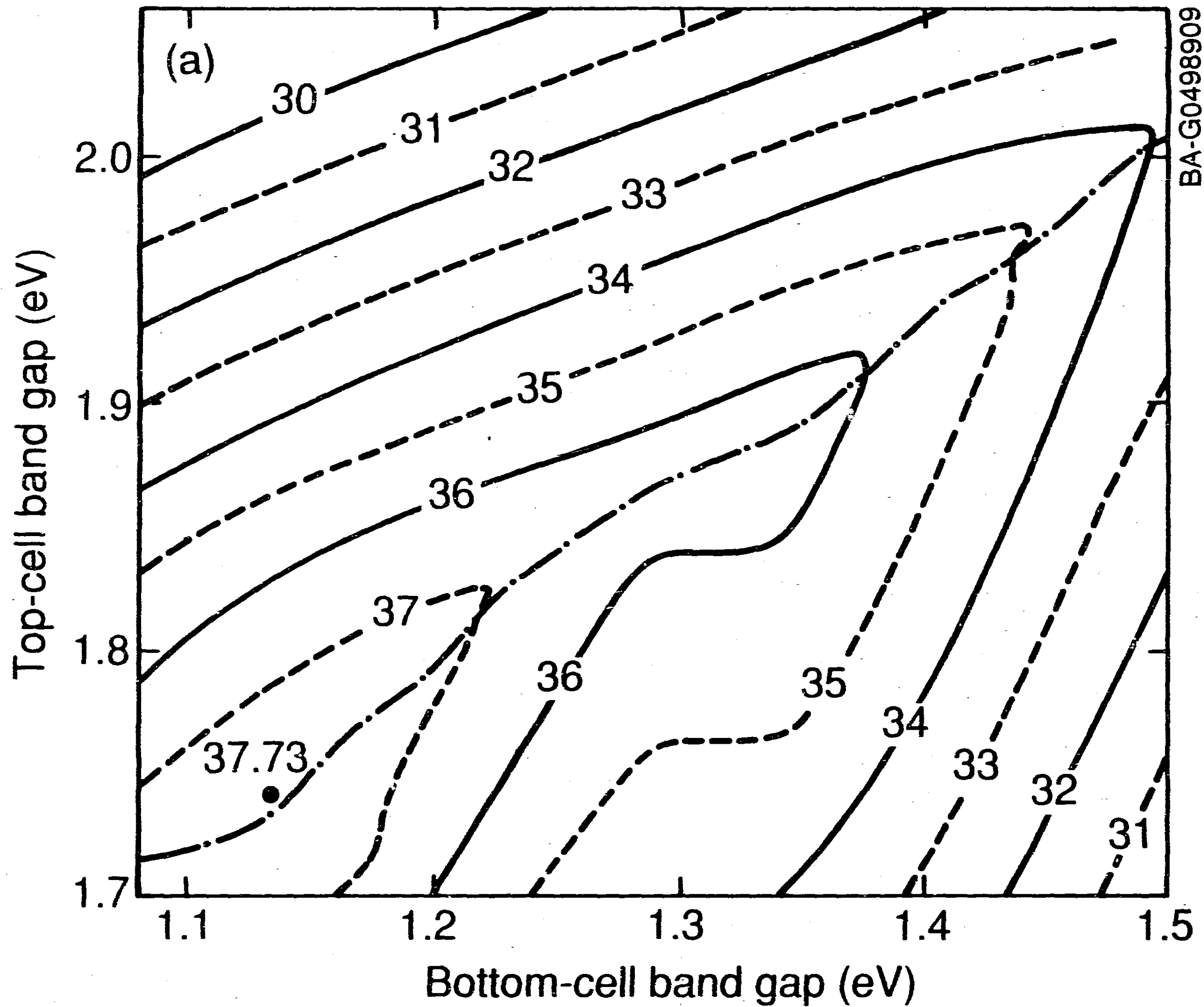

Figure 5-9. **Isoefficiency contour plots.** (a) and (c) show isoefficiency plots for two-junction, series-connected tandem structures under AM1.5 global, one-sun illumination at 300 K. J_o and α were calculated using model A for the top cell and model B for the bottom cell. The top cell thickness was (a) adjusted for current matching and (c) infinite (b) represents the isoefficiency contour plot showing the top cell thicknesses used for the calculation of Figure 5-3(a).

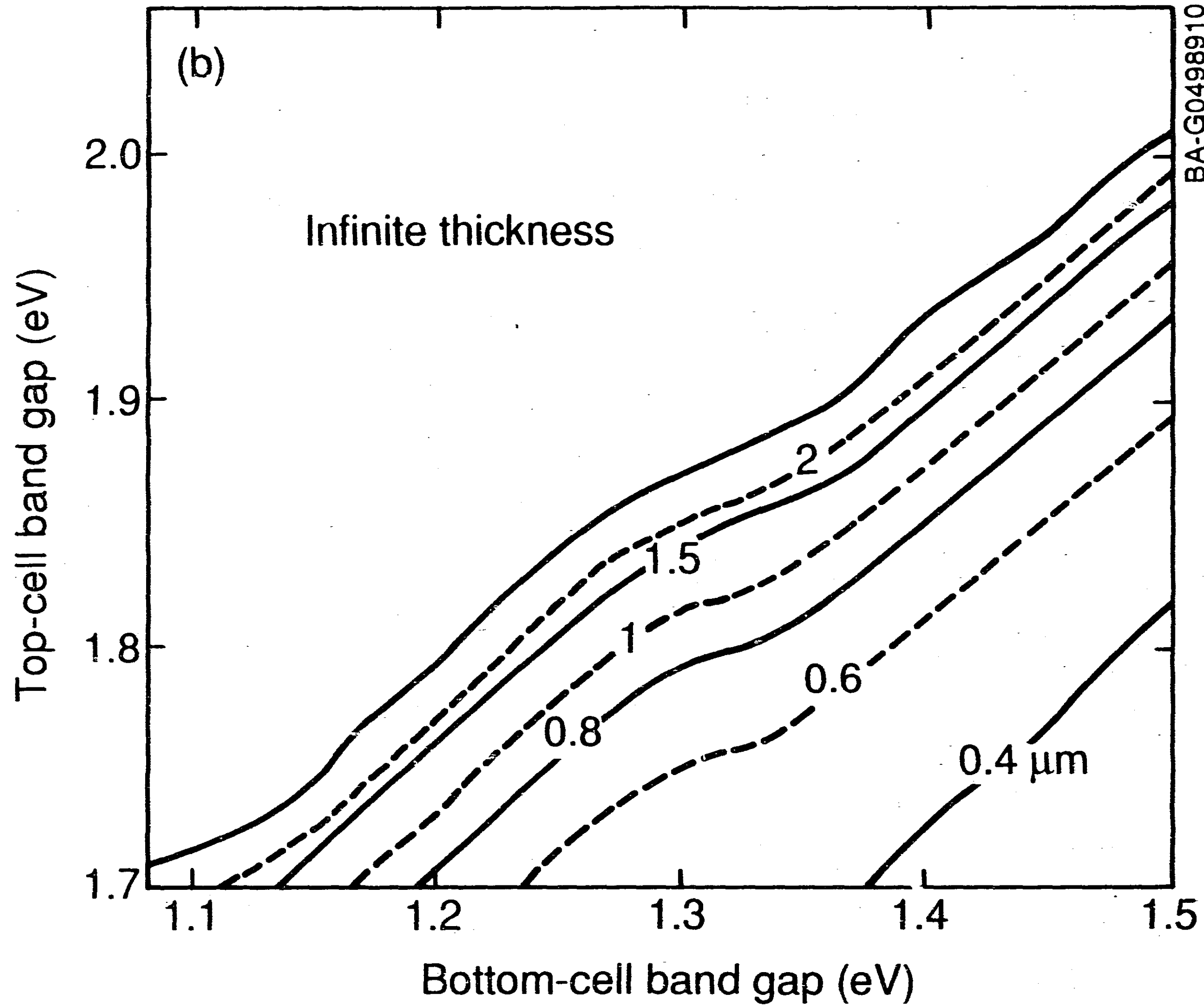

Figure 5-9. **Isoefficiency contour plots.** (a) and (c) show isoefficiency plots for two-junction, series-connected tandem structures under AM1.5 global, one-sun illumination at 300 K. J_o and α were calculated using model A for the top cell and model B for the bottom cell. The top cell thickness was (a) adjusted for current matching and (c) infinite (b) represents the isoefficiency contour plot showing the top cell thicknesses used for the calculation of Figure 5-3(a). (Continued)

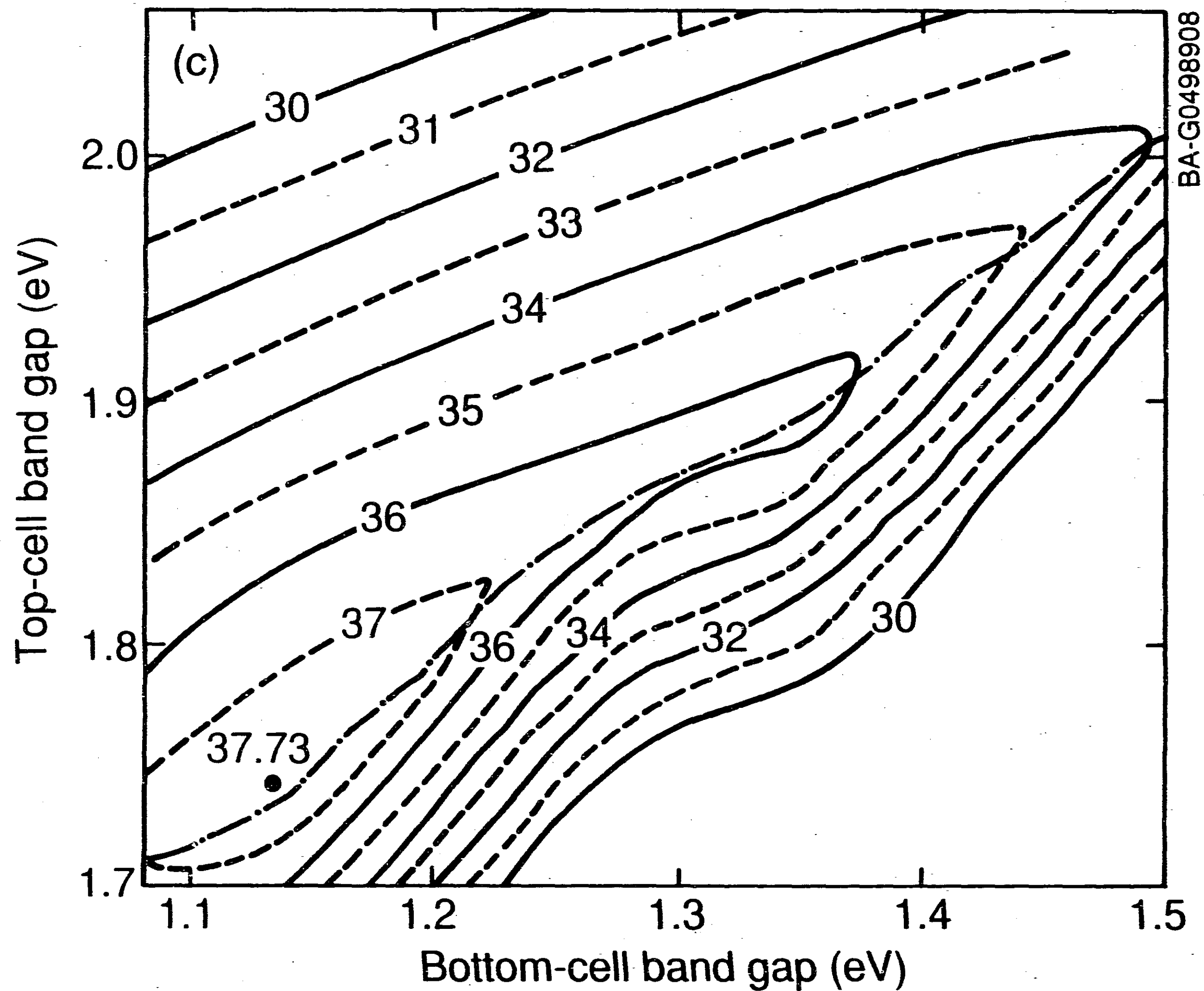

Figure 5-9. **Isoefficiency contour plots.** (a) and (c) show isoefficiency plots for two-junction, series-connected tandem structures under AM1.5 global, one-sun illumination at 300 K. J_o and α were calculated using model A for the top cell and model B for the bottom cell. The top cell thickness was (a) adjusted for current matching and (c) infinite (b) represents the isoefficiency contour plot showing the top cell thicknesses used for the calculation of Figure 5-3(a). (Concluded)

used for the top cell J_o and α calculations. Figure 5-10 shows the isoefficiency plots for the AM1.5 direct normal spectrum. Models B and A were used for the top cells in Figures 5-10(a) and 5-10(b), respectively.

Comparison of Figures 5-8(a) and 5-8(b) or Figures 5-9(a) and 5-9(c) shows the effect of varying the thickness of the top cell. Some of the efficiencies increase significantly when the top cell is thinned. In particular, for the lattice-matched material systems with band-gap combinations of 1.424 eV (GaAs)/1.90 eV ($Ga_{0.5}In_{0.5}P$), 0.7 eV ($Ga_{0.5}In_{0.5}As$)/1.35 eV (InP), and 0.8 eV (Ge, direct gap)/1.424 eV (GaAs) thinning, the top cell increases the theoretical efficiencies from 32% to 35%, from 28% to 32%, and from 28% to 34%, respectively. The stated efficiences for the Ge/GaAs combination are not accurate since germanium has a lower, indirect gap; nevertheless, the stated increase in efficiency should occur when the top cell is thinned.

The effect of thinning the top cell can be understood better by studying curves A, B, and C of Figure 5-11(a), which show the efficiency of a tandem structure with a bottom cell band gap of 1.424 eV as a function of top cell band gap. Curve A represents the efficiency when the top cell is required to have an infinite thickness. Curve B was calculated by varying the thickness of the top cell to obtain current-matched conditions, but without recalculating J_o. This gives an increase in J_{sc} but no change in V_{oc}. Curve C shows the effect of recalculating J_o for the thinner layer. The smaller J_o results in an increase in V_{oc} as shown in the upper half of the graph and, therefore, an increase in efficiency. Comparison of curves A, B, and C shows that the primary advantage of using thinner top cells is a gain in J_{sc}, but that in cases of low surface recombination, an additional gain is made in V_{oc}.

The gain in V_{oc} will be less than that shown in Figure 5-11(a) when the surface-recombination velocities are not zero. The combined effects of surface-recombination velocity and thinning of the cell are shown in Figure 5-12. For simplicity, we consider only the effect of recombination at one surface. In this case the subscripts refer to recombination in the p-type material. This is done by setting $S_h\sqrt{\tau_h D_h} = 1$ (which is equivalent to setting $S_h L_h/D_h = 1$), making J_o independent of the n-layer thickness. The relative V_{oc} is then a function of x_p/L_e and $S_e L_e/D_e$, which are dimensionless expressions for the p-layer thickness and p-layer surface-recombination velocity, respectively. For $S_e L_e/D_e = 1$, the V_{oc} does not vary with the p-layer thickness. For lower surface-recombination velocities, the V_{oc} increases as the p layer is thinned. However, it should be noted that the V_{oc} is expected to decrease as the cell is thinned when the surface-recombination velocity is high. The same graph is equally applicable to n-type material if all subscripts are replaced appropriately.

The thicknesses used for the calculations in Figure 5-11(a) are noted at the top of that figure and are replotted for easy reference in Figure 5-13. The only practical limitations for implementing these thinner cells are control of the layer thickness and uniformity. This can be evaluated from Figure 5-13, which shows the efficiency and bottom cell and top cell currents as a function of top cell thickness and band gap, assuming a bottom cell with band gap 1.424 eV. If one assumes that the thickness can be controlled to ±10%, a band gap as low as 1.85 eV still has an ideal efficiency of between 33% and 34%.

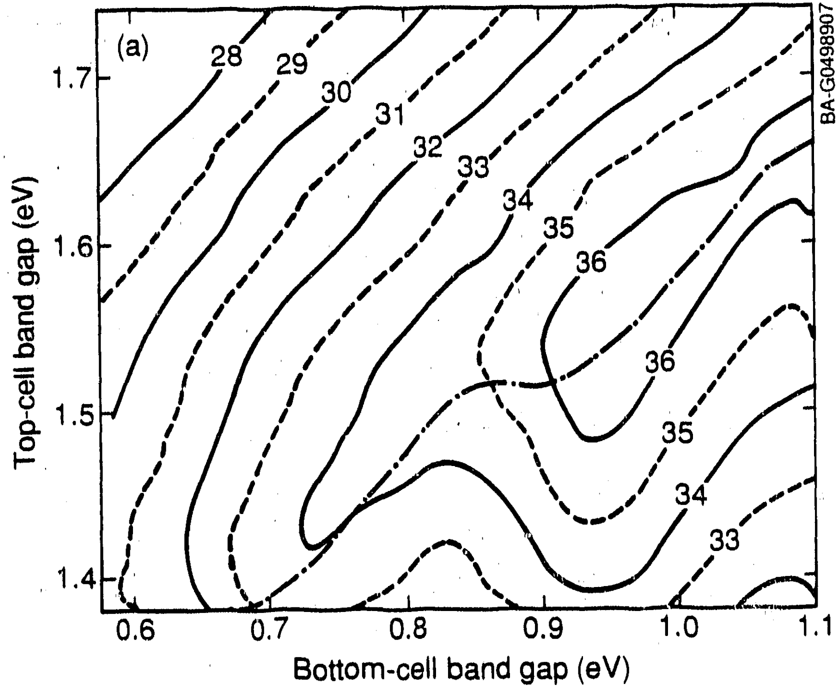

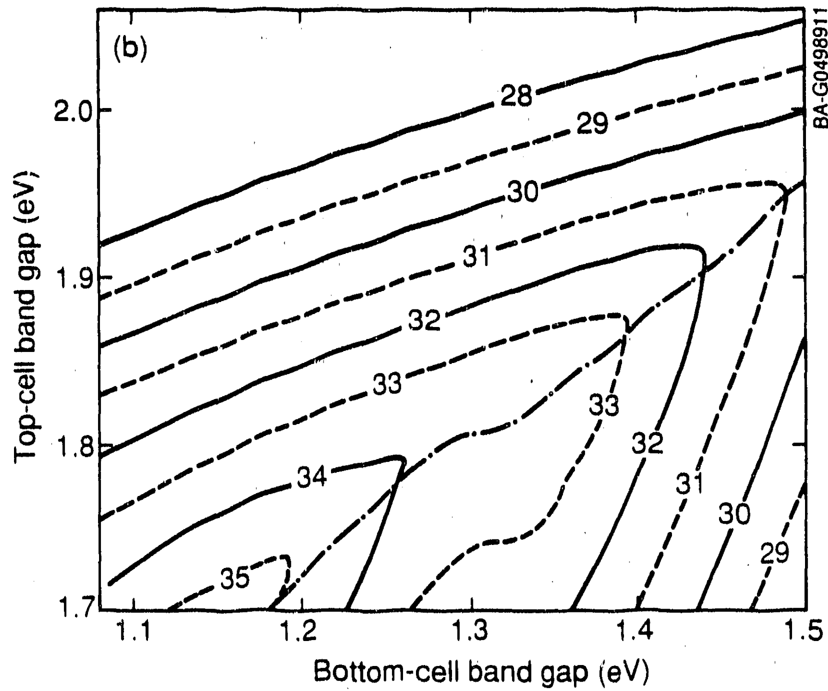

Figure 5-10. Isoefficiency plots for two-junction, series-connected tandem structures under AM1.5 direct, one-sun illumination at 300 K. J_o and α were calculated using (a) model B for both cells and (b) model A for the top cell and model B for the bottom cell. The top cell thickness was adjusted for current matching.

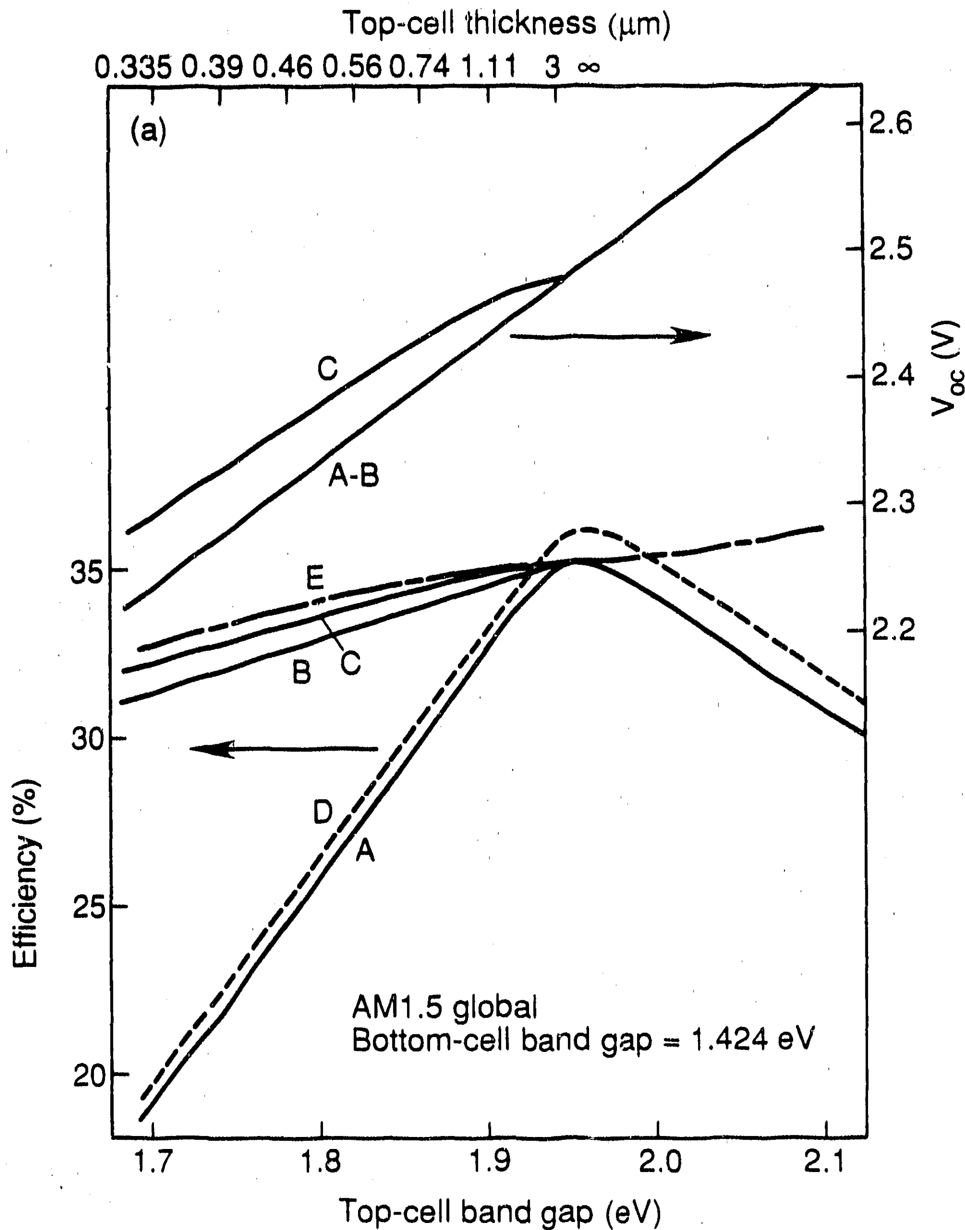

Figure 5-11. Efficiency of a tandem structure. (a) The efficiency and V_{oc} as a function of top cell band gap for a bottom cell with band gap of 1.424 eV and AM1.5 global irradiation. Curve A assumes an infinite thickness for the top cell. Curve B varies the top cell thickness to achieve current matching but does not recalculate J_o. Curve C repeats curve B but includes a recalculation of J_o. Curves A–C use model A for the top cell and model B for the bottom cell. Curve D uses model B for both cells and an infinite thickness for the top cell. (b) and (c) show efficiency curves A and C as described in (a), except that AMO and AM1.5 direct normal irradiance spectra were used in (b) and (c), respectively.

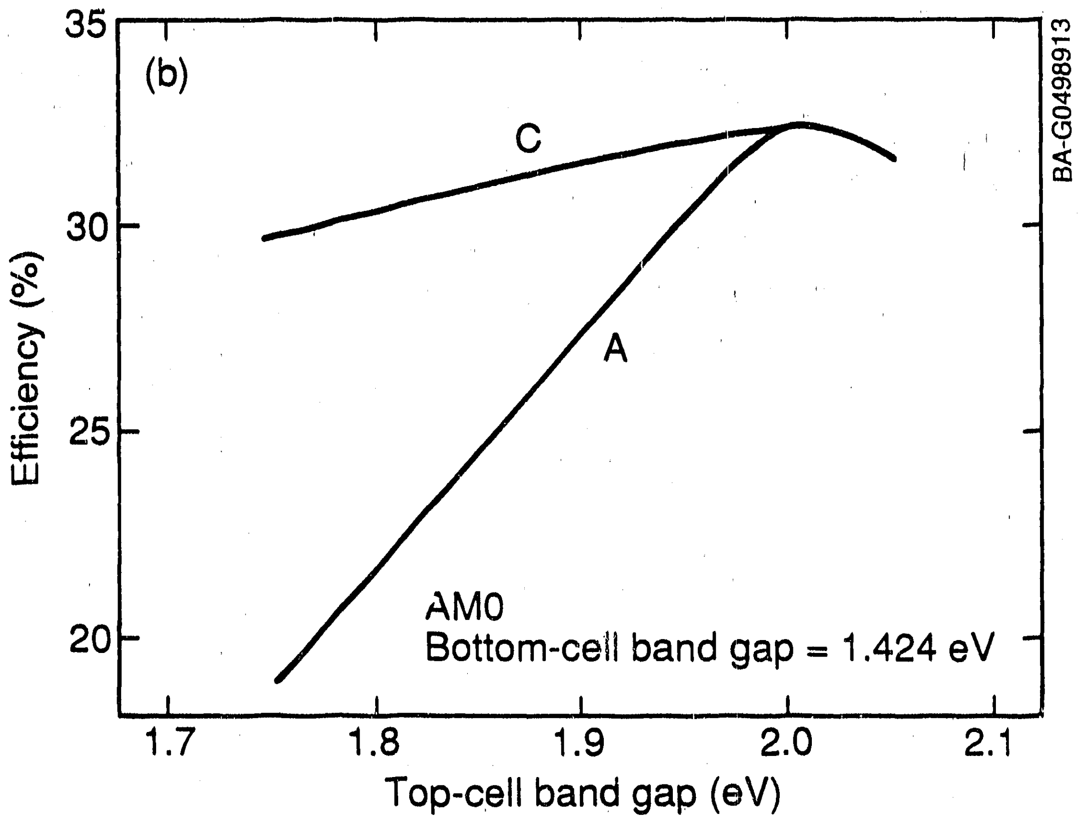

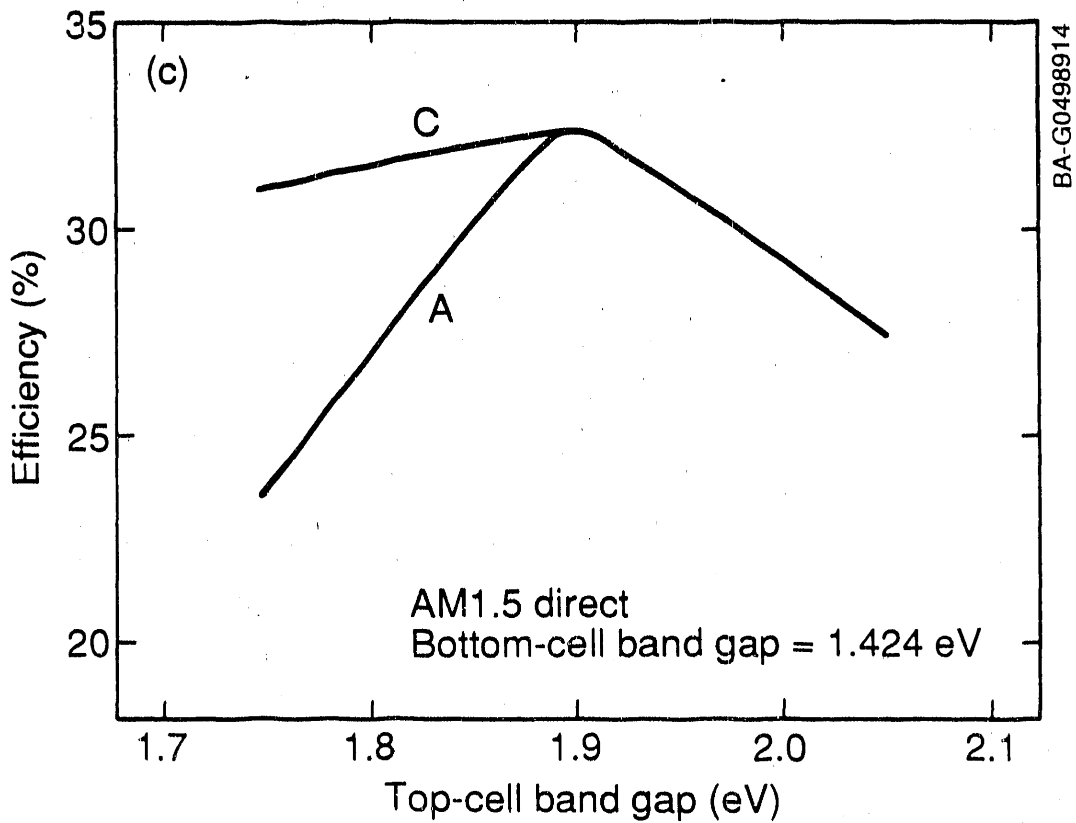

Figure 5-11. Efficiency of a tandem structure (Concluded)

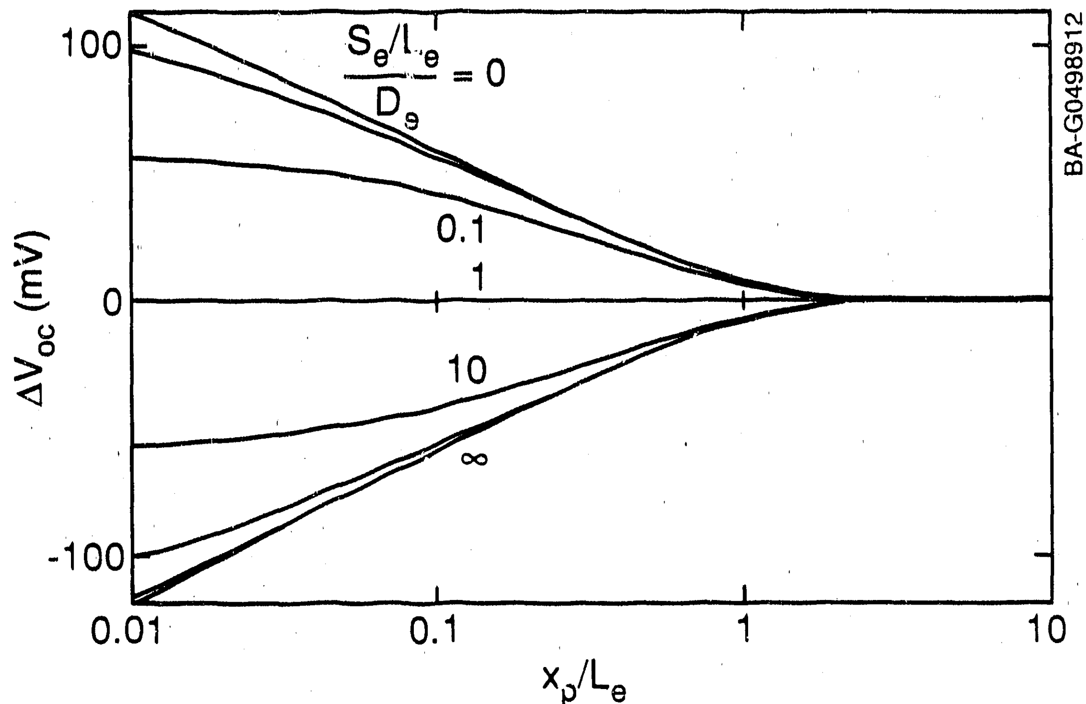

Figure 5-12. The effect of p-layer thickness and surface recombination on V_{oc}. Dimensionless variables are used for the p-layer thickness (thickness/electron diffusion length) and the surface recombination (recombination velocity*electron diffusion length/electron diffusion coefficient). The change in V_{oc} is shown for various surface-recombination ratios, as labeled on the graph.

However, a band gap as low as 1.70 eV is not practical since a 10% variation of thickness would result in a variation of several efficiency points. Figure 5-14 is of particular interest for the GaAs/$GaInP_2$ system since the band gap of $GaInP_2$ varies anomalously with deposition conditions from about 1.82 eV to about 1.90 eV [5,20]. Figures 5-13 and 5-14 predict an optimal top cell thickness of about 0.75 μm for a GaAs/$GaInP_2$ cell with top cell band gap of 1.85-1.86 eV.

We were able to fabricate a current-matched, 27%-efficient tandem cell with a top cell band gap of 1.85-1.86 eV using a thickness of about 0.9 μm [15]. Given the assumptions of the model (no surface recombination, which is an especially bad assumption for the top cell) and experimental uncertainties (in the absorption coefficient and thickness measurements), this is very good agreement between theory and experiment. Strictly speaking, the optimal top cell thickness would be achieved for the current-matched condition at the maximum-power point, rather than under short-circuit conditions as we have calculated. However, this difference is quite small, as can be seen from Figure 5-14.

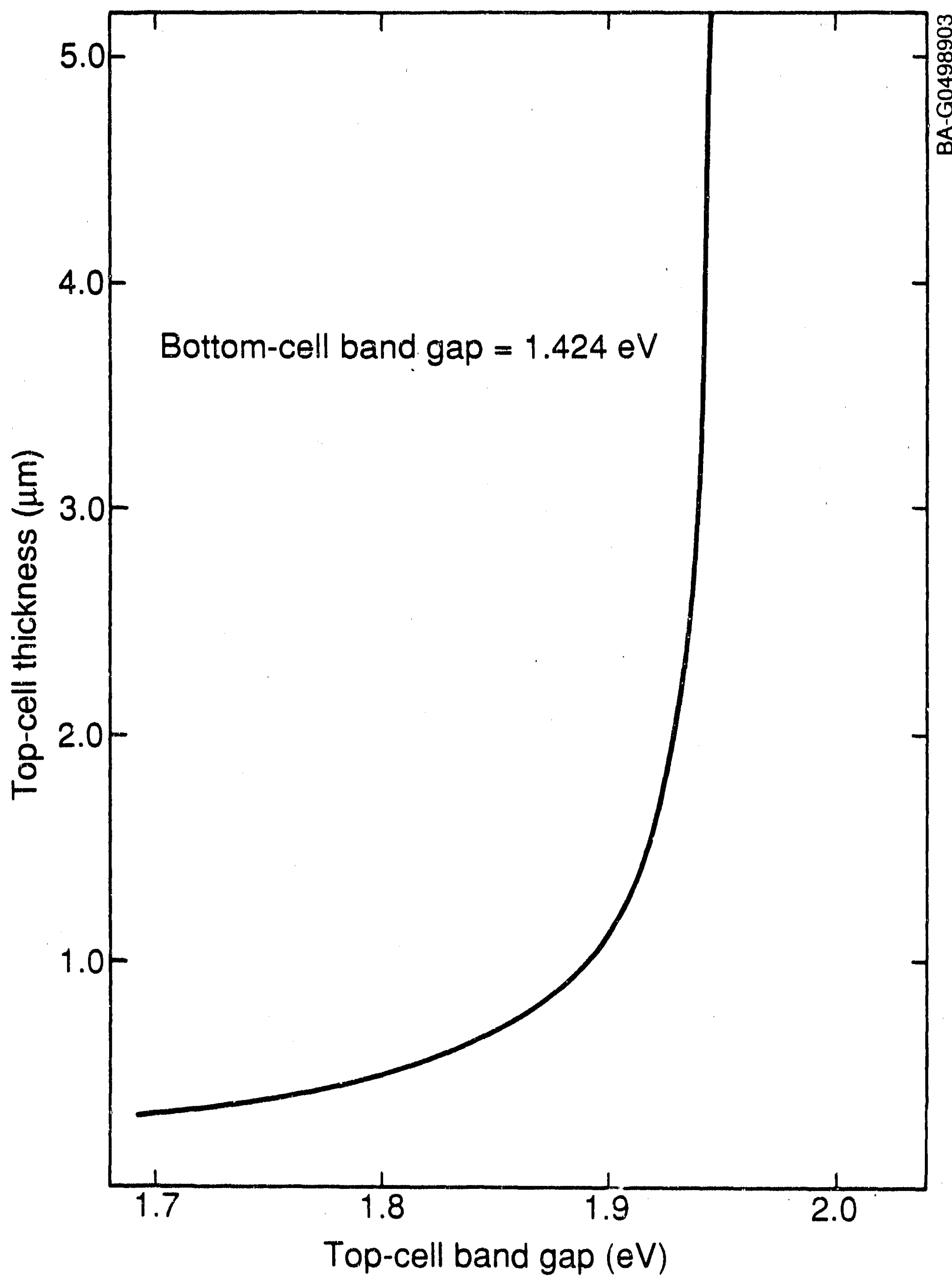

Figure 5-13. Top cell thickness as a function of top cell band gap to achieve the current-matched condition for a bottom cell with a band gap 1.424 eV. Model A was used for the absorption calculation. These thicknesses were used for calculation of curves B and C in Figure 5-11.

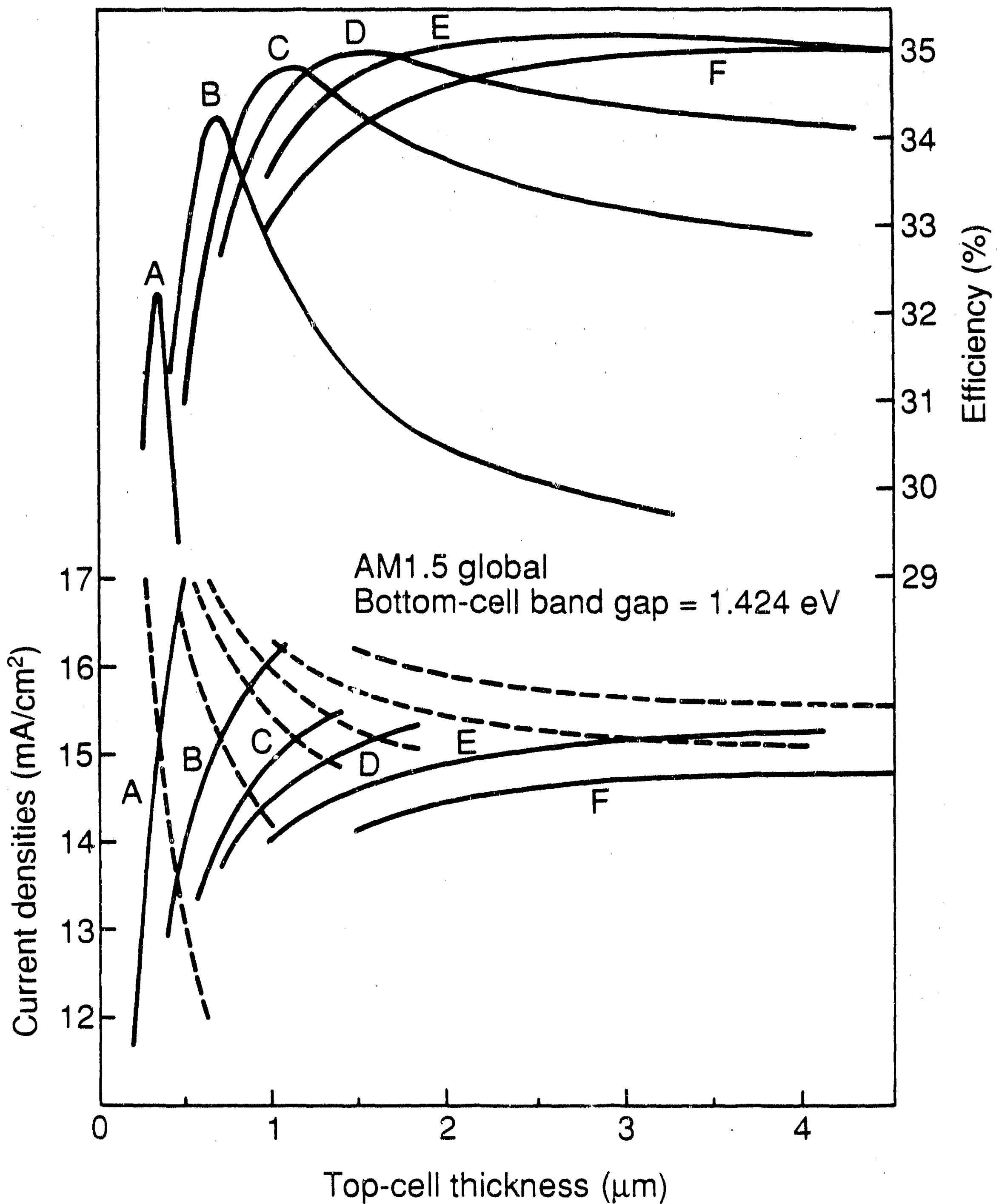

Figure 5-14. The lower portion of the figure shows the top cell (solid line) and bottom cell (dashed line) currents as a function of top cell thickness and band gap. The upper portion shows the corresponding tandem-cell efficiencies. A band gap of 1.424 eV and model B were used for the bottom cell. Model A and band gaps of (A) 1.70 eV, (B) 1.85 eV, (C) 1.90 eV, (D) 1.92 eV, (E) 1.94 eV, and (F) 1.96 eV were used for the top cell.

The efficiency of the series-connected tandem cells under different irradiance spectra can be compared in Figures 5-8 through 5-10 or Figures 5-11(a)-(c). Using the AM0 and AM1.5 direct normal spectra, respectively, Figures 5-11(b) and 5-11(c) show the efficiencies obtained for both the thinned and infinitely thick top cells as shown in Figure 5-11(a). At lower air mass, the spectrum has more short-wavelength light, increasing the optimal top cell band gap for a GaAs bottom cell. However, the effect of thinning the top cell is roughly equivalent in each case. The top cell thicknesses used in Figure 5-11(a) and plotted in Figure 5-13 would be almost identical for Figures 5-11(b) and 5-11(c) if correction is made for the difference in optimal top cell band gap.

The effect of using the different material properties (models A and B) for calculation of J_o and α of the top cell can be seen by comparing Figures 5-8 and 5-9 or, more quantitatively, by comparing curves A and D in Figure 5-11(a). All the efficiencies are shifted by almost the same amount; the maximum efficiency is obtained at an essentially constant set of band gaps regardless of the material model. However, the magnitude of the change (1% absolute) is significant. This is especially true since the two chosen material models are both based on III-V compounds and may differ less than two arbitrarily chosen materials would. Clearly, the projected efficiency should be recalculated using the known material properties of any materials under consideration. However, since the material properties of new materials are not always known, the calculated graphs are useful in choosing which new materials to study.

From previous calculations we have also assumed that the material properties were independent of band gap. Writing J_o in the form used by Fan [1], Nell [16], and Wanlass [17]:

$$J_o = C\, T^3 \exp(-E_g/kT) .$$

For infinite thickness, we used C = 43.3, and 6.17 mA/cm^2K^3 for models A and B, respectively. These differ only slightly from those used previously: 50 mA/cm^2K^3 [1] and 17.9 mA/cm^2K^3 [16,17], respectively.

The data showing the thicknesses required for current matching [Figures 5-9(b) and 5-13] were all obtained using model A for the top cell. These results can easily be generalized to other systems by increasing or decreasing the thickness proportionally when the absorption coefficient is smaller or larger, respectively.

5.4 The Effect of Selenium Doping on the Optical and Structural Properties of $Ga_{0.5}In_{0.5}P$

$GaInP_2$ has recently attracted considerable attention for both technological and scientific reasons. Because it is lattice-matched to GaAs and has a band gap in the visible range, it is an excellent material for diode lasers, light-emitting diodes, and cascade solar cells [21]. Scientifically, it is of interest because its band gap, at constant composition, varies with growth parameters [5,22,23]. This anomalous variation has been related to spontaneous ordering of the gallium and indium on the group III sublattice [20,24,25,26]. This spontaneous ordering apparently occurs by a surface mechanism [27] in spite of the fact that the bulk disordered structure has been shown, both theoretically [28] and experimentally [29], to be lower in energy.

Recently, zinc and magnesium doping have been shown to decrease the ordering and increase the band gap of $GaInP_2$ films when the p-type carrier concentration exceeded about $10^{18}/cm^3$ [30,31]. Because zinc has often been used as a catalyst for disordering of various superlattices [20,29,32], it was hypothesized that the mechanism for the zinc- and magnesium-induced disordering was related to diffusion of the p-type dopants through the growing film [30]. The current study reports selenium-induced disordering similar to that reported for zinc and magnesium. This result is unexpected since selenium usually diffuses much more slowly than zinc and magnesium, and since selenium is an n-type dopant, residing on the group V instead of the group III sublattice. We also report a smoothing effect of selenium doping on the surface morphology of $GaInP_2$.

The $GaInP_2$ films were grown by atmospheric pressure CVD as described in Section 5.2.1. Hydrogen selenide was used as the dopant source, giving very similar results to those reported previously [33]. Hydrogen, diffused through palladium, was used as the carrier gas. GaAs wafers, 2° off (100) toward (110), were used as the substrates after cleaning with 2:1:10 aqueous $NH_3:H_2O_2:H_2O$. The films were 2 μm thick, grown in 20 min.

The carrier concentrations were measured by an electrochemical capacitance-voltage technique, using a Polaron profiler. Van der Pauw-Hall effect measurements were done on some of the samples. The absolute accuracy of the carrier concentration measurement was a factor of two, while the precision was 10%-20%. The results from the two methods agreed well. The selenium content of the films is not necessarily equal to the electron concentration [33]. At very high selenium contents the electron concentration falls dramatically. The films with high selenium content but low electron concentration had band gaps and ordering more consistent with lightly doped films. We report here only the carrier concentration, since the absolute selenium content has a less consistent effect on the band gap and ordering.

The lattice mismatch was measured by double-crystal, rocking-mode x-ray diffraction. All samples reported here exhibited a relative lattice mismatch of less than 0.001. Corrections to the band-gap energy for any deviations from the lattice-matched composition were less than 5 meV.

The band gaps were measured by electrochemical photocurrent spectroscopy [9]. Figure 5-15 shows examples of the data. The photocurrent generated by light from a monochromator is plotted as a function of photon energy (E). The band gap (E_g) was obtained by fitting the photocurrent to Eqs. 5-1 and 5-2:

$$\text{photocurrent} = \text{constant}/(1 + 1/\alpha L) \;, \qquad (5\text{-}9)$$

where L is the minority-carrier diffusion length, and α is the absorption coefficient [9]:

$$\alpha(E) = \text{constant}*(E-E_g)^{1/2} \;. \qquad (5\text{-}10)$$

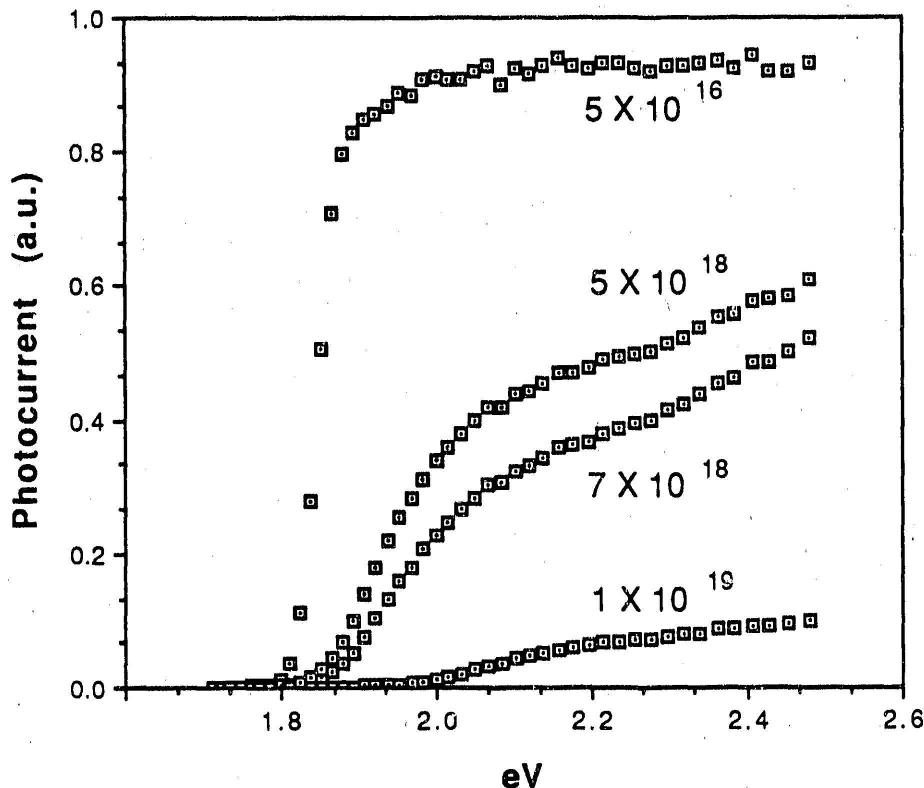

Figure 5-15. Electrochemical photocurrent (arbitrary units) as a function of photon energy for four $GaInP_2$ samples of variable selenium content with carrier concentrations ranging from 5 × $10^{16}/cm^3$ to $10^{19}/cm^3$. All were grown at 670°C.

A correction to E_g was made for the Burstein-Moss effect for those samples with carrier concentrations higher than 3 × $10^{18}/cm^3$. This correction is necessary since the measured ("apparent") band gap of a degenerately doped semiconductor is higher than the actual band gap [34]. The correction factor for the effect of degenerate doping was calculated by modeling the photocurrent spectroscopy according to Eqs. 5-1, 5-3, and 5-4:

$$\alpha(E) = \text{constant} * \frac{(E-E_g)^{\frac{1}{2}} e^{(E-E_f)/kT}}{e^{(E-E_f)/kT} + 1} \tag{5-11}$$

where E_f is the Fermi level, T is the temperature, and k is Boltzmann's constant. For a given E_f, the carrier concentration (n) was calculated assuming an effective mass (m^*) of 0.11 electron masses [35].

$$n = \int_{E_c}^{\infty} \frac{8\pi\,[2(E-E_c)]^{\frac{1}{2}}\, m^{*3/2} dE}{h^3\,(e^{(E-E_f)/kT} + 1)} \tag{5-12}$$

where E_c is the conduction band energy.

The uncertainty of this model is especially large for values of E_f that are significantly above the conduction band because of an uncertainty in the effective mass (which may not even be constant for all films) and the existence of additional states at the X and L points. Non-parabolicity of the Γ-point conduction band may also introduce some error. Nevertheless, the model gives results that are qualitatively similar to those obtained for GaAs [36] and is sufficient given the scope of this document.

The photographs of the surfaces were taken using a scanning laser microscope with differential phase constant (Lasersharp, distributed by Bio-Rad). The contrast was electronically enhanced to show the differences between smooth films. The smoothest films reported here are essentially featureless under examination with a standard microscope.

The ordering was investigated by transmission electron microscopy using plan-view specimens, thinned chemically with a bromine/methanol solution. The extent of ordering was estimated subjectively from the dark-field images. The electron diffraction data were presented in more detail in a separate publication [37].

Table 5-2 summarizes the data, including the band gaps, corrected band gaps, carrier concentrations, and amount of order for each of the films at the three growth temperatures (T_g) studied. The ordered volumes, reported as "medium, weak, very weak, and disordered," we believe correspond to 10%-50%, ~ 1%, < 0.1%, and not detectable, respectively [37]. At each growth temperature, an increase in the selenium content leads to an increase in the band gap and a decrease in the observed amount of ordering. For films grown at 670°C, an abrupt decrease in the ordering occurs at a carrier concentration of $10^{19}/cm^3$. At the same carrier concentration, an increase in the band gap is also observed. The uncertainty in the band gap of the highly doped film is large both because of uncertainty in the model of the Burstein-Moss effect and because the high carrier concentration (small minority-carrier diffusion length) causes a shallow edge on the photocurrent (as seen in Figure 5-15), decreasing the precision and accuracy with which the band gap can be measured. The photoluminescent (PL) line width also increased so that measurement of the band gap by PL presented no advantage over the method used. It is not possible to determine whether the small increase in the apparent band gap for the films doped to 5 and $7 \times 10^{18}/cm^3$ is caused by the Burstein-Moss effect or whether it is a result of less extensive ordering of the films. Gomyo et al. show a very similar increase in band gap for selenium-doped films grown with slightly smaller carrier concentrations [38]. Because they see the effect for films with carrier concentrations lower than that at which the Burstein-Moss effect causes a shift in the apparent band gap, they conclude that this shift in the band gap is a manifestation of the extent of order.

The change from the ordered to the disordered state occurs at a smaller carrier concentration for films grown at 740°C than those grown at 670°C. Since the Burstein-Moss shift is unimportant for $GaInP_2$ films doped at $3 \times 10^{18}/cm^3$, the interpretation of these results is more straightforward.

For each set of films grown at a constant growth temperature, a clear "on-off" correlation exists between the band gap and the ordered volume (i.e., a significant increase of the band gap and decrease in the ordered volume are

Table 5-2.

T_g (°C)	n(/cm^3)	Correction	E_g(eV) Before Burstein-Moss Correction	E_g(eV) After Burstein-Moss Ordered Volume (%)**
670	~1×10^{19}	1.96	1.88 ± 40 meV	weak
670	7×10^{18}	1.875	1.825 ± 20 meV	medium
670	5×10^{18}	1.865	1.845 ± 10 meV	medium
670*	5×10^{16}	1.823	1.830 ± 5 meV	medium
740	3×10^{18}	1.915	1.915 ± 5 meV	disordered
740	2×10^{18}	1.885	1.885 ± 5 meV	medium
740*	4×10^{16}	1.880	1.880 ± 5 meV	medium
600	2×10^{19}	1.96	1.9 ± 60 meV	disordered
600	5×10^{17}	1.885	1.885 ± 5 meV	very weak
600*	2×10^{16}	1.880	1.88 ± 5 meV	very weak

*Nominally undoped.

**Estimated from dark-field superlattice images.

observed for the same doping levels). However, if films grown at 600° and 740°C are compared, the correlation is not as clear. At both 600° and 740°C, band gaps of 1.88-1.885 eV were reported. However, films grown at 740°C with a band gap of 1.88-1.885 eV appear to be substantially ordered as shown in the dark-field image, while those grown at 600°C with similar band gaps exhibit almost no ordering. This observation is consistent with the observations of Kondow et al. [26] but conflicts with the observations of Gomyo et al. [24]. The discrepancy may be related to the fact that the order parameter of a thin film is very difficult to measure. (X-ray diffraction of very thin samples is difficult, and the scattering of electrons is not understood well enough to give a quantitative order parameter from the electron diffraction superlattice-spot intensity.) We have chosen to estimate the ordering from the dark-field images, but this method only shows that some ordering exists in a large volume of the films grown at 740°C. We cannot conclude anything about the extent of the ordering within the ordered volume. It is quite likely that the superlattice spots result from regions of alternating $Ga_{0.5-\delta}In_{0.5+\delta}P$ and $Ga_{0.5+\delta}In_{0.5-\delta}P$ layers where $0<\delta<0.5$, especially since Kondow et al. [39] have observed $Ga_{0.7}In_{0.3}P$ films that are ordered with the same symmetry as $Ga_{0.5}In_{0.5}P$ films. It may be that at high-growth temperatures, the ordered domains become less perfectly ordered but are still abundant, while at low-growth temperatures, very few ordered domains are formed. Our attempts to accurately quantify the order parameter using x-ray powder diffraction have

been unsuccessful in establishing a correlation between the band gap and the order parameter [40].

The disordering of the $GaInP_2$ films by selenium doping is very similar to that reported previously for zinc- and magnesium-doped films. Our observations of zinc-induced disordering are very similar to those previously reported, except that slightly more (about a factor of 3) zinc was required to disorder the films. The change from ordered to disordered films takes place as the carrier concentration is increased above $10^{18}/cm^3$ for zinc [30,31], magnesium [30], and selenium. The exact numbers differ slightly depending on the laboratory and the dopant, but these differences are less than the experimental uncertainty. This similarity between the three dopants is surprising since the effect was originally attributed [30] to fast diffusion of the zinc, which is known to disorder not only $GaInP_2$ but also large period superlattices [24,29,32]. Although the bulk diffusion constants of the dopants in $GaInP_2$ are not known, selenium is a much slower diffuser than zinc in GaAs [41]. It is unlikely that selenium, zinc, and magnesium would all have such similar effects if the mechanism for all three were related to diffusion.

The similarity between the effects of zinc, magnesium, and selenium suggests that the disordering mechanism could be a colligative-type effect (i.e., dependent on the number and not the identity or diffusivity of the dopant). This seems quite plausible because impurities are known to affect the phase stability of many systems. In this case, the ordered surface structure may be destabilized by the presence of an impurity regardless of whether the impurity is zinc, magnesium, or selenium.

However, Gomyo et al. [38] have recently found that of the n-type dopants, selenium affects the ordering very similarly to zinc and magnesium, but silicon causes disordering at a much lower concentration (between 10^{16} and $4 \times 10^{17}/cm^3$) [38]. It is possible that the difference has to do with the fact that silicon can be either a p- or an n-type dopant, affecting the total carrier concentration, but this seems unlikely since no evidence of compensation has been found for silicon doping at electron concentrations less than $4 \times 10^{18}/cm^3$ [42]. Therefore, the observations of Gomyo et al. are evidence against a colligative-type mechanism.

The proposal that selenium affects the stability of an ordered surface phase implies a strong interaction between selenium and the surface of $GaInP_2$. This is supported by observations that link selenium and the surface morphology of $GaInP_2$. All $GaInP_2$ films grown under optimal conditions are specular and mirror-like to the naked eye. However, under closer examination, we have observed that $GaInP_2$ films exhibit unusual surface morphologies [43]. For films grown on (100) GaAs substrates misoriented 2° toward (110), there appears to be a correlation between surface roughness and band gap [43]. Films with anomalously low band gaps show the greatest roughness, while films with normal (high) band gaps are very smooth.

The photographs in Figure 5-16 show the effect of selenium doping on the surface morphology of $GaInP_2$ films. All of these films appear mirror-like to the naked eye. The two doped samples are so smooth that their diffuse reflectance is less than their photoluminescence (i.e., when a green laser [0.5 mW] is shone on the surface, the eye sees the red light from the photoluminescence

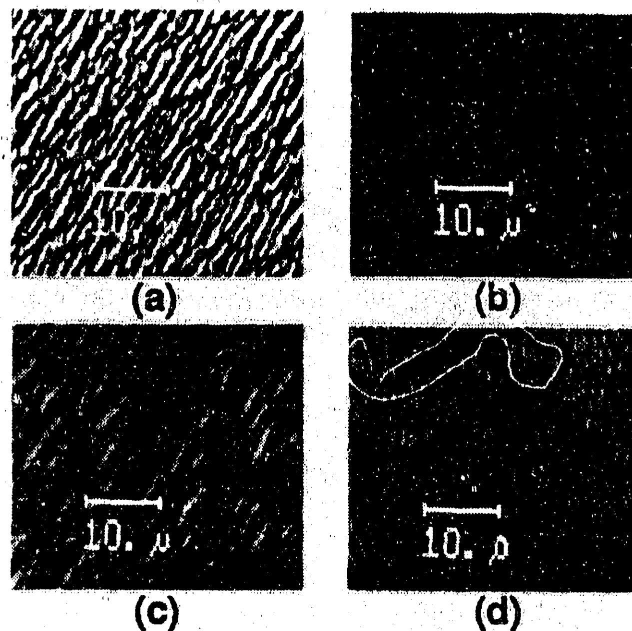

Figure 5-16. Photographs of samples: (a) undoped, grown at 670°C, (b) Se-doped $10^{19}/cm^3$, grown at 670°C; (c) undoped, grown at 740°C; and (d) Se-doped $10^{19}/cm^3$, grown at 740°C. The contrasts have been electronically enhanced to highlight the differences, resulting in saturation of the amplifier in the case of (a). The 10-μm markers show the scale.

rather than a diffusely reflected green laser light). These two smooth samples, shown in Figures 5-16(b) and 5-16(d), also have high band gaps, just as samples grown at high and low temperatures have smooth surfaces and high band gaps [43].

Although the relationship between the surface morphology and the ordering is not clear, both are influenced by surface kinetics. Just as the selenium may affect the ordering by being an impurity on the surface, it also influences the mechanism by which the surface becomes rough or smooth.

5.5 On-line Purifiers for CVD

The objective of this work was to evaluate the efficacy of the ATM Epigrade Purifier for on-line purification of arsine and phosphine. The basic approach was to use MOCVD to deposit various III-V materials, with and without the use of the purifier, and, using a newly developed photoelectrochemical spectroscopy technique, characterize the minority carrier transport properties of the deposit. The following is a brief discussion of the experimental techniques and the final results obtained to date.

Two Epigrade Purifiers were installed on the arsine and phosphine lines downstream of their flow control using a procedure similar to that contained

in the purifier operating instructions. In addition, before the purifier was opened to arsine, phoshine, or hydrogen, each line, including the bypass portion of the purifier, was purged with H_2 for 3 days at a flow of 50 cc/min. The purifiers were then conditioned with arsine or phosphine according to the purifier operating instructions.

GaAs, GaAlAs, and GaAlInP layers were grown and then characterized. For the initial phase of this work, the primary characterization tool was the electrochemical/photocurrent spectroscopy technique described by Kurtz and Olson [9]. From this technique one can obtain relative photoresponse and background carrier concentration. These measurements, including sample preparation, can be made very rapidly so that the rate-limiting step in obtaining results is the deposition process and associated factors such as yield or run-to-run reproducibility. Because of yield or reproducibility problems, a minimum number of runs are required to measure a given response with reasonable precision. In the following, some results will be presented for which the minimum number of growth runs has not been made. They are, therefore, considered preliminary results and are included only for purposes of completeness.

The first seven depositions after installing the arsine purifier were undoped GaAs runs, four with the purifier on and three with the purifier off (bypass valve open and the inlet and outlet valves closed). For all seven runs, the growth temperature, growth rate, and V/III ratio were 700°C, 200 nm/min, and 28, respectively. Statistically, the purifier has no effect on the white light photocurrent or N_D-N_A, the background carrier concentration. This is a case, however, where more data are needed because of a lack of reproducibility (i.e., the standard error of the measured effect is greater than the measured effect itself).

For AlGaAs, the growth temperature is increased to 750°C. All other growth parameters were similar to those used for the growth of GaAs. After an initial period of experimentation, a series of 18 AlGaAs growth runs was made, nine with the purifier on and nine with it off. Two runs (one each) were rejected because of anomalously low photocurrents, possibly due to a leak at the joint between the reactor inlet and the injection manifold.

Undoped, the AlGaAs is p-type with a hole concentration of 2-3 $\times$ $10^{16}/cm^3$. As discussed earlier, the hole concentration is unaffected by the state of the purifier. However, the photocurrent of the AlGaAs layers is definitely enhanced by the action of the purifier. The average photocurrent of the AlGaAs grown using the untreated arsine is 6.2 mA/cm^2. With the purifier on, the average photocurrent increases 10% to 6.8 mA/cm^2. The standard error of the difference between these two averages is 0.26 mA/cm^2. The probability that there is no real difference between the two treatments (purifier on or off) is therefore only 0.03.

AlGaAs was doped with selenium to a level of 4-5 $\times$ $10^{17}/cm^3$. All other conditions were the same as described earlier. A total of four growth runs were made, two for each treatment. The average photocurrent of the AlGaAs grown using the untreated arsine was 2.84 mA/cm^2. With the purifier on, the average photocurrent increased 37% to 3.88 mA/cm^2. The standard error of the difference is 0.43 mA/cm^2, implying that there is 0.16 chance that there is no real difference between the two average photocurrents or treatments.

These results are consistent with known properties of oxygen in AlGaAs. It is likely that the oxygen deep level in AlGaAs will have an effect on the minority carrier transport properties that is carrier-type dependent. If oxygen is a deep acceptor in AlGaAs, then in p-type material it would be negatively charged and as such should exhibit a low capture cross-section for minority carrier electrons. In n-type AlGaAs, oxygen acceptors would be neutral and therefore much more effective at trapping minority carrier holes. All of this implies that n-type AlGaAs should be more sensitive than p-type AlGaAs to oxygen contamination and, consequently, to any efforts to reduce the oxygen contamination.

GaAlInP with a band gap of ~2.15 eV was grown to test the phosphine purifier. When this material was grown no difference was found between the on and off modes. We decided to add a measureable, known impurity to the gas stream. Water vapor carried by hydrogen was injected into the phosphine line upstream of the purifier in concentrations of 0 - 4000 ppm. From 0 - 400 ppm water, there was still no difference in the on and off purifier modes. At 4000 ppm, there was degradation in the electronic properties of the material without the purifier in-line.

The results show that the phosphine purifier will remove impurities from a gas stream. It is more interesting to note that at high-impurity concentrations, GaAlInP suffered no ill effects. This implies that some self-gettering process not yet understood occurs in the vapor phase. This observation lends support to the group's proposal that the GaInP group of compounds grown in cascade cell structures is much less sensitive to impurity problems than the GaAlAs group of compounds.

5.6 References

1. J. C. C. Fan, B. Y. Tsaur, and B. J. Palm, in Proceedings of the 16th IEEE Photovoltaics Specialists Conference (IEEE, New York), 1982, p. 692.

2. S. M. Bedair, J. A. Hutchby, J. P. C. Chiang, M. Simons, and J. R. Hauser, in Proceedings of the 15th IEEE Photovoltaics Specialists Conference (IEEE, New York), 1981, p. 21.

3. J. M. Olson and A. Kibbler, J. Cryst. Growth 77 (1986) p. 182.

4. J. M. Olson, A. E. Kibbler, and S. R. Kurtz, in Proceedings of the 19th IEEE Photovoltaic Specialists Conference (IEEE, New York), 1987, p. 285.

5. S. R. Kurtz, J. M. Olson, and A. Kibbler, Solar Cells 24 (1988) p. 307.

6. A. Saletes, A. Rudra, P. Basmaji, J. F. Carlin, M. Leroux, J. P. Contour, P. Gibart, and C. Verie, in Proceedings of the 19th IEEE Photovoltaic Specialists Conference (IEEE, New York), 1987, p. 124.

7. T. Glatfelter and J. Burdick, in Proceedings of the 19th IEEE Photovoltaic Specialists Conference (IEEE, New York), 1987, p. 1187.

8. B.-C. Chung, G. F. Virshup, S. Hikido, and N. R. Kaminar, Appl. Phys. Lett. 55 (1989) p. 1741.

9. S. R. Kurtz and J. M. Olson, in Proceedings of 19th IEEE Photovoltaics Specialists Conference (IEEE, New York), 1987, p. 823.

10. J. S. Yuan, M. T. Tsai, C. H. Chen, R. M. Cohen, and G. B. Stringfellow, J. Appl. Phys. 60 (1986) p. 1346.

11. Y. Ohba, M. Ishikawa, H. Sugawara, M. Yamamoto, and T. Nakanisi, J. Cryst. Growth 77 (1986) p. 374.

12. G. H. Olsen and M. Ettenberg, in Crystal Growth Theory and Technique, Vol. 2, C. H. L. Goodman, ed. (Plenum Press, New York), 1978, p. 47.

13. J. M. Olson, R. K. Ahrenkiel, D. J. Dunlavy, Brian Keyes, and A. E. Kibbler, Appl. Phys. Lett. 55 (1989) p. 1208.

14. J. J. Loferski, J. Appl. Phys. 27 (1956) p. 777.

15. J. M. Olson, S. R. Kurtz, A. E. Kibbler, and P. Faine, Appl. Phys. Lett. (accepted for publication).

16. M. E. Nell and A. M. Barnett, IEEE Trans. Electron Devices ED-34 (1987) p. 257.

17. M. W. Wanlass, K. A. Emery, T. A. Gessert, G. S. Horner, C. R. Osterwald, and T. J. Coutts, to be published in Solar Cells.

18. R. Hulstrom, R. Bird, and C. Riordan, Solar Cells 15 (1985) p. 365.

19. The calculations are discussed in more detail in Refs. 4-6 and in books such as Martin A. Green, Solar Cells, Operating Principles, Technology, and System Applications (Prentice-Hall, Englewood Cliffs, New Jersey), 1982, pp. 62-101; Alan L. Fahrenbruch and R. H. Bube, Fundamentals of Solar Cells Photovoltaic Solar Energy Conversion (Academic Press, New York), 1983, pp. 210-243.

20. A. Gomyo, T. Suzuki, and S. Iijima, Phys. Rev. Lett. 60 (1988) p. 2645.

21. J. M. Olson, S. R. Kurtz, and A. E. Kibbler, in Proceedings of the 20th IEEE Photovoltaic Specialists Conference, Las Vegas, Nevada, (IEEE, New York), 1988, p. 777.

22. A. Gomyo, K. Kobayashi, S. Kawata, I. Hino, T. Suzuki, and T. Yuasa, J. Cryst. Growth 77 (1986) p. 367.

23. Y. Ohba, M. Ishikawa, H. Sugawara, M. Yamamoto, and T. Nakanisi, J. Cryst. Growth 77 (1986) p. 374.

24. A. Gomyo, T. Suzuki, K. Kobayashi, S. Kawata, I. Hino, and T. Yuasa, Appl. Phys. Lett. 50 (1987) p. 673.

25. T. Suzuki, A. Gomyo, S. Iijima, K. Kobayashi, S. Kawata, I. Hino, and T. Yuasa, Jap. J. Appl. Phys. 27 (1988) p. 2098.

26. M. Kondow, H. Kakibayashi, S. Minagawa, Y. Inoue, T. Nishino, and Y. Hamakawa, Appl. Phys. Lett. 53 (1988) p. 2053.

27. T. Suzuki, A. Gomyo, and S. Iijima, J. Cryst. Growth 93 (1988) p. 396.

28. J. E. Bernard, L. G. Ferreira, S.-H. Wei, and A. Zunger, Phys. Rev. B38 (1988) p. 6338.

29. F. P. Dabkowski, P. Gavrilovic, K. Meehan, W. Stutius, J. E. Williams, M. A. Shahid, and S. Mahajan, Appl. Phys. Lett. 52 (1988) p. 2142.

30. T. Suzuki, A. Gomyo, I. Hino, K. Kobayashi, S. Kawata, and S. Iijima, Jap. J. Appl. Phys. 27 (1988) L1549.

31. E. Morita, M. Ikeda, O. Kumagai, and K. Kaneko, Appl. Phys. Lett. 53 (1988) p. 2164.

32. W. D. Laidig, N. Holonyak, Jr., M. D. Camras, K. Hess, J. J. Coleman, P. D. Dapkus, and J. Bardeen, Appl. Phys. Lett. 38 (1981) p. 776. J. W. Lee and W. D. Laidig, J. Elec. Mat. 13 (1984) p. 147.

33. T. Iwamoto, K. Mori, M. Mizuta, and H. Kukimoto, J. Cryst. Growth 68 (1984) p. 27.

34. Elias Burstein, Phys. Rev. 93 (1954) p. 632.

35. C. Alibert, G. Bordure, A. Laugier, and J. Chevallier, Phys. Rev. B6 (1972) p. 1301. Alibert et al. report the effective masses for bulk $Ga_xIn_{1-x}P$. These may differ for $GaInP_2$ films with anomalously low band gaps.

36. M. Druminski, H.-D. Wolf, K.-H. Zschauer, and K. Wittmaack, J. Cryst. Growth 57 (1982) p. 318.

37. J. P. Goral, S. Kurtz, J. M. Olson, and A. Kibbler, J. Elec. Mat. (1989).

38. A. Gomyo, H. Hotta, I. Hino, S. Kawata, K. Kobayashi, and T. Suzuki, Jap. J. Appl. Phys. 28 (1989) L1330.

39. M. Kondow, H. Kakibayashi, T. Tanaka, and S. Minagawa, Phys. Rev. Lett. 63 (1989) p. 884.

40. S. R. Kurtz, J. M. Olson, and A. Kibbler, Appl. Phys. Lett. 54 (1989) p. 718.

41. The diffusion coefficient of selenium in GaAs at 700°C was measured to be 3×10^{-18} cm^2/s by B. Goldstein, Phys. Rev. 121 (1961) p. 1305; that of zinc in GaAs is concentration dependent and about 10^{-12} cm^2/s for the conditions of interest, H. C. Casey, Jr., M. B. Panish, and L. L. Chang, Phys. Rev. 162 (1967) p. 660.

42. H. Hotta, I. Hino, and T. Suzuki, J. Cryst. Growth 93 (1988) p. 618.

43. J. M. Olson, S. R. Kurtz, A. Kibbler, to be published.

6.0 SOLID-STATE THEORY

Investigators

A. Zunger, Principal Scientist and Group Leader
D. M. Wood, Senior Scientist (to August, 1989)
S. Froyen, Staff Scientist
S.-H. Wei, Research Associate
R. Dandrea, OER-BES Post-Doctoral Scientist
Z. W. Lu, OER-BES Post-Doctoral Scientist (from June, 1989)
J. E. Bernard, DDF Post-Doctoral Scientist

6.1 Introduction

The past 10 years have witnessed dramatic developments and breakthroughs in theoretical physics techniques aimed at atomic-level understanding of the electronic structure of superconductors, metals, clusters, alloys, and other quantum behavior that underlies the properties of real materials. It is now possible to predict from "first principles" the optical, magnetic, electrical, and thermodynamic properties of some simple materials before measurements are done. At the same time, equally dramatic developments occurred in our ability to grow in the laboratory "artificial" crystal structures through atomic-level control of the growth process [e.g., by molecular beam epitaxy (MBE) and organo-metallic vapor phase epitaxy (OM-VPE)]. Many crystal structures, consisting of particular architecture of atomic positions (even those not present in nature) can now be grown on demand.

The primary mission of the solid-state theory research effort is to (1) bring state-of-the-art methods and ideas of condensed matter theory into the realm of photovoltaic materials, and thus (2) develop a fundamental understanding of the elements that constitute and enhance solar cell performance, and (3) use this knowledge to design novel photovoltaic materials that could be grown and tested in the laboratory by modern crystal growth techniques. The second mission is to analyze the properties of existing materials. Unlike simple devices (e.g., the transistor), the underlying complexity of solar cells in terms of their chemical constitution, diverse atomic structures, defects, interfaces, and varying degrees of order leads to a dependence of their performance (e.g., efficiency) on a very large number of material parameters that are difficult to disentangle and isolate. Solid-state theory research attempts to address these problems by modeling the electronic structure of prototype systems that isolate these effects. This includes modeling of the basic electronic structure of

- Defects and impurities in semiconductors
- Optical properties of alloys
- Stability and thermodynamics of superlattices
- Band gaps of novel ternary semiconductors
- Surfaces and interfaces of semiconductors.

This type of research is aimed at parallel theoretical and experimental studies and is intended to ensure that photovoltaics will continuously benefit from breakthroughs done in other areas of condensed matter physics. This approach supplements the more conventional trial-and-error approaches to design.

This report summarizes work in FY 1989 in the following areas (specific references to papers published on work in this reporting period are given in brackets and listed in Section 6.9):

- Stability and band offsets of heterovalent superlattices Si/GaP, Ge/GaAs, and Si/GaAs [1]
- Temperature-composition phase diagrams of bulk GaInP, AℓGaAs, and GaAsSb [2,3]
- Structures, thermodynamics, and optical properties of epitaxial alloys [4,5]
- Stability of strain layer superlattices [6]
- Electronic structure of H_2 in palladium: can solid-state effects explain "cold fusion"? [7,8]
- Ordering in semiconductor alloys [9]
- Band structure of random alloys [10].

This section describes progress along these lines; work partially funded by the Office of Energy Research/Basic Energy Sciences (OER-BES) is indicated by an asterisk. Published references pertaining to work carried out during this reporting period follow the title of each subsection.

6.2 Stability and Band Offsets of Heterovalent Superlattices Si/GaP, Ge/GaAs, and Si/GaAs [1]

Heteropolar interfaces form whenever a III-V material is combined with the elemental semiconductors silicon and germanium. To systematically study the electronic structure and stability of such interfaces, Dandrea, Froyen, and Zunger [1] have performed first principles pseudopotential calculations for the following column IV/column III-V semiconductor superlattices: Si/GaP, Ge/GaAs, and Si/GaAs. Ge/GaAs interfaces and superlattices have in the past been extensively studied as prototypical examples of lattice-matched IV/III-V systems. In addition, the lattice-matched Si/GaP system and the strained Si/GaAs system were selected as two systems of experimental interest. Among the superlattice directions included in this study, two ([001] and [111]) have polar interfaces and one [110] has a nonpolar interface. Each interface in the polar superlattices contains either only III-IV or IV-V bonds. Such non-octet bonds give rise to partially occupied, localized, interface states. Provided that such ideal interfaces can be manufactured, these states lead to charged interfaces and very large, oscillating electric fields in the superlattice direction. Such polar interfaces are likely to be unfavorable and reconstruction (intermixing) of the atoms at the interfaces will take place to eliminate the fields. Dandrea, Froyen, and Zunger systematically studied the relative stability of both the polar and the nonpolar interfaces, including reconstructions, for the three IV/III-V systems. This enabled them to present a simple two-parameter model that successfully described the energetics for all the interfaces considered and allowed them to model the energetics of more complicated interfacial reconstructions. They also presented the valence band offsets for all superlattices without residual electric fields. For the reconstructed interfaces these depend strongly on the type of reconstruction and can therefore be used as a probe into the structure of the experimentally grown interfaces through comparison to the measured band offsets.

The calculated total energies for the superlattices with respect to unstrained constituents are given in Table 6-1. Also tabulated for the lattice-mismatched Si-GaAs case are energies of the strained constituents (indicated by n=∞). Also shown, in Figure 6-1 are the energies per 4n atoms as a function of n for the unrelaxed Si-GaP superlattices. For a given value of n, the [111] superlattices have the lowest energy. This is because these superlattices have only half the number of non-octet bonds (all are along the [111] direction) compared to [001] and [110] superlattices with the same n.

Note that the non-octet bonds always come in pairs: there are equal numbers of III-IV bonds and IV-V bonds. From electron counting, a III-IV bond is expected to behave as an acceptor, with 1/4 electron missing, and a IV-V bond as a donor, with 1/4 extra electron. These donors and acceptors would exist as interface states at uncompensated interfaces. However, in the superlattices, there is the possibility for compensation where the extra electrons in the IV-V bonds transfer to the III-IV bonds, gaining energy of the order of the gap. For nonpolar interfaces, where both types of bonds are present, the charge transfer occurs within a given interface, and the compensation is expected to be complete. For the polar [001] and [111] interfaces, however, where each interface contains one type of bond only, compensation involves inter-interface charge transfer, producing electric fields and a potential drop across each sublayer. The potential drop is proportional to both the charge transfer and n, and since the potential difference cannot exceed the band gap, the charge transfer must go as 1/n for large n. Note that this charge-transfer argument predicts the electric fields to run from the IV-V donor interface to the III-IV acceptor interface in all unreconstructed polar superlattices. We indeed find this to be the case.

The fields can be eliminated and the compensation improved by swapping atoms between interfaces (e.g., one-half of the silicon atoms at the phosphorus interface with one-half of the gallium atoms at the gallium interface). This allows the compensation to take place intra-interface. For the [001] superlattices, the reconstruction does not create additional non-octet bonds and is expected to be energetically favorable. For n = 1, the reconstruction increases the energy (see Table 6-1) presumably because the layers are too thin. For n = 2, there are four possible reconstructions: a III-IV (cation) or a IV-V (anion) swap, and atoms can be swapped directly above one another in the [001] direction (vertical) or not directly above on another (staggered). All reconstructions lower the energy considerably compared to the unreconstructed superlattices, and the vertical swap appears to be favored by a small amount. The energy difference between swapping the anion or cation is negligible for Ge/GaAs and favors a cation swap for Si/GaP and Si/GaAs. These energy differences are small, however, and a more complicated combination of anion and cation swaps cannot be ruled out. For the [111] superlattices, each swap would increase the number of non-octet bonds by four. Complete intra-interfacial compensation is achieved by swapping every fourth interface atom. This results in a 50% increase in the number of non-octet bonds and considering the large energy difference between the unreconstructed [111] and the nearly optimally compensated [110] superlattices, a [111] reconstruction would appear unlikely to be energy lowering. This will be investigated further below using an energy model.

Table 6-1. Calculated Total Energies of Ideal and Reconstructed Heteropolar Superlattices. The reconstructed superlattices are described in the text. The energies in parentheses refer to unrelaxed geometries with the atoms in their ideal zincblende positions. The energies are given in eV per four atoms. We estimate an uncertainty in the values of up to 20 meV.

$\vec{G}$	n	Reconstruction	Energy Si/GaP	Energy Ge/GaAs	Energy Si/GaAs
[001]	1	No	0.485(0.499)	0.393(0.448)	0.489
		Yes	(0.505)	(0.453)	-
	2	No	0.343(0.360)	0.257(0.271)	0.367
		Cation vertical	0.216(0.248)	0.182(0.205)	0.245
		Cation staggered	-	(0.227)	-
		Anion vertical	0.236(0.249)	0.178(0.200)	0.265
		Anion staggered	-	(0.227)	-
	3	No	0.232(0.257)	0.196(0.205)	-
	∞	No	0.0	0.0	0.043
[110]	1	No	0.485(0.499)	0.393(0.448)	0.507
	2	No	0.125(0.189)	0.124(0.146)	0.184
	3	No	0.109(0.149)	(0.136)	-
	4	No	0.069(0.103)	-	-
	∞	No	0.0	0.0	0.054
[111]	1	No	0.118(0.167)	0.131(0.137)	0.192
	2	No	0.089(0.116)	-	0.158
	3	No	0.077(0.097)	-	-
	∞	No	0.0	0.0	0.054

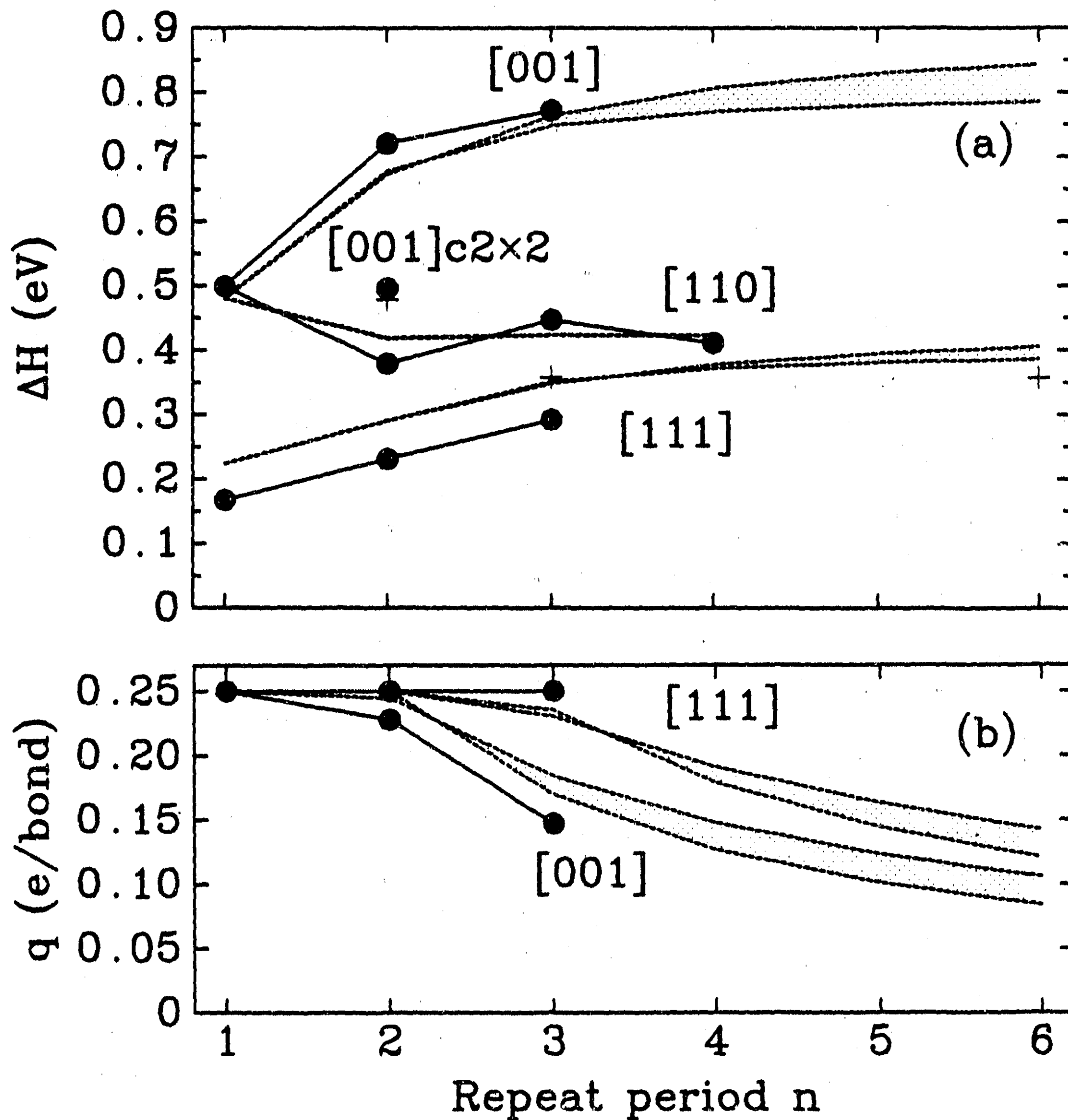

Figure 6-1. Calculated and modeled total energies of nonisovalent, unrelaxed Si-GaP superlattices. The energies are given in eV per 4n atoms with zero at the energy of the segregated constituents. The reconstructured superlattices are described in the text. The modeled energies (dashed lines) are calculated from Eq. 6-2 and correspond to a range of the parameter. The extreme values are $\varepsilon_g(0) = 0.8$ eV, $I = 0.20$ eV, $U^D + U_A = 1.71$ eV and $\varepsilon_g(0) = 1.2$ eV, $I = 0.22$ eV, $U^D + U_A = 3.52$ eV.

Formation energies for non-isovalent superlattices are an order of magnitude larger than for the isovalent ones. The following develops a model that captures the major physics of the results. The model consists of two terms: the first is the energy, I, of the uncompensated non-octet bond (actually the average of a pair of III-IV and IV-V bonds); the second is the energy gained in the donor-to-acceptor compensation transfer. To calculate the second term,

start with the difference between the donor and acceptor energy levels. To first order in the donor-acceptor charge transfer q, the energy level difference is given by

$$\varepsilon_g(q) = \varepsilon_g(0) - \frac{1}{\varepsilon_0}(V^D_{Mad} + V^A_{Mad})q - (U^D + U^A)q \ , \qquad (6\text{-}1)$$

where $\varepsilon_g(0)$ is the uncompensated energy difference; q is the donor-acceptor charge transfer; V^D_{Mad} and V^A_{Mad} are the electrostatic Madelung potentials at the donor and acceptor bond, respectively, resulting from an unscreened charge transfer of one electron; ε_0 is the static dielectric constant; and U^D and U^A are the intra-bond electron repulsion (this includes both electrostatic and exchange-correlation contributions). Equation 6-1 can be derived from the local density approximation (LDA) total energy expression using linear response and by assuming that the donor and acceptor states are localized, spherical, and centered at the bonds. The integral of Eq. 6-1 with respect to q is the total energy change upon a donor-to-acceptor charge transfer q. Thus the superlattice total energy per pair of non-octet bonds becomes

$$E_{Total} = 2I - \int_0^q \varepsilon_g(q)\, dq = 2I - \varepsilon_g(0)q + \frac{1}{2\varepsilon_0}(V^D_{Mad} + V^A_{Mad})q^2 + \frac{1}{2}(U^D + U^A)q^2 \ . \qquad (6\text{-}2)$$

The charge transfer q is calculated from Eq. 6-1 by setting $\varepsilon_g(q) = 0$ and then limiting q to a maximum of 0.25 electrons. Because q achieves close to its fully compensated value, 0.25, in all cases except for n = 3 [001], one cannot fit all the parameters in Eq. 6-2 independently. Most of the superlattice energy differences are thus determined by the Madelung terms, which are not fit but calculated, and the remaining parameters are only used to fit the overall energy scale. ε_0 has been set equal to 10.4 (the average of Si and GaP). To improve the robustness of the fit, we also fit the n = 3 charge transfer (calculated to be 0.15 electrons) in addition to the total energies. Fitting the non-octet bond energy, I, and the electron repulsion, $U^D + U^A$, Eq. 6-2 reproduces the calculated energies with fair accuracy (see Figure 6-1). There are still insufficient data to fit $\varepsilon_g(0)$ as an independent parameter. Indeed $\varepsilon_g(0)$ can be chosen over a range of values from 0.6-0.2 eV without affecting the accuracy fit [changes in $\varepsilon_g(0)$ are offset by changes in $U^D + U^A$].

The accuracy of the model is remarkable considering its simplicity and its crude assumptions. In particular, it is assumed that charges on neighboring bonds are fully screened (using ε_0). Such charged, neighboring bonds occur in the [001] and the reconstructed [111] superlattices. This is certainly not true and the fit can be improved by a factor of two by introducing one additional parameter to account for the repulsion between equal charges on neighboring bonds.

Using the model one can investigate other possible structures. Figure 6-1 shows the model energies of some longer period superlattices. This extrapolation becomes somewhat uncertain because of its dependence on the choice for $\varepsilon_g(0)$. The figure therefore shows results for a range of $\varepsilon_g(0)$ between 0.8-1.2 eV. Estimated energies for the reconstructed [111] superlattices with a vertical cation or anion swap (the model does not distinguish the two) is also given. Note that the n = 3 superlattice will not reconstruct (according to the model) but that the n = 6 will.

Finally, the calculation allows an estimate of band offsets. For the polar interfaces, the electric fields make an estimate of the offsets impossible. However, for the nonpolar [110] and the reconstructed [001] interfaces, reliable estimates can be obtained even in superlattices as thin as n = 2. The resulting calculated valence band offsets are tabulated in Table 6-2. For the lattice mismatched Si/GaAs system on silicon, the offset for the average of the strain split valence band maximum of GaAs is given.

Table 6-2. Calculated Strain-Averaged Valence Band Offsets (in eV) for [001] Reconstructed and [110] Unreconstructed Superlattices. A positive valence band offset puts the valence band maximum on the column IV sublattice. $\vec{G}$ denotes orientation.

		Valence Band Offset		
$\vec{G}$	Reconstruction	Si/GaP	Ge/GaAs	Si/GaAs
[001]	Cation vertical	0.8	0.7	0.3
	Anion vertical	0.0	0.1	-0.5
[110]	No	0.45	0.5	0.1

Dandrea, Froyen, and Zunger [1] conclude that the formation energies of non-isovalent superlattices are mostly determined by the energy of non-octet III-IV and IV-V bonds and electrostatic interactions between these. They have formulated a simple model that incorporates these effects and that successfully describes our formation energies calculated from first-principles methods. It would appear that such interactions should also be an integral part of any successful description of non-isovalent alloys. They found that [001] superlattices with their charged polar interfaces are unstable with respect to interface reconstructions that remove the interface charges, even for periods as short as n = 2. The similarly polar [111] superlattices are the most stable superlattices (among [001], [110], and [111]), and they estimate that these are stable against reconstruction up to n = 3.

6.3 Temperature-Composition Phase Diagrams of Bulk GaInP, AℓGaAs, and GaAsSb [2,3]

Simple binary semiconductors such as Si, Ge, GaP, GaAs, InP, and AℓAs have been used as the "core materials" for a wide range of electronic and opto-electronic device integrated circuits (IC), very-large-scale-integration (VLSI), light-emitting diodes (LED), lasers, solar cells, detectors, etc. Since the existing list of such simple semiconductors provides but a limited range of materials properties (band gaps, carrier mobilities, lattice parameters), it has been a common practice to form solid solutions A_xB_{1-x} of the parent compounds A and B, attempting thereby to obtain materials properties that are intermediate between those of A and B. These alloys are grown either

in bulk form or epitaxially on a substrate. Unlike the parent semiconductors A and B, the alloys A_xB_{1-x} are (1) disordered and, therefore, generally have lesser electron mobility; and (2) structurally unstable toward low-temperature disproportionation into their binary constituents. (Their mixing enthalpy ΔH is positive, so their free energy ΔH-TS is negative only at sufficiently high temperature T, where the -TS entropy term overwhelms ΔH.) Until recently, it was believed that all such isovalent semiconductor pairs A and B (where A and B are either IV-IV, III-V, or II-I semiconductors) exist either as disproportionation products A+B or as disordered solid solutions A_xB_{1-x}. In 1985 and 1986, we predicted theoretically that hitherto unknown long-range ordered stoichiometric intersemiconductor compounds A_nB_{4-n} $(1 \le n \le 3)$ can be thermodynamically more stable (below some growth temperature T_c) than the disordered alloy. Such ordered compounds form a novel class of semiconductors in that (1) their crystal structures are unprecedented in conventional semiconductor physics (they can appear in tetragonal CuAuI-like, rhombohedral CuPt-like, or chalcopyrite-like modifications), (2) their band structures (hence, band gaps, effective masses, etc.) differ from either the average of the constituents or from those of the disordered alloy, and (3) some of them are thermodynamically more stable (i.e., have lower ΔH) than the equivalent disordered alloy.

In this work we have calculated the phase diagrams of those semiconductor alloys often used in photovoltaic cells (e.g., GaAlAs, GaInP, and InGaAs). The procedure used is as follows (for details, see Ref. 2): We select a set of N_s periodic structures {s}, compute the excess total energies $\{\Delta E(s,V)\}$ from electronic structure theory, and obtain by inversion the N_s interaction energy functions $\{J_f(V)\}$. This set is then used in the cluster expansion to predict the total energies $\{\Delta E(s',V)\}$ for another set $\{s'\} \neq \{s\}$ of periodic structures. This prediction is compared with the directly calculated values of $\Delta E(s',V)$ from electronic structure theory. The difference between the energies $\{\Delta E(s'V)\}$ obtained from the series expansion prediction and the "exact" linearized augmented plane wave (LAPW) excess energies is then minimized by varying the number and types of figures {F} used in the cluster expansion, thus establishing the minimum sizes of K and M required to produce a given maximum error we are prepared to tolerate. Our study of isovalent zincblende semiconductor alloys showed that to achieve a relative error of only a few percentage points in ΔE requires retention of up to fourth fcc neighbors for M and up to four-body nearest neighbor for K. These include eight $J_{k,m}$ terms: (1) a normalization term $J_{0,1}$; (2) a sites-only term $J_{1,1}$; (3) four-pair interaction terms $J_{2,1}$, $J_{2,2}$, $J_{2,3}$, and $J_{2,4}$ between first, second, third, and fourth fcc neighbors, respectively (abbreviated in what follows as J_2, K_2, L_2, and M_2, respectively); and (4) a three-body $J_{3,1}$ and a four-body $J_{4,1}$ nearest-neighbor terms. Our previous study also established an optimal set of structures {s} consistent with the above requirements. Having established a "complete" set of interaction energies {J}, we use these in an Ising Hamiltonian, which describes the thermodynamics of the alloy. The Ising Hamiltonian is then solved by the Monte Carlo and by the Cluster Variation methods.

Figure 6-2 shows the reduced mixing enthalpy ("interaction parameter")

$$\hat{\Omega}(x,T) = \Delta H(x,T)/x(1-x) \qquad (6\text{-}3)$$

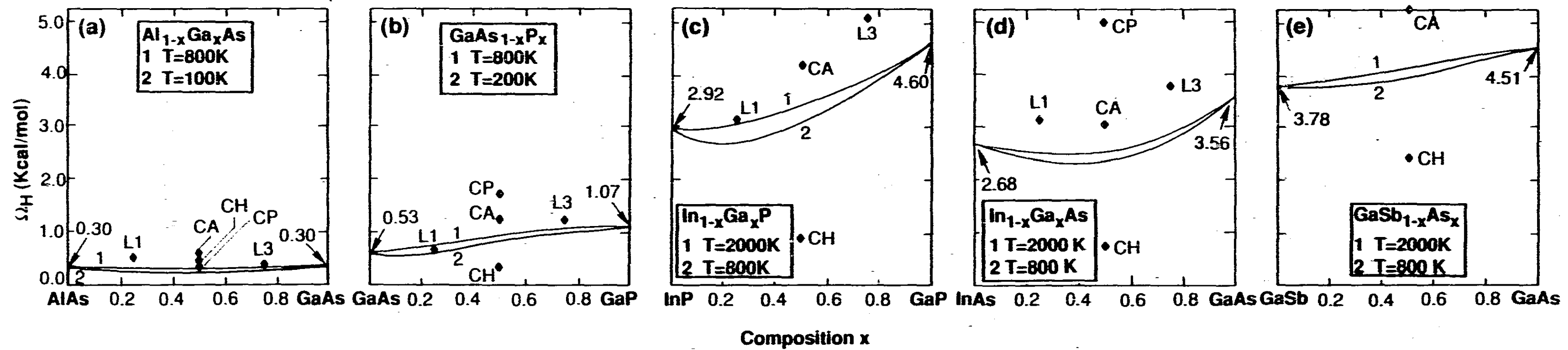

Figure 6-2. Calculated reduced enthalpy for the disordered alloy (solid lines) and for ordered compounds (diamonds)

for the disordered alloy at two temperature (solid lines), and the analogous quantity (reduced formation enthalpy) for the ordered compounds s at T = 0

$$\hat{\Omega}_s(X_s, T = 0) = \Delta E(s,V_s)/X_s(1-X_s) , \qquad (6-4)$$

(depicted as solid diamonds).

The basic features of our results in Figure 6-2 are as follows:

1. For size-mismatched alloys, the (201)-type structures such as chalcopyrite have a lower enthalpy than the disordered alloy. We will see below that this leads to metastable long-range ordering of size-mismatched semiconductor alloys, as observed in liquid-phase epitaxy (LPE) growth (Nakayama and Fujita) of $In_{1-x}Ga_xAs$ and in vapor growth (Jen et al.) of $GaSb_{1-x}As_x$.

2. For size-matched alloys, the disordered alloys have a lower enthalpy than any of the simple ordered structures studied; hence, no thermodynamically mandated ordering is expected in size-matched semiconductor alloys. The CuAu-I-like ordering observed by Kuan et al. in $A\ell_{1-x}Ga_xAs$ is likely to be surface-induced.

3. The CuPt ordering recently observed in epitaxial growth of size-mismatched semiconductor alloys is characterized by a considerably higher enthalpy than the disordered alloy; hence, bulk effects produce neither stable nor metastable CuPt ordering in size-mismatched semiconductor alloys.

4. $\hat{\Omega}(x,T)$ has a significant composition dependence neglected by most phenomenological models (e.g., Panish and Ilegems). Note that when B is the smallest of the two atoms in $A_{1-x}B_x$, we find that $\hat{\Omega}(0) < \hat{\Omega}(1)$. This reflects the fact that more energy is required to incorporate a large atom A in a small host crystal B (i.e., $x \to 1$) than to incorporate a smaller atom B in a large host crystal A (i.e., $x \to 0$).

Figure 6-3 depicts the calculated phase diagrams of the five III-V alloy systems in the high-temperature range where disordered alloys exist. The calculations show the binodal ("miscibility") line as well as the spinodal. The binodal is the line in the (x,T) plane where the A-rich and B-rich disordered phases have equal chemical potentials μ. The spinodal line describes the limit of metastability of the disordered phase when $d^2F/dx^2 = d\mu/dx = 0$, F being the free energy. In all cases, we find that the thermodynamically stable ground state corresponds to phase separation. The phase diagrams are generally asymmetric with respect to $x = 1/2$.

Experimental data on the solid-state part of semiconductor alloy phase diagrams are fragmentary: Although detailed data exist on the high-temperature liquid and solidus lines, the low atomic diffusion constants at lower temperatures make such studies in solid semiconductors difficult. A notable exception is the recent data of Ishida et al. for $GaSb_{1-x}As_x$ shown in Figure 6-3(e) and exhibiting close agreement with the calculation.

The persistently lower formation enthalpy of the ABC_2 chalcopyrite structure relative to the disordered phase in size-mismatched alloys (Figure 6-2) suggests the possibility of metastable long-range ordering into this structure. We calculated the temperature limit of stability for this phase, according to

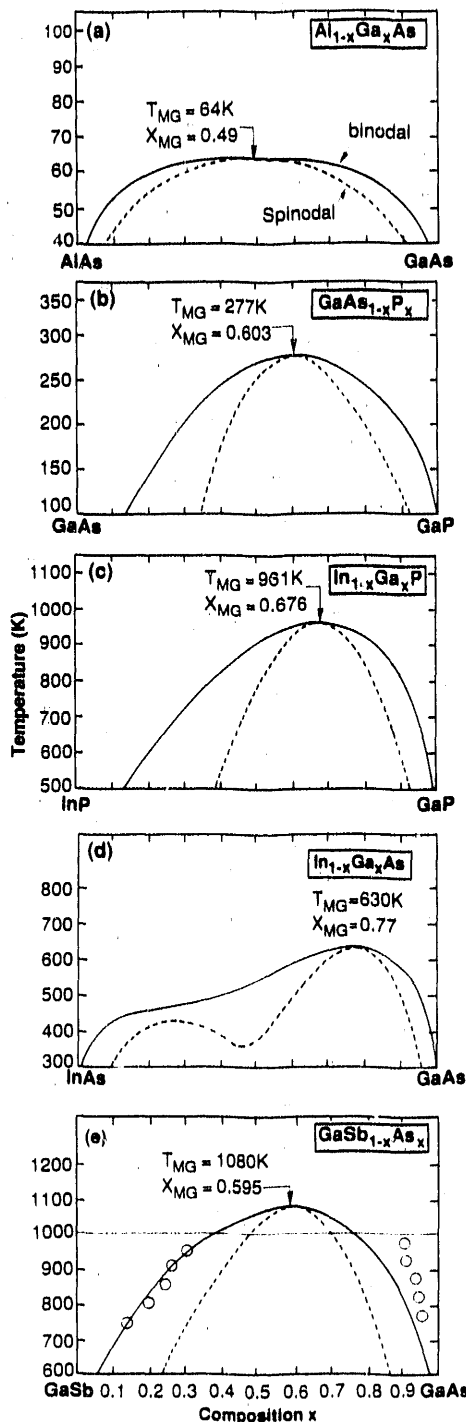

Figure 6-3. Calculated phase diagrams for the III-V alloys (a) $AP_{1-x}Ga_xAs$, (b) $GaAs_{1-x}P_x$, (c) $In_{1-x}Ga_xP$, (d) $In_{1-x}Ga_xAs$, and (e) $GaSb_{1-x}As_x$. The solid (dashed) lines give the binodal (spinodal) lines. Low-temperature ordered phases are not shown. The arrows point to the maximum miscibility gap (MG) temperatures and compositions. The circles in (e) are the recent experimental data of I. Shida et al.; the horizontal line represents the peritectic line.

$$\frac{\partial^2 F}{\partial x^2} = 0 \; . \qquad (6\text{-}5)$$

At thermodynamic equilibrium, the system phase separates below T_{MG} into AC-rich plus BC-rich mixtures, while above T_{MG} a homogeneous alloy persists. If, however, phase separation is kinetically inhibited, metastable long-range ordering will persist below T_c. These structures are metastable in a very specific manner: They are more stable below T_c than the homogeneous disordered alloy but unstable with respect to phase separation. Note that other ordered structures such as CuPt or CuAuI are not metastable; they are unstable both with respect to disordering and phase separation.

6.4 Structures, Thermodynamics, and Optical Properties of Epitaxial Alloys [4,5]

The most widely used semiconductors are the indirect band-gap materials silicon and germanium. Most applications in opto-electronics, however, require semiconducting materials with direct band gaps. If silicon or germanium could somehow be manufactured with direct band gaps of the appropriate magnitude, their already mature technology could be harnessed in integrated optics. One way to modify the electronic structure of a material is to impose additional structural order, e.g., by ordering the atoms of a disordered alloy into a superlattice. Such order will modify the Brillouin zone of the material and may cause the electron energy bands to fold, making previously indirect transitions direct. This possibility has spurred the current interest in short-period superlattices of silicon and germanium, in particular superlattices grown in the [001] direction. Here X and points along the Δ symmetry direction fold to the center, $\bar{\Gamma}$, of the superlattice Brillouin zone, raising the possibility of a direct band-gap material. Growth of such materials has recently become possible through MBE. Pearsall et al. studied electroreflectance of Si_nGe_n superlattices on (001)Si for n = 1, 2, 4, and 6 and observed new optical transitions at 0.76, 1.25, 1.70, and 2.31 eV for n = 4.

Motivated by these results, we studied the electronic structure for such superlattices. Our work in the previous report dealt with [001]-oriented superlattices. There the system is direct only on a germanium substrate; most experiments, however, are done on a silicon substrate. To investigate the possibility for a direct band-gap superlattice on a silicon substrate, we have performed calculations for Si_nGe_n[110] superlattices on silicon for n = 4, 6, and 8. Figure 6-4 shows planar-averaged wave functions $|\psi|^2$ for the $\bar{\Gamma}$ folding states in the n = 6 superlattice.

The valence band maximum is located at $\bar{\Gamma}$. The states are now completely split by the substrate-induced strain as well as by interaction between folded-in states of the same symmetry. The uppermost valence band state, $\bar{\Gamma}_{v1}$, is localized on the germanium sublattice [see Figure 6-4(c)], and its energy approaches the germanium valence band edge as the superlattice thickness increases.

The lowest conduction band at $\bar{\Gamma}$, $\bar{X}^{001}_{c1}$, is formed by a folded-in [001] $\bar{X}$ state. The symmetry of this state changes with n, causing a small shift upward for n = 6 as it interacts with the valence band state $\bar{\Gamma}_{v2}$. This is also seen in the complementary nature of the wave functions [see Figure 6-4(b) and 6-4(d)]. There is a small residual downward dispersion immediately away from $\bar{\Gamma}$, reflecting the downward dispersion from X to the conduction band minimum at Δ in the

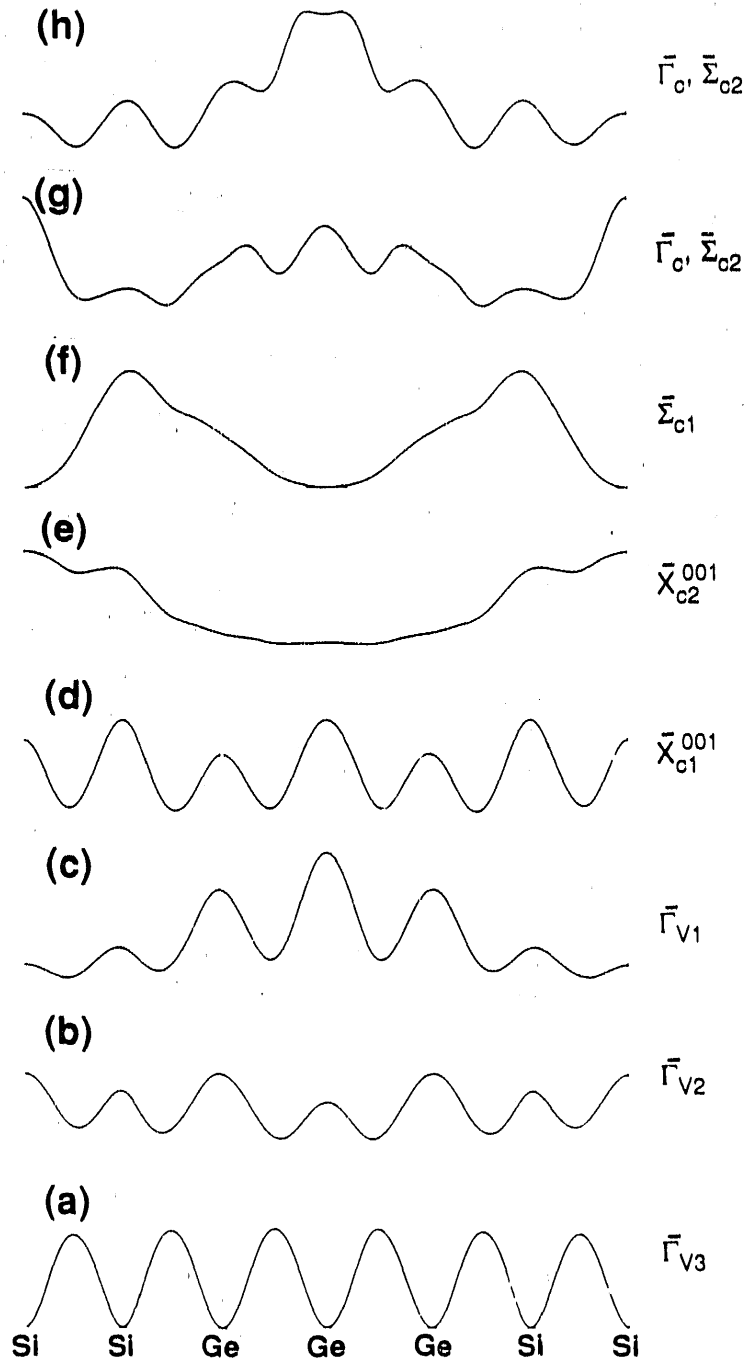

Figure 6-4. [110] planar-averaged wave functions $\bar{\Gamma}$ folding states in the [110] Si_6Ge_6 superlattice on a silicon substrate

alloy. This dispersion amounts to 35, 72, and 50 meV for n = 4, 6, and 8, respectively. For comparison, the dispersion of the folded-in [001] X states in [001]-oriented superlattices is 99, 85, and 12 meV for n = 2, 4, and 6, respectively, grown on silicon and 114 meV for the n = 4 superlattice grown on

germanium. The folding of states along the superlattice direction Σ does not lead to low energy states until n = 6, when a point close to K folds, and n = 8, when the K point itself folds. For n = 6, the folding state labeled $\bar{\Sigma}_{c2}$ interacts strongly with the original alloy Γ'_{2c} state (both of B_{1u} symmetry), making identification of their origins in alloy states impossible. The $\bar{\Gamma}$ folding conduction band states are delocalized with the exception of the $\bar{X}^{001}_{c2}$ state, which is localized on the silicon sublattice, and the upper of the $\bar{\Gamma}_c,\bar{\Sigma}_{c2}$ pair, which is localized on the germanium sublattice [see Figures 6-4(e) and 6-4(g)].

Matrix elements for transitions to states folded from the [001]X point are smaller than those folded from the Σ or K points and are much smaller for n = 4 and 8. For the new optically allowed transitions, the LDA-corrected energies are 0.96 and 1.14 eV for n = 4; 1.12, 1.27, and 1.43 eV for n = 6; and 0.97 and 1.15 eV for n = 8. The minimum indirect gaps (to $\bar{\Delta}^{001}_{min}$) are 0.74, 0.97, and 0.89 eV, respectively.

In summary, we have shown that short-period silicon-germanium superlattices exhibit new low-energy optical transitions and that they are excellent candidates for direct band-gap materials. Superlattices oriented in the [001] direction show the highest promise to be direct. Because of the strain splitting of the X valleys, the superlattices should be grown on silicon/germanium alloy (with more than 50% germanium) or germanium substrates. If a silicon substrate must be used, superlattices grown in the [110] direction exhibit quasi-direct band gaps, i.e., $\bar{\Gamma}$ is lower in energy than $\bar{X}$, but the superlattice is nevertheless indirect because of a small downward dispersion (of the order k_BT) of the lowest conduction band away from $\bar{\Gamma}$.

Our second project on properties of epitaxial systems involves band-gap narrowing in alloys [5]. Recent theoretical predictions and experimental observations demonstrated that isovalent pseudobinary $A_{1-x}B_xC$ semiconductor alloys can order into CuAu-like (CA), chalcopyrite (CH), and CuPt-like (CP) structures. We have calculated the band gaps of seven alloys in each of these three structures, as well as those of the random (R) alloys at the same 50%-50% composition. We found ordering-induced band-gap narrowing with respect to the linearly averaged gaps of the binary constituents and analyzed the physical origins for these variations.

Our calculated direct $\Gamma_{VBM} \rightarrow \Gamma_{1c}$ band gaps (Figure 6-5) generally increase in the sequence

$$E_{CP} < E_{CA} < E_R < E_{CH} < \bar{E} , \quad (6\text{-}6)$$

where $\bar{E}$ denotes the 50%-50% average of the direct gaps of the binary constituents (the only exceptions are $E_{CH} \gtrsim \bar{E}$ for lattice-matched $AlGaAs_2$ and $CdHgTe_2$). We see that the band-gap narrowing δ (with respect to the average gap of the binary constituents) is generally small in the chalcopyrite structure but can be very large in the CuPt phase. In fact, we predict that δ_{CP} is

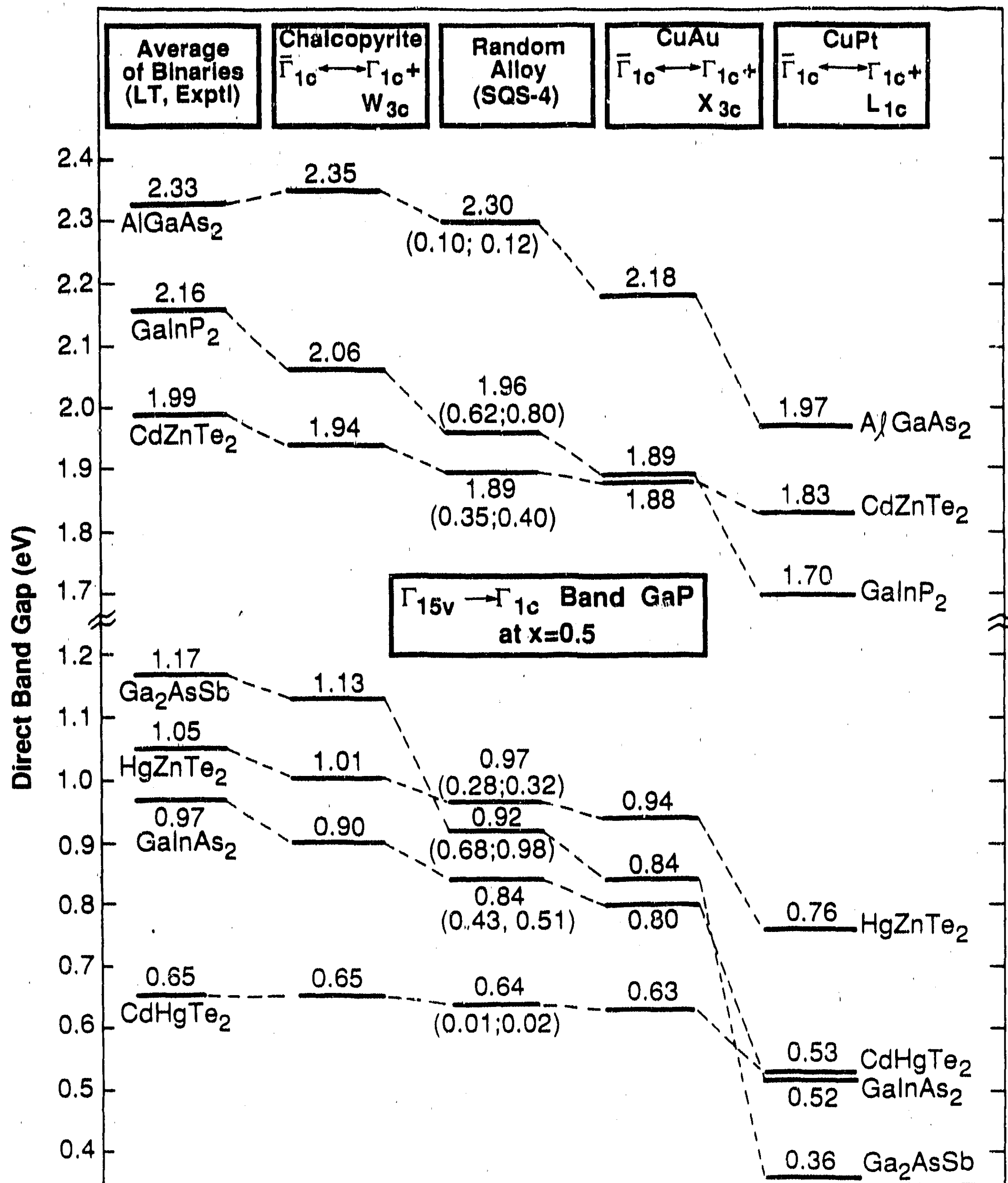

Figure 6-5. Predicted low-temperature direct band gaps $\Gamma_{VBM} \rightarrow \Gamma_{1c}$ of seven ABC_2 semiconducting systems in the CA, CH, CP, and random (SQS-4) structures. The numbers in parentheses are bowing coefficients for the random alloy with (first number) or without (second number) crystal-field average, respectively. [A=(001) superlattice (SL); CH=(201) SL; CP=(111) SL.]

so large that $AlGaAs_2$ becomes a direct-gap material in this structure, despite the fact that the corresponding 50%-50% random alloy and the CA structure of the alloy have indirect band gaps. The large variation of the band gaps

(~0.81 eV for Ga_2AsSb) with ordering highlights the possibility of tuning alloy band gaps at a fixed composition by selecting growth conditions that favor a particular structure (provided that the samples are uniform). These variations in E_g with ordering could be used as an optical fingerprint to detect particular forms of ordering in a sample. The variation is generally smaller for II-VI systems than for III-V systems. It is interesting to see in Figure 6-5 some cases of "band-gap crossings" for different systems in different structures. For instance, $GaInP_2$ has a larger gap than $CdZnTe_2$ both in the CH structure and in the random alloy; yet the opposite is predicted to be true in the CP structure. Similarly, $CdHgTe_2$ has a smaller gap than Ga_2AsSb in the CH, CA, and random structures; yet in the CuPt structure, Ga_2AsSb has a smaller gap than $CdHgTe_2$.

6.5 Stability of Strain Layer Superlattices [6]

Artificial growth of A_pB_p superlattices (SLs) is based on a series of sequential exposures of a substrate to pure compound A, then pure B, etc., thus largely circumventing the thermodynamically controlled simultaneous reaction $xA + (1 - x)B \rightleftarrows A_xB_{1-x}(\gamma)$, which could have otherwise produced a variety of microscopic arrangements γ ranging from disordered alloys to phase separation. Diffusion barriers present in the SL make it uncertain whether its apparent stability reflects these barriers or a genuine thermodynamic preference of γ = SL over γ = disordered or γ-phase separated. Postgrowth stability is addressed experimentally by reducing these kinetic barriers. Indeed, the introduction of fast-diffusing impurities catalyzes the disordering of semiconductor SLs. To clarify these issues, we use first-principles methods to investigate the excess enthalpy of the above reaction for a range of ternary III-V and II-VI semiconductor SLs as a function of repeat period p and orientation G=[001], [110], [111], and [201], as well as for their 50%-50% disordered alloys. A number of universal features are discovered. Figure 6-6 shows the results for GaAsP. Our basic conclusions are as follows:

1. In the $p \rightarrow \infty$ limit we find the universal order

$$\Delta H([001]) < \Delta H[201]) < \Delta H([110]) < \Delta H([111]) \quad , \qquad (6\text{-}7)$$

which simply reflects the different elastic energies induced by the various epitaxial growth directions. Hence the conventional [001] growth direction is indeed the stablest for long-period SLs.

2. For short-period SLs, the stability sequence differs (Figure 6-6), reflecting interfacial effects rather than the constituent's strain. To analyze this, it is useful to think of the interfacial energy I(p,G) as having a classical "strain-relief" piece I_{SR} due to atomic relaxation near the interface and a "charge-exchange" piece I_{CE} due to interfacial electronic charge redistributions. To isolate the first contribution, we have calculated $\Delta H(p,G)$ using the purely elastic valence force field (VFF) model. The results for GaP-GaAs [Figure 6-6(b)] illustrate that for G = [001] and [111], $\Delta H(p)$ is nearly constant and hence $I_{SR} \approx 0$, while for G = [110] and [201], $\Delta H(p)$ for small p is well below the $p=\infty$ values, and so $I_{SR} << 0$. This reflects large energy-lowering relaxations of interfacial atoms for these latter orientations (for $p \geq 2$; for p = 1, the [001], [110], and [201] SLs are identical), and leads universally to the p = 2 [201] SLs (chalcopyrites) having the lowest SL energy.

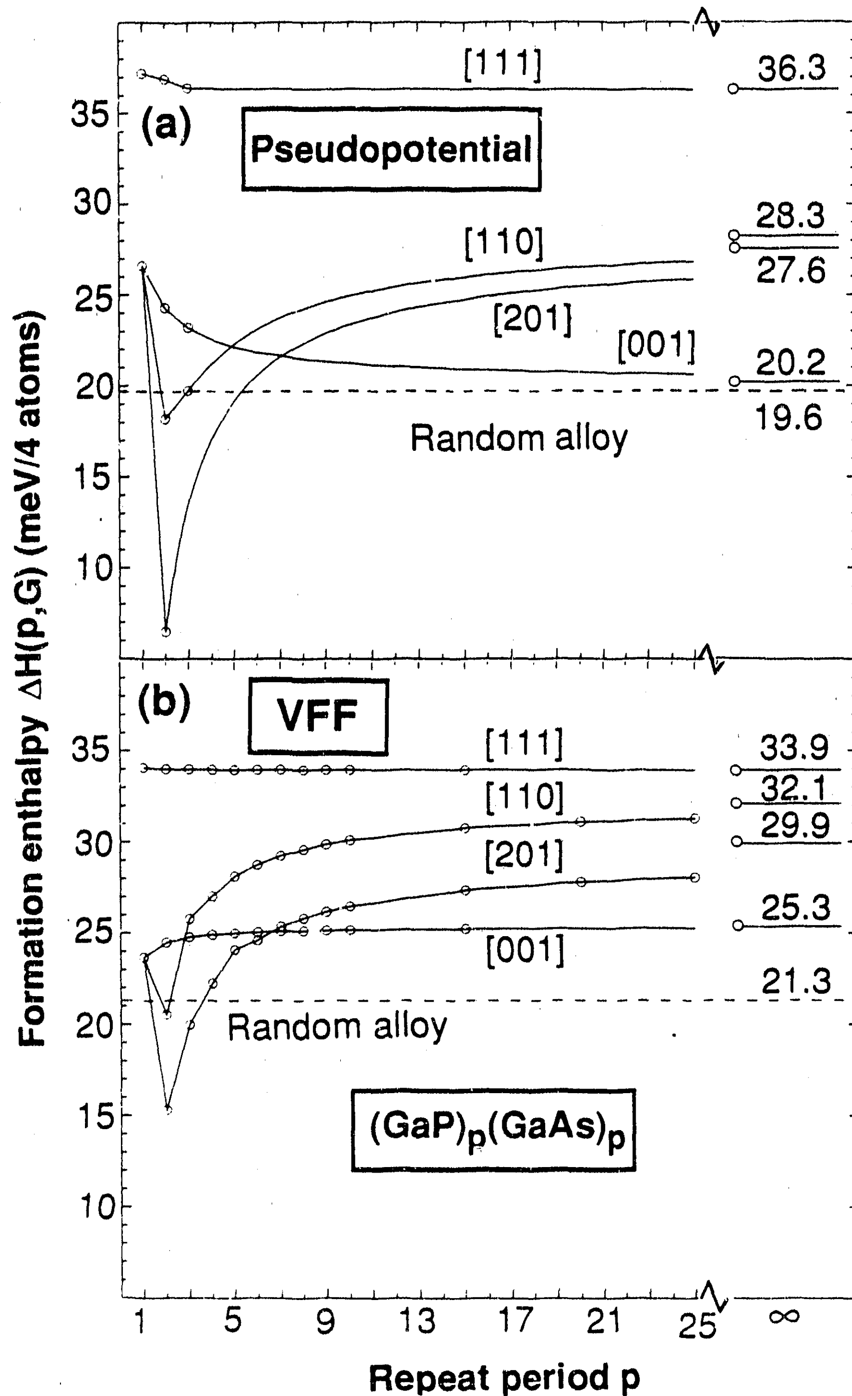

Figure 6-6. Formation enthalpy of $(GaP)_p(GaAs)_p$ vs repeat period p and orientation G. (a) First-principles pseudopotential calculations. (b) VFF calculations. The strain energies of the epitaxially deformed binaries ($p = \infty$) are shown at the right.

3. As the [001] interfacial energy is controlled by I_{CE}, it is natural to inspect the self-consistent charge rearrangement in these systems relative to their epitaxially deformed binaries. Figure 6-7 (and similar constructs for other systems) shows that overall charge is always transferred from the constituent with the smaller to that with the larger lattice constant. We find that whether this direction of size-mismatch-induced charge transfer is stabilizing ($I < 0$) or destabilizing ($I > 0$) depends on whether it also coincides with the direction mandated by electronegativities: Transfer to a more (less) electronegative region leads to $I < 0$ ($I > 0$). Our results, in general, follow the interfacial energy rule for lattice-mismatched systems, stating that I([001]) is negative (positive) if the smaller of the two constituents has a smaller (larger) electronegativity.

To test these ideas, we calculated $\delta H(1,[001])$ for AlX-InX, with X=P or As. The rule predicts a negative interfacial energy ($\chi_{Al} = 1.5$, $\chi_{In} = 1.7$), and we indeed find $\delta H = -35$ and -33 meV/(4 atoms) for X = P and As, respectively.

6.6 Electronic Structure of H_2 in Palladium: Can Solid-State Effects Explain "Cold Fusion"? [7,8]

Recent claims of observation of room-temperature (cold) nuclear fusion in deuterated transition metal electrodes have rekindled interest in the physics of dense deuterium in the field of metallic electrons and transition atoms. Of recent interest here is the Born-Oppenheimer energy surface E(R) of two deuterium atoms at a distance R, since both the vibrational wave-function $\psi(R)$ of diatomic deuterim [determining the fusion rate $\Lambda = A|\psi(R=0)|^2$] and the tunneling barrier penetration factor B depend sensitively on E(R). Previous estimates of Λ and B assumed the free space form of E(R) of gaseous H_2 [bound at $R_{eq} = 0.74$ Å by $E(R_{eq}) \approx 4.7$ eV/2H; because the electronic E(R) is independent of the isotope mass effects, the discussion below applies equally to H and D]. Since the equilibrium distance R_{eq} for the isolated H_2 molecule is too large to grant sufficient tunneling events, various solid-state R_{eq}-shortening mechanisms were sought. It was hoped, for example, that the existence of a metal lattice (e.g., fcc palladium) in which deuterium is embedded could grant a large coulomb screening effect, hence, substantially reduce the D-D tunneling distance and enhance the fusion rate.

In an attempt to further clarify some of the solid-state aspects of cold fusion and to gain a better understanding of metal hydride systems in general, we have used first-principles self-consistent total energy methods within the local density formalism to systematically predict the stability of various periodic arrangements of atomic and diatomic hydrogen in fcc palladium. We studied various orientations of H_2 in fcc palladium, finding that [111] is the most stable; a molecule in any other orientation will spontaneously reorient along [111]. However, we find that in this orientation, the system can further lower its energy by dissociating into two hydrogen atoms each at a tetrahedral interstitial site, leading thereby to a yet longer hydrogen-hydrogen separation. Subsequent penetration of the diffusion barriers (0.3 eV) leads then to an exothermic hopping into the octahedral sites. Bringing two such octahedrally positioned hydrogen atoms to the equilibrium internuclear separation of an isolated H_2 molecule requires an investment of 2.4 eV/2H; the same reaction in the gas phase emits 4.7 eV/2H. Our findings can be summarized as follows:

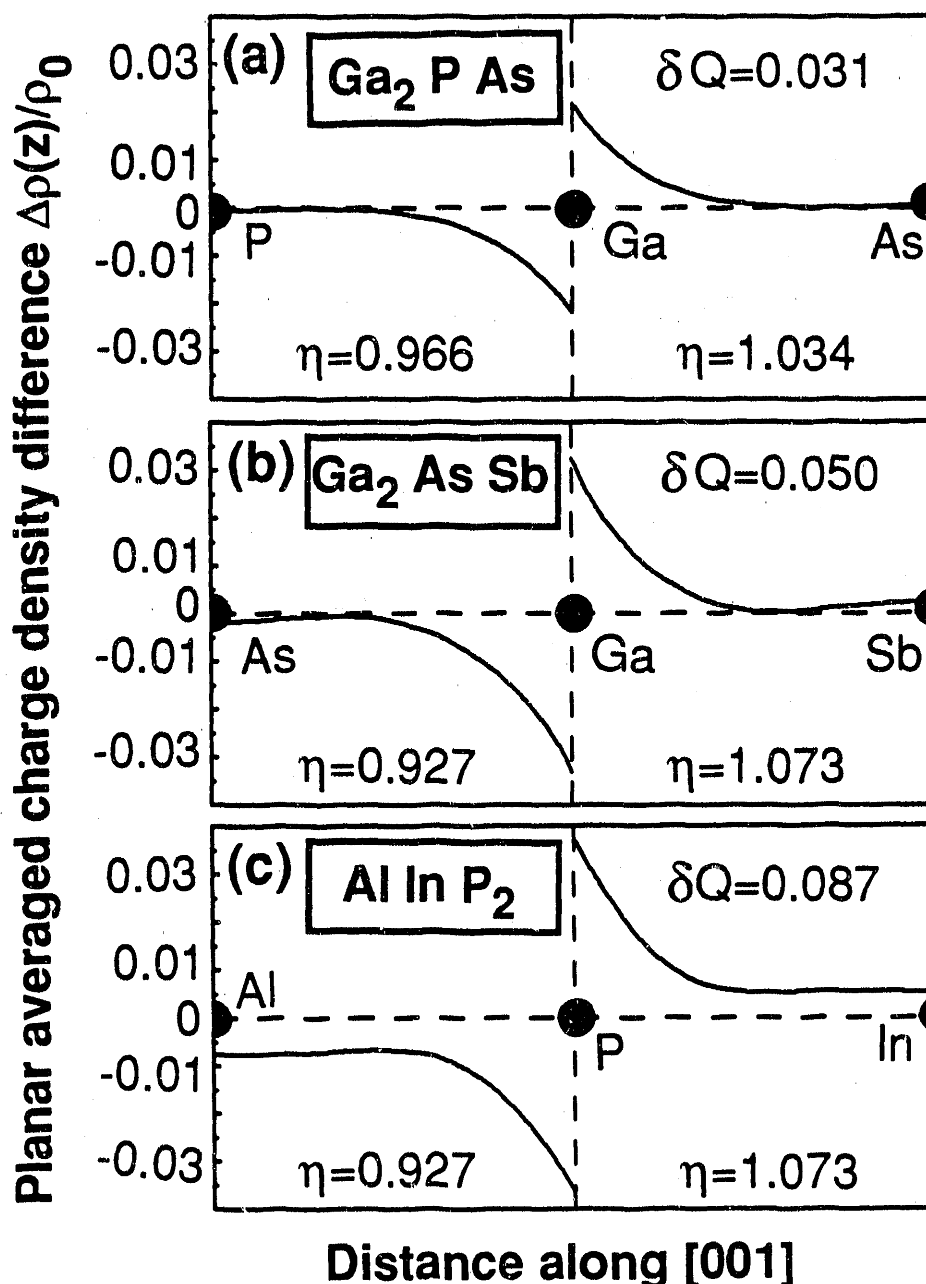

Figure 6-7. Charge-density differences (SL minus epitaxial binary, averaged in planes orthogonal to [001]) for three p = 1 [001] SLs, in units of the mean SL valence charge density ρ_0. $\eta=c/a_s$ is the tetragonal distortion in each half of the SL, and δQ is the number of electrons (per SL unit cell) transferred between the two halves.

Dilute hydrogen in palladium: We model the small-α (dilute) limit by placing a hydrogen atom at the octahedral (O) center of an fcc palladium cubic unit cell (α = 0.25, Pd_4H, denoted as SC in Figure 6-8). The calculated octahedral formation enthalpy ΔH_O = -0.28 eV/H is exothermic; it is in fair agreement with the observed formation enthalpy of ~ -0.14 to -0.16 eV/H.

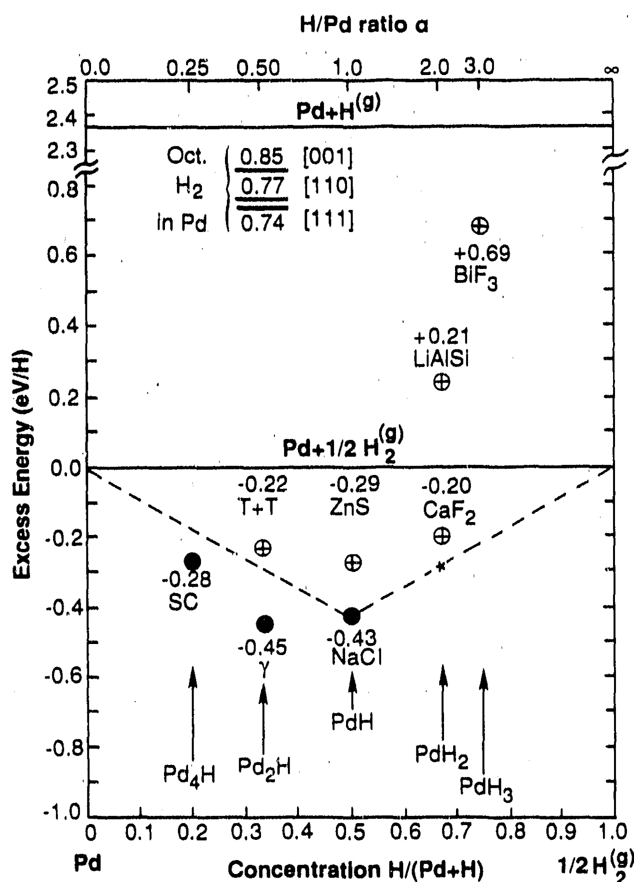

Figure 6-8. **Calculated formation enthalpies $\Delta H(PdH_\alpha)$ with respect to $Pd^{(s)}$ + $1/2\ H_2^{(g)}$ or $Pd^{(s)}$ + $H^{(g)}$.** Solid circles: stable phases; open circles: unstable phases (see text for notation of crystal structures). The results for α = 0.5 (except the γ phase) are calculated at fixed lattice constant (a = 4.00 Å); others are calculated at their respective equilibrium values.

Higher α values and ordered phases: The fcc structure of palladium [with palladium at the (0,0,0) position] has two tetrahedral (T) interstitial sites [at a(1/4,1/4,1/4) and a(3/4,3/4,3/4)] and a single octahedral (O) interstitial site [at a(1/2,1/2,1/2)], all empty in pure palladium. Partial or full occupation of these sites by hydrogen leads to a number of possible ordered phases. For α = 0.5, we can occupy, in an ordered fashion, one-half of the oxygen sites by hydrogen, forming the observed low-temperature tetragonal γ phase Pd_4H_2 of space group $I4_1/amd$, or D_{4h}^{19}. Alternatively, one can occupy both tetrahedral sites along the [111] direction, forming the "T+T structure" of Pd_4H_2 also with α = 0.5. For α = 1, we can occupy either the O site to form the NaCl structure of PdH or occupy one of the T sites, to form the ZnS structure of PdH. For α = 2, it is possible to occupy all the T sites, forming the CaF_2 structure, or occupy one T and one O site to form the LiAlSi-like structure of PdH_2. Finally, for α = 3, occupation of all three interstitial holes (2T + O) forms the BiF_3 structure of PdH_3.

We find that

1. ΔH is negative for all but the LiAℓSi and BiF_3 structure of PdH_2 and PdH_3, respectively; if formed, these two compounds would disproportionate, releasing their ΔHs thermally.

2. $\Delta H_\alpha < 0$ is a necessary but not a sufficient condition to imply local stability of structure α. For example, the CaF_2 structure of PdH_2 has a higher ΔH than PdH + 1/2 $H_2^{(g)}$ (a point denoted in Figure 6-8 by an asterisk on the dashed tie-line); hence, despite its $\Delta H_\alpha < 0$, if formed, it too will decompose into these components, releasing the corresponding heat.

3. For $\alpha \leq 1$, the system shows preference for occupation of O over T, since T has a shorter Pd-H distance of $(\sqrt{3}\ a/4)$ relative to that for O: $(a/2)$. On the other hand, for larger α (e.g., $\alpha = 2$), we find that the system prefers occupation of two T sites over occupation of O + T, since the H-H distance is shorter in the latter case, leading to a stronger H-H repulsion.

Diatomic hydrogen in palladium: We next inquire whether there exists a metastable phase of H_2 dimer in palladium with smaller R_{eq} than the free-space value. We model this system at $\alpha = 0.5$ by an octahedrally centered H_2 molecule inside an fcc cube with interatomic separation R and orientation $\vec{G}$. Varying R at a = 4.00 Å (close to the calculated equilibrium lattice constant) for the orientations $\vec{G}$ = [111], [001], and [110], we find the Born-Oppenheimer energy curves $E[a_{eq}, \vec{G}, R]$ shown in Figure 6-9. The basic results are:

1. Octahedrally centered diatomic H_2, kept at its gas phase internuclear separation $E_{eq}[H_2^{(2)}]$ is unstable by as much as ~1.5 eV with respect to disproportionation into $Pd^{(s)} + H_2$ for all principal orientations (Figures 6-8 and 6-9).

2. A few local minima exist in the energy surface, corresponding to metastable molecules. However, all are characterized by H-H internuclear separations larger than the free-space value (denoted as "gas phase eq. dist" in Figure 6-9).

Clearly, none of the equilibrium structures shown in Figures 6-8 and 6-9 are conducive to cold fusion, since the equilibrium hydrogen-hydrogen distance in palladium is considerably larger than that of the free molecule (Figure 6-9). Consistent with other studies, equilibrium fusion rates must be enormously smaller than what was previously thought. Use of free H_2 potential to estimate fusion probabilities inside palladium would seem unreasonable. We conclude that there are no spectacular solid-state effects (e.g., enhanced effective masses) that would significantly reduce R_{eq}.

6.7 Ordering in Semiconductor Alloys [9]

In this project we addressed the following questions: (1) Is a bulk $(AC)_p(BC)_p$ SL thermodynamically stable or unstable with respect to either phase-separation into its binary constituents p(AC) + p(BC) or disordering into a random $A_{0.5}B_{0.5}C$ alloy? (2) How does this stability depend on the SL

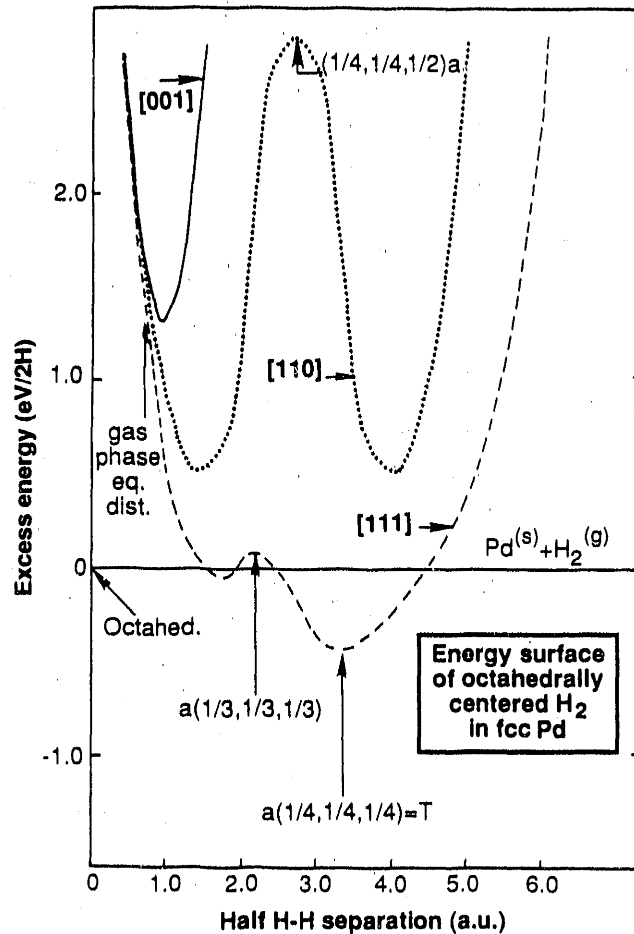

Figure 6-9. Calculated excess energy of the octahedrally centered H_2 molecule in fcc Pd at a = 4.00 Å for three orientations $\vec{G}$ as a function of the H-H distance

repeat period p or orientation G? (3) How does the condition of coherent epitaxial registry with a substrate or existence of a free surface during growth affect stability? (4) What overall classes of stability/metastability/instability are to be expected for II-VI and III-V SLs? We start by reviewing previous ideas on this subject. These are based on two facts: (1) classic thermodynamic models of alloys characterized their energy by a single constant interaction parameter (e.g., the nearest-neighbor pair interaction) and (2) all known disordered (D) semiconductor alloys have positive mixing enthalpies $\Delta H^{(D)} \geq 0$. These two points led proponents of early models of pseudobinary $A_{1-x}B_xC$ semiconductor alloys to assume that the interactions between the units forming these alloys are repulsive. The source of this repulsion was identified as the elastic energy associated with packing a lattice with A and B atoms of dissimilar sizes. It followed then that $\Delta H^{(S)}$ must be positive also for many other atomic arrangements at the same composition [e.g., for ordered structures (S) such as SLs]. The purely repulsive nature of these interactions suggested that as the disordered alloy is cooled down, the system first exhibits clustering (enhancement of the populations of pure AC-like and BC-like clusters relative to those in random distribution),

then a miscibility gap and phase separation. Ordering would then not exist except by virtue of artificial (e.g., shutter-controlled) growth of (super) structures. This behavior is opposite to that in ordering intermetallic alloys (e.g., $Cu_{1-x}Au_x$), where attractive interactions lead to $\Delta H^{(S)} < 0$; cooling the disordered alloy leads then to anticlustering (reduction of the populations of the pure clusters relative to those in a random distribution with the same composition), followed eventually by the formation of stable, long-range-ordered compounds at some stoichiometric compositions. In the classic models, based on a single interaction parameter of a definite sign, phase-separation [expected when $\Delta H^{(D)}>0$] and ordering [expected when $\Delta H^{(S)}<0$] are taken to be mutually exclusive phenomena.

It is now becoming clear that this picture is flawed. Indeed ΔH reflects a competition between attractive and repulsive forces; however, the balance is different in ordered versus disordered phases of the same system; hence, $\Delta H^{(D)}>0$ can be consistent both with ordering and anticlustering. We have performed a series of calculations which show this.

We have calculated the formation enthalpy

$$\Delta H^{(\gamma)} = E^{(\gamma)}(V_{\gamma}) - (1-x)E^{(AC)}(V_{AC}) - xE^{(BC)}(V_{BC}) , \qquad (6\text{-}8)$$

for a series of 50%-50% isovalent semiconductors in four phases γ: ordered CH, CA-like, and CP-like, and the disordered alloy. The three ordered arrangements can be described as $(AC)_p(BC)_p$ SLs of repeat period p and orientation G: CH is p = 2; G = [201], CA is p = 1, G = [001]; and CP is p = 1, G = [111]. We have used the local density formalism, as implemented in the LAPW method and the nonlocal pseudopotential method. For each structure, we first calculate self-consistently its potential and band structure, then use the variational charge density and wave functions to compute the total energy, including all coulomb and exchange-correlation interactions. Structural parameters are optimized to reach the minimum total energy. $\Delta H^{(D)}(x,T)$ for the disordered alloy is then obtained by solving the fcc Ising Hamiltonian using the cluster-variation method. We include up to four-body and fourth fcc-neighbor interaction energies. These are extracted from the total energy calculations of the ordered compounds. The results are depicted in Figure 6-10. We conclude the following:

1. As correctly noted by the classic alloy theories, the elastic contribution to the enthalpy is positive and increases with the relative A-B size difference and with covalency. However, the substitution energy ε_s is negative for size-mismatched systems and becomes more negative as the relative size difference and covalency increase. Hence, size difference is the cause of repulsion (through elastic volume deformation) and attraction (due to charge transfer and SL relaxation) at the same time.

2. Clustering depends on $\{\varepsilon_s\}$ only. Size-mismatched systems have $\varepsilon_s < 0$, hence, they will exhibit anticlustering; whereas since size-matched alloys have $\varepsilon_s > 0$, they will show clustering.

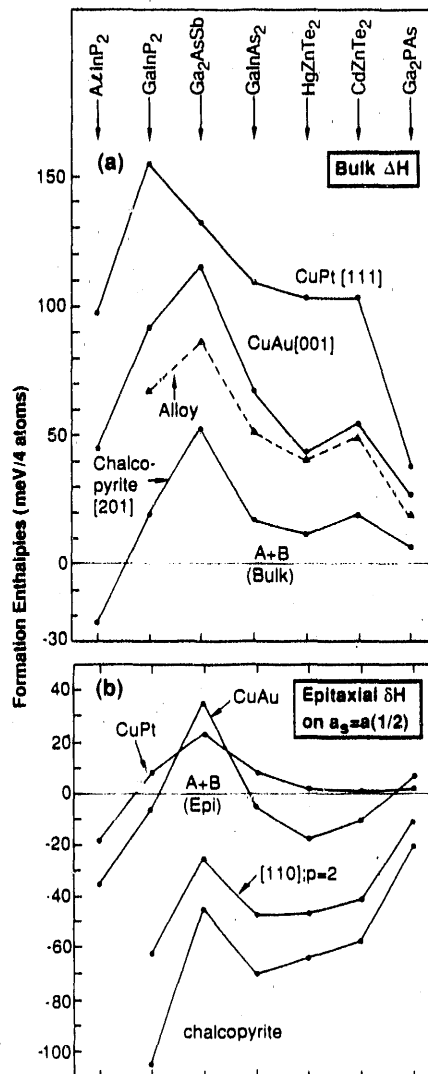

Figure 6-10. Calculated (a) bulk and (b) epitaxial formation enthalpies

3. In size-mismatched alloys, CH has universally the most favorable substitution energy. Since $\Delta H(CH)<\Delta H^{(D)}$, it could order metastably or even stably ($\Delta H(CH)<0$ for $AlInP_2$). The S = CA and CP structures have $\Delta H^{(S)}>\Delta H^{(D)}>0$ and are unstable with respect to disordering. The sequence is different for size-matched alloys where bulk ordering is not expected for any S.

4. We distinguish here between (see Figure 6-11) unstable bulk ordering (type I) where the ordered phase S is less stable than both the disordered alloy and phase separation; Figures 6-11(a) and 6-11(b), metastable bulk ordering (type II), where the ordered phase is more stable than one of the two alternatives but less stable than the other; Figures 6-11(c) and 6-11(d) and stable bulk ordering (type III), where the ordered system is more stable than both alternatives; and Figures 6-11(e) and 6-11(f). In the absence of competition between attraction and repulsion, classic models using continuum

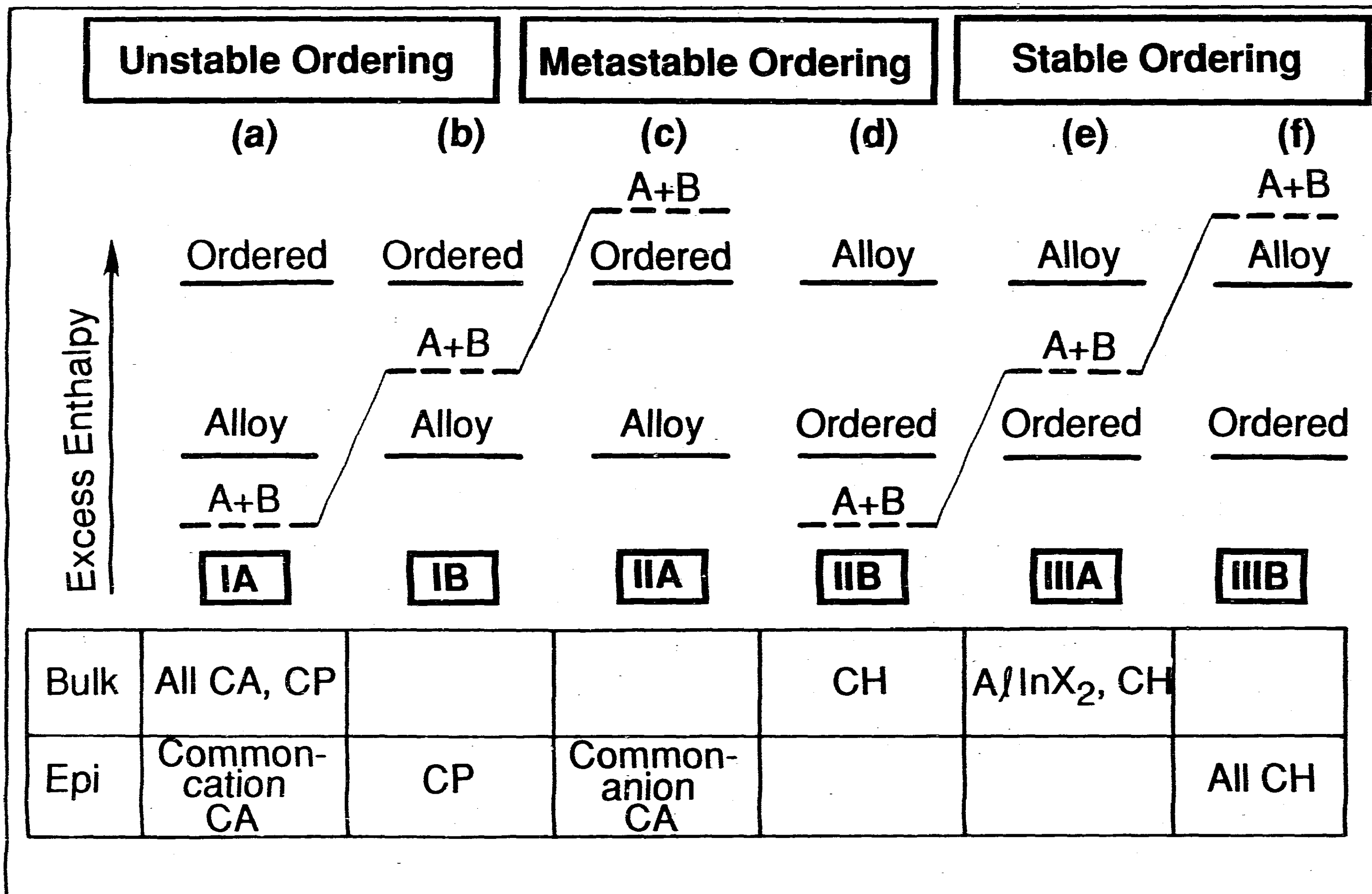

Figure 6-11. Classification of types of ordering according to enthalpies

elasticity depicted all semiconductor alloys to be essentially of type IA (or possibly IIB). Summarizing the results in Figure 6-11 shows that other types of ordering exist as well, much like the case in intermetallic systems.

So far we have dealt with bulk systems that are free to adjust to reach their absolute minimum energies. This is appropriate to "free-floating" (melt or solution) growth. In coherent epitaxial growth, on the other hand, the growing phase and its constituents AC and BC are constrained for sufficiently thin films, to adopt the substrate's lattice constant a_s in the plane perpendicular to G. The appropriate epitaxial formation enthalpy $\delta H^{(\gamma)}(a_s,\tilde{G})$ is then taken with respect to the energies $E^{(AC)}(a_s,\tilde{G})$ and $E^{(BC)}(a_s,\tilde{G})$ of the constituents deformed to the substrate's dimension $\tilde{a}_s$ and relaxed in the direction parallel to G. For a substrate lattice-matched to the growing phase γ (but not to its constituents), this constraint can lower the epitaxial δH by raising the energy of the (epitaxial) constituents. Figure 6-10(b) shows our calculated epitaxial energies for $a_s = a(x = 1/2)$. The figure demonstrates the following:

1. Unstable bulk ordering (IA, e.g., all CAs and CPs) can be transformed epitaxially into metastable ordering (IIA, e.g., many of the common-anion CAs). Likewise, metastable bulk ordering (IIB) can be transformed into stable epitaxial ordering (IIIB, e.g., CHs). This is consistent with the observation of [201] ordering in LPE growth of $GaInAs_2$.

1. The epitaxial destabilization of the constituents also reduces the enthalpy of the disordered alloy (and reduces its compositional derivative). Hence, the alloy can be stable with respect to phase separation to far lower temperatures than in bulk. Indeed, bulk-immiscible systems (GaP_xSb_{1-x}) become epitaxially miscible.

Our foregoing discussion of epitaxial stability dealt with constrained total energy minimization without the presence of a free surface, e.g., as appropriate to LPE growth. Metal-organic chemical vapor deposition (MOCVD) and MBE growth, on the other hand, do involve a free surface; the energy-minimizing atomic configuration at the surface can then be different than in bulk. To the extent that this is so, and that subsequent coverage of the surface freezes its structure, a surface-induced configuration can grow to macroscopic dimensions. Indeed, our calculations for epitaxially constrained $Ga_{0.5}In_{0.5}P$ on a lattice-matched GaAs substrate with a free [001] surface show that the order of stability of Figure 6-9(b) is changed: One of the two possible CP-type ordering vectors is now more stable than CH. Recent observations of spontaneous CP ordering are hence likely to reflect surface-induced thermodynamic ordering. Denoting by T_b the ordering temperature appropriate for 3-D epitaxial growth (e.g., LPE), this predicts that postgrowth annealing at a growth temperature T_g will yield, if sufficient atomic mobility exists, the epitaxial ordering of Figure 6-10(b) (if $T_g < T_b$) or the disordered phase (if $T_g > T_b$).

6.8 Band Structure of Random Alloys [10]

One of the significant realizations to emerge from recent electronic structure calculations of crystals, impurities, and surfaces is that electronic properties sensitively reflect the details of the microscopic atomic arrangements, including small changes in atomic positions (relaxation). Yet, many theories

of substitutional $A_{1-x}B_x$ random alloys are nonstructural in that they consider only the average occupations by <A> or <B> of sites, removing from the theory the informational content associated with the geometrical arrangements of atoms around a site. Such is the virtual crystal approximation (VCA), where the alloy is assumed to have a single, <AB> averaged type of site, or the site coherent potential approximation (S-CPA), where all A's and separately all B's are assumed equivalent and each is embedded in a structureless, uniform average medium; structural relaxation is excluded in both approaches. Experimental techniques capable of probing the average local properties of alloys have, however, clearly demonstrated the important role played by the microscopic atomic structure. For example, even in homogeneous $A_{1-x}B_x$ alloys without short- or long-range order, the average A-A, A-B, and B-B distances are generally different; in semiconductor alloys, similar atomic relaxations have been shown to control the band gaps and thermodynamic quantities. On the other hand, the obvious difficulty with structural theories of alloys arises from the fact that even in the simplest case of a binary system with N sites, there are 2^N possible atomic configurations whose total energy needs to be structurally relaxed, then averaged. One then proceeds in practice either by selecting a smaller number of "representative" configurations (e.g., the Monte Carlo approach) or a single periodic structure with a random distribution of A and B atoms on its N sites. While these techniques explicitly specify the alloy structure and can hence incorporate atomic relaxation, they approach the statistical limit as slowly as $N^{-1/2}$. Therefore, they involve a rather large number of configurations (e.g., ^{5} ~10^6 in Monte Carlo studies) or large cell sizes (e.g., >10^3 atoms), for which first-principles self-consistent calculations (currently restricted to $N \le 50$ atoms) are still impractical. We show here that by selective occupation of the N lattice sites by A and B atoms, one can construct special periodic "quasi-random structures" (SQS) that mimic, for finite N, the correlation functions of an infinite substitutional random alloy far more closely than does the standard approach of occupying each of the N sites randomly by A or B. While both approaches produce the same results for $N \to \infty$, the present approach produces excellent approximations already for $N = O(10)$, hence affords application of accurate electronic structure methods for calculating structural, optical, and thermodynamic properties of random alloys.

Unlike the S-CPA or the VCA, the SQS exhibits a distribution of local environments of inequivalent A (or B) atoms; hence, when treated by conventional band structure methods, one can simply incorporate in them realistic atomic relaxations and charge redistribution. Unlike cluster expansion methods, the SQS approach is capable of depicting directly the electronic charge distribution in a random alloy and does not require evaluation of interaction parameters from a truncated expansion.

We have applied self-consistently the local density formalism, as implemented by the LAPW and nonlocal pseudopotential band structure methods, to a range of pseudobinary $A_{0.5}B_{0.5}C$ semiconductor SQSs. Here, the carbon atoms reside on the nominally common sublattice (so the actual number of atoms per cell is 2N); all A, B, and C atomic positions are allowed to relax (without atomic interchanges) so as to minimize the total energy. A direct band structure calculation of the total energy of a structurally relaxed SQS (taken with respect to the energies of the binary constituents AC and BC at equilibrium) approximates the excess energy $\Delta H(x = 1/2)$ of a random alloy. Such direct calculations for SQS-2 and SQS-4 are compared in Table 6-3 to results obtained

by the cluster expansion. Table 6-3 shows that a single calculation even on SQS-4 reproduces well, without resort to statistical calculations, the corresponding results obtained from the full statistical mechanics simulation; the latter agrees well with measured excess enthalpies. We have also calculated the relativistic band structures of the SQSs for the seven semiconductor alloys using the LAPW method. Table 6-3 gives the optical bowing coefficient $b = 4[\bar{E}_g(1/2) - E_g(1/2)]$ of the direct alloy band gap at composition $x = 1/2$ (where $\bar{E}_g$ denotes the concentration-weighted band gap of the binary constituents; note that due to the difference taken in b, the local density error cancels to first order). For comparison, we also give the calculated results for the CP structure and experimental data for the disordered alloy. We see that parameter-free, self-consistent calculations on the SQS-N converges well and reproduces the experimental trends. It is important to note that neglect of structural relaxation (as done in VCA and S-CPA methods) leads to huge errors in size-mismatched alloys; e.g., we find that b(SQS-2) for unrelaxed Ga_2SbAs is 0.34 eV instead of 1.30 eV for the relaxed structure, and that ΔH is 237 meV instead of 115 meV. For GaAsP, ΔH is 60.2 meV instead of 16.5 meV.

Such SQSs can be easily generalized to other compositions or lattice types (bcc, diamondlike) and open the way for extending the application of first-principles electronic structure techniques to a variety of metal and semiconductor alloys.

Table 6-3. Mixing Enthalpies ΔH(x=1/2) of the Random Alloy, in meV/4-atoms, as Obtained by the LAPW and Pseudopotential Calculations on SQSs and from a Cluster Expansion on Eight Periodic Structures. To achieve convergence in the latter, interactions extending to the 4th fcc neighbors were included.

	LAPW							Pseudo-potential	
	AlAs GaAs	GaSb GaAs	InAs GaAs	GaP InP	HgTe CdTe	ZnTe CdTe	HgTe ZnTe	GaP GaAs	AlAs GaAs
$\Delta H^{(R)}(1/2)$									
CuPt	7.5	132	108.5	155.4	9.8	103.5	103.3	31.6	10.7
SQS-2	11.5	115	66.7	91.0	12.1	54.2	42.5	26.1	13.7
SQS-4	6.0	80	47.3	73.0	9.8	56.1	49.1	13.9	10.5
Cluster Expansion (T=∞)	6.6	91	58.8	81.5	8.4	55.3	47.6	19.5	10.5

6.9 References

Articles indicated with an asterisk describe work partially supported by OER/BES.

1. R. G. Dandrea, S. Froyen, and A. Zunger, "Stability and Band Offsets of Heterovalent Superlattices: Si-GaP, Ge-GaAs, and Si-GeAs," Phys. Rev. B, Rapid Communication 42 (1990) p. 3213.

2. S.-H. Wei, L. G. Ferreira, and A. Zunger, "First Principles Calculation of Temperature-Composition Phase Diagrams of Semiconductor Alloys," Phys. Rev. B41 (1990) pp. 8240-8269.

3. L. G. Ferreira, S.-H. Wei, and A. Zunger, "Stability, Electronic Structure, and Phase Diagrams of Novel Inter-Semiconductor Compounds," submitted to Int. J. Supercompt.

4. S. Froyen, D. M. Wood, and A. Zunger, "Electronic Structure of Ultrathin SiGe Strained Superlattices: The Possibility of Direct Band Gaps," Thin Solid Films, 183 (1989) pp. 33-48.

*5. S.-H. Wei and A. Zunger, "Band Gap Narrowing in Ordered and Disordered Semiconductor Alloys," Appl. Phys. Lett. 56 (1990) pp. 662-664.

*6. R. G. Dandrea, J. E. Bernard, S.-H. Wei, and A. Zunger, "Stability of Coherently Strained Semiconductor Superlattices," Phys. Rev. Lett. 64 (1990) pp. 36-39.

*7. S.-H. Wei and A. Zunger, "Stability of Atomic and Diatomic Hydrogen in fcc Palladium," Solid State Commun. 73 (1990) p. 327.

*8. S.-H. Wei and A. Zunger, "Instability of Diatomic Deuterium in Palladium," J. Fusion Energy (in press).

9. J. E. Bernard, R. G. Dandrea, L. G. Ferreira, S. Froyen, S.-H. Wei, and A. Zunger, "Ordering in Semiconductor Alloys," Appl. Phys. Lett. 56 (1990) pp. 731-733.

10. A. Zunger, S.-H. Wei, L. G. Ferreira, and J. E. Bernard, "Special Quasirandom Structures," Phys. Rev. Lett. 64 (1990) pp. 353-356.

7.0 LASER RAMAN AND LUMINESCENCE SPECTROSCOPY

Investigator

A. Mascarenhas, Staff Scientist

7.1 Introduction

The primary objective of this research is to understand the opto-electronic properties of solid-state materials used for solar cell applications by studying their radiative recombination mechanisms. The principal technique we have utilized for elucidating such information is low-temperature photoluminescence. These experiments, combined with polarization studies, enable the selection rules for the optical transitions to be determined and thereby provide crucial information about the intrinsic electronic band structure exhibited by photovoltaic materials. The opto-electronic properties manifested are determined by the final structure and bonding achieved in the materials grown for photovoltaic applications. A direct probe of the lattice structure is possible through Raman scattering spectroscopy. Raman scattering studies enable the determination of the normal vibrational mode frequencies and their symmetries. This provides useful clues about the dynamic behavior of the lattice structure, its bonding, and its symmetry. In the past three years, we have exploited the above-mentioned spectroscopic techniques to investigate the microcrystalline behavior of amorphous semiconductors and the role of phonons in high-T_c superconductivity. During the past year, we have focused our attention on spontaneous ordering and lattice dynamics.

7.1.1 Investigating the Phenomenon of Spontaneous Ordering in $GaInP_2$

The experimental research by the III-V High Efficiency Solar Cell group at the Solar Energy Research Institute (SERI) on the growth of a $GaInP_2$/GaAs tandem solar cell has indicated that at the lattice-matched composition, the band gap of the $GaInP_2$ cell is sometimes lower than the theoretically expected value because of spontaneous ordering of the alloy. This results in small deterioration of the optimal solar cell efficiency obtained. Over the past few years, there has also been an extensive effort made by the Solid-State Theory group at SERI to model and to understand this phenomenon. We have conducted spectroscopic measurements involving polarization photoluminscence studies on $GaInP_2$ in an attempt to understand the anomalous band-gap lowering observed in $GaInP_2$. These studies [1] have resulted in the first experimental evidence for the spontaneous breaking of cubic symmetry in the band structure of organo-metallic vapor phase epitaxy (OMVPE)-grown $GaInP_2$. We showed how this effect is related to the spontaneous ordering of the alloy and its correlation with the anomalous lowering of the band gap of these films.

7.1.2 Raman Scattering Investigations of the Lattice Dynamics of $Cu_xAg_{1-x}InSe_2$ and $CuIn_xGa_{1-x}Se_2$

The Semiconductor Crystal Growth group at SERI has recently grown crystals of the quaternary chalcopyrite semiconductors $Cu_xAg_{1-x}InSe$ and $CuIn_xGa_{1-x}Se_2$ to investigate these materials as possible candidates for solar cell devices. In these solid solution mixtures, which have the chalcopyrite structure, copper and indium are ordered relative to each other but are randomly replaced by

silver or gallium, respectively. We have conducted Raman scattering experiments to study the effects of disorder in the cation sublattices by monitoring its effects on the zone center phonon frequencies and by comparing the behavior of the quaternary solid solutions with their end point extremes--$CuInSe_2$, $CuGaSe_2$, and $AgInSe_2$. Since the solid-state phase ordering transitions that occur during crystal growth are potential contributors to crystal cracking problems often experienced with those systems, Raman scattering studies are valuable for probing and understanding this phenomenon. Our studies on these alloys have demonstrated the coexistence of two-mode and one-mode alloy behavior, which is exhibited in the Raman scattering from zone center normal modes.

7.2 Polarized Band-Edge Photoluminescence and Ordering in $GaInP_2$

Spontaneous long-range ordering into the CuAuI, CuPt, and chalcopyrite structures has recently been observed in several normally disordered isovalent III-V alloys $A_xB_{1-x}C$ [2]. In the case of the alloy $GaInP_2$ grown by OMVPE on (001) GaAs substrates, electron diffraction studies reveal ordering of the cations on the group III sublattice along $[\bar{1}11]$ or $[1\bar{1}1]$, two of the four <111>-type directions (see Figure 7-1) [3-6]. A mechanism for this spontaneous long-range ordering has been proposed [7]. This mechanism consists of the alignment of gallium and indium atoms into a series of alternate [110] direction gallium atom lines within each (001) plane, which is caused by the anisotropic site occupation affinity for column III atoms because of their large bond-length difference, and the asymmetry in the direction for the dangling bonds; and the in-phase alignment of two gallium lines belonging to adjacent (001) ordered planes, which is caused by the selective settling of gallium atoms on the (111)B microfacets of [110] step arrays. Thus, although bulk $GaInP_2$ is metastable [8] with respect to phase separation, the long-range ordering observed during epitaxial growth is a result of surface thermodynamic effects rather than bulk thermodynamic effects [9].

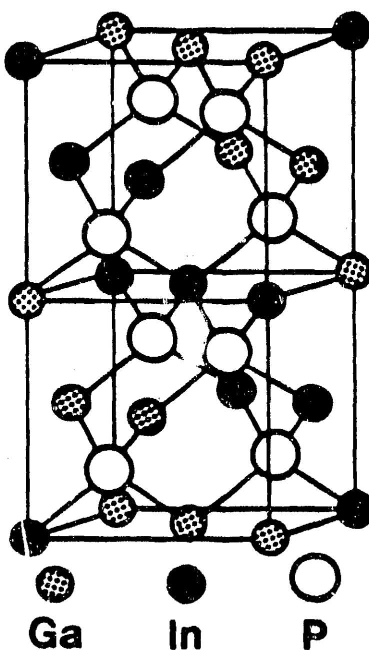

Figure 7-1. Crystal structure showing the unit cell of the perfectly ordered alloy $GaInP_2$

Even at a fixed composition, the band gap of OMVPE-grown $GaInP_2$ varies with the reactor growth temperature, reaching a minimum at about 670°C [10-12]. Excellent qualitative correlation between the degree of sublattice ordering and the lowering of the band gap in $GaInP_2$ has been reported [3]. However, we have no conclusive evidence that the band-gap lowering is a result of spontaneous ordering. In the ordered alloy, the size of the Brillouin zone is halved due to the doubling of the unit cell. As a result of this, the conduction band state at the L point is zone-folded back to the Γ point. This new state has the same symmetry as the conduction band at Γ^2 and lies just above it. The repulsion between these like-symmetry states results in a lowering of the band gap of the ordered alloy [2]. In addition, the reduced symmetry should result in a crystal field splitting of the valence band, but this has not been previously observed.

We presented the first experimental evidence for the spontaneous breakdown of cubic symmetry in the band structure of spontaneously ordered films of $Ga_{0.52}In_{0.48}P$ grown by OMVPE on (001) GaAs substrates, misoriented 2° toward $(0\bar{1}\bar{1})$. Our results verify a direct correlation between the valence band splitting, band-gap lowering, and ordering. For exciting light linearly polarized along the [110] or $[1\bar{1}0]$ crystal axes, we observe a shift in the energies of the room temperature photoluminescence (PL) peaks for polarizations parallel ($\parallel$) and perpendicular ($\perp$) to that of the exciting light. The magnitude of this shift shows a correlation with the anomalous lowering of the energy gap of these films. The PL emission corresponding to each of these peaks shows a preference for polarization along the [110] or $[1\bar{1}0]$ crystal axes, respectively. The relative intensity of these two peaks for exciting light polarized along [110] differs from the relative intensity of the two peaks for exciting light polarized along $[1\bar{1}0]$. These results demonstrate an anisotropy between the [110] and $[1\bar{1}0]$ crystal axes, which are equivalent directions in the cubic symmetry point group $\bar{4}3m$. The violations of cubic symmetry emerge as a natural consequence if the selection rules for optical transitions are derived for a band structure whose symmetry is that of the subgroup R3m instead of the full space group $F\bar{4}3m$. The results are consistent with those found in structural measurements showing evidence of ordering in GaInP [6-9].

Growth of $Ga_{0.52}In_{0.48}P$ films by OMVPE has been described earlier [13]. Samples #1 and #2 were grown at 700° and 750°C, respectively. X-ray double crystal rocking curves indicate that the lattice mismatch between the films and substrate is less than 0.1%, and so the effects of strain on the bond structure can be neglected. Electron diffraction studies reveal a higher degree of ordering in Sample #1 as compared to Sample #2. The PL was measured at room temperature using a perfect backscattering geometry [14]. A HeNe laser was used for the excitation. Exciting light was incident along the z direction, which is normal to the (001) face of the sample. PL emission in the -z direction was analyzed for polarization $\parallel$ and $\perp$ to that of the exciting light E_i. The energy gap of sample #1 is 1.83 eV, approximately 70 meV lower than the band gap of fully random alloy $Ga_{0.52}In_{0.48}P$ grown by liquid phase epitaxy [2]. The PL emission spectra for excitation polarized along I) the [110] and II) the $[1\bar{1}0]$ crystal axes of this sample are shown in Figures 7-2(a), 7-2(b), and Figures 7-2(c), 7-2(d), respectively. The energy positions E_A and E_B of peaks A and B, respectively, remain unchanged for case I) and case II). The energy difference $\Delta_{AB} = E_A - E_B = 10$ meV. The energy gap of sample #2 is 30 meV larger than that of sample #1. Figure 7-3

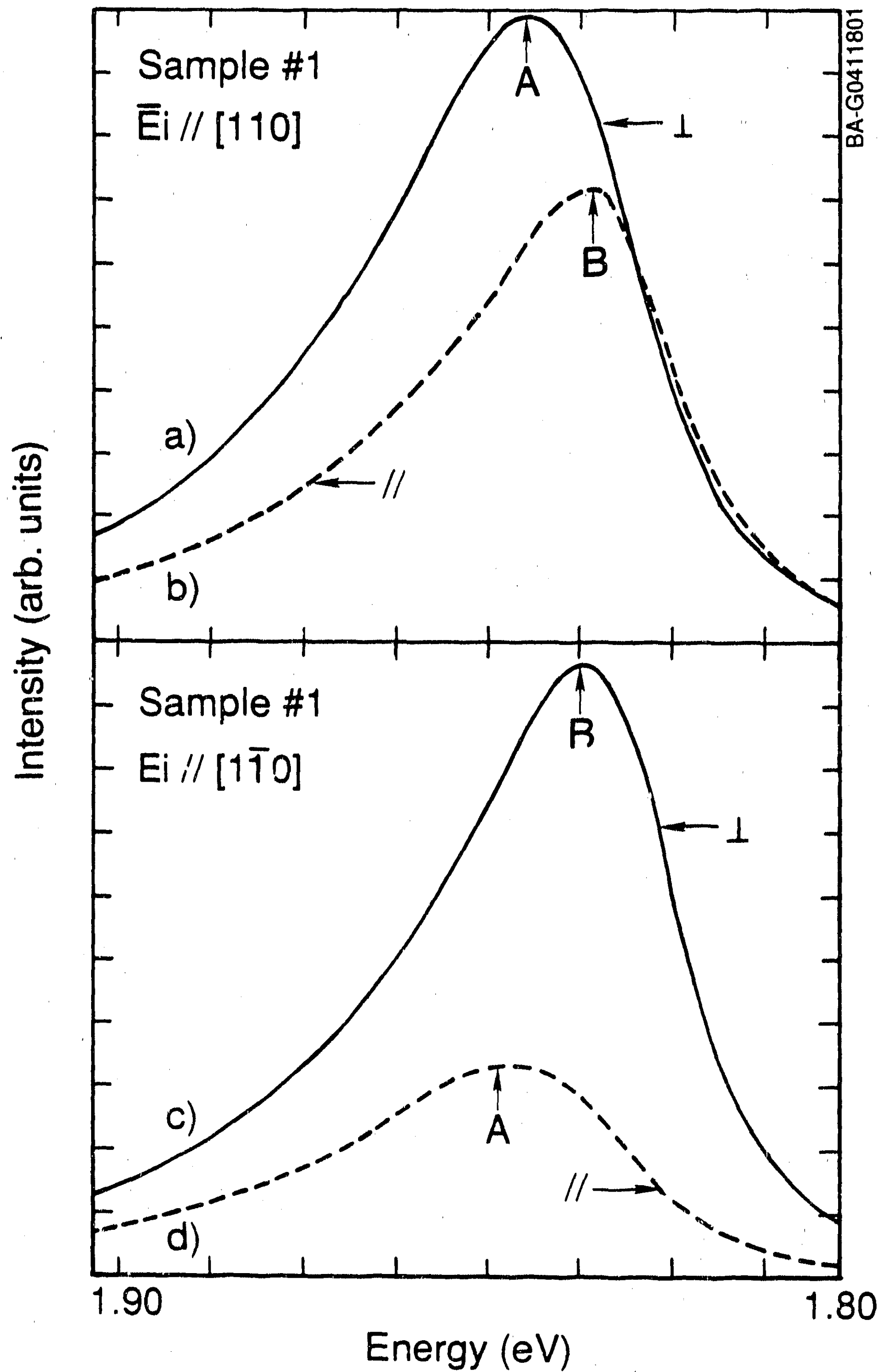

Figure 7-2. For sample 1: PL emission polarized (curve a) ⊥, (curve b) ∥ for E_i ∥ [110] and (curve c) ⊥, (curve d) ∥ for E_i ∥ [1$\bar{1}$0]

shows that the PL from sample #2 exhibits polarization features similar to those of sample #1. However, for this sample, $\Delta_{AB} = E_A - E_B = 2$ meV. To illustrate the polarization features of PL from a material that possesses the full cubic symmetry of $F\bar{4}3m$, we have performed similar measurements on the (001) face of an $A\ell_{0.28}Ga_{0.72}As$ sample. The PL spectra are shown in Figure 7-4. Here, peaks A and B have the same energy. If $I_{\perp}$ is the intensity of PL polarized $\perp$ to $\bar{E}_i$, and $I_{\parallel}$ is the intensity of PL polarized $\parallel$ to $\bar{E}_i$, ${}^{110}R = {}^{110}[\frac{I_{\perp}}{I_{\parallel}}]_p$ is the ratio of the peaks of these intensities when $\bar{E}_i \parallel [110]$, and ${}^{1\bar{1}0}R = {}^{1\bar{1}0}[\frac{I_{\perp}}{I_{\parallel}}]_p$ is the corresponding ratio when $\bar{E}_i \parallel [1\bar{1}0]$. In $A\ell_{0.28}Ga_{0.72}As$, ${}^{1\bar{1}0}R = {}^{110}R > 1$. This linear polarization of the luminescence is due to the anisotropic momentum distribution of photocreated electrons [15]. Since the two ratios are equal, the PL shows no preference between equivalent directions in the point group $\bar{4}3m$, consistent with the cubic symmetry of $A\ell_{0.28}Ga_{0.72}As$. However, for $Ga_{0.52}In_{0.48}P$, ${}^{110}R > {}^{110}R > 1$, indicating a spontaneous breakdown of cubic symmetry.

We now consider the selection rules for optical transitions in $Ga_{0.52}In_{0.48}P$ using a band structure with a symmetry of the subgroup R3m instead of the full space group $F\bar{4}3m$, and show that the above-mentioned discrepancies are a consequence of the reduced symmetry of this subgroup. We start by assuming that the cations are disordered on the group III sublattice. For this situation, the symmetry of the band structure at the Γ point is described by the double group of $\bar{4}3m$ [as shown in Figure 7-5(a)]. Next, the cations are assumed to order on the group III sublattice. Perfect ordering leads to a GaP/InP monolayer superlattice. Partial ordering leads to a superlattice composed of alternating gallium-rich ($Ga_{0.52+x}In_{0.48-x}P$) and indium-rich ($Ga_{0.52-x}In_{0.48+x}P$) monolayers. For both situations, however, the crystal symmetry changes abruptly from $F\bar{4}3m$. If the new symmetry is similar to one of the subgroups of $F\bar{4}3m$, then the change can be described as a second order phase transition [16]. Such a structural transformation is continuous. This makes it possible to treat the effects of ordering as a perturbation on the band structure of the disordered alloy. We assume the new symmetry to be described by the subgroup R3m. At the Γ point, the evolution of the band structure in the environment of reduced symmetry is determined by the correlation of the point double groups of 3m and 43m [as shown in Figure 7-5(b)]. If ordering is assumed to occur along $[1\bar{1}1]$, then this is the direction of the symmetry axes $\hat{z}'$ of the rhombohedral group 3m. The $[1\bar{1}1]$ and $[\bar{1}11]$ directions define a plane whose normal is along [110]. We chose this as the $\hat{y}'$ axes. The $[1\bar{1}0]$ and [110] axes transform into the $[10\sqrt{2}]$ and $[0\bar{1}0]$ directions, respectively, in the primed coordinate system. The selection rules for optical transitions from the conduction band to the valence band (at

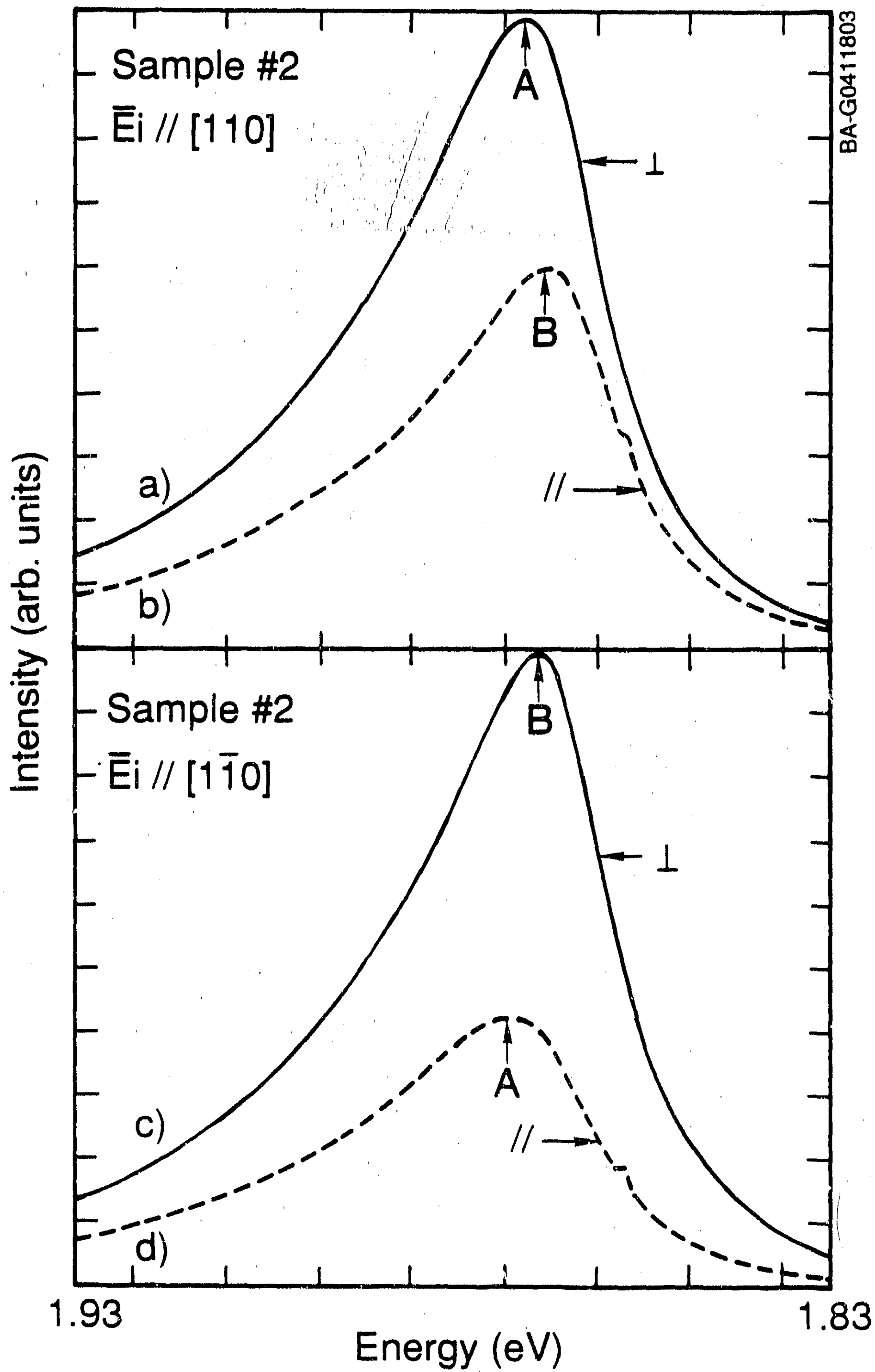

Figure 7-3. For sample 2: PL emission polarized (curve a) ⊥, (curve b) ∥ for E_i ∥[110] and (curve c) ⊥, (curve d) ∥ for E_i ∥ [1$\bar{1}$0]

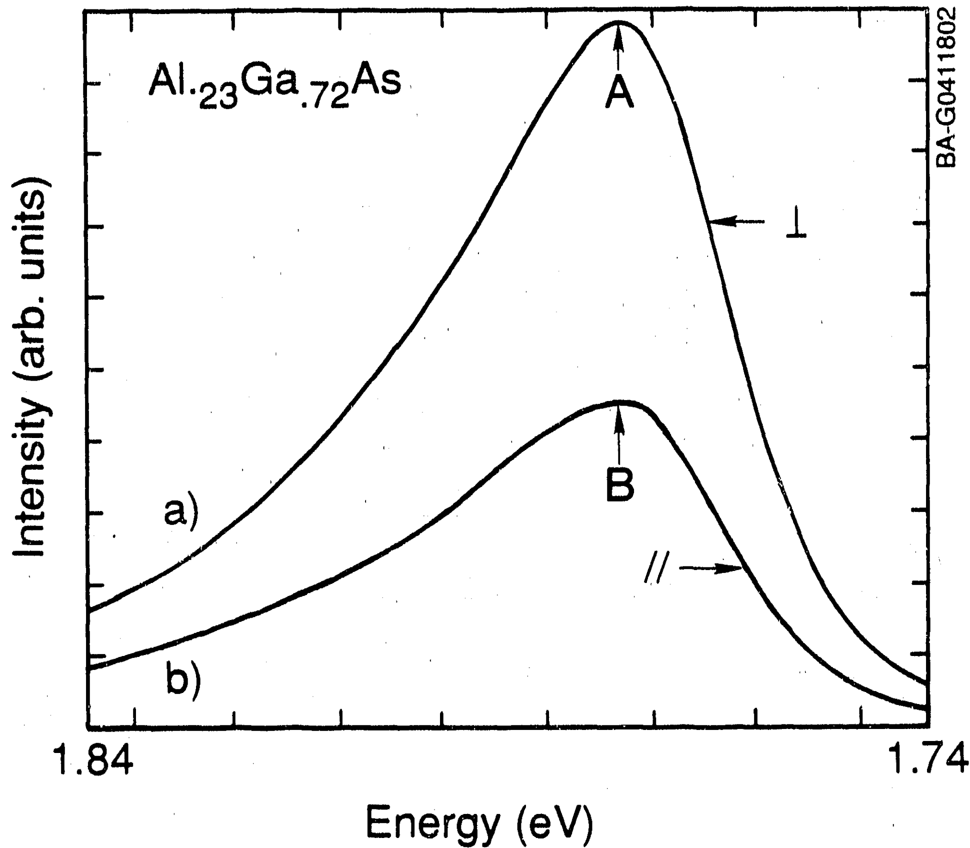

Figure 7-4. For the $Al_{0.28}Ga_{0.72}As$ sample: PL emission polarized (curve a) ⊥ and (curve b) ∥ for E_i ∥ [110] or [1$\bar{1}$0]

Γ) and vice versa are derived by determining the nonvanishing momentum matrix elements between these states, for exciting light with polarization components along $\hat{x}'$, $\hat{y}'$, and $\hat{z}'$. PL emission polarized along $\hat{x}'$ and $\hat{y}'$ is allowed for transitions from Γ_6^c to Γ_4^v, Γ_5^v, and $\Gamma_6^v(2)$. PL emission polarized along $\hat{z}'$ is allowed only for transitions from Γ_6^c to $\Gamma_6^v(2)$. The transitions Γ_6^c to Γ_6^v (1) have been ignored since at room temperature, kT is much less than the spin-orbit splitting.

If $(I_A)_\alpha$ is the intensity of PL emission with energy E_A and polarization along α (where α = x', y', z'), and $(I_B)_\alpha$ is the intensity of PL emission with energy E_B and polarization along α (where α = x', y'), then

$$ {}^{1\bar{1}0}\left[\frac{I_\perp}{I_\parallel}\right] = \frac{{}^{1\bar{1}0}[(I_B)_{y'} + (I_A)_{y'}]_{110}}{{}^{1\bar{1}0}\left[\frac{2}{3}(I_A)_{z'} + \frac{1}{3}\{(I_B)_{x'} + (I_A)_{x'}\}\right]_{1\bar{1}0}} \quad (7\text{-}1) $$

$$ {}^{110}\left[\frac{I_\perp}{I_\parallel}\right] = \frac{{}^{110}\left[\frac{2}{3}(I_A)_{z'} + \frac{1}{3}\{(I_B)_{x'} + (I_A)_{x'}\}\right]_{1\bar{1}0}}{{}^{110}[(I_B)_{y'} + (I_A)_{y'}]_{110}} \;. \quad (7\text{-}2) $$

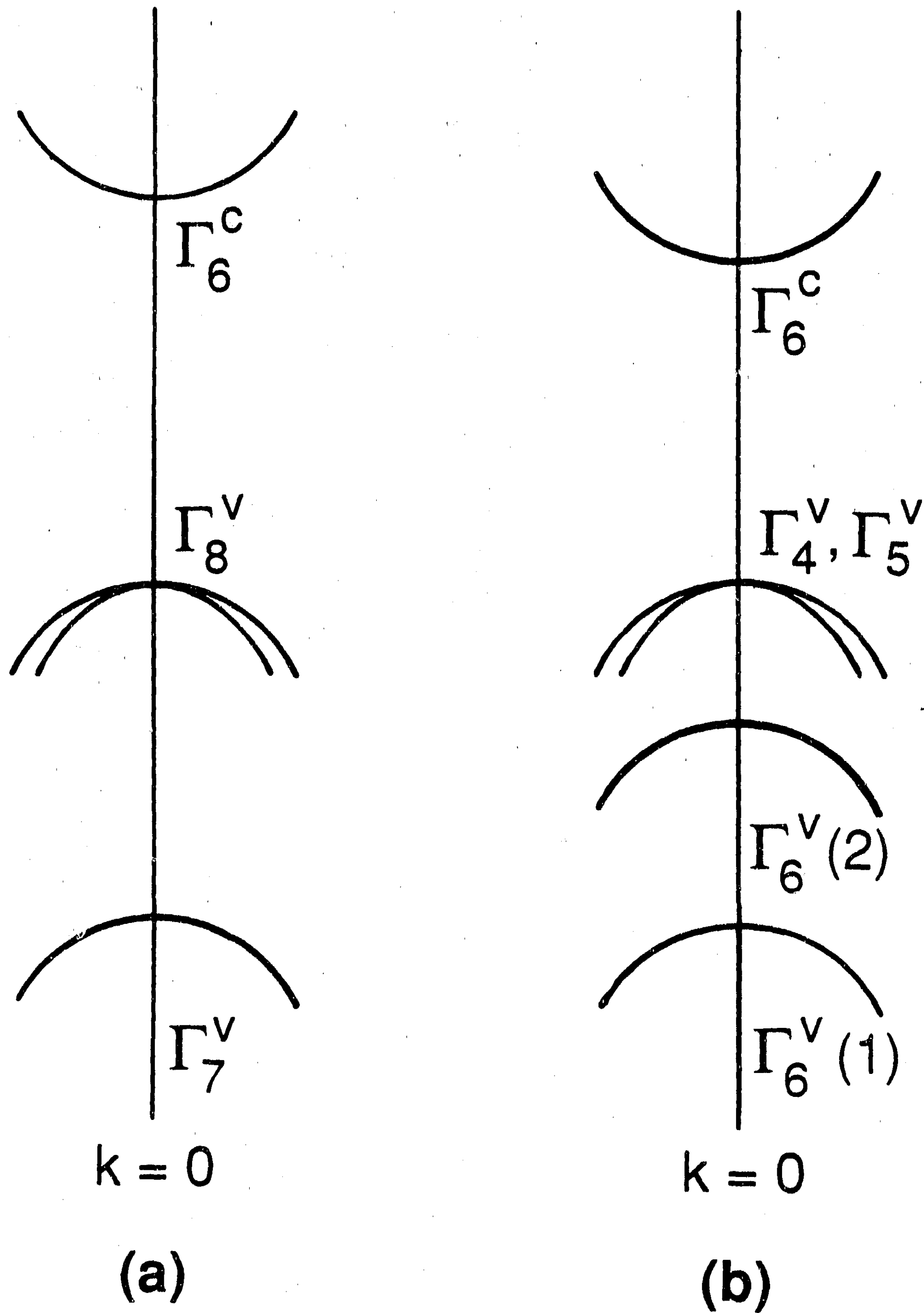

Figure 7-5. Symmetry of the conduction and valence bands at the Γ point for (a) disordered and (b) ordered $Ga_{0.52}In_{0.48}P$

The superscripts and subscripts in Eqs. 7-1 and 7-2 are used to distinguish between the polarization of the exciting light and the PL emission, respectively. $\Delta_{AB} = E_A - E_B$ corresponds to the crystal field splitting. For the PL emission polarized along $[1\bar{1}0]$, the matrix elements $<\Gamma_4^v|y'|\Gamma_6^c>$, $<\Gamma_5^v|y'|\Gamma_6^c>$, and $<\Gamma_6^v(2)|y'|\Gamma_6^c>$ are each non-zero. The heavy and light hole valence subbands Γ_4^v and Γ_5^v comprise $J_{z'} = \pm \frac{3}{2}$ states ($J_{z'}$ is the z' component of the total angular momentum) whereas $\Gamma_6^v(2)$ comprises $J_{zi} = \pm$ ¹Å² states. Also, Γ_4^v and Γ_5^v lie above $\Gamma_6^v(2)$ by energy Δ_{AB}. Hence, PL emission polarized along $[1\bar{1}0]$ results predominantly from the recombination between Γ_6^c and Γ_4^v, Γ_5^v, which yields the dominant peak B at energy E_B. Since the numerator and denominator of Eqs. 7-1 and 7-2 are reversed, PL emission polarized along [110] yields peak A as the dominant peak. The peak in the numerator of Eq. 7-1 is at energy E_B, whereas the peak in its denominator is at energy E_A. The reverse is true for Eq. 7-2. Since $E_B < E_A$, PL transitions with energy E_B are favored with respect to those with energy E_A. Thus, ${}^{110}R > {}^{110}R$. Due to the anisotropic distribution of photocreated electrons, each of these ratios is greater than unity [15] (i.e., ${}^{110}R > {}^{110}R > 1$).

In conclusion, it is possible to explain the spontaneous breaking of cubic symmetry in the band structure of the $Ga_{0.52}In_{0.48}P$ samples as a result of spontaneous ordering of this alloy along the [111] axis. Since ordering along the $[\bar{1}11]$ axes would have led to similar results, but ordering along [111] or $[11\bar{1}]$ would not, the results indicate that the samples are ordered predominantly along the $[1\bar{1}1]$ or $[\bar{1}11]$ axes, in agreement with electron diffraction studies and the current understanding of the ordering mechanism. Our results verify a direct correlation between the valence band splitting, bandgap lowering, and ordering.

7.3 Two-Mode Behavior in Raman Spectrum of $CuIn_xGa_{1-x}Se_2$

$CuInSe_2$ and $CuGaSe_2$ are $A^IB^{III}C^{VI}$-type ternary compounds, which are electrochemical analogs of $A^{II}B^{VI}$-binary alloys. However, in the ternary alloys, the cations A and B are ordered on two different sublattices, resulting in the chalcopyrite structure with space group symmetry D_{2d}^{12}. In the solid-solution mixtures ($CuIn_xGa_{1-x}Se_2$) of these two ternary compounds, the chalcopyrite structure is retained; but unlike the ternary end point constituents, in the quaternaries, there is substitutional disorder on the group V cation sublattice. The physical consequences of this are manifested in the lattice dynamic behavior of the materials, which can be studied experimentally by using Raman scattering to probe the zone center phonon frequencies. The lattice dynamic behavior of solid-solution mixtures of two different II-VI or III-V binary alloys has been well studied, both experimentally and theoretically. Some ternary alloys exhibit a two-mode behavior in their phonon spectrum whereas others exhibit a one-mode behavior. It is therefore of interest to examine the lattice dynamic behavior of the alloy $CuIn_xGa_{1-x}Se_2$ over the entire range of composition so as to investigate whether such quaternary alloy systems exhibit similar one-mode or two-mode behavior.

The Raman spectrum of $CuInSe_2$ and $CuGaSe_2$ shown in Figures 7-6 and 7-7 exhibit modes at 176, 212, 234 cm^{-1}, and 188, 252, 274 cm^{-1}, respectively. The dominant modes observed at 176 and 188 cm^{-1} are A symmetry vibrational modes due to Se-Se anion vibrations in $CuInSe_2$ and $CuGaSe_2$. The modes at 212 and 234 cm^{-1} in $CuInSe_2$ are due to the E symmetry TO and B_2 symmetry LO vibrations, respectively. In $CuGaSe_2$ these modes are observed at 252 and 274 cm^{-1}. Figures 7-8 and 7-9 show the A_1 and B_2 + E symmetry vibrations observed in the quaternary alloy $CuIn_xGa_{1-x}Se_2$ for several values of x between that of the end point constituents. The A_1 symmetry vibration shows a smooth, continuous decrease in frequency from that of $CuGaSe_2$ to that of $CuInSe_2$, which is characteristic of a one-mode behavior for this phonon mode in the quaternary. In contrast, for very small values of x, the frequencies of the B_2 and E modes converge to that of the local mode of indium in $CuGaSe_2$; whereas for values of x close to unity, these modes converge to that of the local mode of gallium in $CuInSe_2$. This is characteristic of a two-mode behavior for the B_2 and E vibrations in the quaternary alloy $CuIn_xGa_{1-x}Se_2$. These vibrations involve the cations on the group III sublattice, and they appear as weak and broad lines in the Raman spectrum of $CuIn_xGa_{1-x}Se_2$, owing to the substitutional disorder present on the sublattice.

To summarize the results of this Raman scattering investigation of $CuIn_xGa_{1-x}Se_2$, our research indicates that the phonons in this alloy show a mixed-mode behavior. The phonons below 200 cm^{-1} exhibit a one-mode behavior, whereas those above 200 cm^{-1} exhibit a two-mode behavior. The information provided by this study should prove useful, not only for using Raman scattering to determine the stoichiometry of $CuIn_xGa_{1-x}Se_2$ but also for studying the extent of disorder present in the material.

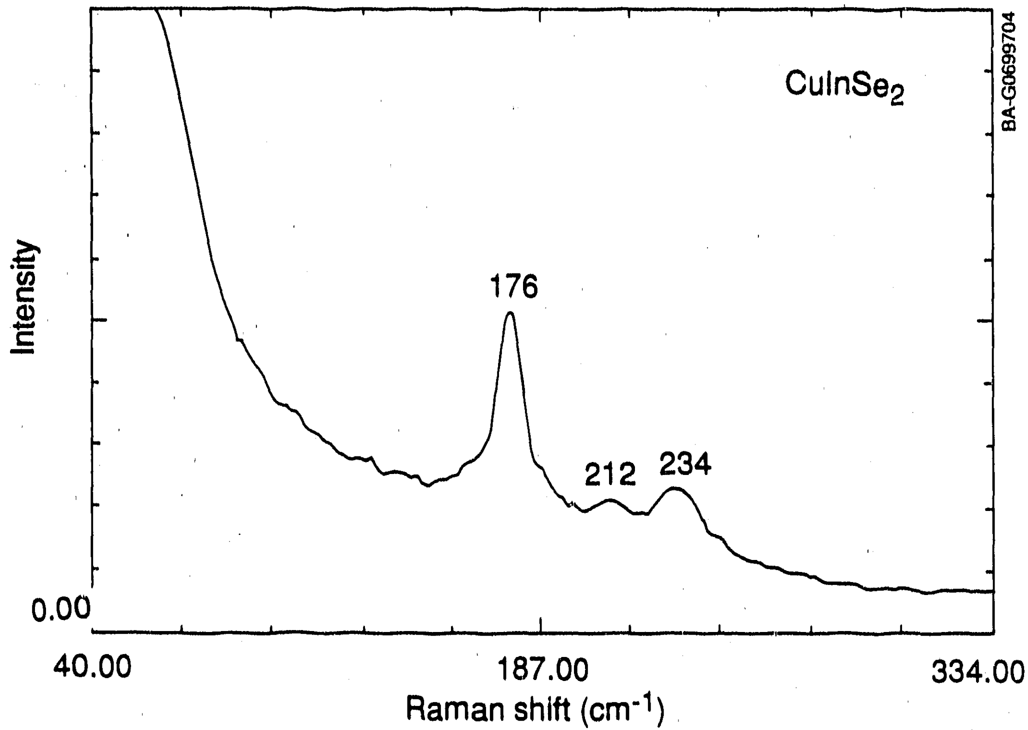

Figure 7-6. Raman spectrum of $CuInSe_2$

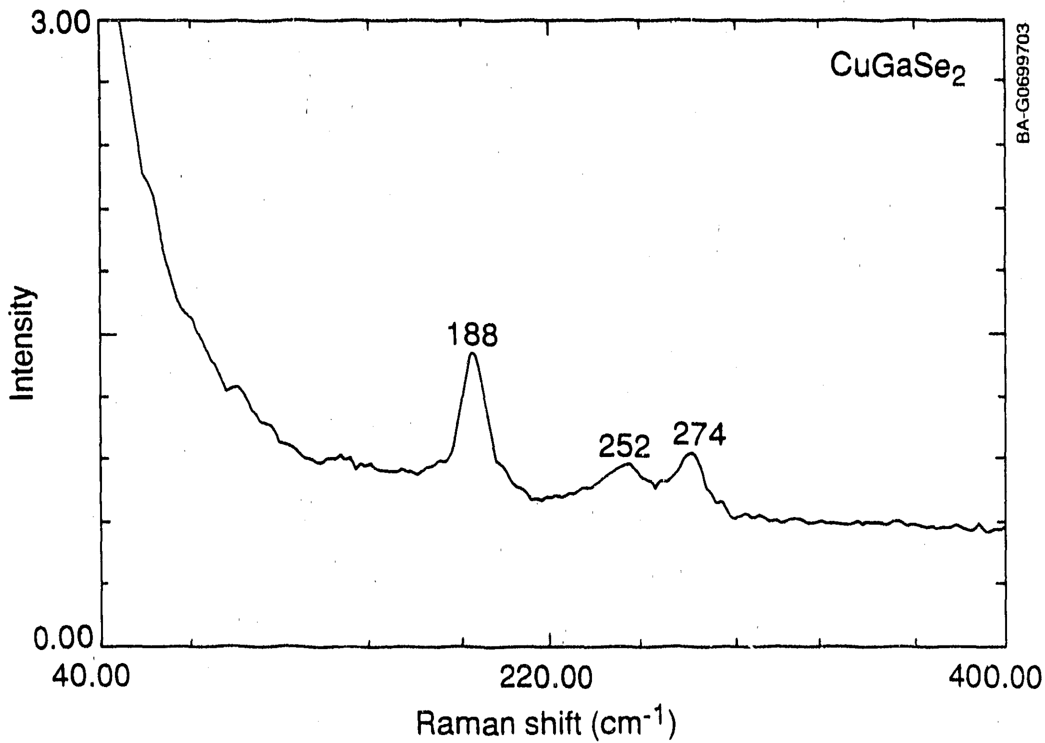

Figure 7-7. Raman spectrum of $CuGaSe_2$

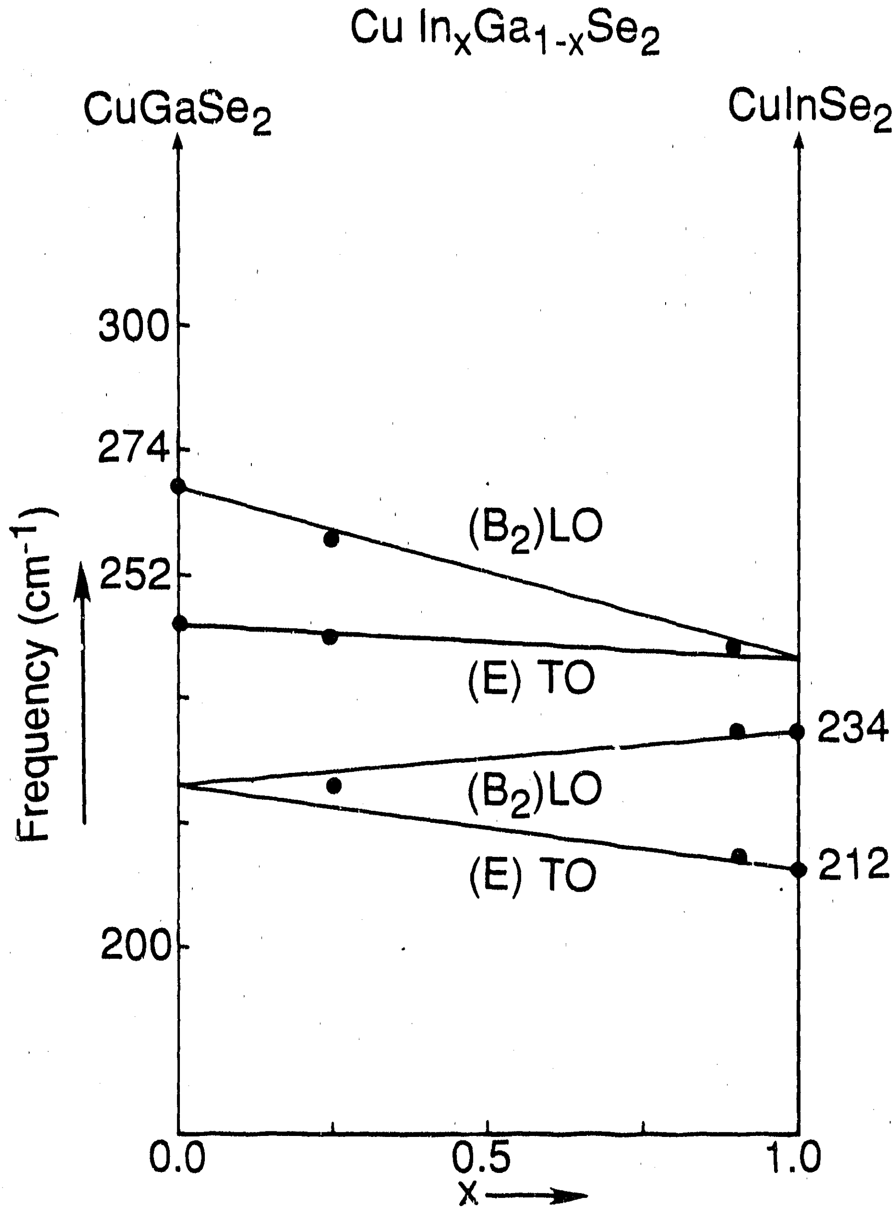

Figure 7-8. Two mode behavior: phonon frequency versus alloy composition for $CuIn_xGa_{1-x}Se_2$

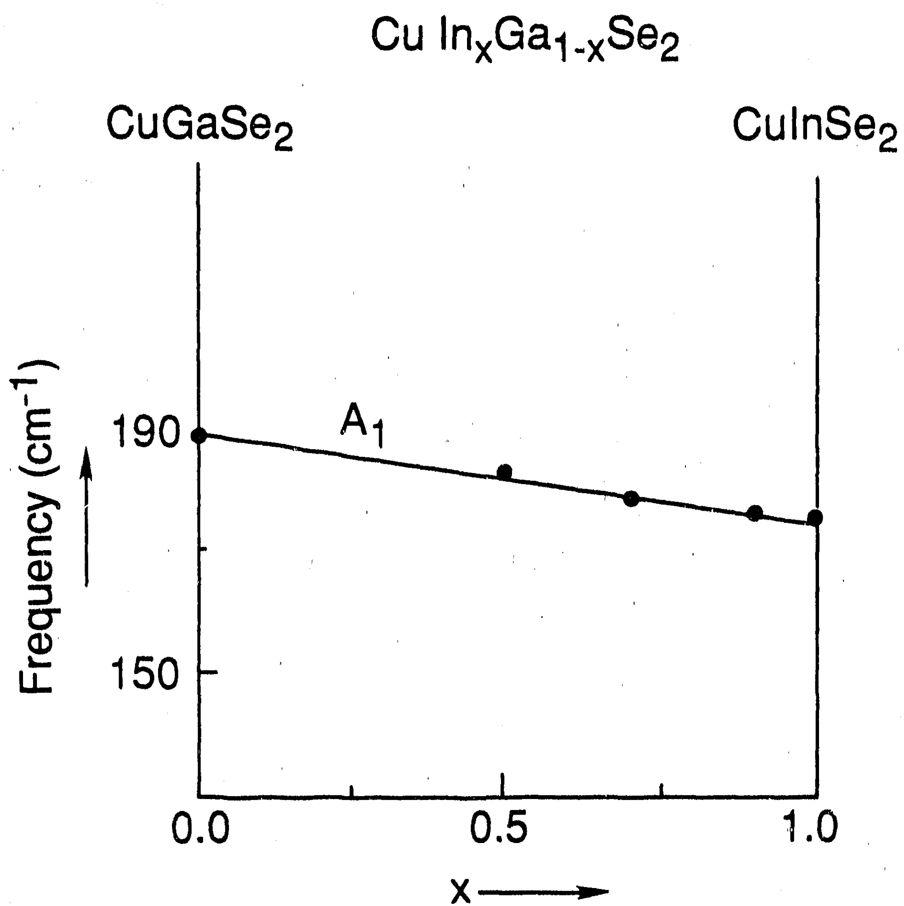

Figure 7-9. One mode behavior: phonon frequency versus alloy composition for $CuIn_xGa_{1-x}Se_2$

7.4 References

1. A. Mascarenhas, S. Kurtz, A. Kibbler, and J. M. Olson, Phys. Rev. Lett. 63 (1989) p. 2108.

2. Su-Huai Wei and Alex Zunger, Phys. Rev. B39 (1989) p. 3279.

3. A. Gomyo, T. Suzuki, and S. Iijima, Phys. Rev. Lett. 60 (1988) p. 2645.

4. J. P. Goral, M. M. Al-Jassim, J. M. Olson and A. Kibbler, in Epitaxy of Semiconductor Layered Structures, edited by R. T. Tung, L. R. Dawson, and R. L. Gunshor (Materials Research Society, Pittsburg), 1988, Mat. Res. Soc. Symp. Proc. Vol. 102, p. 583.

5. P. Bellon, J. P. Chevalier, G. P. Martin, E. Dupont-Nivet, C. Thiebaut, and J. P. Andre, Appl. Phys. Lett. 52 (1988) p. 567.

6. S. McKernan, B. C. DeCooman, C. B. Carter, D. P. Bour, and J. R. Shealy, J. Mater. Res.,3 (1988) p. 406.

7. A. Gomyo, K. Kobayashi, S. Kawata, I. Hino, T. Suzuki, and T. Yuasa, J. Cryst. Growth 77 (1986) p. 367.

8. Y. Ohba, M. Ishikawa, H. Sugawara, M. Yamamoto, and T. Nakanishi, J. Cryst. Growth 77 (1986) p. 374.

9. S. R. Kurtz, J. M. Olson, and A. Kibbler, Solar Cells 24 (1988) p. 307.

10. T. Suzuki, A. Gomyo, and S. Iijima, J. Cryst. Growth 93 (1988) p. 396.

11. F. P. Dabkowski, P. Gavrilovic, K. Meehan, W. Stutius, J. E. Williams, M. A. Shahid, and S. Mahajan, Appl. Phys. Lett. 52 (1988) p. 2142.

12. J. E. Bernard, L. G. Ferreira, S.-H. Wei, and A. Zunger, Phys. Rev. B38 (1988) p. 6338.

13. J. M. Olson and A. Kibbler, J. Cryst. Growth 77 (1986) p. 182.

14. J. B. Hopkins, L. A. Farrow, and G. J. Fisanick, Appl. Phys. Lett. 44:5 (1984) p. 535.

15. V. D. Dymnikov, M. I. D'yakonov, and N. I. Perel', Sov. Phys. JETP 44:6 (1976) p. 1252.

16. L. D. Landau and E. M. Lifshitz, Statistical Physics (Pergamon Press, Oxford), 1969, Chapter 14.

Document Control Page	1. SERI Report No. SERI/TP-212-3675	2. NTIS Accession No. DE91002128	3. Recipient's Accession No.
4. Title and Subtitle Annual Report, Solid State Photovoltaic Research Branch, FY 1989			5. Publication Date September 1990 6.
7. Author(s) Solid State Research Branch			8. Performing Organization Rept. No.
9. Performing Organization Name and Address Solar Energy Research Institute 1617 Cole Blvd. Golden, CO 80401			10. Project/Task/Work Unit No. PV130101 11. Contract (C) or Grant (G) No. (C) (G)
12. Sponsoring Organization Name and Address			13. Type of Report & Period Covered Technical Progress Report 14.
15. Supplementary Notes			

16. Abstract (Limit: 200 words)

This report summarizes the progress of the Solid State Photovoltaic Research Branch of the Solar Energy Research Institute (SERI) from October 1, 1988 through September 30, 1989. Six technical sections of the report cover the main areas of SERI's in-house solid state photovoltaic research: Semiconductor Crystal Growth, Amorphous Silicon Research, Polycrystalline Thin Films, III-V High-Efficiency Photovoltaic Cells, Solid State Theory, and Laser Raman and Photoluminescence Spectroscopy. Principal achievements and experimental details of the current work are covered in each section. Each section was written by the group leader principally in charge of the work. The task in each case was to explain the purpose and major accomplishments of the branch's work in the context of the U. S. Department of Energy's National Photovoltaic Research Program Plans.

17. Document Analysis

a. Descriptors

photovoltaic cells ; amorphous state ; silicon solar cells ; thin films ; crystal growth ; gallium arsenide solar cells ; electron microscopy ; solid-state physics ; chalcogenides ; semiconductor materials ; solar cells

b. Identifiers/Open-Ended Terms

c. UC Categories

270

18. Availability Statement	19. No. of Pages
National Technical Information Service U.S. Department of Commerce 5285 Port Royal Road Springfield, VA 22161	288 20. Price A13

Form No. 0069E (6-30-87)

END

DATE FILMED

02 / 20 / 91